Surface Phaces on Silicon

Preparation, Strucrurs, and Propoties

V.G. LIFSHITS, A.A. SARANIN, and A.V.ZOTOV

Contents

Preface

It is safe to say that modern surface science had its origins in the early 1960s. Of course, the surface-related phenomena e.g. adsorption, catalysis, thin film growth, etc. had been investigated long before, and it was then that the achievements in vacuum technology provided the feasibility to obtain ultra-high vacuum reliably and, thus, to conduct experiments with what are commonly called atomically clean crystal surfaces. It was found that many adsorbates form ordered extremely thin layers since their thicknesses vary typically in the range from a fraction to a few atomic layers, they can even be defined as two-dimensional (2D) with specific structure, composition, and properties different from those of bulk materials. The study of various problems related to the formation, atomic and electronic structure and properties of these 2D layers or *surface phases* the latter term being increasingly in use became a promising avenue of materials science. Another important trend in the investigations concerns the determination of the role of surface phases in different surface phenomena which indeed say, in the case of adsorption, desorption, surface diffusion, surface reactions, etc. appeared to be governed mainly by the formation or occurrence of different surface phases.

Since silicon attracts particular attention as the main material of semiconductor electronics, the surface phases on silicon have been studied extensively by a number of groups throughout the world over an extended period of about the last 30 years and, as a result, a great amount of varied information has been accumulated by the scientific community. These numerous results are spread over a large number of publications and, when someone starts the investigation of a particular system, he often has to overcome a serious problem of finding the necessary information. We did have problems in our own research practice since making a comprehensive bibliography takes a lot of time and effort. So, about four years ago, we initiated the preparation of this handbook on Surface Phases on Silicon. To our knowledge, nothing like this has been published before except for several review papers that cover only selected points of this subject.

The handbook was designed as a guide for researchers working in the field of surface science. It consists of two non-equivalent parts. Part I contains preliminary comments concerning the definition of the term “surface phases”, a brief description of the basics of two-dimensional crystallography, and certain background information about the formation and characterization of surface phases on silicon. Part I plays an auxiliary role and its task is to remind the reader of the basic notions of surface science. The main information is accumulated in Part II that is devoted to the particular “adsorbate/Si” systems. It contains information on more than 300 surface structures formed on clean Si(111), Si(100), and Si(110) surfaces in the presence of foreign atoms at submonolayer coverages, as well as those without adsorbates. The data on 64 adsorbates are reviewed including methods of preparation of surface phases conventionally, in the form “coverage-temperature” formation phase diagrams, models of their atomic structure and a description of the surface properties and surface-related phenomena like desorption, surface diffusion, reactivity, etc. During the preparation of the handbook, about 3000 references have been studied starting from very early works like those of Farnsworth and co-workers and of Lander and Morrison and up to the publications of the middle of 1993.

Since surface science is a rapidly developing branch of materials science, the present volume reflects only the status of knowledge about surface phases on silicon to the middle of 1993. Thus, one can see that the chapters devoted to particular adsorbates differ greatly in size and completeness depending on the extent to which these "adsorbate/Si" systems have been investigated: While there is an abundance of data for selected adsorbates say, H, Ag, Au, etc., there are only a few publications for the others say, Mg, Se, Hg, etc. and some "adsorbate/Si" systems have not been studied at all say, for Be, Zr, Cd, etc.

So, the handbook not only contains the available information about surface phases on silicon but also provides the reader with the feasibility to conclude what promising scientific problems are waiting to be solved. We hope therefore that the present handbook will be useful for researchers and will stimulate further investigations of surface phases on silicon. An additional point to emphasize is that, though the data accumulated in the handbook concerns only surfaces of crystalline silicon, many phenomena described here are also believed to be common for other possible "adsorbate/crystal" systems.

Vladivostok, December 1993

V. G. Lifshits, A. A. Saranin,
and A. V. Zotov

Acknowledgments

We have benefited greatly from the kind co-operation of many researchers well known for their contribution to surface science who have supplied us with an up-to-date collection of their papers on this subject. Therefore, we would like to express our gratitude to:

J. J. Boland, J. E. Demuth and R. J. Hamers, IBM T. J. Watson Research Center, Yorktown Heights, USA.
T. -C. Chiang, University of Illinois at Urbana, Champaign, Urbana, USA.
J. Derrien, CNRS, Grenoble, France.
L. C. Feldman and H -J. Gossmann, AT&T Bell Laboratories, Murray Hill, USA.
G. Gewinner, Universite de Haute Alsace, Mulhouse, France.
J. A. Golovchenko, Harvard University, Cambridge, USA.
M. Hanbucken and H. Neddermeyer, Institut fur Experimentalphysik der Ruhr-Universitat, Bochum, Germany
A. Ichimiya, Nagoya University, Nagoya, Japan.
A. Kawazu, Y. Murata and H. Tochihara, The University of Tokyo, Tokyo, Japan.
S. Kono, Tohoku University, Sendai, Japan.
G. Le Lay, CRMC-2-CNRS, Marseille, France.
S. R. Leone, National Bureau of Standards, University of Colorado, Boulder, USA.
I. Lindau, Stanford Synchrotron Radiation Laboratory, Stanford, USA.
R. Miranda, Universidad Autonoma de Madrid, Madrid, Spain.
J. Nogami, Stanford University, Stanford, USA.
I. Ohdomari, Waseda University, Tokyo, Japan.
M. A. Olmstead, University of California, Los Angeles, USA.
K. Oura and K. Ueda, Osaka University, Osaka, Japan.
G. Rossi, Laboratorium fur Festkorperphysik, Zurich, Switzerland.
F. Salvan, U. A. CNRS, Grenoble, France.
C. A. Sebenne, Universite Pierre et Marie Curie, Paris, France.
K. Takayanagi, Y. Tanishiro and K. Yagi, Tokyo Institute of Technology, Tokyo, Japan.
C. Tatsuyama, Toyama University, Toyama, Japan.
R. I. G. Uhrberg, Linkoping Institute of Technology, Linkoping, Sweden.
T. Urano, Kobe University, Kobe, Japan.
E. D. Williams, University of Maryland, Maryland, USA.
R. S. Williams, University of California, Los Angeles, USA.
Y. Yamamoto, JEOL Ltd, Tokyo, Japan.

and many other scientists.

The preparation of this handbook would have been impossible without the continued interest and technical assistance of many people employed in the Science and Technology Center for Semiconductor Microelectronics at the Institute of Automation and Control Processes of the Far Eastern Branch of the Russian Academy of Sciences. Particularly, our sincere thanks

are expressed to Dr E. A. Khramtsova for stimulating discussions and invaluable help starting from the creation of the database of references and extending throughout all stages of the manuscript preparation. Also our sincere thanks are expressed to academician V. P. Myasnikov, Head of the Institute of Automation and Control Processes for encouragement throughout the work. Our sincere appreciation is extended to Ms O. V. Bekhtereva for computer typesetting the manuscript and for her useful comments on the form of material presentation in the handbook. The assistance of Mr L. I. Ziegelman, Mrs O. L. Tarasova, and Mr A. B. Chub in the creation of the reference database, computer-drawing of illustrations and processing of the manuscript is also gratefully acknowledged.

The part of our own results included in the book were obtained under support from the Russian Foundation of the Fundamental Research.

Last but not least we wish to thank the staff of John Wiley & Sons Ltd and especially Dr Philip Hastings (Publishing Editor), Dr Jonathan Agbenyega (Publishing Editor), Mrs Vanessa Lutman (Editorial Assistant), and Mrs Monica Twine (Senior Production Editor) for their help in all stages of the book preparation.

Abbreviations

AED	Auger electron diffraction
AES	Auger electron spectroscopy
AIUPS	Angle-integrated ultraviolet photoelectron spectroscopy
AREELS	Angle-resolved electron energy loss spectroscopy
ARPES	Angle-resolved photoelectron spectroscopy
ARUPS	Angle-resolved ultraviolet photoelectron spectroscopy
CITS	Current imaging tunneling spectroscopy
CMTA	Constant momentum transfer averaging
DAS	Dimer–adatom–stacking fault (model)
EELFS	Electron energy loss fine structure
ELS	Energy loss spectroscopy
ERDA	Elastic recoil detection analysis
ESD, ESDIAD	Electron-stimulated desorption ion angular distribution
EXAFS	Extended X-ray absorption fine structure
FI-STM	Field ion-scanning tunneling microscopy
HREELS	High resolution electron energy loss spectroscopy
HRIRS	High resolution infra-red spectroscopy
HT	High temperature
IAES	Ion-induced Auger electron spectroscopy
ICISS	Impact-collision ion scattering spectroscopy
INS	Ion-neutralization spectroscopy
IPES, IP	Inverse photoemission spectroscopy
IR	Infra-red
ISS	Ion scattering spectroscopy
KRIPES	K-resolved inverse photoelectron spectroscopy
LEED	Low-energy electron diffraction
LEELS	Low-energy electron energy loss spectroscopy
LEEM	Low-energy electron microscopy
LEISS	Low-energy ion scattering spectroscopy
LERIS	Low-energy recoil ion spectroscopy

LITD	Laser-induced thermal desorption
LNT	Liquid nitrogen temperature
MBE	Molecular beam epitaxy
MDS	Metastable-atom de-excitation spectroscopy
MEED	Medium-energy electron diffraction
MEIS	Medium-energy ion spectroscopy
MIR	Multiple internal reflection
ML	Monolayer
MS	Mass spectroscopy
NEXAFS	Near-edge X-ray absorption fine structure
NMR	Nuclear magnetic resonance
NRA	Nuclear reaction analysis
PES	Photoelectron spectroscopy
PEXAFS	Photoelectron extended X-ray absorption fine structure
PYS	Photoelectron yield spectroscopy
QMS	Quadrupole mass spectroscopy
RBS	Rutherford backscattering spectroscopy
REM	Reflection electron microscopy
RHEED	Reflection high-energy electron diffraction
RHEELS	Reflection high-energy electron loss spectroscopy
RT	Room temperature
SEM	Scanning electron microscopy
SEXAFS	Surface extended X-ray absorption fine structure
SI	Surface ionization
SIMS, SSIMS	Static secondary ion mass spectrometry
SPE	Solid phase epitaxy
STM	Scanning tunneling microscopy
STS	Scanning tunneling spectroscopy
TCS	Total current spectroscopy
TDS	Thermal desorption spectroscopy
TED	Transmission electron diffraction
TEM	Transmission electron microscopy
TOF	Time-of-flight
TPD	Temperature-programmed desorption
TRAXS	Total reflection angle X-ray spectroscopy
UHV	Ultra high vacuum
UPS	Ultraviolet photoelectron spectroscopy
UV	Ultraviolet
WF	Work function
XAES	X-ray induced Auger electron spectroscopy
XPD, XPED	X-ray photoelectron diffraction
XPS	X-ray photoelectron spectroscopy
XRD	X-ray diffraction
XSW, XSWIS	X-ray standing wave interference spectroscopy

Part I

PRELIMINARY COMMENTS

1. Preliminary Comments

1. INTRODACTION

Surface phases is a rather specific object of materials science. So, before the presentation of the data on the particular surface phases on silicon, it seems useful to provide the reader with certain preliminary comments on the general features of surface phases. The items to be treated concern the definition of the term “surface phases”, formalism for the description of the periodic two-dimensional structures (i.e. the two-dimensional crystallography), and background information on the preparation and characterization of surface phases. However, these subjects are presented here in a very brief (almost abstract-like) manner, just to highlight the most significant features in the investigation of surface phases. The interested reader can readily find more complete information elsewhere. It concerns especially the experimental techniques of thin film growth under ultra-high vacuum conditions and the methods of surface analysis, since both these themes are well reflected in many excellent books and review articles.

2. WHAT SURFACE PHASES ARE

The present handbook contains a review of the data on the surface phases on Si surfaces, including the information on the experimental conditions required for the formation of the given surface phase, presentation of the available models of their atomic arrangement and description of the different surface phenomena related to the formation or occurrence of the surface phases.

Though a large number of publications have been devoted to the above subjects, it is not safe to say that the term “surface phase” is commonly used in surface science literature since other terms like “surface superstructures”, “reconstructions”, “two-dimensional (or 2D) structures”, etc. are also used as synonyms of what we call surface phases. This situation is believed to result from the fact that surface science is currently a rapidly-developing branch of materials science and is still far from the status of the “classical” science with its well-adopted system of definitions, concepts, and terminology.

It is hazardous to offer any new generalization, so we do not pretend to give a strict definition but rather try to explain the meaning we attribute to the term “surface phases”. We consider surface phases on silicon as extremely thin layers in an equilibrium state with crystalline silicon (with the layer thickness of the order of monoatomic layer) which composition, structure, and properties definitely differ from those of the corresponding planes of bulk silicon and bulk adsorbate, as well as bulk adsorbate-silicon compound if available. In other words, the surface phase is a specific near-surface region with its own characteristics. This definition is not ingenious since the close idea that the interface between two phases differ radically in properties from both phases has gained now a general acceptance.

Among other properties, the geometrical structure is believed to be the most fundamental one for identification of the particular surface phase. So, the surface phases are usually labeled in accordance with their periodicity with respect to the underlying Si crystal plane, e.g. Si(111)3×1–Ag surface phase (or even 3×1–Ag phase for brevity). In the handbook, we treat primarily the ordered surface phases, although disordered (amorphous) surface phases can also be formed. Some surface phases can occur in several azimuthal orientations. So the surface that contains domains of a given phase in different orientations might be considered as a "polycrystalline" surface phase, while the surface of one phase in a single orientation might be considered as a two-dimensional analog of a single crystal. It seems evident that the distinction between the multi-domain (or polycrystalline) phases and the disordered phase is to a great extent a matter of convenience depending on the critical domain size.

Each surface phase exists in a particular temperature and adsorbate concentration interval where it basically preserves its structure. Though the well-ordered surface phase is associated with a definite composition (i.e. with a definite concentration of adsorbate), it remains stable with certain variation of its composition through the formation of such structural defects as vacancies and adatoms. However, when the variation of composition is beyond the region of stability of the given phase, another one might be formed. This process usually takes place in selected local regions. So, it is quite a common situation that the domains of different surface phases coexist at the surface.

It should be mentioned that the presence of foreign atoms of adsorbate at the surface is not a critical requirement for the formation of surface phases since the near-surface layers of atomically clean silicon planes are themselves surface phases. They have atomic geometries significantly different from those of corresponding planes in the bulk (e.g. the structure of the Si(100) surface is characterized by the dimerization of the topmost Si atoms and the equilibrium Si(111) surface has a very complicated structure with a periodicity seven times greater than that of the (111) plane in bulk Si.) Furthermore, silicon surfaces exhibit very specific properties. For example, the main feature of the electronic structure of the clean Si(111)7×7 surface is the existence of the half-filled surface band, i.e. the Si(111)7×7 surface has a metallic character in sharp contrast to bulk silicon which is well known to be a semiconductor material.

While the presence of foreign atoms is not necessary for the formation of surface phases, as mentioned above, the Si atoms of the substrate play an essential role in any case. This concerns both the structure and properties of the forming surface phase. On one hand, the ordering of the adsorbate atoms occurs in the potential relief of the underlying Si substrate (as a result, the periodicity of most surface phases is multiple that of the Si substrate plane). On the other hand, Si atoms are inevitably involved in the structure of the surface phase since, even in the case when the topmost atomic layer does not contain silicon atoms, the rearrangement (relaxation) should take place of the few deeper Si layers. It can therefore be concluded that the formation process, structure, and properties of the surface phases are governed by the interaction of adsorbate atoms with each other, by the interaction of adsorbate atoms with Si atoms of the substrate, as well as by interaction between near-surface Si atoms.

Surface phases manifest themselves in many surface-related phenomena. The most obvious example is the Stranski–Krastanov mode of thin film growth which is typical for the majority of adsorbates on silicon. According to this growth mode, the first stage of growth consists in the formation of the two-dimensional adsorbate layer (or Stranski–Krastanov layer) which is essentially the surface phase. The sequential formation of several surface phases with increasing concentration of adsorbate is also possible (and indeed occur often) at this stage. In the latter case, the completion of the 2D layer growth corresponds to the formation of the last surface phase with the maximum possible concentration of adsorbate atoms. Afterwards, i.e. when no additional adsorbate atoms can be adopted into the surface phase, the growth of three-dimensional islands of adsorbate takes place.

Another glowing example refers to surface diffusion since surface diffusion of adsorbate is often accompanied by the formation of surface phases with the diffusion coefficient being different for the various phases. The adsorbate bonding energy also usually varies from one surface phase to another which should influence such surface process such as desorption. Desorption proceeds through the formation of the surface phases in the sequence opposite to that observed during adsorption and desorption kinetics and/or desorption activation energy might be noticeably different for various surface phases. The difference in the composition and atomic structure of surface phases results naturally in the variation of electronic structure, surface reactivity, and different physical properties. The list of example phenomena which depend on or are related to the formation or existence of surface phases can be expanded.

3. BASICS OF TWO-DIMENSIONAL CRYSTALLOGRAPHY

Two methods for the description of the two-dimensional lattices of surface phases used conventionally. The first one was proposed by Park and Madden [1] and consists in the determination of the matrix which establishes a link between the basic translation vectors of the surface under consideration and those of the ideal (unreconstructed) substrate surface. That is, if $\mathbf{a}$ and $\mathbf{b}$ are the basic translation vectors of the substrate lattice, while $\mathbf{a}_\mathrm{s}$ and $\mathbf{b}_\mathrm{s}$ are the basic translation vectors of the surface phase, than they can be linked by the equations

$$\mathbf{a}_\mathrm{s} = G_{11}\mathbf{a} + G_{12}\mathbf{b}$$

$$\mathbf{b}_\mathrm{s} = G_{21}\mathbf{a} + G_{22}\mathbf{b}$$

where four coefficients, G_{ij}, form the required matrix

$$G = \begin{pmatrix} G_{11} & G_{12} \\ G_{21} & G_{22} \end{pmatrix}$$

The values of G_{ij} determine whether the structure of the surface phase is commensurate or incommensurate. The commensurability means that a rational relationship between the vectors $\mathbf{a}_\mathrm{s}, \mathbf{b}_\mathrm{s}$ and $\mathbf{a}, \mathbf{b}$ can be established. If there is no rational relationship between the unit vectors of the surface phase and the substrate, the surface phase is incommensurate. In other words, the incommensurate superstructure is registered in-plane incoherently with the underlying substrate lattice.

The second method for the description of two-dimensional lattices was proposed by Wood [2]. This method is the one most used now though it is less versatile than the above matrix notation. In the Wood description, the ratio of the surface periods and those of the unreconstructed substrate are given as well as an angle of rotation which makes the unit mesh of the surface to be aligned with the basic translation vectors of the substrate. That is, if an adsorbate A induces on the Si(hkl) surface the reconstruction with the basic translation vectors of $|\mathbf{a}_\mathrm{s}| = m|\mathbf{a}|$ and $|\mathbf{b}_\mathrm{s}| = n|\mathbf{b}|$ and with the rotation angle of ϕ, then this surface structure is labeled Si(hkl)$m \times n$–$R\phi°$–A. The surface mesh may be centered, in which case the notation would be $c(m \times n)$.

To illustrate both kinds of description, we consider the simple example of the surface structure induced by the adsorption of one-third monolayer of Al onto the Si(111) surface. Figure 1(a) shows schematically the atomic arrangement of such a surface. Here the open circles denote the top Si atoms of the Si(111) plane which occupy almost bulk-like positions

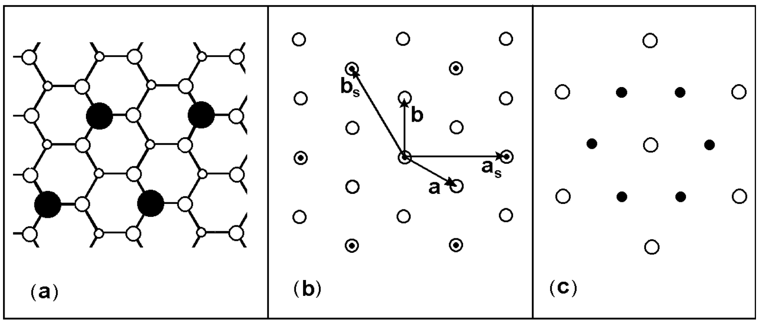

Fig 1. An illustration of the Si(111)$\sqrt{3}\times\sqrt{3}$—$R30°$ superstructure. (a) Model of the atomic arrangement of the Si(111)$\sqrt{3}\times\sqrt{3}$—$R30°$–Al surface phase. Open circles denote the Si atoms of the top Si double-layer. Al adatoms are shown by solid circles; (b) The real-space Si(111)$\sqrt{3}\times\sqrt{3}$—$R30°$ superlattice (shown in double circles) superposed on the Si(111)1 × 1 lattice. The basic translation vectors, $\mathbf{a}_s, \mathbf{b}_s$, of $\sqrt{3}\times\sqrt{3}$ superlattice and those, $\mathbf{a}$, $\mathbf{b}$, of the 1 × 1 lattice are shown; (c) Sketch of the LEED pattern (reciprocal lattice) of the Si(111)$\sqrt{3}\times\sqrt{3}$—$R30°$ structure. Normal spots are shown by open circles and extra reflections are shown by closed circles

and large solid circles are Al adatoms. The real lattice of this surface structure (solid circles) and the lattice of the unreconstructed Si(111) substrate (open circles) are shown in Fig. 1(b). One can easily see from the latter figure that the above structure is described as Si(111)$\sqrt{3}\times\sqrt{3}$—$R30°$–Al in Wood's notation and as a Si(111)$\begin{pmatrix} 2 & 1 \\ -1 & 1 \end{pmatrix}$–Al in the matrix notation of Park and Madden. The pattern of the reciprocal two-dimensional lattice can be obtained directly using surface-sensitive diffraction methods such as low energy electron diffraction (LEED) or reflection high energy electron diffraction (RHEED), and Fig. 1(c) shows a sketch of the LEED pattern (reciprocal lattice) from the above structure. Normal reflections which correspond to the unreconstructed Si(111)1 × 1 surface are shown by open circles and extra-reflections (or super-reflections), the sign of the Si(111)$\sqrt{3}\times\sqrt{3}$—$R30°$ superstructure, are shown by double circles.

It should be mentioned that the Wood description is appropriate only in cases when the rotation angle is the same for both the basic translation vectors (i.e. for $\mathbf{a_s}$ and $\mathbf{b_s}$ with relation to $\mathbf{a}$ and $\mathbf{b}$, respectively). Otherwise, only the matrix notation can provide an accurate description. However, sometimes in the literature less rigorous notation (of the Wood's-like type) is used with the addition of the necessary comments or even without them when it concerns well known structures. The most prominent example is the clean Si(110) surface. The reconstruction of this surface is properly described in matrix notation as Si(110)$\begin{pmatrix} 2 & 2 \\ 17 & 1 \end{pmatrix}$. However, it is often labeled as Si(110)"2 × 16" with quotes indicating that the basic translation vectors of this reconstruction cannot be aligned along the bulk symmetry axes by any rotation (the unit mesh of the "2 × 16" structure is non-rectangular in contrast to the rectangular (1 × 1) mesh).

As for the surface structures on the Si(110) surface, the following important point is worth making. The basic translation vectors of the unreconstructed Si(110)1 × 1 surface are 1/2 $[\bar{1}10]$ and [001] as shown in Fig. 2. The lengths of these vectors are not equal to each other (unlike the cases of the Si(111) and Si(100) surfaces) and the sequence of writing the unit vectors becomes essential for the precise description of the surface structures. For example, the surface superstructure shown in Fig. 2 would be written as Si(110)5 × 4 if one defines the basic translation vectors as $\mathbf{a} = 1/2\ [\bar{1}10]$ and $\mathbf{b} = [001]$, but it would be Si(110)4 × 5 with $\mathbf{a} = [00\bar{1}]$ and $\mathbf{b} = 1/2\ [\bar{1}10]$. At the present, there is no universally adopted sequence of the Si(110) unit vectors and this fact certainly leads to confusion in the literature. In this book,

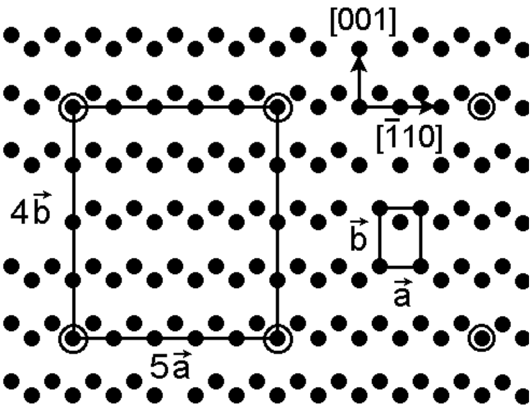

Fig 2. Sketch of the Si(110) plane. Closed circles show the top Si atoms. Double circles represent the rods of the Si(110)1 × 5 superlattice. The unit cells and basic translation vectors of the Si(110)1 × 1 lattice and Si(110)5 × 4 superlattice are shown

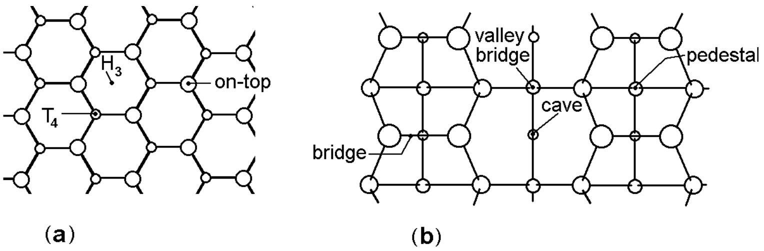

Fig 3. The various possible adsorption sites on (a) unreconstructed Si(111)1 × 1 and (b) reconstructed Si(100)2 × 1 surfaces

we define the basic translation vectors of the Si(110) plane as **a** = 1/2[$\bar{1}$10] and **b** = [001], since they seem to be currently in the most common use.

The ordered surface structures are formed by adsorbate atoms occupying regular sites on silicon surfaces. A great variety of atomic arrangements exists even for the similar structures. For example, in the Si(111)$\sqrt{3} \times \sqrt{3}$—$R30°$ structure of group 3 atoms (Al, In, Ga) there is one adatom in each ($\sqrt{3} \times \sqrt{3}$) unit cell as shown in Fig. 1(a). The arrangement of the Si(111)$\sqrt{3} \times \sqrt{3}$—$R30°$–Sb includes the adsorbate trimers. The Si(111)$\sqrt{3} \times \sqrt{3}$—$R30°$–B structure is built of Si adatoms while B atoms occupy the substitutional sites below Si adatoms. The Si(111)$\sqrt{3} \times \sqrt{3}$—$R30°$–Ag and Si(111)$\sqrt{3} \times \sqrt{3}$—$R30°$–Au structures are so complicated that there is no consensus on their atomic arrangements despite the abundance of experimental data. So there are a lot of possible bonding sites for adatoms on the silicon surfaces and it is probably not possible to label them all. However, there are several main bonding sites which have the conventions.

In the case of Si(111), these are "on-top", H_3, and T_4 sites (see Fig. 3(a)). In the "on-top" position, the adatom resides directly above the Si atom of the top Si(111) layer. In both the H_3 and T_4 sites, the adatom is situated in the center of the triangle formed by three top Si atoms on the Si(111) surface, but, in the case of the H_3 site, it is above the Si atom in the fourth layer and, in the case of the T_4 site, it is above the Si atom in the second layer. The adatom has three neighboring Si atoms in the H_3 position and four in the T_4 site.

The labeled adsorption sites on the reconstructed Si(100)2 × 1 surface are the "bridge", "valley bridge", "cave", and "pedestal" sites. These adsorption positions are shown in Fig. 3(b). To our knowledge, there are no commonly accepted terms for the adsorption sites on the Si(110) surface.

4. EXPERIMENTAL BACKGROUND

4.1. VACUUM, SURFACE CLEANING, AND ABSORBTION

The importance of the the use of surface phenomena for different practical applications has long been accepted but the origination of contemporary surface science only dates from the early 1960s. It is safe to state that the most significant reason for such a situation is that it was not until the 1960s that the development of the vacuum technology made it possible to achieve and maintain the ultra-high vacuum (UHV) reliably. As a direct consequence, the feasibility for conducting experiments with the atomically clean crystal surfaces (including those of silicon) became apparent. Moreover, the number of surface phenomena found many years ago were put into practice for surface characterization (e.g. low energy electron diffraction and Auger electron emission were discovered as early as 1927 and 1925, respectively, but became powerful tools for monitoring surface structure and chemical composition only in the 1960s).

The rigid requirement for ultra-high vacuum conditions both at the stages of formation and investigation of surface phases becomes clear from the following simple estimation: one can easily obtain from the kinetic theory of gases that the flux f of the molecules impinging to the surface from the environment is given by the expression:

$$f = p(2\pi mkT)^{-1/2}.$$

Here p is the pressure, m is the mass of the molecule, k is the Boltzmann constant, and T is the temperature.

We take as an example O_2 molecules ($m \approx 5.4 \times 10^{-23}$ g) and the room temperature of the environment ($T \approx 300$ K). If we assume the sticking probability to be unity (i.e. all impinging molecules are left on the surface) and define the density of one monoatomic layer as 10^{15} cm^{-2} (which is in fact close to the real values for silicon surfaces), we can see that the time of adsorption of one monolayer is

about 3 s	at	$p \approx 10^{-6}$ Torr
about 5 min	at	$p \approx 10^{-8}$ Torr
about 1 hour	at	$p \approx 10^{-9}$ Torr

Thus, it means that for the preservation of the value of surface pollution below the level of a few per cent of a monolayer throughout the experiment for the duration of about one hour vacuum no worse than 10^{-10} Torr is required. Though our estimation refers to the most unfavourable cases, it is commonly accepted now that reliable results on the formation, structure, and properties of surface phases can be obtained only in vacuum of the order of 10^{-10} Torr and better.

The modern ultra-high vacuum equipment assures the required vacuum conditions. However, the sample is introduced to the UHV chamber from the ambient air and, hence, a definite *in situ* cleaning procedure is necessary to obtain the atomically clean surface. There have been a great number of investigations devoted to the design of methods to produce extremely clean Si substrate surfaces (mainly, for the growth of the homoepitaxial Si films of the device quality) and this research work is still in progress. At the moment, three main cleaning procedures are employed *in situ*, namely, annealing, ion bombardment followed by annealing and cleavage. (It should be mentioned that except for the case of cleavage, before the insertion into the UHV chamber the Si sample has undergone several stages of *ex situ* treatment, including mechanical and chemical polishing to produce the mirror smooth surface, chemical cleaning to remove the organic contaminations etc.).

The cleaning of the Si sample by ultra-high vacuum annealing seems to be in most general use now. The annealing at about 1200 °C is used conventionally to evaporate the thin native

SiO_2 layer and to remove the possible carbon contamination. This cleaning procedure in most cases produces the clean Si surfaces with a good ordering. Recently a serious effort has been mounted to reduce the required annealing temperatures. The most promising results were obtained by using the chemical pretreatment in which the clean thin SiO_2 layer free from carbon contaminations is produced on the Si sample surface. The forming Si oxide layer can be removed at temperatures as low as about 800 °C.

The usage of ion bombardment is also directed towards reducing the temperature of the heat treatment. In this method, the contaminated surface layer is sputtered by the ions (usually, Ar^+) with energy of 0.5–5.0 keV. However, there are the side-effects of ion bombardment, namely, the disordering (amorphization) of the surface often accompanied by the penetration of Ar to the subsurface region. To restore the ordered structure of the surface the sample requires annealing at about 700–800 °C. The best results are achieved after several "sputtering/annealing" cycles.

Upon cleavage, only the clean Si(111) surface can be produced. It should be noted that the cleaved Si(111) surface is metastable and differs greatly from the equilibrium surface obtained in the above two procedures both in structure and properties.

Among the exotic cleaning procedures, pulse laser irradiation and etching of the oxide layer by the flux of Si or metal atoms (In, Ga) might be mentioned. In the first method, the short laser pulse causes the rapid melting and solidification of the surface region thousands of angstroms deep. The surface after irradiation is free from contamination but as revealed in recent investigations it is highly inhomogeneous and contains considerable residual disorder. In the second method, the Si or metal atoms arriving at the sample surface and held at about 600–800 °C react with the oxide layer with the formation of the volatile products. However, this method has certain serious shortcomings: first, it is unlikely to remove carbon contaminations from the Si surface and, second, it leads in most cases to the roughening of the surface.

Once the atomically clean surface is obtained, the deposition of small amounts of certain adsorbate is conducted to form the desired surface phase. Most solid substances are deposited by thermal evaporation in vacuum. Depending on many circumstances (the temperature of evaporation of material, the reactivity of material, the experimental design, etc.) a great variety of different sources for the deposition of adsorbates are employed [3]. The tungsten filament or basket with a melted drop of the material to be evaporated make up the simplest deposition sources. These kinds of sources, though quite sufficient for qualitative investigations, do not provide the possibility to maintain the reproducible calibrated rate of deposition. So, in modern UHV installations, the effusion cells are employed conventionally [4]. In effusion cells, the evaporated material is held in the crucible which is heated by radiation from a resistance-heated source (conventionally, a refractory metal wire). The thermocouple is attached to the crucible to provide the temperature (and, thus, the evaporation rate) control. Multiple radiation shields surround the heater to improve both the thermal efficiency and temperature stability. The whole effusion cell has an integral water-cooled or liquid nitrogen-cooled surround. Special attention is paid to the material of the crucible which should withstand high temperatures, be of high purity and be chemically inert with respect to evaporated material. The preferred present-day crucible material is a pyrolytic boron nitride, although some other materials are also employed, say, ultra-pure graphite, sapphire, quartz, etc.

Another type of deposition source that should be mentioned are electron-beam and laser-radiation heated sources. The heating of the source material by the flux of electrons or photons is favorable since it can be concentrated on just the evaporating material so that surroundings can be maintained at relatively low temperatures. The electron-beam and laser-radiation heated sources are especially valuable for evaporation of refractory materials.

However, these kinds of sources usually produce relatively large fluxes and, therefore, are employed for the fabrication of rather thick films.

Selected elements have sufficiently high vapor pressure at temperatures below the melting point (e.g. Pd, Mo, Fe, Ni, Si) and they can be evaporated via sublimation by passing electrical current directly through wires or bars made of these materials.

When adsorbates are molecules or atoms of gases, the Si sample is exposed to the gas which is conventionally delivered to the vacuum chamber through the leak valve. Here the requirements for the purity of gases are very high. The composition of a pure gas, i.e. whether it consists of atoms or molecules, is very important since the reactivity of gases with respect to silicon might differ greatly in both cases. For example, the reaction of silicon surfaces with atomic nitrogen or hydrogen is much more pronounced in comparison with molecular gases.

The exposure unit that has been universally accepted in literature is Langmuir (L) (1 L $=$ 10^{-6} Torr s). It should be said, however, that the exposure units characterize the experimental procedure only but not the actual amount of atoms (or molecules) adsorbed at the surface since sticking probability may differ from unity. Moreover, the number of atoms (or molecules) impinging to the surface at the exposure of 1 L depends on the mass of the gas particles and the gas temperature.

So, in order to characterize the surface density of foreign atoms constituting the surface phase, the coverage units, monolayers (ML), are used. One monolayer (ML) is defined as the areal density of the topmost atoms of the corresponding unreconstructed Si plane, i.e. 7.8×10^{14} cm^{-2} for Si(111), 6.9×10^{14} cm^{-2} for Si(100) and 9.6×10^{14} cm^{-2} for Si(110). Coverage is symbolized conventionally in literature by Greek *theta* (θ).

Sometimes thickness units (Å, nm) are employed under the assumption that the volume density of the adsorbate film coincides with that of the corresponding bulk material. So the thickness of the submonolayer film simply equals the product of the areal density of adsorbate atoms on the surface and the atomic volume occupied by one adsorbate atom. For the reader's convenience (if he would like to convert the coverage units to thickness units or vice versa), the thickness of one monolayer of different materials on the main Si surfaces are given in Supplement 1.

4.2. METHODS OF SURFACE ANALYSIS

In the general case of characterization of the particular surface phase, sometimes one is interested in its atomic and electronic structure, its chemical composition, surface morphology, as well as in its physical and chemical characteristics. To obtain such information a large number of various methods for surface analysis is used at present. In most cases, these methods employ electron, photon, or ion beams to probe the surface under investigation. Each one of the methods is specifically sensitive to one (or several) feature of the surface phase. Therefore, the combination of several complementary methods is usually required for obtaining conclusive information about the structure and properties of the surface phases.

The experimental methods of surface analysis are given a great deal of attention in the literature and there is an abundance of books and journal papers concerning the specific methods. Therefore, we present below only a brief summary of the main aspects of the surface-sensitive methods of analysis which are currently in common use.

Electron Diffraction Methods

Low-energy electron diffraction (LEED) is the routine method for surface structure analysis [5, 6]. The technique of diffraction is sensitive to the periodic order and low-energy electrons with energy in the 20–300 eV range provide the needed surface sensitivity. Therefore, LEED is well suited for characterization of the surface ordered structures. Though the LEED technique primarily gives information about the size and shape of the two-dimensional surface unit mesh, the consideration of the surface atomic arrangement on the basis of the LEED data is also possible. Usual procedure involves in the latter case the comparison of the I–V (reflection intensity versus electron energy) curves calculated for a given atomic model with those recorded in the LEED experiment. However, the kinematic theory is no longer valid for the LEED due to the multiple-scattering effects. This imposes the serious computation problems associated with the dynamical calculations.

Another type of electron diffraction widely used for surface analysis is reflection high energy electron diffraction (RHEED) [7] which employs an electron with the energy of 30–100 keV. The feature of glancing incidence makes RHEED sensitive to surface rather than to bulk structure. The usual geometry of RHEED, when the electron gun and phosphorescent screen are positioned remotely from the substrate, makes it possible to observe the RHEED patterns during growth processes. In the first approximation, the results of RHEED experiments can be considered by utilizing kinematic theory. However, the more accurate consideration of the surface atomic geametry requires the complicated dynamic analysis, as in the case of LEED.

These difficulties are essentially avoided in UHV transmission electron diffraction (TED) since the single-scattering approximation of diffraction can be more safely assumed in TED than in LEED and RHEED [8, 9]. TED can be successfully applied to the analysis of the surface-parallel atom positions. This can be illustrated by the pronounced result of the conclusive determination of the complex dimer–adatom stacking fault structure of the Si(111)7×7 surface by Takayanagi *et al.* [8, 9] by means of TED. However, the TED technique has been rarely applied hitherto for a limited number of surface structures.

Auger Electron Spectroscopy

Auger electron spectroscopy (AES) is one of the most used techniques for the analysis of surface chemical composition [10, 11]. It provides the possibility to detect all except H and He elements of the Periodic Table presented in a few near-surface atomic layers. Thus, AES is widely employed for quantitative estimations of adsorbate coverages. The thin film growth mode can be characterized by monitoring of the adsorbate Auger peak amplitude versus deposition time. The changes in the electronic structure of the system with adsorption are also manifested in the changes in Auger spectra.

Electrons (and, rarely, photons and ions) are employed to excite Auger electrons. The use of electrons has the advantage that the incident electron beam might be focused, thus giving spatial resolution ≈ 0.1 μm. Although AES is usually considered as the non-destructive method, in some cases, processes such as electron-stimulated desorption or heating of the target may result in undesirable consequences.

Photoelectron and Photoemission Spectroscopies

Photoelectron and photoemission spectroscopies have proved to be extremely powerful techniques for the determination of the electronic properties and surface atomic structure of solids [10–15]. Depending on the photon energy, one can distinguish between ultra-violet photoelectron spectroscopy (UPS) and X-ray photoelectron spectroscopy (XPS) for photon energy lower than 42 eV and greater than 1 keV, respectively, the first one being used to study the occupied valence electrons state and the second the core states. The recent application of synchrotron radiation provides the possibility to obtain continuous radiation from infra-red to strong X-ray, which give the ability to adjust photon energy for a given electron transition and, thus, provide the maximum sensitivity for the surface region [16].

There are several kinds of the photoelectron techniques. The extremely important kind of photoelectron spectroscopy is the angle-resolved photoelectron spectroscopy (ARPES) [17] which allows the determination of complete surface state band structure.

It should be mentioned further that it is well established that photoelectrons or Auger electrons excited from core levels show intensity variations with angles that are caused solely by diffraction [14]. These intensity variations are used for the determination of surface atomic geometry in the techniques called X-ray photoelectron diffraction (XPD) and Auger electron diffraction (AED).

In inverse photoemission spectroscopy (IPES), the sample is probed by an electron beam and emitted photons are detected [15]. IPES makes it possible to obtain complete information about unoccupied electronic states.

Ion Scattering Spectroscopy

In conventional ion scattering spectroscopy (ISS), the monoenergetic ion beam collides with the surface under investigation and the backscattered spectrum of ions is recorded [6]. The backscattered spectrum carries information about the surface structure and its composition. The recent improvement of this method has been achieved by the development of the impact-collision ion scattering spectroscopy (ICISS) [18, 19] in which the experimental scattering angle is fixed close to 180° to ensure that the detected ions have scattered from near-surface atoms. This specialization of the scattering condition minimizes the contribution of multiple scattering to the detected yield and simplifies the interpretation of the angular dependence of the backscattered yield as a function of the sample orientation with respect to the ion beam.

ICISS and its modifications are powerful methods for surface structure determination. The primary advantages of ion scattering methods is that, first, they provide detailed structural information in real space rather than in reciprocal space as for diffraction or photoemission, and, second, long-range order at the surface is not necessary for ISS analysis. However, it should be noted that the interpretation of results from ion scattering spectroscopy is strongly model dependent.

SEXAFS

Surface extended X-ray absorption fine structure spectroscopy (SEXAFS) is the surface-sensitive application of the EXAFS technique, which, owing to synchrotron radiation, has become a key tool for the determination of the local structure in surface phases [20, 21]. It enables to choose the kind of atoms in which the neighbouring environment is of interest. SEXAFS does not need long-range order and is insensitive to the direction of the bonds: the same precision is obtained in all the directions. The classical employment of SEXAFS is for the determination of bond lengths between adsorbed atoms and the surface substrate atoms and coordination numbers. The typical accuracy is usually better than 0.03 Å on bond lengths.

X-ray Diffraction

Though X-ray diffraction (XRD) has been used for many years to study the structure of crystalline and amorphous materials, only in recent years has XRD has been widely applied to the study of the surfaces [22]. This fact is closely connected with the rapidly increasing number of possibilities for doing experiments at synchrotron X-ray facilities with highly intensive, well-collimated X-ray beams. When the X-ray beam is incident to the surface at glancing angles, thereby limiting the penetration of the X-rays into the bulk crystal, the surface sensitivity is considerably enhanced. This can be less than one layer of atoms to obtain the superlattice reflections from a reconstructed surface. X-ray diffraction provides a good ability to solve surface structures owing to the fact that, in many cases, X-rays interact weakly with the matter and, thus, the kinematical approach is quite sufficient to analyze the experimental data.

X-ray Standing Wave Interference Spectroscopy

The X-ray standing wave (XSW) technique relies on the interference between the incident and the diffracted waves when an X-ray plane wave is Bragg diffracted by a perfect crystal [23,24]. This method gives valuable information about adsorption sites of foreign atoms on a single crystal surface for adsorbate coverages as small as 0.01 ML. It allows the determination of vertical position with respect to the diffraction plane. However, the XSW technique is insensitive to the in-plane geometry of the adsorbate layer.

Scanning Tunneling Microscopy

Since its advent in 1982 by Binnig and Rohrer [25], scanning tunneling microscopy (STM) has steadily become established and is now becoming an indispensable tool for surface analysis. In the STM, a metallic tip is advanced towards the sample to the distance at which the wavefunctions of the tip and sample start to overlap. The application of a small bias voltage between tip and sample results in the tunneling electron current which flows through the gap separating sample and tip and is detected by apparatus. Scanning the tip along the sample surface provides the possibility for real-space imaging of the geometric and electronic properties of surfaces on a scale which extends to atomic dimensions [26,27]. STM has proved to be an extremely powerful technique for the determination of the local surface atomic and electronic structures. The structural information obtained by this method is unique as most surface probes average the information on a large number of atoms. STM combined with other complementary surface-sensitive techniques has permitted the reliable elucidation of a great body of the surface structures.

However, it is well understood now that, as STM is sensitive to the electronic structure of the atoms, the atomic features seen by STM do not always simply allow the determination of atom positions in the outermost layer of a sample surface. In this sense, STM image reflects the spatial distribution of a certain range of electronic states.

REFERENCES

[1] R. L. Park and H. H. Madden, *Surf. Sci.* **11** (1968) 188.
[2] E. A. Wood, *J. Appl. Phys.* **35** (1964) 1306.
[3] *Handbook of Thin Films Technology*, Ed. L. I. Maissel and R. Glang, McGraw-Hill Book Company (1970).
[4] M. A. Herman and H. Sitter, *Molecular Beam Epitaxy. Fundamentals and Current Status*, Springer-Verlag, Berlin (1989).
[5] M. A. Van Hove, W. H. Wienberg and C. M. Chan, *Low-energy Electron Diffraction: Experiment, Theory and Surface Structure Determination*, Springer, West Berlin (1986).
[6] D. P. Woodruff and T. A. Delchar, *Modern Techniques of Surface Science*, Cambridge University Press, Cambridge (1986).
[7] J. E. Mahan, K. M. Geib, G. Y. Robinson and R. G. Long, J. Vac. Sci. Technol. A **8** (1990) 3692.
[8] K. Takayanagi, Y. Tanishiro, S. Takahashi and M. Takahashi, *Surf. Sci.* **164** (1985) 367.
[9] K. Takayanagi, *J. Microscopy* **136** (1984) 287.
[10] *Practical Surface Analysis by Auger and X-ray Photoelectron Spectroscopy*, Ed. D. Briggs and M. P. Seach, John Wiley & Sons, London (1983).
[11] *Electron and Ion Spectroscopy*, Ed. L. Fiermans, J. Vennik, and W. Deceyser, Plenum Press, New York (1978).
[12] T. Chiang, *CRC Critical Reviews in Solid State and Materials Sciences* **14** (1988) 269.
[13] S. Kono, *Springer Series in Solid State Science*, **81** (1988) 253.

[14] S. Kono, Y. Enta, T. Abukawa, N. Nakamura, K. Anno and S. Suzuki, *Phys. Scripta* **31** (1990) 96.

[15] F. J. Himpsel, *Surf. Sci. Repts.* **12** (1990) 1.

[16] P. H. Fuoss, K. S. Liang and P. Eisenberger, in *Synchrotron Radiation Research: Advances in Surface and Low-Dimensional Science*, Ed. R. Z. Bachrach, Plenum, New York (1986).

[17] G. V. Hansson and R. I. G. Uhrberg, *Surf. Sci. Repts.* **9** (1988) 197.

[18] R. S. Daley and R. S. Williams, *Nucl. Instrum. Meth. Phys. Res. B* **45** (1990) 380.

[19] F. Shoji, K. Oura and T. Hanawa, *Nucl. Instrum. Meth. Phys. Res. B* **36** (1989) 23.

[20] G. Rossi, D. Chandesris, P. Roubin and J. Lecante, *Surf. Sci.* **168** (1986) 787.

[21] M. De Crescenzi, J. Derrien, L. Lozzi, P. Picizzi and S. Santucci, *Surface Interface Analysis* **16** (1990) 111.

[22] R. Feidenhans'l, *Surf. Sci. Repts.* **10** (1989) 105.

[23] S. Lagomarsino and F. Scarinci, *Vuoto: Sci. e Tecn.* **19** (1989) 87.

[24] J. R. Patel and J. A. Golovchenko, *Phys. Rev. Lett.* **50** (1983) 1858.

[25] G. Binnig and H. Rohrer, *Surf. Sci.* **126** (1983) 236.

[26] F. Salvan, A. Humbert, P. Dumas and F. Thibaudau, *Ann. Phys. Fr.* **13** (1988) 133.

[27] R. M. Tromp, *J. Phys. :Cond. Matt.* **1** (1989) 10211.

Part II

REVIEW OF SURFACE PHASES ON SILICON

2. Introduction

In this part of the handbook we will attempt a review of the data available in literature on the surface phases on silicon. The surface phases of atomically clean Si surfaces will be our initial concern. Then we shall address the surface phases formed upon adsorption of different elements on the Si surfaces. Each one of the 63 chapters is devoted to the single given adsorbate. The arrangement of the chapter is as follows: The data for each of the main Si substrate orientations, (111), (100), and (110), are presented in a separate section within the chapter. The section is opened by the list of the surface structures observed in the system under consideration followed by the first subsection entitled “Phase diagram”. In this subsection, the known results on the surface phase preparation are accumulated. The most convenient way for the presentation of a such information is a formation phase diagram built in the “coverage–temperature” coordinates, for example like the schematic one shown in Fig. 1.

The formation phase diagrams can be determined in several kinds of experiments. First, the adsorbate can be deposited on to the Si substrate held at a fixed temperature. After each deposition step, the surface reconstruction is elucidated (usually, by means of LEED or RHEED). The set of experimental dots in such a measurement occupies the pass **A** on Fig. 1. This procedure if repeated at different temperatures provides the possibility for the determination of the coverage and temperature ranges at which certain surface phases exist. The graphic presentation of these data produces the required formation phase diagram.

Second, the adsorbate film of a fixed coverage can be formed at room temperature and then annealed at progressively higher temperatures. In this case, the LEED (RHEED) patterns are recorded and indexed after each annealing step (see pass **B** on Fig. 1). Annealing at high temperatures might result in the noticeable desorption of the adsorbate atoms from the surface and the actual pass (marked as **B′**) should deviate from the vertical pass **B** towards the lower coverages. So, it is essential to distinguish between the case when the “coverage” axis shows the adsorbate coverage of a RT deposit before annealing (e.g. determined by means of a quartz crystal thickness monitor) and the case when the coverages of adsorbate left at the surface after annealing (e.g. determined by means of AES) is shown. In the latter case, the experiments might involve the RT deposition of a “thick” film followed by annealing to cause the isothermal desorption of the adsorbate. It is obvious that the corresponding pass (marked by **C**) is opposite to the pass **A**.

Another essential remark is as follows: in most investigations, before the LEED (RHEED) observations the heating is interrupted and the sample is cooled to room temperature. However, sometimes the LEED (RHEED) observations are performed with the “hot” sample. The ability to detect the reversible phase transformations on the surface upon heating/cooling is unique to this kind of experiment.

Thus, when giving the particular formation phase diagram, we always present it with brief comments which clarify its origin. Though we have tried to give the formation phase diagrams for each system, it has been impossible to do this when the required phase diagrams

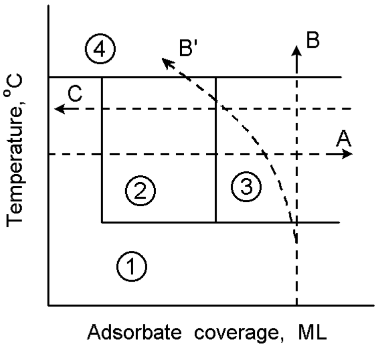

Fig 1. Schematic "formation phase diagram". The regions of occurrence of the surface structures 1, 2, 3, and 4 are shown by solid lines. The passes **A**, **B**, **B′**, **C** (dashed lines) illustrate the different kinds of experiments (see the text)

are not available in literature or the phase preparation procedures cannot be reported in terms of the phase diagrams described above. In the latter cases, the subsection "Phase diagram" constitutes the description of how the surface phases can be formed. When it seems convenient and essential, the "Phase diagram" subsection is divided into more particular subdivisions (e.g. "RT growth", "HT growth", "Deposition on to cleaved Si(111)2 × 1", etc.).

While describing the completion of the stage of surface phase formation we usually present a brief summary of the results on the formation of thicker film. It concerns especially the silicide-forming adsorbates since, in this case, it is rather difficult to make a clear distinction between the surface phases and extra-thin silicide layers.

The second subsection is called "Structure". It accumulates the available information on the geometric structure (i.e. atomic arrangement) of the surface phases. Since all submonolayer systems have not attracted the same interest, the reliability of the proposed structure models varies greatly from one system to another. In the worst cases, the models are proposed tentatively on a basis of a simple "coverage-symmetry" consideration and are highly speculative. However, in the best cases, the geometric structure is elucidated from the abundance of data obtained by several groups using a wide set of complementary surface-sensitive methods. There are numerous occasions when several structure models of one particular surface phase have been proposed by different authors and there is not enough evidence to choose the preferential one. In such an event, we list all models with the description of the kind of data used for the construction of the models so that the reader can make his own choice.

The last subsection, namely, "Properties" is devoted to the surface properties and surface processes or phenomena related to the formation and occurrence of the surface phases of adsorbates on silicon surfaces. These are, for example, desorption, surface diffusion and electromigration of adsorbate atoms, the variations of the electronic structure with the adsorption, chemical passivation or promoted reactivity of the Si surfaces with the adsorbate layers as compared with that for the Si surfaces without them, etc.

A list of references can be found towards the end of each chapter. The handbook, in turn is accompanied by a set of four Supplements. Supplement 1 shows the thicknesses of one monolayer of different adsorbates on the main silicon surfaces, Si(111), Si(100), Si(110). Supplement 2 and Supplement 3 present the list of superstructures which are known to be formed on silicon surfaces. These supplements differ in the form of material presentation: while Supplement 2 shows the superstructures that are induced by the given adsorbate, Supplement 3 shows the adsorbates that induce the given superstructure. Finally, in Supplement 4, sketches of the LEED patterns (reciprocal lattices) of the known superstructures are given.

3. Atomically-clean Silicon Surfaces

(Si)

SILICON

1. (111) ORIENTATION

The 7×7, 2×1, and 1×1 reconstructions were reproducibly obtained in many investigations. The 2×2, 3×3, 5×5, 9×9, $c(4\times2)$ and $\sqrt{3}\times\sqrt{3}$—$R30^\circ$ structures were reported in several papers to exist at local regions of the Si(111) surface and (or) to result from specific treatments.

1.1. PHASE DIAGRAM

The 7×7, 2×1, and 1×1 reconstructions were reproducibly obtained in many investigations. The 2×2, 3×3, 5×5, 9×9, $c(4\times2)$ and $\sqrt{3}\times\sqrt{3}$—$R30^\circ$ structures were reported in several papers to exist at local regions of the Si(111) surface and (or) to result from specific treatments.

1.1. PHASE DIAGRAM

When an Si sample is cleaved in ultra-high vacuum at low temperatures, a 2×1-reconstructed (111) silicon surface is produced. A 2×1 LEED pattern is observed from the freshly cleaved surface as soon as the apparatus can record, namely within a few seconds [1]. The 2×1 structure forms even when cleavage is carried out at close to liquid He temperatures [2].

It was shown that, for good flat cleavages, the half-order spots appear in only one of the three azimuths possible and the preferred direction is related to the direction of propagation of the crack that causes the cleavage [3].

The 2×1 structure is metastable and it converts irreversibly to a 7×7 structure upon heating at temperatures ranging from about 210 to 600 °C (the transition temperature increases with increasing step density) [4–16]. In the early work of Lander *et al.* [4], the intermediate 5×5 structure was observed. However, the intermediate 5×5 structure was not detected in subsequent works, but in some cases an apparent 1×1 LEED pattern was observed [7–9]. The 5×5 structure has again been found in recent investigations [11–16].

Feenstra and Lutz [14–16] found that there are two distinct reaction paths by which $2\times1\rightarrow7\times7$ surface transformation occurs. In the first path, the 2×1 surface becomes covered with adatoms and converts to a somewhat disordered arrangement containing simple adatom structures and small 5×5 and 7×7 domains. This surface, which displays an apparent 1×1 LEED pattern, orders subsequently and forms the 7×7 structure. This reaction path was expressed as:

$$2\times1+\text{adatoms}\rightarrow\text{adatoms}/1\times1,\ 5\times5,\ 7\times7\rightarrow7\times7$$

In the second path, the transformation from the 2×1 surface to a well-ordered 5×5 surface occurs via the growth from small 5×5 domains. At sufficiently high temperatures the 5×5 structure converts to the 7×7 structure. This second reaction path was written as:

$$2 \times 1 \rightarrow 5 \times 5 \rightarrow 7 \times 7$$

Feenstra and Lutz suggested that the occurrence of one or the other of two possible reaction paths depends on the density of nucleation sites (steps or domain boundaries) which provide the surface with excess adatoms. The surface with few nucleation sites can transform into a well-ordered 5×5 structure (the second reaction path), while a surface with many nucleation sites tends to form the 7×7 structure (the first reaction path) [14].

The 7×7 is the lowest-energy structure for the Si(111) surface. This structure can be easily produced on the Si(111) surface in many ways: by heat treatment at above 950 °C of mechanically and chemically polished Si(111) wafers, or by argon ion bombardment followed by similar, but shorter, annealing or by low-temperature heating of cleaved Si(111) samples as described above.

It should be pointed out that, though the 7×7 structure is commonly attributed to the atomically-clean equilibrium Si(111) surface, Ohdomari [17–19] suggested that oxygen might play an essential role in stabilizing the 7×7 reconstruction.

When the 7×7 reconstructed Si(111) surface is heated above about 850 °C, the 7×7 LEED pattern changes to a 1×1 surface [20–36]. This transition is reversible and, upon slow cooling of the 1×1 surface through the transition temperature region, the 7×7 reconstruction is restored. Reflection electron microscopy [27, 28] and low-energy electron microscopy [34] established that, in transformations between 7×7 and 1×1 surface structures, the surface steps act as nucleation sites: on cooling the 7×7 structure nucleates at the upper edge of the monoatomic steps and grows along the upper terraces, while on heating the reverse process takes place.

If the surface is cooled very rapidly (quenched), the 1×1 LEED pattern remains [37, 38]. Though, at first glance, the high-temperature and quenched surfaces show the 1×1 structure, closer inspection of their diffraction patterns reveals the presence of certain additional features. The diffuse spots at about $\sqrt{3} \times \sqrt{3}$—$R30°$ positions were observed in RHEED [39] and LEED [40] studies of the high-temperature 1×1 surface. Furthermore, very weak half-order LEED reflections were detected on the LEED patterns both from the high-temperature 1×1 phase [31] and quenched 1×1 surface [38]. The STM observations [33] evidenced the presence of regions with 2×1 structure at the rapidly cooled surface and those of 2×2 structure if the cooling rate is slower.

The 1×1 surface is observed also at room temperature after pulse laser irradiation (typically, 15 nsec pulse with a dose of about 1 J/cm^2) [31, 41–57]. It is accepted that this treatment leads to melting of the Si crystal to a depth of several thousands of angstroms followed by liquid-phase epitaxial regrowth from the unmelted substrate. The laser-treated Si(111) surface displays an apparent 1×1 LEED pattern with some slight intensity enhancement at half-order positions [31, 47–49, 57, 58]. The STM observations revealed that $c(4 \times 2)$ and 2×2 regions populate the ordered parts of the surface after laser annealing [58, 59].

Annealing to 750 °C is required to return the laser-treated Si(111) surface to its equilibrium 7×7 structure [57, 60]. Upon annealing at a lower temperature of 600 °C, regions with 5×5, 7×7, 9×9, and $\sqrt{3} \times \sqrt{3}$—$R30°$ structures were detected by STM [58].

The observation of $\sqrt{3} \times \sqrt{3}$—$R30°$ reconstruction on the clean Si(111) surface was reported also in Refs [61, 62]. In Ref. [61], the $\sqrt{3} \times \sqrt{3}$—$R30°$ LEED pattern was observed from the Si(111) sample which was rapidly annealed for 5 sec at 1000 °C after intense bombardment with 1 keV Ar ions. An STM study of Ref. [62] revealed the development of a

$\sqrt{3} \times \sqrt{3}$—$R30^\circ$ reconstruction on the terraces of a width of less than the size of the 7×7 unit cell. The stepped Si surface was prepared by non-uniform heating of an initially flat Si(111) sample.

A number of metastable reconstructions is observed upon Si homoepitaxial growth at low temperatures i.e., in kinetically limited regime. In early works by Thomas and Francombe [63–66], the observation of the 5×5 LEED pattern from Si epitaxial layer grown at about 500–600 °C was reported. This result found a confirmation in the RHEED studies of Nakahara and Ichimiya [67–69] who observed a mixed phase of 5×5 and 7×7 for growth temperatures from 380 to 600 °C.

In a recent STM study of low-temperature (300–500 °C) nucleation and growth of epitaxial Si on Si(111) [70–72], it was shown that epitaxial Si islands can adopt 3×3, 5×5 and 9×9 structures, while on extremely small islands, a 2×2 structure is also sometimes observed. The 5×5 reconstruction is the only one of the above reconstructions that can cover extended areas, while 2×2, 3×3 and 9×9 were never observed with more than one or two unit cells together.

Nakahara and Ichimiya [73] reported that the coexistent regions of 5×5 and 7×7 phases are formed during SPE crystallization of the amorphous–Si/Si(111) interface at 500–600 °C. However, upon further annealing at 600 °C, the 5×5 domains are rearranged into 7×7 via disordered regions. In contrast, after MBE growth at 600 °C, the 5×5 structure remains and does not disappear during annealing at 600 °C, presumably, due to the lack of the disordered regions at the surface.

1.2. STRUCTURE

1.2.1. Si(111)2 × 1

The 2×1-reconstructed Si(111) surface obtained by cleavage in ultra-high vacuum has been studied using different experimental techniques, LEED [74–76], PES 8, 77–80], EELS [81–85], optical characterizations [86–93], ion scattering [94, 95], STM [96–99], and theoretical calculations [100, 106].

The major data obtained are consistent with the π-bonded chain model which was proposed by Pandey [107, 108] and modified by Northrup and Cohen [101]. Pandey proposed a drastic restructuring of the surface in which the bonds between half of the second and third layer atoms are broken to induce a zig-zag chain structure of the first and second layer atoms. Northrup and Cohen suggested a buckling (tilting) of the chains. The resulting structure model is shown in Fig. 1.

However, there is not unanimous agreement concerning the validity of the chain model. Notably, this model does not provide satisfactory fit to LEED data [74, 76] (the R-factor was never below 0.4). Haneman [1, 10, 109] also argued that the subsurface bond breaking required on formation of the π-bonded chain structure cannot occur at room or lower temperature cleavage.

Recently, Haneman proposed an alternative model, namely, a three-bond-scission model [1, 10, 109] shown in Fig. 2. The proposed model is based on the assumption that cleavage takes place along the (111) plane by scission of three bonds per atom between the closely spaced double layers of Si atoms. The chains form due to the motion of atoms towards each other along the [112] direction. The chains can tilt since the underlying symmetry is different for the atoms moving to the left and to the right (see Fig. 2). Haneman speculated that the three-bond-scission model provides a more natural starting point for the conversion to 7×7 structure upon heating than the chain model, explains the correlation of preferred 2×1 domain orientation to cleavage direction and accounts for the observation of less damage in the surface for cleavage along [112] relative to cleavage along [110]. However he accepted that

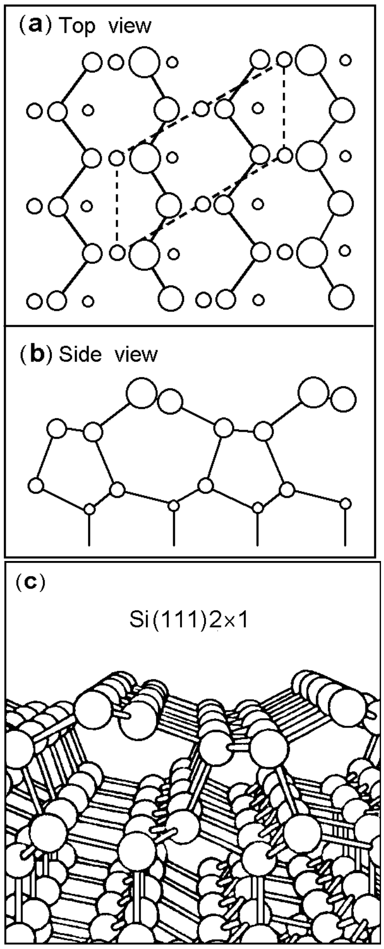

Fig 1. π-bonded chain model of a cleaved Si(111)2×1 surface. (a)Top view, (b) side view. Circle size represents depth: the larger circles are in the top layer. The surface unit cell is shown in dashed lines. (c) View of ball-and-stick model (from Ref. [101]). (*Reproduced by permission of Elsevier Science Publishers BV*)

definite conclusions must await detailed comparison with the relevant data and optimization of the structure [1, 10, 109].

1.2.2. Si(111)1 × 1

There are three types of clean Si(111) surfaces that show an apparent 1 × 1 LEED pattern (usually, with faint half-order reflections): (1) heated at temperatures above about 850 °C, (2) rapidly quenched from high temperatures to room temperature and (3) pulse laser annealed.

Phaneuf and Williams [31] suggested that the laser-quenched surface is made of 2 × 2 arrangements of adatoms on a partially disordered substrate, while the high-temperature equilibrium surface contains a random arrangement of adatoms whose relative positions show a tendency to be two spacings apart.

A random distribution of adatoms which are located at both the H_3 and T_4 sites is also a basic feature of the models for high-temperature 1 × 1 derived from the analysis of LEED data by Iwasaki *et al.* [40] and proposed in the RHEED study of Kohmoto and Ichimiya [110]. The latter authors also outlined that the structure occurring at high temperatures is different from the quenched surface structures. Pashley *et al.* [33] revealed by STM the presence of 2 × 1 or 2 × 2-reconstructed areas at the quenched surface depending on the cooling rate. The STM study by Becker *et al.* [58,59] of the laser-annealed surface showed that this surface

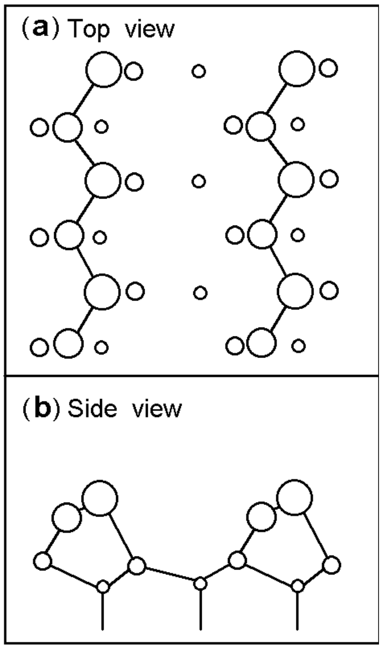

Fig 2. Three-bond scission model of a cleaved Si(111)2×1 surface (top and side view). Atoms decrease in size with depth. Top chains are tilted (from Ref. [109]). (*Reproduced by permission of American Institute of Physics*)

has a rather disordered structure but also contains small domains of 2 × 2 and $c(4 \times 2)$ reconstructions. The latter structures are consistent with a simple model of alternating rows of 2 × 2 and $c(4 \times 2)$ adatoms on T_4 sites on a 1 × 1 substrate [59].

It should be mentioned that STM results showed that the quenched (111) surfaces are inhomogeneously structured and, hence, there is a serious problem associated with deriving conclusions about their structures from surface averaging techniques such as LEED and ion scattering. This is believed to be the reason that various LEED and ISS experiments failed to agree on the nature of the apparent 1×1 LEED pattern with proposed models, including, ideal bulk-like termination with a minor relaxation [44, 56], somewhat disordered 7 × 7 structure [49, 51, 53] and a graphite-like structure [55].

1.2.3. Si(111)7 × 7

The 7 × 7 structure of the clean Si(111) surface has been studied exhaustively over a period of 25 years, and many models have been proposed. The situation to 1981 has been reviewed by Haneman [111], to 1984 by Takayanagi *et al.* [112], and to 1986 by Haneman [1]. The concept of adatoms in the outermost layer was proposed by Harrison [113] many years ago. Key experiments using CMTA LEED [114] and ISS [51, 115] revealed non-cubic stacking in the selvedge. Binnig *et al.* [116] in 1983 obtained the first STM picture of this surface, which showed triangular units with deep holes at the vertices and smaller holes along the boundaries of the triangles. This led Himpsel [117], McRae [118], and Bennett *et al.* [119] to propose independent models in which the 7 × 7 unit cell is divided into two equal triangles with different stacking. A key contribution was made by Himpsel [117] and McRae [118], who showed that rebonding of Si atoms across the boundary between the faulted and unfaulted triangular regions results in two dimers, a ring of 12 atoms and two rings of 8 atoms in exact agreement with features in the earlier STM image [116]. Finally, Takayanagi *et al.* using TED [112] correctly pieced together a model with dimers, adatoms, and stacking-faults (DAS).

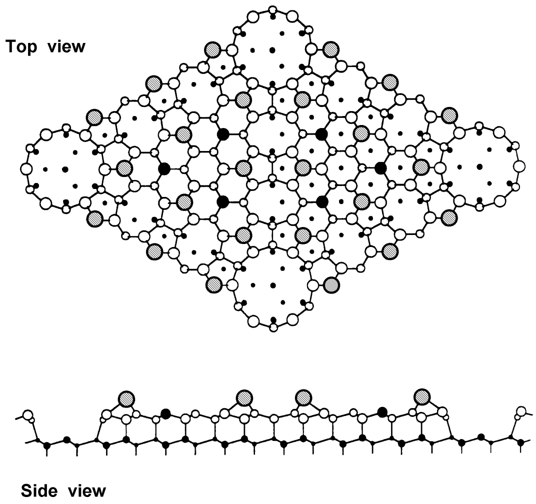

Fig 3. DAS model of the Si(111)7×7 surface. (a) Top view. Atoms on (111) layers at decreasing heights are indicated by circles of decreasing sizes. Heavily outlined circles represent 12 adatoms. Large open circles represent atoms in the stacking fault layer. Smaller open circles represent atoms in the dimer layer. Solid circles and dots represent atoms in the unreconstructed layer beneath the reconstructed surface. (b) Side view. Larger open and solid circles indicate atoms on the $(\bar{1}01)$ plane parallel to the long diagonal across the corner vacancies of the 7×7 unit cell. Smaller open and solid circles indicate atoms on the next $(\bar{1}01)$ plane (from Ref. [112]). (*Reproduced by permission of Elsevier Science Publishers BV*)

In accordance with the original work of Takayanagi *et al.* [112] a three-dimensional structure model of the Si(111)7×7 surface is shown in Fig. 3, (a) top view and (b) side view ($(\bar{1}01)$ projection). In the top view, atoms on (111) layers at decreasing heights (Z coordinate) are shown by circles of decreasing sizes. The structure consists of a two-layer reconstruction in which the rest-atom double layer is capped by an adatom layer. The rest-atom layer consists of triangular subunits with a 1×1 structure which are either faulted or unfaulted with respect to the bulk layer beneath. These subunits are bounded by dimer-row domain walls which intersect to produce holes at the corners of the cell. The adatom layer consists of six adatoms arranged locally in a 2×2 structure above the shallow hollows within each triangular subunit. Thus, the DAS model consists of 9 dimers and 12 adatoms per unit cell. The DAS model contains 19 dangling bonds: 12 from the adatoms, 6 from atoms which are in the stacking fault layer but are not bonded to the adatoms and one from the atom below the vacancy. The number of dangling bonds is the smallest among various models so far proposed. Therefore, the DAS model can have the lowest energy among them [112].

In the DAS model, all atoms except those in dimers are located at sites of the unreconstructed (111) layers of the normal spacing [112]. Many of them, however, are at positions of unusual atom coordinations. Therefore, they must have slight relaxation of the positions both in the surface-parallel and surface-normal directions. It should be noted, that until now there is no accurate total energy calculation and coordinate optimization of the 7×7 structure because the size of such a project is too large for present day computers [120].

The vertical structure of the DAS model was investigated by LEED [114, 121], RHEED [122,123], XSW [124], X-ray diffraction [125], and X-ray reflectivity [120]. While these results are completely consistent with the DAS model, they disagree somewhat on the exact position of the layers. The absolute position of the surface layers relative to the distant bulk shows a significant expansion for X-ray reflectivity experiments by Robinson and Vlieg [120], but differs from the LEED [114, 121], RHEED [122, 123], and XSW [124] results. Figure 4 shows a side view of part of the DAS model that defines the parameterization of the layer positions.

Fig [.]

Table

1. Values of mean interlayer spacing. Values are in Å (from Ref. [120]).

Spacing (Fig. 4)	Ideal value	Experimental			Theoretical calculations	
		X-ray reflectivity (Ref. [120])	RHEED (Ref. [123])	LEED (Ref. [121])	LDA* (Ref. [274])	Semi-emp. (Ref. [127])
Ad–1a	0.78	1.58	1.23	1.21	1.14	1.25
1a–1b	0.78	0.85	0.83	0.84	0.80	0.88
1b–2a	2.35	2.41	2.34	2.26	2.37	2.35
2a–2b	0.78	0.75	0.68	0.72	0.76	0.66
2b–3a	2.35	2.35	2.35	2.33	2.36	2.35
3a–3b	0.78	0.78	0.78	0.78	0.78	0.78

* Local density approximation.

Fig [.]

Table

2. List of the dimer bond lengths (from Ref. [123]).

Dimer length (Å)	Method	Ref.
2.56	TED	[112]
2.43	Theory	[127]
2.44	TED, STM, GXD	[275]
2.49	XRD	[125]
2.45	Dynamic LEED	[121]
3.24	Kinematic RHEED	[276]

Table 1 gives the values for interlayer spacings derived from the literature by averaging and conversion to common units [120]. Many kinds of the dimer bond length that have been reported now are listed in Table 2 in accordance with Ref. [123]. Most of the atoms in the first and all second layer atoms have displacements parallel to the surface. The magnitudes of these displacements are greater for the first layer atoms (∼ 0.2 Å) and less (0.01–0.08 Å) for the second layer atoms [114, 121, 126–128].

The DAS model of Takayanagi *et al.* [112] proposed in 1985 is supported by abundant experimental and theoretical evidence with a variety of methods and is no longer questioned seriously [120]. The DAS model has now been widely accepted as the best model.

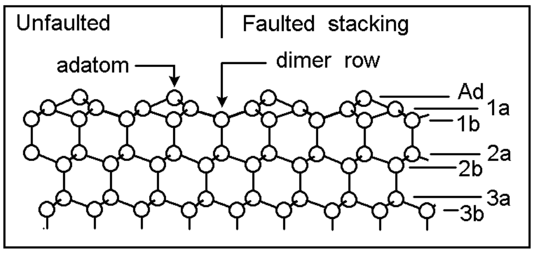

Fig 4. Ball-and-stick diagram of the DAS model of the reconstructed Si(111)7 × 7 surface viewed from the side. All atoms are in unrelaxed "ideal" positions indicated in Table 1. The layer notations used in the Table 1 are defined (from Ref. [120]). (*Reproduced by permission of Elsevier Science Publishers BV*)

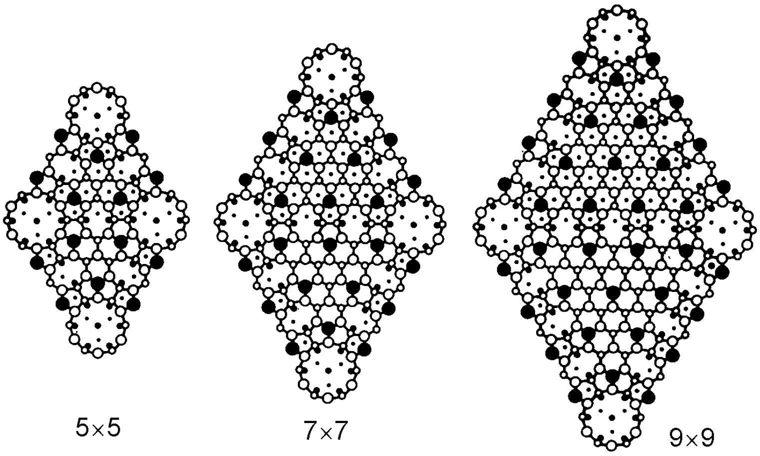

Fig 5. Top view of 5 × 5, 7 × 7, and 9 × 9 structures according to dimer-adatom-stacking fault model. Shaded large circles are adatoms. Open circles are atoms in the partially faulted double layers directly below. Filled circles are the bulk unreconstructed double layer of the bulk (from Ref. [58]). (*Reproduced by permission of the publishers of Journal of Physical Review Letters*)

1.2.4. Si(111)3 × 3, Si(111)5 × 5, and Si(111)9 × 9

The 3 × 3, 5 × 5, and 9 × 9 reconstructions are related closely to the 7 × 7 one as members of the dimer-adatom-stacking fault family [58, 59, 70, 126, 129–131]. The structures for the 5 × 5, 7 × 7, and 9 × 9 reconstructions are illustrated in Fig. 5 from Ref. [58]. The 3 × 3 structure (not shown in Fig. 5) consists only of a ring of adatoms which interconnects to form cornerholes with its surrounding adatoms [70].

Certain peculiarities in the atomic arrangement and electronic structure of the 5 × 5 phase were derived in the theoretical study of Adams and Sankey [132]. Particularly, they found that adatoms on the faulted side of the 5 × 5 unit cell are higher than the adatoms on the unfaulted side; the adatom dangling-bond states are primarily filled on the faulted side, and primarily empty on the unfaulted side. These theoretical predictions are in agreement with STM images [59] of filled and unfilled states on the Si(111)5 × 5 phase.

1.2.5. Si(111)$\sqrt{3} \times \sqrt{3}$—*R*30°

There is no consensus about the atomic arrangement of the $\sqrt{3} \times \sqrt{3}$—$R30°$ structure on the clean Si(111) surface. While Fan *et al.* [61] examining the LEED *I–V* curves suggested the vacancy model (a first-layer Si atom in each $\sqrt{3} \times \sqrt{3}$ unit cell is missing), both Becker *et al.* [58] and Berghaus *et al.* [62] explained the $\sqrt{3} \times \sqrt{3}$ reconstruction by saturating dangling bonds of the ideal Si(111) surface by Si adatoms. It should be said, however, that the preparation procedures for the formation of $\sqrt{3} \times \sqrt{3}$ reconstructed surfaces differ greatly and the resultant surfaces may not be similar to each other.

2. (100) ORIENTATION

The surface reconstructions observed on Si(100) are 2 × 1, $c(4 \times 2)$, 2 × 2, and $c(4 \times 4)$.

2.1. PHASE DIAGRAM

The clean Si(100) surface usually displays a two-domain 2 × 1 reconstruction. These domains are related by a 90° rotation, i.e. their surface periodicities are 2 × 1 and 1 × 2.

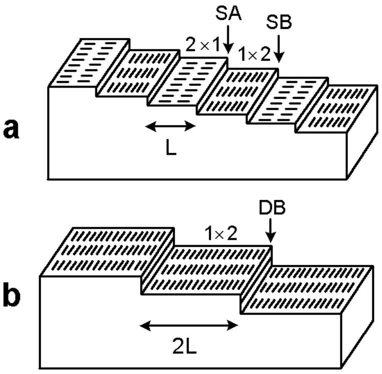

Fig 6. Schematic representation of the (a) single-layer and (b) double-layer step structures of a vicinal Si(100) surface. The surface misorientation φ is related to the terrace width L by $\mathrm{tg}(\varphi) = Z_{\mathrm{Si}}/L$, where $Z_{\mathrm{Si}} = 1.36$ Å is the height of a single-layer step (from Ref. [145]). (*Reproduced by permission of the publishers of Journal of Physical Review Letters*)

It is commonly accepted that the Si(100)2 × 1 reconstruction is caused by formation of Si dimers that are arranged in parallel rows. There are two possible dimer orientations with dimer bonds directed either along [011] or [$0\bar{1}1$]. Monolayer-high steps separate domains with 2 × 1 and 1 × 2 symmetry. However, if the surface misorientation is accommodated by double-layer steps, the single orientation is formed as illustrated in Fig. 6.

Chadi [133,134] calculated the formation energies of single- and double-layer steps on the Si(100) surface. He found that for both types of steps the orientation of dimers relative to the step edge has an important effect on the step energy. Chadi labelled the downward step running parallel to the dimer rows as A type and that running perpendicular to the dimer rows as B type (see Fig. 6). The most significant result of the calculations is that although the A type single-layer (SA) step has the lowest energy, the B type double layer (DB) steps become energetically more favorable over single-layer SA+SB steps on (100) surfaces misoriented towards [011] or [$0\bar{1}1$] axes.

These calculations are in a good agreement with experimental observations that, for surface misorientation $\varphi \geq 4°$, a surface that originally exhibits domains of 2 × 1 and 1 × 2 reconstructions becomes single-domain reconstructed after extended high-temperature annealing (at about 900 to 1100 °C) [135–149].

Sakamoto and Hashiguchi [150] reported the formation of a single-domain Si(100)2 × 1 structure after annealing a well-oriented (100) surface at a temperature of 1000 °C for 20 min. The subsequent REM observations [137, 151, 152] confirmed the preferential growth of one type of reconstructed domain but revealed that single-layer steps are not removed completely by annealing.

An interesting result was obtained by Latyshev *et al.* [153] and Kahata and Yagi [154] in their REM studies of structural transformations on a Si(100) surface heated by direct current. It was found that the direction of current affects the step motion at sublimation and, thus, determines the portions of the surface occupied by 2 × 1 and 1 × 2 domains. If the directions of current and step motion under sublimation coincide, almost the whole surface has the structure with direction of dimerization normal to the steps. If the directions of the current and the steps motion are opposite, the surface is mainly characterized by the structure in which thedirection of dimerization is parallel to the steps (Fig. 7). The change-over from one type of surface to the other with changing direction of the current during sublimation was found to be reversible.

The formation of a single-domain Si(100) surface was also detected during Si molecular beam epitaxy on Si(100) misoriented by 0.5° towards [110] [146, 155–159]. The growth was conducted at temperatures of 450–550 °C. It was found that SB steps advance much faster than SA steps forming a nearly perfect single-domain structure with straight, double-layer steps. However, Sakamoto *et al.* [156] mentioned that the forming single-domain surface is not stable. When Si deposition is terminated and the sample is kept at the growth temperature, a two-domain surfaces is restored within a few minutes.

Men *et al.* [160] studying the Si(100) surface under an externally applied stress showed that bending a nominally flat Si(100) sample at 550–800 °C produces unequal populations of the 2×1 and 1×2 domains (the domain compressed along the dimer bond is favored). The effect was found to saturate at a strain of about 0.1% when 90% of the surface is occupied by the favorable domain (Fig. 8).

Although the 2×1 structure is stable from room temperature up to melting point, it is not a ground state of the Si(100) surface.The theoretical works by Ihm *et al.* [161] and Saxena *et al.* [162] predicted an order–disorder transition on the Si(100) surface from a lower-energy (and higher-order-periodicity) $c(4 \times 2)$ structure to a less ordered 2×1 structure above a critical temperature of about 250 K. This transition was detected in a LEED study by Tabata *et al.* [163] at about 200 K.

The observation of the $c(4 \times 2)$ reconstructed Si(100) surface was reported in several papers [164–170]. The preparation procedure usually included high-temperature annealing and slow cooling at a rate of about 1 °C/s. Enta *et al.* [170] reported that half-order streak lines noticed in the LEED pattern at room temperature changed to quarter-order spots as the temperature decreased and sharp $c(4 \times 2)$ LEED spots were observed for the tested temperature range of 200–280 K.

The regions of $c(4\times2)$ symmetry and 2×2 symmetry were detected in addition to the 2×1 reconstructed surface in STM observations of clean Si(100) samples [171–173]. The presence of 2×2 reconstructed (and possibly $c(2 \times 2)$ reconstructed) regions was also manifested in the He diffraction study [167–169].

In a number of studies [63, 174–180], the formation of the $c(4 \times 4)$ reconstruction was observed as a result of different treatments of the clean Si(100) surface: The $c(4\times4)$ structure was formed by Kato *et al.* [174] using special surface processing at a hydrogen exposure higher than 10^4 L and afterwards annealing. The hydrogen-covered Si(100) surface shows a 1×1 dihydride bulk-like structure. Upon annealing at above 500 °C, all hydrogen atoms are

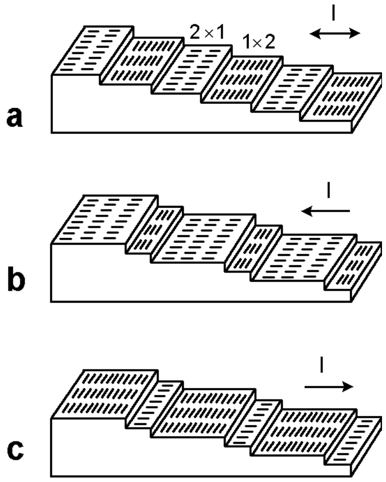

Fig 7. A schematic of the Si(100) surface structure in the process of sublimation when heating by direct current. The direction of electrical current coincides (b) and opposite (c) with the direction of step motion upon sublimation (from Ref. [153]). (*Reproduced by permission of Elsevier Science Publishers BV*)

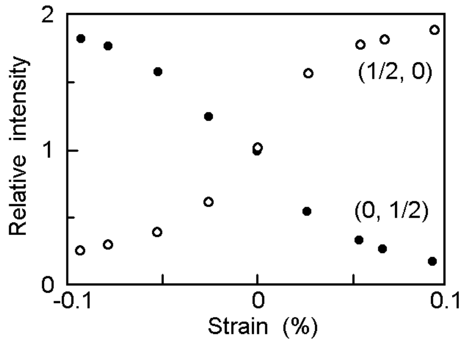

Fig 8. The ratio of the intensity of the $(\frac{1}{2}, 0)$ and $(0, \frac{1}{2})$ LEED reflections to their values at zero strain plotted as a functions of the calculated surface strain. The data were measured at a fixed position along the bar for various deflections of the end (from Ref. [160]). (*Reproduced by permission of the publishers of Journal of Physical Review Letters*)

thermally desorbed and the 2 × 1 structure of the clean Si(100) appears. By annealing at 570–690 °C, this 2 × 1 structure changes into the $c(4\times4)$ structure which converts irreversibly into the 2 × 1 structure by annealing above 690 °C [174].

The above technique seems to be the most reliable and has been employed successfully to produce $c(4\times4)$ in Refs [174,179,180]. However, several other procedures have been reported: Thomas and Francombe [63] and Sakamoto *et al.* [175] observed the $c(4\times4)$ reconstruction during Si epitaxial growth on Si(100) at 600–700 °C and 700–800 °C, respectively. Another way of preparing $c(4\times4)$ was reported by Wang *et al.* [176] who prepared the surface by cooling a sample from 1100 °C and keeping it at 600 °C for 5 min. Finally, Mokler *et al.* [177, 178] obtained a $c(4\times4)$ reconstruction during Si growth on Si(100) at about 645 °C using a disilane gas source.

2.2. STRUCTURE

2.2.1. Si(100)2 × 1

It is well recognized now that the basic element of the Si(100)2 × 1 unit cell is a Si–Si dimer (i.e. two Si atoms in the top layer bonded to each other). The dimerization of Si atoms on the Si(100) plane was proposed as long ago as 1959 by Schlier and Farnsworth [181] and was confirmed definitely in recent STM observations [171–173].

However, many questions regarding the details of the reconstruction are still not resolved. One major question which is addressed in the most recent works is whether the dimers are parallel to the surface (symmetric) or buckled (asymmetric, i.e. one member atom is higher from the surface than the other) (see Fig. 9). There is no consensus yet and though the majority of the theoretical and experimental works support the buckled dimers model [138, 182–198], the symmetric dimers are favored in several works [199–202]. The compromise viewpoint expressed in a number of publications [203–206] implies that as the calculated energy difference between the symmetric and asymmetric dimers is very small (e.g. it is only ∼ 0.02 eV according to Ref. [203]), it is therefore quite possible that both kinds of dimers could coexist on the surface.

The STM observations [171–173] have clarified the situation only partially. STM images show the presence of both buckled and non-buckled dimers in roughly equal amounts as well as a high density (∼ 10%) of vacancy type defects (missing dimers). In defect-free areas only symmetric dimers are observed while buckled dimers appear to be stabilized near surface defects. However, the authors [173] pointed that they were unable to ascertain whether the symmetric-looking dimers are truly symmetric or whether the STM image is only sensitive

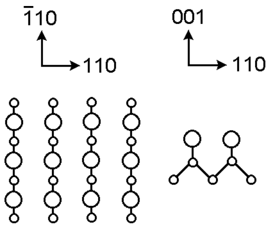

(a) ideal 1×1

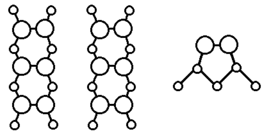

(b) 2×1 with symmetric dimers

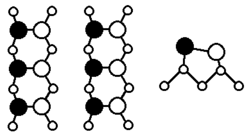

(c) 2×1 with buckled dimers

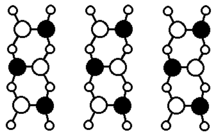

(d) 2×2

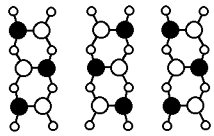

(e) c(4×2)

Fig 9. Various reconstructions of the Si(100) surface based on the surface-dimer model: (a) Ideal bulk-terminated surface; (b) 2×1 reconstruction with symmetric dimers; (c) 2×1 reconstruction with buckled dimers (top and side views); (d) 2×2 reconstruction and (e) $c(4 \times 2)$ reconstructions (top views). Large circles represent the surface atoms, solid circles are the surface atoms that are displaced out of the surface. The smaller circles represent atoms in the first subsurface layer. (*Reproduced by permission of the publishers of Journal of Physical Review B*)

to the time-average position of dimers which may flip dynamically on a time scale shorter than the STM measurement time. The idea that buckled dimers may rapidly interconvert with symmetric dimers or simply flip found theoretical support in Refs [197, 207].

Moreover, the results of several theoretical works [208–210] showed that biasing the surface, used in STM experiments, can visibly influence the resulting surface image. In the case of the 2×1 reconstruction of the Si(100) surface this means that one can expect STM images to show symmetric dimers even if the dimers in the unbiased surface are buckled.

2.2.2. Si(100)$c(4 \times 2)$ and Si(100)2×2

As was shown by STM observations [171–173], the formation of long-range $c(4 \times 2)$ and 2×2 reconstructions is connected with the ordering of buckled dimers. The alternating buckled dimers give rise to $c(4 \times 2)$ and 2×2 symmetries when adjacent rows are out-of-phase and in-phase, respectively (see Fig. 9).

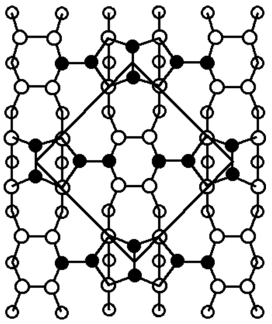

Fig 10. Structure model of the $c(4 \times 4)$ structure. Solid circles are used to highlight the surface atoms. The square outlines a $c(4 \times 4)$ primitive cell (from Ref. [180]). (*Reproduced by permission of the publishers of Journal of Physical Review B*)

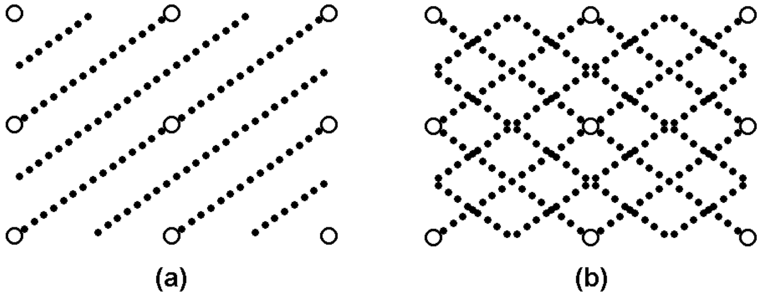

Fig 11. Sketches of the LEED patterns (reciprocal lattices) of Si(110)"2×16" : (a) corresponds to a single-domain structure and (b) to double-domain structure. (*Reproduced by permission of the publishers of Japanese Journal of Applied Physics*)

2.2.3. Si(100)$c(4 \times 4)$

Initially, it was proposed that the $c(4 \times 4)$ reconstruction results from an ordering of missing dimer defects [174]. However, the missing dimer model appeared to be inconsistent with the STM data of Refs [179, 180]. So Uhrberg *et al.* [180] proposed a new model based on the detailed analysis of STM images and first-principles total energy calculations. A sketch of this model is shown in Fig. 10. The main feature of the model is the presence of two types of surface dimers oriented parallel and perpendicular to the underlying 2×1 dimer rows.

3. (110) ORIENTATION

The clean Si(110) displays "2×16" (sometimes "2×32"), 1×1, and 1×2 reconstructions.

3.1. PHASE DIAGRAM

Various reconstructions have been observed on the Si(110) surface depending on the relevant heat treatments [37, 211–218]. However, only the "2×16" structure was shown to exist at the clean Si(110) surface, while other reconstructions, 5×4, 1×2, 1×5, 1×7, 1×9, etc. were found to be induced at small amounts of nickel impurities which are easily trapped by the surface from different uncontrolled sources [213, 214, 217–220].

The quotes in the notation of the "2×16" structure indicate that the reconstruction is not aligned along the bulk symmetry axes (see Fig. 11). The "2×16" structure is best described in matrix notation as $\begin{pmatrix} 17 & 1 \\ 2 & 2 \end{pmatrix}$.

The "2×16" structure is formed after annealing of the Si(110) surface at 1000–1300 °C if, at all stages of sample preparation and mounting, precautions are taken to prevent contact of the sample with any Ni containing environment [218]. The "2 × 16" structure exists in two domains with rows of LEED extra spots along the [11] and $[1\bar{1}]$ directions of the reciprocal two-dimensional Si(110) lattice, as can be seen in Fig. 11(b). The single-domain phase is formed on the vicinal Si(110) surfaces with high off-angles [221] or can be obtained by prolonged heating of low off-angle surfaces [218].

Ichinokawa *et al.* [213, 222] and Yamamoto *et al.* [214, 223] reported that the "2 × 16" structure transforms into a 1 × 1 structure at about 750 °C. The phase transition is reversible and the temperature range of the transition spreads over 30–40 °C.

Cowan and Golovchenko [224] and de Jong *et al.* [50] found that pulse laser irradiation of the Si(110) surface invariably produces a well-developed 1 × 2 structure.

Ampo *et al.* [217] reported that the clean Si(110) surface sometimes shows a "2 × 32" structure, which is essentially similar to a "2 × 16" structure but with twice greater periodicity. However, it should be pointed out that the "2 × 32" structure has never been detected by other groups.

3.2. STRUCTURE

3.2.1. Si(110) "2 × 16"

As proposed by Ampo *et al.* [217] and confirmed later in the STM study by Hoeven *et al.* [225], the "2 × 16" reconstructed Si(110) surface is formed by a periodic up and down sequence of terraces in a step height of the one Si(110) bulk layer spacing (1.9 Å). The width of the terraces is eight times larger than a periodicity of the 1 × 1 unit mesh and step edges are along the $[\bar{1}12]$ or the $[1\bar{1}2]$ directions. The fine, well-resolved STM image of the Si(110) "2 × 16" surface obtained recently by Yamamoto *et al.* [226] revealed the presence of zigzag chains consisting of Si adatoms on both the upper and lower terraces. Based on the above results, a structural model was proposed in Ref. [226]. Fig. 12 shows the schematic illustration of a side view of the model and Fig. 13 presents the top view of the atomic arrangement of "2 × 16" structure.

STM observations of Refs [225, 227, 228] revealed, in addition to a "2 × 16" reconstruction, the presence of regions where the terraces, typically alternated up and down in the Si(110) plane, are arranged in an up–up sequence forming faceted planes with (17 15 1), $(17\ 15\ \bar{1})$, (15 17 1) and $(15\ 17\ \bar{1})$ indices. The presence of these faceted planes was claimed first in the LEED study by Olshanetsky and Shklyaev [212].

4. PROPERTIES

4.1. Si SURFACE SELF-DIFFUSION

The reliable determination of parameters of Si adatom migration on the Si surfaces is a very complex problem for experimental investigation. Information regarding Si surface migration

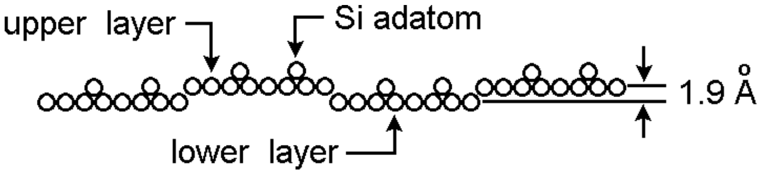

Fig 12. Schematic illustrations of the cross-section of the model for the Si(110) "2 × 16" structure (from Ref. [226]). (*Reproduced by permission of the publishers of Japanese Journal of Applied Physics*)

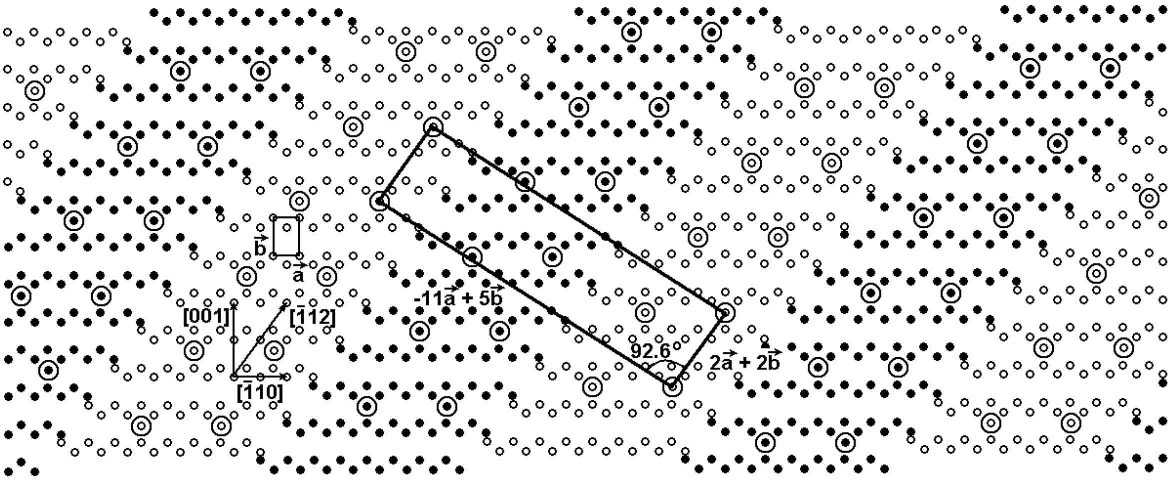

Fig 13. The atomic arrangement of the Si(110)"2 × 16" structure deduced from STM results. The rectangle represents the unit mesh of the "2 × 16" structure. Axial lengths are 1.3 Å and 50.2 Å and the axial angle is 92.6 °. Small open circles are atoms on the upper (110) terrace. Small solid circles are atoms on the lower (110) terrace. Double circles represent Si adatoms (from Ref. [226]). (*Reproduced by permission of the publishers of Japanese Journal of Applied Physics*)

is presently obtained indirectly, usually, by modeling growth measurements and determining which migration properties give a reasonable fit to the data. Even the simplest models which are used in these studies involve several parameters which cannot be derived directly from experimental data. This results in the spread of values for activation energy of migration.

In the case of Si diffusion on the Si(111) surface, the values obtained by fitting experimental data with models range from 0.2 to 1.6 eV [229]. Even as a high value as 3.6 ± 0.8 eV was reported in Ref. [67]. However, in the majority of publications, the values of about 1.3 eV have been reported [230–234]. These values are in agreement with the results of theoretical study [235] which yields

$$D = 2.15 \times 10^{-3} \exp(-1.51\text{eV}/kT)\ \text{cm}^2/\text{s}$$

for Si atom diffusion on a reconstructed Si(111)7 × 7 surface.

The migration of Si atoms on the Si(100)2 × 1 surface has been investigated in a large number of theoretical works [236–245]. The results obtained in the majority of calculations suggest that the barriers to diffusion are highly anisotropic and strongly favor the migration of Si adatoms along the dimer rows. However, there is no consensus concerning the passage of the easy diffusion: while the calculations of Toh and Ong [244] favor the migration between the dimer rows, Sristava and Garrison [243], Zhang *et al.* [239,240] and Huang and Allen [241] reported that the Si adatom probably remains on top of the dimer row.

Sristava and Garrison [243,246] suggested further that the dominant mechanism of adatom diffusion is intimately intertwined with the surface reconstruction. The dimers are opening and closing as the adatom diffuses on the dimer row. The macroscopic diffusion process was calculated to follow the Arrhenius form with $D = 5.7 \times 10^{-3} \exp(-0.75\ \text{eV}/kT)\ \text{cm}^2/\text{s}$ [243], while the diffusion coefficient to Si–adatom migration perpendicular to the dimer rows was found to be $D_\perp = 4.8 \times 10^{-3} \exp(-1.2\ \text{eV}/kT)\ \text{cm}^2/\text{s}$ [246].

Several other quantitative results have been reported earlier. Toh and Ong [244] estimated the effective activation energy for the quasi-one-dimensional motion to be 0.325 eV. Brocks *et al.* [242] obtained 0.6 eV for the migration along the dimer rows (the same value was also reported by Miyazaki *et al.* [238]) and 1.0 eV across the rows. Huang and Allen [241] considered the diffusion of Si adatoms and dimers on a Si(100) surface. The determined

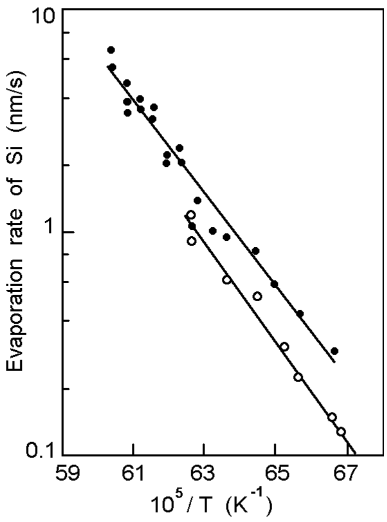

Fig 14. Evaporation rate of Si versus reciprocal temperature. Closed circles represent the data of Ref. [253], open circles the data of Ref. [254]. (*Reproduced by permission of Elsevier Science Publishers BV*)

diffusion barrier for an isolated adatom (~ 1.2 eV) appeared to be about 0.5 eV lower than that for dimer diffusion.

As compared to the recent activity in the theoretical treatment of a Si surface diffusion on Si(100), there is little experimental information [247–252]. In an early work of Gavriljuk *et al.* [247], the mass transport during smoothing off the Si(100) surface roughness upon annealing at 1050–1200 °C was studied by means of a light-scattering technique. The activation energy (~ 2.2 eV) determined in Ref. [247] for surface self-diffusion is believed to be overestimated. The authors suggested that this value includes the energy for Si adatom formation and the energy for Si adatom migration.

In recent works by Mo *et al.* [248–251], the self-diffusion of Si adatoms was investigated by STM analysis of the number density of stable islands formed during submonolayer Si deposition at 75–300 °C. The results confirmed that the diffusion is highly anisotropic with "fast direction" along the dimer rows. The determined values (an activation energy of 0.67 ± 0.08 eV and a prefactor of $\sim 10^{-3}$ cm^2/s) is in reasonable agreement with the recent theoretical results of Refs [238, 242, 243].

Elswijk *et al.* [252] also derived the activation energy of Si surface diffusion from the STM data of Si homoepitaxial growth on Si(100) but obtained the value of 1.15 ± 0.1 eV.

4.2. Si DESORPTION

The most recent publication on the evaporation of silicon is the work of Souchiere and Vu Thien Binh [253], in which the evaporation rate of Si has been determined, under well-controlled experimental conditions, directly from sample geometry variations, and the data obtained have been compared with the previously reported results.

Souchiere and Vu Thien Binh [253] found that, for the temperature range between 1225 and 1390 °C, the evaporation rate does not depend on a sample orientation and is described by an Arrhenius-type relation, $1.21 \times 10^6 \exp(-4.10 \text{ eV}/kT)$ cm/s. The plot of this dependence is shown in Fig. 14 in comparison with the data of the weight loss measurements of the early work of Batdorf and Smits [254]. In the latter work and several other publications, the activation energy of Si sublimation has been reported to be 4.55 eV [254], 4.30 eV [255], 4.56 eV [256], all values being in good agreement with the result of Ref. [253].

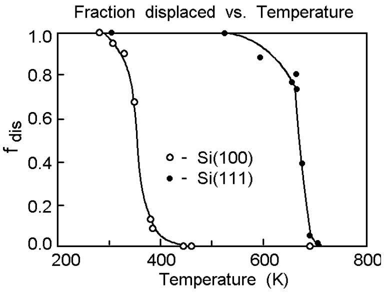

Fig 15. Ion channeling yields versus growth temperature of 300-Å Si films grown on Si(100) and Si(111) at a rate of 0.3 Å/s (from Ref. [265]). (*Reproduced by permission of American Institute of Physics*)

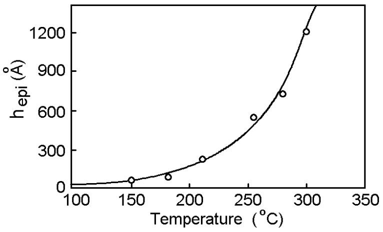

Fig 16. Temperature dependence of the limited epitaxial thickness h_{epi} for Si deposition on to Si(100) at a rate of 0.7 Å/s (from Ref. [264]). (*Reproduced by permission of Elsevier Science Publishers BV*)

4.3. Si MOLECULAR BEAM EPITAXY

When Si is deposited in ultra-high vacuum on to the atomically clean Si crystalline surfaces heated to a suitable temperature, the growth of epitaxial Si film occurs. This method of epitaxial growth is known as Si molecular beam epitaxy (Si–MBE) and the minimal temperature required for the epitaxial growth is defined as epitaxial temperature (T_{epi}). The determination of the epitaxial temperature is the fundamental question of the Si MBE growth and also attracts interest for the purposes of application of MBE as a low-temperature device fabrication process [257–266].

The epitaxial temperature was found to differ for different surfaces. For the Si(100) surface, T_{epi} is $\sim 350\,^{\circ}\mathrm{C}$ lower than that for the Si(111) surface. This result is illustrated by Fig. 15 which shows the temperature dependence of the fraction of disordered atoms determined in He^{+} ion channeling measurements for thin Si films grown on Si(100) and Si(111) substrates. The difference in the behavior of these two surfaces was interpreted as a consequence of the different nature of their surface structures [259, 265]. While Si atoms deposited on to the Si(111) surface tend to occupy "adatom" or "faulted" sites (that are not a continuation of the bulk crystal structure), Si atoms arriving on to Si(100) surface have the possibility to relax directly into bulk-like epitaxial sites [265].

Recently, Eaglesham *et al.* [264] have pointed out that the notion of a T_{epi} is not appropriate in a description of the transition from the growth of amorphous film towards the growth of epitaxial film. They have demonstrated that there is rather a limiting thickness h_{epi} for epitaxial film, beyond which the amorphous phase nucleates. For Si MBE on Si(100), the epitaxial thickness is 10–30 Å at room temperature and increases rapidly at higher temperatures (see Fig. 16). The activation energy deduced from the Arrhenius plot of $\ln(h_{\mathrm{epi}})$ versus $1/T$ was found to be rate-dependent and changes from 0.4 to 1.5 eV with the increase of growth rate from 0.7 Å/s to 11 Å/s [264].

The nature of the limited thickness epitaxy has not been determined conclusively hitherto: while Jorke *et al.* [263] proposed a model based on a continuous build-up of disorder in the

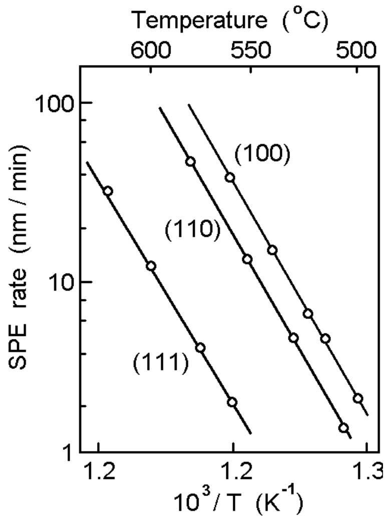

Fig 17. Temperature dependence of the SPE rate for (100), (110), and (111) Si substrate orientations (from Ref. [273]). (*Reproduced by permission of Elsevier Science Publishers BV*)

growing film, Eaglesham *et al.* [264] and Maki *et al.* [267] suggested that the surface roughness built up during the early stages of growth plays a central role in nucleating the amorphous phase.

4.4. AMORPHOUS Si OVERGROWTH AND Si SOLID PHASE EPITAXY

In recent publications of Gibson *et al.* [268] and Sakai *et al.* [269], it was reported that the 7×7 reconstruction of the Si(111) surface (i.e. the vacuum–solid interface) preserves upon RT Si deposition (i.e. at the buried solid–solid interface). The 7 × 7 structure is, however, modified by the disappearance of the adatoms and the ordering of two layers on the amorphous Si side of the interface [270, 271]. In contrast, the Si(100)2 × 1 reconstruction is not preserved after amorphous Si deposition [268].

If the amorphous Si film on the Si crystalline surface is heated to a temperature of about 500–600 °C, it crystallizes epitaxially in a solid phase epitaxial (SPE) regime. SPE growth proceeds mainly by translation of the amorphous–crystalline interface from the substrate to the outer surface of the film. (However, it also involves certain lateral growth and rearrangement of domains of different reconstructions at the final stage of crystallization [73].)

Gibson *et al.* [268] reported that in the case of the Si(111)7×7 substrate, if the amorphous–crystalline interface is moved nominally 15 Å, the 7 × 7 periodicity is removed. The result of the TEM study of Sakai *et al.* [272] showed that transformation from a 7×7 to 1×1 structure proceeds laterally through a modification of the dimer structure prior to the vertical SPE growth of amorphous Si.

The rate of interface motion (SPE rate) is very sensitive to the substrate orientation which means that the atomic configuration of the amorphous–crystalline interface plays a dominant role in the SPE growth. The SPE growth rate is the highest in (100) samples and is about 2 and 20 times that in (110) and (100) samples respectively. However, the activation energy is the same (∼ 3 eV) for all samples (Fig. 17).

The structural perfection of the grown epitaxial films is also strongly dependent on the orientation of the underlying substrate as one can see in Fig. 18. While the Si films SPE grown on Si(111) are faulted, the epitaxial films grown on Si(100) exhibit good crystalline quality comparable with that of the perfect single-crystalline Si substrate [273].

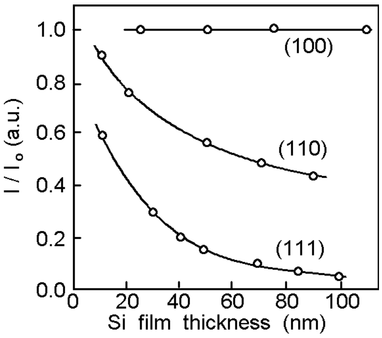

Fig 18. Structural perfection of the films determined from LEED intensity data versus film thickness. The annealing temperature is 600 °C (from Ref. [273]). (*Reproduced by permission of Elsevier Science Publishers BV*)

REFERENCES

[1] D. Haneman, *Rep. Prog. Phys.* **50** (1987) 1045.
[2] V. Yu. Aristov, I. E. Batov and V. A. Grazhulis, *Surf. Sci.* **132** (1983) 73.
[3] M. Sacchi, M. Sancrotti, O. Sakho and G. Rossi, Appl. *Surf. Sci.* **56–58** (1992) 563.
[4] J. J. Lander, G. W. Gobeli and J. Morrison, *J. Appl. Phys.* **34** (1963) 2298.
[5] M. Erbudak and T. E. Fischer, *Phys. Rev. Lett.* **29** (1972) 732.
[6] F. Bauerle, W. Monch and M. Henzler, *J. Appl. Phys.* **43** (1972) 3917.
[7] M. Henzler, *Surf. Sci.* **36** (1973) 109.
[8] J. E. Rowe and J. C. Phillips, *Phys. Rev. Lett.* **32** (1974) 1315.
[9] P. P. Auer and W. Monch, *Surf. Sci.* **80** (1979) 45.
[10] D. Haneman and A. A. Chernov, *Surf. Sci.* **215** (1989) 135.
[11] R. I. G. Uhrberg, E. Landemark and L. S. O. Johansson, *Phys. Rev. B* **39** (1989) 13525.
[12] D. Haneman, J. J. Rownd and M. G. Lagally, *Surf. Sci.* **224** (1989) L965.
[13] B. Garni, D. E. Savage and M. G. Lagally, *Surf. Sci.* **235** (1990) L324.
[14] R. M. Feenstra and M. A. Lutz, *Phys. Rev. B* **42** (1990) 5391.
[15] R. M. Feenstra and M. A. Lutz, *Surf. Sci.* **243** (1991) 151.
[16] R. M. Feenstra and M. A. Lutz, *J. Vac. Sci. Technol. B* **9** (1991) 716.
[17] I. Ohdomari, *Surf. Sci.* **227** (1990) L125.
[18] I. Ohdomari, *Surf. Sci.* **271** (1992) 170.
[19] I. Ohdomari, Appl. *Surf. Sci.* **56–58** (1992) 20.
[20] J. J. Lander, *Surf. Sci.* **1** (1964) 125.
[21] J. V. Florio and W. D. Robertson, *Surf. Sci.* **22** (1970) 459.
[22] J. V. Florio and W. D. Robertson, *Surf. Sci.* **24** (1971) 173.
[23] T. Yokotsuka, S. Kono, S. Suzuki and T. Sagawa, *Solid State Commun.* **39** (1981) 1001.
[24] P. A. Bennett and M. B. Webb, *Surf. Sci.* **104** (1981) 74.
[25] M. B. Webb and P. A. Bennett, *J. Vac. Sci. Technol.* **18** (1981) 847.
[26] N. Osakabe, Y. Tanishiro, K. Yagi and G. Honjo, *Surf. Sci.* **97** (1980) 393.
[27] N. Osakabe, K. Yagi and G. Honjo, *Japan J. Appl. Phys.* **19** (1980) L309.
[28] N. Osakabe, Y. Tanishiro, K. Yagi and G. Honjo, *Surf. Sci.* **109** (1981) 353.
[29] Y. Tanishiro, K. Takayanagi and K. Yagi, *Ultramicroscopy* **11** (1983) 95.
[30] E. G. McRae and R. A. Malic, *Surf. Sci.* **161** (1985) 25.
[31] R. J. Phaneuf and E. D. Williams, *Phys. Rev. B* **35** (1987) 4155.
[32] A. B. Latyshev, A. L. Aseev and S. I. Stenin, *Pisma v GETF* **47** (1988) 448.
[33] M. D. Pashley, K. W. Haberern and W. Friday, *J. Vac. Sci. Technol.* A **6** (1988) 488.
[34] W. Telieps and E. Bauer, *Surf. Sci.* **162** (1985) 163.
[35] K. Hricovini, G. Le Lay, M. Abraham and J. E. Bonnet, *Phys. Rev. B* **41** (1990) 1258.
[36] A. V. Latyshev, A. B. Krasilnikov, A. L. Aseev, L. V. Sokolov and S. I. Stenin, *Surf. Sci.* **254** (1991) 90.

[37] H. D. Hagstrum and G. E. Becker, *Phys. Rev. B* **8** (1973) 1580.
[38] W. S. Yang and F. Jona, *Phys. Rev. B* **28** (1983) 1178.
[39] S. Ino, *Japan J. Appl. Phys.* **16** (1977) 891.
[40] H. Iwasaki, S. Hasegawa, M. Akizuki, S. -T. Li, S. Nakamura and J. Kanamori, *J. Phys. Soc. Jap.* **56** (1987) 3425.
[41] D. M. Zehner, C. W. White and G. W. Ownby, *Surf. Sci.* **92** (1980) L67.
[42] D. M. Zehner, C. W. White and G. W. Ownby, *Appl. Phys. Lett.* **36** (1980) 56.
[43] D. M. Zehner, C. W. White and G. W. Ownby, *Appl. Phys. Lett.* **37** (1980) 456.
[44] D. M. Zehner, J. R. Noonan, H. L. Davis and C. W. White, *J. Vac. Sci. Technol.* **18** (1981) 852.
[45] D. E. Eastman, P. Heimann, F. J. Himpsel and B. Reihl, *Phys. Rev. B* **24** (1981) 3647.
[46] D. M. Zehner and C. W. White, *Mat. Res. Soc. Symp. Proc.* **13** (1983) 317.
[47] Y. J. Chabal, J. E. Rowe and D. A. Zwemer, *Phys. Rev. Lett.* **46** (1981) 600.
[48] Y. J. Chabal, J. E. Rowe and S. B. Christman, *Phys. Rev. B* **24** (1981) 3303.
[49] Y. J. Chabal, J. E. Rowe and S. B. Christman, *J. Vac. Sci. Technol.* **20** (1982) 763.
[50] T. de Jong, L. Smit, V. V. Korablev, R. M. Tromp and F. W. Saris, Appl. *Surf. Sci.* **10** (1982) 10.
[51] R. M. Tromp, E. J. Van Loenen, M. Iwami and F. W. Saris, *Solid State Commun.* **44** (1982) 971.
[52] R. J. Nemanich and D. Haneman, *Appl. Phys. Lett.* **40** (1982) 785.
[53] H. Kobayashi, K. Edamoto, M. Onchi and M. Nishijima, *Solid State Commun.* **44** (1982) 1449.
[54] J. M. Moison and M. Bensoussan, *Surf. Sci.* **126** (1983) 294.
[55] G. J. R. Jones and B. W. Holland, *Solid State Commun.* **53** (1985) 45.
[56] F. Jona, P. M. Marcus, H. L. Davis and J. R. Noonan, *Phys. Rev. B* **33** (1986) 4005.
[57] R. J. Phaneuf and E. D. Williams, *Surf. Sci.* **195** (1988) 330.
[58] R. S. Becker, J. A. Golovchenko, G. S. Higashi and B. S. Swartzentruber, *Phys. Rev. Lett.* **57** (1986) 1020.
[59] R. S. Becker, B. S. Swartzentruber, J. S. Vickers and T. Klitsner, *Phys. Rev. B* **39** (1989) 1633.
[60] W. Radlik and H. Neddermeyer, *Surf. Sci.* **195** (1988) 195.
[61] W. C. Fan, A. Ignatiev, H. Huang and S. Y. Tong, *Phys. Rev. Lett.* **62** (1989) 1516.
[62] Th. Berghaus, A. Brodde, H. Neddermeyer and St. Tosch, *Surf. Sci.* **181** (1987) 340.
[63] R. N. Thomas and M. H. Francombe, *Appl. Phys. Lett.* **11** (1967) 108.
[64] R. N. Thomas and M. H. Francombe, *Appl. Phys. Lett.* **11** (1967) 134.
[65] R. N. Thomas and M. H. Francombe, *Appl. Phys. Lett.* **17** (1970) 80.
[66] R. N. Thomas and M. H. Francombe, *Surf. Sci.* **25** (1971) 357.
[67] H. Nakahara and A. Ichimiya, *Surf. Sci.* **241** (1991) 124.
[68] H. Nakahara and A. Ichimiya, *J. Cryst. Growth* **95** (1989) 472.
[69] H. Nakahara and A. Ichimiya, *Surf. Sci.* **242** (1991) 162.
[70] U. K. Kohler, J. E. Demuth and R. J. Hamers, *J. Vac. Sci. Technol.* A **7** (1989) 2860.
[71] R. J. Hamers, U. K. Kohler and J. E. Demuth, *Ultramicroscopy* **31** (1989) 10.
[72] A. Ichimiya, T. Hashizume, K. Ishiyama, K. Motai and T. Sakurai, *Ultramicroscopy* **42–44** (1992) 910.
[73] H. Nakahara and A. Ichimiya, *J. Cryst. Growth* **99** (1990) 514.
[74] F. G. Himpsel, P. M. Marcus, R. Tromp, I. P. Batra, M. R. Cook, F. Jona and H. F. Liu, *Phys. Rev. B* **30** (1984) 2257.
[75] R. Feder and W. Monch, *Solid State Commun.* **50** (1984) 311.
[76] H. Sakama, A. Kawazu and K. Ueda, *Phys. Rev. B* **34** (1986) 1367.
[77] F. J. Himpsel, P. Heimann and D. E. Eastman, *Phys. Rev. B* **24** (1981) 2003.
[78] F. Houzay, G. M. Guichar, R. Pinchaux and Y. Petroff, *J. Vac. Sci. Technol.* **18** (1981) 860.
[79] P. Martensson, G. V. Hansson and P. Chiaradia, *Phys. Rev. B* **31** (1985) 2581.
[80] P. Martensson, A. Cricenti and G. V. Hansson, *Phys. Rev. B* **32** (1985) 6959.

[81] U. Del Pennino, M. G. Betti, C. Mariani, C. M. Bertoni, S. Nannarone, I. Abbati, L. Braicovich and A. Rizzi, *Surf. Sci.* **189–190** (1987) 689.

[82] A. Selloni and R. Del Sole, *Surf. Sci.* **168** (1986) 35.

[83] U. Del Pennino, M. G. Betti, C. Mariani, S. Nannarone, C. M. Bertoni, I. Abbati and A. Rizzi, *Phys. Rev. B* **39** (1989) 10380.

[84] N. J. DiNardo, J. E. Demuth, W. A. Trompson and Ph. Avouris, *Phys. Rev. B* **31** (1985) 4077.

[85] N. J. DiNardo, W. A. Thompson, A. J. Schell-Sorokin and J. E. Demuth, *Phys. Rev. B* **34** (1986) 3007.

[86] M. A. Olmstead and N. M. Amer, *Phys. Rev. B* **33** (1986) 2564.

[87] A. Bianconi, R. Del Sole, A. Selloni, P. Chiaradia, M. Fanfoni and I. Davoli, *Solid State Commun.* **64** (1987) 1313.

[88] P. Chiaradia, A. Cricenti, S. Selci and G. Charotti, *Phys. Rev. Lett.* **52** (1984) 1145.

[89] M. A. Olmstead and N. M. Amer, *Phys. Rev. Lett.* **52** (1984) 1148.

[90] A. Stockhausen, T. U. Kampen and W. Monch, Appl. *Surf. Sci.* **56–58** (1992) 795.

[91] D. Straub, L. Ley and F. G. Himpsel, *Phys. Rev. Lett.* **54** (1985) 142.

[92] M. A. Olmstead, *Surf. Sci. Repts.* **6** (1987) 159.

[93] L. Reining and R. Del Sole, *Phys. Rev. Lett.* **67** (1991) 3816.

[94] R. M. Tromp, L. Smit and J. F. Van der Veen, *Phys. Rev. Lett.* **51** (1983) 1672.

[95] L. Smit, R. M. Tromp and J. F. Van der Veen, *Surf. Sci.* **163** (1985) 315.

[96] R. M. Feenstra, W. A. Thompson and A. P. Fein, *Phys. Rev. Lett.* **56** (1986) 608.

[97] R. M. Feenstra, W. A. Thompson and A. P. Fein, *J. Vac. Sci. Technol. A* **4** (1986) 1315.

[98] J. A. Stroscio, R. M. Feenstra and A. P. Fein, *Phys. Rev. Lett.* **57** (1986) 2579.

[99] J. A. Stroscio, R. M. Feenstra and A. P. Fein, *J. Vac. Sci. Technol. A* **5** (1987) 838.

[100] J. E. Northrup and M. L. Cohen, *Phys. Rev. Lett.* **49** (1982) 1349.

[101] J. E. Northrup and M. L. Cohen, *Phys. Rev. B* **27** (1983) 6553.

[102] E. M. Pearson, T. Halicioglu and W. A. Tiller, *J. Vac. Sci. Technol. A* **5** (1987) 293.

[103] L. Miglio, P. Santini, P. Ruggerone and G. Benedek, *Surf. Sci.* **211–212** (1989) 335.

[104] B. I. Craig and P. V. Smith, *Surf. Sci.* **225** (1990) 225.

[105] O. L. Alerhand, J. D. Joannopoulos and E. J. Mele, *Phys. Rev. B* **39** (1989) 12622.

[106] R. M. Feenstra, *Phys. Rev. B* **44** (1991) 13791.

[107] K. C. Pandey, *Phys. Rev. Lett.* **47** (1981) 1913.

[108] K. C. Pandey, *Phys. Rev. Lett.* **49** (1982) 223.

[109] D. Haneman and M. G. Lagally, *J. Vac. Sci. Technol. B* **6** (1988) 1451.

[110] S. Kohmoto and A. Ichimiya, *Surf. Sci.* **223** (1989) 400.

[111] D. Haneman, *Advances in Phys.* **31** (1982) 165.

[112] K. Takayanagi, Y. Tanishiro, S. Takahashi and M. Takahashi, *Surf. Sci.* **164** (1985) 367.

[113] W. A. Harrison, *Surf. Sci.* **55** (1976) 1.

[114] H. Huang, S. Y. Tong, W. E. Packard and M. B. Webb, *Phys. Lett. A* **130** (1988) 166.

[115] R. J. Culbertson, L. C. Feldman and P. J. Silverman, *Phys. Rev. Lett.* **45** (1980) 2043.

[116] G. Binning, H. Rohrer, Ch. Gerber and E. Weibel, *Phys. Rev. Lett.* **50** (1983) 120.

[117] F. J. Himpsel, *Phys. Rev. B* **27** (1983) 7782.

[118] E. G. McRae, *Phys. Rev. B* **28** (1983) 2305.

[119] P. A. Bennett, L. C. Feldman, Y. Kuk, E. G. McRae and J. E. Rowe, *Phys. Rev. B* **28** (1983) 3656.

[120] I. K. Robinson and E. Vlieg, *Surf. Sci.* **261** (1992) 123.

[121] S. Y. Tong, H. Huang, C. M. Wei, W. E. Packard, F. K. Men, G. S. Glander and M. B. Webb, *J. Vac. Sci. Technol. A* **6** (1988) 615.

[122] A. Ichimiya, *Surf. Sci.* **192** (1987) L893.

[123] Y. Horio and A. Ichimiya, *Surf. Sci.* **219** (1989) 128.

[124] S. M. Durbin, L. E. Berman, B. W. Batterman and J. M. Blakely, *Phys. Rev. Lett.* **56** (1986) 236.

[125] I. K. Robinson, *J. Vac. Sci. Technol. A* **6** (1988) 1966.
[126] G. -X. Qian and D. J. Chadi, *J. Vac. Sci. Technol. B* **4** (1986) 1079.
[127] G. -X. Qian and D. J. Chadi, *Phys. Rev. B* **35** (1987) 1288.
[128] J. Yanagisawa and A. Yoshimori, *Surf. Sci.* **231** (1990) 297.
[129] T. Yamaguchi, *Phys. Rev. B* **31** (1985) 5297.
[130] K. Takayanagi and Y. Tanishiro, *Phys. Rev. B* **34** (1986) 1034.
[131] D. Vanderbilt, *Phys. Rev. B* **36** (1987) 6209.
[132] G. B. Adams and O. F. Sankey, *Phys. Rev. Lett.* **67** (1991) 867.
[133] D. J. Chadi, *Phys. Rev. Lett.* **59** (1987) 1691.
[134] D. J. Chadi, *Ultramicroscopy* **31** (1989) 1.
[135] R. Kaplan, *Surf. Sci.* **93** (1980) 145.
[136] B. Z. Olshanetsky and A. A. Shklyaev, *Surf. Sci.* **82** (1979) 445.
[137] N. Inoue and K. Yagi, *Appl. Phys. Lett.* **55** (1989) 1400.
[138] R. D. Bringans, R. I. G. Uhrberg, M. A. Olmstead and R. Z. Bachrach, *Phys. Rev. B* **34** (1986) 7447.
[139] D. Saloner, J. A. Martin, M. C. Tringides, D. E. Savage, C. E. Aumann and M. G. Lagally, *J. Appl. Phys.* **61** (1987) 2884.
[140] P. E. Wierenga, J. A. Kubby and J. E. Griffith, *Phys. Rev. Lett.* **59** (1987) 2169.
[141] T. Nakayama, Y. Tanishiro and K. Takayanagi, *Japan J. Appl. Phys.* **26** (1987) L280.
[142] C. E. Aumann, D. E. Savage, R. Kariotis and M. G. Lagally, *J. Vac. Sci. Technol. A* **6** (1988) 1963.
[143] J. E. Griffith, J. A. Kubby, P. E. Wierenga, R. S. Becker and J. S. Vickers, *J. Vac. Sci. Technol. A* **6** (1988) 493.
[144] J. E. Griffith, G. P. Kochanski, J. A. Kubby and P. E. Wierenga, *J. Vac. Sci. Technol. A* **7** (1989) 1914.
[145] O. L. Alerhand, A. N. Berker, J. D. Joannopoulos and D. Vanderbilt, *Phys. Rev. Lett.* **64** (1990) 2406.
[146] K. Sakamoto, T. Sakamoto, K. Miki and S. Nagao, *J. Electrochem. Soc.* **136** (1989) 2705.
[147] Miguel J. J. De, C. E. Aumann, R. Kariotis and M. G. Lagally, *Phys. Rev. Lett.* **67** (1991) 2830.
[148] J. J. Demiguel, C. E. Aumann, S. G. Jaloviar, R. Kariotis and M. G. Lagally, *Phys. Rev. B* **46** (1992) 10257.
[149] C. E. Aumann, J. J. Demiguel, R. Kariotis and M. G. Lagally, *Surf. Sci.* **275** (1992) 1.
[150] T. Sakamoto and G. Hashiguchi, *Japan J. Appl. Phys.* **25** (1986) L78.
[151] N. Inoue, Y. Tanishiro and K. Yagi, *Japan J. Appl. Phys.* **26** (1987) L293.
[152] T. Nakayama, Y. Tanishiro and K. Takayanagi, *Japan J. Appl. Phys.* **26** (1987) L1186.
[153] A. V. Latyshev, A. L. Aseev, A. B. Krasilnikov and S. I. Stenin, *Surf. Sci.* **227** (1990) 24.
[154] H. Kahata and K. Yagi, *Japan J. Appl. Phys.* **28** (1989) L858.
[155] N. Aizaki and T. Tatsumi, *Surf. Sci.* **174** (1986) 658.
[156] K. Sakamoto, K. Miki and T. Sakamoto, *Thin Solid Films* **183** (1989) 229.
[157] A. J. Hoeven, E. J. Van Loenen, D. Dijkkamp, J. M. Lenssinck and J. Dieleman, *Thin Solid Films* **183** (1989) 263.
[158] A. J. Hoeven, D. Dijkkamp, E. J. Van Loenen, J. M. Lenssinck and J. Dieleman, *J. Vac. Sci. Technol. A* **8** (1990) 207.
[159] C. Roland and G. H. Gilmer, *Phys. Rev. B* **46** (1992) 13437.
[160] F. K. Men, W. E. Packard and M. B. Webb, *Phys. Rev. Lett.* **61** (1988) 2469.
[161] J. Ihm, D. H. Lee, J. D. Joannopoulos and J. J. Xiong, *Phys. Rev. Lett.* **51** (1983) 1872.
[162] A. Saxena, E. T. Gawlinski and J. D. Gunton, *Surf. Sci.* **160** (1985) 618.
[163] T. Tabata, T. Aruga and Y. Murata, *Surf. Sci.* **179** (1987) L63.
[164] J. J. Lander and J. Morrison, *J. Chem. Phys.* **37** (1962) 729.

[165] R. E. Weber and W. T. Peria, *J. Appl. Phys.* **38** (1967) 4355.
[166] T. D. Poppendieck, T. C. Ngoc and M. B. Webb, *Surf. Sci.* **75** (1978) 287.
[167] M. J. Cardillo and G. E. Becker, *Phys. Rev. Lett.* **40** (1978) 1148.
[168] M. J. Cardillo and G. E. Becker, *Phys. Rev. B* **21** (1980) 1497.
[169] M. J. Cardillo and W. R. Lambert, *Surf. Sci.* **168** (1986) 724.
[170] Y. Enta, S. Suzuki and S. Kono, *Phys. Rev. Lett.* **65** (1990) 2704.
[171] R. M. Tromp, R. J. Hamers and J. E. Demuth, *Phys. Rev. Lett.* **55** (1985) 1303.
[172] R. J. Hamers, R. M. Tromp and J. E. Demuth, *Phys. Rev. B* **34** (1986) 5343.
[173] R. J. Hamers, R. M. Tromp and J. E. Demuth, *Surf. Sci.* **181** (1987) 346.
[174] K. Kato, T. Ide, T. Nishimori and T. Ichinokawa, *Surf. Sci.* **207** (1988) 177.
[175] T. Sakamoto, T. Takahashi, E. Suzuki, A. Shoji, H. Kawanami, Y. Komiya and Y. Tarui, *Surf. Sci.* **86** (1979) 102.
[176] H. -C. Wang, R. -F. Lin and X. Wang, *Phys. Rev. B* **36** (1987) 7712.
[177] S. M. Mokler, W. K. Liu, N. Ohtani and B. A. Joyce, *Appl. Phys. Lett.* **58** (1991) 3419.
[178] W. K. Liu, S. M. Mokler, N. Ohtani, C. Roberts and B. A. Joyce, *Surf. Sci.* **264** (1992) 301.
[179] T. Ide and T. Mizutani, *Phys. Rev. B* **45** (1992) 1447.
[180] R. I. G. Uhrberg, J. E. Northrup, D. K. Biegelsen, R. D. Bringans and L. E. Swartz, *Phys. Rev. B* **46** (1992) 10251.
[181] R. E. Schlier and H. E. Farnsworth, *J. Chem. Phys.* **30** (1959) 917.
[182] D. J. Chadi, *Phys. Rev. Lett.* **43** (1979) 43.
[183] M. T. Yin and M. L. Cohen, *Phys. Rev. B* **24** (1981) 2303.
[184] J. Ihm, M. L. Cohen and D. J. Chadi, *Phys. Rev. B* **21** (1980) 4592.
[185] R. M. Tromp, R. G. Smeenk, F. W. Saris and D. J. Chadi, *Surf. Sci.* **133** (1983) 137.
[186] H. H. Farrell, F. Stucki, J. Anderson, D. J. Frankel, G. J. Lapeyre, and M. Levinson, *Phys. Rev. B* **30** (1984) 721.
[187] F. F. Abraham and I. P. Batra, *Surf. Sci.* **163** (1985) L752.
[188] O. L. Alerhand and E. J. Mele, *Phys. Rev. B* **35** (1987) 5533.
[189] S. Aduru and J. W. Rabalais, *Surf. Sci.* **205** (1988) 269.
[190] C. K. Ong and B. C. Chan, *J. Phys. :Cond. Matt.* **1** (1989) 3931.
[191] A. Mazur and J. Pollmann, *Surf. Sci.* **225** (1990) 72.
[192] N. Jedrecy, M. Sauvage-Simkin, R. Pinchaux, J. Massies, N. Greiser and V. H. Etgens, *Surf. Sci.* **230** (1990) 197.
[193] E. Landemark, C. J. Karlsson, Y. C. Chao and R. I. G. Uhrberg, *Phys. Rev. Lett.* **69** (1992) 1588.
[194] R. A. Wolkow, *Phys. Rev. Lett.* **68** (1992) 2636.
[195] L. S. O. Johansson and B. Reihl, *Surf. Sci.* **269–270** (1992) 810.
[196] G. K. Wertheim, D. M. Riffe, L. E. Rowe and P. H. Citrin, *Phys. Rev. Lett.* **67** (1991) 120.
[197] J. Dabrowski and M. Scheffler, Appl. *Surf. Sci.* **56–58** (1992) 15.
[198] H. Kageshima and M. Tsukada, *Phys. Rev. B* **46** (1992) 6928.
[199] A. Redondo and W. A. Goddard III, *J. Vac. Sci. Technol.* **21** (1982) 344.
[200] K. E. Khor and S. D. Das Sarma, *Phys. Rev. B* **36** (1987) 7733.
[201] E. Artacho and F. Yndurian, *Phys. Rev. Lett.* **62** (1989) 2491.
[202] L. S. O. Johansson, R. I. G. Uhrberg, P. Martensson and G. V. Hansson, *Phys. Rev. B* **42** (1990) 1305.
[203] S. Tang, A. J. Freeman and B. Delley, *Phys. Rev. B* **45** (1992) 1776.
[204] T. Hoshino, S. Oikawa, M. Tsuda and I. Ohdomari, *Phys. Rev. B* **44** (1991) 11248.
[205] M. Tsuda, T. Hoshino, S. Oikawa and I. Ohdomari, *Phys. Rev. B* **44** (1991) 11241.
[206] R. Wiesendanger, D. Burgler, G. Tarrach, H. -J. Guntherodt, I. V. Shvets and J. M. D. Coey, *Surf. Sci.* **274** (1992) 93.
[207] P. C. Weakliem, G. W. Smith and E. A. Carter, *Surf. Sci.* **232** (1990) L219.
[208] P. Badziag, W. S. Verwoerd and M. A. Van Hove, *Phys. Rev. B* **43** (1991) 2058.

[209] Greg P. Kochanski and Joseph E. Griffith, *Surf. Sci.* **249** (1991) L293.
[210] K. Watanabe and K. Watanabe, *J. Phys. Soc. Jap.* **61** (1992) 419.
[211] F. Jona, *IBM J. Res. Dev.* **9** (1965) 375.
[212] B. Z. Olshanetsky and A. A. Shklyaev, *Surf. Sci.* **67** (1977) 581.
[213] T. Ichinokawa, H. Ampo, S. Miura and A. Tamura, *Phys. Rev. B* **31** (1985) 5183.
[214] Y. Yamamoto, S. Ino and T. Ichikawa, *Japan J. Appl. Phys.* **25** (1986) L331.
[215] B. A. Nesterenko, A. V. Brovii and A. I. Sorokovykh, *Surf. Sci.* **171** (1986) 495.
[216] R. S. Becker, B. S. Swartzentruber and J. S. Vickers, *J. Vac. Sci. Technol. A* **6** (1988) 472.
[217] H. Ampo, S. Miura, K. Kato, Y. Ohkawa and A. Tamura, *Phys. Rev. B* **34** (1986) 2329.
[218] B. A. Nesterenko, Appl. *Surf. Sci.* **33–34** (1988) 21.
[219] T. Oyama, S. Ohi, A. Kawazu and G. Tominaga, *Surf. Sci.* **109** (1981) 82.
[220] Y. Yamamoto, *Japan J. Appl. Phys.* **31** (1992) 2544.
[221] Y. Ishikawa, Y. Hosokawa, I. Hagaguchi and T. Ichinokawa, *Surf. Sci.* **187** (1987) L606.
[222] T. Ichinokawa, N. Yamagami, H. Ampo and A. Tamura, *Phys. Rev. B* **28** (1983) 6151.
[223] Y. Yamamoto, T. Sueyoshi, T. Sato and M. Iwatsuki, *Japan J. Appl. Phys.* **32** (1993) L532.
[224] P. L. Cowan and J. A. Golovchenko, *J. Vac. Sci. Technol.* **17** (1980) 1197.
[225] A. J. Hoeven, D. Dijkkamp, E. J. Van Loenen and P. J. G. M. Van Hooft, *Surf. Sci.* **211–212** (1989) 165.
[226] Y. Yamamoto, S. Kitamura and M. Iwatsuki, *Japan J. Appl. Phys.* **31** (1992) L635.
[227] E. J. Van Loenen, D. Dijkkamp and A. J. Hoeven, *J. Microscopy* **152** (1988) 487.
[228] Y. Yamamoto, T. Sueyoshi, T. Sato and M. Iwatsuki, *Japan J. Appl. Phys.* **32** (1993) 1808.
[229] F. G. Allen and E. Kasper, in *Silicon Molecular Beam Epitaxy*, vol. 1, Eds. E. Kasper and J. C. Bean (CRC Press, Boca Raton, FL, 1988) p. 65.
[230] S. M. Bedair, *Surf. Sci.* **42** (1974) 595.
[231] M. Ishikawa and T. Doi, *Appl. Phys. Lett.* **50** (1987) 1141.
[232] R. F. C. Farrow, *J. Electrochem. Soc.* **121** (1974) 899.
[233] E. Kasper, *Appl. Phys. A* **28** (1982) 129.
[234] P. Ashu, C. C. Matthai and T. -H. Shen, *Surf. Sci.* **251–252** (1991) 955.
[235] P. M. Agrawal, D. L. Thompson and L. M. Raff, *J. Chem. Phys.* **91** (1989) 6463.
[236] I. NoorBatcha, L. M. Raff and D. L. Thompson, *J. Chem. Phys.* **81** (1984) 3715.
[237] S. Stoyanov, *J. Cryst. Growth* **94** (1989) 751.
[238] T. Miyazaki, H. Hiramoto and M. Okazaki, *Japan J. Appl. Phys.* **29** (1990) L1165.
[239] Z. Zhang, Y. -T. Lu and H. Metiu, *Surf. Sci.* **248** (1991) L250.
[240] Y. -T. Lu, Z. Zhang and H. Metiu, *Surf. Sci.* **257** (1991) 199.
[241] Z. -H. Huang and R. E. Allen, *J. Vac. Sci. Technol. A* **9** (1991) 876.
[242] G. Brocks, P. J. Kelly and R. Car, *Phys. Rev. Lett.* **66** (1991) 1729.
[243] D. Srivastava and B. J. Garrison, *J. Chem. Phys.* **95** (1991) 6885.
[244] C. P. Toh and C. K. Ong, *Phys. Rev. B* **45** (1992) 11120.
[245] C. Roland and G. H. Gilmer, *Phys. Rev. B* **46** (1992) 13428.
[246] D. Srivastava and B. J. Garrison, *Phys. Rev. B* **46** (1992) 1472.
[247] Yu. L. Gavriljuk, Y. S. Kaganovskii, V. G. Lifshits, *Kristallographiya* **26** (1981) 561.
[248] Y. M. Mo, R. Kariotis, B. S. Swartzentruber, M. B. Webb and M. G. Lagally, *J. Vac. Sci. Technol. A* **8** (1990) 201.
[249] Y. W. Mo, J. Kleiner, M. B. Webb and M. G. Lagally, *Phys. Rev. Lett.* **66** (1991) 1998.
[250] Y. -W. Mo and M. G. Lagally, *Surf. Sci.* **248** (1991) 313.
[251] Y. -W. Mo, J. Kleiner, M. B. Webb and M. G. Lagally, *Surf. Sci.* **268** (1992) 275.
[252] H. B. Elswijk, A. J. Hoeven, E. J. van Loenen and D. Dijkkamp, *Appl. Phys. Lett.* **9** (1991) 451.
[253] J. L. Souchiere and Vu Thien Binh, *Surf. Sci.* **168** (1986) 52.

[254] R. L. Batfdorf and F. M. Smits, *J. Appl. Phys.* **30** (1959) 259.

[255] J. Drowart, G. De Maria and M. G. Inghram, *J. Chem. Phys.* **29** (1958) 1015.

[256] S. Kono, L. J. Hanekamp and A. Van Silfhout, *Surf. Sci.* **65** (1977) 633.

[257] F. Jona, *Appl. Phys. Lett.* **9** (1966) 235.

[258] T. de Jong, W. R. S. Douma, L. Smit, V. V. Korablev and F. W. Saris, *J. Vac. Sci. Technol. B* **1** (1983) 888.

[259] H. -J. Gossmann and L. C. Feldman, *Appl. Phys. A* **38** (1985) 171.

[260] H. Jorke, H. Kibbel, F. Schaffler, A. Casel, H. -J. Herzog and E. Kasper, *J. Cryst. Growth* **95** (1989) 484.

[261] H. Jorke, H. Kibbel, F. Schafler and H. -J. Herzog, *Thin Solid Films* **183** (1989) 307.

[262] H. Jorke, H. Kibbel, F. Schaffler, A. Casel, H. -J. Herzog and E. Kasper, *Appl. Phys. Lett.* **54** (1989) 819.

[263] H. Jorke, H. -J. Herzog and H. Kibbel, *Phys. Rev. B* **40** (1989) 2005.

[264] D. J. Eaglesham, H. -J. Gossmann, M. Cerullo, L. N. Pfeiffer and K. W. West, *J. Cryst. Growth* **111** (1991) 833.

[265] R. L. Headrick, B. E. Weir, A. F. J. Levi, B. S. Freer, J. Bevk and L. C. Feldman, *J. Vac. Sci. Technol. A* **9** (1991) 2269.

[266] D. J. Eaglesham, H. -J. Gossmann and M. Cerullo, *Phys. Rev. Lett.* **65** (1990) 1227.

[267] K. Maki, Y. Shigeta and T. Kuroda, *J. Cryst. Growth* **115** (1991) 567.

[268] J. M. Gibson, H. -J. Gossmann, J. C. Bean, R. T. Tung and L. C. Feldman, *Phys. Rev. Lett.* **56** (1986) 355.

[269] A. Sakai, T. Tatsumi and K. Ishida, *Surf. Sci.* **224** (1989) L956.

[270] I. K. Robinson, W. K. Waskiewicz, R. T. Tung and J. Bohr, *Phys. Rev. Lett.* **57** (1986) 2714.

[271] I. K. Robinson, *Phys. Rev. B* **35** (1987) 3910.

[272] A. Sakai, T. Tatsumi, I. Hirosawa, H. Ono and K. Ishida, *Surf. Sci.* **249** (1991) L300.

[273] A. V. Zotov and V. V. Korobtsov, *J. Cryst. Growth* **98** (1989) 519.

[274] R. D. Meade and D. Vanderbilt, *Phys. Rev. B* **40** (1989) 3905.

[275] W. S. Yang and R. G. Zhao, in *Asia Pacific Symposium on Surface Physics*, Ed. Xie Xide (World Scientific, Singapore, 1987) p. 36.

[276] Z. C. Wu and J. Schowalter, *J. Vac. Sci. Technol. B* **6** (1988) 1457.

4. Adsorbates on Silicon Surfaces

(Ag)

SILVER

1. (111) ORIENTATION

Ag is known to induce several reconstructions on the Si(111) surface, namely, 2×1, 1×1, $\sqrt{7} \times \sqrt{7}$, 3×1, 6×1, $\delta(7 \times 7)$, $\sqrt{3} \times \sqrt{3}$.

1.1. PHASE DIAGRAM

1.1.1. Growth on the Cleaved Si(111)2×1 Surface

Initial stages of Ag adsorption on to the Si(111)2×1 surface have been investigated by LEED, AES [1–8], UPS [4], PES [9] and PYS [5,7].

At RT it had been established [3,4] that the growth of Ag on Si(111)2×1 proceeds basically in a layer-by-layer-like fashion (Frank–van der Merve mechanism) or Stranski–Krastanov mechanism with very flat islands. However, low temperature experiments [1] confirm the Stranski–Krastanov growth mode at RT. In accordance with the observation of Iwami *et al.* [9] Ag islands formation starts above 0.7 ML.

RT growth

At RT on a cleaved Si(111) surface Ag induces a large variety of LEED patterns corresponding to structures Si(111)2×1, Si(111)1×1, Si(111)$\sqrt{7}\times\sqrt{7}$—$R\pm19.1^\circ$, three-domain Si(111)3×1, and Ag(111)1×1. Bolmont *et al.* [5] were the first to report the formation of an ordered silver overlayer exhibiting a $\sqrt{7}\times\sqrt{7}$—$R\pm19.1^\circ$ LEED structure superposed on the remaining 2×1 pattern of the reconstructed silicon. $\sqrt{7} \times \sqrt{7}$ starts to develop at a coverage of about 0.3 ML [5]. The sharpest diagrams were obtained at coverages slightly below $\theta = 1$ ML ($\theta \simeq 2/3$ ML in Refs [5,7] and $\theta \simeq 6/7$ ML in Refs [3,4]).

Diffuse three-domain Si(111)3×1–Ag LEED patterns were observed only by Le Lay *et al.* [6] and Grazhulis *et al.* [1,2], while Si(111)1×1 only by Grazhulis *et al.* [1,2]. Si(111)$\sqrt{7}\times\sqrt{7}$—$R\pm19.1^\circ$ had two domains symmetrical about (110) plane. The results of various authors are summarized in Fig. 1. In fact, between about 1 and 2 ML of silver, the four sets of patterns can be observed together, as shown in Fig. 2.

LT Growth

The results of low temperature ($\sim$ 8 K) deposition of Ag on to cleaved Si(111) surface and subsequent heating can be summarized as follows [1]:

(a) At $\theta < 0.4 \div 0.5$ ML, Si(111)2×1 structure remains up to RT, but, at $\theta \geq 0.4 \div 0.5$ ML, an irreversible phase transition of Si(111)$2 \times 1 \rightarrow$ Si(111)1×1 type occurs. The temperature of transition depends on θ and for $\theta \approx 0.5$, 0.7 and 1 ML is 230, 180, and 130 K, respectively.

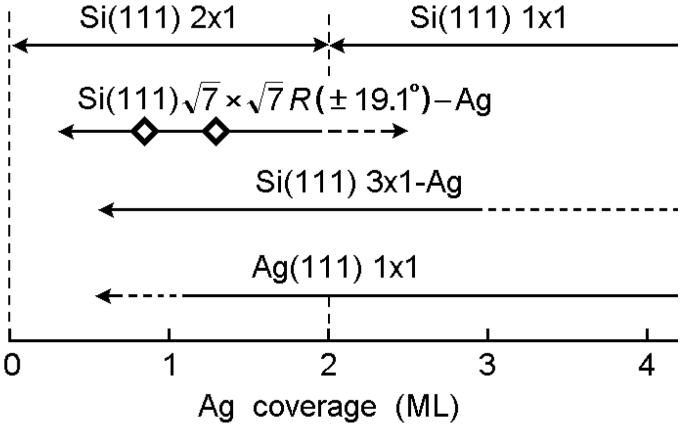

Fig 1. LEED structures of RT deposited Ag on to the Si(111)2 × 1 surface. ◇ denotes the sharpest obtained LEED pattern

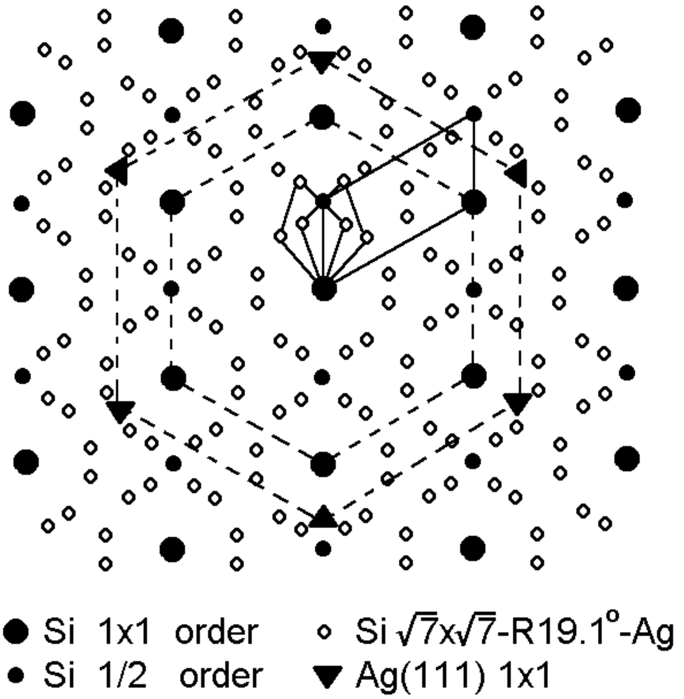

Fig 2. Drawing of the superposed Si(111)2 × 1, Si(111)$\sqrt{7} \times \sqrt{7}$—$R \pm 19.1°$–Ag, Si(111)3 × 1–Ag, Ag(111)1 × 1 LEED diagrams (from Ref. [5]). (*Reproduced by permission of the publishers of Journal of Physical Review B*)

(b) At $0.2 \div 0.3 \leq \theta \leq 1$ ML, for temperatures greater ≈ 130 K, the Si(111)$\sqrt{7} \times \sqrt{7}$—$R \pm 19.1°$–Ag LEED patterns appears.

(c) At $0.7 \leq \theta \leq 3 \div 4$ ML, for temperatures greater ≈ 100 K, the diffuse three-domain Si(111)3 × 1–Ag LEED patterns appear.

(d) At $\theta \geq 0.7$ ML, for temperatures greater ≈ 100 K, the Ag(111)1 × 1 LEED patterns appears.

(e) At $3 \div 4 < \theta < 11$ ML, for $T \geq 100$ K, the Ag(111)1 × 1 structure is observed and, at about 280 K, the appearance of the Si(111)1 × 1 structure occurs.

1.1.2. RT Growth on Si(111)7 × 7

Many of the results imply that the Stranski–Krastanov mode typical for HT growth still occurs at room temperature, though with a large number of thin, flat islands [10–16]. The latter explains the fact that the RT growth of Ag has been considered in a number of papers [4, 6, 17, 18] as following the Frank–Van der Merve growth mode.

The 2D layer was reported to complete at about 2/3 to 1 ML [4, 6, 12, 14–16, 18, 19]. LEED and RHEED observations revealed a vanishing of the 1/7 order spots and increasing of a background at this growth stage. Kohmoto and Ichimiya [19] speculated that the RHEED pattern of the initial 7 × 7 reconstruction changes gradually with Ag adsorption up to about 1/2 ML into another 7×7 pattern, which is similar to $\delta(7\times7)$ patterns observed by adsorption of alkali metals and hydrogen [20, 21].

The appearance of a weak fading $\sqrt{3}\times\sqrt{3}$ pattern was reported by Le Lay *et al.* [4, 6, 18] but it was not confirmed by other investigators.

The Ag clusters forming atop the intermediate 2D layer under further Ag deposition display a Ag (111) texture pattern with considerable azimuthal alignment [4, 6, 12, 14, 18, 22].

The impact-collision ion-scattering spectroscopy results revealed that the epitaxial Ag(111) film grown at RT consists of type A and type B domains of Ag(111), with type B being rotated 180° about the surface normal [22].

1.1.3. HT Growth

The general behavior of Ag deposits on the Si(111) surface is reflected at the schematic phase diagram from Ref. [4] (Fig. 3).

Beyond about 200 °C the growth process of Ag on the Si(111) surface proceeds according to the Stranski–Krastanov mode with nucleation of 3D crystallites after completion of an overlayer which displays a $\sqrt{3}\times\sqrt{3}$—$R30°$ LEED and RHEED pattern [4, 10, 12–15, 17–19, 23–26]. There is no consensus on the coverage at saturation of the $\sqrt{3}\times\sqrt{3}$—$R30°$–Ag surface phase. This value was considered to be 1/3 ML in early works [23, 24] and later various works gave different coverages in the range from 2/3 to 1 ML [4, 10, 12, 14, 18, 19]. Le Lay speculated that the mode of preparation of the clean Si(111)7 × 7 surface has some influence on the completion of the $\sqrt{3}\times\sqrt{3}$—$R30°$ Ag surface phase [4]. Recently Raynerd *et al.* [27, 28] have demonstrated definitely that the coverage of the $\sqrt{3}\times\sqrt{3}$ layer is history dependent. The silver coverage θ was observed to be $\theta\approx1$ ML for deposition temperature

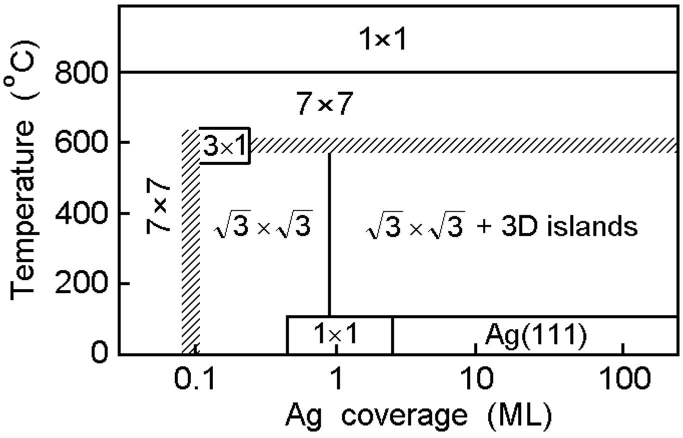

Fig 3. Schematic phase diagram for the Ag/Si(111) interface (from Ref. [4]). (*Reproduced by permission of Elsevier Science Publishers BV*)

$T \geq 700$ K and $\theta \approx 2/3$ for $T \leq 620$ K. STM investigation of the $\sqrt{3} \times \sqrt{3}$ domain growth processes by Ohnishi *et al.* [29] also indicates their dependence upon deposition conditions. After anneal at 350 °C RT deposited Ag, small Ag islands change into $\sqrt{3} \times \sqrt{3}$–Ag domains on the terraces without diffusion of Ag atoms to the step edges. On the other hand, when Ag is deposited on a hot substrate of about 350 °C, the $\sqrt{3} \times \sqrt{3}$–Ag domains nucleate mainly at the step edge. Moreover, two kinds of $\sqrt{3} \times \sqrt{3}$–Ag domains are found in either case: one domain is geometrically higher than the other domain [29].

Bauer and Poppa [24] and Shoji *et al.* [26] reported that Ag adsorption yields initially (i.e. before the appearance of the $\sqrt{3} \times \sqrt{3}$—$R30°$ structure) a 3 × 1 LEED pattern in three equivalent orientations. However, this 3 × 1 structure was more conventionally produced by the heating of the $\sqrt{3} \times \sqrt{3}$—$R30°$ structure in the desorption region ($T \geq 550°$) [4, 14, 15, 18, 19, 25, 26, 30, 31]. The 3 × 1 structure was considered to be completed at 1/3 ML Ag coverage [4, 14, 15, 18].

The 3 × 1–Ag structure is stable at slightly elevated temperatures around 250 °C. Upon cooling below 200 °C, it converts to 6 × 1 structure [14, 15, 30, 32, 33].

1.2. STRUCTURE

1.2.1. Si(111)$\sqrt{3} \times \sqrt{3}$—$R30°$–Ag

Since the first observation of the $\sqrt{3} \times \sqrt{3}$ LEED pattern by Spiegel [23] in 1967, the Si(111)$\sqrt{3} \times \sqrt{3}$—$R30°$–Ag surface has received considerable experimental attention. The atomic geometry of this surface has been studied using a wide variety of surface sensitive probes: AES [3, 4, 12, 14, 27, 28, 34, 35], LEED [3, 12, 14, 15, 36], ISS [14, 22, 35, 37–42], XPD [43–47], RHEED [3, 4, 34, 48, 49], SEXAFS [50,51], PES [12, 47, 52, 53], STM [29, 33, 55–62], XRD [42, 63–67], ISS [11, 68–71], XSW [72], UHV REM [73] and TDS [53]. Despite the abundance of information on the Si(111)$\sqrt{3} \times \sqrt{3}$—$R30°$–Ag structure, to date there is no consensus on the geometric structure of the surface at monolayer and submonolayer coverages of Ag. There are conflicting results in the literature involving both the Ag coverage needed to form a saturated $\sqrt{3} \times \sqrt{3}$ structure and whether the Si substrate reconstruction plays an important role in the formation of the $\sqrt{3} \times \sqrt{3}$ cell [68]. Some studies claim that $\theta = 2/3$ ML, while others have found $\theta = 1$ ML.

The basis for the controversy over the structure of the Si(111)$\sqrt{3} \times \sqrt{3}$—$R30°$–Ag surface may arise from the fact that most techniques are only sensitive to one particular feature of the system: total coverage (AES), local geometric structure (SEXAFS), structure in the perpendicular direction (LEED, RHEED), electronic/geometrical structure of the outermost layer (STM), or in-plane projected surface structure (XRD). The interpretation of results from ISS is strongly model-dependent.

In the past, many models have been proposed for the $\sqrt{3} \times \sqrt{3}$—$R30°$–Ag structure. Neglecting details of the various models, one can distinguish between two classes of competing models [63]. The first one has two Ag atoms, which form a honeycomb, and is completed by a varying number of Si atoms displaced from bulk positions (Ag honeycomb model). The second model consists of three Ag atoms, which form a trimer, has a Si honeycomb on the surface, and may have some additional Si atoms (Si honeycomb model). With the observation of a honeycomb structure on the Si(111)$\sqrt{3} \times \sqrt{3}$—$R30°$–Ag surface by STM [55–58], the discussion on the geometric structure of the $\sqrt{3} \times \sqrt{3}$ unit cell has been focused on these two classes of models. In one STM study, the honeycomb was attributed to Ag (Wilson and Chiang Refs [55, 57, 58]), in the other to Si (Demuth *et al.* Refs [54, 56]). Recently, Katayama *et al.* [70] proposed a modified honeycomb-chained trimer (HCT) model, which is consistent with most of the reported experimental results. Below, we first give a short outline of the earlier proposed models (see Fig. 4), and finally we discuss the modified HCT model.

The first structural models for $\sqrt{3} \times \sqrt{3}$–Ag on Si(111) were suggested from coverage considerations. Spiegel [23] associated this structure with 1/3 ML.

(a) *Simple honeycomb (HC) model* (Fig. 4(a)). Aono *et al.* [39] determined the Ag–Ag interatomic distances in the $\sqrt{3} \times \sqrt{3}$—$R30°$ structure using ICISS and found that the honeycomb arrangement of Ag atoms, first proposed by Le Lay *et al.* [18] takes place based on LEED and AES data. Ag atoms are located above the topmost Si layer. Wilson and Chiang [55, 57, 58] demonstrated that the honeycomb feature observed in STM are registered at threefold hollow sites of the Si(111) surface. TDS data of Markert *et al.* [53] also supported the Ag honeycomb arrangement.

(b) *Missing top layer (MTL) model* (Fig. 4(b)). From a kinematical analysis of the X-ray diffraction patterns Kono *et al.* [45] found that a buried honeycomb framework of Ag atoms is formed on the surface with the first layer Si atoms distorted laterally. The model consists of Ag atoms in the threefold hollow sites of the first Si layer; the longitudinal distance $d_\perp$ is 0.15 ± 0.1 Å below the first Si layer. The first layer Si atoms are contracted toward the center of the hollow of the honeycomb; the lateral distance S of a side of the Si triangle is 2.7 ± 0.2 Å $d_{\mathrm{Ag-Si}} = 2.62 \pm 0.08$ Å [44]. STM results of Wilson and Chiang [55, 57, 58] confirm the location of Ag atoms in the threefold hollow sites of the Si(111) surface.

Recently Bullock *et al.* [43] proposed a new two-domain MTL Ag honeycomb model. In one domain, the Ag atoms of the honeycomb do not have a fourth layer Si atom directly under them, and in the other, they do. The first of these domains is very nearly the structure proposed by Kono *et al.* [45].

(c) *Embedded honeycomb (EHC) model* (Fig. 4(c)). It has been revealed from ISS experiments by Saitoh *et al.* [14, 35] that the silver atoms form honeycombs, and are slightly embedded in the threefold hollows below the first and above the second layer. The LEED/CMTA method applied to the Si(111)$\sqrt{3} \times \sqrt{3}$—$R30°$–Ag structure shows that the Ag layer is embedded by 0.7 Å while the separation between the second and third Si layers is contracted by 1.05 Å [15, 36]. The distance between Ag and Si is 2.48 ± 0.04 Å as determined by SEXAFS by Stöhr *et al.* [51].

(d) *Trimer (T) model* (Fig. 4(d)). Trimer model was proposed by Wehking *et al.* [12] from the coverage consideration, and later was confirmed from the ARUPS and surface-core level chemical shifts data by Hansson *et al.* [52]. Using the technique of the ICISS, Sumitomo *et al.* [22] showed that the Ag-trimer (as well as HCT) model, residing on top of Si, is more likely.

(e) *Substitutional trimer (ST) model* (Fig. 4(e)). From the RHEED intensity analysis Horio and Ichimiya [34, 49] proposed the ST model. The silver atoms are embedded below the silicon topmost layer of about 0.25 ± 0.05 Å and the $\sqrt{3} \times \sqrt{3}$—$R30°$–Ag surface structure is accomplished at $\theta \approx 1$ ML.

CITS was used to examine possible model structures for the $\sqrt{3} \times \sqrt{3}$—$R30°$–Ag structure by Demuth *et al.* [54,56]. Support was found for a structure composed of Ag trimers embedded below the top layer of threefold coordinated Si atoms. Using the technique of ICISS Porter *et al.* [37,38] showed that the separation of the Si and Ag layers is 0.7 ± 0.3 Å and the Si–Ag bond length is 2.66 ± 0.3 Å.

(f) *Honeycomb chained trimer (HCT) model* (Fig. 4(f)). Based on X-ray intensity versus energy curves measured both for the integral- and fractional-order spots Takahashi *et al.* [64] proposed a modified trimer model with three Ag atoms in the $\sqrt{3} \times \sqrt{3}$ unit cell, in which triangles made of Ag atoms are chained in a honeycomb arrangement. The distance between the nearest neighbor Ag atoms (3.39 Å) are about twice the van der Waals radius. The

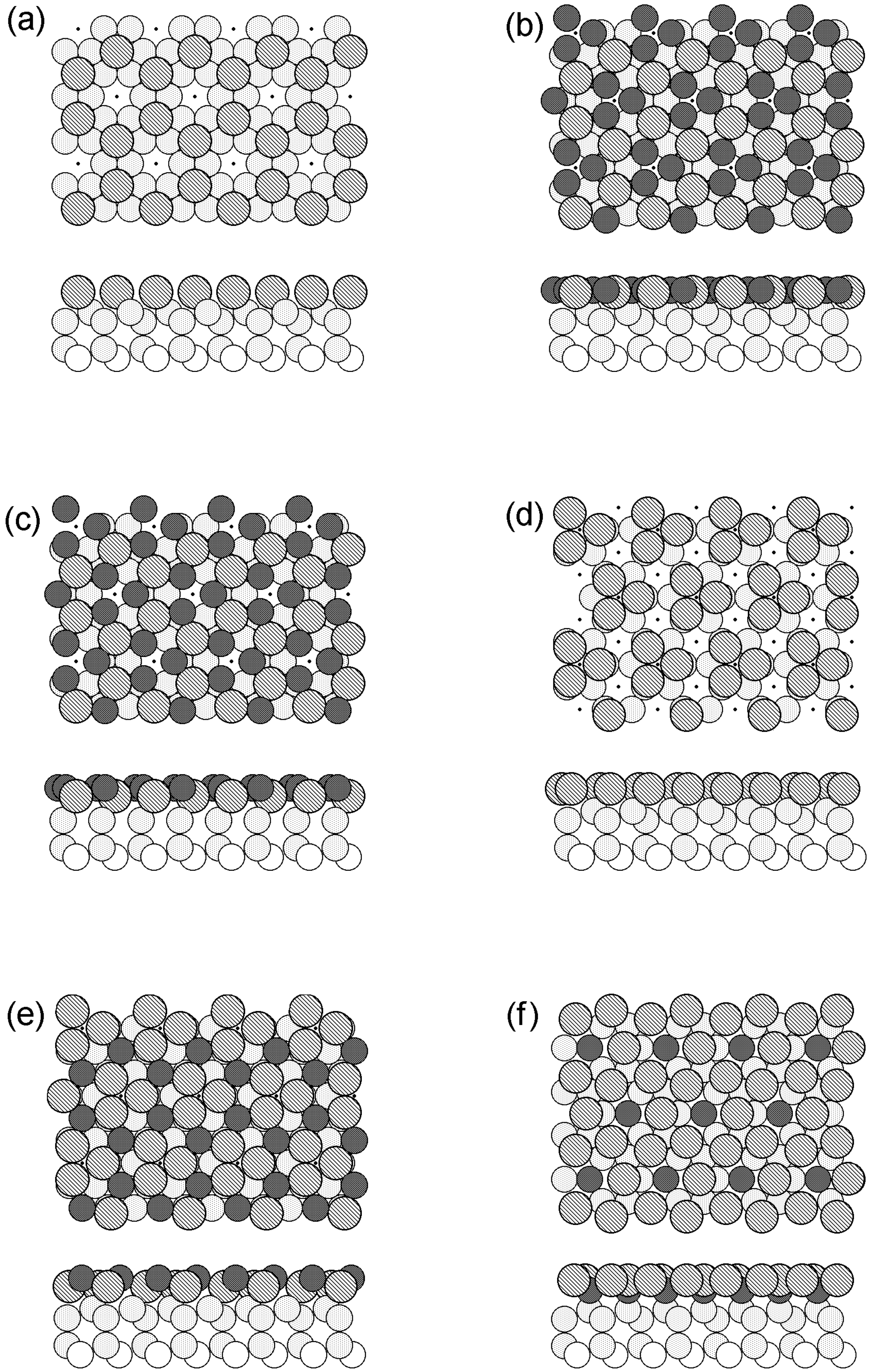

Fig 4 continued overleaf

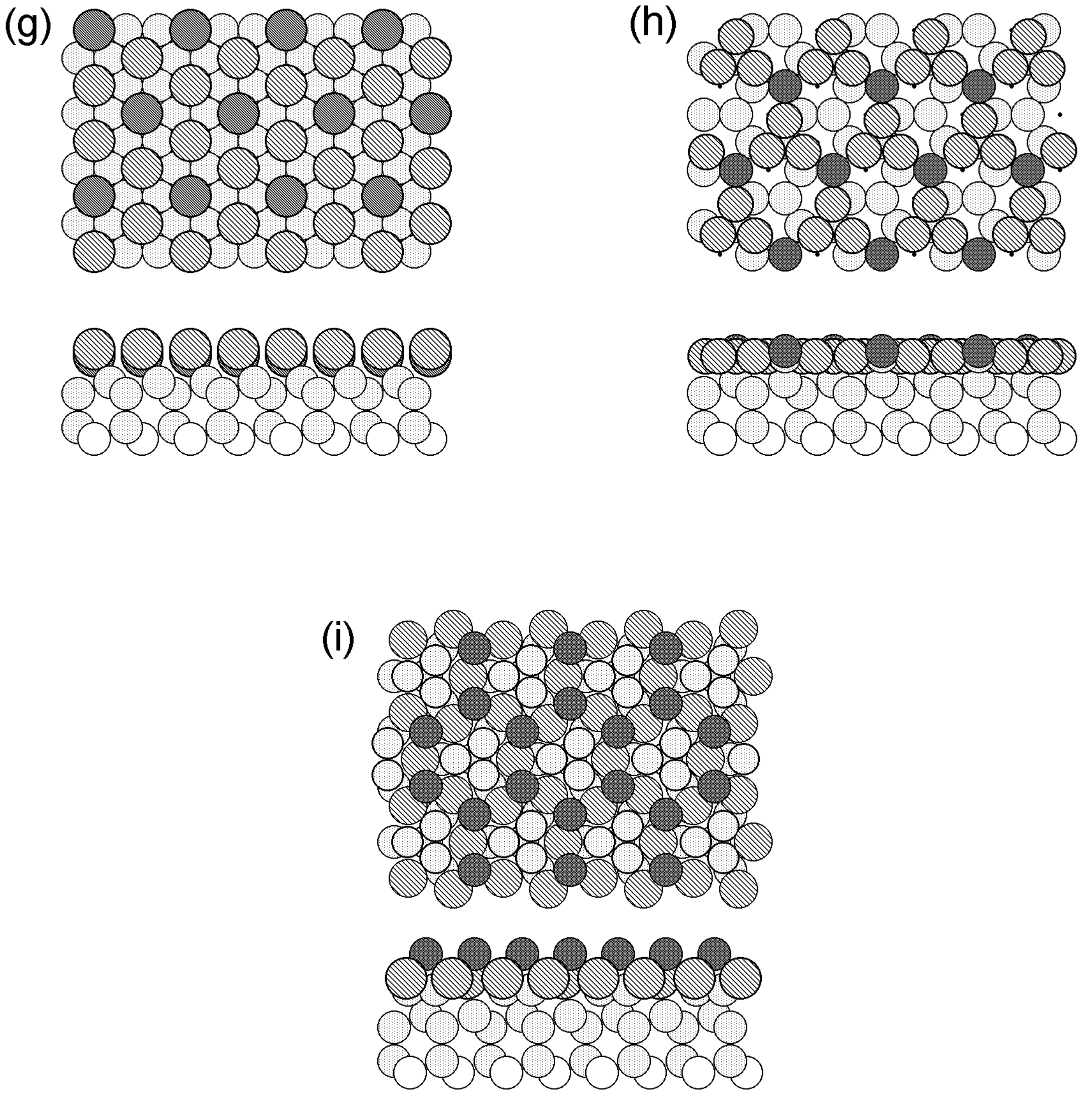

Fig 4. Top and side views of proposed structural models for the Si(111)$\sqrt{3} \times \sqrt{3}$–Ag surface: (a) simple honeycomb (HC) model, (b) missing top layer (MTL) model, (c) embedded honeycomb (EHC) model, (d) trimer (T) model, (e) substitutional trimer (ST) model, (f) honeycomb chained trimer (HCT) model, (g) centered hexagon (CH) model, (h) silicon adatom vacancy (SAV) model, (i) silver-honeycomb chained trimer (SHCT) model. The cross-hatched circles represent Ag atoms, the darker circles Si (from Ref. [41]). (*Reproduced by permission of Elsevier Science Publishers BV*)

height of the Ag layer measured from the ideal first Si layer is 2.9 ± 0.1 Å. TOF ICISS data of Sumitomo *et al.* [22] and ICISS data of Williams *et al.* [40, 41] confirmed the HCT model.

(g) *Centered hexagon (CH) model* (Fig. 4(g)). The CH model was proposed by Le Lay *et al.* [3] based on RHEED and AES data. If an extra atom sits in the center of graphite-like hexagons of the honeycomb structure, but at a slightly different height (-0.3 Å) as compared to the atoms in the initial honeycomb arrangement, a stable structure may be reached with $\theta = 1$ ML.

Recently, an asymmetric structural model with $\theta = 1$ ML was sought as suggested by an analysis of XPD patterns by Kono *et al.* [46]. The model consists of three domains of a symmetrically identical structure in which Ag of two thirds of a ML forms a quasi-honeycomb arrangement and Ag of one third of a ML resides on an off-center site in the hollow of the

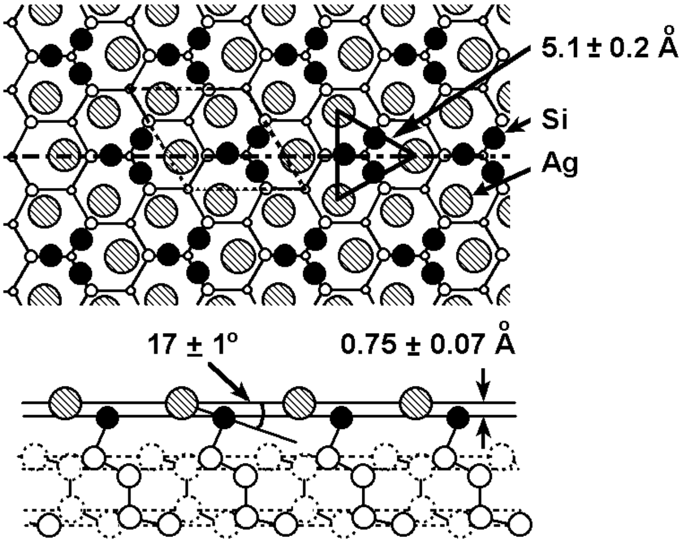

Fig 5. Modified HCT model for the structure of the $\sqrt{3}\times\sqrt{3}$–Ag surface (from Ref. [70]). (*Reproduced by permission of the publishers of Journal of Physical Review Letters*)

quasi-honeycomb, ∼ 0.45 Å below it.

(h) *Silicon adatom vacancy (SAV) model* (Fig. 4(h)). The SAV model is composed of a layer of silicon adatoms nearly coplanar with a trimerized layer of silver [68]. One of the Si adatoms in the $\sqrt{3}\times\sqrt{3}$ unit cell is 0.2 Å higher with respect to the silver layer and another coplanar. The best agreement with the MEIS results was obtained for an Ag–Ag distance of 2.8 Å. The outermost silicon double layer is severely distorted by both the adatoms and by vacancies in the inner half of the double layer. There is one vacancy per $\sqrt{3}\times\sqrt{3}$ unit cell located in the center of trimers.

(i) *Silver-honeycomb chained trimer (SHCT) model* (Fig. 4(i)). The SHCT was proposed by Vlieg *et al.* [63,66] from surface XRD. The Ag atoms in the unit cell are surrounded by six Si atoms: two from the top honeycomb at a distance of 2.63 ± 0.15 Å, three from the second Si layer, of which two are at a distance of 2.57 ± 0.05 Å and one at 2.63 ± 0.06 Å, and one Si atom from the underlying double layer which is at a distance of 2.7 ± 0.8 Å. These distances are between the values for bulk Si and bulk Ag, which are 2.3 Å and 2.88 Å respectively.

Si atoms in the second layer are displaced toward each other and form a trimer with an interatomic distance of 2.25 ± 0.06 Å. Ag–Ag distance is 3.45 Å.

(j) *Modified honeycomb chained trimer (HCT).*

The structure of the $\sqrt{3}\times\sqrt{3}$–Ag surface has been analyzed with a novel form of LEISS spectroscopy (coaxial impact collision ion scattering spectroscopy (CAICISS)) and energy minimization calculations by Katayama *et al.* [70] and the modified HCT model has been proposed. This model is as follows (see Fig. 5). The topmost layer is formed by Ag atoms with the HCT arrangement [67] in which the intratrimer Ag–Ag distance is 5.1 ± 0.2 Å. Below the Ag HCT layer by 0.75 ± 0.07 Å, there is a Si trimer layer (three Si atoms per unit cell), and this Si trimer layer is followed by bulk-like Si layers. Since the Si–Si bond between the Si trimer layer is tilted from the normal surface, the second bulk-like Si layer is split into honeycomb and $\sqrt{3}\times\sqrt{3}$ layers with a large interlayer distance of about 0.6 Å.

Table 1 is compiled to present a direct comparison of Ag trimer sizes for a modified HCT model from the works of various investigators who used a variety of different techniques to study the $\sqrt{3}\times\sqrt{3}$–Ag surface. One can see that the values are in reasonably satisfactory agreement with each other.

Table 1. Comparison of trimer sizes proposed by different investigators* (from Ref. [71])

Ref.	Trimer size (Å)
CAICISS [71]	4.7 ± 0.2
RHEED [48]	(5.29)
XRD [64]	(5.07 ± 0.1)
CAICISS [70]	5.1 ± 0.2
Theory [60]	(4.95)

*Numbers in parentheses are deduced from other structural parameters quoted in those references.

As mentioned above, at the present time, a modified honeycomb chained trimer (HCT) model is consistent with most of the reported experimental results. Experimental support comes from XRD [63, 64], RHEED [48], XSW [72], ISS [70, 71], STM [59] and TED [73]. Theoretical support comes from electronic structure calculations [60, 61, 74].

1.2.2. Si(111)3 × 1–Ag

From the AES (Le Lay *et al.* [3, 4, 18]) and ICISS (Aono *et al.* [39]) data the saturation coverage of the 3×1 phase was estimated to be 1/3 ML. This result based on the assumption that the saturation coverage for the Si(111)$\sqrt{3} \times \sqrt{3}$—$R30°$–Ag surface was 2/3 ML. The value $\theta \sim 1/3$ ML led straightforwardly to the model shown in Fig. 6. Ag atoms are on threefold adsorption sites and form linear chains. ICISS [39] and AREELS [75] experiments showed that Ag atoms at the Si(111)3×1–Ag surface are located above the topmost Si layer. A theoretical interpretation of the 3×1 phase [76] suggested that adsorption takes place on top sites.

From the other point of view [77], Ag does not participate in the 3×1 long-range ordered structure and serves only to induce the surface reconstruction. This result was obtained from the measurements of LEED I–V curves for the 3×1 structures. The metal adsorbate which induce the 3×1 reconstruction is at coverage below 1/3 ML. A proposed missing-row model of the 3×1 reconstruction of the Si(111) surface induced by Ag adsorption is shown in Fig. 4 (see Chapter Li, section 1.2.2).

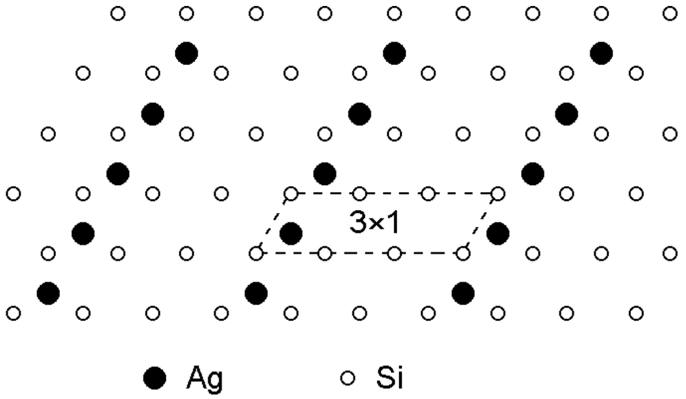

Fig 6. Model of the Si(111)3×1–Ag structure $\theta = 1/3$ (from Ref. [4]). (*Reproduced by permission of Elsevier Science Publishers BV*)

1.2.3. Si(111)6 × 1–Ag

Gotoh and Ino [32] were the first to observe this structure by RHEED. They remarked that all one-sixth order superlattice spots were visible in the [112] incidence azimuth of the primary electron beam but that some of them missed in the [110] incidence azimuth. An explanation for this peculiar behavior in terms of double diffraction enhanced through excitation of surface waves was proposed by Ichikawa and Ino [78]. They assumed a coverage of $\theta = 1/3$ ML for the 6 × 1 structure as for the 3 × 1 structure. The structural model consists of two parallel Ag chains in which the atoms are displaced along the chains and opposite in direction. Le Lay *et al.* [3] showed that the results of Ichikawa and Ino [78] concerning the missing spots of the LEED pattern contradict the experimentally observed LEED pattern of the 6 × 1–Ag structure. Taking into account the energetically unfavorable displacement of the silver atoms from their equilibrium position Le Lay *et al.* [3] proposed the structural model with $\theta = 1/6$ ML. The atomic arrangement in this structure is the same as that shown for the 3 × 1 phase in Fig. 6 but with one row of Ag over two missing ($\theta = 1/6$ ML at saturation).

1.2.4. Si(111)δ(7 × 7)–Ag

Kohmoto and Ichimiya [19] reported that during RT deposition of Ag starting at ~ 0.25 ML and up to about 0.5 ML, the 7×7 reconstruction is different from that of the clean Si(111)7×7 surface. The developing of the RHEED pattern of this surface structure is characterized by the decrease of intensities of half-order spots ((3/7, 4/7), and so on), while weak fractional-order spots along the [10] direction gain in intensity. Such intensity distribution is similar to that of hydrogen covered Si(111)7 × 7 [20]. The latter structure was named $\delta(7 \times 7)$ in Ref. [21]. So, Kohmoto and Ichimiya designated the Ag-induced 7 × 7 reconstruction as a $\delta(7 \times 7)$–Ag structure. Following an analysis of the $\delta(7 \times 7)$–H structure [20] based on the DAS model, they concluded that the $\delta(7 \times 7)$–Ag structure results from the cutting off of the backbonds of Si adatoms by Ag adsorption [19].

However, Tosch and Neddermeyer [79] proposed from their STM results on the initial stages of Ag condensation ($\theta \approx 1/3$ ML) on Si(111)7 × 7 at substrate temperatures of 90 and 130 °C, that Ag atoms are bonded to the inner adatoms and the dangling bonds of the second atomic layer of the DAS structure. This conclusion was derived from the observation of ring-like structures on the inner adatoms which show a triangular distortion. It was also shown in Ref. [79] that the underlying 7 × 7 reconstructed Si(111) surface is not changed by deposition of Ag at substrate temperatures below 130 °C.

1.2.5. Si(111)$\sqrt{7} \times \sqrt{7}$—*R*19.1°–Ag

The structural model for this structure was proposed by Le Lay *et al.* [3, 4]. However, the experimental methods used in these works (LEED, AES) did not provide direct information on the atomic arrangement of this phase and the structural model proposed being, as a consequence, only guessed. From the break in the Auger condensation curves a coverage of $\theta \approx 6/7$ indicates a probable completion of the $\sqrt{7} \times \sqrt{7}$ overlayer. Supposing that the Ag atoms in the $\sqrt{7} \times \sqrt{7}$ ad-layer are in the threefold hollow sites on the non-reconstructed Si(111)1 × 1 surface, the proposed model corresponds to an ordered array of ad-vacancies ($\theta = 1/7$) in the silver overlayer (Fig. 7). Si(111)$\sqrt{7} \times \sqrt{7}$—*R*19.1°–Ag structure forms only on the cleavage structure of Si and not on Si(111)7 × 7. The reason is probably that the 2 × 1 reconstruction of Si(111) which is metastable can more easily transform to a 1 × 1 structure than the 7 × 7 stable one.

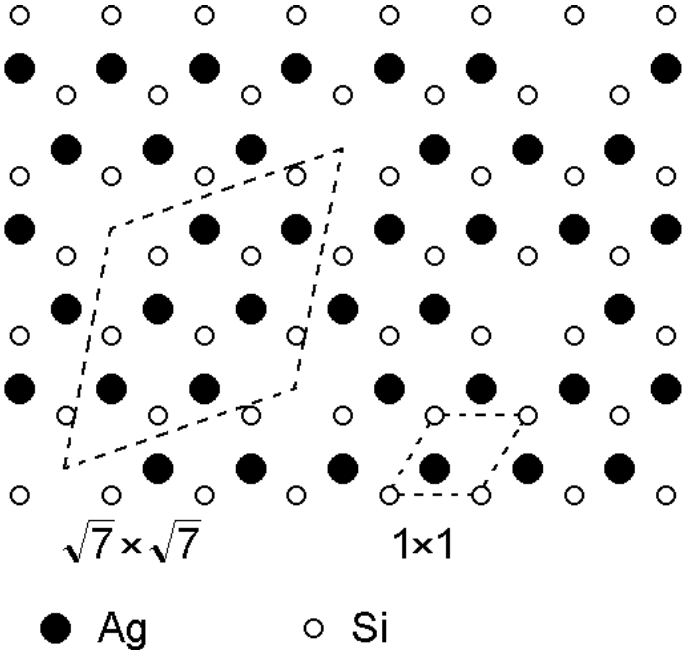

Fig 7. Model of the Si(111)$\sqrt{7}\times\sqrt{7}$—$R19.1^\circ$–Ag structure (from Ref. [4]). (*Reproduced by permission of Elsevier Science Publishers BV*)

1.3. PROPERTIES

1.3.1. Desorption

Le Lay, Manneville, and Kern were the first to study the desorption of the 2D phases of a Ag/Si(111) system at temperatures ranging from 550 to 650 °C [18].

The three distinct steps were clearly detected in the desorption process. The first step, indicated by a plateau in the isothermal desorption plot of the Ag and Si AES peak amplitudes versus time (Fig. 8), corresponds to the desorption of the 3D crystallites. A first break in the intensity-*versus* time curve indicates the beginning of the desorption of the 2D layer. The accompanied LEED observations revealed that the first segment corresponds to the desorption of the $\sqrt{3}\times\sqrt{3}$—$R30^\circ$ phase, the second one to the desorption of the 3×1 phase. The break at $\theta \sim 1/3$ ML shows the value at completion of the 3×1 phase [20].

The linearity of the isotherms of Fig. 8 clearly indicates the zero order desorption, in which the desorption rate is independent of the adsorbed amount: $\theta = \theta_0 kt$. The zero order desorption was confirmed later by Hasegawa *et al.* [30] and Kohmoto and Ichimiya [19]. It was derived theoretically in Ref. [80] that zero order kinetics correspond to the case when the 2D phase desorbes indirectly via a dilute adsorbed gas of isolated atoms provided that the reverse flux from the 2D gas to the 2D phase is far greater than the desorbing flux from the adsorbed gas to vacuum. The desorption (cohesive) energies and the vibrational frequencies determined in Ref. [18] are, respectively:

$E_d = 65$ kcal mole^{-1} (2.82 eV) $\qquad \nu = 1.8\times 10^{12}$ s^{-1}

for the $\sqrt{3}\times\sqrt{3}$—$R30^\circ$ phase,

$E_d = 68$ kcal mole^{-1} (2.95 eV) $\qquad \nu = 2.3\times 10^{12}$ s^{-1}

for the 3×1 phase.

The similar values of desorption energies (64 kcal mole^{-1} for the $\sqrt{3}\times\sqrt{3}$—$R30^\circ$ phase and 69 kcal mole^{-1} for the 3×1 phase) were determined in Ref. [30].

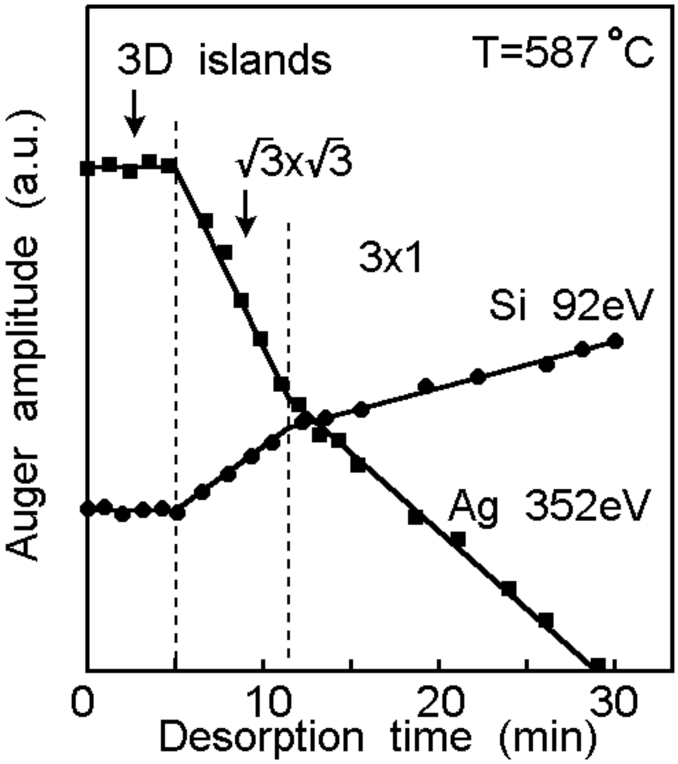

Fig 8. Isothermal (T = 587 °C) desorption plot of the Ag 352 eV and Si 92 eV peak-to-peak Auger amplitudes versus time (from Ref. [18]). (*Reproduced by permission of Elsevier Science Publishers BV*)

1.3.2. Diffusion and Electromigration

The Ag mass transport on Si(111) was studied in several works [81–85].

Boutaoui *et al.* [84] studied the spreading of RT deposited Ag strip upon annealing. They found that the spreading kinetics obtained at lower temperatures, where no desorption occurs, fit the $t^{3/4}$ law (Fig. 9). This law corresponds to the number of atoms leaving an island per unit time. Thus extension of the spreading zone must be controlled by the extraction of Ag atoms from 3D islands. The activation energy of 2.4 eV determined in Ref. [84] is very large compared to the 0.35 eV found by Doust *et al.* [83]. In the latter work, Ag atoms were evaporated on to the substrate held at temperatures higher than 450 °C, where no nucleation of Ag 3D islands occurs. Thus the spreading process is controlled by the diffusion of Ag adatoms on the $\sqrt{3} \times \sqrt{3}$—$R30°$–Ag layer.

Yasunaga *et al.* [85–88] reported the electromigration in the Ag/Si(111) system, i.e. the directional spread of an Ag thin-film patch over Si(111) surface with the application of direct current to the Si substrate. The patch of the Ag thin film spreads on the cathode side over the clean Si(111)7 × 7. The spread-out layer had a constant (about 1 ML) Ag coverage with the $\sqrt{3} \times \sqrt{3}$—$R30°$ structure. On the anode side of the Ag patch no significant movement was detected.

Using Si(111) substrates with a variety of dope levels, Yasunaga *et al.* [86,87] found that the electromigration velocity of the Ag patch decreases in same way as the electric field applied to the substrate with increasing dope level. Thus, the driving force for electromigration was proven to be directly proportional to the electrical field available on the surface for Ag/Si(111). The effective charge was derived from the analysis of the spread of a patch of Ag deposit to be $+1e \sim +4e$ for the Ag adatom on the Si(111)$\sqrt{3} \times \sqrt{3}$–Ag.

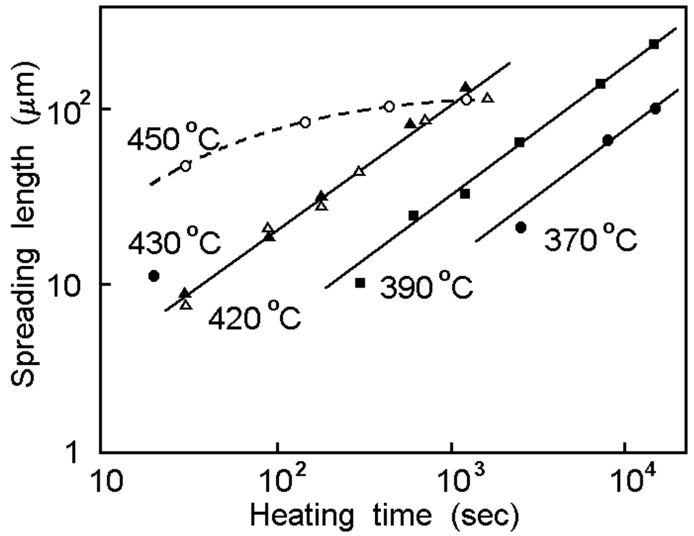

Fig 9. Spreading kinetics obtained by plotting the spreading length versus the heating time at different temperatures (from Ref. [84]). (*Reproduced by permission of Elsevier Science Publishers BV*)

1.3.3. Oxidation of the Si(111)–Ag Surface

It was suggested from the data of photoemission analysis [89] that the $\sqrt{3}\times\sqrt{3}$–Ag structure passivates the (111) surface for oxidation. However, the subsequent soft X-ray photoelectron spectroscopy investigation [90] did not confirm this proposition. The Si(111)$\sqrt{3}\times\sqrt{3}$–Ag surface is not passivated against oxidation if the exposure is higher than 10^6 L O_2. This surface has a lower oxidation rate compared to the clean Si(111)7 × 7 surface but it is not totally inactive to oxidation below the exposure of 10^6 L O_2. As for the as-deposited disordered Ag/Si(111) layer, no passivation stage exists for such a surface [90–92].

2. (100) ORIENTATION

No Ag-induced ordered reconstructions are known for the Ag/Si(100) system.

2.1. PHASE DIAGRAM

LEED [4, 13, 93] and RHEED [94] investigations did not reveal the formation of any new ordered reconstruction upon Ag adsorption on Si(100) as indicated in the phase diagram from Ref. [4] (see Fig. 10). At low Ag coverage, the Ag adatoms are dispersed, and each Ag adatom bonds two Si surface atoms as revealed by high-resolution core-level photoemission spectroscopy [95–97] (see Fig. 11, showing Ag-to-Si bonding coordination number as a function of Ag coverage). This result and the fact that distance between Si dimer rows (5.3 Å [98–100]) is about twice as large as the Ag–Si bond length (2.5 Å [51]) imply a bonding site between two neighboring Si surface dimers (see Fig. 12). This assumption was proved by STM observations [101, 102]. It was also shown in the STM investigations that some Ag adatoms form short linear chains both within the dimer grooves [101] and in the direction perpendicular to the direction of the Si dimer rows [102].

AES [103] and STM [104] data led to the interpretation that 3D islands nucleate at the very early stages of Ag condensation. This is also seen in Fig. 11. The Ag-to-Si coordination number equals 2 for Ag adatoms in the grooves between the Si dimers, as shown in Fig. 12, and it will be less than 2 after Ag islands form on the surface. The gradual decrease of coordination number with increasing Ag coverage without abrupt transition at 0.5 ML coverage indicates

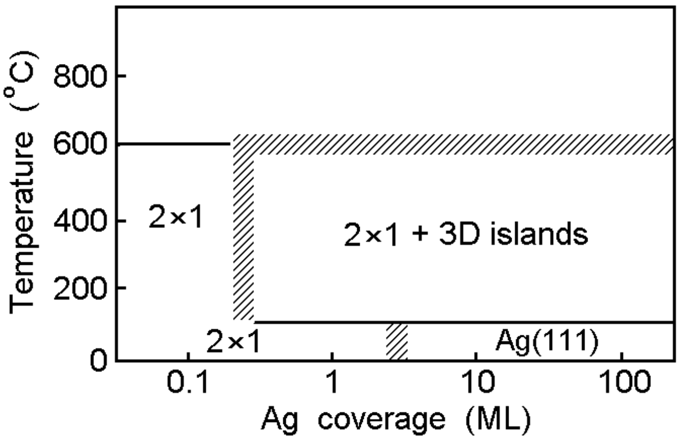

Fig 10. Schematic phase diagram of the Ag/Si(100) system (from Ref. [4]). (*Reproduced by permission of Elsevier Science Publishers BV*)

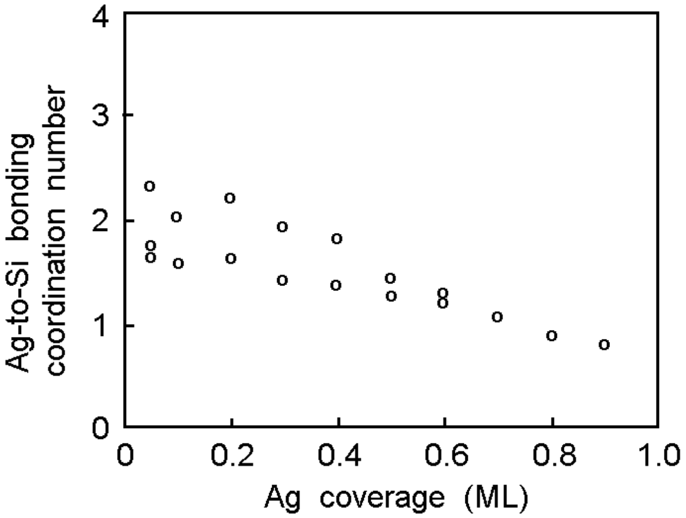

Fig 11. Ag-to-Si bonding coordination number as a function of Ag coverage. This is the average number of Si atoms affected by each Ag adatom (from Ref. [95]). (*Reproduced by permission of the publishers of Journal of Physical Review B*)

that the sample consists of Ag adatoms in the grooves and Ag islands at all stages of Ag adsorption.

Ag islands showed preferential Ag(111) ∥ Si(100) orientation [10, 13, 95, 101, 103, 105]. However Ag(100)- and Ag(110)-oriented crystallites were also detected for Ag/Si(100) system [93,101,106].

3. (110) ORIENTATION

The $\begin{pmatrix} 9 & 3 \\ -9 & 3 \end{pmatrix}$, 5×4, and 1×1 structures are formed on a Si(110) surface depending on Ag coverage and heat treatment.

3.1. PHASE DIAGRAM

The phase diagram for theAg/Si(110) system shown in Fig. 13 was determined by Yamamoto in the RHEED–TRAXS (reflection high energy electron diffraction–total reflection angle X-

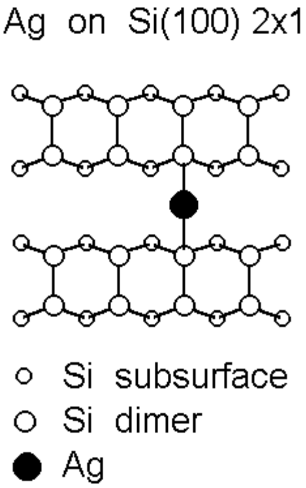

Fig 12. Top view of a structural model for an isolated Ag adatom bonded on to Si(100)2 × 1 (from Ref. [95]). (*Reproduced by permission of the publishers of Journal of Physical Review B*)

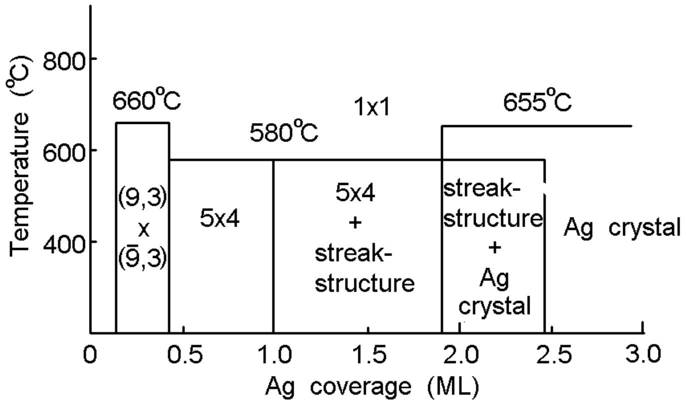

Fig 13. The two-dimensional phase diagram of the Ag/Si(110) system (from Ref. [107]). (*Reproduced by permission of the publishers of Japanese Journal of Applied Physics*)

ray spectroscopy) study [107].

When Ag is deposited on to the Si(110) surface held at 500 °C, the $\begin{pmatrix} 9 & 3 \\ -9 & 3 \end{pmatrix}$ structure appears in the range of Ag coverages from 0.14 to 0.44 ML. Figure 14(a) shows the reciprocal lattice and (b) the real lattice of this structure. One can see in Fig. 14(b), that the structure can also be written as $c(18 \times 6)$.

When the surface showing $c(18 \times 6)$ structure is heated, the structure transforms into a 1×1 structure at 660 °C. Upon cooling to room temperature, the 1×1 structure does not transform clearly into the $c(18 \times 6)$ structure at 660 °C. Thus, the phase transition between $\begin{pmatrix} 9 & 3 \\ -9 & 3 \end{pmatrix}$ and the 1×1 structure is irreversible.

When from 0.44 to 1.0 ML of RT deposited Ag is annealed at 500 °C, the 5×4 structure is observed. The reciprocal and real lattices of the 5×4 structure are shown in Fig. 15. The 5×4 structure was found to transform reversibly into 1×1 structure at 580 °C.

In the Ag coverage range from 1.0 to 1.92 ML, the diffraction pattern where the spots of the 5×4 structure and streaks are mixed is observed upon annealing at 500 °C. On basis of the streak positions at the RHEED pattern, Yamamoto suggested that the streak structure corresponds to the Ag chains in which Ag atoms are arranged regularly at 2.7 Å intervals in the $[\bar{1}10]$ direction, but are not aligned in the [001] direction. The mixed structure reversibly

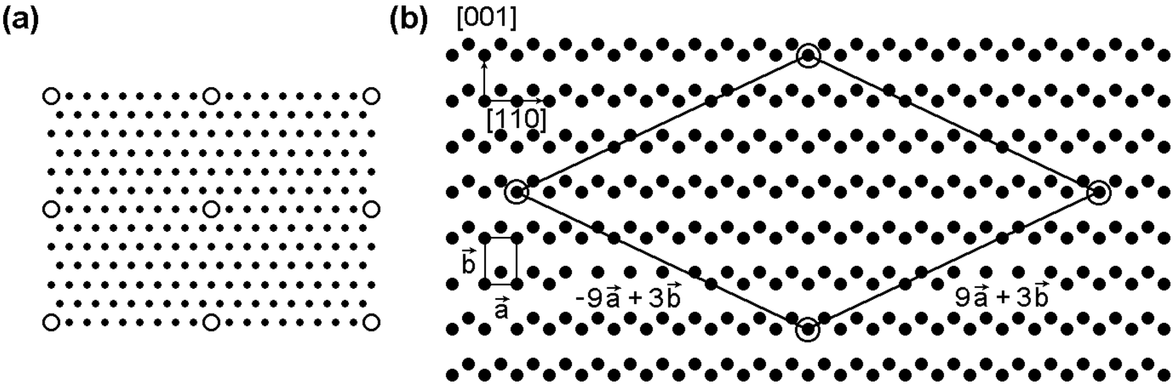

Fig 14. (a) The reciprocal lattice and (b) the real lattice of the Si(110) $\begin{pmatrix} 9 & 3 \\ -9 & 3 \end{pmatrix}$–Ag (or Si(110)–$c(18 \times 6)$–Ag) structure. The solid circles in (b) represent the Si atoms on the Si(110) plane and the double circles the corners of the unit mesh of the superstructure (from Ref. [107]). (*Reproduced by permission of the publishers of Japanese Journal of Applied Physics*)

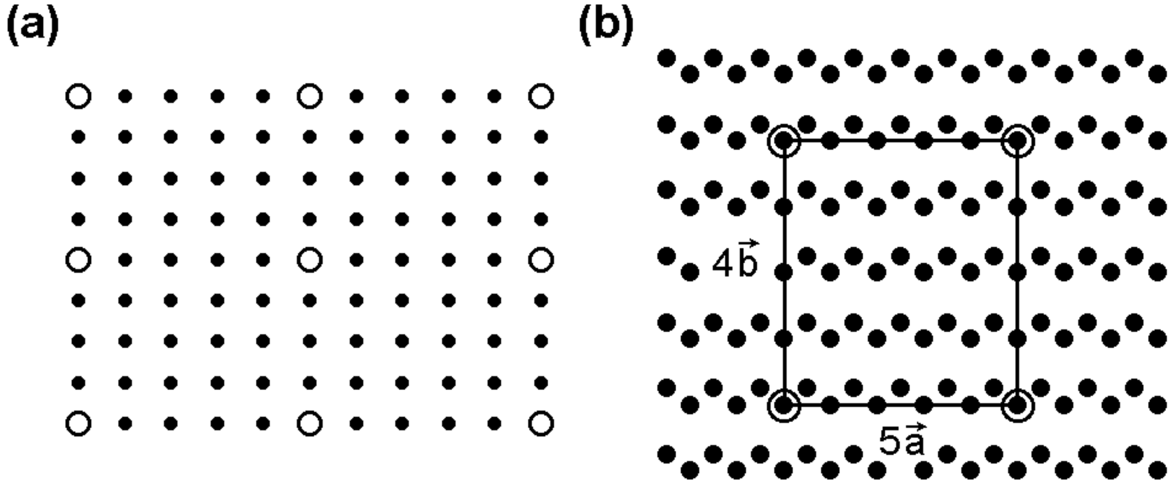

Fig 15. (a) The reciprocal lattice and (b) the real lattice of the Si(110)5×4–Ag structure. The solid circles in (b) represent the Si atoms on the Si(110) plane and the double circles the corners of the unit mesh of the superstructure (from Ref. [107]). (*Reproduced by permission of the publishers of Japanese Journal of Applied Physics*)

transforms into the 1 × 1 structure at 580 °C.

Upon annealing at 500 °C of 1.92 to 2.47 ML Ag, the superposition of the streak structure and the Ag single crystal is detected. The streak structure reversibly transforms into the 1 × 1 structure at 580 °C. Meanwhile, the Ag single crystal irreversibly transforms into the 1 × 1 structure at 655 °C.

When Ag coverage exceeds 2.47 ML, Ag crystals grow epitaxially in the Stranski–Krastanov mode. The orientation of epitaxial Ag crystals is (112)Ag ∥ (110)Si and [111]Ag ∥ [001]Si [107].

REFERENCES

[1] V. Yu. Aristov, I. L. Bolotin, V. A. Grazhulis and V. M. Zhilin, *Sov. Phys. -JETP* **64** (1986) 832.

[2] V. A. Grazhulis, *Appl. Surf. Sci.* **33-34** (1988) 1.

[3] G. Le Lay, A. Chauvet, M. Manneville and R. Kern, *Appl. Surf. Sci.* **9** (1981) 190.

[4] G. Le Lay, *Surf. Sci.* **132** (1983) 169.
[5] D. Bolmont, P. Chen, C. A. Sebenne and F. Proix, *Phys. Rev. B* **24** (1981) 4552.
[6] G. Le Lay, G. Quentel, J. P. Faurie and A. Masson, *Thin Solid Films* **35** (1976) 273.
[7] D. Bolmont, *Helv. Phys. Acta* **56** (1983) 483.
[8] M. Morooka, H. Tomokage, H. Kitagawa and M. Yoshida, *Japan J. Appl. Phys.* **24** (1985) 133.
[9] M. Iwami, M. Kubota, T. Koyama, H. Tochihara and Y. Murata, *Phys. Rev. B* **38** (1988) 1047.
[10] M. Hanbucken, M. Futamoto and J. A. Venables, *Surf. Sci.* **147** (1984) 433.
[11] E. J. Van Loenen, M. Iwami, R. M. Tromp and J. F. Van der Veen, *Surf. Sci.* **137** (1984) 1.
[12] F. Wehking, H. Beckermann and R. Niedermayer, *Surf. Sci.* **71** (1978) 364.
[13] M. Hanbucken, H. Neddermeyer and P. Rupieper, *Thin Solid Films* **90** (1982) 37.
[14] M. Saitoh, F. Shoji, K. Oura and T. Hanawa, *Surf. Sci.* **112** (1981) 306.
[15] Y. Terada, T. Yoshizuka, K. Oura and T. Hanawa, *Surf. Sci.* **114** (1982) 65.
[16] M. Housley, R. Heckingbottom and C. J. Todd, *Surf. Sci.* **68** (1977) 179.
[17] J. A. Venables, J. Derrien and A. P. Janssen, *Surf. Sci.* **95** (1980) 411.
[18] G. Le Lay, M. Manneville and R. Kern, *Surf. Sci.* **72** (1978) 405.
[19] S. Kohmoto and A. Ichimiya, *Appl. Surf. Sci.* **33–34** (1988) 45.
[20] A. Ichimiya and S. Mizuno, *Surf. Sci.* **191** (1987) L765.
[21] H. Daimon and S. Ino, *Surf. Sci.* **164** (1985) 320.
[22] K. Sumimoto, K. Tanaka, Y. Izawa, I. Katayama, F. Shoji, K. Oura and T. Hanawa, *Appl. Surf. Sci.* **41–42** (1989) 112.
[23] K. Spiegel, *Surf. Sci.* **7** (1967) 125.
[24] E. Bauer and H. Poppa, *Thin Solid Films* **12** (1972) 167.
[25] G. Le Lay, G. Quentel, J. P. Faurie and A. Masson, *Thin Solid Films* **35** (1976) 289.
[26] F. Shoji, M. Watamori, T. Kuroi, K. Oura and T. Hanawa, J. Phys. D **22** (1989) 169.
[27] G. Raynerd, T. N. Doust and J. A. Venables, *Surf. Sci.* **261** (1992) 251.
[28] G. Raynerd, M. Hardiman and J. A. Venables, *Phys. Rev. B* **44** (1991) 13803.
[29] H. Ohnishi, I. Katayama, Y. Ohba, F. Shoji and K. Oura, *Japan J. Appl. Phys.* **32** (1993) 2920.
[30] S. Hasegawa, H. Daimon and S. Ino, *Surf. Sci.* **186** (1987) 138.
[31] A. W. D. Van der Gon and R. M. Tromp, *Phys. Rev. Lett.* **69** (1992) 3519.
[32] Y. Gotoh and S. Ino, *Japan J. Appl. Phys.* **17** (1978) 2097.
[33] S. Ino and Y. Gotoh, *Japan J. Appl. Phys.* **16** (1977) 2261.
[34] Y. Horio and A. Ichimiya, *Surf. Sci.* **164** (1985) 589.
[35] M. Saitoh, F. Shoji, K. Oura and T. Hanawa, *Japan J. Appl. Phys.* **19** (1980) L421.
[36] Y. Terada, T. Yoshizuka, K. Oura and T. Hanawa, *Japan J. Appl. Phys.* **20** (1981) L333.
[37] T. L. Porter, C. S. Chang and I. S. T. Tsong, *Phys. Rev. Lett.* **60** (1988) 1739.
[38] C. S. Chang, T. L. Porter and I. S. T. Tsong, *J. Vac. Sci. Technol. A* **7** (1989) 1906.
[39] M. Aono, R. Souda, C. Oshima and Y. Ishizawa, *Surf. Sci.* **168** (1986) 713.
[40] R. S. Williams, R. S. Daley, J. H. Huang and R. M. Charatan, *Appl. Surf. Sci.* **41–42** (1989) 70.
[41] R. S. Daley, R. M. Charatan and R. S. Williams, *Surf. Sci.* **240** (1990) 136.
[42] T. Takahashi, S. Nakatani, N. Okamoto, T. Ishikawa and S. Kikuta, *Techn. Rept. ISSP. A* (1990) 1.
[43] E. L. Bullock, G. S. Herman, M. Yamada, D. J. Friedman and C. S. Fadley, *Phys. Rev. B* **41** (1990) 1703.
[44] S. Kono, K. Higashiyama and T. Sagawa, *Surf. Sci.* **165** (1986) 21.
[45] S. Kono, H. Sakurai, K. Higashiyama and T. Sagawa, *Surf. Sci.* **130** (1983) L299.
[46] S. Kono, T. Abukawa, N. Nakamura and K. Anno, *Japan J. Appl. Phys.* **28** (1989) L1278.

[47] S. Kono, K. Higashiyama, T. Kinoshita, T. Miyahara, H. Kato, H. Ohsawa, Y. Enta, F. Maeda and Y. Yaegashi, *Phys. Rev. Lett.* **58** (1987) 1555.

[48] A. Ichimiya, S. Kohmoto, T. Fujii and Y. Horio, *Appl. Surf. Sci.* **41–42** (1989) 82.

[49] Y. Horio and A. Ichimiya, *Surf. Sci.* **133** (1983) 393.

[50] J. Stohr and R. Jaeger, *J. Vac. Sci. Technol.* **21** (1982) 619.

[51] J. Stohr, R. Jaeger, G. Rossi, T. Kendelewicz and I. Lindau, *Surf. Sci.* **134** (1983) 813.

[52] G. V. Hansson, R. Z. Bachrach, R. S. Bauer and P. Chiaradia, *Phys. Rev. Lett.* **46** (1981) 1033.

[53] K. Markert, P. Pervan, W. Heichler and K. Wandelt, *J. Vac. Sci. Technol. A* **7** (1989) 2873.

[54] J. E. Demuth, E. J. Van Loenen, R. M. Tromp and R. J. Hamers, *J. Vac. Sci. Technol. B* **6** (1988) 18.

[55] R. J. Wilson and S. Chiang, *Phys. Rev. Lett.* **59** (1987) 2329.

[56] E. J. Van Loenen, J. E. Demuth, R. M. Tromp and R. J. Hamers, *Phys. Rev. Lett.* **58** (1987) 373.

[57] R. J. Wilson and S. Chiang, *Phys. Rev. Lett.* **58** (1987) 369.

[58] R. J. Wilson and S. Chiang, *J. Vac. Sci. Technol. A* **6** (1988) 800.

[59] K. J. Wan, X. F. Lin and J. Nogami, *Phys. Rev. B* **45** (1992) 9509.

[60] S. Watanabe, M. Aono and M. Tsukada, *Phys. Rev. B* **44** (1991) 8330.

[61] S. Watanabe, M. Aono and M. Tsukada, *Appl. Surf. Sci.* **60–61** (1992) 437.

[62] A. Shibata, Y. Kimura and K. Takayanagi, *Surf. Sci.* **275** (1992) L697.

[63] E. Vlieg, D. A. W. Van der Gon, J. F. Van der Veen, J. E. MacDonald and C. Norris, *Surf. Sci.* **209** (1989) 100.

[64] T. Takahashi, S. Nakatani, N. Okamoto, T. Ishikawa and S. Kikuta, *Japan J. Appl. Phys.* **27** (1988) L753.

[65] T. Takahashi, S. Nakatani, N. Okamoto, T. Ishikawa and S. Kikuta, Rev. Sci. Instrum. **60** (1989) 2365.

[66] E. Vlieg and J. F. Van der Veen, *Appl. Surf. Sci.* **41-42** (1989) 62.

[67] T. Takahashi, S. Nakatani, N. Okamoto and T. Ishikawa, *Surf. Sci.* **242** (1991) 54.

[68] M. Copel and R. M. Tromp, *Phys. Rev. B* **39** (1989) 12688.

[69] K. Oura, M. Watamori, F. Shoji and T. Hanawa, *Phys. Rev. B* **38** (1988) 10146.

[70] M. Katayama, R. S. Williams, M. Kato, E. Nomura and M. Aono, *Phys. Rev. Lett.* **66** (1991) 2762.

[71] S. Chaudhury, R. S. Williams, M. Katayama and M. Aono, *Surf. Sci.* **294** (1993) 93.

[72] E. Vlieg, E. F. Fontes and J. R. Patel, *Phys. Rev. B* **43** (1991) 7185.

[73] Y. Tanishiro, K. Takayanagi and K. Yagi, *Surf. Sci.* **258** (1991) L687.

[74] Y. G. Ding, C. T. Chan and K. M. Ho, *Phys. Rev. Lett.* **67** (1991) 1454.

[75] K. Horioka, H. Iwasaki, S. Maruno, S. -T. Li and S. Nakamura, *Surf. Sci.* **136** (1984) 121.

[76] V. Barone, G. Del Re, G. Le Lay and R. Kern, *Surf. Sci.* **99** (1980) 223.

[77] W. C. Fan and A. Ignatiev, *Phys. Rev. B* **41** (1990) 3592.

[78] T. Ichikawa and S. Ino, *Surf. Sci.* **97** (1980) 489.

[79] St. Tosch and H. Neddermeyer, *Phys. Rev. Lett.* **61** (1988) 349.

[80] G. Le Lay, M. Manneville and R. Kern, *Surf. Sci.* **65** (1977) 261.

[81] M. Futamoto, M. Hanbucken, C. J. Harland, G. W. Jones and J. A. Venables, *Surf. Sci.* **150** (1985) 430.

[82] M. Hanbucken, T. N. Doust, O. Osasona, G. Le Lay and J. A. Venables, *Surf. Sci.* **168** (1986) 133.

[83] T. Doust, F. L. Metcalfe and J. A. Venables, *Ultramicroscopy* **31** (1989) 116.

[84] N. Boutaoui, H. Roux and M. Tholomier, *Surf. Sci.* **239** (1990) 213.

[85] H. Yasunaga, S. Sakomura, T. Asaoka, S. Kanayama, N. Okuyama and A. Natori, *Japan J. Appl. Phys.* **27** (1988) L1603.

[86] H. Yasunaga and S. Yoda, *Japan J. Appl. Phys.* **30** (1991) 1822.

[87] N. -J. Wu, H. Yasunaga and A. Natori, *Surf. Sci.* **260** (1992) 75.

[88] H. Yasunaga, N. -J. Wu, S. Yoda, T. Aida and K. Sakamoto, *Appl. Surf. Sci.* **60–61** (1992) 64.

[89] A. Cros, F. Houzay, G. M. Guichar and R. Pinchaux, *Surf. Sci.* **116** (1982) L232.

[90] J. -J. Yeh, D. J. Friedman, R. Cao and I. Lindau, *J. Vac. Sci. Technol. A* **4** (1986) 1479.

[91] G. Rossi, L. Caliari, I. Abbati, L. Braicovich, I. Lindau and W. E. Spicer, *Surf. Sci.* **116** (1982) L202.

[92] I. Abbati, C. Rossi, L. Caliari, L. Braicovich, I. Lindau and W. E. Spicer, *J. Vac. Sci. Technol.* **21** (1982) 409.

[93] T. Hanawa and K. Oura, *Japan J. Appl. Phys.* **16** (1977) 519.

[94] K. Nishimori, H. Tokutaka, T. Tamon, S. Kishida and N. Ishihara, *Surf. Sci.* **242** (1991) 157.

[95] A. Samsavar, T. Miller and T. -C. Chiang, *Phys. Rev. B* **38** (1988) 9889.

[96] T. -C. Chiang, *Mat. Res. Soc. Symp. Proc.* **143** (1989) 55.

[97] D. H. Rich, A. Samsavar, T. Miller and T. -C. Chiang, Phys. Scripta **41** (1990) 83.

[98] J. A. Appelbaum and D. R. Hamann, *Surf. Sci.* **74** (1978) 21.

[99] C. W. Van Hasselt, M. A. Verheijen and Th. Rasing, *Phys. Rev. B* **42** (1990) 9263.

[100] R. J. Hamers, R. M. Tromp and J. E. Demuth, *Phys. Rev. B* **34** (1986) 5343.

[101] A. Samsavar, E. S. Hirschorn, F. M. Leibsle and T. -C. Chiang, *Phys. Rev. Lett.* **63** (1989) 2830.

[102] T. Hashizume, R. J. Hamers, J. E. Demuth, K. Markert and T. Sakurai, *Techn. Rept. ISSP. A.* N2178 (1989) 1.

[103] M. Hanbucken and H. Neddermeyer, *Surf. Sci.* **114** (1982) 563.

[104] D. Badt, A. Brodde, St. Tosch and H. Neddermeyer, *J. Vac. Sci. Technol. A* **8** (1990) 251.

[105] M. Hanbucken and G. Le Lay, *Surf. Sci.* **168** (1986) 122.

[106] Y. Kimura and K. Takayanagi, *Surf. Sci.* **276** (1992) 166.

[107] Y. Yamamoto, *Japan J. Appl. Phys.* **31** (1992) 2241.

(Al)

ALUMINUM

1. (111) ORIENTATION

Several reconstructions were found for the Al/Si(111) system. These are $\sqrt{3}\times\sqrt{3}$—$R30°$, $\sqrt{7}\times\sqrt{7}$—$R19.1°, 2\times 1, 1\times 1, \gamma(7\times 7)$, and 4.5×4.5.

1.1. PHASE DIAGRAM

The formation of the Si(111)–Al interface was examined for three different cases, namely, (a) during Al deposition on to the cleaved Si(111)2×1 surface held at room temperature; (b) during Al deposition on to the Si(111)7×7 surface held at RT and (c) during high temperature growth (at the deposition of Al on to the Si(111) surface held at high temperature or annealing of the Al layer deposited at RT). Each case is characterized by the individual growth mode and reconstruction observed.

1.1.1. RT Deposition on to Cleaved Si(111)2×1

The initial stages of Al growth on the Si(111)2×1 surface during RT Al deposition were examined by LEED–AES [1–5].

According to the LEED and AES observations of Chen *et al.* [3], the $\sqrt{3}\times\sqrt{3}$ superstructure appears around 0.2 ML of Al on the Si(111)2×1 surface and completely replaces the 2×1 pattern at about 0.3–0.4 ML. Then, at nearly 1 ML it transforms into the Si(111)1×1 structure [2–4]. After deposition of about 4 ML of Al, the Al(111)1×1 spots are observed with the Al$[1\bar{1}0]\parallel$ Si$[1\bar{1}0]$, which replace finally the Si(111)1×1 structure in the LEED pattern [3].

In contrast, Kelly *et al.* [1] reported that the $\sqrt{3}\times\sqrt{3}$ structure forming at about 0.5 ML of Al remains visible up to coverage of nearly 1.5 ML. At about 1.5 ML of Al, a complicated pattern with a strong diffuse background appears. This pattern suggests a reconstruction incommensurate with respect to the substrate.

1.1.2. RT Deposition on to Si(111)7×7

For RT Al deposition on to the Si(111)7×7 surface no new superstructure is observed, whereas LEED characterization shows only progressive blurring of the LEED pattern up to about 2 ML of Al [6].

1.1.3. HT Growth

The sequence of aluminum structures on Si(111)7×7 versus coverage is represented in Fig. 1.

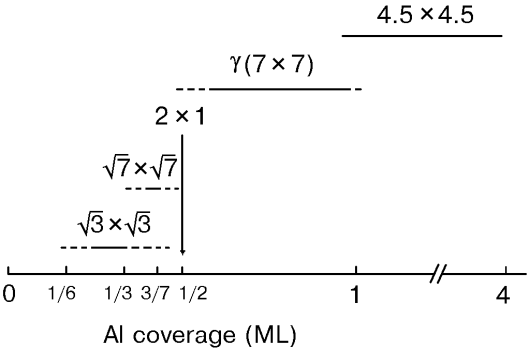

Fig 1. Sequence of the LEED pattern versus aluminum coverage (at the deposition on to the heated Si(111)7 × 7 surface or annealing of Al layer deposited at RT). (*Reproduced by permission of the publishers of Journal of Physical Review B*)

The Si(111)$\sqrt{3} \times \sqrt{3}$–Al structure can be formed by evaporating $\sim$ 2 ML of Al on to the Si(111)7 × 7 surface and then annealing at 850 °C for 30 s (after annealing the amount of Al is a 1/3 ML) or by evaporating $\approx$ 1/3 ML of Al on to the hot (500–700 °C) Si(111) 7 × 7 substrate [7]. Deposition on to the hot surface generally produces overlayers with a higher degree of long-range order [8]. The $\sqrt{3} \times \sqrt{3}$–Al structure was found to exhibit a reversible order–disorder transition at about 800 °C [7, 9].

According to STM [8], at Al coverage slightly higher then 1/3 ML, the local regions with $\sqrt{7} \times \sqrt{7}$ structure coexist with the $\sqrt{3} \times \sqrt{3}$ structure. The completed Si(111)$\sqrt{7} \times \sqrt{7}$—R19.1°–Al overlayer can be prepared by heating the $\sqrt{3} \times \sqrt{3}$ surface to 600 °C and depositing an additional $\simeq$ 1/5 ML of Al [7].

The Si(111)2 × 1–Al structure was observed in STM only [8] when $\simeq$ 0.5 ML Al was deposited on Si(111), followed by a short anneal to 820 °C for 15 s. This structure has not been reported in any other studies of Al/Si(111), presumably because it occupies only a small fraction of the surface and because it may require unusual preparation conditions.

Above 3/7 ML coverage, a new surface structure is observed which was called in the early work of Lander and Morrison [7] a $\gamma(7 \times 7)$ phase. The periodicity of this phase was reexamined by Hamers [8] using STM and by Nishikata *et al.* [10] using LEED. Hamers [8] determined the lattice constant of the $\gamma(7 \times 7)$–Al reconstruction to equal the (6.9 ± 0.2) periods of the Si(111)1 × 1 lattice. In contrast, Nishikata it et al. [10] reported this structure to be incommensurate one with the periodicity close to 9 × 9. This "γ–phase" can be formed either by depositing 1–2 ML Al and heating to 700° [8] or by evaporating 1 ML Al on to the hot (500–800 °C) Si(111) surface. The Al coverages of the $\gamma(7 \times 7)$ overlayer are between 0.5 and 1 ML.

The Si(111)4.5 × 4.5–Al structure was reported only by Li *et al.* [11]. It was formed by depositing 0.6–4.5 ML Al on to the Si(111)$\sqrt{3} \times \sqrt{3}$–Al substrate held at 350 °C.

1.2. STRUCTURE

1.2.1. Si(111)$\sqrt{3} \times \sqrt{3}$—R30°–Al

The Si(111)$\sqrt{3} \times \sqrt{3}$—R30°–Al phase has been studied with a variety of surface-sensitive techniques: LEED [1, 7], ARUPS [12–16], KRIPES [17], EELS [18–20], IAES [21], STM [8, 22–25], dynamical LEED [10, 26], as well as theoretically by using the band-structure–total energy minimization calculations [27] and the first-principle molecular-dynamical simulations [28].

At 1/3 ML Al coverage, the most natural model for the $\sqrt{3} \times \sqrt{3}$ overlayer is a simple adatom structure in which Al atoms adsorb atop a bulk-like Si(111) lattice. In this model,

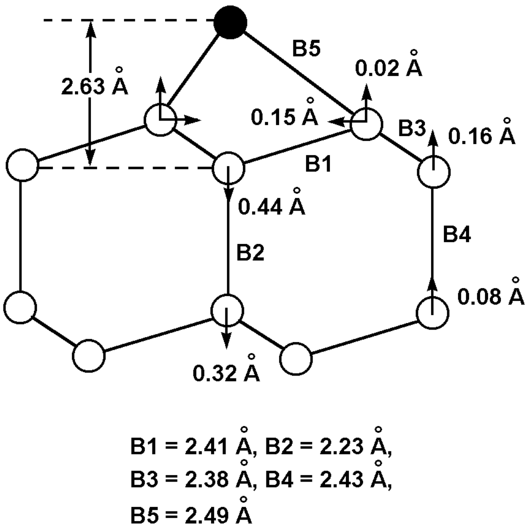

Fig 2. The preferred Si(111)$\sqrt{3}\times\sqrt{3}$—$R30°$–Al structure, with Al (solid circle) occupying the T_4 site. Arrows refer to atomic displacements from bulk sites (from Ref. [26]). (*Reproduced by permission of the publishers of Journal of Physical Review B*)

each Al adatom saturates three Si dangling bonds. By arranging the Al adatoms in a $\sqrt{3}\times\sqrt{3}$ geometry, complete saturation of all silicon dangling bonds is achieved at 1/3 ML Al. There are, however, two different types of threefold-symmetrical sites on Si(111), one above the Si atom in the fourth layer (H_3 sites) and one above the Si atom in the second layer (T_4 sites).

In the pioneer work [7], Lander and Morrison proposed an adatom model in which the Al atoms occupy the H_3 sites. An alternative geometry was suggested by a theoretical study of Northrup [27] with the Al adatoms in the T_4 sites. These sites were found to be more stable than the H_3 sites by 0.3 eV/adatom. The STM results [8, 22, 25] and photoemission results [12–14, 17] favor the T_4 site over the H_3 site. This preference is also based on Northrup's calculation [27], which predict a band-gap of 1.5 eV for the T_4 model, but only 0.8 eV for the H_3 model. The band-gap of nearly 2 eV as observed by STM and photoemission measurements is significantly larger than Northrup's prediction for either model, but is closer to the predictions for the T_4 model. Additional support for the T_4 model is provided by experimental measurements of the band dispersions for both occupied [17] and unoccupied states [12–14], which show better agreement with the T_4 model than with H_3 model. In addition, the results of quantitative dynamical LEED intensity analysis of the Si(111)$\sqrt{3}\times\sqrt{3}$—$R30°$–Al structure conducted by Huang *et al.* [26] and Nishikata *et al.* [10] confirm T_4 model. The positions of the Al adatoms and all atoms in the first three layers of the substrate as determined in Ref. [26] are indicated in Fig. 2. The geometries obtained in another LEED study [10] and in the theoretical studies [27, 28] are almost the same.

Thus, it is safe to conclude that the T_4 site is the correct adsorption site for the Al adatoms in the Si(111)$\sqrt{3}\times\sqrt{3}$—$R30°$–Al structure.

1.2.2. Si(111)$\sqrt{7}\times\sqrt{7}$—R19.1°–Al

The Si(111)$\sqrt{7}\times\sqrt{7}$—$R19.1°$–Al structure was found by Lander and Morrison [7]. This reconstruction has been studied by LEED [1, 7], ARUPS [16], IAES [21], HREELS [1] and STM [8, 24]. According to STM [8], there are three Al adatoms per $\sqrt{7}\times\sqrt{7}$ unit cell. Since the bulk-truncated Si(111) surface has seven Si atoms in each $\sqrt{7}\times\sqrt{7}$ unit cell, this places the local Al coverage at 3/7 (=0.43) ML. This 3/7 ML Al coverage is consistent with previous AES–LEED–ARUPS study [16], in which it was determined that the $\sqrt{7}\times\sqrt{7}$ structure arises

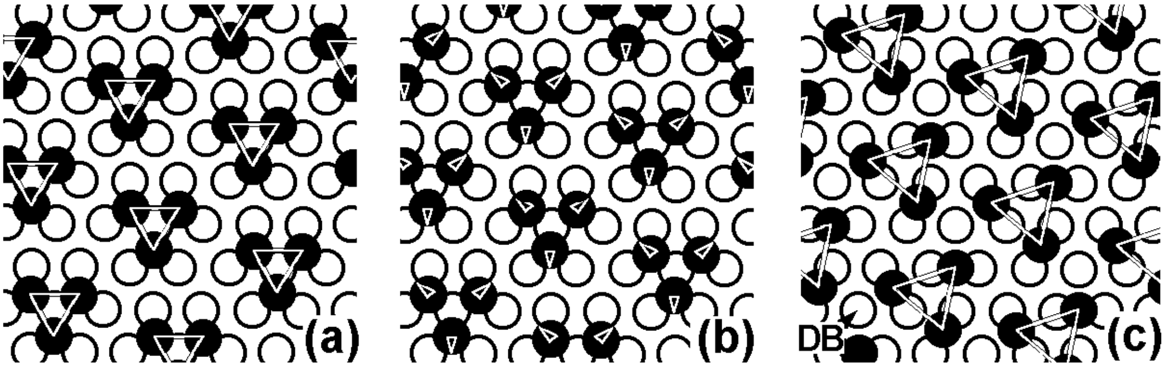

Fig 3. Models for the $\sqrt{7}\times\sqrt{7}$ structure: (a) Hansson's model (from Ref. [16]), (b) radial displacement of Al adatoms due to overcoordination of central Si atoms, (c) new model for $\sqrt{3}\times\sqrt{3}$ resulting from the radial displacements (from Ref. [8]). (*Reproduced by permission of the publishers of Journal of Physical Review B*)

at Al coverages between 0.25 and 0.5 ML.

The structural model of the $\sqrt{7}\times\sqrt{7}$—$R19.1°$–Al was proposed in the early work of Hansson *et al.* [16] (Fig. 3(a)). The model was based on ARUPS results, but it was not confirmed in the subsequent STM investigations [8]. In this model (Fig. 3(a)) lines connecting pairs of aluminum adatoms within each trimer should be oriented parallel to the $[1\bar{1}0]$ direction. In contrast, the STM images show that the clusters are rotated by nearly 15°. The agreement with STM measurements can be achieved by displacing the Al adatoms in each cluster radially outward on to equivalent twofold sites, as in Fig. 3(b). This radial displacement moves Al adatoms from adjacent clusters closer together, in effect forming new sets of clusters, as shown in Fig. 3(c) [8]. Lines connecting pairs of adatoms in the new clusters are rotated by 10.9° with respect to $[1\bar{1}0]$, and Al adatoms within each cluster are separated by $\sqrt{7}a/2 = 5.1$ Å. Both the rotational orientation and the individual atom separations predicted by this new model are in excellent agreement with the STM measurements [8].

1.2.3. Si(111)2×1–Al

The 2 × 1 structure was occasionally observed in STM when $\simeq$ 0.5 ML Al was deposited on Si(111) followed by a short anneal to 800 °C for 15 s [8]. The rare occurrence of this structure and the limited amount of data obtained permit only speculation about its origin. However, the corrugation profiles are consistent with its assignment as a 2 × 1 reconstruction of the clean Si(111) surface [8].

1.2.4. Si(111)7×7–Al "γ-phase"

The 7 × 7–Al structure arises at Al coverages between 0.5 and 1 ML. STM images of this overlayer [8] show an irregular arrangement of triangle-shaped structures. Although triangles have slightly irregular sizes and shapes, there is a clear tendency for the edges of the triangular regions to be aligned along the principal (111) surface lattice directions. The 7 × 7–Al overlayer exhibits poor short-range order, but it has a good long-range order. The triangles are separated by jagged troughs approximately 0.4 Å deep. No significant structure is observed within the islands. In order to determine the most likely locations for the Al atoms in the 7 × 7–Al structure, the STM data [8] were compared with theoretical density-of-states calculations by Chelikowsky [29] for Lander's model [7] (the Al atoms are substituting for all Si atoms in the outermost atomic layer) and with calculations by Zhang and Schlüter [30] for the upper model (adatoms directly above the Si atoms of the outermost double layer). The

STM data (Fig. 4) indicate that at coverage of $\simeq 1$ ML the Al most likely substitutes for the Si atoms in the outermost atomic layer of the Si(111) lattice. The origin of the 7×7 periodicity and detailed atomic arrangement at the boundaries of the triangular regions remain uncertain.

1.3. PROPERTIES

1.3.1. Electronic Properties

According to ARUPS [12, 14, 16, 31], KRIPES [17], and STM [8, 22–24], at low coverage the $\sqrt{3} \times \sqrt{3}$–Al structure clearly leads to a semiconducting surface with a large gap, as the Al adatoms eliminate the midgap states originating on the Si "dangling bonds". The only states remaining near the midgap are those arising from the Si substitutional defects [8, 12, 13, 23]. When the coverage of aluminum is increased from 1/3 to 3/7 ML, the bonding-site symmetry shifts from the T_4 site to twofold site [8]. Adopting the twofold site also allows for significant covalent bonding between the Al adatoms themselves, resulting in additional partially delocalized bonding states between three Al adatoms and the long Si dangling bond in each $\sqrt{7} \times \sqrt{7}$ unit cell [8, 24]. Although this "cooperative" bonding state is somewhat more delocalized than the direct Al–Si bonding states, it is not truly metallic since it is still limited in spatial extent. It is only at the highest coverage, and in the coincident formation of the 7×7–Al overlayer, that metallic character is observed. This is also true in RT deposition, where Kelly *et al.* [19] showed using HREELS that, at low temperatures, deposition of Al on to Si(111)7×7 results in Schottky-barrier formation which correlates with the onset of metallic character near 1 ML Al coverage. The metallic character is also evident from the very small amplitude of the STM corrugation probing both empty and filled states, since the accompanying delocalization of the wave functions reduces the local corrugation amplitude

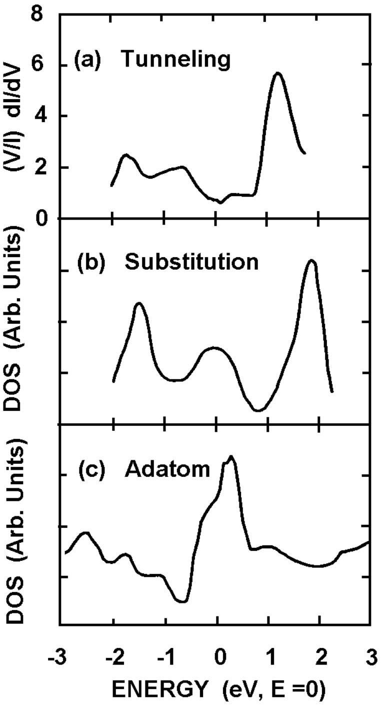

Fig 4. (a) Tunneling spectroscopy results for Si(111)7×7–Al structure, (b) density of states predicted by Chelikowsky for the Al substitution model (from Ref. [29]), and (c) density of states predicted by Zhang and Schlüter for Al–adatom model (from Ref. [30]). (*Reproduced by permission of the publishers of Journal of Physical Review B*)

over the individual atoms (which are no longer observed) [8].

Thereby the changes in atomic geometry are directly related to changes in the local electronic structure, which changes from semiconducting at low coverages to metallic at a coverage of ≃ 1 ML.

2. (100) ORIENTATION

Aluminum induces several reconstructions on the Si(100) surface. These are 2×2, 2×3, 4×5, 1×7, and $c(4 \times 12)$ structures.

2.1. PHASE DIAGRAM

2.1.1. RT Deposition

Only a few works are devoted to RT deposition of Al on the Si(100) surface [7, 32–34] and the results of different authors are not always in agreement.

In the early work, Lander and Morrison [7] reported that Al deposition about one-half monolayer on to the Si(100) surface produces a disordered phase at RT. Annealing above 500 °C causes surface reconstruction on to etch pits with well-developed Si(111) surfaces. These data do not agree with the results of subsequent publications [32–25] and Murakami *et al.* [35] observed that, upon Al deposition at RT, the two-domain 2×1 LEED pattern changes into the 2×2 LEED pattern with increasing θ_{Al} up to 1/2 ML. At Al coverages beyond 1/2 ML, the background of the 2×2 structure becomes high and the spots become weak. At a certain coverage above 1 ML, the (1/2, 1/2) spots disappear and a weak two domain 2×1 LEED pattern remains. By further deposition of Al it changes into a high background pattern without diffraction spots. Nogami *et al.* [32] confirmed these data by STM.

Hasan *et al.* [34] investigated growth of Al on Si(100)2×1 using *in situ* RHEED, LEED and AES and *ex situ* TEM and SEM. RHEED observation during growth demonstrated a continuous change from the original Si(100)2×1 pattern to a 1×1 pattern after deposition of 2 ML. According to the AES and RHEED results, growth of Al is two-dimensional up to an Al coverage of ~ 2 ML and quasi-two-dimensional up to $\theta_{\mathrm{Al}} \approx 4$ ML. At this coverage (4 ML), an Al(110) bulk diffraction pattern was observed with RHEED demonstrating the growth of Al(110) crystals.

The extreme sensitivity of Al to contamination, especially to oxygen-containing molecules, can cause some inconsistency in the results obtained by different authors.

2.1.2. HT Deposition

The phase diagram for the Al/Si(100) system was reported first by Ide *et al.* in Ref. [33] (Fig. 5). The surface phases were formed by Al deposition on to the heated Si(100) surface.

Upon Al deposition at 300 °C, a two-domain 2×3 LEED pattern appears at about 1/3 ML. The 1/3 fractional order spots are streaky along the direction parallel to the threefold axis. Beyond 1/3 ML, it becomes a mixed pattern of 2×3 and a weak 2×2 and further deposition beyond 0.4 ML changes it into a 1×1 structure.

Upon Al deposition at 400 °C, a two-domain 4×5 LEED pattern appears at coverages between 0.3 and 0.4 ML. Every fractional-order spot is weaker than those of the other LEED patterns observed in the Si(100)–Al system. Beyond 0.4 ML, the pattern changes gradually into 1×1.

For a substrate temperature of 500 °C, a 1×7 LEED pattern occurs at coverages ranging from 0.3 to 0.4 ML and a diffuse $c(4 \times 12)$ LEED pattern is observed at Al coverages from 0.4

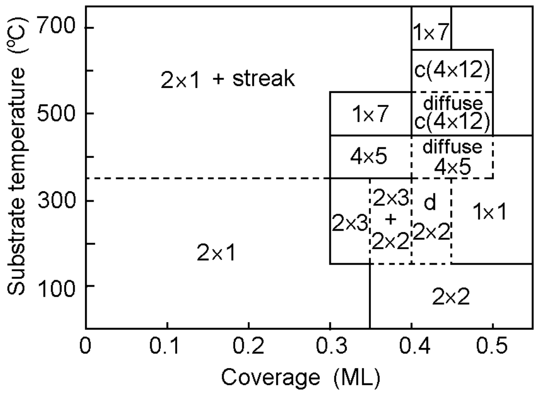

Fig 5. Formation diagram of surface structures on the Si(100)–Al phases for coverages less than 1 ML and at substrate temperatures from room temperature up to 700°C (from Ref. [33]). (*Reproduced by permission of Elsevier Science Publishers BV*)

to 0.5 ML. The sharp two-domain $c(4 \times 12)$ LEED pattern is observed upon Al deposition at 600 °C. Every spot of this $c(4 \times 12)$ pattern appears to be sharper than those of other patterns. At 700 °C, the streaky 2×1 LEED pattern transforms to a two-domain 1×7 one beyond 0.4 ML.

In the experiment of Ref. [33], no more than 0.5 ML could be deposited above a substrate temperature of 600°C. This indicates that sticking coefficient of Al falls off abruptly beyond 0.5 ML saturation coverage at these growth temperatures.

The main results of Ref. [33] were reproduced in the later work of Murakami *et al.* [35] with a few exceptions: The authors of Ref. [35] did not obtain the $c(4 \times 12)$ structure at 500–600°C and observed a poorly ordered 4×1 structure instead of 4×5 one at about 400°C.

2.2. STRUCTURE

2.2.1. Si(100)2×2–Al and Si(100)2×3–Al

Below 0.5 ML Al, the 2×2 and 2×3 phases are detected by LEED [33,35] and STM [32]. In Ref. [33], the structure for these phases was proposed. It involves the placement of Al dimers between the Si dimer rows (Fig. 6). The subsequent STM studies [32] provided strong support for this model. The metal atoms are adsorbed on the surface as dimers. The dimers are arranged in rows, as seen in the STM images. When these rows are $3a$ ($2a$) apart, local areas of 2×3 and 2×2 order are formed. (Here, a is a periodicity of the unreconstructed Si(100) surface.) One can see that proposed 2×3 and 2×2 structures correspond to 0.3 ML and 0.5 ML coverages, respectively. The 2×2 arrangement at 0.5 ML is the densest possible packing of rows in this structure. When the Al dimers are packed in the 2×2 phase, all dangling bonds in the underlying Si surface are terminated. On top of this layer, Al forms three-dimensional clusters [32].

One final point addressed in Ref. [32] concerns the two possible configurations in which Al dimers could be placed on the Si(100) surface, namely, with Al dimers either perpendicular or parallel to the underlying Si dimers (see Fig. 7). STM did not provide enough evidence to choose the preferential configuration. This was done by Northrup *et al.* [36] on the basis of first principles total energy calculations which showed that parallel dimer configuration (Fig. 7(b)) has a significantly lower surface energy than the orthogonal dimer configuration.

3. (110) ORIENTATION

The $\begin{pmatrix} 3 & 0 \\ -1 & 4 \end{pmatrix}$, $\begin{pmatrix} 9 & 0 \\ -2 & 1 \end{pmatrix}$, 1×2, and 1×1 reconstructions were found for the Al/Si(110) system.

3.1. PHASE DIAGRAM

The formation of the two-dimensional phase diagram of the Al/Si(110) system as deduced by Zotov *et al.* [37] from LEED–AES observations is shown in Fig. 8. In the experiment, Al deposition was carried step by step at a given substrate temperature. After each step, the sample was cooled to room temperature for LEED–AES observations.

When Al is deposited on to the Si(110) substrate held at 600 to 700 °C, two well-defined Al-induced reconstructions are observed sequentially. The first one is the two-domain "4×6" structure which exists at Al coverages from 0.16 to 0.3 ML and the second one is the two-domain "1×9" structure occurring from 0.3 ML up to saturated Al coverage of 0.5 ML. Sketches of the LEED patterns (reciprocal lattices) for single- and two-domain "4×6" and "1×9" phases are shown in Fig. 9. The quotes in the notation of "4×6" and "1×9" structures indicate that these reconstructions are not aligned along the bulk symmetry axes. They can be expressed more strictly in matrix notation as $\begin{pmatrix} 3 & 0 \\ -1 & 4 \end{pmatrix}$ for "4×6" and $\begin{pmatrix} 9 & 0 \\ -2 & 1 \end{pmatrix}$ for "1×9".

Yamamoto [38] using RHEED also revealed the formation of two superstructers at high temperatures (780 °C), labeled as $(3,3) \times (\bar{2},1)$ (i.e. $\begin{pmatrix} 3 & 3 \\ -2 & 1 \end{pmatrix}$) and 3×8. While the $(3,3) \times (\bar{2},1)$ corresponds definitely to "1×9", the 3×8 is believed to correspond to "4×6".

The Al growth at temperatures from 600 down to about 500 °C is similar to that described above, i.e. sequential formation of "4×6" and "1×9" phases is observed. However, the critical Al coverages at which structural transformation from "4×6" to "1×9" occurs shifts towards higher coverages. The LEED patterns from "4×6" and "1×9" phases become gradually less sharp and bright with decreasing growth temperature.

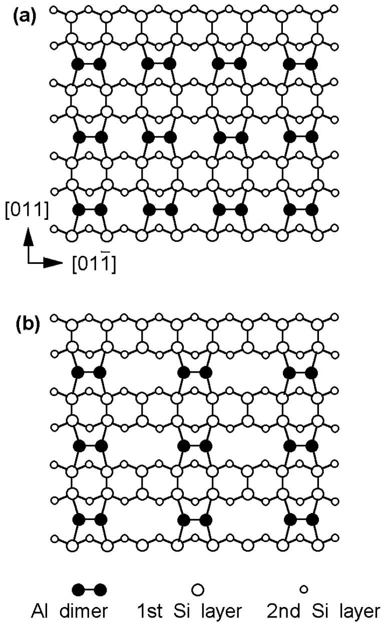

Fig 6. Structure models of (a) 2×2 and (b) 2×3 surfaces (from Ref. [33]). (*Reproduced by permission of Elsevier Science Publishers BV*)

(a) 2x2 ortogonal ad-dimer

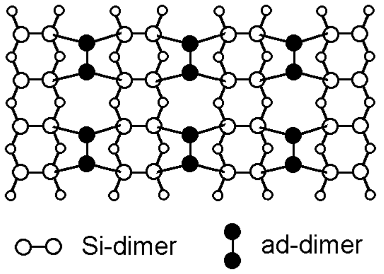

(b) 2x2 parallel ad-dimer

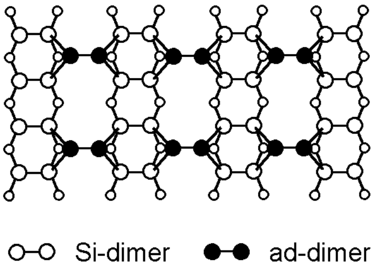

Fig 7. Two possible bonding arrangements of Al dimers on the surface. The Al dimers are positioned either perpendicular (a) or parallel (b) to the underlying Si dimers (from Ref. [36]). (*Reproduced by permission of the publishers of Journal of Physical Review B*)

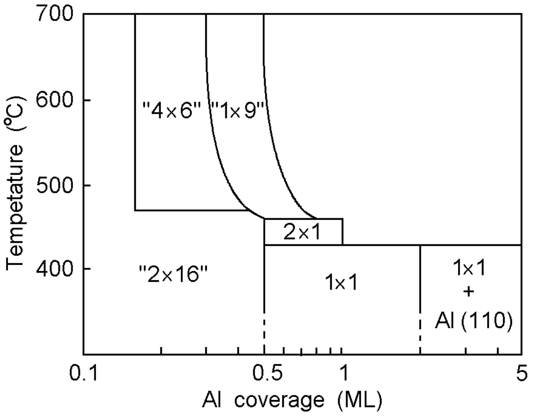

Fig 8. Two-dimensional phase diagram of Al/Si(110) system (from Ref. [37]). (*Reproduced by permission of Elsevier Science Publishers BV*)

Upon deposition of Al at about 450 °C, a new structure, 1×2 , appears at about 0.5 ML and occurs up to Al coverage saturation at about 1 ML. The 1×2 phase was found to exist in a very narrow temperature interval from about 430 to 460 °C.

Upon Al deposition below 430 °C, a 1×1 LEED pattern is observed at coverages beyond 0.5 ML. At these growth temperatures, the Al layer does not saturate at a certain coverage and Al deposition on to the 1×1 phase results in the appearance of the LEED spots corresponding to epitaxial Al(110).

Al deposition at room temperature gradually enhances the background and eliminates all diffraction spots in the LEED pattern. This result indicates the formation of the disordered film.

The annealing of the RT Al deposit produces one of the phases described above depending on Al coverage and annealing temperature. For example, annealing of several ML thick Al films produces sequentially a 1×1 phase at 400 °C, a 1×2 phase at 450 °C and "1×9" phase at 600 °C.

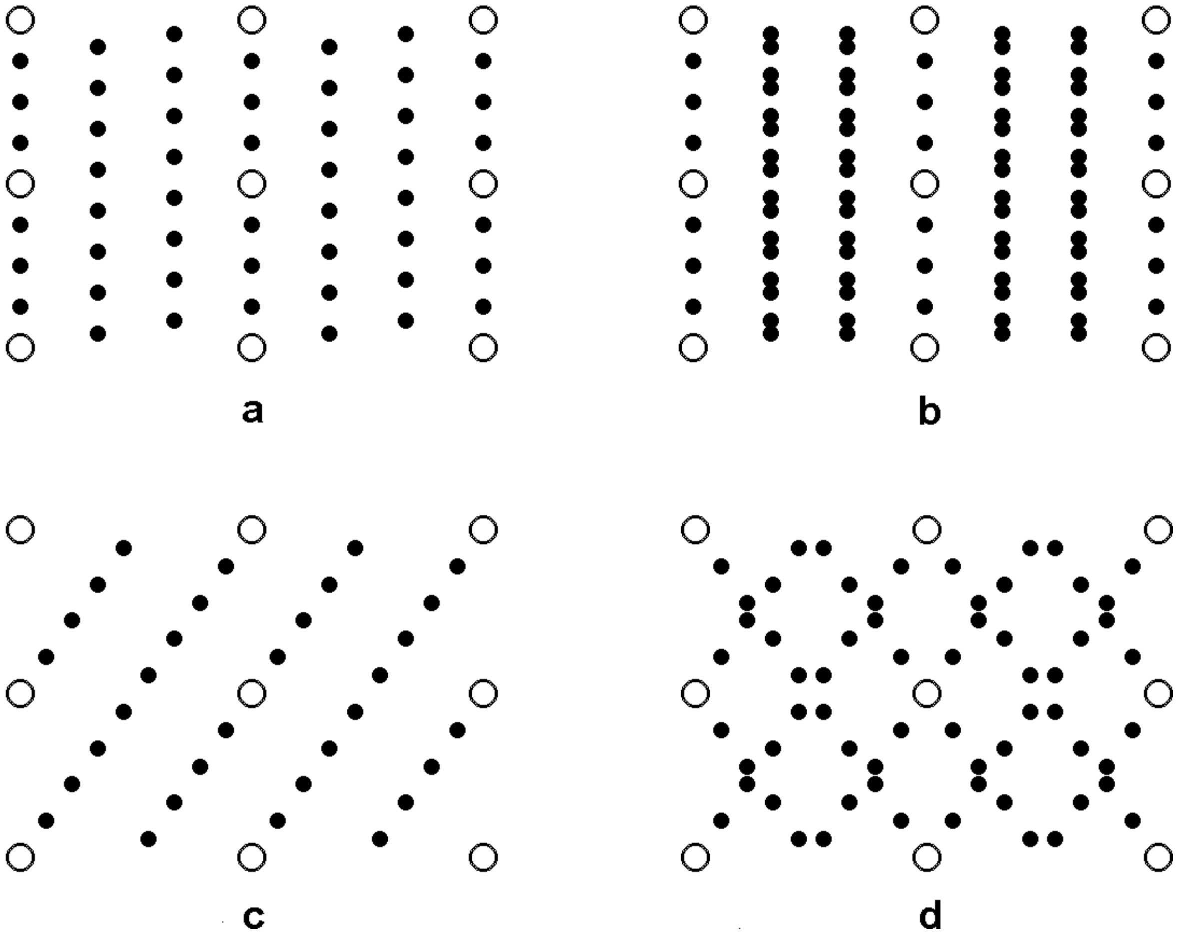

Fig 9. Sketches of LEED patterns (reciprocal lattices) for (a) single-domain and (b) two-domain "4 × 6" structure. (c) and (d), the same for "1 × 9" structure. Open circles are fundamental spots, closed circles are fractional order spots (from Ref. [37]). (*Reproduced by permission of Elsevier Science Publishers BV*)

REFERENCES

[1] M. K. Kelly, G. Margaritondo, J. A. Anderson, D. J. Frankel and G. J. Lapeyre, *J. Vac. Sci. Technol. A* **4** (1986) 1396.

[2] C. A. Sebenne, in *Proc. 17th Int. Conf. Phys. Semic.* , Eds. J. D. Chadi and W. A. Harrison, Springer-Verlag (1985) 143.

[3] P. Chen, D. Bolmont and C. A. Sebenne, *J. Phys. C* **17** (1984) 4897.

[4] A. W. Parke, A. McKinley, R. H. Williams and G. P. Srivastava, *J. Phys. C* **13** (1980) L369.

[5] K. L. I. Kobayashi, F. Gerken, J. Barth and C. Kunz, *Solid State Commun.* **39** (1981) 851.

[6] W. S. Yang, S. C. Wu and F. Jona, *Surf. Sci.* **169** (1986) 383.

[7] J. J. Lander and J. Morrison, *Surf. Sci.* **2** (1964) 553.

[8] R. J. Hamers, *Phys. Rev. B* **40** (1989) 1657.

[9] R. Q. Hwang, E. D. Williams and R. L. Park, *Surf. Sci.* **193** (1988) L53.

[10] K. Nishikata, K. Murakami, M. Yoshimura and A. Kawazu, *Surf. Sci.* **269–270** (1992) 995.

[11] S. -T. Li, S. Hasegawa, N. Yamashita and H. Nakashima, *Appl. Surf. Sci.* **41-42** (1989) 118.

[12] T. Kinoshita, S. Kono and T. Sagawa, *Phys. Rev. B* **32** (1985) 2714.

[13] R. I. G. Uhrberg, G. V. Hansson, J. M. Nicholls, P. E. S. Persson and S. A. Flodstrom, *Phys. Rev. B* **31** (1985) 3805.

[14] T. Kinoshita, S. Kono and T. Sagawa, *Solid State Commun.* **56** (1985) 681.

[15] G. V. Hansson, R. Z. Bachrach, R. S. Bauer and P. Chiaradia, *J. Vac. Sci. Technol.* **18** (1981) 550.

[16] G. V. Hansson, R. Z. Bachrach, R. S. Bauer and P. Chiaradia, *Phys. Rev. Lett.* **46** (1981) 1033.

[17] J. M. Nicholls, B. Reihl and J. E. Northrup, *Phys. Rev. B* **35** (1987) 4137.

[18] M. K. Kelly, G. Margaritondo, J. A. Anderson, D. J. Frankel and G. J. Lapeyre, *J. Vac. Sci. Technol. A* **3** (1985) 1481.

[19] M. K. Kelly, G. Margaritondo, L. Papagno and G. J. Lapeyre, *Phys. Rev. B* **34** (1986) 6011.

[20] S. -T. Li, S. Hasegawa, S. Nakamura and S. Nakashima, *Japan J. Appl. Phys.* **30** (1991) L1671.

[21] T. Aizawa, T. Tsuno, H. Daimon and S. Ino, *Phys. Rev. B* **36** (1987) 9107.

[22] R. J. Hamers and J. E. Demuth, *J. Vac. Sci. Technol. A* **6** (1988) 512.

[23] R. J. Hamers and J. E. Demuth, *Phys. Rev. Lett.* **60** (1988) 2527.

[24] R. J. Hamers, *J. Vac. Sci. Technol. B* **6** (1988) 1462.

[25] T. Takaoka, M. Yoshimura, T. Yao, T. Sato, T. Sueyoshi and M. Iwatsuki, *Mat. Res. Soc. Simp. Proc.* **295** (1993) 59.

[26] H. Huang, S. Y. Tong, W. S. Yang, H. D. Shih and F. Jona, *Phys. Rev. B* **42** (1990) 7483.

[27] J. E. Northrup, *Phys. Rev. Lett.* **53** (1984) 683.

[28] H. Tsuge, M. Arai and T. Fugiwara, *Japan J. Appl. Phys.* **30** (1991) L1583.

[29] J. R. Chelikowsky, *Phys. Rev. B* **16** (1977) 3618.

[30] H. I. Zhang and M. Schlüter, *Phys. Rev. B* **18** (1978) 1923.

[31] G. V. Hansson, J. M. Nicholls, P. Martensson and R. I. G. Uhrberg, *Surf. Sci.* **168** (1986) 105.

[32] J. Nogami, A. A. Baski and C. F. Quate, *Phys. Rev. B* **44** (1991) 1415.

[33] T. Ide, T. Nishimori and T. Ichinokawa, *Surf. Sci.* **209** (1989) 335.

[34] M. -A. Hasan, G. Radnoczi, J. -E. Sundgren and G. H. Hansson, *Surf. Sci.* **236** (1990) 53.

[35] K. -I. Murakami, K. Nishikata, M. Yoshimura and A. Kawazu, *Appl. Surf. Sci.* **60–61** (1992) 146.

[36] J. E. Northrup, M. C. Schabel, C. J. Karlsson and R. I. G. Uhrberg, *Phys. Rev. B* **44** (1991) 13799.

[37] A. V. Zotov, E. A. Khramtsova, V. G. Lifshits, A. T. Kharchenko, S. V. Ryzhkov and A. N. Demidchik, *Surf. Sci.* **277** (1992) L77.

[38] Y. Yamamoto, *Japan J. Appl. Phys.* **31** (1992) L53.

(Ar)

ARGON

1. (111) ORIENTATION

The physisorption of Ar on the Si(111)7×7 surface does not change the initial silicon reconstruction.

1.1. PHASE DIAGRAM

The physisorption of Ar on the Si(111)7×7 surface can occur only at low sample temperature (23 K) [1]. Since the interaction is weak, the substrate is not affected. Particular, superstructures are not eliminated or modified. UPS measurements of the coverage-dependent electron binding energies distinguish three submonolayer types of adsorption sites of Ar on Si(111)7×7 [2]. Thermal desorption spectroscopy also resolved three different adsorption sites with energy in the range from 70 to 110 MeV [1]. The desorption temperature of adsorbed Ar is about 50 K [1]. At low temperatures (< 31 K) the multilayer physisorption occurs.

REFERENCES

[1] J. W. Bartha, U. Barienbruch and M. Henzler, *J. Phys. C* **19** (1986) 2459.

[2] J. E. Demuth and A. J. Schell-Sorokin, *J. Vac. Sci. Technol. A* **2** (1984) 808.

(As)

ARSENIC

1. (111) ORIENTATION

Arsenic removes the reconstruction of the Si(111)7 × 7 surface and forms a well-defined 1 × 1 structure.

1.1. PHASE DIAGRAM

The Si(111)1 × 1–As surface phase is formed by annealing the clean Si(111) surface while exposing it to As_4 flux. To produce a well-ordered 1 × 1–As surface the procedure proposed by Olmstead *et al.* [1, 2] is usually employed: during exposures, the sample is briefly flashed to high temperature of 850 to 1050 °C and then allowed to cool in the arsenic flux to about 350 °C. The As coverage in saturation for 1 × 1–As phase is reported to be slightly less than 1 ML. Two studies using medium-energy ion scattering determined the coverage to be 0.92 ± 0.05 ML [3] and 0.93 ± 0.04 ML [10] which is consistent with the value (~ 0.93 ML) determined by the X-ray standing-wave technique [5].

When the Si(111) surface is kept at a constant temperature of 350 °C at arsenic exposure, the resultant 1×1–As phase is not well ordered, but arsenic coverage remains close to 1 ML [6]. Exposures at higher constant temperature result in improvement of the structural perfection of 1 × 1–As phase but lead to the decrease of As coverage (e.g., the structural quality of the phase formed at 600 °C coincides with that of the phase prepared by cooling in the As beam from high temperature, but the coverage obtained is only 0.5 ML).

1.2. STRUCTURE

1.2.1. Si(111)1 × 1–As

The atomic structure of the Si(111)1 × 1–As surface phase has been studied by several groups using different experimental techniques, namely, scanning tunneling microscopy [6–8], X-ray standing waves [5, 9], medium energy ion scattering [3, 6, 10, 11] and angle-resolved photoelectron spectroscopy [1, 2, 6, 12]. All studies agree on the model where the As atoms replace the outermost Si atoms of the Si(111) surface as shown in Fig. 1. Both experimental measurements [5, 6, 10] and theoretical studies [1, 13, 14] indicated that As atoms lie about 0.2 Å above the position for perfectly terminated bulk silicon (see Fig. 2 and Table 1).

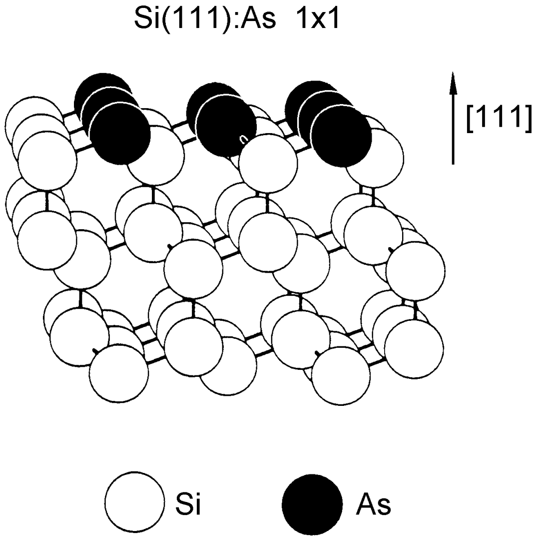

Fig 1. Model of the Si(111):As 1 × 1 surface (from Ref. [2]). (*Reproduced by permission of the publishers of Journal of Physical Review B*)

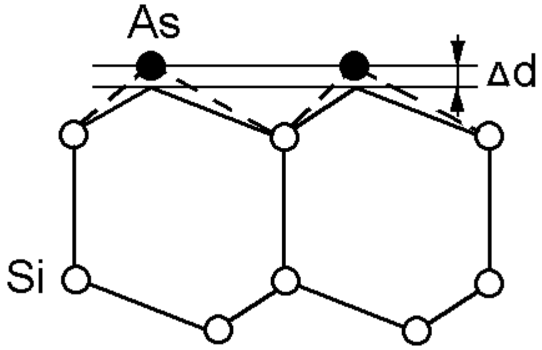

Fig 2. Outwards relaxation of arsenic–silicon spacing from the bulk silicon interplanar spacing. The values determined for Δd are summarized in Table 1. (*Reproduced by permission of the publishers of Journal of Physical Review B*)

1.3. PROPERTIES

1.3.1. Desorption

The desorption of As from the Si(111)1 × 1–As phase becomes significant at temperatures above 700 °C [2,15]. Zinke-Allmang *et al.* [15] showed that As atoms desorb according to a 2nd order kinetic law (Fig. 3) and the desorption rate constant $k(T)$ fits the Arrhenius type equation: $K(T) = K_0 \exp(-E_{\mathrm{des}}/kT)$ with $E_{\mathrm{des}} = 4.3 \pm 0.5$ eV and $K_0 = 10^{18\pm3}$ ML^{-1} s^{-1} (Fig. 4). The high pre-exponential factor for the desorption process was suggested as an indication that adsorbed As atoms are relatively immobile.

1.3.2. Passivation

The Si(111)1 × 1–As surface has been shown to be extremely passive against reaction with gas atoms [2,5,10,12,16]. This property has been investigated by exposing As-terminated Si(111) surface to controlled amounts of oxygen, air and hydrogen. It was found that both the 10^7 L oxygen and the 10^{11} L air exposure has only a minor effect on the surface as revealed by angle-resolved photoemission [2,12,16] and X-ray standing-wave [5] techniques.

This stability with respect to surface contamination is strongly indicative of saturation

Fig [.] **Table**

1. Results for the change in the arsenic–silicon interplanar spacing (Δd).

Δd (Å)	Technique	Reference
0.17 ± 0.3	X-ray	[5]
0.24 ± 0.06	MEIS	[10]
0.2 ± 0.1	MEIS	[6]
0.25	Theory	[13]
0.19	Theory	[1]
0.16	Theory	[14]

of all surface bonds. Samples with an uncompleted 1 × 1–As phase are much less resistant to contamination [10].

The As terminated surface is, however, not highly passivated with respect to atomic hydrogen. Hydrogen exposure (in the presence of a hot filament) causes a disordering of a Si(111)1 × 1–As surface [2, 5, 16]. But the original surface can be returned by annealing (600 °C/2 min), showing that the H atoms adsorb on to the Si(111)1 × 1–As surface rather than disrupt it [12, 16].

2. (100) ORIENTATION

Arsenic terminated Si(100) has a 1 × 2 superstructure. In the case of a single-domain Si(100)2 × 1 substrate, adsorption of arsenic causes the LEED pattern to rotate from 2 × 1 to 1 × 2 [17, 18]. In the case of the As overlayer growth on the two-domain Si(100)2 × 1 surface, a two-domain 2 × 1 LEED pattern with considerably sharper spots occurs [19, 20].

2.1. PHASE DIAGRAM

The Si(100)1 × 2–As surface phase is obtained by the same procedure as the Si(111)1 × 1–As surface, i.e. by the interaction of the As_4 beam with the Si surface either heated at a constant temperature of 350 – 400 °C [19, 21, 22] or cooled from 750 to 400 °C [17, 23]. The Si(100)1 × 2–As phase is completed at about 1 ML As [22].

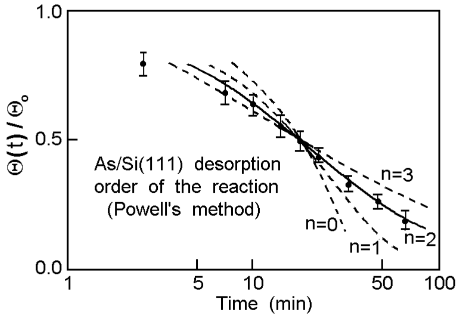

Fig 3. Desorption measurements for As on Si(111) at 750 °C. Data analysis by Powell's method for n, the order of the kinetic law. The solid line ($n = 2$) is in best agreement with the data (from Ref. [15]). (*Reproduced by permission of Elsevier Science Publishers BV*)

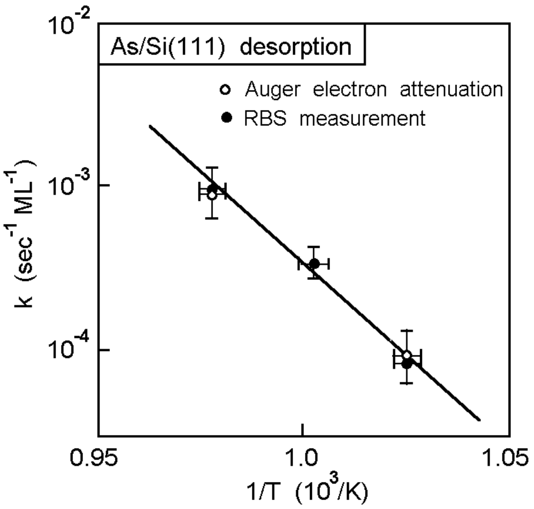

Fig 4. Arrhenius plot for the rates of desorption of As from Si(111) (from Ref. [15]). (*Reproduced by permission of Elsevier Science Publishers BV*)

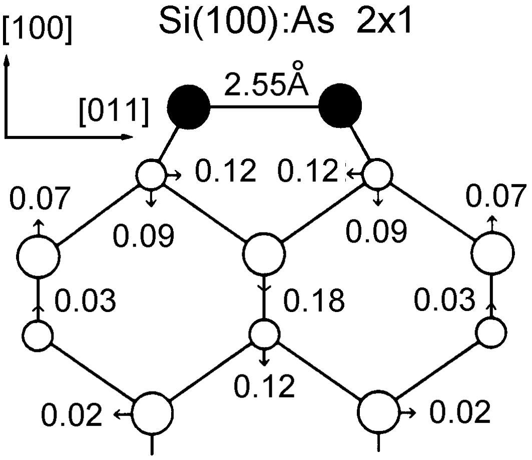

Fig 5. Side view of the As–As dimer model of the Si(100)1 × 2–As surface with As atoms shaded. The bond length between the As atoms and the subsurface displacements are indicated in angstroms (from Ref. [21]). (*Reproduced by permission of the publishers of Journal of Physical Review Letters*)

2.2. STRUCTURE

2.2.1. Si(100)1 × 2–As

Uhrberg *et al.* [17,19,21] proposed that the structure of the Si(100)1 × 2–As surface is caused by the formation of symmetric As–As dimers with an interatomic distance of 2.55 Å. In this model, each As atom bonds to two Si atoms and to the other As atom of the dimer (see Fig. 5). As a result, all As atoms are threefold coordinated with a doubly occupied lone-pair state. This model is consistent with the data of photoemission spectroscopy [12,17,19,21], low-energy neutral impact collision ion scattering [17], X-ray standing-wave technique [23], grazing incidence X-ray diffraction [22], and scanning tunneling microscopy [8]. The latter investigation [8] has shown also that As deposition on Si(100) results in elimination of missing dimer defects characteristic of the native Si(100)2 × 1 surface.

Using the X-ray standing-wave technique, the distance of the As atoms from the unrelaxed, ideal (100) surface was determined to be 1.26 ± 0.01 Å [23] which is close to the calculated value of 1.32 Å [21].

2.3. PROPERTIES

2.3.1. Passivation

The interaction of oxygen with the Si(100)–As surface was studied by Zhong *et al.* [24]. It was shown that the As layer is a good passivation film for the Si(100) surface. The oxygen coverage at saturation on the Si(100)–As surface is 0.5 ML, half of that on the clean Si(100) surface, *i. e.* , the adsorption sites are reduced by one-half with the existence of the As layer. The initial sticking coefficient of oxygen on the Si(100)2 × 1–As surface is 5.6×10^{-3}, which is ten times less than that for a clean Si(100) surface.

REFERENCES

[1] M. A. Olmstead, R. D. Bringans, R. I. G. Uhrberg and R. Z. Bachrach, *Phys. Rev. B* **34** (1986) 6041.
[2] R. I. G. Uhrberg, R. D. Bringans, M. A. Olmstead, R. Z. Bachrach and J. E. Northrup, *Phys. Rev. B* **35** (1987) 3945.
[3] M. W. Copel and R. M. Tromp, *Phys. Rev. B* **37** (1988) 2766.
[4] R. L. Headrick and W. R. Graham, *Phys. Rev. B* **37** (1988) 1051.
[5] L. R. Patel, J. A. Golovchenko, P. E. Freeland and H. -J. Gossmann, *Phys. Rev. B* **36** (1987) 7715.
[6] M. Copel, R. M. Tromp and U. K. Kohler, *Phys. Rev. B* **37** (1988) 10756.
[7] R. S. Becker, B. S. Swartzentruber, J. S. Vickers, M. S. Hybertsen and S. G. Louie, *Phys. Rev. Lett.* **60** (1988) 116.
[8] R. S. Becker, T. Klitsner and J. S. Vickers, *J. Microscopy* **152** (1988) 157.
[9] J. R. Patel, J. Zegenhagen, P. E. Freeland, M. S. Hybertsen, J. A. Golovchenko and D. M. Chen, *J. Vac. Sci. Technol. B* **7** (1989) 894.
[10] R. L. Headrick and W. R. Graham, *Phys. Rev. B* **37** (1988) 1051.
[11] R. L. Headrick and W. R. Graham, *J. Vac. Sci. Technol. A* **6** (1988) 637.
[12] R. D. Bringans and M. A. Olmstead, *J. Vac. Sci. Technol. B* **7** (1989) 1232.
[13] C. H. Patterson and R. P. Messmer, *Phys. Rev. B* **39** (1989) 1372.
[14] M. S. Hybertsen and S. G. Louie, *Phys. Rev. B* **38** (1988) 4033.
[15] M. Zinke-Allmang, L. C. Feldman, J. R. Patel and J. C. Tully, *Surf. Sci.* **197** (1988) 1.
[16] R. I. G. Uhrberg, R. D. Bringans, M. A. Olmstead, R. Z. Bachrach and J. E. Northrup, *in Proceedings of the 18th Int. Conf. Phys. Semiconduc. , Stockholm, 1986,* **1** (1987) 89.
[17] R. D. Bringans, R. I. G. Uhrberg, M. A. Olmstead and R. Z. Bachrach, *Phys. Rev. B* **34** (1986) 7447.
[18] M. Uneta, Y. Watanabe, Y. Fukuda and Y. Ohmachi, *Japan J. Appl. Phys.* **29** (1990) L17.
[19] R. I. G. Uhrberg, R. D. Bringans, R. Z. Bachrach and J. E. Northrup, *J. Vac. Sci. Technol. A* **4** (1986) 1259.
[20] H. Niehus, K. Mann, B. N. Eldridge and M. L. Yu, *J. Vac. Sci. Technol. A* **6** (1988) 625.
[21] R. I. G. Uhrberg, R. D. Bringans, R. Z. Bachrach and J. E. Northrup, *Phys. Rev. Lett.* **56** (1986) 520.
[22] N. Jedrecy, M. Sauvage-Simkin, R. Pinchaux, J. Massies, N. Greiser and V. H. Etgens, *Surf. Sci.* **230** (1990) 197.
[23] J. Zegenhagen, J. R. Patel, B. M. Kincaid, J. A. Golovchenko, J. B. Mock, P. E. Freeland and R. J. Malik, *Appl. Phys. Lett.* **53** (1988) 252.
[24] Z. T. Zhong, D. W. Wang, Y. Fan and C. F. Li, *J. Vac. Sci. Technol. B* **7** (1989) 1084.

(Au)

GOLD

1. (111) ORIENTATION

Au is known to induce 5×1 (5×2), $\sqrt{3} \times \sqrt{3}$, and 6×6 ordered reconstructions on the Si(111) surface.

1.1. PHASE DIAGRAM

1.1.1. RT Deposition

No Au-induced ordered structures are formed at the RT gold deposition on to Si(111)7×7 or cleaved Si(111)2×1 surfaces. LEED observations [1–8] revealed that in both cases the fractional order spots of the corresponding LEED pattern vanish readily for Au coverages in the submonolayer range. A 1×1 structure is then observed up to 1 ML. Beyond this coverage, the integral-order reflections disappear progressively and only a diffuse background is seen suggesting an amorphous character of the Au–Si interface.

As for the growth mode and composition of the grown film, most of the studies [2–5, 7, 9–14] agree on the behavior of the interface for Au coverages exceeding 3–4 ML: Au and Si react at the interface at RT forming an intermixed phase between silicon and the metal; the constituent atoms of the Si substrate are released from this alloyed region and segregate to the outer surface of the Au film forming a Si-rich surface monolayer with composition close to that of the Au_4Si eutectic.

However, there is some controversy on the very first stages (from a fraction of 1 ML to 1–2 ML Au) of Au/Si(111) interface formation. The basic disagreement concerns the question whether the reaction of the Au film with Si substrate occurs only when Au film exceeds a critical thickness typically of 1 to 5 monolayers (as was suggested by Hiraki [12–14], Le Lay [3], Perfetti *et al.* [4, 5], Iwami *et al.* [11, 15] and Katzer and Meinel [16]) or the silicon-metal reaction starts at the very beginning of the interface formation (as was suggested by Braicovich *et al.* [17–19], Dallaporta and Cros [20], and Houzay *et al.* [6]).

The discrepancies in the published results were surmised to arise from slightly different preparation conditions which would result in different substrate temperatures [7] and from the difficulty of analyzing a strongly inhomogeneous interface [20].

1.1.2. HT Growth

The Au/Si(111) submonolayer interfaces reconstruct at high temperatures into 5×1, $\sqrt{3} \times \sqrt{3}$, and 6×6 structures depending on the Au coverage. These ordered surface structures can

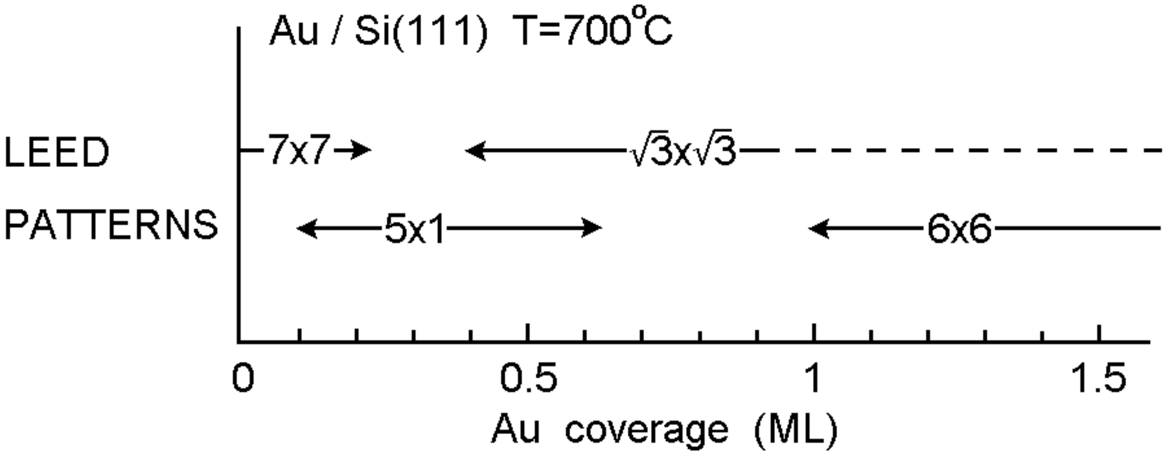

Fig 1. Sequence of LEED structures after cooling to room temperature when the Au atoms were deposited on to the Si(111) substrate at about 700 °C (from Ref. [21]). (*Reproduced by permission of Elsevier Science Publishers BV*)

be produced either by Au deposition on to the heated Si(111) substrate [2, 3, 21–28] or by annealing of the RT deposited Au film [29–37].

Upon deposition at high temperatures (beyond ~ 400 °C) the growth of Au on Si(111) follows the Stranski–Krastanov mode [3, 23, 24]. After successive formation of 5×1, $\sqrt{3}\times\sqrt{3}$, and 6×6 surface phases (see Fig.1), the 3D growth of gold crystallites is observed at Au coverages exceeding ~ 1.5 ML. *In situ* RHEED observations [3] revealed that the parallel orientation (111)Au $\parallel$ (111)Si, $[1\bar{1}0]$Au $\parallel$ $[1\bar{1}1]$Si of gold crystallites is dominating. (Though it is commonly accepted that the formation of the $\sqrt{3}\times\sqrt{3}$ structure is preceded by the formation of the 5×1 structure, Shibata *et al.* [38] found using STM that the formation of the 5×1 structure is suppressed at substrate temperatures from 200 to 280 °C and the $\sqrt{3}\times\sqrt{3}$ structure is formed from the beginning of Au deposition at this temperature range, while the 5×1 structure is formed above 320 °C. The STM study of Hasegawa *et al.* [39] revealed that the 5×1 structure grows at a step edge and expands towards both the higher and lower terraces.)

In the case of annealing of the disordered Au/Si(111) interface formed at RT, the annealing temperature exceeding 400 °C is necessary to induce the formation of the ordered reconstructions. For Au coverages less than about 2 ML, the composition of the Au deposit does not change upon annealing, while the disordered structure transforms into the ordered 5×1, $\sqrt{3}\times\sqrt{3}$, or 6×6 structures (see Fig.2). The coverage limits in which the different structures are observed are in agreement with those determined in Au deposition on to the heated Si(111) substrate (see Fig.3).

In Au films several monolayers thick, the annealing causes the agglomeration of Au atoms into metallic islands (which are possibly covered by Au–Si intermixed layer [31]). The area between islands is covered by 6×6 [31] or $\sqrt{3}\times\sqrt{3}$ [30] surface phases.

At temperatures above 800 °C, desorption of Au atoms from the surface takes place resulting in successive transformations towards the Au/Si(111) surface phases with lower Au surface concentrations, i.e. from a 6×6 phase with 3D islands to a 6×6 phase without islands, then to $\sqrt{3}\times\sqrt{3}$ and 5×1 phases and finally to the clean Si(111)7×7 surface [40].

A notable fact is that, for $\theta\geq1$ ML Au the 6×6 structure converts to a $\sqrt{3}\times\sqrt{3}$ structure, when the 6×6 surface is heated at 700 °C and heating is stopped suddenly. When this surface with $\sqrt{3}\times\sqrt{3}$ structure is annealed several times at 450 °C for ~ 5 min or heated once to 700 °C and kept at 450 °C for ~ 5 min and then cooled slowly to RT, a well-ordered 6×6 LEED pattern is recovered [24].

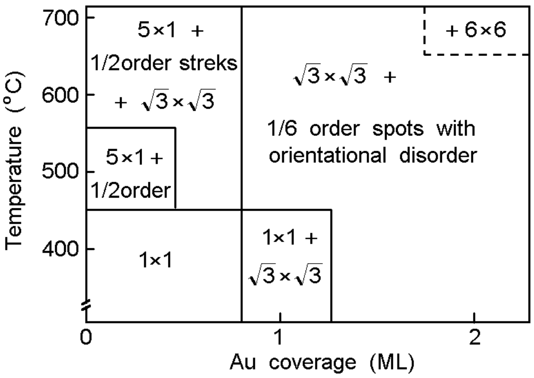

Fig 2. Summary of the LEED results versus coverage and annealing temperature of Au/cleaved Si(111) (from Ref. [31]). (*Reproduced by permission of American Institute of Physics*)

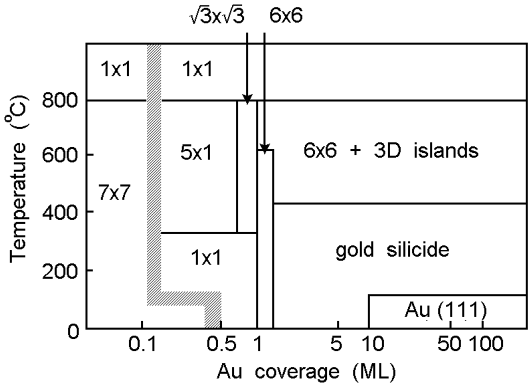

Fig 3. Schematic phase diagram of the Au/Si(111) system for the case of Au deposition on to the heated Si(111) substrate (from Ref. [91]). (*Reproduced by permission of Elsevier Science Publishers BV*)

Another interesting finding is the reversible transformation of the 5 × 1 structure to the 1×1 structure at 750 °C detected by RHEED [41] and UHV reflection electron microscopy [25].

1.2. STRUCTURE

1.2.1. Si(111)5 × 1–Au (Si(111)5 × 2–Au)

The results of the early analysis of the 5 × 1 structure by Le Lay and Faurie [2] suggested that there are two Au strings for every five Si substrate rows, corresponding to the 0.4 ML coverage at saturation. This structure exists in three equivalent domains respecting the threefold rotational symmetry of the substrate. The Au strings are alternately spaced two and three unit cells apart, forming a rowlike structure with double strings separated by a three unit cell spacing. All Au atoms are assumed to sit on equivalent sites. Later, substitutional, on top, and embedded sites with onefold, twofold, or threefold coordination have all been suggested [21, 42–44]. All of these models appear unable to describe features seen in the STM images.

In the recent STM investigations of Si(111)5 × 1–Au surface by Hasegawa *et al.* [33] and Baski *et al.* [32], STM images reveal an asymmetric structure with a two-unit cell periodicity along any given row. The phase of this two-unit cell periodicity is not correlated between rows, however, preventing any long-range 5 × 2 order. This observation is in agreement with the LEED data. Usually a 5 × 1–Au LEED pattern is accompanied by diffuse streaks running through the half-order positions [31–45], although the LEED spots belonging to the

5×1 pattern are sharp. The occurrence of this streak was also observed in X-ray diffraction experiments [46–48]. Lipson and Singer [45] were the first who proposed that the structure is not 5×1, but rather 5×2 with one-dimensional disorder between the 5×1 subunits.

Based on grazing-incidence XRD data Schamper *et al.* [46] proposed the possible structural model of 5×1 Au reconstruction. The main features of this structure are partially occupied rows of gold atoms in low symmetry. The density of Au atoms is highly asymmetric in the direction perpendicular to the rows. The substrate atoms in the top double layer are shifted up to 1 Å from their bulk position. Possible local arrangement of this structure is shown in Fig. 4. The occupation factors of different Au sites are 1.0 for (1), 0.76 for (2), 0.48 for (3), 0.66 for (4), and 0.22 for (5). The structure has a disordered 5×2 periodicity due to the variation of the interatomic Au–Au distances within a row in the $[0\bar{1}1]$ direction. The results show the tendency of Au to form small clusters. The structure model agrees well with recent STM topographs [32, 33, 49] and is consistent with X-ray standing wave measurements [42] in so far as only low-symmetry adsorption sites are occupied. However, the coverage obtained for this model (0.7 ML) is differ from recent results of Bauer [50] 0.443 ± 0.008 ML for the saturation coverage of the 5×1 phase and also from results of Daimon *et al.* [51] 0.43 ± 0.14 ML.

Recent STM topographs at higher resolution than those previously published reveal a detailed structure in the 5×2 unit cells [52]. One of the observed structures is strikingly similar to one of the local atomic arrangement, proposed by Schamper *et al.* [46].

1.2.2. Si(111)$\sqrt{3} \times \sqrt{3}$—$R30°$–Au

Au-induced $\sqrt{3} \times \sqrt{3}$—$R30°$ reconstruction has been investigated by a variety of experimental techniques, including LEED [2, 3, 31, 33–35, 47, 53–59], AES [2, 3, 31, 53] ARUPS [57], STM [33, 53, 54, 58, 60–64], XRD [47, 48], ICISS [34–36, 55, 56],MEIS [65, 66], and TED [28]. Nevertheless, many fundamental questions concerning the reconstruction are still under debate, such as the nominal saturation coverage, the position of the metal atoms, and the degree of Si substrate displacements [66].

As mentioned above, there is a reversible conversion of $\sqrt{3} \times \sqrt{3}$ to the 6×6 structure at the constant Au coverage. This fact implies that the unusual $\sqrt{3} \times \sqrt{3}$ LEED patterns are due to early stages of the formation of a 6×6 surface [24] and suggests the similarity of local arrangements of $\sqrt{3} \times \sqrt{3}$ and 6×6 structures. This similarity was also confirmed by X-ray diffraction experiments (Feidenhans'l *et al.* [47, 48]), and STM experiments (Nogami

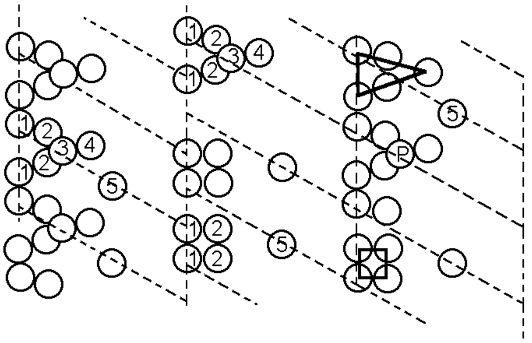

Fig 4. Possible local atomic arrangements according to the splitting and the partial occupation of the Au sites 1–5. Different configurations agree with round, rectangular, triangular units, and protrusions observed by STM [32]. Dashed lines indicate the primitive 2×5 unit cell. Adjacent rows of 2×5 cells may be shifted according to the one-dimensional disordering in the $[\bar{2}11]$ direction (from Ref. [46]). (*Reproduced by permission of the publishers of Journal of Physical Review B*)

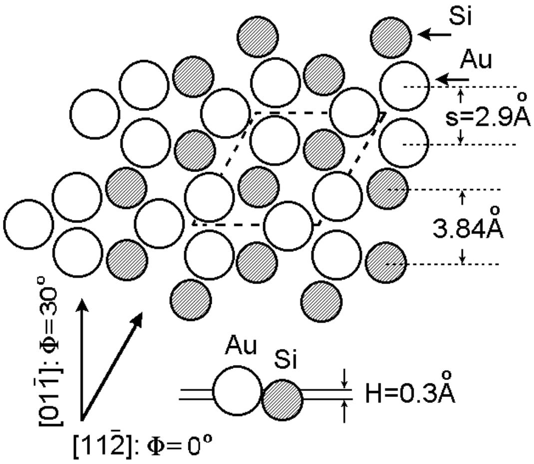

Fig 5. Top and side views of the MTC model for the Si(111)$\sqrt{3} \times \sqrt{3}$—$R30°$–Au surface (from Ref. [55]). (***Reproduced by permission of the publishers of Journal of Physical Review Letters***)

et al. [58, 64], and Salvan *et al.* [53]). According to STM results of Nogami *et al.* [58] the transition between $\sqrt{3} \times \sqrt{3}$ and the 6×6 reconstructions of the Au/Si(111) surface is unusual in that, as the Au coverage increases, there is a continuous evolution of the surface structure with Au coverage, rather than a simple change in the relative abundances of two distinct, well-ordered phases. STM images show that the $\sqrt{3} \times \sqrt{3}$ structure is broken up into sub-100 Å domains that decrease in size with increasing Au coverage.

Two of the most popular general types of models for the $\sqrt{3} \times \sqrt{3}$—$R30°$–Au surfaces are the honeycomb model and the triplet model [65]. The nominal saturation coverage for the honeycomb model is 2/3 ML, while it is 1 ML for the triplet model.

The first structural model was proposed by Le Lay *et al.* [2, 3] based on the AES and LEED data. This model consists of Au trimer in the T_4 position. The Au coverage was estimated to be 1 ML.

Two separate investigations of the $\sqrt{3} \times \sqrt{3}$ Au surface using ICISS led to the proposal of two different models despite the fact that the ion yields were very similar. Oura *et al.* [55] proposed a modified triplet coplanar (MTC) model whereby the Au atoms form a triplet cluster that resides 0.3 Å above the top Si plane (Fig. 5). In this model there is one top layer Si vacancy per $\sqrt{3} \times \sqrt{3}$—$R30°$ unit cell, allowing the Au atoms to collapse towards each other and the vacancy. On the other hand, Huang *et al.* [34–36, 56] concluded that a surface with 70% Au honeycombs and 30% centered Au honeycombs (resulting Au coverage is 0.77 ML) gives the best fit to their data. The Au atoms are about 2 Å above the top Si plane in the H_3 sites and the additional 0.1 ML of Au atoms are located 0.3 Å below these regular honeycombs. The underlying Si atoms are not displaced markedly from their ideal bulk positions.

Recently Chester and Gustafsson [65, 66] using MEIS found that none of the previously proposed models are compatible with their ion scattering data. Reasonable agreement between simulated yields and experimental data was found for the missing top layer twisted trimer (MTLTT) model. This model contains twisted Au trimers that reside on top of a missing top layer Si lattice. The proposed MTLTT model is similar to the trimer model proposed by Kono *et al.* [67] to explain X-ray PED data from the $\sqrt{3} \times \sqrt{3}$–Ag surface, where the Ag trimers also substitute for the top layer Si atoms. Within the context of the MTLTT model, two structures were found to be consistent with the ion scattering data (Fig. 6). Both involve Au trimers and top layer Si triads that rotate about H_3 sites of the Si bulk lattice. Details of the both structures are elucidated in Table 1. The difference between the two is

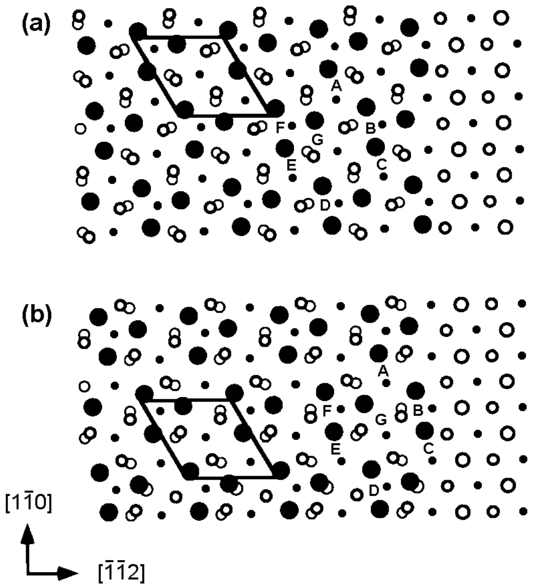

Fig 6. Top view of the MTLTT model for the Si(111)$\sqrt{3} \times \sqrt{3}$—$R30°$–Au surface. For (a) the Si trimers are twisted in the same sense as the Au trimers (structure 1), while in (b) they are rotated in the opposite sense (structure 2) (from Ref [66]) (*Reproduced by permission of Elsevier Science Publishers BV*)

Fig [.] **Table**

1. Optimal simulation parameters for the MTLTT models: $d_{\mathrm{Au-Au}}$ and $d_{\mathrm{Si-Si}}$ are the Au–Au trimer and top layer Si–Si triad atom distances, respectively; θ_{Au} and θ_{Si} are the Au trimer and Si triad rotation angles, respectively; and $\mathrm{Z}_{\mathrm{Au-Si}}$ is the Au distance above the top layer Si plane (from Ref. [66])

Parameters*	Structure 1	Structure 2
$d_{\mathrm{Au-Au}}$	3.0 ± 0.1	2.9 ± 0.1
θ_{Au}	$12° \pm 3°$	$12° \pm 3°$
$d_{\mathrm{Si-Si}}$	3.2 ± 0.1	3.2 ± 0.1
θ_{Si}	$18° \pm 3°$	$-17° \pm 3°$
Z_{Au-Si}	1.6 ± 0.1	1.8 ± 0.1

Fig [.]

*All distances are in angstroms.

predominantly in the rotational orientation of the Si triads with respect to the rotation of Au trimers.

Recently Ding *et al.* [68] based on the honeycomb chained trimer (HCT-1) model for the $\sqrt{3} \times \sqrt{3}$-Ag structure [69] proposed a conjugate HCT-1 (CHCT-1) model for the $\sqrt{3} \times \sqrt{3}$–Au surface. Among various models proposed by experiments, the CHCT-1 model is closest to the models proposed by Chester and Gustafsson [65,66]. Calculations of Ding *et al.* [68] have shown that the CHCT-1 model is the energetically most favorable structure. This structural model is shown in Fig. 7. Two ordered arrays, one of Si trimers and one of Au trimers, both centered about the third layer Si atoms. The size of Au trimer is 2.83 Å and the Au–Si interlayer distance is 0.56 Å. In accordance with the LEED experiment and quantitative intensity analysis of Quinn *et al.* [59] among the many proposed models reported in the literature, CHCT-1 is the only one that fits their experimental data satisfactory.

1.2.3. Si(111)6 × 6–Au

As mentioned above, the local arrangement of the 6 × 6 structure is very similar to the $\sqrt{3} \times \sqrt{3}$ structure. This similarity was demonstrated by the LEED results of Higashiyama *et al.* [24], STM results of Salvan *et al.* [53] and Nogami *et al.* [58], ICISS results of Huang and Williams [35, 36] and XRD results of Feidenhans'l *et al.* [47]. The difference between $\sqrt{3} \times \sqrt{3}$ and 6 × 6 structure was noted by X-ray diffraction experiments of Feidenhans'l *et al.* [47]. According their observation the distance between the $\sqrt{3}$ subunits is slightly longer in the 6 × 6 structure than in the $\sqrt{3} \times \sqrt{3}$ structure.

Based on the ICISS data Huang and Williams [35, 36] proposed a structural model of the Si(111)6 × 6–Au structure. This model consists of a honeycomb in which 75% of Au hexagons have an additional Au atom in the center. The centered Au atoms sit slightly below (−0.3 Å) the other Au atoms in the hexagon array (Fig. 8). The empty hexagon centers are indicated by a star, and the 6 × 6 unit cell is outlined. The total Au coverage for the proposed 6 × 6 structure in the 20 : 80 mixture of the honeycomb and the centered hexagons would be 0.93 ML. This model is not in contradiction with the similarity of local arrangement of 6 × 6 and $\sqrt{3} \times \sqrt{3}$ structures and has 30 : 70 mixture for the $\sqrt{3} \times \sqrt{3}$ structure (see Si(111)$\sqrt{3} \times \sqrt{3}$—$R30°$–Au).

1.3. PROPERTIES

1.3.1. Desorption

The Au desorption from the Si(111) surface at temperatures in the range 800 to 920 °C was studied by Le Lay *et al.* [3, 40] using LEED and AES. Desorption isotherms show four distinct kinetic steps as can be seen in Fig. 9. While the first step corresponds to the desorption of the 3D crystallites, each of the next three steps is connected with the vanishing of one Au/Si(111) surface phase i.e. 6 × 6, $\sqrt{3} \times \sqrt{3}$ and 5 × 1. In each case the reaction is zero order ($\theta = -Kt + \text{const}$) which is a characteristic of the indirect desorption of 2D islands via a 2D dilute adsorbed gas. The desorption energies and the vibrational frequencies determined in the desorption experiments for Au/Si(111) surface phases are:

$$E = 76 \text{ kcal mole}^{-1}(3.3 \text{ eV}), \qquad \nu = 9 \times 10^{12} \text{ s}^{-1}$$

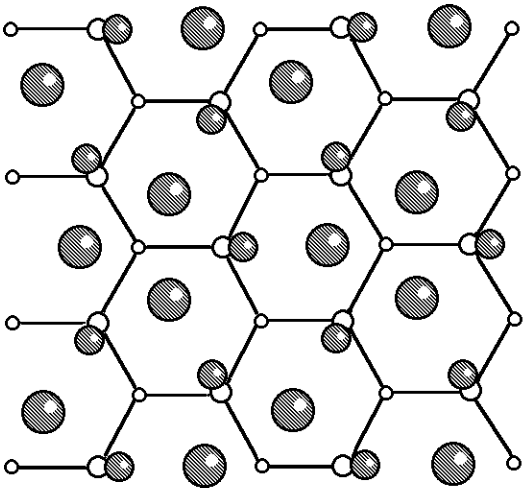

Fig 7. Top view of the CHCT-1 structure model for the Si(111)$\sqrt{3} \times \sqrt{3}$—$R30°$–Au surface (from Ref. [68]). (*Reproduced by permission of Elsevier Science Publishers BV*)

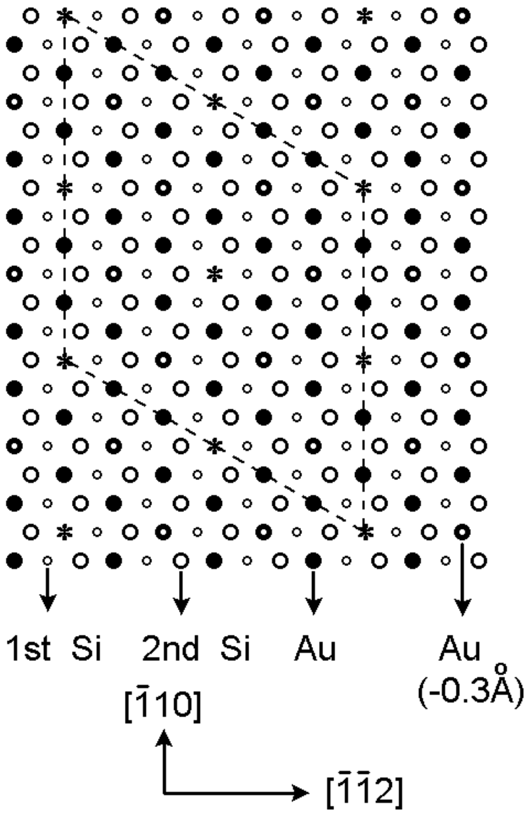

Fig 8. A top view of the proposed model for the Si(111)6 × 6–Au surface (from Ref. [36]). (*Reproduced by permission of the publishers of Journal of Physical Review B*)

for the 6 × 6 phase,

$$E = 82 \text{ kcal mole}^{-1}(3.6 \text{ eV}), \qquad \nu = 1.5 \times 10^{13} \text{ s}^{-1}$$

for the $\sqrt{3} \times \sqrt{3}$ phase,

$$E = 85 \text{ kcal mole}^{-1}(3.7 \text{ eV}), \qquad \nu = 1.7 \times 10^{13} \text{ s}^{-1}$$

for the 5 × 1 phase.

1.3.2. Surface Diffusion

The one-dimensional gold diffusion process over the Si(111) clean surface was studied by Gavriljuk and Lifshits [70–72] using AES and LEED. In the experiment, diffusion of Au atoms out of a gold strip about 10 ML thick and 1 mm wide was monitored in the temperature range 500–900 °C. In the initial period of annealing, the continuous Au film disintegrates into separate 3D islands which covered about 5% of the area. The surface area within the strip between the islands is occupied by a $\sqrt{3} \times \sqrt{3}$ surface phase. The Au diffusion proceeds via the release of Au atoms from the islands and the motion of thus formed adatoms over the surface phase out of the strip. When the 3D islands are depleted, diffusion is significantly retarded.

The spreading of the Au overlayer was found to be accompanied by the formation of the ordered Au-induced reconstructions. One can see in Fig. 10 that Au concentration profiles consist of regions with different slopes corresponding to regions of different structures on the surface. This implies that the diffusivity varies from one phase to another. The diffusion

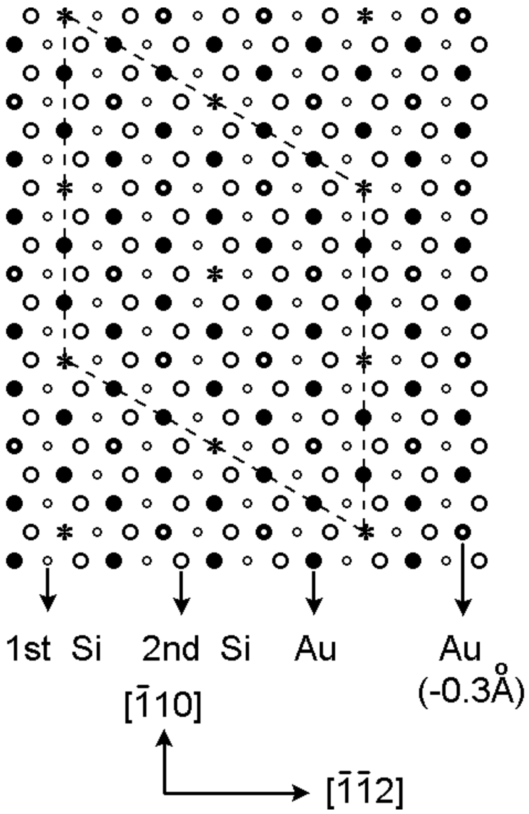

Fig 9. Desorption isotherms of Au/Si(111); Auger intensities versus desorption time at 865 °C: desorption of 3D crystallites—(1); desorption of 6×6 - (2), $\sqrt{3} \times \sqrt{3}$ - (3) and 5×1 - (4) surface phases (from Ref. [3]). (*Reproduced by permission of Elsevier Science Publishers BV*)

Fig [.]

Table **2**. Diffusion constants for different Au/Si(111) surface phases (from Ref. [72])

Phase	D_0 ($\mathrm{m}^2\ \mathrm{s}^{-1}$)	E (eV)
$\sqrt{3} \times \sqrt{3}$	0.7×10^{-4}	1.3
5×1	4.75×10^{-3}	1.6
7×7	0.12	2.0

constants for different phases in the Au/Si(111) system determined in experiments are presented in Table 2. The difference in activation energy of migration of the adatoms on the various phases leads to the possibility of controlling the concentration profile by adjusting the annealing temperature. One can see in Fig. 10(a), that at 660 °C diffusion proceeds through the propagation of the $\sqrt{3} \times \sqrt{3}$ phase only. This is connected with the fact that at this temperature the coefficient of diffusion of Au adatoms is greater for the $\sqrt{3} \times \sqrt{3}$ phase than for the 5×1 phase.

An unusual result related to the diffusion in gold submonolayer over Si(111), namely, the Au oscillatory diffusion, was achieved by Ichinokawa *et al.* [73]. In this work, a gold-deposited area of 0.1 mm diameter and several monolayers thick was annealed at 700 °C. In the diffusion process, the concentric oscillatory rings of the $\sqrt{3} \times \sqrt{3}$ and 5×1 structures were formed in an area of 0.4 mm diameter and observed by the dark field image in scanning LEED microscopy. The satisfactory physical explanation of this phenomenon has not yet been received.

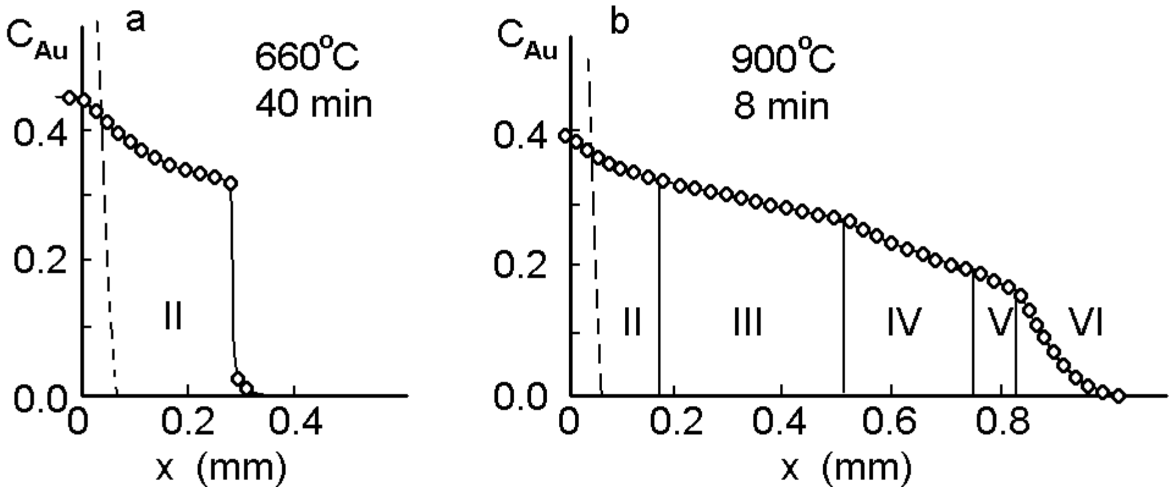

Fig 10. Concentration profiles obtained for Au surface diffusion on Si(111) at (a) 660 °C, (b) 900 °C. Regions of different structures: (II) $\sqrt{3} \times \sqrt{3}$; (III) $\sqrt{3} \times \sqrt{3} + 5 \times 1$; (IV) 5×1; (V) $5 \times 1 + 7 \times 7$; (VI) 7×7. Dashed line shows the Au strip edge (from Ref. [72]). (*Reproduced by permission of Elsevier Science Publishers BV*)

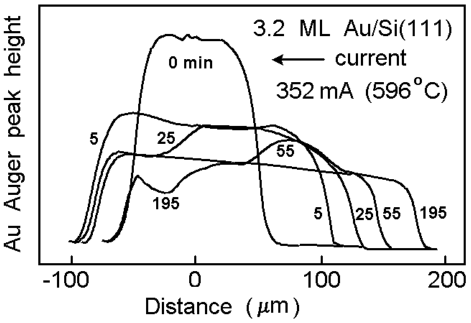

Fig 11. The movement of an Au patch with a deposition coverage of 3.2 ML under the presence of a given d.c. current of 352 mA is indicated by successive Auger line profiles (from Ref. [75]). (*Reproduced by permission of Elsevier Science Publishers BV*)

1.3.3. Electromigration

The surface electromigration of Au atoms on Si(111) was studied using methods of reflection electron microscopy [74] and scanning Auger microscopy [75]. In the experiment, a patch of Au film several monolayers thick was deposited on to a Si(111) 7 × 7 surface. The movement of the patch was then examined applying a d.c. current. It was shown that, in addition to isotropic spreading due to surface diffusion, the Au overlayer exhibits a directional movement towards the anode (see Fig. 11).

The movement of the Au overlayer was found to consist of three distinct processes: (1) fast isotropic spreading supplemented by the directional movement over the layer of about 1 ML in coverage, (2) the advance of the leading edge on the anode side at the expense of the Au coverages from 1 to 0.7 ML on the cathode side and (3) a slow directional movement of the overlayer as a whole causing an oscillatory profile on the cathode side [75].

All three processes are clearly reflected in the dependence of the displacement of the leading edge on the anode side versus annealing time shown in Fig. 12. The lateral flux of atoms at the leading edge was estimated to be 8.1×10^8 and 2.0×10^8 atoms/cm s for a d.c. current of 352 mA (596 °C) in processes 2 and 3, respectively. The activation energy of the flux is 0.77 eV (process 2) and 1.2 eV (process 3), regarding the transport as a thermally activated process.

Yasunaga and Sasuga [75] suggested that process 1 includes the transformation of as-deposited Au film into a $\sqrt{3} \times \sqrt{3}$ reconstructed surface phase ($\theta_{\mathrm{Au}} = 1$ ML) with 3D islands randomly distributed and spreading of the surface phase until Au adatoms are no longer supplied from the islands on account of their extinction. In process 2, the mobile adatoms come from the surface phase by thermal activation. They are similarly carried towards the anode mainly over the surface phase (2D layer of 1 ML). However, as a result of the supply of Au adatoms, the 2D layer reduces in coverage from 1.0 to 0.7 ML (presumably, to 5×1 phase) on the cathode side. After the Au overlayer becomes 0.7 ML in coverage everywhere, the adatoms are supplied by releasing atoms from the 2D layer itself. This corresponds to a process 3 leading to the formation of an oscillatory profile on the cathode side.

1.3.4. Oxidation

The reactivity of the Au/Si(111) surface with respect to oxidation was found to depend dramatically on the surface structure and, hence, on the local environment of Si atoms at the surface.

In an amorphous RT an Au–Si interface catalytic action of gold atoms on the oxidation of Si(111) was observed [76–79] Exposure of an Si surface covered by a few Au monolayers to oxygen induces the overgrowth of a SiO_2-like phase even at room temperature as opposed to a clean Si(111) which cannot be oxidized to SiO_2 in these conditions. In the latter case a chemisorbed oxygen monolayer is formed.

Contrarily to the enhanced oxygen uptake observed on an amorphous Au–Si interface, the ordered Si(111)$\sqrt{3} \times \sqrt{3}$–Au surface phase is insensitive to oxidation. After the exposure of the $\sqrt{3} \times \sqrt{3}$ surface to an oxygen dose of 6×10^4 L (10^{-4} Torr during 10 min.), the photoemission spectrum is almost unchanged and Auger analysis shows no trace of oxygen [6,80].

2. (100) ORIENTATION

Several reconstructions, 1×1, and $c(8 \times 2)$, 5×1 (or $\sqrt{26} \times 1$), $\sqrt{26} \times 3$, and $c(2 \times 18)$ were detected in the Au/Si(100).

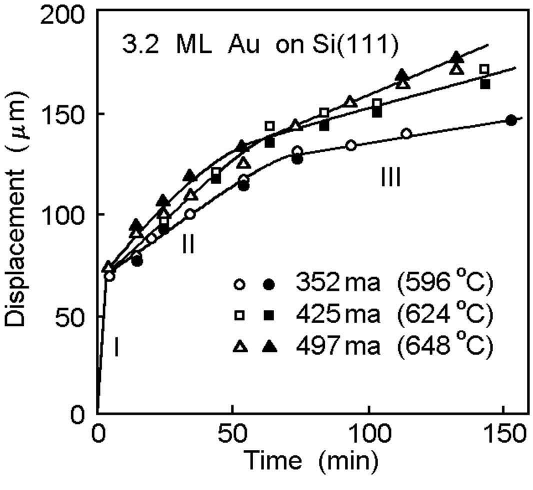

Fig 12. The movement of the leading edge of the Au overlayer with time of d.c. power supply. Three distinct processes are evident (from Ref. [75]). (*Reproduced by permission of Elsevier Science Publishers BV*)

2.1. PHASE DIAGRAM

2.1.1. RT Growth

LEED observations of Refs [81–83] showed that, upon RT deposition of Au, the initial 2×1 reconstruction pattern of clean Si(100) becomes gradually diffuse and a 1×1 structure appears at about 1 ML Au. With further increase of Au coverage, a 1×1 pattern fades and disappears completely at about 3.5–5 ML Au. However, according to the LEED data of Oura and Hanawa [81], at relatively high Au exposures, certain features become detectable at the LEED pattern: these are a very diffuse and weak ring at about 3 nm of Au deposition which was suggested to indicate the formation of gold silicide layer and new diffuse spots arranged on a circle at about 30 nm of Au deposition which were analyzed as due to Au(111)$\|$ Si(100) having six azimuthally rotated orientations. It should be noted that Hanbücken *et al.* [82] using TED found another orientation of overgrown Au layer, namely, Au(100) $\|$ Si(100).

As for chemical RT interaction in the Au/Si(100) system, it is now agreed that the Au/Si interface is strongly intermixed. However, there is still disagreement whether a critical thickness of the metal deposit is required to trigger the intermixing reaction [82, 84–86].

2.1.2. HT Growth

Oura and Hanawa [81] showed that crystalline gold silicide thin layers are formed on the RT grown Au (111) film after heat treatment at $100 \div 400\,^\circ$C, while heat treatment over $450\,^\circ$C leads to agglomeration of the film, producing a series of Au-induced superstructures: A few minutes heating in a temperature range of 450–700 °C produces Si(100)$c(8 \times 2)$–Au structure which converts to the $\sqrt{26} \times 1$ structure accompanied with faint 1/3 order streaky LEED spots at around 750 °C, the streaky spots separating into distinct spots accompanied with faint half-order streaks after heating over 800 °C [81,87]. This pattern can be tentatively interpreted as $\sqrt{26} \times 3$ plus disordered Si(100)2×1, the former disappears completely leaving the Si(100)2×1 pattern after heating over 1000 °C. In Fig. 13 the superstructures are illustrated on the 2D reciprocal lattice. The notation $\sqrt{26} \times 1$ was used instead of 5×1 by Oura *et al.* [81, 87] for the sake of convenience. They are really the same structures. The condition of the appearance of the superstructures is schematically represented in Fig. 14, together with that for silicide and Au(111) [81]. Coverages of Au for the completion of $c(8 \times 2)$, $\sqrt{26} \times 1$, and $\sqrt{26} \times 3$ were not determined exactly, but a 0.5 ML for $c(8 \times 2)$ and a 1 ML for $\sqrt{26} \times 3$ were estimated from the exposure assuming a sticking coefficient of unity. In the figure, the temperatures distinguishing three superstructures do not mean definite transition temperatures but indicate a temperature at which a rapid transition takes place, higher temperatures being necessary for specimens of thicker Au deposit.

In a recent REM study of surface electromigration of Au on Si(100), Yamanaka *et al.* [88] detected the formation of the novel reconstruction, $c(2 \times 18)$. The $c(2 \times 18)$ structure was always formed when the d.c. current was in the [011] direction but when the current was in the [010] direction the $\sqrt{26} \times 1$ structure was usually formed. Current of 330 mA was passed through the B-doped Si specimen ($1 \times 10 \times 0.4$ mm^3 in size, a few ohm-cm) in this experiment.

3. (110) ORIENTATION

The ordered reconstructions found for the Au/Si(110) system are 1×2, 2×5, $\begin{pmatrix} 4 & 0 \\ -1 & 3 \end{pmatrix}$, and 1×1.

3.1. PHASE DIAGRAM

The phase diagram for Au submonolayers on Si(110) was drawn by Yamamoto in Ref. [89] (see Fig. 15).

When Au is deposited at room temperature, the intensity of the "2 × 16" superlattice reflections become weaker and, at coverages exceeding 0.3 ML, a 1 × 1 structure is observed.

When the sample temperature is raised gradually the 1 × 2, 2 × 5, or $\begin{pmatrix} 4 & 0 \\ -1 & 3 \end{pmatrix}$ superstructures (Fig. 16) are formed at 440 °C depending on the adsorbed amounts of Au. These transitions are irreversible and, upon cooling to room temperatures, the 1 × 2, 2 × 5, and $\begin{pmatrix} 4 & 0 \\ -1 & 3 \end{pmatrix}$ superstructures persist. It should be said that the formation of the two-domain $\begin{pmatrix} 4 & 0 \\ -1 & 3 \end{pmatrix}$ structure was reported first by Green and Bauer [90].

The heating of the samples to the high temperature results in the transformation of the above mentioned reconstructions into the 1 × 1 structure. The transformation occurs at 970 °C for the 1 × 2 phase, at 750 °C for the 2 × 5 phase and at 850 °C for the $\begin{pmatrix} 4 & 0 \\ -1 & 3 \end{pmatrix}$ phase. This phase transition is reversible.

3.2. STRUCTURE

Yamamoto [89] proposed the structure models for the Si(110)–Au phases. The proposed models are based on the consideration of the observed RHEED patterns and Au coverages determined by X-ray spectroscopy. It was assumed that Au joins three Si atoms and saturates the three dangling bonds.

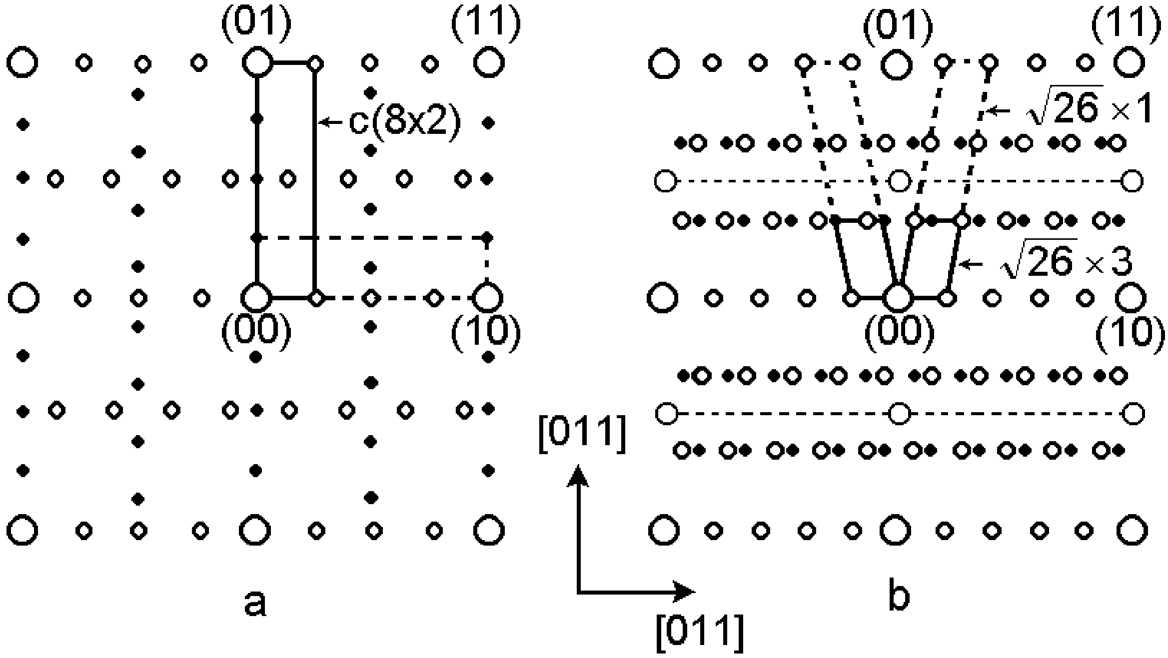

Fig 13. Schematic illustration of the LEED pattern. (a) $c(8 \times 2)$, (b) $\sqrt{26} \times 1$, $\sqrt{26} \times 3$. LEED pattern observed is a superposition of those from possible domains: two domains possible for $c(8 \times 2)$ as shown in (a) and four domains for $\sqrt{26} \times 1$ or $\sqrt{26} \times 3$ but only two are shown in (b) (from Ref. [87]). (*Reproduced by permission of the publishers of Japanese Journal of Applied Physics*)

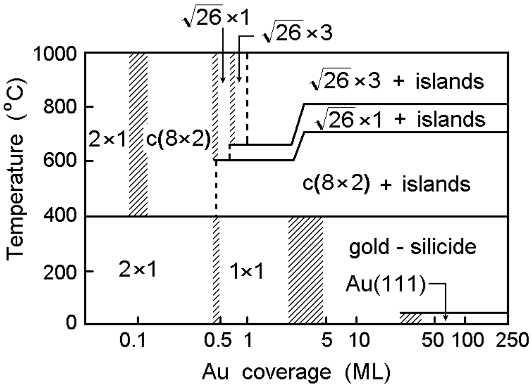

Fig 14. Formation phase diagram of the Au/Si(100) system (from Ref. [81]). (*Reproduced by permission of Elsevier Science Publishers BV*)

3.2.1. Si(110)1 × 2–Au

The proposed arrangement of Au atoms for the 1 × 2 structure is shown in Fig. 17(a). This model has an Au coverage of 0.25 ML which is consistent with an experimental value of 0.08–0.26 ML.

3.2.2. Si(110)2 × 5–Au

The 2 × 5–Au structure is a specific 2 × 5 structure because characteristic streaks are observed in the diffraction pattern. Disregarding the streaks, the corresponding real lattice is that of a 5 × 1 structure, but the existence of the streaks running structure.

In the proposed model two types of arrangement are assumed, C and D (see Fig. 17(b)). The arrangement order of C and D is random, and this produces the characteristic streaks. In this model, the Au coverage is 0.45 ML, while the amount detected by X-ray spectroscopy is 0.28–0.46 ML.

The $\begin{pmatrix} 4 & 0 \\ -1 & 3 \end{pmatrix}$ structure occurs between 0.46 and 1.23 ML Au. If Au is adsorbed at the same site as in 1 × 2 and 2 × 5 structures, 0.5 ML becomes the adsorption limit. So, in the proposed model, Au atoms making Au–Au metallic bonds over 0.5 ML are involved. These atoms are shown by the oblique circles in Fig. 17(c).

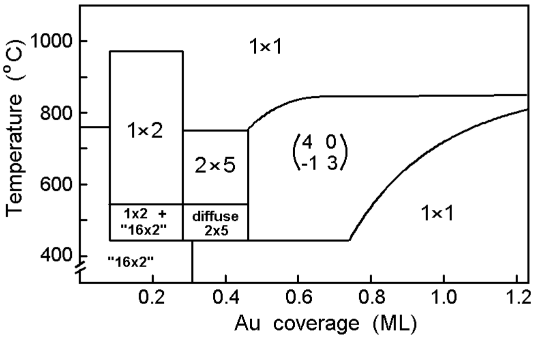

Fig 15. Two-dimensional phase diagram representing the phase transitions between the structures in the Au/Si(110) system. The abscissa represents the amount of RT adsorbed Au and the ordinate the sample temperature (from Ref. [89]). (*Reproduced by permission of Elsevier Science Publishers BV*)

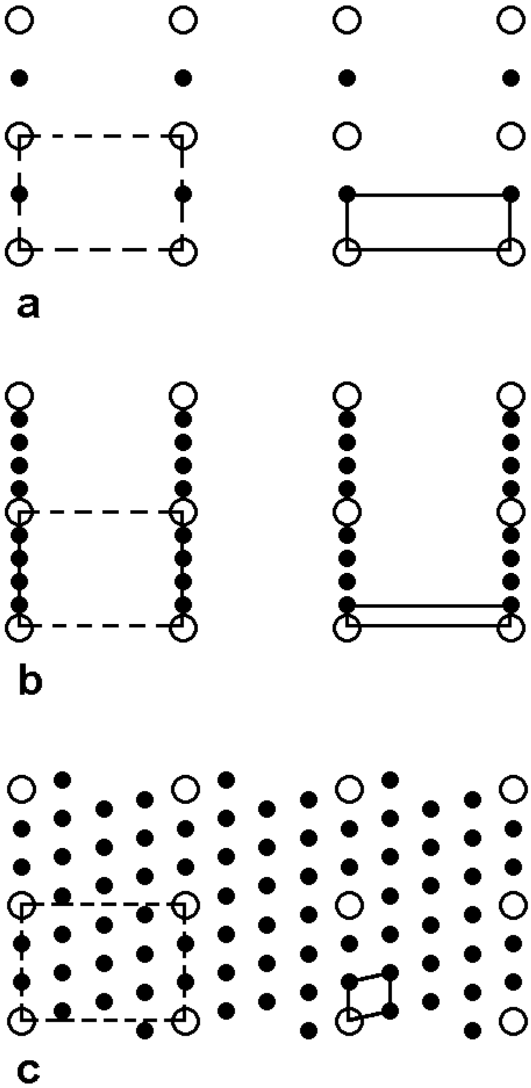

Fig 16. The reciprocal lattice of the (a) 1×2, (b) 2×5, and (c) $\begin{pmatrix} 4 & 0 \\ -1 & 3 \end{pmatrix}$ structures. The open circles are normal spots and solid circles are fractional-order spots. The unit mesh of the reciprocal lattice of superstructure is shown in solid lines, the unit mesh of the reciprocal Si(110)1×1 lattice is shown in dashed lines (from Ref. [89]). (*Reproduced by permission of Elsevier Science Publishers BV*)

REFERENCES

[1] G. Le Lay, G. Quentel, J. P. Faurie and A. Masson, *Thin Solid Films* **35** (1976) 273.
[2] G. Le Lay and J. P. Faurie, *Surf. Sci.* **69** (1977) 295.
[3] G. Le Lay, *J. Cryst. Growth* **54** (1981) 551.
[4] P. Perfetti, S. Nannarone, F. Patella, C. Quaresima, A. Savoia, F. Cerrina and M. Capozi, *Solid State Commun.* **35** (1980) 151.
[5] P. Perfetti, S. Nannarone, F. Patella, C. Quaresima, M. Capozi, A. Savoia and G. Ottaviani, *Phys. Rev. B* **26** (1982) 1125.
[6] F. Houzay, G. M. Guichar, A. Cros, F. Salvan, R. Pinchaux and J. Derrien, *Physica B* **117–118** (1983) 840.
[7] A. Taleb-Ibrahimi, C. A. Sebenne, D. Bolmont and P. Chen, *Surf. Sci.* **146** (1984) 229.
[8] F. Houzay, G. M. Guichar, A. Cros, F. Salvan, R. Pinchaux and J. Derrien, *J. Phys. C* **15** (1982) 7065.
[9] A. K. Green and G. Bauer, *J. Appl. Phys.* **47** (1976) 1284.

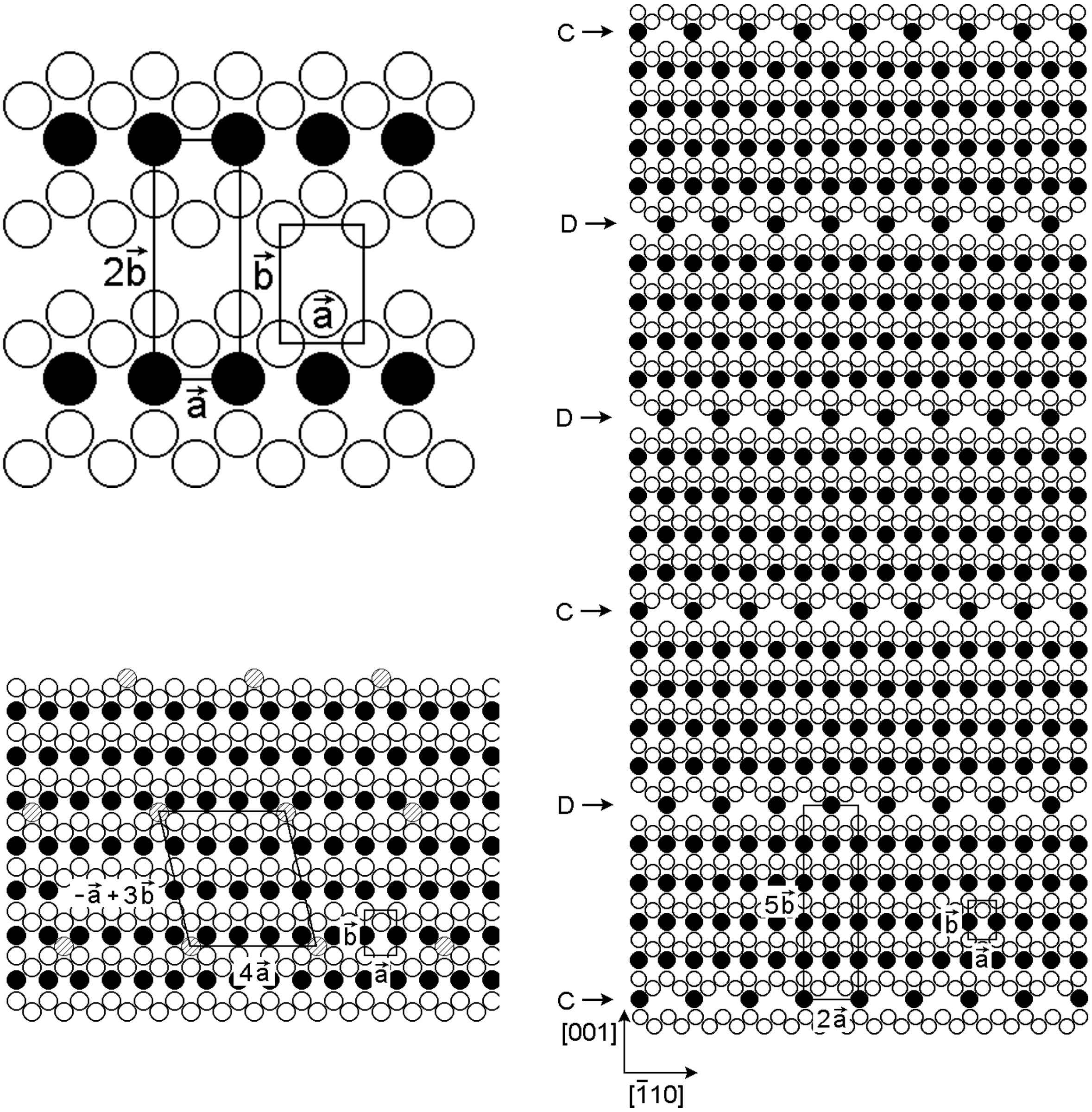

Fig 17. Arrangement of the Au atoms for the (a) 1 × 2, (b) 2 × 5 and (c) $\begin{pmatrix} 4 & 0 \\ -1 & 3 \end{pmatrix}$ structures. The open circles represent Si atoms, the solid circles Au atoms up to 0.5 ML and the oblique circles Au atoms over 0.5 ML (from Ref. [89]). (*Reproduced by permission of Elsevier Science Publishers BV*)

[10] M. T. Thomas and D. L. Styris, *Phys. Status Solidi(b)* **57** (1973) K83.
[11] M. Iwami, T. Terada, H. Tochihara, M. Kubota and Y. Murata, *Surf. Sci.* **194** (1988) 115.
[12] K. Okuno, T. Ito, M. Iwami and A. Hiraki, *Solid State Commun.* **34** (1980) 493.
[13] A. Hiraki, Japan *J. Appl. Phys.* **22** (1983) 549.
[14] A. Hiraki, *Surf. Sci. Repts.* **3** (1983) 357
[15] M. Iwami, M. Kubota, T. Koyama, H. Tochihara and Y. Murata, *Phys. Rev. B* **38** (1988) 1047
[16] D. Katzer and K. Meinel, *J. Cryst. Growth* **98** (1989) 690
[17] L. Braicovich, C. M. Garner, P. R. Skeath, C. Y. Su, P. W. Chye, I. Lindau and W. E. Spicer, *Phys. Rev. B* **20** (1979) 5131
[18] I. Abbati, L. Braicovich, A. Franciosi, I. Lindau, P. R. Skeath, C. Y. Su and W. E. Spicer, J. Vac. Sci. Technol. **17** (1980) 930

[19] I. Abbati, L. Braicovich and A. Franciosi, *Solid State Commun.* **33** (1980) 881

[20] H. Dallaporta and A. Cros, *Surf. Sci.* **178** (1986) 64

[21] Y. Yabuuchi, F. Shoji, K. Oura and T. Hanawa, *Surf. Sci.* **131** (1983) L412

[22] K. Oura and T. Hanawa, Semicond. Technol. , Tokyo (1984) 197

[23] E. Bauer and H. Poppa, *Thin Solid Films* **12** (1972) 167.

[24] K. Higashiyama, S. Kono and T. Sagawa, Japan *J. Appl. Phys.* **25** (1986) L117.

[25] N. Osakabe, Y. Tanishiro, K. Yagi and G. Honjo, *Surf. Sci.* **97** (1980) 393.

[26] Y. Tanishiro and K. Takayanagi, *Ultramicroscopy* **31** (1989) 20.

[27] Y. Tanishiro and K. Yagi, *Surf. Sci.* **234** (1990) 37.

[28] S. Takahashi, Y. Tanishiro and K. Takayanagi, *Surf. Sci.* **242** (1991) 73.

[29] G. Le Lay, G. Quentel, J. P. Faurie and A. Masson, *Thin Solid Films* **35** (1976) 289.

[30] V. G. Lifshits, V. B. Akilov and Yu. L. Gavriljuk, *Solid State Commun.* **40** (1981) 429.

[31] A. Taleb-Ibrahimi, C. A. Sebenne and F. Proix, *J. Vac. Sci. Technol. A* **4** (1986) 2331.

[32] A. A. Baski, J. Nogami and C. F. Quate, *Phys. Rev. B* **41** (1990) 10247.

[33] T. Hasegawa, K. Takata, S. Hosaka and S. Hosoki, *J. Vac. Sci. Technol. A* **8** (1990) 241.

[34] R. S. Williams, R. S. Daley, J. H. Huang and R. M. Charatan, Appl. *Surf. Sci.* **41–42** (1989) 70.

[35] J. H. Huang and R. S. Williams, *J. Vac. Sci. Technol. A* **6** (1988) 689.

[36] J. H. Huang and R. S. Williams, *Phys. Rev. B* **38** (1988) 4022.

[37] J. Yuhara, M. Inoue and K. Morita, *J. Vac. Sci. Technol. A* **10** (1992) 334.

[38] A. Shibata, Y. Kimura and K. Takayanagi, *Surf. Sci.* **273** (1992) L430.

[39] T. Hasegawa, S. Hosaka and Sh. Hosoki, Japan *J. Appl. Phys.* **31** (1992) L1492.

[40] G. Le Lay, M. Manneville and R. Kern, *Surf. Sci.* **65** (1977) 261.

[41] S. Ino, Japan *J. Appl. Phys.* **16** (1977) 891.

[42] L. E. Berman, B. W. Batterman and J. M. Blakely, *Phys. Rev. B* **38** (1988) 5397.

[43] J. H. Huang and R. S. Williams, *Surf. Sci.* **204** (1988) 445.

[44] S. M. Durbin, L. E. Berman, B. W. Batterman and J. M. Blakely, *Phys. Rev. B* **33** (1986) 4402.

[45] H. Lipson and K. E. Singer, *J. Phys. C* **7** (1974) 12.

[46] Ch. Schamper, W. Moritz and H. Schulz, *Phys. Rev. B* **43** (1991) 12130.

[47] R. Feidenhans'l, F. Grey, M. Nielsen and R. L. Johnson, in *Kinetics of Ordering and Growth at Surface, Plenum Press, New York* (1990) 189.

[48] R. Feidenhans'l, F. Grey, J. Bohr, M. Nielsen and R. L. Johnson, *Colloque De Physique* **50** (1989) C7-175.

[49] T. Hasegawa, K. Takata, S. Hosaka and S. Hosoki, *J. Vac. Sci. Technol. B* **9** (1991) 758.

[50] E. Bauer, *Surf. Sci.* **250** (1991) L379.

[51] H. Daimon, C. Chung, S. Ino and Y. Watanabe, *Surf. Sci.* **235** (1990) 142.

[52] J. D. O'Mahony, C. H. Patterson, J. F. McGilp, F. M. Leibsle, P. Weightman and C. F. J. Flipse, *Surf. Sci.* **277** (1992) L57.

[53] F. Salvan, H. Fuchs, A. Baratoff and G. Binnig, *Surf. Sci.* **162** (1985) 634.

[54] F. Salvan, A. Humbert, P. Dumas and F. Thibaudau, *Ann. Phys. Fr.* **13** (1988) 133.

[55] K. Oura, M. Katayama, F. Shoji and T. Hanawa, Phys. Rev. Lett. **55** (1985) 1486.

[56] R. S. Daley, J. H. Huang and R. S. Williams, *Surf. Sci.* **202** (1988) L577.

[57] C. J. Karlsson, E. Landemark, L. S. O. Johansson and R. I. G. Uhrberg, *Phys. Rev. B* **42** (1990) 9546.

[58] J. Nogami, A. A. Baski and C. F. Quate, *Phys. Rev. Lett.* **65** (1990) 1611.

[59] J. Quinn, F. Jona and P. M. Marcus, *Phys. Rev. B* **46** (1992) 7288.

[60] Ph. Dumas, A. Humbert, G. Mathieu, P. Mathiez, C. Mouttet, R. Rolland, F. Salvan and F. Thibaudau, *J. Vac. Sci. Technol. A* **6** (1988) 517.

[61] F. Salvan, F. Thibaudau, Ph. Dumas and A. Humbert, in *Metallization and Metal–Semiconductor Interfaces*, Ed. I. P. Batra (Plenum Press, New York, 1989) p.315.

[62] Ph. Dumas, A. Humbert, G. Mathieu, P. Mathiez, C. Mouttet, R. Rolland, F. Salvan, F. Thibaudau and St. Tosch, *Phys. Scripta* **38** (1988) 244.

[63] A. Baratoff, G. Binnig, H. Fuchs, F. Salvan and E. Stoll, *Surf. Sci.* **168** (1986) 734.

[64] J. Nogami, A. A. Baski and C. F. Quate, *Phys. Rev. Lett.* **65** (1990) 2211.
[65] M. Chester and T. Gustafsson, *Phys. Rev. B* **42** (1990) 9233.
[66] M. Chester and T. Gustafsson, *Surf. Sci.* **256** (1991) 135.
[67] S. Kono, K. Higashiyama and T. Sagawa, *Surf. Sci.* **165** (1986) 21.
[68] Y. G. Ding, C. T. Chan and K. M. Ho, *Surf. Sci.* **275** (1992) L691.
[69] Y. G. Ding, C. T. Chan and K. M. Ho, *Phys. Rev. Lett.* **67** (1991) 1454.
[70] Yu. L. Gavriljuk and V. G. Lifshits *Poverkhnost* N4 (1983) 82.
[71] Yu. L. Gavriljuk and V. G. Lifshits, Phys. Chem. Mech. Surf. **2** (1984) 1091.
[72] V. G. Lifshits, V. B. Akilov, B. K. Churusov and Yu. L. Gavriljuk, *Surf. Sci.* **222** (1989) 21.
[73] T. Ichinokawa, I. Hamaguchi and M. Hibino, *Surf. Sci.* **209** (1989) L144.
[74] A. Yamanaka, K. Yagi and H. Yasunaga, *Ultramicroscopy* **29** (1989) 161.
[75] H. Yasunaga and E. Sasuga, *Surf. Sci.* **231** (1990) 263.
[76] W. Telieps and E. Bauer, *Ultramicroscopy* **17** (1985) 57.
[77] A. Cros, F. Salvan, M. Commandre and J. Derrien, *Surf. Sci.* **103** (1981) L109.
[78] A. Cros, J. Derrien and F. Salvan, *Surf. Sci.* **110** (1981) 471.
[79] I. Abbati, C. Rossi, L. Caliari, L. Braicovich, I. Lindau and W. E. Spicer, J. Vac. Sci. Technol. **21** (1982) 409.
[80] A. Cros, F. Houzay, G. M. Guichar and R. Pinchaux, *Surf. Sci.* **116** (1982) L232.
[81] K. Oura and T. Hanawa, *Surf. Sci.* **82** (1979) 202.
[82] M. Hanbucken, Z. Imam, J. J. Metois and G. Le Lay, *Surf. Sci.* **162** (1985) 628.
[83] Z. H. Lu, T. K. Sham, K. Griffiths and P. R. Norton, *Solid State Commun.* **76** (1990) 113.
[84] M. Hanbucken, G. Le Lay and V. Vlassov, in *Proceedings of 18th International Conference on Physics of Semiconductors* **1** (1987) 347.
[85] K. Hricovini, J. E. Bonnet, B. Carriere, J. P. Deville, M. Hanbucken and G. Le Lay, *Surf. Sci.* **211–212** (1989) 630.
[86] H. S. Jin, T. Ito and W. M. Gibson, *J. Vac. Sci. Technol. A* **3** (1985) 942.
[87] K. Oura, Y. Makino and T. Hanawa, Japan *J. Appl. Phys.* **15** (1976) 737.
[88] A. Yamanaka, Y. Tanishiro and K. Yagi, *Surf. Sci.* **264** (1992) 55.
[89] Y. Yamamoto, *Surf. Sci.* **271** (1992) 407.
[90] A. K. Green and E. Bauer, *Surf. Sci.* **103** (1981) L127.
[91] G. Le Lay, *Surf. Sci.* **132** (1983) 169.

(B)

BORON

1. (111) ORIENTATION

Boron was found to induce $\sqrt{3} \times \sqrt{3}$—$R30°$ reconstruction of the Si(111) surface. The 1×1 structure was detected in several works before the formation of the $\sqrt{3} \times \sqrt{3}$—$R30°$ structure.

1.1. PHASE DIAGRAM

Two main techniques are employed to prepare the Si(111)$\sqrt{3} \times \sqrt{3}$–B surface.

First, B is deposited from a B-containing compound, say, HBO_2. At a substrate temperature above 700 °C, HBO_2 dissolves and only B is deposited on to the surface [1]. The 2D phase diagram representing this case is shown in Fig. 1.

In the second preparation, heavily boron-doped Si(111) wafers (i.e. with B bulk concentration exceeding the value of 10^{19}B cm^{-3}), are annealed at elevated temperatures [2–5]. The boron accumulation at the surface at annealing temperatures of 900–1100 °C proceeds due to the segregation phenomena. The surface accumulation of B at 1250 – 1350 °C results from the fact that the evaporation rate of boron atoms from a silicon surface is considerably lower than that of silicon atoms.

Figure 2 shows the kinetics of the accumulation of B on the surface and simultaneous phase transformations as revealed by Korobtsov *et al.* in the LEED–AES study [3]. Boron surface concentration in Fig. 2 is expressed in units of atomic percent since, at annealing, boron is accumulated not only at the surface but in a rather thick (more than 100 Å) near-

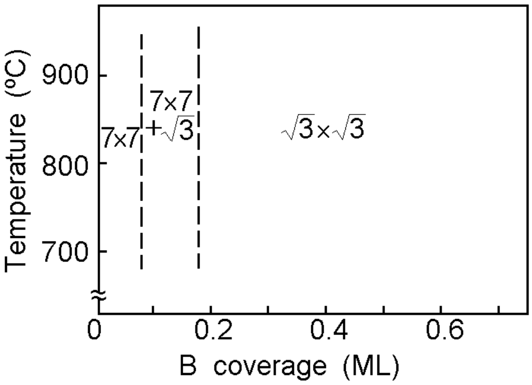

Fig 1. RHEED pattern dependence on the substrate temperature during deposition and B coverage. RHEED observation was performed at room temperature (from Ref. [1]). (*Reproduced by permission of Elsevier Science Publishers BV)*

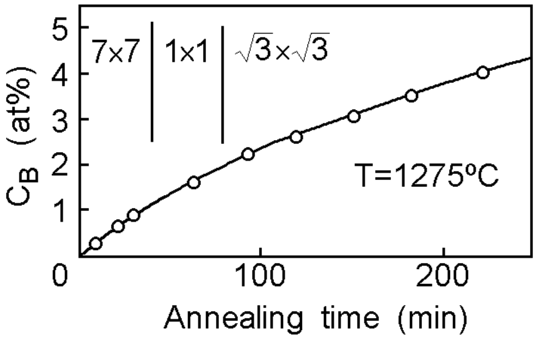

Fig 2. Evolution of surface structure and composition of 0.005 ohm-cm B-doped Si(111) sample during annealing at 1275 °C according to LEED–AES data (from Ref. [6]). (*Reproduced by permission of Elsevier Science Publishers BV)*

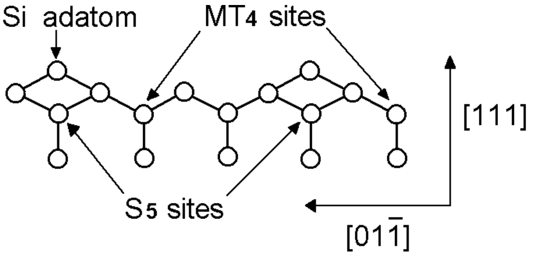

Fig 3. Structural models of a Si(111)$\sqrt{3} \times \sqrt{3}$—$R30°$–B phase. Both S_5 and MT_4 boron bonding sites are shown. The majority of the experimental results support the S_5 model (from *Journal of Microscopy*, **152** (1988) 751). (*Reproduced by permission of Blackwell Scientific Publications, Ltd)*

surface region [3]. The B-enriched region is much thicker than the escape depth of Auger electrons. Hence, the near-surface region probed by AES acts as a Si-B binary phase with nearly constant composition. This proves the usage of atomic percent units. However, the B surface concentration in at% can be easily converted to coverage units (fraction of ML). For example, 1/3 ML corresponds to about 15 at% [6].

In Refs [3–5, 7, 8], the 1 × 1 structure was observed during annealing as an intermediate structure between 7 × 7 and $\sqrt{3} \times \sqrt{3}$—$R30°$–B. It appears at about 0.03 ML (see Fig. 2). However, the 1 × 1 structure was not detected during boron deposition [1].

1.2. STRUCTURE

1.2.1 Si(111)$\sqrt{3} \times \sqrt{3}$—$R30°$–B

According to AES data of Refs [1,3], the $\sqrt{3} \times \sqrt{3}$—$R30°$–B surface phase is completed at 1/3 ML B coverage.

The majority of experimental data obtained with different techniques, namely, STM [9–13], X-ray diffraction [14], quantitative LEED intensity analysis [15], core-level photoelectron spectroscopy [16,17] is consistent with the model in which the boron atom is below the surface in the fivefold-coordinated substitutional (S_5) site under a silicon T_4 adatom (Fig. 3).

In the pioneer STM study of $\sqrt{3} \times \sqrt{3}$—$R30°$–B [7,8,18], another structural model (so called MT_4 model) was proposed. In this model, B atoms occupy the sites marked as "MT_4 sites" in Fig. 3. The model was based on the observation of the absence of mirror symmetry with respect to the short diagonal of the $\sqrt{3} \times \sqrt{3}$ unit cell. However, this observation was not confirmed in the subsequent STM investigations [9–13]. The MT_4 model is also in contradiction with X-ray diffraction data of Ref. [14].

The first-principles total energy calculations [9,13,19] revealed that among other candidates the S_5 model corresponds to the lowest-energy configuration. Hence, it is safe to state that the S_5 arrangement is the most plausible basic structure of the $\sqrt{3}\times\sqrt{3}$—$R30°$–B phase.

The particular features of the Si(111)$\sqrt{3}\times\sqrt{3}$–B surface were considered by Luo *et al.* [20] with the high energy He$^+$-ion channeling technique. The experimental results showed large average atomic displacements (0.25 Å) parallel to the reconstructed (111) surface, but smaller displacements (0.1 Å) perpendicular to the [110] axial direction.

1.3. PROPERTIES

1.3.1. Thermal Stability

The $\sqrt{3}\times\sqrt{3}$—$R30°$–B structure is very stable against the heating and it cannot be removed by heat treatment even at temperatures near the melting point [2, 3]. The stability of the $\sqrt{3}\times\sqrt{3}$—$R30°$–B surface is considered to be due to the relief of subsurface strain by short B–Si bonds [13].

1.3.2. Passivation

The ordered subsurface B atoms were found to passivate surface Si atoms and reduce drastically the reactivity of the Si(111) surface with respect to hydrogen [2, 21], oxygen [2, 22] and ammonia (NH_3) [23] gases: Ohnishi [2] reported that the $\sqrt{3}\times\sqrt{3}$—$R30°$–B structure remains unchanged after being treated at 600–1100 °C in hydrogen gas of an exposure of about 1000 L. Chen *et al.* [21] showed that interaction of atomic hydrogen with the Si(111)$\sqrt{3}\times\sqrt{3}$–B surface results in reduced saturation coverage of hydrogen (as compared to Si(111)7 × 7 surface) and, hence, leads to the suppression of SiH_4 formation.

Besides the inhibition of the thermal oxidation (no changes in the $\sqrt{3}\times\sqrt{3}$—$R30°$ LEED pattern were detected upon 100 L exposure in oxygen gas at 530–700 °C [2]), an analogous suppression of the photo-oxidation process was found by Bozso and Avouris [22].

Avouris *et al.* [23] showed by STM that exposure of the Si(111)$\sqrt{3}\times\sqrt{3}$–B surface to several hundreds of L of NH_3 at room temperature leads to very little reaction in contrast to the Si(111)7 × 7 surface, where NH_3 exposure of a few L is sufficient to cause an extensive reaction.

In the case of Cu thin film growth on Si(111)$\sqrt{3}\times\sqrt{3}$–B surface [24], both room temperature and high temperature Cu/$\sqrt{3}\times\sqrt{3}$–B interfaces are characterized by a drastic diminution of the interaction between Cu and Si atoms. The Cu–Si intermixing is strongly reduced and is only present at large coverages (dozens of ML). AES observations indicated that the Stranski–Krastanov growth mode typical for the Cu/Si(111)7 × 7 system is replaced by the Volmer–Weber mode for the Cu/Si(111)$\sqrt{3}\times\sqrt{3}$–B suggesting that under these conditions Cu does not wet the surface.

The passivation of the surface was considered to be obtained through charge transfer from Si adatoms to the substitutional B atoms [13, 24, 25].

1.3.3. Tunnel-diode Effect on an Atomic Scale

The uncompleted Si(111)$\sqrt{3}\times\sqrt{3}$—$R30°$–B phase has been used in Refs [12, 23, 26] for a beautiful demonstration of the tunnel-diode effect in structures of atomic dimensions. These structures involve a tunnel-diode configuration formed by specific sites at the surface and STM tip. It has been shown that several defect sites can exhibit negative differential resistance (NDR) regions in I–V curves.

As an example, Fig. 4 shows the I–V curve with NDR obtained over a "B-free" site adjacent to several "B-occupied" sites. The "B-occupied" site corresponds to the Si adatom

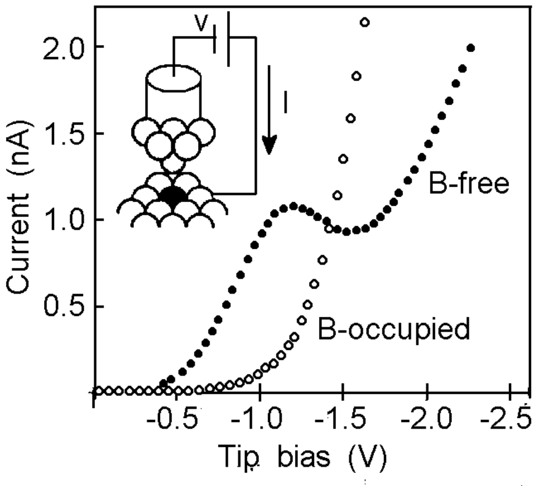

Fig 4. *I–V* curves for the case of negative tip bias, acquired with the tip over boron-occupied and boron-free sites in regions of substantial mixing of the two types of sites (see text). Inset shows geometry of the tunneling device (from Ref. [12]). (*Reprinted with permission from Nature, © 1989, Macmillan Magazines Limited*)

site directly above a substitutional B atom, while the “B-free” site to a site above Si atom. The conductance anomaly is stable and repeatable, both for individual atomic sites and different samples. No such feature is detected for “B-occupied” positions, or in large areas of “B-free” sites.

1.3.4. Si Overgrowth on $\sqrt{3} \times \sqrt{3}$—$R30°$–B

After RT deposition of amorphous Si on to the Si(111)$\sqrt{3} \times \sqrt{3}$—$R30°$–B surface, the buried interface preserves the $\sqrt{3} \times \sqrt{3}$ reconstruction [14, 27–32]. This is clearly seen in Fig. 5 showing the X-ray diffraction profile of

The arrays of ordered $\sqrt{3} \times \sqrt{3}$–B structure at the buried interface still remain even after epitaxial overgrowth of Si via molecular beam epitaxy with deposition temperature of 600 °C [27] or via solid phase epitaxy with an annealing temperature of 540–600 °C [28, 29]. In the latter case, as much as from 15% [28] to 33% [29] of the boron remains in an ordered $\sqrt{3} \times \sqrt{3}$ array.

An interesting effect of surface reconstruction on the orientation of homoepitaxial silicon films was found for Si epitaxy on the Si(111)$\sqrt{3} \times \sqrt{3}$–B surface [32, 33]. It was shown that single-crystalline Si films grown at 400 °C on the $\sqrt{3} \times \sqrt{3}$—$R30°$–B surface phase are rotated 180° about the surface normal with respect to the substrate. The films grown on the 7 × 7 reconstructed Si(111) surface under identical conditions have untwined orientation (Fig. 6).

2. (100) ORIENTATION

The 2×1 reconstruction induced by boron was found by Headrick *et al.* [32, 34]. The symmetry of the LEED pattern from this structure is similar to that from the clean Si(100)2 × 1 surface but these LEED patterns differ apparently in the intensity distribution of diffraction spots.

2.1. PHASE DIAGRAM

The 2 × 1–B surface phase is completed at 0.5 ML coverage upon boron deposition on to the Si(100) surface held at 500 °C. Boron in excess of 0.5 ML does not occupy a well-ordered site

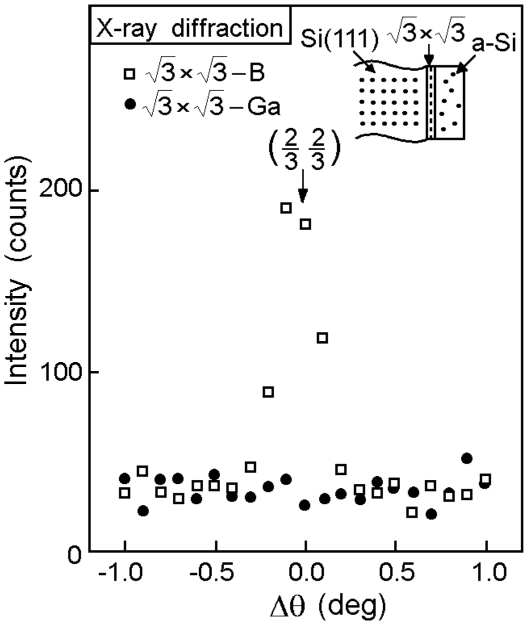

Fig 5. Rocking scan through the (2/3, 2/3) surface X-ray diffraction rod for buried boron surface structure on Si(111). The thickness of the amorphous Si overlayer is 50 Å. The data for the buried gallium phase which does not preserve the ordered $\sqrt{3} \times \sqrt{3}$—$R30°$ reconstruction is shown for comparison (from Ref. [28]). (*Reproduced by permission of American Institute of Physics*)

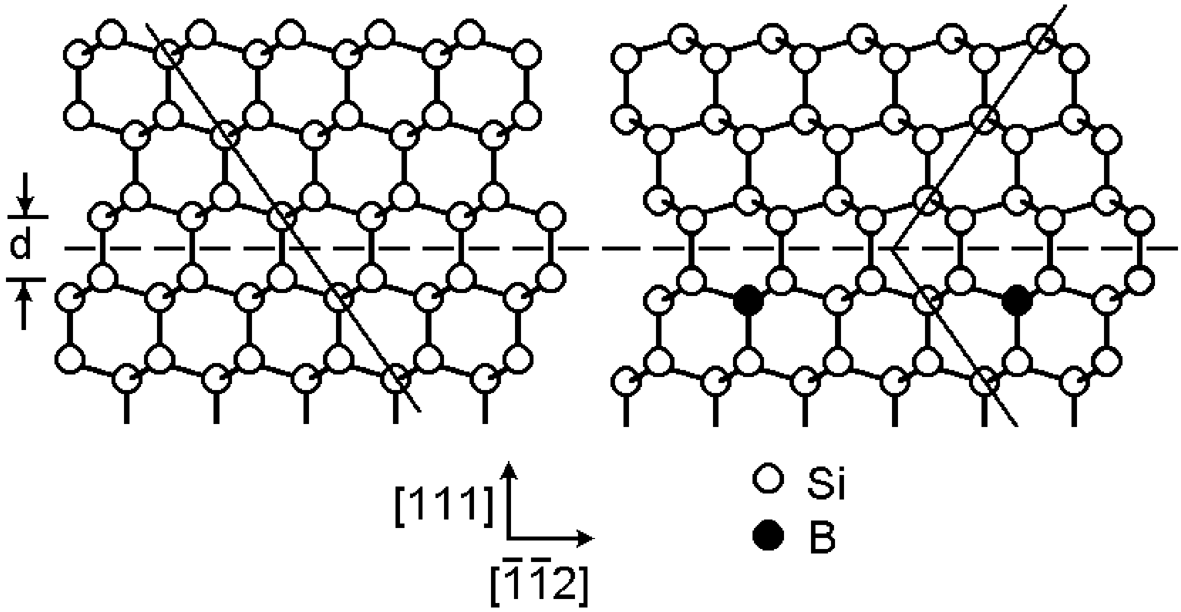

Fig 6. Ball-and-stick models for the film orientation and interface structure for 0—(left) and 0.33—(right) ML boron coverages. The $\sqrt{3} \times \sqrt{3}$ reconstruction of the interface is introduced because boron occupies substitutional sites, occupying every third site in a single monolayer at the interface (from Ref. [33]). (*Reproduced by permission of the publishers of Journal of Physical Review Letters)*

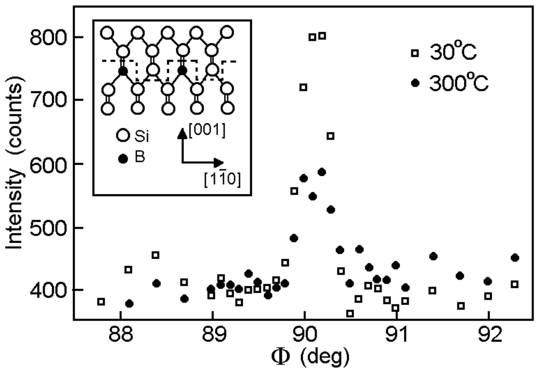

Fig 7. Grazing incidence X-ray diffraction azimuthal scans through the (3/2, 0) diffraction spots for Si(100)2×1–B buried structure capped by growth at room temperature and at 300 °C. The boron coverage was 0.5 ML in both cases and silicon growth rate was 0.1 Å/sec. The inset shows a model of the 2×1 structure at the buried interface (from Ref. [32]). (*Reproduced by permission of American Institute of Physics)*

as reflected in the increasing of background in LEED and sharp decreasing of intensity of half-order grazing-incidence X-ray diffraction reflections [34].

2.2. PROPERTIES

2.2.1. Si Overgrowth on Si(100)2 × 1–B

Headrick *et al.* [32, 34, 35] found that 2×1–B reconstruction can be preserved within high-quality crystalline silicon by low-temperature epitaxial overgrowth at about 300 °C. The grazing incidence X-ray diffraction data (see Fig. 7) indicate that about 50% of the boron remains in the 2×1- ordered layer. The inset in Fig. 7 shows a model of the buried 2×1-reconstructed interface; the dashed line separates the original B-covered surface from the covering silicon layer.

2.2.2. Conductivity of Buried Si(100)2 × 1–B

The strong correlation between the formation of 2×1–B surface phase and electrical activity of boron after subsequent epitaxial Si overgrowth was shown in Ref. [34]. The p-type carrier density increases linearly with B coverage up to 0.5 ML with about 65% boron incorporating in electrically active sites. At B coverage exceeding 0.5 ML, no further increase in carrier density was observed (Fig. 8). The mobility of about 20 cm^2 V^{-1} s^{-1} obtained for the buried 2×1–B phase is comparable with the values for very high boron concentrations in bulk silicon.

3. (110) ORIENTATION

The $\begin{pmatrix} 10 & 0 \\ -2 & 1 \end{pmatrix}$ reconstruction was detected in the B/Si(110) system at low B coverages.

3.1. PHASE DIAGRAM

The formation of the ordered surface phases in the submonolayer B/Si(110) system was studied by Zotov *et al.* [36] by means of LEED and AES. In the experiment, boron was accumulated at the surface *via* high-temperature (900–1300 °C) annealing of heavily B-doped Si(110) sample with B bulk concentration of about 10^{20} cm^{-3}. Despite a great number of

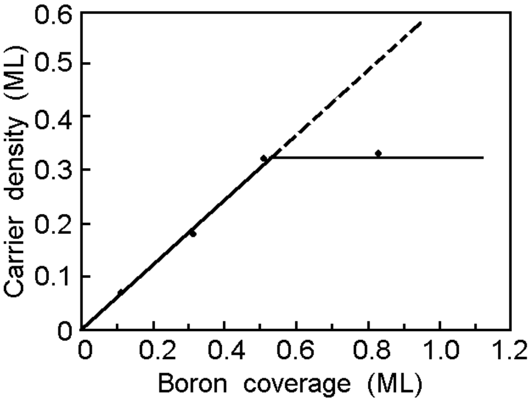

Fig 8. Carrier density at 4.2 K as a function of boron coverage for boron monolayer doping layers. Ordered Si(100)2 × 1–B surfaces were capped at room temperature and annealed at 400 °C for 1 minute (from Ref. [34]). (*Reproduced by permission of American Institute of Physics)*

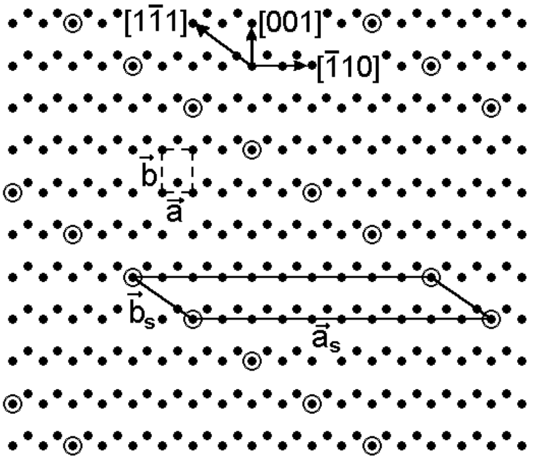

Fig 9. The real lattice of the Si(110)$\begin{pmatrix} 10 & 0 \\ -2 & 1 \end{pmatrix}$–B structure. The solid circles represent the Si atoms on the Si(110) plane and the double circles represent the corners of the unit mesh of the superstructure (from Ref. [36]). (*Reproduced by permission of Elsevier Science Publishers BV)*

different heat treatments examined in the work, the authors of Ref. [36] were unable to exceed the value of about 0.1 ML at B coverage.

It was found that, at B coverages starting from 0.07 ML, the Si(110)$\begin{pmatrix} 10 & 0 \\ -2 & 1 \end{pmatrix}$ superstructure is formed. The real lattice of this structure is shown in Fig. 9. The basic translation vectors of the reciprocal lattice of the superstructure are $\mathbf{a}_s^* = \frac{1}{10}\mathbf{a}^* + \frac{2}{10}\mathbf{b}^*$ and $\mathbf{b}_s^* = \mathbf{b}^*$. The superstructure occurs in two domain orientations, so the LEED pattern of this superstructure shows up as rows of reflections along the [12] and [$\bar{1}$2] directions of the reciprocal 2D lattice of the Si(110) surface (see Fig. 10).

The close examination of the LEED patterns showed that the 10th order reflections are elongated along the [12] directions and even a number of additional weak reflections are present in the [12] rows of the reflections. However, it was impossible to determine the periodicity associated with the “additional” reflections. Considering the real lattice of the Si(110)$\begin{pmatrix} 10 & 0 \\ -2 & 1 \end{pmatrix}$–B structure shown in Fig. 9, it was suggested that this kind of LEED pattern probably corresponds to the structure in which the periodicity along the [1$\bar{1}$1] direction (i.e. within the [1$\bar{1}$1] rows) is well defined, while the ordering of these rows is not perfect (either

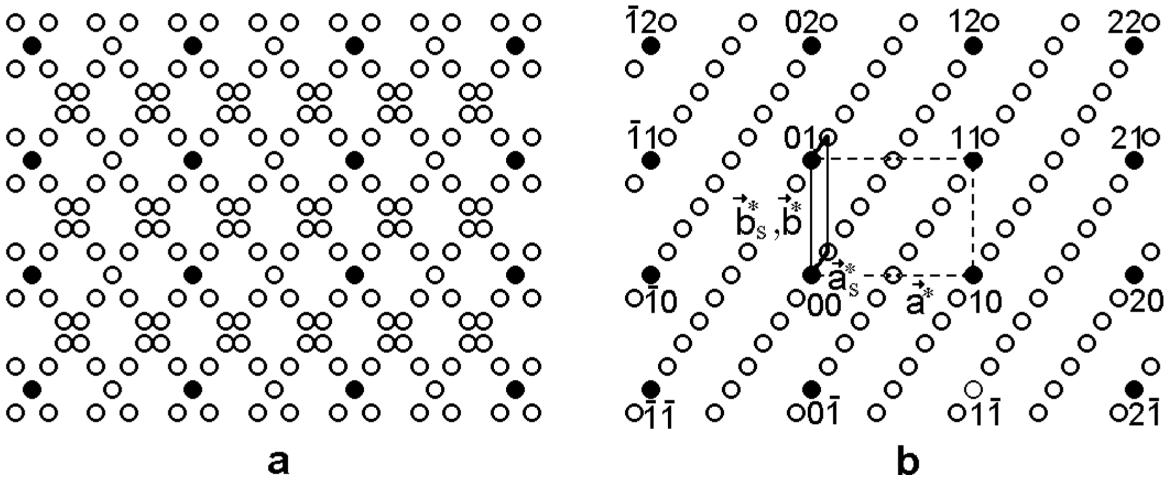

Fig 10. (a) Sketch of the LEED pattern for the two-domain Si(110)$\begin{pmatrix} 10 & 0 \\ -2 & 1 \end{pmatrix}$–B structure. (b) Reciprocal lattice of the Si(110)$\begin{pmatrix} 10 & 0 \\ -2 & 1 \end{pmatrix}$–B structure. The solid circles represent the reciprocal lattice rods of the Si(110) plane and open circles represent the reciprocal lattice rods for the superstructure. The unit mesh of the Si(110) plane is shown in broken lines and the unit mesh of the superstructure is shown in solid lines (from Ref. [36]). (*Reproduced by permission of Elsevier Science Publishers BV)*

the domains with periodicity other than 10**a** are also present on the surface, or 10**a** is an average value of a certain range of periodicities occurring along the [$\bar{1}$10] direction).

Since the B coverages examined in Ref. [36] were limited by the value of 0.1 ML, the question of whether the apparent non-perfect ordering in the $\begin{pmatrix} 10 & 0 \\ -2 & 1 \end{pmatrix}$ superstructure is a specific feature of this B-induced reconstruction or is it a sequence of a deficiency of the surface-accumulated boron for the formation of the completed well-ordered surface phase has remained open.

REFERENCES

[1] H. Hirayama, T. Tatsumi and N. Aizaki, *Surf. Sci.* **193** (1988) L47.
[2] N. Ohnishi, Japan *J. Appl. Phys.* **10** (1971) 517.
[3] V. V. Korobtsov, V. G. Lifshits and A. V. Zotov, *Surf. Sci.* **195** (1988) 466.
[4] A. V. Zotov, V. V. Korobtsov and V. G. Lifshits, *Poverhnost* N8 (1988) 77
[5] S. Bensalah, J. -P. Lacharme and C. A. Sebenne, *Surf. Sci.* **211–212** (1989) 586.
[6] A. V. Zotov and V. G. Lifshits, *J. Cryst. Growth* **121** (1992) 88.
[7] Ph. Dumas, F. Thibaudau and F. Salvan, *J. Microscopy* **152** (1988) 751.
[8] F. Thibaudau, Ph. Dumas, P. Mathiez, A. Humbert, D. Satti and F. Salvan, *Surf. Sci.* **211–212** (1989) 148.
[9] P. J. Bedrossian, R. D. Meade, K. Mortensen, D. M. Chen, J. A. Golovchenko and D. Vanderbilt, *Phys. Rev. Lett.* **63** (1989) 1257.
[10] P. Bedrossian, K. Mortensen, D. M. Chen and J. A. Golovchenko, *Phys. Rev. B* **41** (1990) 7545.
[11] P. Bedrossian, K. Mortensen, D. M. Chen and J. A. Golovchenko, *Nucl. Instrum. Meth. Phys. Res. B* **48** (1990) 296.
[12] P. Bedrossian, D. M. Chen, K. Mortensen and J. A. Golovchenko, Nature **342** (1989) 258.
[13] I. -W. Lyo, E. Kaxiras and Ph. Avouris, *Phys. Rev. Lett.* **63** (1989) 1261.

[14] R. L. Headrick, I. K. Robinson, E. Vlieg and L. C. Feldman, *Phys. Rev. Lett.* **63** (1989) 1253.

[15] H. Huang, S. Y. Tong, J. Quinn and F. Jona, *Phys. Rev. B* **41** (1990) 3276.

[16] A. B. McLean, L. J. Terminello and F. J. Himpsel, *Phys. Rev. B* **41** (1990) 7694.

[17] T. M. Grehk, P. Martensson and J. M. Nicholls, *Phys. Rev. B* **46** (1992) 2357.

[18] F. Salvan, F. Thibaudau and Ph. Dumas, Appl. *Surf. Sci.* **41–42** (1989) 88.

[19] E. Kaxiras, K. C. Pandey, F. J. Himpsel and R. M. Tromp, *Phys. Rev. B* **41** (1990) 1262.

[20] L. Luo, G. A. Smith, S. Hashimoto and W. M. Gibson, *Radiat. Eff. and Defects Solids* **111–112** (1989) 125

[21] P. J. Chen, M. L. Colaianni and J. T.Yates Jr., *J. Appl. Phys.* **70** (1991) 2954.

[22] F. Bozso and Ph. Avouris, *Phys. Rev. B* **44** (1991) 9129.

[23] Ph. Avouris, I. -W. Lyo, F. Bozso and E. Kaxiras, *J. Vac. Sci. Technol. A* **8** (1990) 3405.

[24] Ph. Mathiez, T. P. Roge, Ph. Dumas and F. Salvan, Appl. *Surf. Sci.* **56–58** (1992) 551.

[25] M. -A. Hasan, J. -E. Sundgren and G. V. Hansson, *Thin Solid Films* **184** (1990) 61.

[26] I. -W. Lyo and Ph. Avouris, *Science* **245** (1989) 1369.

[27] K. Akimoto, J. Mizuki, I. Hirosawa, T. Tatsumi, H. Hirayama, N. Aizaki and J. Matsui, *Ext. Abst. 19th Conf. Solid St.* (1987) 463.

[28] R. L. Headrick, L. C. Feldman and I. K. Robinson, *Appl. Phys. Lett.* **55** (1989) 442.

[29] K. Akimoto, I. Hirosawa, T. Tatsumi and H. Hirayama, *Appl. Phys. Lett.* **56** (1990) 1225.

[30] T. Tatsumi, I. Hirosawa, T. Niino, H. Hirayama and J. Mizuki, *Appl. Phys. Lett.* **57** (1990) 73.

[31] R. L. Headrick, A. F. J. Levi, H. S. Luftman, J. Kovalchick and L. C. Feldman, *Phys. Rev. B* **43** (1991) 14711.

[32] R. L. Headrick, B. E. Weir, A. F. J. Levi, B. S. Freer, J. Bevk and L. C. Feldman, *J. Vac. Sci. Technol. A* **9** (1991) 2269.

[33] R. L. Headrick, B. E. Weir, J. Bevk, B. S. Freer, D. J. Eaglesham and L. C. Feldman, *Phys. Rev. Lett.* **65** (1990) 1128.

[34] R. L. Headrick, B. E. Weir, A. F. J. Levi, D. J. Eaglesham and L. C. Feldman, *Appl. Phys. Lett.* **57** (1990) 2779.

[35] B. E. Weir, R. L. Headrick, Q. Shen, L. C. Feldman, M. S. Hybertsen, M. Needels, M. Schluter and T. R. Hart, *Phys. Rev. B* **46** (1992) 12861.

[36] A. V. Zotov, S. V. Ryzhkov and V. G. Lifshits, *Surf. Sci.* **295** (1993) L1005.

(Ba)

BARIUM

1. (111) ORIENTATION

No ordered structures were observed during Ba deposition on the Si(111) surface.

1.1. PHASE DIAGRAM

Core photoemission study of the early stages of the Ba/Si(111) interface formation was performed by Abbati *et al.* [1]. With increasing Ba coverages from 0.2 to 4.4 ML their results strongly suggests the formation of a reacted interfacial layer whose overgrowth is basically uniform, i.e. without strong clustering effects.

2. (100) ORIENTATION

Three long-range ordered structures, 2×3, 1×2, and 2×4, have been observed at submonolayer Ba coverage on Si(100).

2.1. PHASE DIAGRAM

Ordered structures of the Ba/Si(100) system have been investigated using LEED and AES by Fan and Ignatiev [2]. The adsorption of Ba produces a disordered Ba overlayer on the surface at RT or below. However, a number of structures are observed after anneal of the Ba surface exposed to a high temperature ($> 700\,^\circ$C). The relationships between the observed surface structures are described in Fig. 1 as a function of Ba coverage and anneal temperature. The first surface structure observed as coverage increased, is a 2×3 phase resulting from Ba adsorption of about 0.3 ML and anneal to about $900\,^\circ$C. With increasing Ba coverage (> 0.4 ML) and repeated anneals to high temperature ($900\,^\circ$C), the intensities of the one-third order beams in the 2×3 pattern gradually decrease while the intensities of the half-order beams increase slightly. Finally, when Ba coverage reaches about 0.5 ML, the 2×3 phase is almost completely converted to a 1×2 phase after anneal to about $900\,^\circ$C. As coverage increases, this 1×2 phase is immediately followed by the appearance of a 2×4 phase component. Further increase in coverage to a full monolayer does not result in additional LEED patterns. AES data of Fan and Ignatiev [3] showed the formation of Ba silicide after Ba exposures of > 1 ML and anneal to about $600\,^\circ$C.

The silicide formation was also confirmed by using XPS and XAES by Weijs *et al.* [4]. Two Ba–Si phases (possibly BaSi and $BaSi_2$) were detected as reaction products upon annealing the Ba/Si(100) system at ~ 550 K. No silicide formation takes place at RT. Weijs *et al.* [5] have found that Ba grows layer-by-layer on the RT Si(100) substrate.

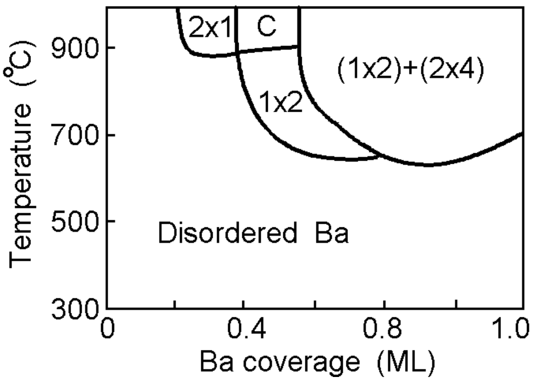

Fig 1. The relationship between the observed surface phases of Ba on the Si(100) surface as a function of anneal temperature and Ba coverage. C indicates a combination of the surface domains of the 2 × 3 and 1 × 2 phases (from Ref. [2]). (*Reproduced by permission of Elsevier Science Publishers BV)*

2.2. STRUCTURE

The possible models for the submonolayer-coverage atomic structures of the Ba/Si(100) system proposed by Fan and Ignatiev [2] on a basis of LEED and AES data [2] are shown on Fig. 2. Within the possible models, a simple atomic chain structure is assumed for the Ba overlayers for the 2 × 3 and 1 × 2 structure. The proposed model for the Si(100)2 × 4–Ba structures is, however, constructed by "zigzag" chains of Ba atoms.

2.3. PROPERTIES

2.3.1. Electronic Properties

The variation of the work function (WF) during Ba deposition on the Si(100) surface is shown in Fig. 3 [6]. At low coverage, a linear decrease in WF is observed. At higher Ba coverage the work function becomes approximately constant around 2.3 eV, which is close to the WF of bulk Ba (2.5 eV).

Upon evaporation of Ba, a lowering of the Schottky barrier by 0.35 eV has been measured by Weijs *et al.* [5].

2.3.2. Oxidation

Thermal oxidation of the Ba/Si(100) surface showed that Ba significantly enhances the oxidation of silicon [3, 7]. At 500 °C and 2.4 ML Ba coverage, the SiO_2 oxides obtained were a factor of 5 thicker than those obtained for the clean unpromoted Si(100) surface [7].

REFERENCES

[1] I. Abbati, L. Braicovich, U. el Pennino, S. Nannarone, G. Rossi and I. Lindau, *Surf. Sci.* **162** (1985) 645.
[2] W. C. Fan and A. Ignatiev, *Surf. Sci.* **253** (1991) 297.
[3] W. C. Fan and A. Ignatiev, *Phys. Rev. B* **44** (1991) 3110.
[4] P. J. W. Weijs, J. C. Fuggle and P. A. M. van der Heide, *Surf. Sci.* **260** (1992) 97.
[5] P. J. W. Weijs, J. F. van Acker, J. C. Fuggle, P. A. M. van der Heide, H. Haak and K. Horn, *Surf. Sci.* **260** (1992) 102.
[6] R. W. J. Hollering, D. Dijkkamp, H. W. L. Lindelauf and van der Heide, *J. Vac. Sci. Technol. A* **8** (1990) 3997.
[7] A. Mesarwi and A. Ignatiev, *J. Vac. Sci. Technol. A* **9** (1991) 2264.

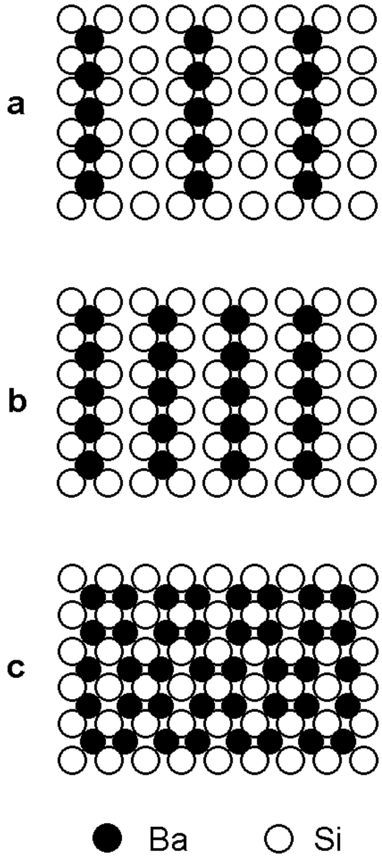

Fig 2. Proposed possible models for the observed long-range ordered Ba/Si(100) structures using chains of Ba atoms: (a) a 2×3 structure ($\theta = 1/3$ ML), (b) a 1×2 structure ($\theta = 1/2$ ML), and (c) a 2×4 structure ($\theta = 1$ ML) (from Ref. [2]). (*Reproduced by permission of Elsevier Science Publishers BV)*

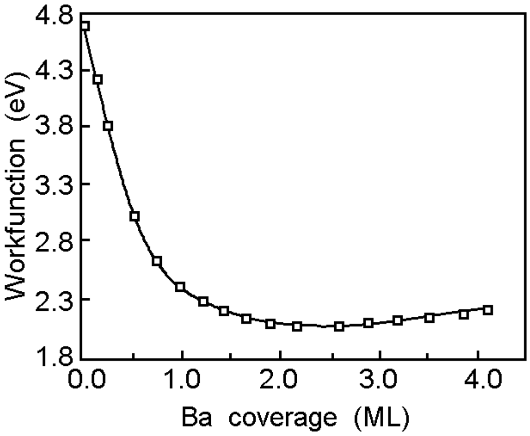

Fig 3. Variation of the work function (WF) during deposition of Ba on a clean Si(100) surface at RT, as measured with XPS (from Ref. [6]). (*Reproduced by permission of American Institute of Physics)*

(Bi)

BISMUTH

1. (111) ORIENTATION

The clear $\sqrt{3} \times \sqrt{3}$—$R30°$ reconstruction and less sharp 1×1 reconstruction were detected for the Bi/Si(111) system depending on growth temperature.

1.1. PHASE DIAGRAM

When deposited on to the heated Si(111) substrate, Bi overlayer grows according to Stranski–Krastanov growth mode. At $\sim 500\,°C$, a LEED pattern of the 2D layer shows a $\sqrt{3} \times \sqrt{3}$—$R30°$ structure, which becomes diffusive with decreasing deposition temperature. When the substrate temperature is kept at $300\,°C$, the 2D layer shows 1×1 reconstruction. The degree of supersaturation, when the onset of bismuth 3D islands growth takes place on the 2D layer is found to be greater than 10 on the 1×1 structure, and 100 on the $\sqrt{3} \times \sqrt{3}$ structure [1–3].

When Bi is deposited on to the RT substrate, the layer-by-layer growth (Frank-van der Merve growth mode) of amorphous Bi occurs on the surface [4].

1.2. STRUCTURE

1.2.1. Si(111)$\sqrt{3} \times \sqrt{3}$—$R30°$–Bi

The $\sqrt{3} \times \sqrt{3}$—$R30°$–Bi was found for the Bi/Si(111) system upon annealing at about $500\,°C$ of RT deposited Bi layer or upon deposition of Bi on to the Si(111) substrate held at about $500\,°C$. This reconstruction was the object of several investigations.

Kawazu and co-workers [1–3] reported that the saturation coverage for $\sqrt{3} \times \sqrt{3}$—$R30°$–Bi is 1/3 ML. From this result they proposed the threefold hollow adatom model equivalent to the H_3 model. This proposition disagrees with the 1 ML trimer model for the $\sqrt{3} \times \sqrt{3}$—$R30°$–Bi surface in which three Bi atoms (trimer) are situated on every $\sqrt{3} \times \sqrt{3}$ site. This model was proposed on the basis of angle-resolved ultraviolet photoelectron spectroscopy [5], X-ray photoelectron diffraction [4], and X-ray diffraction data [6–8]. The above controversy was resolved by Wan *et al.* [9, 10] who revealed the occurrence of two distinct $\sqrt{3} \times \sqrt{3}$–Bi phases at 1/3 ML and 1 ML Bi coverages. On the basis of quantitative analysis of I–V LEED curves, it was concluded in Refs [9, 10] that, at 1/3 ML, Bi atoms adsorb on the T_4 sites and, at 1 ML, Bi atoms form trimers centered on the T_4 position (see Fig. 1).

The analysis of X-ray intensity versus energy curves of Refs [6–8, 11] gave information on the position of surface atoms with respect to bulk crystal. It was shown that the interatomic distance of Bi atoms in trimer is 3.08 ± 0.08 Å and spacing between the Bi and the first layer Si atoms is 2.68 ± 0.02 Å. (The corresponding values determined from LEED data in Ref. [9]

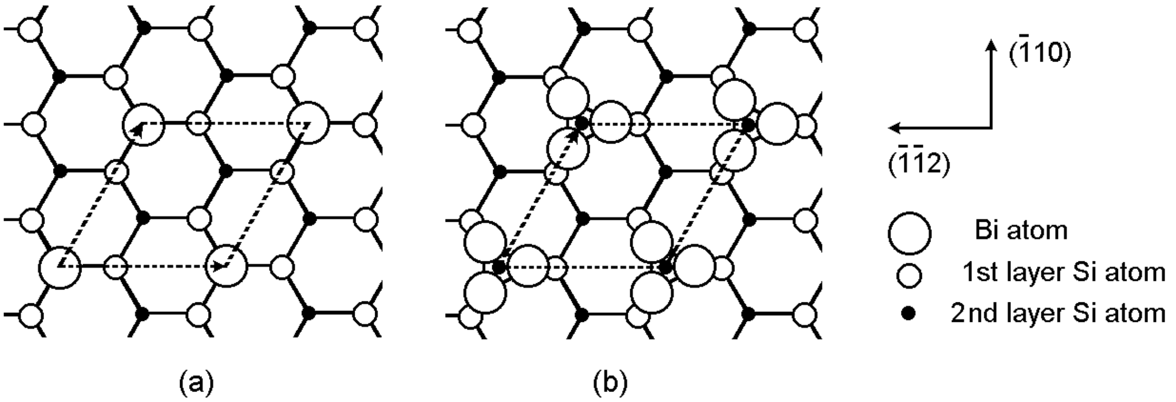

Fig 1. Top views of the structures proposed for two Si(111)$\sqrt{3} \times \sqrt{3}$–Bi surface phases: (a) with 1/3 ML Bi coverage; (b) with 1 ML Bi coverage. Dashed lines show the size of the $\sqrt{3} \times \sqrt{3}$ unit cell (from Ref. [10]). (*Reproduced by permission of Elsevier Science Publishers BV)*

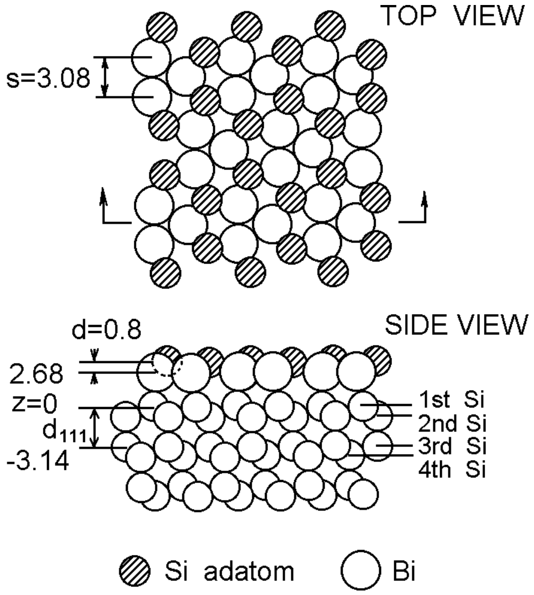

Fig 2. Top and side views of the trimer model with Si adatoms forming a honeycomb structure (from Ref. [7]). (*Reproduced by permission of Elsevier Science Publishers BV)*

are 2.93 Å and 2.210 Å, respectively.) The center of the trimer in the T_4 site was found to be favored rather than in the H_3 one. The displacements of the first and second layer Si atoms were shown to be small and at most 0.15 Å.

In addition, it was suggested in Ref. [7] that a Si adatom layer making a honeycomb structure exists 0.80 ± 0.20 Å above the Bi layer. This suggestion improved the R factor: the R factor, being 0.17 when only the adsorbed Bi layer was taken into account, reduced to 0.12. However, it was pointed out in Ref. [8] that the accuracy of the data was not high enough owing to the weak intensities of the diffracted X-ray to prove the existence of the Si adatoms unambiguously. The structural Bi trimer model of the Si(111)$\sqrt{3} \times \sqrt{3}$—$R30°$–Bi surface with Si adatoms forming a honeycomb structure is shown in Fig. 2.

1.3. PROPERTIES

1.3.1. Desorption

Kawazu *et al.* [1] reported that the $\sqrt{3} \times \sqrt{3}$—$R30°$–Bi surface phase with 1/3 ML Bi coverage has a desorption energy of about 2.4 eV. This value was obtained assuming the first-order desorption kinetics.

1.3.2. Electronic Properties

The ARUPS study of Kinoshita *et al.* [5] revealed the semiconducting nature of $\sqrt{3} \times \sqrt{3}$—$R30°$–Bi surface showing the existence of at least four occupied surface-state bands.

2. (100) ORIENTATION

Several ordered reconstructions have been detected for the submonolayer Bi/Si(100) system, namely, 2×1, 1×1, and $2 \times n$.

2.1. PHASE DIAGRAM

2.1.1. Low Temperature Growth

The growth of the Bi overlayer on Si(100) at low temperatures (< 280 K) proceeds to Frank-Van der Merwe mechanism, the Bi overlayer being disordered and uniform [12].

2.1.2. HT Growth

It is agreed that deposited Bi grows on the Si(100) surface at temperatures exceeding about 300 K in the Stranski–Krastanov mode [12–14]. However, the results on the structure of the 2D Bi layer vary from one publication to another: Kawazu *et al.* [13] reported that the 2D bismuth layer saturates at about 0.5 ML and displays a 2×1 pattern with weak fractional-order spots. Fan *et al.* [12,15] reported a 1×1 reconstruction at about 1 ML Bi. Hanada and Kawai [16] in a recent RHEED study of Bi desorption have observed the $2 \times n$ structures on Si(100) with about 1 ML of Bi. The nth order RHEED spots move away from fundamental spots continuously over the range from 1/13 to 1/5 as the temperature is elevated from 260 to 550 °C (Fig. 3). The Bi coverage is (0.95 ± 0.04) ML and (0.81 ± 0.04) ML for n=13 and n=5, respectively.

2.2. STRUCTURE

2.2.1. Si(100)1 × 1–Bi

The atomic structure of the 1×1–Bi phase was studied by Fan *et al.* [15] using both LEED experiments and the dynamical calculations. It was concluded that the Bi atoms on the Si(100) surface have no long-range ordered structure, but they stabilize the 1×1 structure of the Si(100) surface. The disordered Bi overlayer is, however, uniform and has the definite coverage of about 1 ML. The best agreement between LEED dynamical calculations and experimental data was achieved for the Si(100)1×1 structural model with a 7% contraction of the first Si-atomic layer spacing [15].

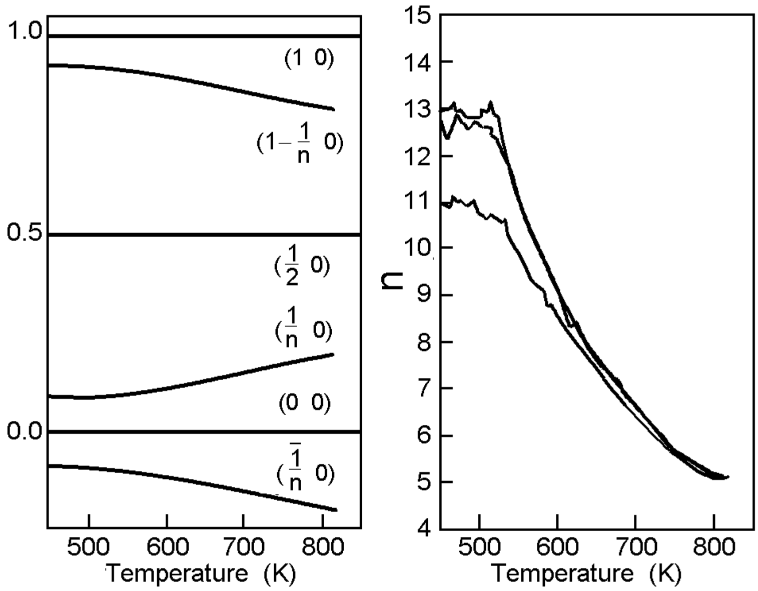

Fig 3. (a) Temperature dependence of the RHEED spot position for Si(100)2 × n–Bi structure. The reflections measured are indicated by two-dimensional reciprocal rod indices. (b) Temperature dependence of the n which is calculated from the position of three nth order reflections in (a). The temperature is elevated at 1 K/s after RT deposition of 2ML (from Ref. [16]). (*Reproduced by permission of Elsevier Science Publishers BV)*

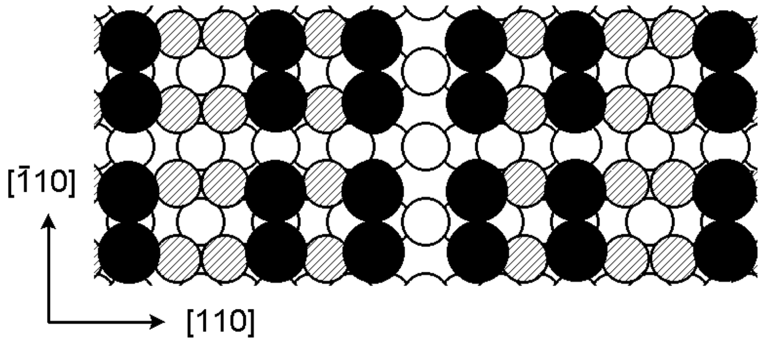

Fig 4. Missing row model for the Si(100)2 × n–Bi surface. For simplicity, the case where $n = 5$ is shown. Missing rows are indicated by triangles (from Ref. [16]). (*Reproduced by permission of Elsevier Science Publishers BV)*

2.2.2. Si(100)2 × n–Bi

Hanada and Kawai [16] proposed a missing row model for the Si(100)2 × n–Bi surface as illustrated in Fig. 4. The model was constructed under the assumptions that Bi atoms saturate all dangling bonds and that the 2 × n structure consists of $(n - 1)/n$ ML Bi.

2.3. PROPERTIES

2.3.1. Desorption

Kawazu *et al.* [13] estimated the desorption energy of Bi from the Si(100)-Bi surface phase to be 2.3 eV and the mean lifetime of a Bi atom to be about 300 s at 470 °C.

2.3.2. Passivation

Yamada and Abe [14] performed the annealing of the 1.7 ML Bi-covered Si(100) samples in an oxygen atmosphere. It was found that pronounced oxidation of the surface starts only with Bi desorption at temperatures above 450 °C. When oxygen adsorbs at the Si(100) surface with a small quantity of Bi (less than about 1/6 ML) no chemical shifts were observed in the Si AES signal. This was suggested to indicate that oxygen does not combine with Si as strong as it does in SiO_2.

3. (110) ORIENTATION

Surface phases having 1×1 and 3×2 reconstructions have been detected for the submonolayer Bi/Si(110) system.

3.1. PHASE DIAGRAM

The adsorption process of Bi on clean Si(110) was studied in Ref. [17] by means of QMS, AES and LEED. It was concluded that the growth conforms to the Stranski–Krastanov mode.

At high temperatures ($T \simeq 450\,°C$), two surface phases were observed. The first surface phase saturates at 1/6 ML Bi coverage and shows a 3×2 structure. The second phase saturates at 1/3 Ml Bi and shows a 1×1 structure.

At low substrate temperatures ($\leq 300\,°C$), only Si(110)1×1 structure is detected even at low Bi coverages.

REFERENCES

[1] A. Kawazu, Y. Saito, N. Ogiwara, T. Otsuki and G. Tominaga, *Surf. Sci.* **86** (1979) 108.
[2] Y. Saito, A. Kawazu and G. Tominaga, *Thin Solid Films* **85** (1981) 275.
[3] Y. Saito, A. Kawazu and G. Tominaga, *Surf. Sci.* **103** (1981) 563.
[4] C. Y. Park, T. Abukawa, K. Higashiyama and S. Kono, Japan *J. Appl. Phys.* **26** (1987) L1335.
[5] T. Kinoshita, S. Kono and H. Nagayoshi, J. Phys. Soc. Jap. **56** (1987) 2511.
[6] T. Takahashi, K. Izumi, T. Ishikawa and S. Kikuta, *Surf. Sci.* **183** (1987) L302.
[7] T. Takahashi, S. Nakatani, T. Ishikawa and S. Kikuta, *Surf. Sci.* **191** (1987) L825.
[8] T. Takahashi, S. Nakatani, N. Okamoto, T. Ishikawa and S. Kikuta, Rev. Sci. Instrum. **60** (1989) 2365.
[9] K. J. Wan, T. Guo, W. K. Ford and J. C. Hermanson, *Phys. Rev. B* **44** (1991) 3471.
[10] K. J. Wan, T. Guo, W. K. Ford and J. C. Hermanson, *Surf. Sci.* **261** (1992) 69.
[11] T. Takahashi, S. Nakatani, N. Okamoto, T. Ishikawa and S. Kikuta, *Techn. Rept. ISSP. A. N* 2033 (1988) 1.
[12] W. C. Fan, A. Ignatiev and N. J. Wu, *Surf. Sci.* **235** (1990) 169.
[13] A. Kawazu, T. Otsuki and G. Tominaga, Japan *J. Appl. Phys.* **20** (1981) 553.
[14] T. Yamada and H. Abe, Japan *J. Appl. Phys.* **29** (1990) L1192.
[15] W. C. Fan, N. J. Wu and A. Ignatiev, *Phys. Rev. B* **45** (1992) 14167.
[16] T. Hanada and M. Kawai, *Surf. Sci.* **242** (1991) 137.
[17] T. Oyama, S. Ohi, A. Kawazu and G. Tominaga, *Surf. Sci.* **109** (1981) 82.

(Br)

BROMINE

1. (111) ORIENTATION

Bromine induces 7 × 7 and 1 × 1 structures on the Si(111) surface.

1.1. PHASE DIAGRAM

When Br is adsorbed on a 7 × 7 reconstructed Si(111) surface, the LEED pattern changes markedly [1]. Except for those seventh-order LEED spots along the lines connecting the first-order spots in the form of a hexagon and a sixfold "star" around each first-order spot, all other fractional order spots vanish. The new pattern is similar to that observed after Cl or H adsorption on Si(111)7 × 7. After tempering the adsorbate at 300 °C the LEED pattern changes fully to 1 × 1.

No change of the LEED pattern was observed when Br was adsorbed on the Si(111)1 × 1 surface [1]. In this case, the Si(111)1 × 1 surface was prepared by a fast cooling of the high temperature 1 × 1 structure.

Br forms a stable, well ordered layer even upon chemical deposition. Usual treatment includes processing in a methanol solution containing 0.05 wt. % Br for 1 min. [2].

1.2. STRUCTURE

The geometrical structure of the Br/Si(111) surface obtained in Br methanol solution has been investigated by means of XSW [1, 3–5] and $^4He^+$ transmission channeling [2]. The upper surface site, which is expected for a monovalent bonding of Br to the Si dangling bond, was found experimentally [2–4] for chemisorption on a mechano-chemically polished surface from a methanol solution. Different authors have obtained the position of Br atoms from 2.56 Å to 2.75 Å above the Si(111) diffraction planes (which, the reader should know, do not correspond to a physical silicon atomic plane [3]). The same preparation technique used on a cleaved surface showed at low coverages the identical result with evidence of a small outward relaxation, but also revealed another position with increasing coverage which agreed with a threefold ionic bonding site H_3 [5, 6].

The first XSW study was carried out *in situ* in ultrahigh vacuum on a Si(111)1 × 1 surface with 1 ML Br by Funke and Materlik [7]. Later, the same authors [1] conducted an XSW study on Br adsorbed on Si(111) for different reconstruction structures, 1 × 1 and 7 × 7. It was clearly shown that Br is adsorbed on the upper surface site in UHV just as it is known to be adsorbed on chemically prepared surfaces [1]. With increasing coverage of Br on 1 × 1, the Si–Br bond length increases from 2.64 Å to 2.76 Å because of the increasing Br–Br layer interaction. On a 7×7 surface, Br records the interior of the unit cell by a local reconstruction.

No evidence was found for a large relaxation of the Si–Br double layer perpendicular to the bulk (111) diffraction planes.

1.3. PROPERTIES

1.3.1. Oxidation

Br renders the Si(111) surface stable against oxidation [8]. This was concluded from a series of STM investigations of a chemically prepared, Br passivated Si(111) surface in ambient conditions. The time-dependent STM investigations show that the Br-passivated surface remains stable for days.

2. (100) ORIENTATION

Br does not change the original 2 × 1 reconstruction.

2.1. PHASE DIAGRAM

The Br/Si(100)2 × 1 interface has been investigated by using XSW and LEED [9] both at RT and for different annealing temperatures up to 600 °C. LEED patterns were 2 × 1 in all cases.

2.2. STRUCTURE

Eteläniemi *et al.* [9] have found a good agreement with their XSW results for adsorption of Br along the dangling bonds of the dimer atoms. Thus, Br atoms saturate the free dangling bonds of the Si(100)2 × 1 surface.

3. (110) ORIENTATION

To our knowledge the Br/Si(110) system has been investigated only in the work of Bedzyk *et al.* [10], where the Br surface phases have been prepared in non-UHV conditions. For this reason the surface reconstruction is unknown.

3.1. PHASE DIAGRAM

To prepare Br layers on the Si(110) surface the sample was processed to a 0.05 % by volume Br methanol solution [10].

3.2. STRUCTURE

Detailed XSW analysis of the position information of chemically deposited Br [10] leads to the conclusion that silicon surface atoms bonded to adsorbed bromine atoms are in extrapolated bulk-like positions.

Direct measurement of the desorption of correlated bromine in air demonstrates the highly stability of the Br/Si surface interface.

REFERENCES

[1] P. Funke and G. Materlik, *Surf. Sci.* **188** (1987) 378.

[2] H. -S. Cheng, L. Luo, M. Okamoto, T. Thundat, S. Hashimoto and W. M. Gibson, *J. Vac. Sci. Technol. A* **5** (1987) 607.

[3] J. A. Golovchenko, J. R. Patel, D. R. Kaplan, P. L. Cowan and M. J. Bedzyk, *Phys. Rev. Lett.* **49** (1982) 560.

[4] G. Materlik, A. Frahm and M. J. Bedzyk, *Phys. Rev. Lett.* **52** (1984) 441.

[5] B. N. Dev, V. Yu. Aristov, N. Hertel, T. Thundat and W. M. Gibson, *J. Vac. Sci. Technol. A* **3** (1985) 975.

[6] B. N. Dev, V. Yu. Aristov, N. Hertel, T. Thundat and W. M. Gibson, *Surf. Sci.* **163** (1985) 457.

[7] P. Funke and G. Materlik, *Solid State Commun.* **54** (1985) 921.

[8] T. Thundat, G. A. Nagahara, U. Knipping and S. M. Lindsay, *Bull. Am. Phys. Soc.* **33** (1988) 572.

[9] V. Etelaniemi, E. G. Michel and G. Materlik, *Surf. Sci.* **251–252** (1991) 483.

[10] M. J. Bedzyk, W. M. Gibson and J. A. Golovchenko, *J. Vac. Sci. Technol.* **20** (1982) 634.

(C)

CARBON

1. (111) ORIENTATION

No ordered surface structures have been found hitherto for the C/Si(111) system.

1.1. PHASE DIAGRAM

While no experimental data on deposition of atomic carbon on to Si(111) surface are available, there are a few works [1,2] devoted to a study of C_{60} fullerene adsorption on the Si(111)7×7 surface.

The fullerenes (C_{60}, C_{70}, C_{76}, and so on) represent a third unique bonding structure for the carbon element, in addition to the well known planar graphite and tetrahedral diamond. The fullerene is a large spherical molecule, which is itself very unique in its stable structure and its large open space. C_{60} can accommodate various elements inside the sphere and its electronic structure can be modified drastically, depending on the type of added element. Discovery of superconductivity in the K-doped C_{60} in 1991 [3] has added even more excitement in C_{60} research.

The adsorption behavior of C_{60} on the Si(111)7×7 surface was studied by Wang *et al.* [1] using STM and by Hong *et al.* [2] using grazing-incidence X-ray diffraction. Contradictory results were obtained in these investigations. Wang *et al.* [1] reported that C_{60} molecules do not form ordered mono/multilayers on the 7×7 surface. In contrast, according to the investigation of Hong *et al.* [2], the thick C_{60} film has the *fcc* structure and is oriented with its [111] direction along the normal surface.

As for submonolayer coverage, the STM observations [1] revealed that there is only one C_{60} adsorbed per half unit, namely a maximum of two molecules per 7×7 unit cell. This is because its diameter is very large (about 7.1 Å). The statistic analysis indicates that fullerene molecules favor the faulted half of a 7×7 unit cell (56%) over the unfaulted half (30%). They occasionally take up the corner vacancy (7%). The C_{60} was also rarely found on the dimer lines.

According to grazing-incidence X-ray diffraction data [2] the C_{60} film about 200 Å (24 molecular layers) thick does not appreciably affect the underlying DAS structure of Si(111). However, the 7×7 reconstruction of the clean silicon surface does not recover by heating the sample, presumably due to decomposition of C_{60} resulting in the SiC formation.

2. (100) ORIENTATION

Other than 1 × 1, no ordered surface structures are observed upon atomic carbon deposition on to Si(100). Meanwhile the fullerene molecules induce c(4 × 3) and c(4 × 4) reconstructions of (100) silicon surface.

2.1. PHASE DIAGRAM

2.1.1. Atomic Carbon Deposition

The RT deposition of carbon on to Si(100)2 × 1 results in the destruction of the initial 2 × 1 structure. The second order reflections disappear after only 0.15 ML of carbon has been deposited [4], then basically the carbon film grows on a 1 × 1 substrate. Auger electron spectroscopy revealed a layer-by-layer growth, at least, up to the fourth layer (the limitation of method) [5]. Within this coverage range, the electronic structure of the carbon atoms evolves from carbidic to diamond-like. After the deposition of the two carbon layers, the topmost layer consists exclusively of carbon atoms as evidenced by low-energy ion scattering experiments [4, 5]. STM images [4, 6] show that the films with thickness of up to 12 Å are characterized by long-range order and crystallinity, with a hexagonal surface lattice. The measured next nearest-neighbor distances range from 2.3 to 2.6 Å.

Effect of annealing on the structure and composition of the carbon diamond-like films was studied by AES and EELS by Martin-Gago *et al.* [4]. For annealing temperatures of less than 700 °C, no changes in the EELS and AES spectra were observed. After heating the film at 950 °C for 10 min both grafitization and formation of silicon carbide were found.

A further increase of temperature, up to 1075 °C, leads to the transformation of the whole carbon into a pure carbidic form. The formation of SiC is accompanied by noticeable interdiffusion of C and Si.

2.1.2. Fullerene Deposition

Field ion-scanning tunneling microscopy was employed to study the monolayer and multilayer adsorption behavior of the C_{60} [7] and C_{84} [8] fullerenes on the Si(100)2 × 1 surface. It was found that the C_{60} and C_{84} molecules reside in the troughs separated by the Si dimer rows. They are distributed randomly on the surface with a minimum separation of 12 Å and 14 Å, respectively, when number density of adsorbed molecules is small.

The first and second layers of C_{60} has only a short-range local ordering. There are two types of structures detected: $c(4 \times 3)$ and $c(4 \times 4)$, with nearest neighbor distance of 9.6 Å and 10.9 Å, respectively. The orderly Stranski–Krastanov mode island formation with the hexagonal packing was observed above the third layer with its lattice constant of 10.4 Å.

For the first and second layers of C_{84}, only the disordered adsorption geometry was observed. When C_{84} was deposited while keeping the substrate at 100 to 150 °C, the fcc (111) crystal with the lattice constant of 17.1 Å forms above the third layer.

REFERENCES

[1] X. -D. Wang, T. Hashizume, H. Shinohara, Y. Saito, Y. Nishina and T. Sakurai, *Japan J. Appl. Phys.* **31** (1992) L983.

[2] H. Hong, W. E. McMahon, P. Zschack, D. -S. Lin, R. D Aburano, H. Chen and T. -C. Chiang, *Appl. Phys. Lett.* **61** (1992) 3127.

[3] A. F, Hebard, M. J. Rossinsky, R. C. Haddon, D. M. Murphy, S. H. Glarum, T. T. M. Palstra, A. P. Ramirez and A. R. Kortan, *Nature* **350** (1991) 600.

[4] J. A. Martin-Gago, J. Fraxedas, S. Ferrer and F. Comin, *Surf. Sci.* **260** (1992) L17.
[5] J. A. Martin, L. Vazquez, P. Bernard, F. Comin and S. Ferrer, *Appl. Phys. Lett.* **57** (1990) 1742.
[6] S. Ferrer, F. Comin, J. A. Martin, L. Vazques and P. Bernard, *Surf. Sci.* **251–252** (1991) 960.
[7] T. Hashizume, X. -D. Wang, Y. Nishina, H. Shinohara, Y. Saito, Y. Kuk and T. Sakurai, *Japan J. Appl. Phys.* **31** (1992) L880.
[8] T. Hashizume, X. D. Wang, Y. Nishina, H. Shinohara, Y. Saito and T. Sakurai, *Japan J. Appl. Phys.* **32** (1993) L132.

(Ca)

CALCIUM

1. (111) ORIENTATION

No ordered structures were observed during Ca deposition on the Si(111) surface while a number of ordered structures (1×1, 2×1, 3×1, 5×1, 2×3, and $\sqrt{3} \times \sqrt{3}$—$R30°$) were found after CaF_2 deposition followed by desorption of F.

1.1. PHASE DIAGRAM

Direct Ca deposition on the Si(111) surface does not induce any ordered structures. When Ca was evaporated on the Si(111) surface at RT only Ca was detected by AES indicating the presence of a thick unreacted layer at the surface [1]. During the subsequent annealing cycle some of the Ca reacted with the Si substrate to form $CaSi_2$. The remainder of the Ca desorbed from the surface. The 2×2 LEED pattern (indexed relative to the Si integer-order beams) was obtained from a $CaSi_2$ surface.

The ordered structures induced by Ca on the Si(111) surface were obtained after CaF_2 deposition and subsequent desorption of F [2–7]. Epitaxial growth of CaF_2 on the Si(111) surface was confirmed only at a substrate temperature of $\sim 600\,°C$ but at other temperatures island growth takes place [7]. As the CaF_2 exposure of the Si(111) surface at $770\,°C$ is increased to slightly above that which corresponds to a 1 ML of CaF_2 the formation of the 1×1 structure takes place [3, 5, 8, 9]. In this first monolayer, the Ca:F ratio is one according to the MEIS study of Tromp *et al.* [8].

Using STM Wolkow *et al.* [4] showed that, at temperatures from 750 to $800\,°C$, deposition of approximately one monolayer of CaF_2 on the Si(111)7×7 surface leads to the appearance of two new structures. One of these may be described as $\sqrt{3} \times \sqrt{3}$—$R30°$, the other phase exhibits rows with somewhat irregular fine structure and is best described as a 2×3 structure. In the monolayer regime, these structures were found to coexist. Upon annealing at $850\,°C$, the surface which is predominantly 2×3 can be largely converted to the $\sqrt{3} \times \sqrt{3}$—$R30°$ structure. It is known that annealing at or above $800\,°C$ leads to preferential desorption of fluorine. The $\sqrt{3} \times \sqrt{3}$—$R30°$ structure may therefore be poorer in fluorine than the 2×3 structure and possibly lacking fluorine altogether. In similar experimental conditions, only the $\sqrt{3} \times \sqrt{3}$—$R30°$ structure was detected by LEED by Rieger *et al.* [10], Karlsson *et al.* [2] and Bouzidi *et al.* [11]. For the $\sqrt{3} \times \sqrt{3}$—$R30°$ reconstruction, Ca is assumed to be bonded to three Si atoms in the threefold-coordinated T_4 or H_3 sites [11]. When thin films of CaF_2 are deposited on to the Si(111)7×7 surface and then annealed at 700–$800\,°C$ for a period of a few minutes, they slowly re-evaporate. At submonolayer coverages, the F to Ca ratio decrease with time until only Ca remains on the Si(111) surface as shown by PES by Olmstead *et al.* [5, 12]. As a function of annealing time, the surface reconstruction (as seen in LEED) undergoes a sequence: $1 \times 1 \rightarrow 2 \times 1 \rightarrow 5 \times 1 \rightarrow 3 \times 1 \rightarrow 7 \times 7$. The 3×1 reconstruction is a stable Si(111)–Ca surface, on which no fluorine is observed. Continued annealing of this surface returns the clean Si(111)7×7 reconstruction. AES measurements of the Ca concentration on this surface are of the order of 1/3 ML of Ca. The 3×1 reconstruction was also observed by Miura *et al.* [7] and Cramm *et al.* [6]. The ISS data of Miura *et al.* [7] gives only a Ca peak from the Si(111)3×1–Ca surface.

2. (100) ORIENTATION

To our knowledge there is no information about the formation of ordered structures when Ca is directly deposited on Si(100) surface. However, in the special case of Si/CaF_2/Si(100) MBE growth 5×1, 6×1, and 8×4 reconstructions were observed.

2.1. PHASE DIAGRAM

When Si was grown heteroepitaxially on a CaF_2/Si(100) structure by MBE, Ca segregation at the Si surface was found by Sasaki and Onoda [13]. This phenomenon is related to the formation of the superstructures on the Si surface. The surface structure was found to change with the Si growth temperature. At 700 °C the RHEED patterns show the Si(100)6×1 structure, at 650 °C, Si(100)5×1 structure and, at 720–760 °C, the RHEED patterns show the 1/4 order surface reconstructions, but they are somewhat complicated. The typical pattern at this temperature range corresponds to the 8×4 structure. The estimated Ca concentration at the Si surface is of the order of 10^{13}–10^{14} cm^{-2}. The larger amount of Ca causes the 5×1 structure, the medium causes the 6×1 structure, and the smaller causes the 8×4 structure.

REFERENCES

[1] J. F. Morar and M. Wittmer, *J. Vac. Sci. Technol. A* **6** (1988) 1340.

[2] U. O. Karlsson, F. J. Himpsel, J. F. Morar, D. Rieger and J. A. Yarmor, *J. Vac. Sci. Technol. B* **4** (1986) 1117.

[3] Ph. Avouris and R. Wolkow, *Appl. Phys. Lett.* **55** (1989) 1074.

[4] R. Wolkow and Ph. Avouris, *J. Microscopy* **152** (1988) 167.

[5] M. A. Olmstead, R. I. G. Uhrberg, R. D. Bringans and R. Z. Bachrach, *J. Vac. Sci. Technol. B* **4** (1986) 1123.

[6] S. Cramm, F. Senf, I. Storjohann, C. Kunz and L. Incoccia, *Physica B* **158** (1989) 660.

[7] K. Miura, R. Souda, T. Aizawa, C. Oshima and Y. Ishizawa, *Solid State Commun.* **72** (1989) 605.

[8] R. M. Tromp, M. C. Reuter, F. K. LeGoues and W. Krakow, *J. Vac. Sci. Technol. A* **7** (1989) 1910.

[9] S. J. Morgan, A. R. Law and R. H. Williams, *Vacuum* **38** (1988) 381.

[10] D. Rieger, F. J. Himpsel, U. O. Karlsson, F. R. McFeely, J. F. Morar and J. A. Yarmoff, *Phys. Rev. B* **34** (1986) 7295.

[11] S. Bouzidi, F. Coletti, J. M. Debever, J. L. Longueville and P. A. Thiry, *Appl. Surf. Sci.* **56–58** (1992) 821.

[12] M. A. Olmstead, R. I. G. Uhrberg, R. D. Bringans and R. Z. Bachrach, *Phys. Rev. B* **35** (1987) 7526.

[13] M. Sasaki and H. Onoda, *J. Appl. Phys.* **59** (1986) 3104.

(Ce)

CERIUM

1. (111) ORIENTATION

$\sqrt{3} \times \sqrt{3}$—$R30°$ and 2 × 2 ordered structures have been detected for the submonolayer Ce/Si(111) system.

1.1. PHASE DIAGRAM

1.1.1. RT Growth

In the case of RT Ce overlayer growth on Si(111)7 × 7, the LEED observations [1] revealed that, for Ce coverages below 0.3 ML (1 ML = 1.6 Å), surface shows a faint 1 × 1 LEED pattern and no reflections are seen for higher coverages.

These observations coincide in general with those for the Ce growth on the cleaved Si(111)2 × 1 surface where the 2 × 1 reconstruction is replaced by 1 × 1 structure at the early stages of Ce chemisorption followed by the disappearance of the spotty LEED pattern [2]. The detailed model of a complex, multistep formation of a RT Ce/Si(111)2 × 1 interface was proposed by Grioni *et al.* [2–4]. The model involves the growth of Ce clusters, Ce/Si reaction to form silicide patches, lateral silicide growth and finally metallic Ce layer overgrowth with surface segregated Si.

1.1.2. HT Growth

Fujimori *et al.* [1] reported that, when the Si(111) surface with 0.3–1 ML of RT deposited Ce is heated to about 350 °C, the $\sqrt{3} \times \sqrt{3}$—$R30°$ reconstruction is observed and the Ce coverage for this structure was found to be 0.35 ± 0.07 ML. Further heating to 450 °C (or heating of the surface with coverages of 0.2 ML of Ce up to 350 °C) results in the formation of a 2 × 2 structure with Ce coverage of 0.20 ± 0.03 ML.

1.2. STRUCTURE

1.2.1. Si(111)$\sqrt{3} \times \sqrt{3}$–Ce

A simple model was proposed for the $\sqrt{3} \times \sqrt{3}$—$R30°$–Ce phase with Ce coverage of 1/3 ML in Ref. [1]. It was assumed that Ce atoms occupy threefold hollow (H_3) sites of the ideal Si(111)1 × 1 surface. Thus, each Ce atom is bonded to three top Si atoms, saturating Si dangling bonds. The H_3 site was believed to be favorable for Ce bonding since a Ce atom in the H_3 site has a structural environment similar to that of bulk $CeSi_2$ in that the Ce atom is coordinated by Si atoms and that these, in turn, are covalently bonded to three neighboring Si atoms [1].

2. (100) ORIENTATION

We have been unable to find any information on the submonolayer Ce/Si(100) interface except for Ref. [5] in which the enhancement of Si oxidation by the Ce monolayer was investigated. In the experiment, the Si(100) surface with 3 Å Ce was annealed at 600 °C and exposed to oxygen at temperatures from RT to 650 °C. The presence of Ce significantly enhances the oxidation (in order to achieve the same oxide thickness in a clean Si(100) sample oxygen exposure a thousand times larger is required). The oxidation of Ce–Si reacted interface leads to a mixed oxide with a Ce:Si:O composition ratio of 1:1:3.

REFERENCES

[1] A. Fujimori, M. Grioni, J. J. Joyce and J. H. Weaver, *Phys. Rev. B* **36** (1987) 1075.

[2] M. Grioni, J. J. Joyce, S. A. Chambers, D. G. O'Neill, M. Del Giudice and J. C. Weaver, *Phys. Rev. Lett.* **53** (1984) 2331.

[3] M. Grioni, J. J. Joyce, M. Del Giudice, D. G. O'Neill and J. H. Weaver, *Phys. Rev. B* **30** (1984) 7370.

[4] A. Fujimori, M. Grioni, J. J. Joyce and J. H. Weaver, *Phys. Rev. B* **31** (1985) 8291.

[5] F. U. Hillebrecht, M. Ronay, D. Rieger and F. J. Himpsel, *Phys. Rev. B* **34** (1986) 5377.

(Cl)

CHLORINE

1. (111) ORIENTATION

Chlorine is known to induce two reconstructions on the Si(111) surface. These are 7×7, and apparent 1×1.

1.1. PHASE DIAGRAMS

Following the first report of the Cl/Si(111) system by Florio and Robertson [1], it has been investigated using a variety of experimental and theoretical methods: LEED [1–3], RHEED [4], AES [1, 2, 4–7], PES [6, 8, 9–11], ARUPS [9,12,13], STM [14–17], TDS [6], SEXAFS [2, 18–21], EELS [4, 5, 7, 22], and theoretically [23–34].

It was found that the periodicity of LEED pattern following the RT temperature adsorption of chlorine on the Si(111)7×7 surface does not change [1]. However, the intensities of the first-order and fractional-order reflections are reduced and the diffuse background scattering is substantially increased, indicative of a disordered layer of adsorbed chlorine. Structural changes, however, do occur upon subsequent heating of the silicon samples, or if the initial adsorption is carried out while the sample is being heated.

Starting with a saturated amorphous layer of chlorine upon the Si(111)7×7 surface, heating to 380 °C for ~ 1 min results in a new pattern of 7th order periodicity, a decrease in diffuse background scattering and a substantial increase of silicon first order reflections. There is complete extinction at all voltages of certain 7th order reflections. Only the following fractional order spots appear: $(h, 0)$, $(0, k)$ for $h, k = 1/7, 2/7, 3/7 \ldots$; and (h, k) for $h+k = 1$, i.e. $(1/7, 6/7), (2/7, 5/7), (3/7, 4/7), \ldots$. Auger data indicate a chlorine coverage $\sim$ 80–90% of the saturation value.

With further heat treatment, at 480 °C for ~ 1 min, resulting in little change in chlorine surface coverage, the fractional order spots disappear and a 1×1 pattern, Si(111)1×1–Cl is observed. With higher temperature heating, the chlorine surface coverage is reduced from $\approx 80\%$ of the maximum saturation value down to $\approx$ 4–5%. For all these values of coverage, a strong 1×1 LEED pattern is observed. Thus, this Si(111)1×1 structure can be of the kind of so-called “impurity-stabilized” structures. The usual procedure in removing the last traces of chlorine is to flash the silicon sample to ≈ 800 °C or above for several seconds. The coverage of chlorine-saturated surface at RT was estimated using AES ($\theta_{\text{sat}} = 1.62$ ML) by Whitman *et al.* [6] (see below).

After saturation adsorption (100–400 L) of chlorine on the Si(111)2×1 cleavage face, LEED shows a primitive 1×1 surface structure [10, 13, 35].

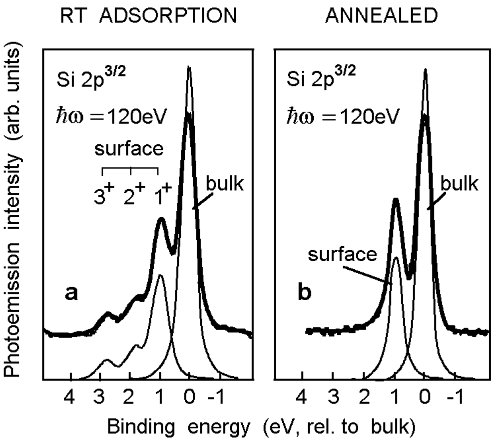

Fig 1. Si $2p$ core-level photoelectron spectra for saturated chlorine adsorption at (a) RT, (b) after annealing this surface to about 400 °C (after subtraction of the Si $2p^{1/2}$ contribution and the background) (from Ref. [8]). (*Reproduced by permission of the publishers of Journal of Physical Review B)*

1.2. STRUCTURE

The structure of the Si(111)7 × 7–Cl phase corresponding to a disordered 7 × 7 LEED pattern with some sharpening of the fractional-order spots after the anneal remains unknown [15]. Chemical interaction of Cl with Si(111)7 × 7 surface at RT results in bonding of silicon atoms to either one, two or three chlorine atoms. This result was obtained using core-level PES by Schnell *et al.* [8,9]. The authors observed Si–$2p$ core-level shifts of 0.93, 1.83, and 2.73 eV to higher binding energy, respectively as shown in Fig. 1(a). After annealing to 400 °C, following Cl adsorption, only monochloride species present on this surface (Fig. 1(b)). The "impurity stabilized" Si(111)1 × 1–Cl structure is believed to be similar to the high-temperature disordered 1 × 1 phase of the clean Si(111) surface [36].

Bonding sites for Cl on Si(111)7×7 were investigated by a variety of experimental methods [2, 9, 18, 19] and theoretically [26–28]. The general accepted conclusion from these works is: Cl occupies the on-top position and the Cl–substrate bond is normal to the surface. SEXAFS measurements of Citrin *et al.* [18–20] have determined an accurate bond length between Si and Cl (2.03 ± 0.03 Å). This value is in good agreement with later results of Purdie *et al.* [21] 2.00 ± 0.02 Å. A number of theoretical calculations [25–28, 34, 37] are in good agreement with this value.

Using STM Boland and Villarrubia [15–17] have studied the structural modifications induced by Cl reaction with the Si(111) 7 × 7 surface in the atomic scale. Initially, a single Cl atom reacts with the adatom (DAS surface structure model) dangling bond. At higher surface coverage, additional Cl atoms insert themselves into the Si–Si backbonds between the adatom and rest-atom layers, producing adatoms that have reacted with two or three Cl atoms.

At saturation coverage, annealing produces extensive mass transport in which most of the adatom layer is stripped away and accumulated in pyramidal Si structures, permitting the complete underlying Si rest-atom layer to be imaged by STM. Much of this layer initially exists as nearly-adatom-free Cl-stabilized 7 × 7 domains, but further annealing converts it slowly to the more favorable bulk-like 1 × 1 structure. Whitman *et al.* [6] estimated the saturation Cl coverage at RT by AES and PES using the facts that annealing the chlorine-saturated surface at ≈ 400 °C produces a surface composed solely of SiCl [8, 9], which STM has shown to consist of the "rest" atom layer with each Si "rest" atom terminated by a Cl atom. If the θ_{Cl} observed after annealing a chlorine-saturated surface to ≈ 400 °C, as described above, is taken to be 1 ML, then the saturation coverage at RT results in $\theta_{\mathrm{sat}} \approx 1.89$ ML. As the 7×7 unit cell has 42 "rest" atoms then $\theta_{\mathrm{sat}} \approx (42/49) \times 1.89 = 1.62$ ML.

On the cleaved Si(111)2×1 surface, in accordance with PES data [10, 13, 35], the Cl adatoms have been found to occupy covalent onefold coordinated sites. Cl–Si bonds are probably tilted with respect to the surface normal.

1.3. PROPERTIES

1.3.1. Desorption

TD spectra following a saturation exposure of chlorine desorption peaks are observed near 300 and 700 °C [6]. At 700 °C, only SiCl^+ and SiCl_2^+ signals are observed, indicating the desorption of SiCl_2. At the lower temperature, a SiCl_3^+ signal is also observed. Hence, both SiCl_4 and some SiCl_2 desorb simultaneously near 300 °C and only SiCl_2 near 700 °C. When $\theta_{\mathrm{Cl}} \leq 0.5$ ML only the high temperature peak associated with the desorption of SiCl_2 is observed. No appreciable Cl_2 desorption is observed from the chlorinated surfaces. From the temperature dependence of the rate constant, an activation energy of 35 kcal/mol (1.5 eV) for the desorption process was measured.

1.3.2. Surface Diffusion

LITD techniques were used to study the surface diffusion of the chlorine on Si(111)7×7 after SiCl_4 adsorption by Gupta *et al.* [38]. No evidence of significant surface chlorine mobility ($D \leq 2 \times 10^{-11}$ cm^2/s) was found for surface temperatures as high as 825 K.

1.3.3. Oxidation

It is found from heating Cl/Si surfaces in O_2 atmospheres that adsorbed Cl atoms suppress oxidation [39, 40]. In the first step of oxidation, Cl atoms desorb by heating, and in the second step the Cl-free areas thus react with O_2 followed by further oxidation proceeding to back-bonds of surface Si atoms. The Si–Cl bonds did not directly react with O_2.

1.3.4. Electron Stimulated Desorption

Electron beam desorption of chlorine from the Si(111) surface can be significant with a focused electron beam [1]. Starting with an ordered 1×1 chlorine structure, the result of beam desorption is a disordered surface. For a beam current of 2 μA at 500 V beam energy and a beam diameter of ≈ 0.05 cm (electron beam density $\approx 6 \times 10^{15}$ electrons/cm^2 s), a chlorine electron beam desorption cross-section* of $\approx 2 \times 10^{19}$ cm^{-2} was calculated.

2. (100) ORIENTATION

On Si(100), the 2×1 periodicity is maintained up to saturation coverage of Cl.

2.1. PHASE DIAGRAM

No obvious degradation of the single-domain LEED patterns was observed on Cl adsorption at RT, suggesting that the 2×1 surface reconstruction is not significantly modified by the adsorbate [41]. AES indicates close to monolayer Cl saturation coverage at RT [41]. While this is consistent with the work of Rowe *et al.* [10], it is significantly lower in later work of Aoto *et al.* [4] (about ≈ 0.25 ML).

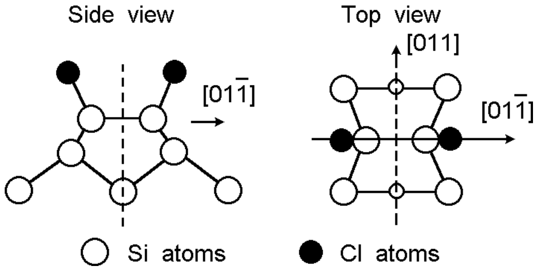

Fig 2. The symmetric dimer model for the Si(100)2 × 1–Cl surface (from Ref. [41]). (*Reproduced by permission of the publishers of Journal of Physical Review B)*

At 100 K, Cl_2 dissociatively chemisorbs on the dangling bonds of Si(100) as reported by Gao *et al.* [42, 43]. At saturation, the surface concentration of Cl is about one Cl atom per Si atom. Heating in UHV at 820 °C for 30 s successfully removes almost all Cl atoms on Cl/Si(100) [7].

2.2. STRUCTURE

In early photoemission studies [10, 35], it was shown that the Cl atoms form covalent bonds with the Si surface atoms on Si(111), and it was asserted that the same conclusion is valid for Cl adsorption on Si(100)2 × 1 [10]. On Si(100), the 2 × 1 periodicity is maintained up to saturation coverage of Cl, suggesting that the Cl atoms bond to Si dimer atoms without breaking the dimer bonds [10]. The expected atomic geometry for the surface is illustrated in Fig. 2. For symmetric dimers, the Cl–Si bond was estimated to be directed $\approx 25°$ off the surface normal, and Cl–Si bond length of 1.95 ± 0.04 Å was determined using SEXAFS and NEXAFS spectroscopies by Thornton *et al.* [2]. Later work of Gao *et al.* [42] for low temperature adsorption is in good agreement with the RT results. HREELS spectra indicate that Cl_2 adsorption at 100 K give a monochloride surface species. Digital ESDIAD measurements revealed that the Si–Cl bond angle for the monochloride is oriented on the vertical plane containing the Si–Si dimer bond and is inclined from the surface normal by $25° \pm 4°$ [42, 43].

Theoretical calculations of Craig and Smith [29] assumed the dissociative adsorption of Cl_2. The adsorption of Cl_2 is found to yield a 2 × 1 symmetric dimer topology with each Si–Cl bond, with the bond length of 2.05 Å, being tilted away from the surface normal at an angle of 14.8°. However, the lowest energy configuration for Cl_2 on the Si(100) surface was determined to be a 2 × 1 bridge site model in which the two chlorine atoms are sited 0.708 Å and 1.132 Å above the surface plane.

2.3. PROPERTIES

2.3.1. Desorption

In accordance with the TPD data of Gao *et al.* [42] the etching products of Si(100) by Cl_2 at elevated temperatures are $SiCl_2$ at about 800 K and a small amount of $SiCl_4$ at about 500 K.

3. (110) ORIENTATION

Cl adsorption on the Si(110) "2 × 16" surface does not significantly change the original reconstruction.

3.1. PHASE DIAGRAM

To our knowledge the interaction of Cl with the Si(110) "2×16" surface was only investigated in a single work of Aoto *et al.* [4] using LEELS, AES, and RHEED. After saturated Cl adsorption, the Si(110) surface exhibited a weakened reconstructed "2 × 16" pattern [4]. The Cl saturated coverage for the Si(110) surface is the same as for the Si(111) surface in accordance with AES observation, i.e. > 1 ML. The resemblance between the Si(110) and Si(100) LEELS peaks related to the Si–Cl bond indicates the similarity of this Si–Cl bond, i.e. being covalent but tilted [4].

REFERENCES

[1] J. V. Florio and W. D. Robertson, *Surf. Sci.* **18** (1969) 398.
[2] G. Thornton, P. L. Wincott, R. McGrath, I. T. McGovern, F. M. Quinn, D. Norman and D. D. Vvedensky, *Surf. Sci.* **211–212** (1989) 959.
[3] J. V. Florio and W. D. Robertson, *Surf. Sci.* **24** (1971) 173.
[4] N. Aoto, E. Ikawa and Y. Kurogi, *Surf. Sci.* **199** (1988) 408.
[5] M. Miyamura, Y. Sakisaka, M. Nishijima and M. Onchi, *Surf. Sci.* **72** (1978) 243.
[6] L. J. Whitman, S. A. Joyce, J. A. Yarmoff, F. R. McFeely and L. J. Terminello, *Surf. Sci.* **232** (1990) 297.
[7] N. Aoto, E. Ikawa, T. Kikkawa and Y. Kurogi, *Surf. Sci.* **250** (1991) 235.
[8] R. D. Schnell, D. Rieger, A. Bogen, F. J. Himpsel, K. Wandelt and W. Steinmann, *Phys. Rev. B* **32** (1985) 8057.
[9] R. D. Schnell, D. Rieger, A. Bogen, F. J. Himpsel, K. Wandelt and W. Steinmann, *Surf. Sci.* **162** (1985) 25
[10] J. E. Rowe, G. Margaritondo and S. B. Christman, *Phys. Rev. B* **16** (1977) 1581.
[11] J. E. Rowe, G. Margaritondo and S. B. Christman, *Phys. Rev. B* **16** (1977) 3648.
[12] P. K. Larsen, N. V. Smith, M. Schluter, H. H. Farrell, K. M. Ho and M. L. Cohen, *Phys. Rev. B* **17** (1977) 2612.
[13] P. K. Larsen, N. V. Smith, M. Schluter, H. H. Farrell, K. M. Ho and M. L. Cohen, *Phys. Rev. B* **17** (1978) 2612.
[14] J. J. Boland, *Surf. Sci.* **244** (1991) 1.
[15] J. J. Boland and J. S. Villarrubia, *Phys. Rev. B* **41** (1990) 9865.
[16] J. S. Villarrubia and J. J. Boland, *Phys. Rev. Lett.* **63** (1989) 306.
[17] J. J. Boland and J. S. Villarrubia, *Science* **248** (1990) 838.
[18] J. E. Rowe and P. H. Citrin, *J. Vac. Sci. Technol.* **21** (1982) 338.
[19] P. H. Citrin and J. E. Rowe, *Surf. Sci.* **132** (1983) 205.
[20] P. H. Citrin, J. E. Rowe and P. Eisenberger, *Phys. Rev. B* **28** (1983) 2299.
[21] D. Purdie, C. A. Muryn, N. S. Prakish, P. L. Winkott, D. S. -L. Law and G. Thornton, *Surf. Sci.* **251–252** (1991) 546.
[22] P. E. Best, *Phys. Rev. B* **19** (1979) 1054.
[23] S. M. Mohapatra, B. N. Dev, K. C. Mishra, N. Sahoo, W. M. Gibson and T. P. Das, *Phys. Rev. B* **38** (1988) 12556.
[24] M. P. Ruzaykin and A. B. Svechnikov, *Poverkhnost* (1988) 59.
[25] C. K. Ong and L. P. Tay, *J. Phys. :Cond. Matt.* **1** (1989) 1071.
[26] G. B. Bachelet and M. Schluter, *J. Vac. Sci. Technol. B* **1** (1983) 726.
[27] K. Zhang and L. Yeh, *J. Vac. Sci. Technol.* **19** (1981) 628.
[28] M. Schluter, *Ultramicroscopy* **14** (1984) 89.
[29] B. I. Craig and P. V. Smith, *Surf. Sci.* **262** (1992) 235.
[30] K. Mednick and C. C. Lin, *Phys. Rev. B* **17** (1978) 4807.
[31] K. Mednick and C. C. Lin, *Surf. Sci.* **81** (1979) 347.
[32] T. Hoshino and M. Tsukada, *Solid State Commun.* **38** (1981) 231.
[33] M. Chen and I. P. Batra, *J. Vac. Sci. Technol.* **16** (1979) 570.

[34] M. Seel and P. S. Bagus, *Phys. Rev. B* **28** (1983) 2023.

[35] M. Schluter, J. E. Rowe, G. Margaritondo, K. M. Ho and M. L. Cohen, *Phys. Rev. Lett.* **37** (1976) 1632.

[36] D. E. Eastman, *J. Vac. Sci. Technol.* **17** (1980) 492.

[37] G. B. Bachelet and M. Schluter, *Phys. Rev. B* **28** (1983) 2302.

[38] P. Gupta, P. A. Coon, B. G. Koehler and S. M. George, *J. Chem. Phys.* **93** (1990) 2827.

[39] N. Aoto, E. Ikawa, T. Kikkawa and Y. Kurogi, *Surf. Sci.* **247** (1991) 21.

[40] N. Aoto, H. Watanabe and T. Kikkawa, *Surf. Sci.* **256** (1991) 361.

[41] L. S. O. Johansson, R. I. G. Uhrberg, R. Lindsay, P. L. Wincott and G. Thornton, *Phys. Rev. B* **42** (1990) 9534.

[42] Q. Gao, C. C. Cheng, P. J. Chen, W. J. Choyke and J. T. Yates, Jr, *Thin Solid Films* **225** (1993) 140.

[43] C. C. Cheng, Q. Gao, W. J. Choyke and J. T. Yates, *Phys. Rev. B* **46** (1992) 12810.

(Co)

COBALT

1. (111) ORIENTATION

The ordered $\sqrt{7} \times \sqrt{7}$, $\sqrt{3} \times \sqrt{3}$, 2×2 (or three domain 2×1), and 1×1 reconstructions were observed for the submonolayer Co/Si(111) system. Except for the $\sqrt{7} \times \sqrt{7}$, these reconstructions were also observed at rather thick Co–silicide layers.

1.1. PHASE DIAGRAM

1.1.1. RT Growth

The formation of the Co/Si(111) interface upon RT Co deposition on to the Si(111)7×7 surface has been extensively investigated with the use of different surface techniques, ARUPS, XPS, LEED, work function measurements [1–6], AES [4, 7], EELS [8, 9], SEXAFS [8, 10], resistivity and Hall effect measurements [11].

The main results can be summarized as follows: Upon Co deposition, the initial 7×7 LEED pattern changes gradually to the 1×1 pattern. At about 2 ML Co coverage, a strong diffuse background is observed, while at 3–4 ML a new but still diffuse 1×1 pattern appears displaying the threefold symmetry, different from that of the Si(111)1×1. It was shown that this pattern reflects the formation of a very thin interfacial silicide with composition close to that of $CoSi_2$ ($\sim$ 4 ML Co ($\sim$ 3.5 Å) react with Si to form $\sim$ 4 unit cells of $CoSi_2$ ($\sim$ 13 Å)). At RT, the interfacial silicide layer is sufficient enough to prevent further Si and/or Co interdiffusion. Some grains of more metal-rich silicides (CoSi and Co_2Si) are detected near the interfacial $CoSi_2$ layer, while at $\theta > 10$ ML an almost pure film of Co grows. The forming of Co film is disordered as indicated by the disappearance of the 1×1 LEED pattern at coverages beyond 5 ML Co.

1.1.2. HT Growth

*

Low-coverage Range (≤ 2.5 ML) It was shown that upon annealing of low-coverage Co film, although chemical bonds between the Co and Si atoms are already initiated, the Co atoms are not yet fully surrounded by Si atoms as in bulk $CoSi_2$ coordination. Some bonds were assumed to be still missing. It was suggested also that the outer last plane of interfacial silicide is composed mostly of Co atoms [1, 2, 12].

Two Co-induced reconstructions, $\sqrt{7} \times \sqrt{7}$ and 2×2, were observed in the submonolayer range by Pirri *et al.* [1, 12] that resulted from depositing Co atoms on to Si(111) substrate held at about 600 °C or annealing at 600 °C RT deposited Co films. The $\sqrt{7} \times \sqrt{7}$ structure is observed at 0.4 ÷ 0.6 ML Co coverage and the 2 × 2 structure (or possibly 2 × 1 with three equivalent domains) at about 1 ML. Between 0.5 and 1 ML, the $\sqrt{7} \times \sqrt{7}$ and 2 × 2 superstructures can be observed together.

Somewhat different results for ordered superstructures in the submonolayer Co/Si(111) system were reported by Wu *et al.* [13]: a $\sqrt{3} \times \sqrt{3}$ structure forms upon annealing 0.4 ML of Co at 650 °C and annealing about 1 ML at 800 °C results in the formation of a $\sqrt{7} \times \sqrt{7}$ structure.

*

High-coverage Range (≥3 ML) When Co coverage is sufficient to reproduce at least one or two unit cells of $CoSi_2$, annealing at about 600 °C produces a flat and continuous $CoSi_2$ layer which shows a 1 × 1 LEED pattern with threefold symmetry [2, 14–16]. The intensity of the background of the 1 × 1 pattern is negligible indicating a very well-ordered phase [12].

An annealing temperature of about 600 °C was found to be optimal for producing a $CoSi_2$ layer since at lower temperatures an incomplete reaction producing other Co richer silicides is detected [8, 15, 17], while annealing at higher temperatures disrupt the $CoSi_2$ film [13–15, 18]. The former case is illustrated in Fig. 1 showing the variation of the Co and Si AES signals versus annealing temperature. The main features clearly seen in Fig. 1 are three plateaux with a constant ratio of Co/Si AES signals. They correspond to the formation of Co_2Si (first plateau, ~ 350–450 °C), CoSi (second plateau, ~ 450–550 °C) and, finally, $CoSi_2$ (plateau at ≥ 600 °C) [15].

Several superstructures were detected by LEED [15, 17] during the silicide formation process. The $\sqrt{3} \times \sqrt{3}$—$R30°$ superstructure was detected for complete Co_2Si phase [17] (or, possibly, when CoSi starts to form [15]). This $\sqrt{3} \times \sqrt{3}$—$R30°$ reconstruction changes to a 1 × 1 structure, which, in turn, transforms into 2 × 2 just before the formation of $CoSi_2$. Finally, a sharp 1 × 1 structure of $CoSi_2$ was observed [15].

The 2 × 2 structure (or, possibly, three-domain 2 × 1) was also detected in Ref. [13] and resulted from annealing of more than 8 ML of Co at 700 °C. This structure converts to 1 × 1 after annealing at 800 °C.

Stalder *et al.* [19] reported the RHEED and STM observation of the three-domain 2 × 1 reconstruction on thin ($d < 45$ Å) strained layers of $CoSi_2$/Si(111). This reconstruction is a stable low-temperature ($T < 180$ °C) structure of the Si-rich $CoSi_2$ surface.

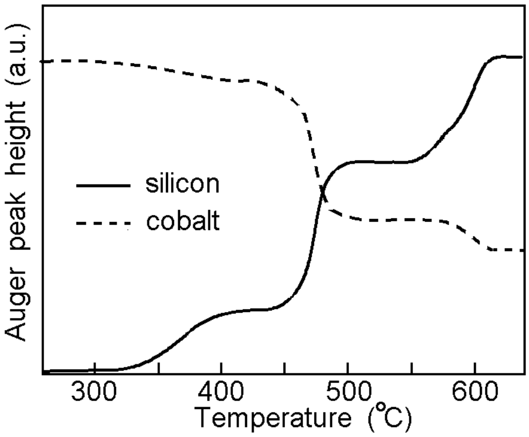

Fig 1. Auger signal variation with formation temperature of the Co/Si(111) interface. Initial Co thickness ~ 33 Å (~ 100 Å of final $CoSi_2$ product). The increasing temperature interdiffusion of Si (outwards) induces an opposite variation of the Si and Co signal. The plateaux correspond to well-defined composition phases (Co_2Si, CoSi, and $CoSi_2$) (from Ref. [15]). (*Reproduced by permission of the American Institute of Physics*)

1.2. STRUCTURE

While the atomic arrangement of the reconstructed surfaces of the Co–silicides has been considered in a number of works (e. g. $CoSi_2(111)1 \times 1$ in Refs [20,21] or $CoSi_2(111)2 \times 1$ in Ref. [19]), the structure of the Si(111)–Co surface phases have not received sufficient interest. We can mention here only the work of Pirri *et al.* [12] in which it was tentatively suggested that the $Si(111)\sqrt{7} \times \sqrt{7}$–Co surface at Co coverage of about 0.5 ML is similar to the Al- or Ag-induced $\sqrt{7} \times \sqrt{7}$-reconstructed Si(111) surface.

2. (100) ORIENTATION

To our knowledge, there is no information in literature concerning the reconstructions induced by submonolayer Co coverages on Si(100) (except the observation of the 2×1 structure of RT deposited 0.5 ML Co). As for the $CoSi_2$ thin films epitaxially grown on Si(100), they display $\sqrt{2} \times \sqrt{2} - R45°$, $3\sqrt{2} \times \sqrt{2} - R45°$ and 2×2 reconstructions depending on growth conditions.

2.1. PHASE DIAGRAM

2.1.1. RT Growth

Gallego *et al.* [22] determined by means of UPS, AES and EELS that, after RT deposition of about 1 ML Co, a single $CoSi_2$-like monolayer forms. Above 1 ML, reaction slows down and a polycrystalline film of metallic Co (with some Si interdiffused) begins to cover the thin interfacial silicide in a layer-by-layer fashion [22].

The suggestions about the mechanism of RT formation of the Co/Si(100) interface different from those above were reported in the SEXAFS–LEED–AES study by Meyerheim *et al.* [23]. They found that, up to about 0.5 ML, Co adsorbed nearly in the plane of the unreconstructed Si(100) surface. At this stage, the 2×1 LEED pattern is still observable, though the brightness of the spots is reduced. At coverages ranging from 0.5 to 2.5 ML, Co atoms penetrate into the Si bulk occupying the interstitial sites. At higher coverages, Co atoms replace the Si host lattice atoms. Finally, at about 19 ML, a Co metallic overlayer starts to grow [23].

Meyerheim *et al.* [23] also reported an observation which can shed light on the discrepancy of the reported results, namely, they found the strong dependence of the RT Co/Si(100) interface formation on the surface preparation procedure. The surface cleaned by sputtering and annealing was shown to be more reactive than the surface prepared by chemical etching followed by *in situ* annealing. Gallego *et al.* [22] exploited the former cleaning procedure, while the main results of Meyerheim *et al.* [23] were obtained on the samples that had undergone the latter cleaning procedure.

2.1.2. HT growth

No results on the HT behavior of the submonolayer Co/Si(100) interface have been previously reported, while there have been a number of publications devoted to the growth of thin epitaxial $CoSi_2$ films (dozensof angstroms thick) on Si(100) substrate [22, 24–31]. The most promising results were obtained by the template method. In this method, a thin $CoSi_2$ layer with thickness of about 10–15 Å (“template”) is formed at the first stage by sequential deposition or co-deposition of Co and Si at RT followed by annealing at temperature (usually of about 450 °C). On the second stage, Co deposition or co-deposition of Co and

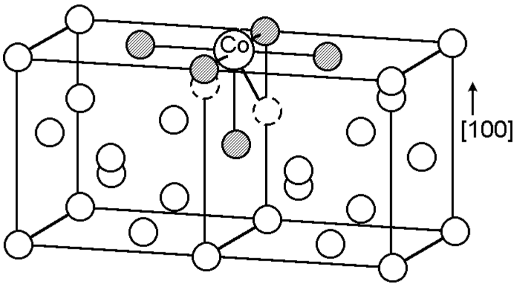

Fig 2. The surface adsorption site as determined for Co evaporated on to Si(100) at about 0.4 ML. Two Si unit cells are shown. Shell A corresponds to two Si atoms shown as open dashed circles, shell B corresponds to five Si atoms shown as hatched circles (from Ref. [23]). (*Reproduced by permission of the publishers of Journal of Physical Review B)*

Si at temperatures ranging from 400 to 650 °C is used to thicken the template to the desired $CoSi_2$ thickness. The grown $CoSi_2$ films usually have a good crystalline quality and display $\sqrt{2} \times \sqrt{2} - R45°$ ($c(2 \times 2)$ in another notation), $3\sqrt{2} \times \sqrt{2} - R45°$ or 2×2 surface reconstructions.

The resultant reconstruction depends on a large body of growth parameters (the way of template formation, growth temperature, the ratio of Co and Si fluxes, etc.). However, the main results can be briefly summarized as follows: the $3\sqrt{2} \times \sqrt{2} - R45°$ reconstruction (occurring in two domains) corresponds to the Si-rich $CoSi_2$ surface (so-called, $CoSi_2$(100)–S), while the Co-rich $CoSi_2$ surface ($CoSi_2$(100)–C) resides in $\sqrt{2} \times \sqrt{2} - R45°$ reconstruction and 2×2 reconstruction is related to the transition from one surface to another. The beautiful result was obtained by Yalisove *et al.* [27] who found that two surface structures, $3\sqrt{2} \times \sqrt{2} - R45°$ and $\sqrt{2} \times \sqrt{2} - R45°$, could be transformed into each other in a reversible manner by the addition of 1 ML of Co or Si followed by annealing at 450 °C.

Stalder *et al.* [31] found that $CoSi_2$(100)–C surface is stable at low temperatures only (T < 500 °C), while the $CoSi_2$(100)-S surface is the stable high temperature phase. The same researchers also found that, apart from the $\sqrt{2} \times \sqrt{2} - R45°$ reconstruction of the $CoSi_2$(100)–C surface, another $\sqrt{2} \times \sqrt{2} - R45°$ occurs on $CoSi_2$(100)–S surface. By STM with atomic-scale resolution, two $\sqrt{2} \times \sqrt{2} - R45°$ reconstructions were clearly distinguished to be attributed to the two different surface structures [31].

In addition, it should be noted that the results of experiments with oxygen [32] and hydrogen [22] adsorption indicate that even the Co-rich $CoSi_2$ surface is terminated by at least one monolayer of Si.

2.2. STRUCTURE

2.2.1. Si(100)2 × 1–Co

The SEXAFS result of Meyerheim *et al.* [23] showed that, for 0.4 ML Co adsorbed on Si(100) at RT, Co environment is composed of two Si atoms located at distance of 2.3 Å (shell A) and five atoms at a distance of 2.8 Å (shell B). This suggests the adsorption site for a Co atom as shown in Fig. 2. The short-range order structure determination shows that upon Co adsorption the 2 × 1 reconstruction of the Si(100) surface is lifted. However, a 2 × 1 LEED pattern is still observable although with reduced brightness of the reflections. Therefore, Meyerheim *et al.* [23] proposed that only adsorption sites in every second [110] row of the Si(100) surface is occupied by Co atoms creating a new 2 × 1 reconstruction.

REFERENCES

[1] C. Pirri, J. C. Peruchetti, G. Gewinner and J. Derrien, *Surf. Sci.* **152–153** (1985) 1106.
[2] J. Derrien, *Surf. Sci.* **168** (1986) 171.
[3] C. Pirri, J. C. Peruchetti, D. Bolmont and G. Gewinner, *Phys. Rev. B* **33** (1986) 4108.
[4] J. Derrien and F. Arnaud d'Avitaya, *J. Vac. Sci. Technol. A* **5** (1987) 2111.
[5] N. Cherief, R. C. Cinti, M. De Crescenzi, J. Derrien, T. A. Nguyen Tan and J. Y. Veuillen, *Appl. Surf. Sci.* **41-42** (1989) 241.
[6] J. Y. Veuillen, T. A. Nguyen Tan, R. C. Cinti, M. De Crescenzi and J. Derrien, *Phys. Rev. B* **39** (1989) 8015.
[7] J. Derrien, M. De Crescenzi, E. Chainet, C. D'Anterroches, C. Pirri, G. Gewinner and J. C. Peruchetti, *Phys. Rev. B* **36** (1987) 6681.
[8] E. Chainet, M. De Crescenzi, J. Derrien, T. A. Nguyen Tan and R. C. Cinti, *Surf. Sci.* **168** (1986) 801.
[9] A. Bensaoula, J. Y. Veuillen and T. A. Nguyen Tan, *Surf. Sci.* **241** (1991) 425.
[10] G. Rossi, A. Santaniello, P. De Padova, X. Jin and D. Chandesris, *Europhys. Lett.* **11** (1990) 235.
[11] J. Y. Veuillen, J. Derrien, P. A. Bados, E. Rosencher and C. D'Anterroches, *Appl. Phys. Lett.* **51** (1987) 1448.
[12] C. Pirri, J. C. Peruchetti, G. Gewinner and J. Derrien, *Phys. Rev. B* **29** (1984) 3391.
[13] S. C. Wu, Z. Q. Wang, Y. S. Li and F. Jona, *Phys. Rev. B* **33** (1986) 2900.
[14] C. Pirri, J. C. Peruchetti and G. Gewinner, *Phys. Rev. B* **30** (1984) 6227.
[15] F. A. D'Avitaya, S. Delage, E. Rosencher and J. Derrien, *J. Vac. Sci. Technol. B* **3** (1985) 770.
[16] N. Roberts and R. J. Needs, *Surf. Sci.* **236** (1990) 112.
[17] C. Pirri, J. C. Peruchetti, G. Gewinner and D. Bolmont, *Solid State Commun.* **57** (1986) 361.
[18] de E. Fresart, J. C. Kao and K. L. Wang, *J. Vac. Sci. Technol. B* **4** (1986) 645.
[19] R. Stalder, H. Sirringhaus, N. Onda and H. von Känel, *Surf. Sci.* **258** (1991) 153.
[20] L. Haderbache, P. Wetzel, C. Pirri, J. C. Peruchetti, D. Bolmont and G. Gewinner, *Appl. Surf. Sci.* **41-42** (1989) 257.
[21] J. Vrijmoeth, A. G. Schins and J. F. Van der Veen, *Phys. Rev. B* **40** (1989) 3121.
[22] J. M. Gallego, R. Miranda, S. L. Molodtsov, C. Laubschat and G. Kaindl, *Surf. Sci.* **239** (1990) 203.
[23] H. L. Meyerheim, U. Dobler and A. Puschmann, *Phys. Rev. B* **44** (1991) 5738.
[24] D. Loretto, J. M. Gibson and S. M. Yalisove, *Phys. Rev. Lett.* **63** (1989) 298.
[25] D. Loretto, J. M. Gibson and S. M. Yalisove, *Thin Solid Films* **184** (1990) 309.
[26] A. H. Van Ommen, C. W. T. Bulle-Lieuwma and C. Langereis, *J. Appl. Phys.* **64** (1988) 2706.
[27] S. M. Yalisove, R. T. Tung and J. L. Batstone, *Mat. Res. Soc. Symp. Proc.* **116** (1988) 439.
[28] R. T. Tung, J. L. Batstone and S. M. Yalisove, *Mat. Res. Soc. Symp. Proc.* **102** (1988) 265.
[29] L. Haderbache, P. Wetzel, C. Pirri, J. C. Peruchetti, D. Bolmont and G. Gewinner, *Thin Solid Films* **184** (1990) 317.
[30] Q. F. Xiao, J. R. Jimenez, L. J. Schowalter, L. Luo, T. E. Mitchell and W. M. Gibson, *Mat. Res. Soc. Symp. Proc.* **220** (1991) 519.
[31] R. Stalder, C. Schwarz, H. Sirringhaus and H. von Känel, *Surf. Sci.* **271** (1992) 355.
[32] R. T. Tung, F. Schrey and S. M. Yalisove, *Appl. Phys. Lett.* **55** (1989) 2005.

(Cr)

CHROMIUM

1. (111) ORIENTATION

The ordered 7×7, 1×1, $\sqrt{3} \times \sqrt{3}$—$R30^\circ$ surface phases and epitaxial $CrSi_2(001)$ silicide in two orientations were observed in the Cr/Si(111) system.

1.1. PHASE DIAGRAM

1.1.1. RT Deposition on to Cleaved Si(111)2 × 1

The formation of the Cr/Si(111) interface upon RT deposition of Cr on to the cleaved Si(111)2×1 surface was studied by Franciosi *et al.* [1–3] and by Lozzi *et al.* [4].

It was found that the 2×1 LEED pattern quickly disappears for very low Cr coverages indicating the formation of the disordered interface [4]. PES results of Refs [1–3] show that the Si(111)2×1 and Cr react at room temperature to form an intermixed region 10–13 Å wide, while, for higher coverages, the formation of a Cr film on top of the intermixed phase occurs with elemental Si segregation at the surface.

The composition of the intermixed layer was considered in Refs [1–4], but the results obtained are not consistent with each other. Lozzi *et al.* [4] using the surface electron energy loss fine structure technique found the formation of $CrSi_2$ for a 3–5 Å thick interface. In contrast, Franciosi *et al.* [1–3] reported that valence-band emission and measured Schottky barrier height of this interface differ from what is expected for a $CrSi_2$/Si interface. They suggested from the comparison of experimental and theoretical results that the intermixed phase is Si rich.

1.1.2. RT Deposition on to Si(111)7 × 7

Lifshits *et al.* [5–7] and Wetzel *et al.* [8] studied the RT growth of Cr on the Si(111)7×7 surface using LEED–AES and LEED–PES work function measurements, respectively.

LEED observations indicated that the original 7×7 LEED pattern fades with Cr deposition: the 7th order reflections are lost at about 1–2 ML Cr coverage and diffuse 1×1 reflections disappear completely after deposition of 4–8 ML Cr. So, at room temperature, no Cr-induced ordered reconstructions are formed at any Cr coverage [5, 8].

Both Lifshits *et al.* [5–7] and Wetzel *et al.* [8] concluded that, prior to the growth of polycrystalline bulk Cr metal, the formation of the intermixed Cr–Si layer is completed at 25–30 ML Cr coverage.

Wetzel *et al.* [8] reported that the stoichiometry of the reacted Cr–Si layer evolves gradually from Si-rich to Cr-rich phases with increasing Cr coverage and the reacted phases are

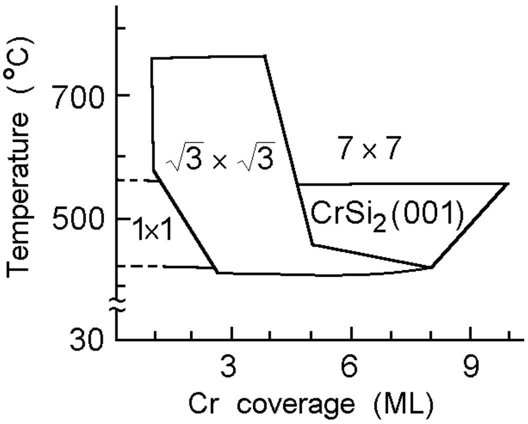

Fig 1. Formation phase diagram of the Cr/Si(111) system (from Ref. [9]). (*Reproduced by permission of the publishers of Poverhost*)

metastable and different from any known bulk silicide. Meanwhile, Lifshits *et al.* [5–7] showed that the forming disordered interface reproduces sequentially the composition and electronic structure of the ordered 1 × 1–Cr, $\sqrt{3} \times \sqrt{3}$–Cr surface phases (formed upon annealing) and bulk Cr_3Si silicide.

1.1.3. HT Growth

The formation phase diagram for the Cr/Si(111) system was determined from the AES–LEED data by Galkin *et al.* [9] and is shown in Fig. 1. In the experiment, Cr was deposited at RT and then the Cr deposit was annealed at higher temperatures. One can see in Fig. 1 that, depending on Cr coverage and annealing temperature, the Si(111)1 × 1, Si(111)$\sqrt{3} \times \sqrt{3}$, Si(111)7 × 7, and epitaxial $CrSi_2$(001)1 × 1 surface structures are formed.

The above results are in a reasonable agreement with the data of Wetzel *et al.* [10, 11] who observed the 1 × 1 structure for Cr coverages below 4 ML and annealing temperature of 450 °C; $\sqrt{3} \times \sqrt{3}$ structure for a coverage range of 4–6 ML and annealing temperatures from 350 to 700 °C (at higher temperatures, the surface converts back to 7 × 7 structure); replacement of the $\sqrt{3} \times \sqrt{3}$ structure by that of epitaxial $CrSi_2$(001) silicide at about 400 °C for Cr coverage of 6–8 ML.

Epitaxial $CrSi_2$ silicide usually occurs in two domains which show up in the LEED pattern as 1.17 × 1.17—$R30°$ and 1.17 × 1.17 − $R0°$ reflections (see Fig. 2). These domain orientations are called A- and B-types and the corresponding epitaxial relationships are: $CrSi_2$(001)/Si(111) with $CrSi_2$[210] ∥ Si[110] and $CrSi_2$(001)/Si(111) with $CrSi_2$[110] ∥ Si[110], respectively [12] (see Fig. 3).

The coexistence of A- and B-type domains was found both in $CrSi_2$ films formed by annealing of RT Cr/Si(111) deposit [7, 9–11] and in $CrSi_2$ films grown upon Cr deposition on to a hot Si(111) substrate [12].

Efforts were made to grow epitaxial $CrSi_2$ films in a single orientation and Haderbache *et al.* [13] found that using a molecular beam epitaxy technique, in which Cr and Si are coevaporated in their stoichiometric ratio on to the Si(111) substrate held at about 450 °C, produces $CrSi_2$ silicide of only A-type orientation. Meanwhile, Plusnin *et al.* [7] obtained a monotype $CrSi_2$ of B-type orientation using the "template" technique and included the formation of the $\sqrt{3} \times \sqrt{3}$–Cr surface phase with Cr coverage of 5–10 ML followed by $CrSi_2$ overgrowth.

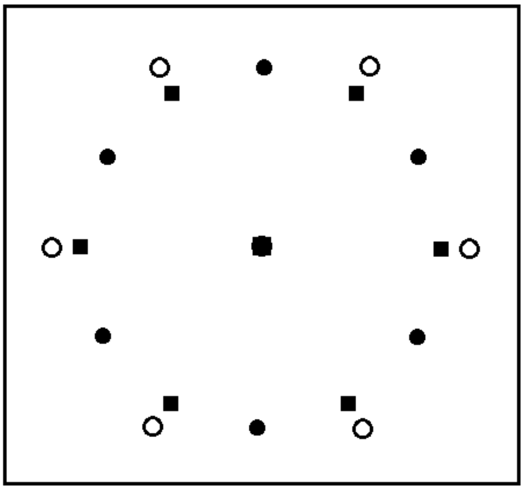

Fig 2. Schematic LEED pattern for epitaxial $CrSi_2$ with two domains: open circles - Si(111); filled circles, 1.17×1.17—$R30°$; filled squares, $1.17 \times 1.17 - R0°$. Only the (00), (10), (01) and equivalent reflections are shown (from Ref. [13]). (*Reproduced by permission of Elsevier Science Publishers BV)*

1.2. STRUCTURE

1.2.1. Si(111)1 × 1–Cr

Wetzel *et al.* [11] concluded from PES data that the compound of the 1 × 1 phase cannot be identified with any known bulk silicide, though there is some similarity with the $CrSi_2$ spectrum. They suggested that, in this phase, the Cr adatoms are merely accommodated in interstitial positions of the Si substrate lattice.

1.2.2. Si(111)$\sqrt{3} \times \sqrt{3}$–Cr

It was concluded in Ref. [11] that the $\sqrt{3} \times \sqrt{3}$ surface structure corresponds to a cubic CrSi silicide. The lattice mismatch for the epitaxial relationship CrSi(111) ∥ Si(111) is only 1.6% and the CrSi(111) lattice fits almost exactly the $\sqrt{3} \times \sqrt{3}$—$R30°$ superlattice of the Si(111) surface. The PES results presented in Ref. [11] confirm this conclusion.

However, Galkin *et al.* [9] pointed out that two Cr–Si phases exist both displaying the $\sqrt{3} \times \sqrt{3}$ reconstruction. This was concluded from the observation of quite different distributions of LEED spot intensities of $\sqrt{3} \times \sqrt{3}$ surfaces at 1–5 ML and 5–10 ML Cr coverages. The compositions of these phases were suggested to be close to $CrSi_3$ and Cr_2Si_3, respectively [9].

2. (100) ORIENTATION

No new surface structures have been detected for the Cr/Si(100) system besides the 2 × 1.

2.1. PHASE DIAGRAM

Zavodinskii *et al.* [14] studied the formation of the Cr/Si(100) interface upon Cr deposition on to the heated ($T = 600$–$800\,°C$) Si(100)2 × 1 substrate. It was found that the original 2 × 1 structure is preserved at the initial stages of deposition and, at about 0.3 ML Cr, the intensity of the 2 × 1 LEED reflections become nearly twice those of a clean Si(100) surface. Authors interpreted this observation as an evidence of the formation of the ordered Si(100)2 × 1–Cr surface phase. EELS results showed that, at this stage, Cr atoms are merely bonded with Si substrate but not with each atom. Upon further deposition, the disordered surface CrSi

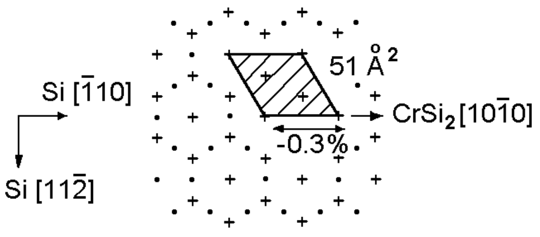

(**a**) Type A

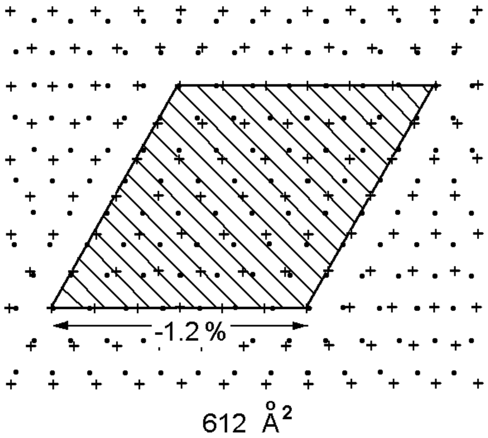

(**b**) Type B

Fig 3. Lattice matching of hexagonal $CrSi_2$ on Si(111): (a) A-type orientation, (b) B-type orientation. Dark dots, Si; crosses, $CrSi_2$. The common unit mesh is shown (from Ref. [12]). (*Reproduced by permission of Elsevier Science Publishers BV)*

silicide begins to form at about 1 ML Cr followed by the growth of polycrystalline $CrSi_2$ islands at about 2.5 ML [14].

2.2. PROPERTIES

2.2.1. Migration of Si Adatoms on Si(100)2 × 1–Cr

Voronov *et al.* [15] studied the diffusional transport of Si adatoms on the Si(100)2 × 1–Cr surface phase in a temperature interval of 940–1200 °C. The results obtained revealed the significant acceleration (by a factor of 25) of Si migration on the Si(100)2 × 1–Cr surface in comparison with that on the clean Si(100)2 × 1 surface.

REFERENCES

[1] A. Franciosi, D. J. Peterman and J. H. Weaver, *J. Vac. Sci. Technol.* **19** (1981) 657.
[2] A. Franciosi, D. J. Peterman, J. H. Weaver and V. L. Moruzzi, *Phys. Rev. B* **25** (1982) 4981.
[3] A. Franciosi, J. H. Weaver, D. G. O'Neill, Y. L. Chabal, J. E. Rowe, J. M. Poate, O. Bisi and C. Calandra, *J. Vac. Sci. Technol.* **21** (1982) 624.
[4] L. Lozzi, M. Passacantando, P. Picozzi, S. Santucci and M. De Crescenzi, *Surf. Sci.* **251–252** (1991) 579.
[5] V. G. Lifshits, V. G. Zavodinskii and N. I. Plusnin, Phys. Chem. Mech. Surf. **2** (1984) 784.
[6] V. G. Lifshits and N. I. Plusnin, *Poverkhnost* N 9 (1984) 78.

[7] N. I. Plusnin, N. G. Galkin, A. N. Kamenev, V. G. Lifshits and S. A. Lobachev, *Poverkhnost* N 9 (1989) 55.

[8] P. Wetzel, C. Pirri, J. C. Peruchetti, D. Bolmont and G. Gewinner, *J. Vac. Sci. Technol. A* **5** (1987) 3359.

[9] N. G. Galkin, V. G. Lifshits and N. I. Plusnin, *Poverkhnost* N 12 (1987) 50.

[10] P. Wetzel, C. Pirri, J. C. Peruchetti, D. Bolmont and G. Gewinner, *Phys. Rev. B* **35** (1987) 5880.

[11] P. Wetzel, C. Pirri, J. C. Peruchetti, D. Bolmont and G. Gewinner, *Solid State Commun.* **65** (1988) 1217.

[12] J. E. Mahan, K. M. Geib, G. Y. Robinson, G. Bai and M. -A. Nicolet, *J. Vac. Sci. Technol. B* **9** (1991) 64.

[13] L. Haderbache, P. Wetzel, C. Pirri, J. C. Peruchetti, D. Bolmont and G. Gewinner, *Surf. Sci.* **209** (1989) L139.

[14] V. G. Zavodinskii, A. V. Voronov and V. G. Lifshits, *Poverkhnost* N 7 (1986) 63.

[15] A. V. Voronov, Yu. L. Gavriluk, V. G. Lifshits and B. K. Churusov, *Poverkhnost* N 8 (1987) 78.

(Cs)

CESIUM

1. (111) ORIENTATION

Cs is known to induce several reconstructions on the Si(111) surface. These are $\delta(7 \times 7)$, 3×1, $\sqrt{3} \times \sqrt{3}$—$R30°$, $c(2 \times 2)$ and incommensurate structures.

1.1. PHASE DIAGRAM

The formation of the Si(111)–Cs interface was examined for two different cases, namely, (a) during Cs deposition on to the cleaved Si(111)2 × 1 surface held at room temperature; (b) during Cs deposition on to the Si(111)7 × 7 surface. Each case is characterized by the individual reconstructions observed.

1.1.1. Cs Deposition on to Cleaved Si(111)2 × 1

Initial stages of Cs adsorption on to the Si(111)2 × 1 surface at RT have been investigated by LEED [1–4], UPS and XPS [3, 5–10], IPES [4], WF changes [1,2], and theoretically [3, 11]. When the Cs deposition starts the peak intensity of the Cs $5p_{3/2}$ emission increases linearly with time and then abruptly becomes constant (Fig.1) [7]. The secondary electron cut-off energy in UPS decreases almost linearly with increase of the Cs coverage until it reaches a saturation value of −3.7 eV [2,4] (Fig. 2). In the saturation region of the cut off and thus of the work function, a well-ordered $\sqrt{3} \times \sqrt{3}$—$R30°$ LEED pattern was observed. This coverage was interpreted as the completion of the first monolayer [2]. In earlier work of Gobeli *et al.* [1], the $\sqrt{3} \times \sqrt{3}$—$R30°$ structure was also observed but the Cs coverage was estimated to be ~ 0.33 ML. Up to 0.5 ML of Cs, an incommensurate quasi-hexagonal structure was observed by Domke *et al.* [3]. A similar LEED pattern was observed by Gobeli *et al.* [1] in the coverage range of $\theta = 0.25 \pm 0.02$ ML. The periodicity of the spots was $2\sqrt{3}$ but some of the spots were missing (Fig. 3). For 1 to 1.5 ML of Cs, a $c(2 \times 2)$ structure was observed [3].

1.1.2. Cs Deposition on to the Si(111)7 × 7

Initial stages of Cs adsorption on to Si(111)7 × 7 surface have been investigated by RHEED [12], LEED [13–20], MDS [21], UPS [14], PES [22,23], AES [15, 19, 20, 24], ISS [15], XSW [19,25,26], EELS [16], FI–STM [27,28] and WF changes [13–15, 18]. During Cs deposition on a Si(111)7 × 7 surface at RT, the $\delta(7 \times 7)$ structure is observed [12]. It requires some (or tens of) minutes of slight annealing to get the RHEED pattern. When the Cs atoms are deposited on the Si(111)7 × 7 surface at about 500 °C, the 3 × 1 superstructure is observed.

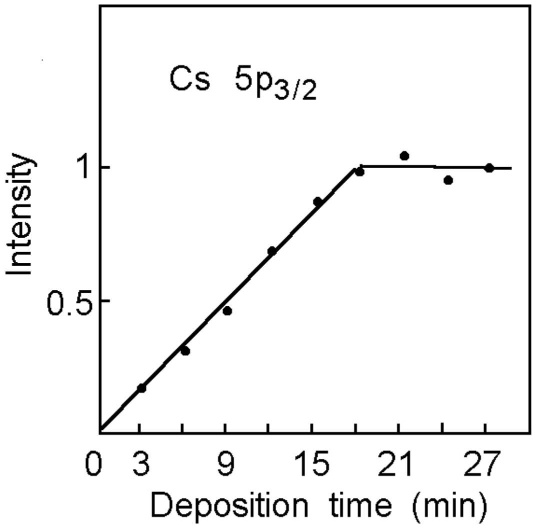

Fig 1. Peak intensity of Cs $5p_{3/2}$ emission versus Cs deposition time (from Ref. [7]). (*Reproduced by permission of Elsevier Science Publishers BV)*

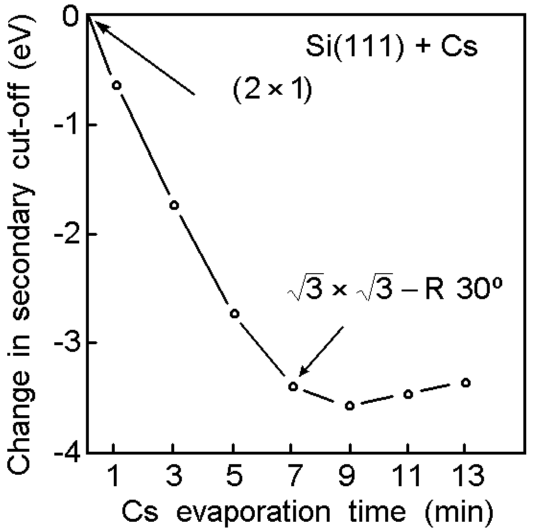

Fig 2. The change in the cut-off energy for secondary electrons in UPS from the Cs/Si(111) surface as a function of Cs evaporation time. The LEED patterns observed at zero coverage and after 7 min are indicated. The latter is attributed to the full monolayer coverage (from Ref. [2]). (*Reproduced by permission of the publishers of Journal of Physical Review B)*

Daimon and Ino [12] proposed that the 3 × 1 structure has two Cs atoms in the 3 × 1 unit mesh by analogy with the Si(111)3 × 1–K structure.

When the Cs atoms are deposited at the substrate temperature of about 150 K, LEED shows no detectable Cs-induced patterns except for a uniform increase in the background intensity [16].

1.2. STRUCTURE

There is no detailed information about the atomic structure of Cs/Si(111) surface phases. But certain remarks can be made based on similarity of the RHEED patterns observed from these phases and those, $\delta(7\times7)$ and 3 × 1, observed at adsorption of other alkali metals.

Cs adsorption on the Si(111)7 × 7 surface has been investigated with the FI–STM by Hashizume *et al.* [27,28]. At the initial coverage (0.005 ML and 0.01 ML), Cs atoms adsorb

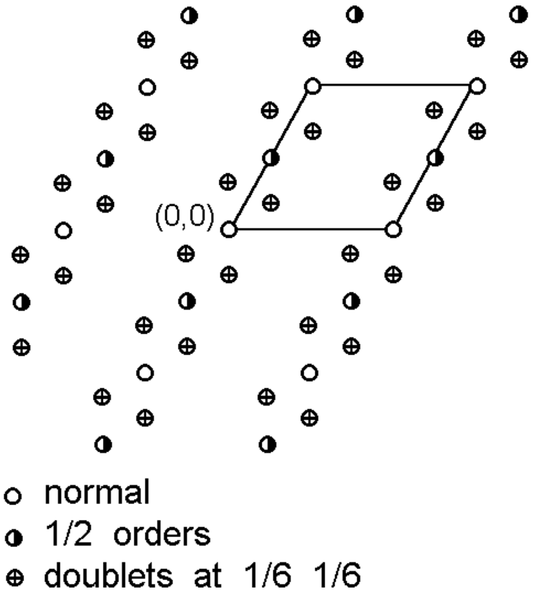

Fig 3. Sketch of LEED pattern from cleaved Si(111), $\theta_{\mathrm{Cs}} \approx 0.25$ (from Ref. [1]). (*Reproduced by permission of American Institute of Physics)*

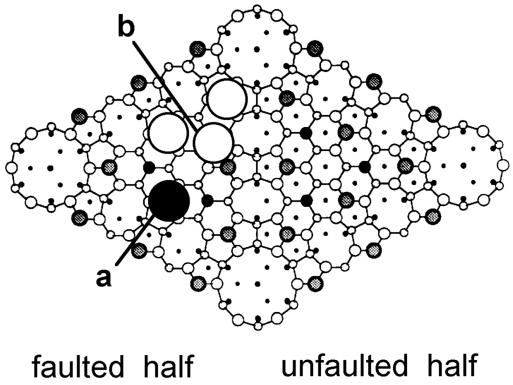

Fig 4. Schematic showing the adsorption geometry of Cs on Si(111)7 × 7 dimer adatoms and stacking fault structure. (a) Shows darkly imaged individual Cs atom, adsorbed at the topmost site of the center adatom position. (b) Shows the brightly imaged Cs trimer (from Ref. [27]). (*Reproduced by permission of American Institute of Physics)*

mainly at the uppermost site of the center adatoms of the DAS structure and are ionized. About 70% of adsorbed Cs atoms are on faulted halves. Some of the adsorbed Cs atoms form clusters (often trimers), which have more covalent character with back-donation of the charge distribution, and those clusters become the dominant species on the surface with increasing coverage. Figure 4 shows the proposed schematic for the adsorption geometry of single and trimer Cs adsorbate on the Si(111)7 × 7 surface.

1.2.1. Si(111)δ(7 × 7)–Cs

The adsorption site of Cs on Si(111)7 × 7 has been investigated by using the XSW technique by Lagomarsino *et al.* [19, 26] and Eteläniemi *et al.* [25]. XSW measurements were carried out using the (111) diffracting planes for RT deposited Cs atoms with Cs coverages ranging from about 0.06 to about 0.15 ML [26]. The measurements showed occupancy of more than one site. The threefold hollow (H_3), the threefold filled (T_4), and all the dangling-bond sites were suggested as possible adsorption sites.

Table 1. The minimum and saturation values of work function for the Cs/Si(111) system

Si(111)	$\Delta\Phi_{\min}$	$\Delta\Phi_{\text{sat}}$	Ref.
2×1	-3.7 eV	-3.4 eV	[2]
7×7	-3.2 eV	—	[14]
7×7	-3.2 eV	-2.9 eV	[13]
7×7	-3.2 eV	-3.1 eV	[15]

The changes in the surface electronic states with increasing Cs coverage have been studied with ARUPS by Magnusson *et al.* [22]. Changes observed predominantly in the emission from the adatom dangling-bond state suggest that bonding of Cs occurs primarily at the adatom site on the Si(111)7 × 7 surface. Secondly, Cs atoms bound to the rest-adatoms dangling bonds. The saturation coverage is thus 18 Cs atoms per 7 × 7 cell. According to XSW results of Eteläniemi *et al.* [25] at saturation coverage (obtained for a layer deposited at RT) the topmost and threefold sites are occupied by Cs atoms. Annealing cycles to 500 °C improve the ordering of the adlayer, and Cs atoms are adsorbed only at threefold sites.

1.3. PROPERTIES

1.3.1. Electronic Properties

The electronic properties of Cs on both Si(111)2 × 1 and Si(111)7 × 7 surfaces have not been determined conclusively and the results of various methods have some contradictions.

Si(111)2×1

In accordance with ARUPS results of Magnusson *et al.* [2], the Si(111) cleaved surface at saturation Cs coverage was found to be semiconducting. But from UPS results of Tochihara *et al.* [5, 6, 10] it was found that a metallic Cs monolayer is formed on Si and nearly a half of the Cs 6*s* band is finally occupied. Theoretical calculations of Ishida *et al.* [11] showed that the bonding π-band of the Si substrate is stable upon Cs adsorption and a partially occupied Cs 6*s* band is newly formed. For thick Cs layers, Cs 5*p* emission from bulk and surface atoms is resolved, resulting in a surface core level shift of 0.23 eV [3].

Si(111)7×7

In accordance with EELS data of Avci [16], the reaction of Cs atoms with the Si(111)7 × 7 surface at 150 K shows two distinct stages. In the initial coverages (≤ 0.3 ML), the Cs atoms transfer their *s* electrons to the Si surface and remain as screened positive centers. For higher coverages (0.3–1 ML), the formation of a metallic layer takes place.

At RT Cs deposition, in accordance with the ARUPS results of Magnusson *et al.* [22], the surface is semiconducting when only adatom sites are occupied, but gets increasingly metallic as saturation is also approached through adsorption at rest-atom sites. Direct evidence of the valence-band charge redistribution with the growth of Cs coverage was obtained in the MDS study by Nishigaki [21].

The core-level shifts were determined with synchrotron-radiation photoemission after Cs adsorption by Lin *et al.* [23]. The results indicate that the chemisorption bond is partially ionic, and the Si surface atoms each have an extra charge of about 0.3 electron after Cs adsorption.

Work Function Changes

Variation of the work function observed during Cs deposition on Si(111) is shown in Fig. 2. The plot reveals a minimum. This minimum was observed on both Si(111)2×1 and Si(111)7×7 surfaces (Table 1). The downward band bending was found to be 0.15 eV [2].

1.3.2. Oxidation

Starnberg *et al.* [29,30] and Franciosi *et al.* [31] have demonstrated that 1 ML of Cs promotes the oxidation of Si(111)7 × 7 by increasing the sticking of O_2, by dissociation of the oxygen molecules, and probably also by weakening the backbonds of the top Si layers so that the initial oxidation takes place already at RT. The Cs stays on top and remains bonded preferentially to Si surface atoms. Annealing at moderate temperature desorbs the Cs completely and leads furthermore to the formation of a more stoichiometric oxide, although with less efficiency than on Si(111)2 × 1. It was suggested that the catalytic mechanism appears to be strongly non-local.

2. (100) ORIENTATION

Cs is known to induce several reconstructions on the Si(100)2 × 1 surface. These are "×3 streak", 4 × 6, 2 × 6, 8 × 4, 2 × 1, 2 × 3, and $c(4 \times 2)$.

2.1. PHASE DIAGRAM

Initial states of Cs adlayer formation on the Si(100)2 × 1 surface have been widely investigated by LEED [13, 32–45], AES [33, 34, 37–43, 45–47], XPS [23, 32, 38, 43, 47–52], XPED [44], ARUPS [38, 46, 48, 49], STM [28], WF measurements [13, 34, 37, 40–42, 46, 50], PEXAFS [53,54], EELS [34, 43, 55], HREELS [43], MEIS [45], TDS [34,37,39,41,42], IR photoemission [56–58], and theoretically [59–64]. Various surface superstructures were observed as Cs was adsorbed at different coverages at either low, intermediate, or high temperature [32, 44].

2.1.1. HT Growth

The adsorption of Cs atoms on to a slightly heated Si(100)2 × 1 surface induces only one ordered phase. Abukawa and Kono [32] have observed the Si(100)$c(4 \times 2)$–Cs superstructure in the temperature range from 300–400 °C and at Cs coverages from 0.5–0.6 ML.

2.1.2. RT Growth

Figure 5(a) shows the experimental phase diagram for substrate temperature (T_s) ≈ 320 K in accordance with the results of Abukawa *et al.* [44]. The horizontal axis indicates Cs coverage (ML) and vertical solid lines correspond to the phase boundaries in which the LEED pattern changes qualitatively. Remaining uncertain phase boundaries are indicated with a dashed line. Shaded areas correspond to the ordered commensurate phases.

For $T_s \approx 320$ K, the phases of "×3 streak" (phase $(4)'$ in Fig.5(a)) and 8 × 4 $(11)'$ were first observed by Abukawa *et al.* [44], in addition to 2 × 3 $(8)'$ and 2 × 1 $(14)'$ which have been reported earlier [32, 33]. Only high background intensity with 2 × 1 spots is found in the region between the ordered phases, which is represented by $(H)'$ in the phase diagram. The uptake of Cs stops at 1 ML having a 2 × 1 order.

2.1.3. Low Temperature Growth

Abukawa *et al.* [44] reported that, for $T_s \approx 110$ K, as well as for $T_s \approx 320$ K, the phases of "×3 streak", 8 × 4 and 2 × 1 are observed at 1/6 ML (phase (4) in Fig.5b), 1/2 ML (11) and 1 ML (14), respectively. Two kinds of 4 × 6 orders appear at 1/4 ML (6) and 3/4 ML (13) for $T_s \approx 110$ K. There is, moreover, a 2 × 6 periodicity at 1/3 ML (8) which corresponds to the 2 × 3 periodicity for $T_s \approx 320$ K and this 2 × 6 phase is remarkable in the sense that it reversibly transforms to 2 × 3 for the $T_s \approx 320$ K. However, the 2 × 6 phase appears diffuse

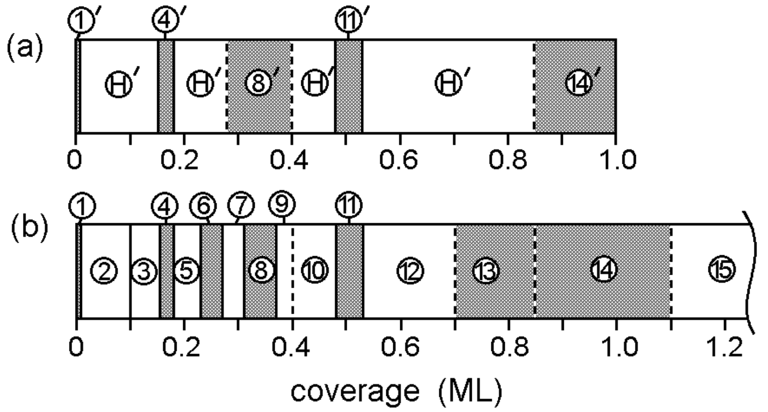

Fig 5. Structural phase diagram derived from a LEED study as a function of coverage for the system Cs/Si(100) for a T_s of $\approx$ 320 K (a), and a T_s of $\approx$ 110 K (b). Shaded areas represent the commensurate ordered phases. The encircled figures and a character with prime denote different phases at $T_s \approx 320$ K: $(1)' = 2 \times 1 + \times 2$ streak, $(4)'$ = "$\times 3$ streak", $(8)' = 2 \times 3$, $(11)' = 8 \times 4$, $(14)' = 2 \times 1$ and $(\mathrm{H})' = 2 \times 1$ + high background. The encircled figures denote different phases at $T_s \approx 110$ K: (1) = $c(4 \times 2)$, (4) = "$\times 3$ streak", (6) = 4×6, (8) = 2×6, (11) = 8×4, (13) = 4×6, (14) = 2×1, (15) = 2×1 + unidentified extra spots and others (2), (3), (5), (7), (9), (10), (12) denote intermediate phases (from Ref. [44]). (*Reproduced by permission of Elsevier Science Publishers BV)*

when 1/3 ML of Cs is initially deposited on to the substrate at $T_s \approx 110$ K and becomes sharp once T_s is raised to $\approx$ 270 K and lowered back to $\approx$ 110 K. The degree of surface order is improved for most of the low-temperature phases by the mild annealing, typically around RT for half a minute under which the desorption of Cs atoms does not take place, and subsequent cooling to $\approx$ 110 K for few minutes.

For a T_s of $\approx$ 110 K, there are intermediate phases between the ordered commensurate phases (2), (3), (5), (7), (9), (10), (12), (15) (see Fig.5(b)). LEED patterns of these intermediate phases could not be attributed to a sum of domains of the neighboring commensurate phases but were explained as a continuous change in its profile with increase in coverage. The detailed description of these intermediate phases one can find in the original work of Abukawa *et al.* [44].

For T_s of $\approx$ 110 K, the uptake of Cs is found to take place more than 1 ML and the second layer of a layer-by-layer growth of Cs starts exactly at 1 ML as judged from a plot of XPS intensity versus deposition time [44]. This is qualitatively consistent with the results of Ortega *et al.* [40] which were obtained at 200 K.

2.2. STRUCTURE

The atomic structure of Si(100)2×1–Cs has been widely investigated both experimentally and theoretically, the structural models for "$\times 3$ streak", 2×3 and 2×6 have been proposed by Abukawa *et al.* [44] while the structure of the 4×6, 8×4, and $c(4 \times 2)$ phases has not been investigated.

2.2.1. Si(100)"×3 Streak"–Cs

The atomic geometry of the "$\times 3$ streak" structure at 1/6 ML has been proposed by Abukawa *et al.* [44]. A schematic illustration of a quadrant of the LEED pattern is shown in Fig. 6 (the solid symbols are not found in the actual LEED pattern and are introduced to explain the structural model of this surface in Fig.7(a)) where sharp spots corresponding to 1×1 and 2×1 periodicities are observed and 1/3 order streak lines run parallel to the connecting line between the (00) and (10) spots. From the characteristics of the "$\times 3$ streak" pattern

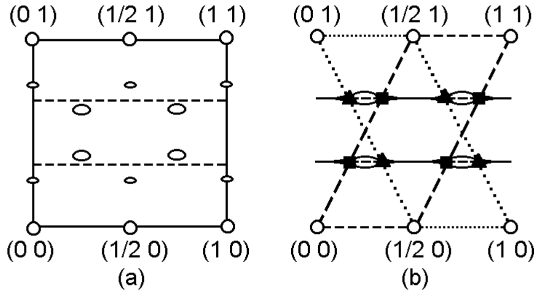

Fig 6. Schematic illustration of LEED pattern observed for a T_s of ≈110 K at 0.1 ML (a) and at 1/6 ML ("×3 streak") (b). (a) and (b) correspond to the initial structure and the final structure of the intermediate phase (3), respectively. The dashed lines in (a) represent the position where a streak appears at 1/6 ML. The spots of (a) near the dashed lines moved and changed its shape and eventually transformed to the "×3 streak" lines with an increase in θ. The solid symbols in (b) are not found in actual LEED patterns but are introduced to explain the structural model in Fig. 7 (from Ref. [44]). (*Reproduced by permission of Elsevier Science Publishers BV)*

the authors [44] deduced the surface structure with $\theta = 1/6$ ML as in Fig. 7(a), in which one-dimensional ×3 Cs arrays are made by placing a Cs atom on every $3a_0$ ($a_0 = 3.84$ Å) site along the substrate ×1 direction (i.e. parallel to the raw Si dimer) and ×3 arrays are located at the interval of $2a_0$, whereas no correlation is held among the ×3 Cs arrays. The 1/3-order streak lines can be explained from this arrangement of Cs atoms as explained later. In addition to this, the sharp 2×1 spots result from the condition that all Cs atoms lie on the 2×1 lattice which is also illustrated in Fig. 7(a). There are three kinds of possible relation between the neighboring ×3 Cs arrays which are represented as A, B, and C in Figs 7(a) and 7(b). Cs atoms in neighboring arrays are arranged parallel to the $2a_0$ unit vector for the type C but are off by a_0 upward or downward in the other two types. The distance between the nearest neighbor Cs atoms is $\sqrt{5}a_0$ in the A and B types, but $2a_0$ in the C type. Except for C, the A and B types are consistent with the XPD patterns observed by Abukawa *et al.* [44]. Thus, Cs atoms are arranged in a similar way as shown in Fig. 7(a).

In Fig. 6(b), it is now possible to explain how the "×3 streaks" are interpreted in terms of a random arrangement of the A and B types [44]. Solid rectangular spots correspond to the reciprocal lattice points of a complete order of A and solid triangular spots to the reciprocal lattice points of a complete order of B. If types A and B are mixed randomly, the corresponding reciprocal lattice points are broadened along the substrate 2× direction resulting in streaky spots similar to those experimentally observed. Therefore, the LEED pattern is qualitatively explained.

2.2.2. Si(100)2 × 6–Cs and Si(100)2 × 3–Cs

The Si(100)2×6–Cs structure forming at $T_s \approx 110$ K reversibly transforms to the Si(100)2×3–Cs one at $T_s \approx 320$ K for 1/3 ML [44]. Based on the comparison of XPD patterns for the two surfaces under the restriction of $\theta = 1/3$ ML and under the assumption that the surface is composed of an overlayer of Cs atom, the structural models for the 2×6 and 2×3 surfaces were proposed by Abukawa *et al.* [44]. The model is shown in Fig.8. In this model, a dimer of Cs atoms is formed on each 2×3 site. From the XPD patterns calculation, the distance between the two Cs atoms of a dimer is found to be 4.5 ± 0.2 Å and the direction of the axis of the Cs dimer is parallel to the ×3 direction.

Two types of structural modulation, which are illustrated in the 2×6 rectangles of Fig. 8, allowed the transition from the 2×3 dimer structure to a 2×6 periodicity. One is a twist modulation, in which the Cs dimers are twisted about its center alternately in the surface

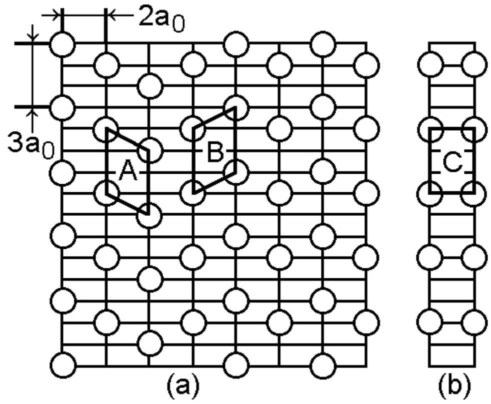

Fig 7. (a) Real-space model for the "×3 streak" surface. Two kinds of arrangement of Cs arrays, A and B, are illustrated to explain the "×3 streak" LEED pattern. (b) Another possible arrangement of Cs arrays, C, for the "×3 streak" surface, which is expected not to be present (see text). Rectangles represent unit cells of the 2 × 1 substrate although actual location of the Cs arrays cannot be specified (from Ref. [44]). (*Reproduced by permission of Elsevier Science Publishers BV)*

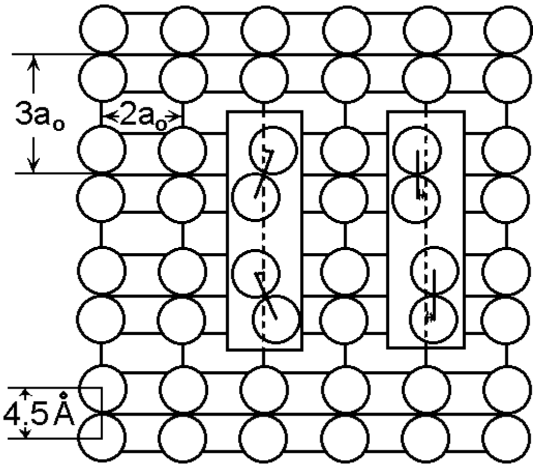

Fig 8. Structural model for the 2 × 3 and 2 × 6 surfaces in which Cs atoms (open circles) are present as dimers on each 2 × 3 site. The substrate 2 × 1 lattice is also illustrated. The two types of 2 × 6 model are drawn in 2 × 6 rectangles: the left one is with twisted modulation of dimers and the right one is with shifted modulation of dimers (see text). One of the modulations is expected to be present randomly for the 2 × 3 surface (from Ref. [44]). (*Reproduced by permission of Elsevier Science Publishers BV)*

plane. The other is a shift modulation, in which the Cs dimers are shifted along the direction perpendicular to their axes alternately in the plane. According to the XPD calculations, the modulation is very little. The twisted angle should be less than ~ 5° in the twist model and the amount of shift should be less than ~ 0.4 Å in the shift model and it is impossible to specify the type of modulation.

2.2.3. Si(100)2 × 3–Cs

The Si(100)2 × 3-Cs structure may now only be qualitatively discussed [59]. Holtom and Gundry [33] observed the 2 × 3 structure for Cs and suggested that at $\theta = 1/3$ ML the 2 × 3 structure is due to Cs atoms at every fourth hollow site. At $\theta = 2/3$ ML, they placed additional atoms at an adjacent site D (see Fig. 3 in Chapter K) next to an hollow site. Batra [65] presented a variation of this model by noting that H and B sites have nearly identical adsorption energy. Hence, he suggested that the site D, invoked by Holtom and

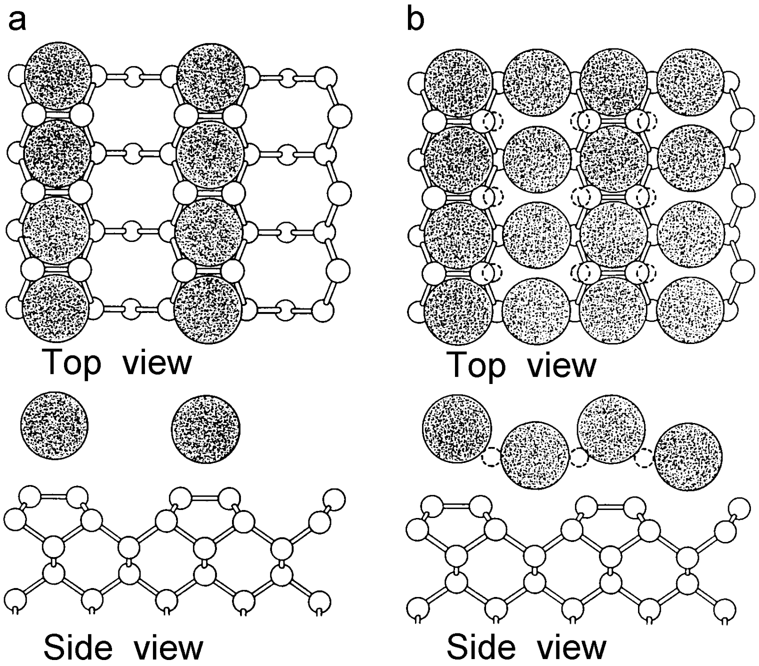

Fig 9. Schematic illustration of models for the Si(100)2×1–Cs. (a) Generally assumed one-dimensional alkali chain model. (b) Alkali double-layer model except that the relationship to the substrate is an assumption. Cs atoms are represented by large shaded circles. The assumed dimerized Si substrate is drawn as a ball-and-stick structure. For the NEA O/Cs/Si(100)2 × 1 surface, the location of oxygen with respect to the Cs-double layer as proposed from the XPD analysis is marked with dashed circles (from Ref. [49]). (*Reproduced by permission of Elsevier Science Publishers BV)*

Gundry [33], should be replaced by the B site. Glander and Webb [66] proposed the removing of every third surface Si atoms and allowing the second-layer atoms beneath them to dimerize. This reconstruction model was considered for the Si(100)2 × 3–Na structure (see also Chapter Na, section* 2.2). Obviously, some further work is required to establish it firmly.

2.2.4. Si(100)2 × 1–Cs

The first structural model of the alkali-saturated surface was proposed by Levine in 1973 [36]. In this model, the alkali atoms occupy the so-called pedestal site between two surface dimers and form one-dimensional alkali chain (Fig.9(a)). The saturation coverage for this model is 0.5 ML. For this structure, calculations of the surface electronic structure predict a one-dimensional conductor behavior. Since then, a one-dimensional alkali chain model and this adsorption site have also been widely used in qualitative discussions for other adsorbates.

In 1987, Enta *et al.* [67] concluded from ARUPS data that the Si(100)2 × 1–K surface is non-metallic. To obtain consistency with the observed semiconducting behavior, a structure with coverage of 1.0 ML was proposed. A subsequent XPD study, performed by Abukawa and Kono [68] showed an enhancement of the photoelectron signal at low exit angles. This was interpreted as forward scattering by K atoms residing above the K emitter atoms. In the double layer model which they subsequently proposed, the coverage is 1.0 ML with 0.5 ML in rows located on the pedestal sites as in the Levine model, and an additional 0.5 ML located in rows in cave sites as shown in Fig. 9(b). The photoelectron diffraction study gave a best-fit corrugation of 1.2 ± 0.1 Å [32] between the lower (cave) and upper (pedestal) Cs rows, with registry to the Si surface assumed. Recently, the absolute saturation coverage of Cs at RT has been measured by using MEIS by Smith *et al.* [45]. The overlayer coverage in this system is 0.97 ± 0.05 ML. This result clearly discriminates between models containing 0.5 and 1.0 ML alkali coverage for the saturated surface. In accordance with the EXAFS investigation of Cs covered Si surface by Kim *et al.* [54], Cs does not significantly modify the structure of the Si(100)2×1 surface. Considering that the K/Si and the Na/Si bond length values reproduce fairly accurately the sum of covalent radii [53, 69] one can assume a Cs–Si bond length of 3.52 ± 0.1 Å.

Possible adsorption sites on the Si(100)2×1 dimerization surface have been discussed in detail both experimentally and theoretically. There have been four high-symmetry adsorption sites suggested: pedestal site, cave site, bridge site and valley-bridge site [36]. Hashizume *et al.* [28] have reported that Cs atoms occupy a site different from those four possible high symmetry sites based on STM investigations in the *low coverage* regime (0.02 ML). They concluded that Cs atoms occupy the off-centered valley bridge site at the initial coverage.

A surface-structural change has been clearly found upon cooling RT Si(100)2×1–Cs to a low temperature (23 K) by Murata *et al.* [70] by using LEED. The authors could not decide what kind of structural change takes place: whether or not it is the Peierls transition expected in the one-dimensional metal system.

In accordance with the TDS results of Kennou *et al.* [34], there are two main binding states of Cs on the Si(100) surface.

2.3. PROPERTIES

2.3.1. Electronic Properties

The electronic properties of Cs on Si(100)2×1 is somewhat diverse. The presence of overlayer plasmon in EELS spectra of Si(100)2×1–Cs seems to support the formation of a metallic monolayer on Si(100) [55]. On the other hand, ARUPS experiments of Kono *et al.* [46, 48] for the Cs overlayer showed that the Si(100)2×1–Cs surfaces are not metallic but they are rather semiconducting. They noted that the bonding between the alkali-metal adatoms and the Si dimers may not be a charge-transfer type but a covalent type. Theoretical calculations of Kato *et al.* [61] showed that the bonding is almost ionic at low coverage, while the covalent character increases with coverage. The data of Ortega *et al.* [40] also indicate that the charge transfer from Cs to Si at completion of the Cs adlayer is not complete. From the core-level and valence-band photoemission spectroscopy data, Soukiassian *et al.* [51] provided evidence that the Cs/Si bonding is covalent. This covalent bond is weak and polarized while plasmon at the alkali metal core level indicates adsorbate rather than substrate metallization.

Variation of the WF observed during Cs deposition on Si(100)2×1 at RT is shown in Fig. 10. The WF decreases, goes through a minimum and then levels-off to a saturation value at the maximum Cs coverage. The values of the WF at minimum and saturation obtained in various works are in satisfactory agreement with each other (Table 2). Theoretical calculations of WF changes during Cs adsorption [60, 61] are in fairly good agreement with experimental results.

2.3.2. Oxidation

Experimental results of various authors [39, 40, 43, 47, 52] indicate that multilayers of Cs deposited on Si(100)2×1 promote the oxidation of Si under subsequent exposure to O_2. The oxygen uptake is enhanced by four orders of magnitude. The cesium can be completely desorbed from the surface at 900 K leaving behind a layer of SiO_2, whose thickness is proportional to the amount of Cs deposited. For a saturation Cs coverage and the same O_2 exposure, the growth of oxides is more pronounced on a stepped than on a non-stepped Si(100)2×1 surface [42]. This is due to the higher coverage of Cs on the stepped surface.

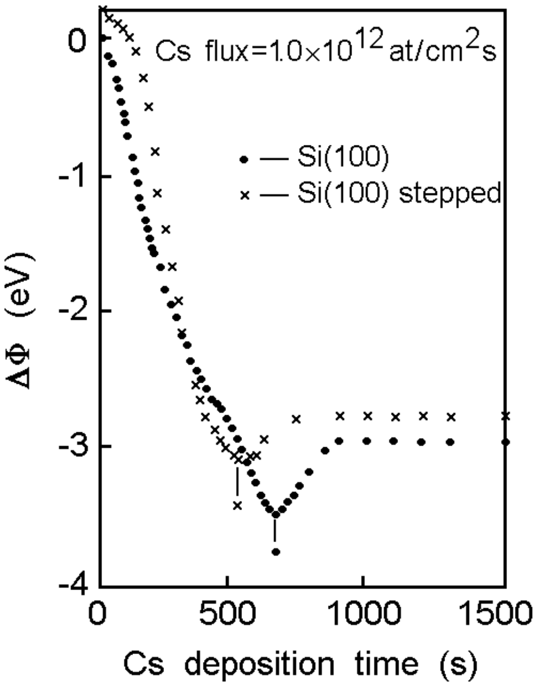

Fig 10. The change of work function versus Cs deposition time at 300 K on the Si(100) (from Ref. [34]). (*Reproduced by permission of Elsevier Science Publishers BV*)

Table 2. The minimum and saturation values of work function for the Cs/Si(100) system (from Ref. [46])

$\Delta\Phi_{\mathrm{min}}$	$\Delta\Phi_{\mathrm{sat}}$	Ref.
−3. 5 eV	−2. 9 eV	[34]
−3. 3 eV	−2. 9 eV	[42]
−3. 6 eV	−2. 1 eV	[41]
−3. 3 eV	−2. 8 eV	[40]
−3. 5 eV	−3. 3 eV	[37]
−3. 57 eV	−3. 11 eV	[46]
−3. 5 eV	−3. 0 eV	[13]
−3. 8 eV	−3. 6 eV	[33]
−3. 7 eV	−3. 2 eV	[72]

The simultaneous coadsorption of Cs and O_2 on the Si(100)2 × 1 surface at RT is very effective on the deposited amount of Cs and O_2 [41]. This effect is faster when the Si substrate is first covered with 1 ML of Cs. Heating at ∼ 800 °C, after coadsorption, removes the Cs completely from the surface, while the oxygen forms SiO_2 with a thickness greater than 35 Å. The possible mechanism of cesium-induced promotion of oxidation of Si(100)2 × 1 is discussed in Refs [40, 43, 47].

2.3.3. Negative Electron Affinity Surface of O/Cs/Si(100)2 × 1

Through the addition of monolayer quantities of Cs and O to an atomically clean Si(100)2 × 1 surface of a p-type single crystal, the negative electron affinity (NEA) surface is achieved [35, 36, 38, 40, 49, 50, 56–58]. In practice, NEA is easiest to achieve with a degenerate p-type semiconductor; then the criteria for NEA is simply that the WF be less than the bandgap.

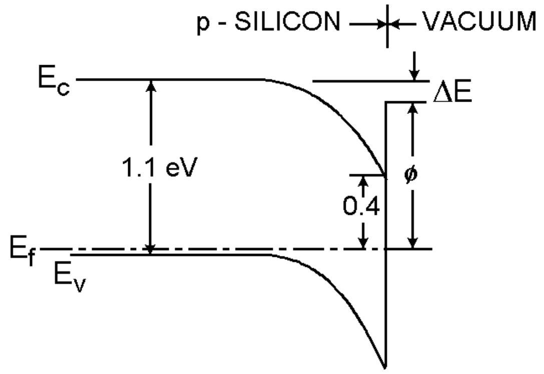

Fig 11. Energy band diagram of the NEA Si(100) surface. ΔE is about 0. 1 eV (from Ref. [58]). (*Reproduced by permission of American Institute of Physics)*

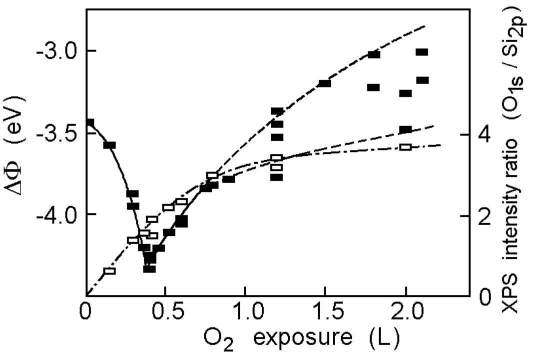

Fig 12. Changes in work function Φ as a function of O_2 exposure (in Langmuir) to a Cs-saturated Si(100)2 × 1 surface. $\Delta\Phi$ in respect to $\Phi = 4.8$ eV of a clean single-domain Si(100) 2 × 1 surface. The scatter in Φ above the O_2 exposure of 1 L means that $\Delta\Phi$ depends on the time duration after the exposure: thus the surface becomes unstable although the oxygen content appears stable (from Ref. [50]). (*Reproduced by permission of the publishers of Japanese Journal of Applied Physics)*

The energy band diagrams of the NEA Si(100) surface is shown in Fig.11. Martinelly [57, 58] found that Si(111), Si(110), and Si(211) samples do not yield NEA.

When a Cs saturated Si(100)2 × 1 surface is exposed to oxygen gas of 1.5×10^{-8} Torr work function Φ decreases sharply to a minimum value of $\Phi \approx 0.5$ eV at 0.4 L although the LEED pattern remains 2 × 1 [50] (Fig. 12). Upon further O_2 exposure, Φ increases and the change in Φ becomes $-3.0 \div -3.5$ eV for O_2 exposure of ≈ 2 L.

The structure of the surface exhibiting the NEA (NEA surface, for brevity) was studied by Levine [36] based on the one-dimensional chains on the ridge of a dimerized-Si(100)2 × 1 surface. It is believed that oxygen atoms exist at the bottom of the grooves of the substrate in between the alkali chains. The structure of the NEA surface of O/Cs/Si(100)2 × 1 was reinvestigated by Abukawa *et al.* [38, 50] on the basis of the double-layer array of alkali atoms. Analysis of XPD patterns for the NEA surface revealed the location of oxygen atoms with respect to the Cs double layer (Fig. 9(b)). It is also inferred that an oxygen atom occupies each of the Si–dimer dangling bonds at the stage of a minimum work function.

3. (110) ORIENTATION

Cs is known to induce three reconstructions on the Si(110) surface. These are 5 × 4, 2 × 2, and 1 × 1 structures.

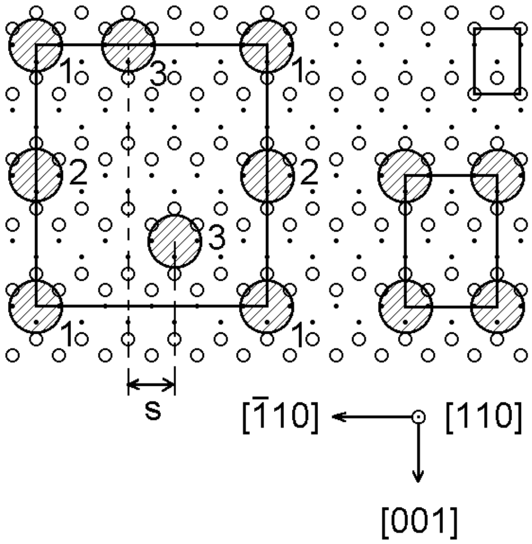

Fig 13. Proposed atomic structure for the Cs adsorption on Si(110). White circles, last-layer silicon atoms; black dots, second-layer silicon atoms; dashed circles, cesium atoms. The 5 × 4, 2 × 2, and 1 × 1 unit cells are displayed (from Ref. [71]). (*Reproduced by permission of Elsevier Science Publishers BV)*

3.1. PHASE DIAGRAM

Initial stages of Cs adlayer formation on the Si(110)"2 × 16" surface were investigated using LEED, AES and XSW only in one work [71]. After RT saturation Cs deposition ($\theta_{\mathrm{Cs}} \simeq$ 0.5 ML), only a 1 × 1 pattern is observed, probably indicating a poor ordering of the adsorbate [71]. After annealing the surface for 40 s at 480 °C (and reducing the coverage to 0.2 ML), a 2 × 2 pattern is observed. The 2 × 2 spots are sharper at 0.15 ML. At a coverage of 0.1 ML, a 5 × 4 pattern appears. After further coverage reduction, the LEED pattern weakens and streaks evolve along the [001] direction ($\theta_{\mathrm{Cs}} \simeq 0.05$ ML), keeping a fivefold periodicity along the [$\bar{1}$10] direction. For coverages between 0.2 and 0.1 ML, and depending on the experimental conditions, the coexistence of 2 × 2 and 5 × 4 spots is observed.

3.2. STRUCTURE

The adsorption site of Cs on Si(110)"2 × 16" has been investigated by Michel *et al.* using XSW [71]. For different Cs coverages and annealing conditions, the experimental results favor the hollow adsorption site where the Cs atom is half-way between the Si atoms nearest the top along the [001] direction. Accepting the adsorption site determined by XSW, the structural models for two observed structures, 2 × 2 and 5 × 4, were proposed by Michel *et al.* [71].

3.2.1. Si(110)2 × 2–Cs

The proposed atomic structure of the 2 × 2 reconstruction is shown in Fig. 13. It corresponds to the Cs coverage of 0.25 ML.

3.2.2. Si(110)5 × 4–Cs

The proposed atomic structure of the 5 × 4 reconstruction is shown in Fig. 13. Considering the coverage at which the 5 × 4 pattern is observed, the authors expect about 4 atoms per unit cell. This structure gives rise to atomic chains along [$\bar{1}$10], formed by a basic unit of two Cs atoms separated by a distance of $2a$ along [$\bar{1}$10]. Its similarity with the 2 × 2 structure would easily explain the appearance of the latter at higher coverages. At lower coverages, streaks are observed along the [001] direction, which would be easily explained by the existence of atomic chains along [$\bar{1}$10].

REFERENCES

[1] G. W. Gobeli, J. J. Lander and J. Morrison, *J. Appl. Phys.* **37** (1966) 203.
[2] K. O. Magnusson and B. Reihl, *Phys. Rev. B* **39** (1989) 10456.
[3] M. Domke, T. Mandel, C. Laubschat and M. Prietsch, *Surf. Sci.* **189–190** (1987) 268.
[4] B. Reihl, K. O. Magnusson, J. M. Nicholls, P. Perfetti and F. Salvan, in *Metallization and Metal-semiconductor Interfaces*, Ed. by Batra I. P. , Plenum (1989) 397.
[5] H. Tochihara, M. Kubota, T. Aruga, M. Miyao and Y. Murata, *Japan J. Appl. Phys.* **23** (1984) L271.
[6] H. Tochihara, M. Kubota and Y. Murata, *Solid State Commun.* **57** (1986) 437.
[7] H. Tochihara, M. Kubota, M. Miyao and Y. Murata, *Surf. Sci.* **158** (1985) 497.
[8] P. Soukiassian, *Surf. Sci.* **172** (1986) L507.
[9] H. Tochihara and Y. Murata, *Surf. Sci.* **172** (1986) L509.
[10] H. Tochihara, M. Kubota, M. Miyao and Y. Murata, *Proc. 17th Int. Conf. Phys. Semic.* (1985) 113.
[11] H. Ishida, K. Terakura and M. Tsukada, *Solid State Commun.* **59** (1986) 365.
[12] H. Daimon and S. Ino, *Surf. Sci.* **164** (1985) 320.
[13] R. E. Weber and W. T. Peria, *Surf. Sci.* **14** (1969) 13.
[14] K. O. Magnusson and B. Reihl, *Phys. Rev. B* **41** (1990) 12071.
[15] U. A. Ditzinger, Ch. Lunau, B. Schieweck, St. Tosch, H. Neddermeyer and M. Hanbucken, *Surf. Sci.* **211–212** (1989) 707.
[16] R. Avci, *J. Vac. Sci. Technol. A* **4** (1986) 1400.
[17] L. Fotiadis and R. Kaplan, *Thin Solid Films* **184** (1990) 415.
[18] P. Wagner, K. Muller and K. Heinz, *Surf. Sci.* **68** (1977) 189.
[19] S. Lagomarsino, F. Scarinci, P. Castrucci, C. Giannini, E. F. Fontes and J. R. Patel, Appl. *Surf. Sci.* **56–58** (1992) 402.
[20] K. Oura, M. Naitoh, F. Shoji, J. Yamane, K. Umezawa and T. Hanawa, *Nucl. Instrum. Meth. Phys. Res. B* **45** (1990) 199.
[21] S. Nishigaki, N. Oishi, S. Matsuda, N. Kawanishi and T. Sasaki, *Phys. Rev. B* **39** (1989) 8048.
[22] K. O. Magnusson, S. Wiklund, R. Dudde and B. Reihl, *Phys. Rev. B* **44** (1991) 5657.
[23] D. -S. Lin, T. Miller and T. -C. Chiang, *Phys. Rev. B* **44** (1991) 10719.
[24] R. E. Weber and W. T. Peria, *J. Appl. Phys.* **38** (1967) 4355.
[25] V. Etelaniemi, E. G. Michel and G. Materlik, *Phys. Rev. B* **44** (1991) 4036.
[26] S. Lagomarsino, F. Scarinci, P. Castrucci and C. Giannini, *Phys. Rev. B* **46** (1992) 13631.
[27] T. Hashizume, K. Motai, Y. Hasegawa, I. Sumita, H. Tanaka, S. Amano, S. Hyodo and T. Sakurai, *J. Vac. Sci. Technol. B* **9** (1991) 745.
[28] T. Hashizume, Y. Hasegawa, I. Sumita and T. Sakurai, *Surf. Sci.* **246** (1991) 189.
[29] H. I. Starnberg, P. Soukiassian, M. H. Bakshi and Z. Hurych, *Phys. Rev. B* **37** (1988) 1315.
[30] H. I. Starnberg, M. H. Bakshi and P. Soukiassian, *J. Vac. Sci. Technol. A* **6** (1988) 1567.
[31] A. Franciosi, P. Soukiassian, P. Philip, S. Chang, A. Wall, A. Raisanen and N. Troullier, *Phys. Rev. B* **35** (1987) 910.
[32] T. Abukawa and S. Kono, *Surf. Sci.* **214** (1989) 141.
[33] R. Holtom and P. M. Gundry, *Surf. Sci.* **63** (1977) 263.
[34] S. Kennou, M. Kamaratos, S. Ladas and C. A. Papageorgopoulos, *Surf. Sci.* **216** (1989) 462.
[35] P. M. Gundry, R. Holtom and V. Leveret, *Surf. Sci.* **43** (1974) 647.
[36] J. D. Levine, *Surf. Sci.* **34** (1973) 90.

[37] M. Kamaratos, S. Kennou and C. A. Papageorgopoulos, *Surf. Sci.* **227** (1990) 43.

[38] T. Abukawa, Y. Enta, T. Kashiwakura, S. Suzuki and S. Kono, *J. Vac. Sci. Technol. A* **8** (1990) 3205.

[39] C. A. Papageorgopoulos and M. Kamaratos, *Surf. Sci.* **221** (1989) 263.

[40] J. E. Ortega, E. M. Oellig, J. Ferron and R. Miranda, *Phys. Rev. B* **36** (1987) 6213.

[41] M. Kamaratos and C. A. Papageorgopoulos, *Surf. Sci.* **219** (1989) 317.

[42] M. Kamaratos, S. Kennou, S. Ladas and C. A. Papageorgopoulos, *J. Phys. :Cond. Matt.* **1** (1989) 6071.

[43] J. A. Schaefer, F. Lodders, Th. Allinger, S. Nannarone, J. Anderson and G. J. Lapeyre, *Surf. Sci.* **211-212** (1989) 1075.

[44] T. Abukawa, T. Okane and S. Kono, *Surf. Sci.* **256** (1991) 370.

[45] A. J. Smith, W. R. Graham and E. W. Plummer, *Surf. Sci.* **243** (1991) L37

[46] Y. Enta, T. Kinoshita, S. Suzuki and S. Kono, *Phys. Rev. B* **39** (1989) 1125

[47] P. Soukiassian, H. I. Starnberg and T. Kendelewicz, Appl. *Surf. Sci.* **41–42** (1989) 395.

[48] S. Kono, *Arabian J. Sci. Eng.* **15** (1990) 293.

[49] S. Kono, Y. Enta, T. Abukawa and T. Kinoshita, Appl. *Surf. Sci.* **41–42** (1989) 75.

[50] T. Abukawa, S. Kono and T. Sakamoto, *Japan J. Appl. Phys.* **28** (1989) L303.

[51] P. Soukiassian, M. H. Bakshi, Z. Hurych and T. M. Gentle, *Surf. Sci.* **221** (1989) L759.

[52] P. Soukissian, M. H. Bakshi, Z. Hurych and T. M. Gentle, *Phys. Rev. B* **35** (1987) 4176.

[53] P. Soukiassian, S. T. Kim, Z. Hurych and J. A. Kubby, *Appl. Surf. Sci.* **56–58** (1992) 394.

[54] S. T. Kim, S. Kapoor and Z. Hurych, *Phys. Rev. B* **44** (1991) 5622.

[55] H. Tochihara and Y. Murata, *Surf. Sci.* **215** (1989) L323.

[56] J. R. Howorth, R. Holtom, A. L. Harmer and E. W. Trawny, *Appl. Phys. Lett.* **21** (1972) 316.

[57] R. U. Martinelli, *Appl. Phys. Lett.* **16** (1970) 261.

[58] R. U. Martinelly, *J. Appl. Phys.* **44** (1973) 2566.

[59] I. P. Batra, *J. Vac. Sci. Technol. A* **8** (1990) 3425.

[60] T. Kato, K. Ohtomi and M. Nakayama, *Surf. Sci.* **158** (1985) 505.

[61] T. Kato, K. Ohtomi and M. Nakayama, *Surf. Sci.* **209** (1989) 131.

[62] H. Ishida, N. Shima and M. Tsukada, *Surf. Sci.* **158** (1985) 438.

[63] H. Ishida, *Phys. Rev. B* **38** (1988) 8006.

[64] Y. Ling and X. Xide, *Surf. Sci.* **247** (1991) L204.

[65] I. P. Batra, *Phys. Rev. B* **39** (1989) 3919.

[66] G. S. Glander and M. B. Webb, *Surf. Sci.* **222** (1989) 64.

[67] Y. Enta, T. Kinoshita, S. Suzuki and S. Kono, *Phys. Rev. B* **36** (1987) 9801.

[68] T. Abukawa and S. Kono, *Phys. Rev. B* **37** (1988) 9097.

[69] T. Kendelewicz, P. Soukiassian, R. S. List, J. C. Woicik, P. Pianetta, I. Lindau and W. E. Spicer, *Phys. Rev. B* **37** (1988) 7115.

[70] Y. Murata, H. Toshihara and M. Kubota, in *Metallization and Metal-Semiconductor Interfaces*, Plenum Press, New York (1989) 367.

[71] E. G. Michel, V. Etelaniemi and G. Materlik, Appl. *Surf. Sci.* **56–58** (1992) 457.

[72] N. Toshihara and Y. Murata, *J. Phys. Soc. Jap.* **51** (1982) 2920.

(Cu)

COPPER

1. (111) ORIENTATION

Cu is known to induce several reconstructions on the Si(111) surface. These are 4 × 1, 4 × 2, 1 × 1 and "5 × 5" (or quasi−5 × 5) structures.

1.1. PHASE DIAGRAM

1.1.1. RT Deposition on to Cleaved Si(111)2 × 1

The initial stages of Cu growth on the Si(111)2 × 1 surface during RT Cu deposition were monitored by LEED, AES, and PES techniques in Refs [1, 2]. The results obtained suggest that the growth of Cu on a 2×1 reconstructed Si(111) surface occur in two steps: first, growth of a mixed two-dimensional Cu–Si alloy and subsequent epitaxial growth of 3D Cu islands. The sequence of reconstructions detected by LEED during the growth process is presented in Fig. 1(a). LEED observations [1] revealed that, at Cu coverage of about 0.5 ML, the initial 2 × 1 reconstruction converts to 4 × 1 structure. At the LEED pattern from this structure, while the 2 × 1 spots remain quite sharp, the new fractional-order spots appear blurred and elongated along the fractional-order line, i.e. the $[\bar{2}11]$ direction. Beyond ∼ 1 ML, LEED indicates the appearance of 4 × 2 reconstruction. This structure remains observable up to about 5 ML of Cu where the Cu(111)$\sqrt{3} \times \sqrt{3}$—$R30^\circ$ pattern starts to be seen. In turn, the latter pattern converts to an hexagonal pattern corresponding to the unreconstructed Cu(111) plane at Cu coverages beyond ∼ 10 ML. This Cu(111)1 × 1 structure is rotated by 30° compared to the Si(111)1 × 1 structure.

1.1.2. RT Deposition on to Si(111)7 × 7

When Cu is deposited on to the 7 × 7 reconstructed Si(111) surface held at RT, the 7 × 7 reconstruction evolves gradually to a Si(111)1 × 1 LEED pattern with the Cu coverage increasing from 0 to 1 ML (Fig. 1(b)). According to the LEED observations of Refs [3, 4], this 1 × 1 structure disappears progressively and vanishes completely at Cu coverage of 3 ML leaving a uniform background up to 10 ML of Cu. In contrast, Kemmann *et al.* [5] reported that a 1 × 1 structure forming at about 1 ML of Cu remains visible up to a coverage of nearly 10 ML.

The STM studies [6–8] of the Cu growth in submonolayer range revealed that, at very low Cu coverages (about 0.05 ML), Cu atoms adsorb preferentially on the center adatoms of the 7 × 7 DAS structure. These Cu atoms are nuclei of the triangular-shaped two-dimensional islands forming at higher coverages (0.3–0.7 ML). The triangular clusters are formed slightly

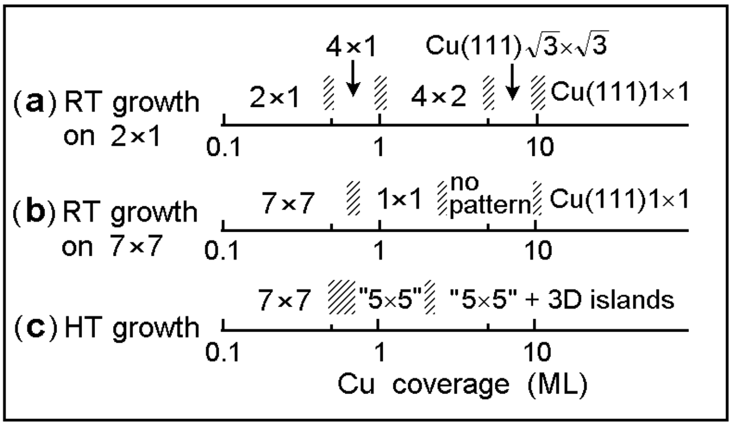

Fig 1. The evolution of the surface reconstruction observed by LEED (a) during RT deposition on to the Si(111)2 × 1 surface (from Ref. [1]); (b) during RT deposition onto Si(111)7 × 7 surface (from Ref. [4]) and (c) during high temperature deposition on to the Si(111)7 × 7 surface (from Ref. [4])

preferentially on the faulted halves of the 7 × 7 unit cells and do not apparently affect the underlying 7 × 7 reconstructed Si(111) substrate.

At coverages beyond 10 ML, a hexagonal LEED pattern is observed rotated by 30° with respect to Si(111)1 × 1. From the size of the unit mesh, Daugy *et al.* [4] concluded that it corresponds either to a (111) face of bulk Cu or to the Si diluted α-phase of Cu–Si alloy which crystallizes in the *fcc* system and has almost the same lattice parameter as pure bulk Cu (3.61 Å). AES observations showed that Cu(111)1 × 1 layer grows beyond 10 ML while the formation of α(Cu–Si) phase with diluted Si at a concentration decreasing from 10% to 0% occurs at Cu coverages of up to 10 ML [4]. The significant intermixing at RT for Cu coverage in excess of around one monolayer (which is necessary for the formation of Cu–Si alloy) was confirmed in Refs [9–11]. ISS results of Yasue *et al.* [12] suggested that the thin Si layer exists on top the film surface up to about 30 ML.

1.1.3. HT Growth

The upper limit for growth of Cu on Si(111) is about 600 °C since above this temperature Cu dissolves into the Si bulk [13] (or possibly evaporates from the surface [14]).

During Cu growth at 300 to 600 °C, the occurrence of a "5 × 5"-like (or the quasi-5 × 5) superstructure was found [4]. For $\theta < 0.8$ ML it coexists with Si(111)7 × 7 and then develops up to $\theta \approx 1.3$ ML. The "5 × 5" surface structure also forms upon annealing of the room temperature Cu deposit at above 300 °C [4, 5, 15, 16]. The sharpest LEED patterns were obtained for an annealing temperature of 600 °C.

At coverages beyond ~ 1.3 ML, the growth of 3D Cu_3Si islands occurs [4, 13–15]. (Fig. 1(c)).

1.2. STRUCTURE

1.2.1. Si(111)1 × 1–Cu

The 1 × 1 reconstruction is formed at room temperature after deposition of about 1 ML of Cu on to the Si(111)7 × 7 surface. It was suggested by Daugy *et al.* [4] that the most probable locations of the adsorbed Cu atoms are the threefold hollow (H_3) sites on the Si(111) surface. This assumption is in agreement with the results of self-consistent total energy calculations of Ref. [17] which reveal that Cu atoms adsorb in H_3 sites with equilibrium heights of 0.74 Å above the plane of the surface Si atoms.

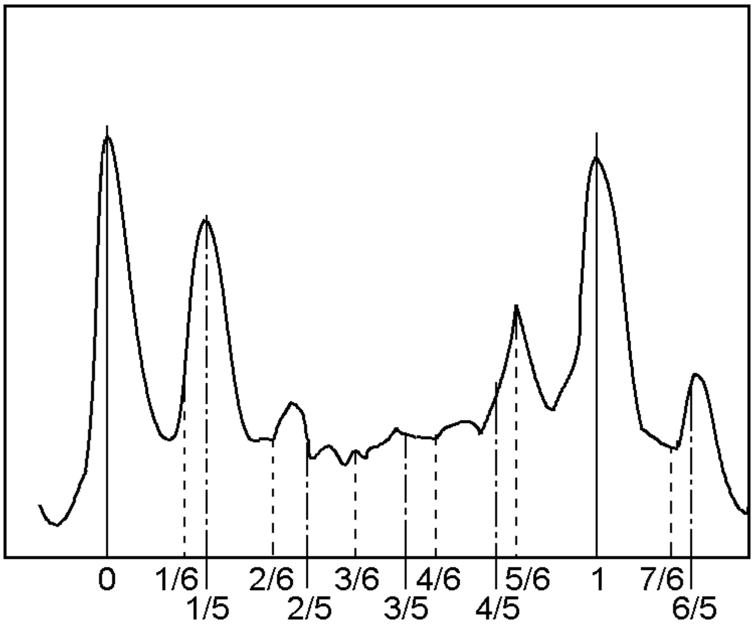

Fig 2. Densitometry scanning of the "5 × 5" LEED pattern. Note that the peaks correspond neither to a 5 × 5 nor to a 6 × 6 pattern (from Ref. [4]). (*Reproduced by permission of Elsevier Science Publishers BV)*

1.2.2. Si(111)"5 × 5"–Cu

It was determined that during high-temperature growth of about 1 ML of Cu on Si(111) a two-dimensional phase is developed which gives rise to a distinct LEED pattern. In the first publications [18, 19], it was ascribed to a 5 × 5 reconstruction. However, later more careful LEED investigations [4, 5] showed that the observed structure is incommensurate. This reconstruction fits neither with a 5 × 5 nor with a 6 × 6 one, as can be seen in Fig. 2 showing the densitometry scanning of the "5 × 5" LEED pattern.

The "5 × 5" structure has been studied by several surface sensitive techniques, LEED [5], UHV reflection electron microscopy [20, 21], diffraction of He atoms [22, 23], STM [7, 24–26], Auger-electron diffraction [27], ARUPS [28, 29], and XSW [30].

Kemmann *et al.* [5] assumed that the "5 × 5" LEED pattern is generated by refraction on the original Si lattice and a second structure on top of the surface due to a two-dimensional Cu–Si phase with a ratio of the reciprocal lattice vectors of 0.816±0.003 (see Fig. 3). However, this assumption was ruled out in the helium diffraction study by Doak and Nguyen [22], where the presence of the periodicity of reconstruction 5.55± 0.05 larger than that of a Si(111)1 × 1 structure was revealed. Since helium atoms do not penetrate into the surface, it is impossible to "mix" diffraction peaks from the outermost layer with those from deeper layers as it can take place with LEED [22]. Thus, the incommensurate "5 × 5" periodicity is a feature of the overlayer only.

REM study [20, 21] showed that development of the "5 × 5" structure proceeds by the growth of islands in the manner which is illustrated schematically in Fig. 4. The islands with "5 × 5" structure were found to nucleate at bilayer steps and grow at the same level on both lower and upper terraces. This growth mode indicates that the islands are not pure Cu islands atop a Si substrate, but rather a mixed Cu–Si layer is formed. The island formation process was shown to involve transport of Si from the upper to the lower terraces [21]. The estimation shows that the mixed layer contains 1.33 ± 0.1 ML of Si and the Cu:Si stoichiometry of the "5 × 5" layer is 1 : 1.2 ± 0.2 [29].

Chambliss and Rhodin [28,29] suggested that the dominant 1×1 regions of the "5×5" layer

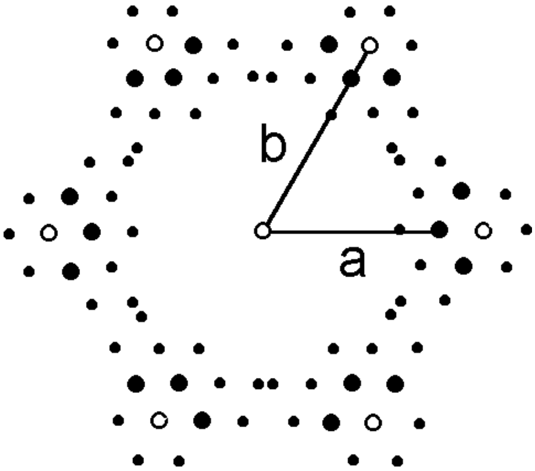

Fig 3. Schematic representation of the "5×5" LEED pattern. The open circles correspond to the first-order Si(111) beams. The size of the circles approximately indicates their intensities (from Ref. [5]). (*Reproduced by permission of Elsevier Science Publishers BV)*

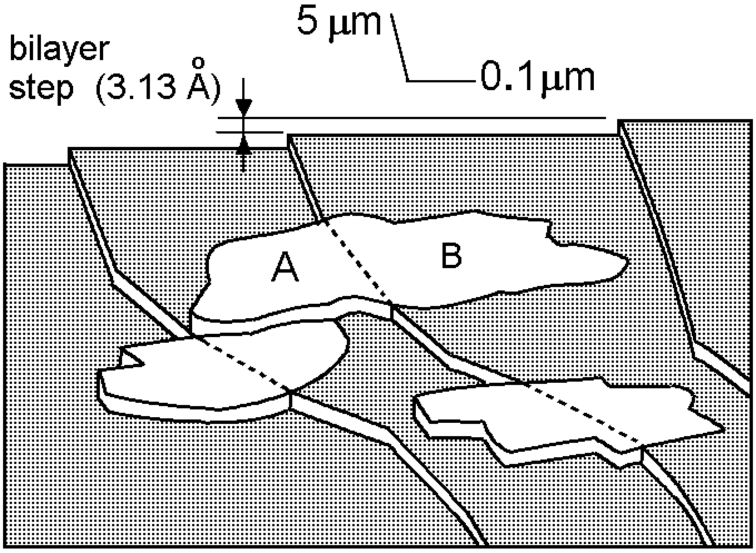

Fig 4. Schematic illustration of the island structure of the partial "5×5" surface as revealed by reflection electron microscopy (Ref. [21]). Light patches are reacted Cu–Si islands, which grow in both directions from bilayer steps, at approximately the height of upper terraces. Fractions of island area above lower terrace (A) and at upper terrace (B) were measured to infer Cu–Si layer composition (from Ref. [29]). (*Reproduced by permission of the publishers of Journal of Physical Review B)*

are composed of a CuSi substitutional structure above a complete Si double layer (Fig. 5(a)). This suggestion is based on the stoichiometry consideration and the comparison of the ARUPS data with band structure calculations. It was found in Ref. [29] that substitutional Cu atom is situated at 3.13 Å above the center of the underlying Si double layer. This position is relaxed inward somewhat from the position of the missing Si in an ideal bilayer, where a strictly substitutional Cu atom would reside [29].

The alternative model of the Cu–Si mixed-layer structure was proposed by Chambers *et al.* [27]. It was suggested that this layer has a $CuSi_2$ interstitial-like structure (as shown in Fig. 5(b)) with Cu atoms residing 0.1 Å below the outer plane of Si atoms. The latter model is in agreement with the Auger-electron diffraction data [27] but does not produce a good agreement with the ARUPS data [29]. The common feature of both models is that the Cu–Si phase forms a nearly planar overlayer.

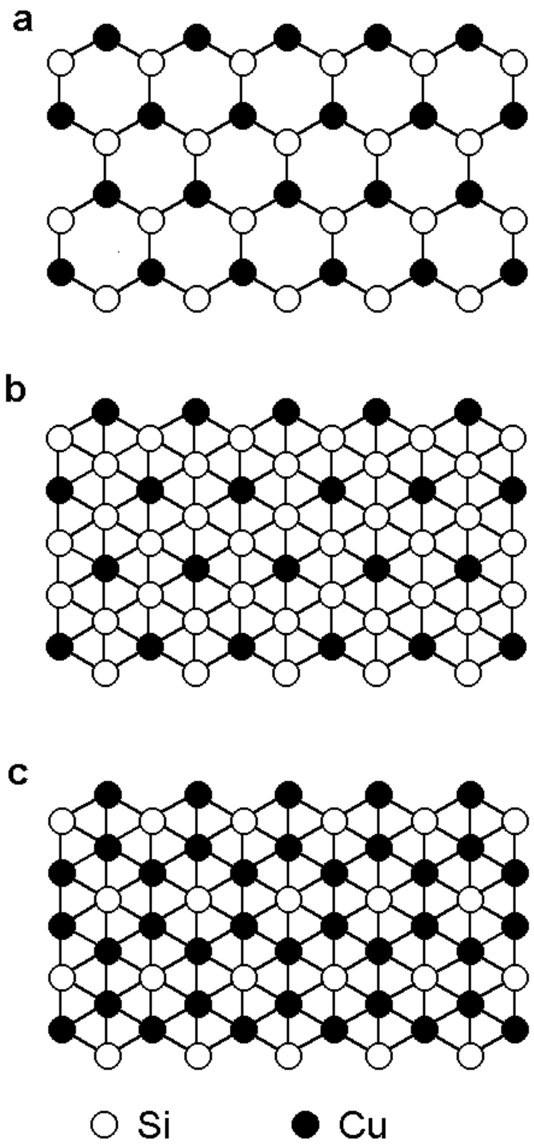

Fig 5. Likely planar models for the "5 × 5" structure: (a) CuSi substitutional structure, (b) $CuSi_2$ interstitial-like structure, and (c) Cu_2Si structure with Cu atoms occupying both interstitial (H_3) and substitutional sites of the upper half of the Si(111) double layer (from Refs [29] and [30]). (*Reproduced by permission of the publishers of Journal of Physical Review B)*

Another model of the Cu–Si layer structure was derived by Zegenhagen *et al.* [30] from XSW data. The overlayer was suggested to consist of an almost planar, close-packed, hexagonal layer as in the previous model but with basically Cu_2Si stoichiometry. The structure is formed by Cu residing in H_3 sites and substituting for Si in the upper half of the Si(111) double layer as shown in Fig. 5(c). It was concluded that the strong compressive strain in the mismatched Cu–Si overlayer leads to an hexagonal network of incommensurations or stacking faults giving rise to the 5.55 × 5.55 domain structure. Complete tiling of the surface was shown to require different types of domains with interior incommensurate lattices rotated by about 3° to achieve the registry at the domain boundaries [30].

STM observations of the "5 × 5" structure have been performed by several groups [7, 24–26]. The results obtained in these investigations can be summarized as follows: the STM image of the "5 × 5" structure consists largely of the hexagonal arrays of spots apparently commensurate with the Si(111) lattice. These arrays are believed to correspond to a Cu–

silicide layer which is coincident with the substrate and likely under severe stress due to the incorporation of Cu into the Si(111) lattice. These regions are broken up by a quasiperiodic array of features with a spacing that varies between five and seven lattice units. These features are craters analogous to the corner holes of the Si(111)7 × 7 which contribute to reduce strain energy. In contrast to the Si(111)7 × 7, the Si(111)"5 × 5"–Cu surface, however, does not contain dimer and adatom configurations as well as stacking fault regions.

1.3. PROPERTIES

1.3.1. Chemical Properties

The Cu layer was found to change significantly the chemical properties of the Si(111) surface and the effect of Cu to be strongly dependent on the structure of the Cu layer.

The RT deposited Cu layer in thickness varying from the fraction of monolayer to several dozens nm was found to enhance the oxidation of the Si(111) surface [31–35]. An enhanced oxidation was elucidated as a catalytic process since no Cu-O bonding was detected [32,33]. In Ref. [17], the catalytic activity of Cu in the synthesis of dimethyldichlorsilane from elemental silicon and methylchloride is reported:

$$\mathrm{Si} + 2\mathrm{CH_3Cl} \xrightarrow{\mathrm{Cu}} (\mathrm{CH_3})_2\mathrm{SiCl_2}$$

The catalytic effect of RT deposited Cu was explained with the disruption of the Si sp^3 environment by the Cu atoms [17, 31].

In contrast, an annealed interface which displays a "5 × 5" LEED pattern is passivated as regard to oxidation [31] and is also inert to atomic hydrogen [36] due to formation of strong directional bonding between Si and Cu atoms.

1.3.2. Surface Electromigration

When a Si sample with a patch of Cu deposit is heated to about 500–600 °C by a direct current, the electromigration of Cu atoms towards the cathode is observed [37, 38]. The electromigration occurs only when the coverage of the Cu deposit is more than 2 ML and the spreading-out uniform layer corresponds to the incommensurate Si(111)"5 × 5"–Cu surface phase [37]. It is interesting to note that, in the early period of annealing of about 10 min, the velocity of Cu propagation (about 2 μm/min) is approximately independent on the d.c. current (150–350 mA) and substrate temperature (500–600 °C) [38].

1.3.3. Electronic Properties

The strong anisotropies in the empty electron-band states of the Si(111)"5 × 5"–Cu phase was found by Sancrotti *et al.* [39, 40] using X-ray absorption spectroscopy. The absorption spectra are strongly dependent on whether the polarization vector is oriented parallel to the surface or nearly normal to it showing a metallic edge in the interface plane and a quasi-gap in the perpendicular direction.

2. (100) ORIENTATION

No well-defined superstructures have been observed in the investigations of Cu/Si(100) system both at RT and HT growth.

2.1. PHASE DIAGRAM

2.1.1. RT Growth

The formation of a Cu/Si(100) interface at room temperature was the object of several investigations [41–47]. It was shown that, upon RT Cu deposition onto Si(100), a continuous amorphous Cu–Si layer is formed. The forming layer is a Cu silicide of an approximate composition of Cu_3Si [43, 45]. For large coverages (about 20 ML), a tendency towards Si surface segregation was detected [45].

In LEED observations [41–44, 46, 47], the initial 2 × 1 pattern of clean Si(100) surface changes gradually with 3 ML Cu coverage to a 1 × 1 pattern which weakens with further Cu deposition and vanishes completely at 8 ML of Cu. No Cu-induced ordered reconstruction was detected in these studies.

2.1.2. HT Growth

The high-temperature growth for the Cu/Si(100) system is conventionally referred to that conducted upon Cu deposition onto Si(100) surface held at temperatures ranging from 130° to 500 °C [5, 42–44, 48, 49]. The growth at these temperatures proceeds in a modified mode of Volmer–Weber growth involving the formation of 3D islands of Cu silicide with the preservation of the unchanged Si(100)2 × 1 surface between the islands [5, 49]. LEED observations show that the 2 × 1 reconstruction gradually becomes diffuse but still remains visible up to 100 ML Cu coverage [41]. The island growth is anisotropic and the long axis of the island corresponds to the direction perpendicular to the Si–Si dimer rows [49].

The puzzling result was obtained in AES measurements which show the very small reduction of the Si Auger signal with increasing Cu coverage as well as the small value of the Cu Auger signal. Two different explanations of this phenomenon were proposed. Hanbucken *et al.* [41–44, 48] suggested that islands are covered with a Si skin of thickness up to 50 Å. This suggestion is based on the SEM and TEM observations. In contrast, Ichinokawa *et al.* [49] concluded from their scanning RHEED and AES data that Cu–silicide islands are not covered by a Si layer. They explained the above AES results as being caused by 3D island formation with a low lateral coverage.

2.2. CHEMICAL PROPERTIES

The effect produced by RT deposition of Cu on to the Si(100) surface is the same as that described above for a RT Cu/Si(111) interface, namely, the enhanced oxidation of silicon surface due to a catalytic activity of Cu atoms at the surface is observed [33–35].

REFERENCES

[1] A. Taleb-Ibrahimi, V. Mercier, C. A. Sebenne, D. Bolmont and P. J. Chen, *Surf. Sci.* **152–153** (1985) 1228.

[2] I. Abbati and M. Grioni, *J. Vac. Sci. Technol.* **19** (1981) 631.

[3] F. Ringeisen, J. Derrien, E. Daugy, J. M. Layet, P. Mathiez and F. Salvan, *J. Vac. Sci. Technol. B* **1** (1983) 546.

[4] E. Daugy, P. Mathiez, F. Salvan and J. M. Layet, *Surf. Sci.* **154** (1985) 267.

[5] H. Kemmann, F. Muller and H. Neddermeyer, *Surf. Sci.* **192** (1987) 11.

[6] St. Tosch and H. Neddermeyer, *J. Microscopy* **152** (1988) 415.

[7] St. Tosch and H. Neddermeyer, *Surf. Sci.* **211–212** (1989) 133.

[8] T. Yasue, T. Koshikawa, H. Tanaka and I. Sumita, *Surf. Sci.* **287–288** (1993) 1025.

[9] S. A. Chambers, G. A. Howell, T. R. Greenlee and J. H. Weaver, *Phys. Rev. B* **31** (1985) 6402.

[10] M. Hanbucken, G. Le Lay and V. Vlassov, *18th Int. Conf. Phys. Semiconduc.* **1** (1987) 347.

[11] S. A. Chambers, T. R. Greenlee, G. A. Howell and J. H. Weaver, *J. Vac. Sci. Technol. A* **3** (1985) 1291.

[12] T. Yasue, C. Park, T. Koshikawa and Y. Kido, *Appl. Surf. Sci.* **70–71** (1993) 428.

[13] M. Mundschau, E. Bauer, W. Telieps and W. Swiech, *J. Appl. Phys.* **65** (1989) 4747.

[14] S. A. Chambers and J. H. Weaver, *J. Vac. Sci. Technol. A* **3** (1985) 1929.

[15] L. Calliari, F. Marchetti and M. Sancrotti, *Phys. Rev. B* **34** (1986) 521.

[16] H. Dallaporta and A. Cros, *Surf. Sci.* **178** (1986) 64.

[17] S. H. Chou, A. J. Freeman, S. Grigoras, T. M. Centle, B. Delley and E. Wimmer, *J. Chem. Phys.* **89** (1988) 5177.

[18] J. T. Grant and T. W. Haas, *Surf. Sci.* **23** (1970) 347.

[19] E. Bauer, *Vacuum* **22** (1972) 539.

[20] K. Takayanagi, *Mat. Res. Soc. Symp. Proc.* **56** (1986) 129.

[21] T. Ishitsuka, K. Takayanagi, Y. Tanishiro and K. Yagi, *Proc. XIth Int. Cong. El. Micr.* **1** (1986) 1347.

[22] R. B. Doak and D. B. Nguyen, *Phys. Rev. B* **40** (1989) 1495.

[23] R. B. Doak, *J. Vac. Sci. Technol. B* **7** (1989) 1252.

[24] J. E. Demuth, U. K. Koehler, R. J. Hamers and P. Kaplan, *Phys. Rev. Lett.* **62** (1989) 641.

[25] R. J. Wilson, S. Chiang and F. Salvan, *Phys. Rev. B* **38** (1988) 12696.

[26] K. Mortensen, *Phys. Rev. Lett.* **66** (1991) 461.

[27] S. A. Chambers, S. B. Anderson and J. H. Weaver, *Phys. Rev. B* **32** (1985) 581.

[28] D. D. Chambliss, T. N. Rhodin and R. V. Kasowski, *J. Vac. Sci. Technol. A* **6** (1988) 1499.

[29] D. D. Chambliss and T. N. Rhodin, *Phys. Rev. B* **42** (1990) 1674.

[30] J. Zegenhagen, E. Fontes, F. Grey and J. R. Patel, *Phys. Rev. B* **46** (1992) 1860.

[31] E. Daugy, P. Mathiez, F. Salvan, J. M. Layet and J. Derrien, *Surf. Sci.* **152–153** (1985) 1239.

[32] I. Abbati, C. Rossi, L. Caliari, L. Braicovich, I. Lindau and W. E. Spicer, J. Vac. Sci. Technol. **21** (1982) 409.

[33] P. J. Moller, *J. Vac. Sci. Technol. A* **5** (1987) 996.

[34] D. Graf, M. Grundner, L. Muhlhoff and M. Dellith, *J. Appl. Phys.* **69** (1991) 7620.

[35] J. Li, H. Yonezawa and T. Shigematsu, *Japan J. Appl. Phys.* **31** (1992) L210.

[36] S. A. Chambers, M. Del Guidice, M. W. Ruckman, S. B. Anderson, J. H. Weaver and G. J. Lapeyre, *J. Vac. Sci. Technol. A* **4** (1986) 1595.

[37] A. Yamanaka and K. Yagi, *Surf. Sci.* **242** (1991) 181.

[38] H. Yasunaga and A. Natori, *Surf. Sci. Repts.* **15** (1992) 205.

[39] M. Sancrotti and G. Rossi, *Phys. Rev. B* **44** (1991) 1958.

[40] M. Sacchi, M. Sancrotti, O. Sakho and G. Rossi, *Appl. Surf. Sci.* **56–58** (1992) 563.

[41] M. Hanbucken, J. J. Metois, P. Mathiez and F. Salvan, *Surf. Sci.* **162** (1985) 622.

[42] M. Hanbucken and G. Le Lay, *Surf. Sci.* **168** (1986) 122.

[43] P. Mathiez, E. Daugy, F. Salvan, J. J. Metois and M. Hanbucken, *Surf. Sci.* **168** (1986) 158.

[44] M. Hanbucken, *Asia Pacific Symposium* (1987) 209.

[45] W. Radlik and H. Neddermeyer, *Surf. Sci.* **195** (1988) 195.

[46] T. Nakahara, S. Ohkura, F. Shoji, T. Hanawa and K. Oura, *Nucl. Instrum. Meth. Phys. Res. B* **45** (1990) 467.

[47] S. Guillet, L. E. Regalado, T. Lopez-Rios and R. Cinti, *Surf. Sci.* **277** (1992) L52.

[48] M. Hanbucken and J. Chazelas, J. Microsc. Spectrosc. Electron. **13** (1988) 349.

[49] T. Ichinokawa, T. Inoue, H. Izumi and Y. Sakai, *Surf. Sci.* **241** (1991) 416.

(Dy)

DYSPROSIUM

1. (111) ORIENTATION

The 1×1 structure was observed for the Dy/Si(111) system.

1.1. PHASE DIAGRAM

Upon depositing < 1 ML of Dy metal on the Si(111) surface at RT, the 7×7 LEED pattern turns into 1×1 [1]. With increasing coverage ($\theta = 1.2$ ML) the LEED pattern becomes ambiguous, indicating that the long range of the surface is lost. Using UPS, XPS, and AES Wang *et al.* [1] showed that the intermixing of Dy and Si atoms takes place during deposition of Dy on to the Si(111) surface at RT for metal coverages ≤ 4.1 ML. After annealing for 30 min at 400 °C, the Dy silicide forms with an atomic concentration ratio of Dy to Si of $\sim 1 : 2$ [1].

Sakho *et al.* [2] deposited monolayers of Dy on Si(111)7×7 surface. After annealing at $T > 600\,^{\circ}$C, the Dy layers convert into epitaxial pseudo-disilicide (DySi_{2-x}) interfaces which are terminated by extra silicon at the surface.

REFERENCES

[1] Y. X. Wang, B. -Q. Li, Y. R. Xing and C. C. Hsu, *J. Vac. Sci. Technol. A* **7** (1989) 2604

[2] O. Sakho, F. Sirotti, M. DeSantis, M. Sacchi and G. Rossi, *Appl. Surf. Sci.* **56–58** (1992) 568.

(Er)

ERBIUM

1. (111) ORIENTATION

One monolayer of Er produces a two-dimensional Er silicide showing a 1 × 1 structure upon annealing, while thicker Er silicides display a $\sqrt{3} \times \sqrt{3}$—$R30°$ reconstruction.

1.1. PHASE DIAGRAM

1.1.1. RT Growth

The LEED observations [1–5] showed that, upon RT deposition of Er, the 7 × 7 pattern gradually evolves over a 0–1 ML coverage range into a blurred 1 × 1 pattern, which disappears completely at higher coverages. This indicates the formation of a rather disordered layer.

The PES results of Refs. [3, 6, 7] suggested that the Er atoms react readily with the Si substrate at the very early stages of deposition ($\theta < 2$ ML) forming a Si-rich amorphous silicide layer. However, the data of a recent PES study of Lollman *et al.* [5] elucidated that an intermixing reaction occurs only when a critical coverage of about 0.8 ML is attained. The formation of the silicide-like layer proceeds in a coverage range of 0.8–2.5 ML followed by the growth of an almost pure Er upper layer.

1.1.2. HT Growth

Paki *et al.* [4] showed that annealing 1 ML Er deposited on Si(111) at RT at 550 °C produces a well-defined 2D silicide resembling a flat single $ErSi_2$ layer. The surface of the silicide layer formed displays a 1 × 1 LEED pattern with sharp spots and very low background intensity.

In the case of thicker Er layers (i.e. with thickness starting from 2 ML up to hundreds of angstroms), the annealing results in the formation of stable $ErSi_{1.7}$ silicide which displays a $\sqrt{3} \times \sqrt{3}$—$R30°$ structure [2, 4, 8–11]. Heating to about 400 °C produces a diffuse $\sqrt{3} \times \sqrt{3}$—$R30°$ LEED pattern but the brightness of the spots and their sharpness increase steadily with temperatures of up to about 900 °C where the spots evolution stops [2, 11]. The structural quality of the Er silicide layers was found to improve by the use of the template growth method [9], codeposition of Er and Si [2, 8], and two-step annealing (sequentially, at 400 °C and 900 °C) [2].

Beyond about 900 °C, the $\sqrt{3} \times \sqrt{3}$—$R30°$ diffraction pattern starts to become faint until the extinction of the $\sqrt{3} \times \sqrt{3}$—$R30°$ reflections accompanied by a mild appearance of the 7 × 7 structure. This observation was attributed to the cracking of the silicide layer out to islands [5]. The temperature of cracking of the silicide layer may be sufficiently lower for extremely thin films, e.g. when 3 ML thick Er film is annealed the reappearance of the 7 × 7 reflections is observed upon annealing at about 650 °C [12].

1.2. STRUCTURE

1.2.1. Si(111)1 × 1–Er

The 1 × 1 surface structure is detected when 1 ML of erbium deposited at RT is annealed at about 550 °C. Paki *et al.* [4] suggested that the forming 2D silicide adopts a structure resembling a single $ErSi_2$ layer (AlB_2 structure) with a reconstructed Si top layer. The reconstruction is similar to the one proposed for the $YSi_{1.7}(0001)$ surface, i.e. , a buckled Si double layer as in bulk Si.

1.2.2. Si(111)$\sqrt{3} \times \sqrt{3}$—$R30°$–Er

It is commonly supposed [2, 4] that a sharp $\sqrt{3} \times \sqrt{3}$ LEED pattern evidences the formation of the epitaxial $ErSi_{1.7}$ silicide. The Si deficiency (1.7 stoichiometry instead of 2) results from the vacancy formation. These vacancies order in a periodic array (where each sixth Si atom is lost), giving rise to $a\sqrt{3} \times \sqrt{3}$—$R30°$ superstructure.

The proposed vacancy model coincides with that proposed for the $\sqrt{3} \times \sqrt{3}$—$R30°$ structure of $YSi_{1.7}$ and $YbSi_{1.7}$ silicides.

1.3. PROPERTIES

1.3.1. Oxidation

The oxidation of $ErSi_{1.7}$ overlayer epitaxially grown on Si(111)7×7 was investigated by Guerfi *et al.* [13] and Veuillen *et al.* [14]. It was found that at room temperature and low oxygen pressure ($\leq 2 \times 10^{-5}$ mbar) it is rather inert: a chemisorption phase of oxygen is detected only after exposures above 100 L. The oxygen chemisorption is accompanied by the change of the LEED pattern from $\sqrt{3} \times \sqrt{3}$—$R30°$ to a faint 1 × 1 at about 1000 L exposure and a complete disappearance of LEED spots upon ∼ 5000 L oxygen exposure. High oxygen pressure (∼ 1 atm) produces a layer of mixed SiO_2, Si suboxides and Er_2O_3.

At 700 °C and under 2×10^{-5} mbar oxygen pressure, the silicide is decomposed with the simultaneous formation of SiO_2 and Er_2O_3. The uppermost layer of this mixed oxide is formed of SiO_2.

REFERENCES

[1] A. W. Parke, A. McKinley, R. H. Williams and G. P. Srivastava, *J. Phys. C* **13** (1980) L369.

[2] F. A. D'Avitaya, P. -A. Badoz, Y. Campidelli, J. A. Chroboczek, J. -Y. Duboz and A. Perio, *Thin Solid Films* **184** (1990) 283.

[3] P. Wetzel, L. Haderbache, C. Pirri, J. C. Peruchetti, D. Bolmont and G. Gewinner, *Phys. Rev. B* **43** (1991) 6620

[4] P. Paki, U. Kafader, P. Wetzel, C. Pirri, J. C. Peruchetti, D. Bolmont and G. Gewinner, *Phys. Rev. B* **45** (1992) 8490.

[5] D. B. B. Lollman,T. A. Nguyen Tan and J. -Y. Veuillen, *Surf. Sci.* **269–270** (1992) 959.

[6] L. Haderbache, P. Wetzel, C. Pirri, J. C. Peruchetti and D. Bolmont, *Appl. Phys. Lett.* **57** (1990) 341.

[7] S. Gokhale, S. Mahamuni, S. V. Deshmukh, V. J. Rao, A. S. Nigavekar and S. K. Kulkarni, *Surf. Sci.* **237** (1990) 127.

[8] F. A. d'Avitaya, A. Perio, J. C. Oberlin, Y. Campidelli and J. A. Chroboczek, *Appl. Phys. Lett.* **54** (1989) 2198.

[9] F. H. Kaatz, M. P. Siegal, W. R. Graham, J. Van der Spiegel and J. J. Santiago, *Thin Solid Films* **184** (1990) 325.

[10] P. Wetzel, L. Haderbache, L. Pirri, J. C. Peruchetti, D. Bolmont and G. Gewinner, *Surf. Sci.* **251–252** (1991) 799.

[11] J. -Y. Veuillen, T. A. Nguyen Tan, D. B. B. Lollman, N. Guerfi and R. Cinti, *Surf. Sci.* **251–252** (1991) 432.

[12] P. Paki, U. Kafader, C. Pirri, J. C. Peruchetti, D. Bolmont and G. Gewinner, *Surf. Sci.* **269–270** (1992) 970.

[13] N. Guerfi, T. A. Nguyen Tan, J. -Y. Veuillen and D. B. Lollman, *Appl. Surf. Sci.* **56–58** (1992) 501.

[14] J. -Y. Veuillen, L. Magaud, D. B. B. Lollman and T. A. Nguyen Tan, *Surf. Sci.* **269–270** (1992) 964.

(Eu)

EUROPIUM

1. (111) ORIENTATION

A set of surface structures, 1 × 1, 2 × 2, 5 × 5, 3 × 3, and 3 × 1 are observed upon heating the Eu/Si(111) interface.

1.1. PHASE DIAGRAM

1.1.1. RT Growth

The formation of the Eu/Si(111) interface at RT deposition of Eu on to the Si(111)7 × 7 surface was studied in Refs. [1–4] by means of electron spectroscopies and LEED.

It was found that the intermixing of Eu and Si is very pronounced and the onset of chemical reaction occurs at about 0.5 ML Eu coverage (1 ML = 3. 8 Å Eu). At this point, the initial 7 × 7 reconstruction is lifted and a 1 × 1 LEED pattern is observed. In turn, the 1 × 1 LEED pattern is destroyed at about 2 ML Eu coverage indicating the growth of the disordered layer.

Henle *et al.* [4] concluded from PES and AES data that the interface formation process has a multistep nature. The first phase reacted which is formed at about 5 Å is chemically inhomogeneous, while the second phase reacted forming at higher coverages is a well-defined silicide type reaction product.

The intermixed reacted interface is wide and an Eu film thickness greater than 50 Å is necessary before a metallic Eu surface is obtained [3].

1.1.2. HT Growth

The evolution of the RT deposited Eu/Si(111) interface upon annealing was studied by Hofmann and Netzer [3] and Henle *et al.* [4] and the results of these investigations are in good agreement with each other.

It was found that upon annealing a sequence of the 1 × 1, 2 × 2, 5 × 5, 3 × 3 and 3 × 1 surface structures are formed with the increase of annealing temperature as shown in the phase diagram in Fig. 1. The appearance of the 1 × 1 and 2 × 2 structures was considered to indicate a transition from a Eu-rich silicide type interfacial compound formed at RT to a Si-rich ordered silicide phase forming at elevated temperatures. In particular, the 2 × 2 structure was believed to correspond to a disilicide $EuSi_2$ stoichiometry. The structures observed at higher temperatures (5 × 5, 3 × 3, 3 × 1) are presumably Si(111)–Eu surface phases, since the Eu content is already very low at that stage [3, 4].

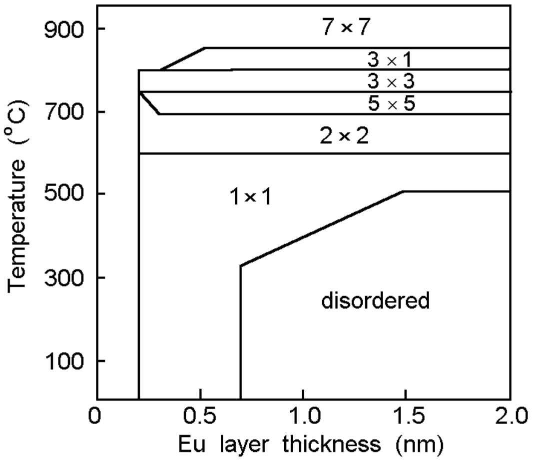

Fig 1. Phase diagram of the Eu/Si(111) system indicating the regions of observation of the LEED structures. In the experiment, the RT deposited Eu/Si(111) interface is annealed sequentially at increasing temperatures. The Eu layer thickness corresponds to that of the as-deposited film (from Ref. [4]). (*Reproduced by permission of Elsevier Science Publishers BV)*

Heating to above 850 °C restores the 7 × 7 reconstruction, but AES still reveals traces of Eu, which cannot be completely removed from the surface.

REFERENCES

[1] G. Rossi, J. Nogami, I. Lindau and J. J. Yeh, *Surf. Sci.* **152–153** (1985) 1247
[2] J. Nogami, C. Carbone, J. J. Yeh, I. Lindau and S. Nannarone, Proc. 17th Int. Conf. Phys. Semic. (1985) 201
[3] R. Hofmann and F. P. Netzer, *Phys. Rev. B* **43** (1991) 9720
[4] W. A. Henle, M. G. Ramsey, F. P. Netzer and K. Horn, *Surf. Sci.* **254** (1991) 182

(F)

FLUORINE

It is generally agreed that SiF_4 is the predominant volatile product in plasma etching of silicon by fluorine-containing gases [1]. This process is practically important in the fabrication of microelectronic devices. For example, CF_4 or XeF_2 plasmas are commonly employed to etch silicon surfaces for pattern transfer [2].

1. (111) ORIENTATION

Fluorine does not produce any reconstructions on the Si(111) surface.

2.1. PHASE DIAGRAM

To the best of our knowledge, the experimental study of the interaction of fluorine atoms with the Si(111) surface and SiF_4 formation was performed using only fluorine-containing gases as a model system. McFeely *et al.* [3] using PES, studied the formation of SiF_y ($y = 1 \div 4$) on the Si(111) surfaces subjected to steady-state etching by XeF_2. The Si($2p$) spectral features of SiF, SiF_2 and SiF_3 were found to shift from that of the bulk towards higher binding energy by approximately 1, 2 and 3 eV, respectively, and SiF_4 was shifted by about 4. 6 eV.

Wen *et al.* [1] investigated the interaction of SiF_4 with the Si(111)7×7 surface at 30 K. Their results indicate that the initial adsorption of SiF_4 results in the formation of SiF and SiF_3: the SiF species have the Si–F bond directed normal to the surface, while the bonds in SiF_3 are not. Subsequent warming of the low-temperature, multi-layer dosed SiF_4covered surface to $T > 100$ K results in a surface that is covered predominantly by SiF and SiF_3.

2. (100) ORIENTATION

Fluorine does not produce any reconstructions on the Si(100) surface.

1.1. PHASE DIAGRAM

The adsorption of molecular and atomic fluorine on the Si(100) surface was experimentally investigated by Engstrom *et al.* [2]. Molecular fluorine was found to adsorb dissociatively on the clean Si(100) surface with an initial probability of adsorption of 0.46 ± 0.02, which is essentially independent of surface temperature ($T_s = 120$–600 K). The coverage–exposure relationship for F_2 is characterized by an initial rapid phase of adsorption, which saturates at a coverage of $\theta_F \simeq 1.5$ ML, followed by a much slower phase of adsorption, which does not saturate.

The adsorption of atomic fluorine is qualitatively different from molecular fluorine. Although the initial probability of adsorption is quite similar, i.e. approximately 0.5 ± 0.3, the adsorption probability of atomic fluorine is only weakly dependent on coverage, decreasing only by a factor of two at a coverage of 3–4 ML.

Temperature-programmed decomposition of silicon–fluoride ad-layers, produced by exposing the clean Si(100) surface at 120 K to a beam of fluorine, yielded SiF_2 (g) and SiF_4 (g) as the only gas phase reaction products. The relative yield of these two gas phase reaction products depends strongly on the initial coverage of fluorine adatoms below ~ 3 ML.

The observation of ion angular distributions originating from electron stimulated desorption of an adsorbed fluorine species by Bozack *et al.* [4] shows that F^+ is emitted from Si(100)2×1 along 4 azimuths corresponding to the principal crystal axes. The F^+ emission angle, $\alpha \approx 36° \pm 5°$ to the surface normal, corresponds closely to the Si–F surface bond direction. This F^+ angular distribution is consistent with F bonding to Si dimers which are in two orthogonal reconstructions on Si(100)2×1.

REFERENCES

[1] C. -R. Wen, S. P. Frigo and R. A. Rosenberg, *Surf. Sci.* **249** (1991) 117.
[2] J. R. Engstrom, M. M. Nelson and T. Engel, *Surf. Sci.* **215** (1989) 437.
[3] F. R. McFeely, J. F. Morar and F. J. Himpsel, *Surf. Sci.* **165** (1986) 277.
[4] M. J. Bozack, M. J. Dresser, W. J. Choyke, P. A. Taylor and J. T. Yates, Jr. , *Surf. Sci.* **184** (1987) L332.

(Fe)

IRON

1. (111) ORIENTATION

The ordered 2×2, $\sqrt{3} \times \sqrt{3}$—$R30°$ and 1×1 surface reconstructions were observed for the Fe/Si(111) system. In rather thick layers epitaxial Fe(111) and β-FeSi$_2$ were detected.

1.1. PHASE DIAGRAM

1.1.1. RT Growth

LEED observations [1–3] revealed that, upon RT Fe deposition on to Si(111)7×7 surface, the initial 7×7 LEED pattern changes to a 1×1 surface at about 0.25 ML Fe coverage (1 ML Fe = 0.9 Å). The 1×1 reflections are sharp up to about 1 ML and then become blurred. The 1×1 structure remains apparent for films several dozens nanometers thick also.

The formation of the Fe/Si(111) interface at room temperature was the object of several investigations [3–11] and the preponderance of the evidence indicates that the interface formation involves the reactive intermixing at the early stages of depositions followed by the growth of pure Fe islands and the formation of the continuous epitaxial Fe(111) film. The onset of the Fe island growth was reported to occur at Fe thicknesses of several angstroms (from 3 to 10 Å according to different publications), while the Fe(111) layer covers the surface completely at thicknesses above a few nanometers.

It should be pointed out that there is a lack of consensus concerning the composition of the intermixed layer. In the majority of investigations [5, 8, 9, 11], the formation of the FeSi-like phase was suggested. In contrast, De Crescenzi *et al.* [10] concluded that, at 1–2 Å Fe coverages, Fe and Si interdiffuse to form the β-FeSi$_2$-like phase at the interface, while for increasing coverages the interfacial region is buried by Fe islands. Zeng *et al.* [11] also did not exclude the formation of FeSi$_2$ at the early stages but their data indicate that this layer would be less extended (0.5 Å). Ufuktepe and Onellion [5] reported that, at about 4 Å Fe coverage, the growth of FeSi is changed by the growth of Fe-rich silicide (for example, Fe$_3$Si at 8 Å). A quite different suggestion was proposed by Li *et al.* [6], namely, the formation of a composition gradient rather than a sharply defined interfacial compound.

1.1.2. HT Growth

Urano *et al.* [1, 2, 12] were the first to build a formation phase diagram of an Fe/Si(111) system shown in Fig. 1. In the experiment (as well as in the most publications), Fe film was deposited at RT and then annealed at higher temperatures. The main features of the phase diagram are that, upon annealing above 400 °C, the LEED pattern changes from a 1×1 to

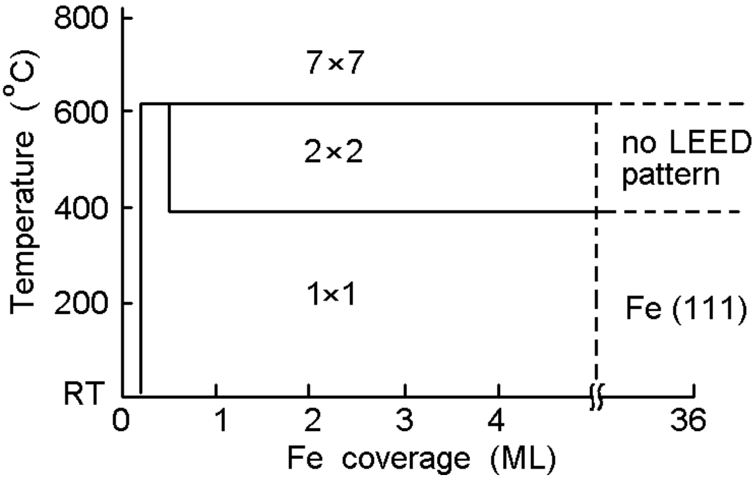

Fig 1. Two-dimensional phase diagram of an iron deposited Si(111) surface. Iron atoms were deposited at room temperature, and each film was annealed at higher temperatures (for 10 min at each temperature). The thickness of the film indicated is that immediately after deposition (from Ref. [12]). (*Reproduced by permission of Elsevier Science Publishers BV)*

2×2 (or three-domain 2×1) superstructure for films of more than 0.5 ML and 1×1 pattern of Fe(111) film dozens of angstroms thick disappears completely into the intense background.

AES results of Urano *et al.* [1,2] suggest that, for films less than 1 ML, Fe atoms remain on the surface up to 600 °C. For films more than 1 ML thick, most of Fe atoms remain on the surface after annealing at temperatures lower than 400 °C but infiltrate into the substrate at higher temperatures.

The results of Urano *et al.* [1,2,12] have been revised in later publications. Gavriljuk *et al.* [3] and Chevrier *et al.* [13] reported the prescence of the $\sqrt{3}\times\sqrt{3}$ structure which was overlooked by Urano *et al.* The formation of the $\sqrt{3}\times\sqrt{3}$ structure was detected in Refs [3,13] upon different preparation conditions, namely, after annealing of 1–2 ML Fe at temperatures above 400 °C in Ref. [3] and upon 300 °C annealing of about 7 ML Fe in Ref. [13].

Another dissimilarity from the results of Urano *et al.* [1,2,12] were found in the investigations of thermal annealing behavior of rather thick (say, 30 Å) Fe(111) films [3, 4, 7, 9, 13, 14]. Upon annealing at 250–400 °C, the LEED and RHEED patterns of Fe(111) are lost and no evidence for crystalline order is left. However, at higher annealing temperatures (450–550 °C) the new and complicated pattern reappears [3, 9, 13]. Careful analysis of the pattern [4, 9] showed that the new epitaxial phase is the orthorhombic β-FeSi$_2$. The relationships of the epitaxy are:

matching planes β-FeSi$_2$(101) || Si(111)
with azimuthal orientations β-FeSi$_2$[010] || Si[011]
and matching planes β-FeSi$_2$(110) || Si(111)
with azimuthal orientations β-FeSi$_2$[001] || Si[011].

The β-FeSi$_2$ (101) or (110) planes, of twofold symmetry, are joined to the sixfold symmetric Si(111) plane, each epitaxy is composed of three equivalent and equiprobable azimuthal orientations.

It is interesting that the temperature at which the epitaxy is coming back is close to the crystallization temperature of the FeSi$_2$ amorphous phase ($T \approx 425\,^\circ$C) [13].

The investigations of the change in the film composition during annealing revealed that the β-FeSi$_2$ formation is preceded by the occurrence of Fe$_3$Si and FeSi phases, Fe$_3$Si being stable at temperatures below 300 °C and FeSi at 300–400 °C [8, 11, 13, 15, 16]. The β-FeSi$_2$ epitaxial layer remains stable up to about 550–650 °C. At higher temperatures, AES and

EELS results reveal the appearance of Si on the surface. Zhu *et al.* [15] explained that this result was due to Si surface segregation, Rizzi *et al.* [17] and Wallart *et al.* [8] attributed this observation to the disruption of the disilicide film with the formation of islands, while Terrasi *et al.* [18] suggested the occurrence of both of the above processes.

1.2. STRUCTURE

1.2.1. Si(111)1 × 1–Fe

Urano *et al.* [12] conducted dynamical analysis of LEED *I–V* curves for a 1 × 1 Fe structure formed by annealing 1 ML Fe at 350 °C. Several models were considered. The best agreement between experimental and calculated curves was reached for a model in which Fe atoms are in 3-fold hollow sites on the Si substrate in which the topmost layer is missing. Two possible spacings between the iron plane and the topmost Si plane, 0.48 Å and 0.93 Å, were obtained. From the point of view of atomic distances, 0.93 Å was suggested as more reasonable [12].

1.2.2. Si(111)2 × 2–Fe

There is a lack of definite results about the atomic arrangement of the 2 × 2 phase. In Ref. [12], Urano *et al.* tested several models for which the 1 × 1 structure was modified for 2 × 2 structure described above (for example, one-fourth of the Fe atoms are replaced with Si atoms, one-fourth of the Fe atoms are omitted and one-fourth of the iron atoms moved perpendicularly). However, good agreement could not be obtained.

Chevrier *et al.* [13] revealed by AES that the 2 × 2 phase has a chemical composition very close to $FeSi_2$. They suggested that this phase is a strained $FeSi_2$ layer which is structurally very close to the CaF_2 structure (β-$FeSi_2$ exhibits, in fact, an already distorted CaF_2 cell) [13].

The latter suggestion received confirmation in the STM study of Vazquez de Parga *et al.* [19] in which it was concluded that the 2 × 2 phase corresponds to $FeSi_2$ crystallizing with the fluorite structure with an almost perfect arrangement of Si adatoms on top of the last Si(111) layer of the fluorite.

1.2.3. Si(111)$\sqrt{3} \times \sqrt{3}$–Fe

Gavriljuk *et al.* [3] concluded from EELS data that the $\sqrt{3} \times \sqrt{3}$ structure corresponds to a two-dimensional FeSi silicide. Later Chevrier *et al.* [13] explained the $\sqrt{3} \times \sqrt{3}$ structure by epitaxy of the FeSi compound with its simple cubic phase and a lattice parameter of 4.4 Å. The proposed epitaxial relationships on the (111) silicon plane are:

FeSi(111) ∥ Si(111) with azimuthal orientations
FeSi[110] ∥ Si[112].

2. (100) ORIENTATION

The ordered reconstructions observed in the Fe/Si(100) system are $c(2 \times 2)$ and 2 × 2 which are associated with the formation of epitaxial silicides.

2.1. PHASE DIAGRAM

2.1.1. RT Growth

LEED observations [4, 20–23] revealed that the 2 × 1 LEED pattern of the Si(100) surface disappears after deposition of the first monolayer of Fe and no other LEED pattern was seen during Fe growth.

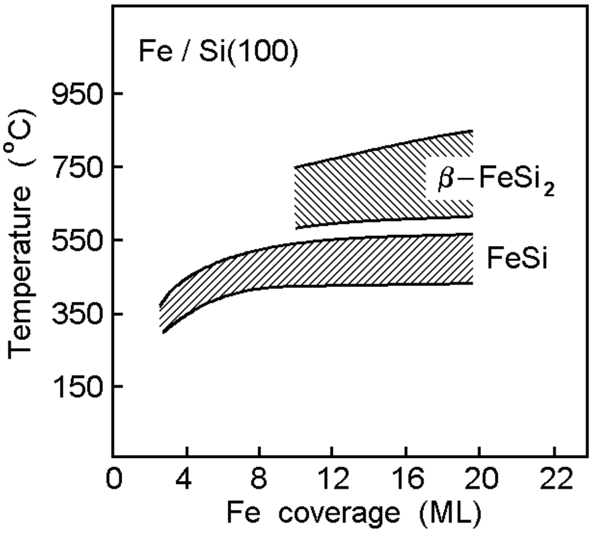

Fig 2. Temperature-coverage phase diagram for the Fe/Si(100) system (from Ref. [26]). (*Reproduced by permission of the publishers of Journal of Physical Review B)*

Gallego *et al.* [20,24,25] concluded from AES, XPS and EELS data that Fe deposition on to Si(100) held at RT results in layer-by-layer growth of polycrystalline, metallic Fe with a small amount of Si (0.1–0.2 ML) interdiffused forming a solid solution. They suggested also that the formation of iron silicides does not occur at room temperature [20]. In contrast, the UPS results of Alvarez *et al.* [26] imply the formation of Fe_3Si at 2–3 ML Fe coverage preceded the growth of unreacted metallic Fe.

2.1.2. HT Growth

The interaction in the Fe/Si(100) system upon annealing and reactive deposition on to the heated substrate has been studied in a number of works [4, 9, 20, 21, 24, 26–28]. However, the majority of publications has been devoted to the growth of films of thickness exceeding the submonolayer range.

It has been shown that depending on growth temperature FeSi and β-$FeSi_2$ phases occur as illustrated by the phase diagram shown in Fig. 2. FeSi is the first phase formed. It is stable at temperatures ranging from 400 to 570 °C [26]. In some cases, a $c(2 \times 2)$ LEED pattern was seen from this surface [20].

At higher temperatures (600–850 °C), the $FeSi_2$ is produced with a layer of Si segregated to the surface [20]. UPS results of Ref. [28] revealed that disilicide grown at these temperatures is the semiconducting β-$FeSi_2$ phase. This surface displays a 2×2 superstructure which is explained by epitaxy of orthorhombic β-$FeSi_2$ on Si(100) according to the epitaxial relationship:

β-$FeSi_2(100) \parallel Si(100)$
with azimuthal orientation:
β-$FeSi_2[010]$ or $[001] \parallel Si[110]$.

However, the ordered reconstruction was not seen in a reproducible fashion, suggesting that very careful conditions must be held to obtain crystallites of epitaxial β-$FeSi_2$ larger than the coherence length of the LEED beams [20]. The possible role of the ordered surface steps in favoring the nucleation of the epitaxial β-$FeSi_2$ phase on Si(100) was discussed by Alvarez *et al.* [28] and this was also observed by Cherief *et al.* [4,21]: while no epitaxial growth was detected on the plane Si(100) surface, the β-$FeSi_2$ epitaxy indicated by appearance of 2×2 reconstruction did occur on the stepped Si(100) surface (The Si(100) surface was misoriented by 5° towards the ⟨110⟩ direction resulting in bilayer steps parallel to ⟨111⟩ direction and ∼ 31 Å wide (100) terraces. This width of terraces corresponds to four unit cells of β-$FeSi_2$(100) planes.) It should be said, however, that Mahan *et al.* [27] observed the growth of ordered β-$FeSi_2$ in the same epitaxial relationship upon deposition at 500 °C on to a plane Si(100) surface.

In Ref. [9], it was reported that co-deposition of Fe and Si at a stoichiometric ratio 1 : 2 at temperatures below 200 °C followed by annealing at 300 °C results in the growth of epitaxial β-$FeSi_2$ which quite surprisingly follows another epitaxial relationship:

β-$FeSi_2$(100) ‖ Si(100)

but with azimuthal orientation:

β-$FeSi_2$[010] and [001] ‖ Si[100]

i.e. rotated by 45° as compared to the orientation described above.

REFERENCES

[1] T. Urano, T. Ogawa, T. Kanaji and F. Fujimoto, *J. Vac. Sci. Technol. A* **5** (1987) 2046.
[2] T. Urano and T. Kanaji, *Appl. Surf. Sci.* **33–34** (1988) 68.
[3] Yu. L. Gavriljuk, L. Y. Kachanova and V. G. Lifshits, *Surf. Sci.* **256** (1991) L589.
[4] N. Cherief, R. C. Cinti, M. De Crescenzi, J. Derrien, T. A. Nguyen Tan and J. Y. Veuillen, *Appl. Surf. Sci.* **41–42** (1989) 241.
[5] Y. Ufuktepe and M. Onellion, *Solid State Commun.* **76** (1990) 191.
[6] B. -Q. Li, M. -R. Ji and J. -R. Wu, *J. Appl. Phys.* **68** (1990) 1099.
[7] F. Scarinci, S. Lagomarsino, C. Giannini, G. Savelli, P. Castrucci, A. Rodia and L. Scopa, *Appl. Surf. Sci.* **56–58** (1992) 444.
[8] X. Wallart, H. S. Zeng, J. P. Nys and G. Dalmai, *Appl. Surf. Sci.* **56–58** (1992) 427.
[9] J. Derrien, J. Chevrier, V. Le Thanh and J. E. Mahan, *Appl. Surf. Sci.* **56–58** (1992) 382.
[10] M. De Crescenzi, G. Gaggiotti, N. Motta, F. Patella and A. Balzarotti, *Phys. Rev. B* **42** (1990) 5871.
[11] H. S. Zeng, X. Wallart, J. P. Nys, G. Dalmi and P. Friedel, *Phys. Rev. B* **44** (1991) 13811.
[12] T. Urano, M. Kaburagi, S. Hogno and T. Kanaji, *Appl. Surf. Sci.* **41–42** (1989) 103.
[13] J. Chevrier, V. Le Thahn, S. Nitsche and J. Derrien, *Appl. Surf. Sci.* **56–58** (1992) 438.
[14] J. De la Figuera, A. L. Vazquez de Parga, J. Alvarez, J. Ibanez, C. Ocal and R. Miranda, *Surf. Sci.* **264** (1992) 45.
[15] Q-G. Zhu, H. Iwasaki, E. D. Williams and R. L. Park, *J. Appl. Phys.* **60** (1986) 2629.
[16] H. C. Cheng, T. R. Yew and L. J. Chen, *J. Appl. Phys.* **57** (1985) 5246.
[17] A. Rizzi, H. Moritz and H. Luth, *J. Vac. Sci. Technol. A* **9** (1991) 912.
[18] A. Terrasi, S. U. Campisano, E. Rimini, Y. Hwu and G. Margaritondo, *Appl. Surf. Sci.* **56–58** (1992) 572.
[19] A. L. Vazquez de Parga, J. De la Figuera, C. Ocal and R. Miranda, *Ultramicroscopy* **42–44** (1992) 845.
[20] J. M. Gallego and R. Miranda, *J. Appl. Phys.* **69** (1991) 1377.
[21] S. Kennou, N. Cherief, R. Cinti and T. A. Nguyen Tan, *Surf. Sci.* **211–212** (1989) 685.
[22] H. H. Weitering, A. R. H. F. Ettema and T. Hibma, *Phys. Rev. B* **45** (1992) 9126.
[23] J. M. Gallego, J. M. Garcia, J. Alvarez and R. Miranda, *Phys. Rev. B* **46** (1992) 13339.
[24] J. M. Gallego, J. Alvarez, J. J. Hinarejos, E. G. Michel and R. Miranda, *Surf. Sci.* **251–252** (1991) 59.
[25] J. M. Gallego and R. Miranda, *J. Appl. Phys.* **63** (1991) 1377.
[26] J. Alvarez, J. J. Hinarejos, E. G. Michel, G. R. Castro and R. Miranda, *Phys. Rev. B* **45** (1992) 14042.

[27] J. E. Mahan, K. M. Geib, G. Y. Robinson, R. G. Long, Y. Xinghua, G. Bai, M. A. Nicolet and M. Nathan, *Appl. Phys. Lett.* **56** (1990) 2126.
[28] J. Alvarez, J. J. Hinarejos, E. G. Michel, J. M. Gallego, A. L. Vazquez de Parga , J. De la Figuera, C. Ocal and R. Miranda, *Appl. Phys. Lett.* **59** (1991) 99.

(Ga)

GALLIUM

1. (111) ORIENTATION

With the increase of coverage, Ga induces 7 × 7, $\sqrt{3} \times \sqrt{3}$—$R30°$, 6.3 × 6.3, 11 × 11, and $6.3\sqrt{3} \times 6.3\sqrt{3}$–$R30°$ reconstructions on the Si(111) surface.

1.1. PHASE DIAGRAM

1.1.1. RT Deposition on to Si(111)2 × 1

The structural transformations of the cleaved Si(111)2 × 1 surface upon RT deposition of Ga were studied by Bolmont *et al.* [1]. It was found that the 2 × 1 LEED pattern remains visible with decreasing intensity up to about 0.2–0.3 ML. Meanwhile, starting from about 0.1 ML, $\sqrt{3} \times \sqrt{3}$—$R30°$ reflections grow in intensity and, after 0.3 ML, the $\sqrt{3} \times \sqrt{3}$—$R30°$ pattern replaces the 2 × 1 pattern. Upon further gallium deposition, the $\sqrt{3} \times \sqrt{3}$—$R30°$ structure is replaced by 1 × 1 structure slightly above 1 ML Ga. The 1 × 1 LEED pattern is still observed at higher Ga coverages. Table 1 summarizes the structural evolution of the Ga/Si(111)2 × 1 system at RT.

AES observations [1] revealed that the RT growth of Ga on Si(111)2 × 1 follows the Stranski–Krastanov growth mode, i.e. after the completion of the 2D layer at about 1 ML Ga the islands of metal start to form.

1.1.2. RT Deposition on to Si(111)7 × 7

Deposition of Ga on to the Si(111)7 × 7 surface held at RT causes a gradual vanishing of the 7 × 7 reflections. When the amount of Ga exceeds 1.5 ML, all 1/7 order reflections disappear and only fundamental reflections remain visible [2].

Table 1. Surface structures observed on cleaved Si(111) upon increasing coverage of Ga deposited at RT (from Ref. [1]).

Ga coverage (ML)	Structure
0-0.1	2 × 1
0.1-0.3	$2 \times 1 + \sqrt{3} \times \sqrt{3}$
0.3-1	$\sqrt{3} \times \sqrt{3}$
> 1	1 × 1

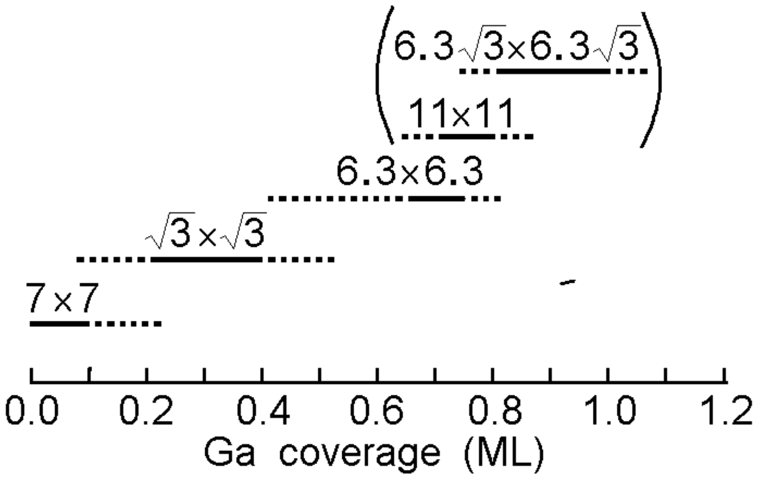

Fig 1. Phase diagram of the Ga/Si(111) system at $T = 550\,°\mathrm{C}$ (from Ref. [6]). (*Reproduced by permission of Blackwell Scientific Publications Ltd)*

1.1.3. HT Growth

A sequence of Ga-induced reconstructions is observed at HT growth of Ga on the Si(111) surface. These observations are summarized in phase diagram for the Ga/Si(111) system shown in Fig. 1. The surface phases were formed by Ga deposition on to the heated Si(111) surface [3–5] or by annealing of the RT deposited Ga layer [2, 6]. The optimal formation temperature was about 550 °C in both cases.

The deviation of the growth temperature towards the higher temperatures causes a decrease in the amount of Ga on the surface by desorption of Ga atoms. At lower temperatures of about 200–400 °C only a 7 × 7 to 6.3 × 6.3 structural change is seen [2], while a series of structural changes, namely $7\times7 \rightarrow \sqrt{3}\times\sqrt{3}$—$R30°$ $\rightarrow 6.3\times6.3 \rightarrow 11\times11 \rightarrow 6.3\sqrt{3}\times6.3\sqrt{3}$—$R30°$ is observed on a surface kept at about 550 °C [2–6].

1.2. STRUCTURE

1.2.1. Si(111)7 × 7–Ga

At low Ga coverage, as it was revealed by STM observations [6], Ga atoms replace Si in the 7 × 7 adatom positions, preserving the 7 × 7 structure.

1.2.2. Si(111)$\sqrt{3}\times\sqrt{3}$—$R30°$–Ga

At about 1/3 ML, Ga induces a $\sqrt{3}\times\sqrt{3}$ reconstruction. The data of X-ray standing-wave measurements [3–5, 7], dynamic analysis of LEED I–V curves [8, 9], photoelectron spectroscopy [10–13], medium-energy ion scattering spectroscopy [14] and theoretical calculations [3, 11, 15–17] are consistent with the T_4 Ga adatom model of Si(111) $\sqrt{3}\times\sqrt{3}$ Ga surface. The T_4 geometry was unambiguously confirmed by STM observations [3, 5, 18] of a surface that exhibits both 7 × 7 and $\sqrt{3}\times\sqrt{3}$ diffraction spots simultaneously (Fig. 2). The corrugation trace of tunneling microscope tip spanning the boundary between the 7 × 7 and $\sqrt{3}\times\sqrt{3}$ structures demonstrates that the T_4 site is populated by the gallium atom. The trace that would have resulted from H_3 configuration is indicated to show that the STM resolves the distinction comfortably.

The goal of locating the gallium atoms perpendicular to the silicon surface was achieved by the X-ray standing-wave interferometry [3–5]. The Ga position was established to be at 1.49 ± 0.03 Å above the upper half of the bulk terminated (111) double plane. This value

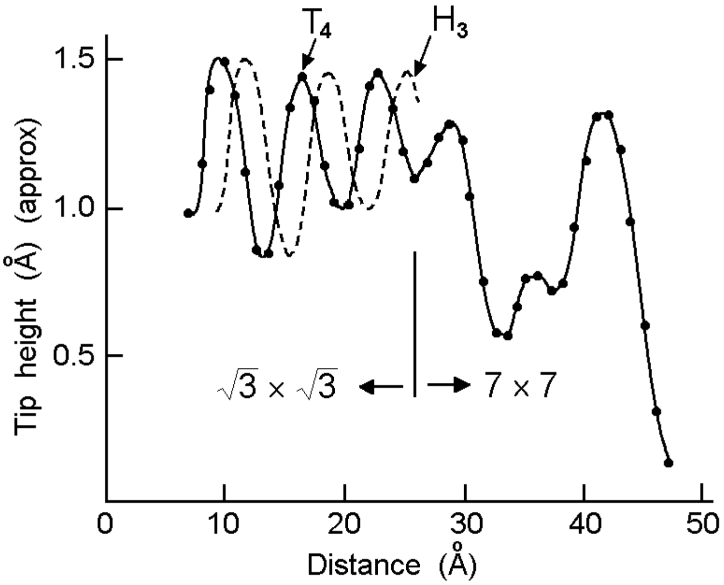

Fig 2. Line scan of top height along the line spanning the 7 × 7–$\sqrt{3} \times \sqrt{3}$ interface. The dotted line shows how the scan would look for H_3 type reconstruction. Heights of atoms in $\sqrt{3} \times \sqrt{3}$ are similar to 7 × 7, confirming the adatom model (from Ref. [3]). (*Reproduced by permission of the publishers of Physical Review B)*

Table 2. The atomic coordinates for the optimum configuration shown in Fig. 3. The x, y, and z axes are parallel to the $[\bar{1}\bar{1}\bar{1}]$, $[\bar{1}2\bar{1}]$ and $[\bar{1}01]$ directions, respectively (from Ref. [9]).

Atom	x (Å)	y (Å)	z (Å)
1	0.00	0.00	0.00
2	1.35	1.05	1.83
3	1.35	−2.10	0.00
4	1.93	3.33	1.92
5	2.57	0.00	0.00
6	4.37	3.33	1.92
7	4.71	0.00	0.00
8	5.22	2.27	0.00
9	5.22	−1.13	1.97

is about 0.15 Å higher than the vertical height of the Ga in the T_4 site obtained by total energy calculations [16,19] and of the optimized surface geometry determined from LEED I–V spectra [9]. The dynamic analysis of LEED I–V spectra [9] also reveals a large deformation of the surface layer resulting from the stable adsorption of Ga atoms (Fig. 3 and Table 2).

1.2.3. Si(111)6.3 × 6.3–Ga and Si(111)11 × 11–Ga

The LEED and RHEED patterns that result from Ga coverages ranging from about 0.5 to 1.0 monolayer show a hexagonal set of spots which surround the 1 × 1 reflections from the substrate [2, 4]. These patterns correspond to incommensurate 6.3 × 6.3 and 11 × 11 superlattices (Fig. 4). According to STM data [4–6, 20], the origin of the 6.3 × 6.3 structure is the superlattice of hexagonally packed supercells of triangular shape spaced 24 Å apart.

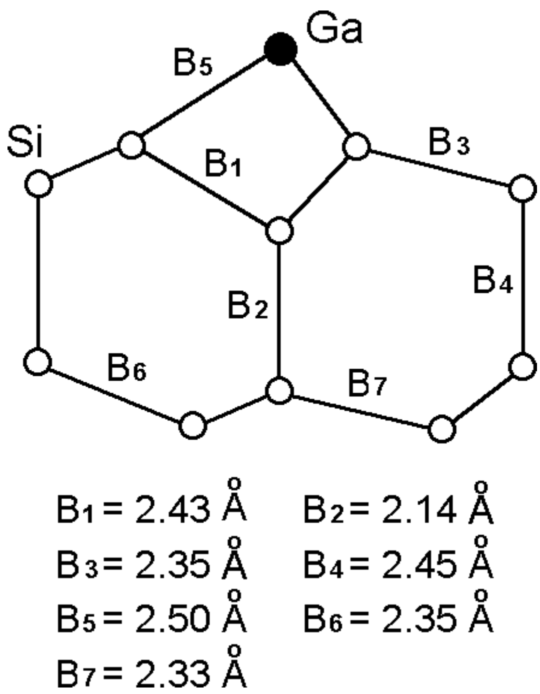

Fig 3. Si(111)$\sqrt{3} \times \sqrt{3}$—$R30°$–Ga structure. Optimized surface geometry from dynamic analysis of LEED *I–V* spectra (from Ref. [9]). (*Reproduced by permission of the publishers of Physical Review B)*

The individual Ga atoms within the supercells, in turn, are packed hexagonally with a 4.1 Å lattice period. The 11 × 11 diffraction reflections might be caused by the 4.1 Å internal periodicity of the supercells, taking into account multiple scattering.

According to X-ray standing-wave measurements [7, 21], Ga atoms occupy the substitutional sites on the topmost silicon (111) double plane. The deduced Ga position is 0.50±0.02 Å below the top half of the extrapolated silicon (111) double plane [4] as shown in Fig. 5. The Ga-induced compression of the outer double layer leads to lateral outward relaxation in that layer to relieve the resulting bond angle stress, at least partially. This relaxation changes the atomic lattice constant from 3.8 to 4.1 Å. The observed boundaries between the supercells then arise as a periodic array of misfit dislocations resulting from the incommensurate relationship between substrate (3.8 Å) and surface (4.1 Å) atomic lattice constants [5].

1.2.4. Si(111)$6.3\sqrt{3} \times 6.3\sqrt{3}$—$R30°$–Ga

The $6.3\sqrt{3} \times 6.3\sqrt{3}$—$R30°$ diffraction pattern is observed at the Ga coverage of about 1 monolayer [2, 5, 20]. STM observations did not reveal obvious manifestation of this pattern and it was emphasized that it might arise from subsurface silicon atom reconstructions [20].

1.3. PROPERTIES

1.3.1. Desorption

Ga desorption from the Si(111) surface was studied by Zinke-Allmang and Feldman [22]. Two distinct branches were evidenced at the thermal desorption curves (Fig. 6). The first branch represents the desorption from pure metal Ga islands, the second branch the desorption from the Ga submonolayer on the Si(111) substrate. The desorption parameters (desorption rate K_0 and activation energy E) were found to be $K_0 = 10^{10\pm3}$ s$^{-1}, E = 2.0 \pm 0.3$ eV for 2D layer and $K_0 = 10^{15\pm3}$ s$^{-1}, E = 2.9 \pm 0.3$ eV for Ga islands (Fig. 7).

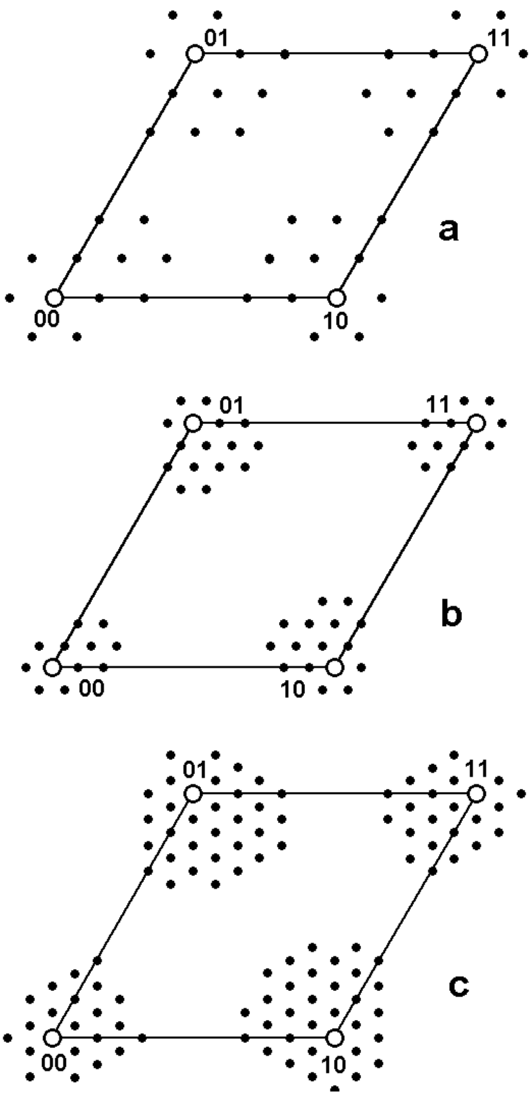

Fig 4. Reciprocal lattices of the (a) 6.3×6.3 structure; (b) 11×11 structure; (c) $6.3\sqrt{3} \times 6.3\sqrt{3}$—$R30^\circ$ structure. The fundamental and fractional order reflections are represented by open and closed circles, respectively (from Ref. [2]). (*Reproduced by permission of the publishers of Japanese Journal of Applied Physics)*

2. (100) ORIENTATION

The ordered surface phases forming in the Ga/Si(100) system are as follows: 2×3, 2×5, 2×2, 8×1, $8 \times n$, 2×1.

2.1. PHASE DIAGRAM

Sakamoto and Kawanami [23] were the first to determine the phase diagram for the Ga/Si(100) system (see Fig. 8). Using the RHEED technique, they found that Ga deposition on to the clean Si(100)2×1 surface from 350 to 680 °C produces sequentially 2×3, 2×5, 2×2, and 8×1 surface structures. They also reported that these serial reconstructions induced by Ga deposition are also observed in the reverse order by Ga re-evaporation from the Ga covered substrate.

In a subsequent LEED–AES study by Bourguignon *et al.* [24], all the above structures were reproduced upon Ga deposition at coverages equal to within ±0.1 ML to the coverages

Table 3. Observed LEED patterns in desorption (T = 840 K) and in deposition ($T \geq 350$ K) (from Ref. [24]).

Observed LEED pattern	Observed coverage θ (ML)*	
	Upon deposition	Upon desorption
Si(100)2×1	≤ 0.1	≤ 0.25 (diffuse)
Si:Ga 3×2	0.15-0.35	—
Si:Ga 5×2	$[\sim 0.4]^{\dagger}$	—
Si:Ga 2×2	0.4–0.55	0.25–0.55
Si:Ga 1×1	—	0.7
Si:Ga 8×1	0.7–0.9	0.75 to ~ 1.5
Incommensurate	—	~ 1.5 to ~ 3
Si:Ga 2×1	≥ 1	≥ 3

* The precision in the indicated coverages below 1 ML is 0.1 ML. † The 5×2 pattern was observed only once. It is also reported in Ref. [23].

reported by Sakamoto and Kawanami for the observation of corresponding RHEED patterns [23]. In addition, the new structure, namely 2×1, was found corresponding to the completion of the monolayer. During thermal desorption, Bourguignon *et al.* [24] detected, at 1.5 to ~ 3 ML, the incommensurate structure for which the LEED pattern is shown in Fig. 9 and the 1×1 structure at 0.7 ML (both structures are not observed upon deposition). However, they did not see the 2×1 structure at 1 ML, as well as the 5×2 and 3×2 structures observed during Ga deposition. The results of the LEED observations of Ref. [24] are summarized in Table 3.

Another question under consideration in Ref. [24] was the growth mode in the Ga/Si(100) system. It was found that the growth mode is drastically affected by the substrate temperature. The Ga/Si Auger peak height ratio *versus* coverage is compatible with a layer-by-layer growth at 25 °C but at higher temperatures a break in the Auger Ga : Si ratio versus time occurs in agreement with a Stranski–Krastanov growth mode. The island formation starts at different coverages depending on temperature, i.e. at 2.5 ML for $T = 60$ °C, at 2 ML for $T = 110$ °C and at 1 ML for $T = 330$ °C (Fig. 10).

In Ref. [25], the results of the LEED observations of the Ga growth on the Si(100) surface held at RT have been presented. The original Si(100)2×1 structure remains visible close to 0.5 ML of Ga and, around 0.75 ML, a faint 2×2 pattern is observed. It is replaced by a

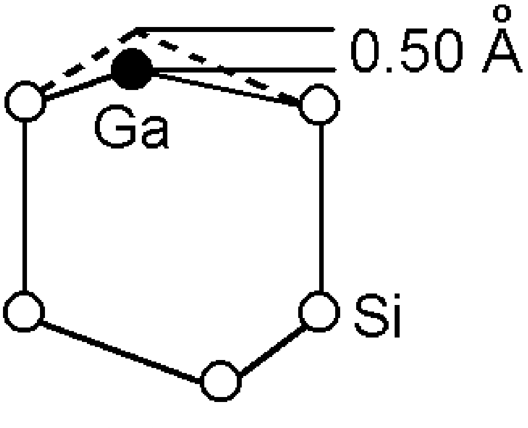

Fig 5. The [1$\bar{1}$0] projection of the (111) planes showing the Ga position at 1 ML coverage (from Ref. [4]). (*Reproduced by permission of American Institute of Physics*)

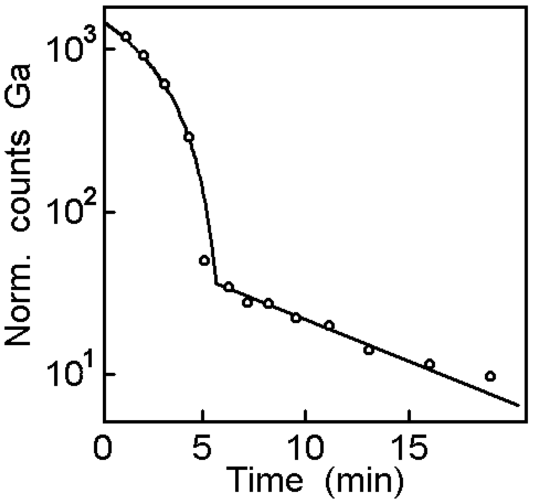

Fig 6. Thermal desorption of 20 ML Ga on Si(111) at 600 °C (from Ref. [22]. (*Reproduced by permission of Elsevier Science Publishers BV)*

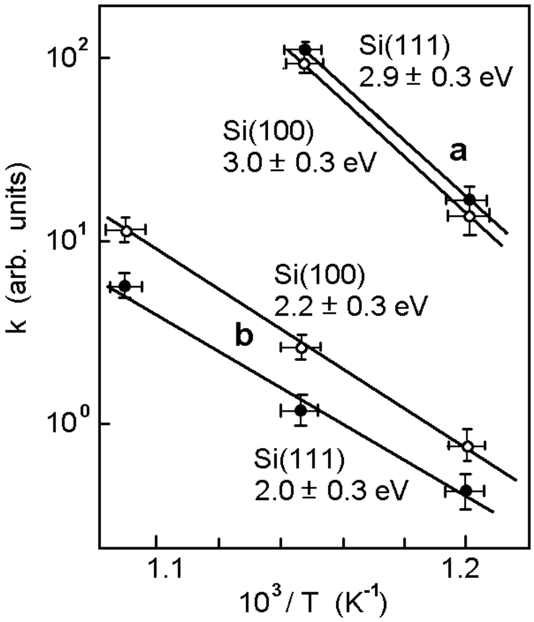

Fig 7. Arrhenius plots for Ga desorption from Si(111) and Si(100). (a) indicates desorption from the islands, (b) indicates desorption from the Ga submonolayer on Si substrate (from Ref. [22]). (*Reproduced by permission of Elsevier Science Publishers BV)*

2 × 1 diagram at 1 ML, which remains observable up to 5 ML. The AES results of Ref. [25] imply the island formation starting from about 1.25 ML in contradiction with conclusion of Ref. [24] about layer-by-layer Ga growth at RT.

2.2. STRUCTURE

2.2.1 Si(100)2 × 3–Ga, Si(100)2 × 5–Ga, Si(100)2 × 2–Ga

Below 0.5 ML Ga, the 2×3, 2×5, and 2×2 phases are detected by LEED [24] and RHEED [23]. In Ref. [24], the structure for these phases was proposed that involved the placement of Ga dimers between the Si dimer rows (Fig. 11). The Ga dimers are aligned in the [011] direction and form rows with two unit cell periodicity along the [0$\bar{1}$1] direction. A three and two unit

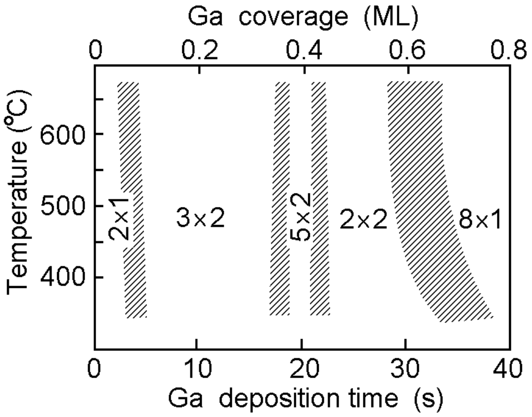

Fig 8. Two-dimensional phase diagram of Ga-induced reconstructions on the Si(100) surface. Hatched areas show transition regions of each neighboring surface structure. Assuming the sticking coefficient to be unity, the Ga coverage corresponding to Ga deposition time is also given (from Ref. [23]). (*Reproduced by permission of Elsevier Science Publishers BV)*

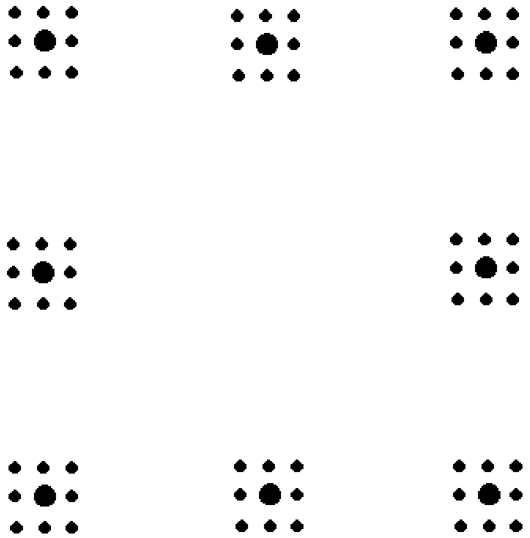

Fig 9. Observed LEED pattern during desorption from Ga multilayer at 840 K and ~ 1.5 ML. Most likely an incommensurate Ga overlayer lies on top of a Si(100)1 × 1 surface, with a Ga/Si lattice size ratio equal to 8/7 (from Ref. [24]). (*Reproduced by permission of Elsevier Science Publishers BV)*

cell spacing between Ga dimer rows defines the periodicity of the 2 × 3 and 2 × 2 phases, respectively. A 2 × 5 phase was believed to arise from an alternation of two and three unit cell spacing along [011] (see Fig. 11). One can see that proposed 2 × 3, 2 × 5, and 2 × 2 structures correspond to 0.33 ML, 0.4 ML and 0.5 ML coverages, respectively, in agreement with phase diagram from Ref. [23] (Fig. 8) and LEED–AES observations of Ref. [24]. The subsequent STM studies [26, 27] provide strong support for the dimer model.

2.2.2. Si(100)8 × 1–Ga, Si(100)8 × *n*–Ga

At coverages above 0.5 ML Ga, LEED [24] and RHEED [23] studies revealed an 8 × 1 reconstruction both upon deposition and upon desorption at 550 °C. An incommensurate phase identified by satellite LEED spots (Fig. 9) was observed, but only upon desorption of higher Ga coverages [24].

In Ref. [27], at coverages between 0.5 and 1 ML the sample exhibited 1/8 LEED satellite spots when prepared at 450 °C. STM observations revealed the presence of an 8 × *n* phase,

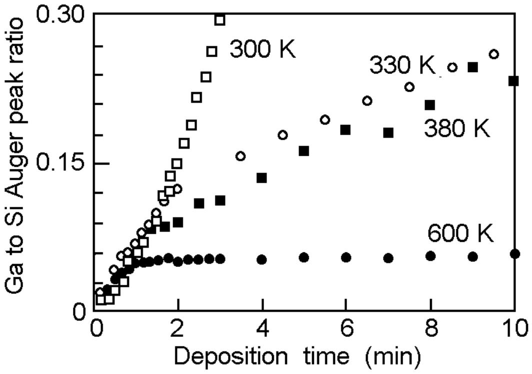

Fig 10. AES Ga (55 eV) to Si (92 eV) peak height ratio versus exposure time for different surface temperatures on Si(100) surfaces. 1 ML corresponds to 0.8 min deposition time of Ga on Si(100) (from Ref. [24]). (*Reproduced by permission of Elsevier Science Publishers BV)*

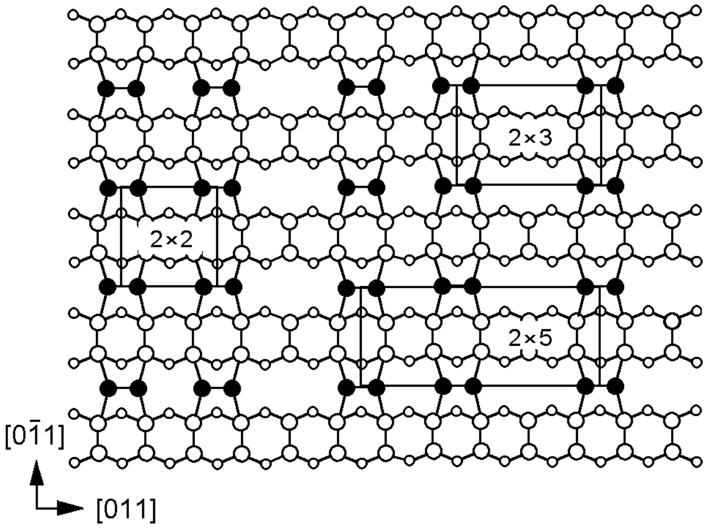

Fig 11. A possible atomic arrangement of 2×2, 2×3, and 2×5 Si(100):Ga phases according to the dimer model of Bourguignon *et al.* (Ref. [24]). (*Reproduced by permission of American Institute of Physics)*

where n usually equals four or five. The detailed nature of the $8 \times n$ phase is not yet known, but does not appear to involve Ga dimers [27].

The correspondence between the $8 \times n$ phase observed by STM and phases detected in LEED studies is unclear.

2.2.3. Si(100)2 × 1–Ga

The 2×1 diffraction pattern is observed for Ga coverage of 1 ML. The authors of Ref. [24] suggested that the structure of the Si(100)2×1–Ga phase is similar to that of the Si(100)2×1–As phase, i.e. Ga dimers forming a monolayer coverage.

2.3. PROPERTIES

Since all Ga surface dangling bonds are satisfied at Ga coverage of 0.5 ML, the Ga bonding should be different for coverages above 0.5 ML. The difference in the nature of chemical bondings is evidenced in the abrupt change of electronic properties and desorption parameters of the Ga/Si(100) system at 0.5 ML coverage.

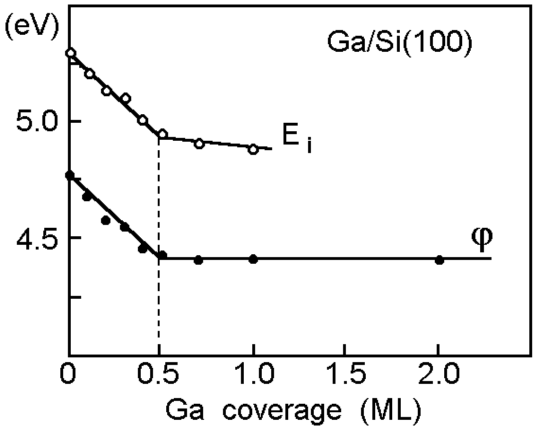

Fig 12. Ionization energy E_i and work function of a Si(100) sample against Ga coverage as deduced from photoemission yield spectra (from Ref. [25]). (*Reproduced by permission of Springer Verlag)*

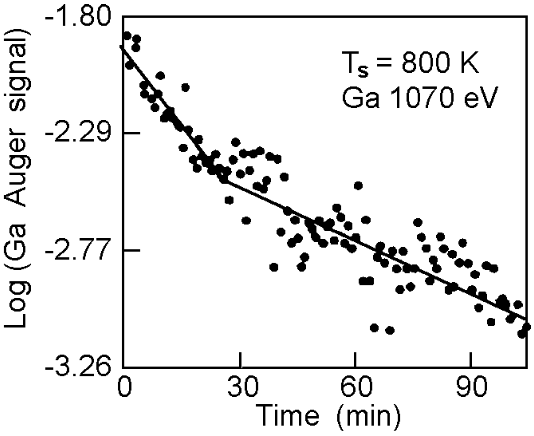

Fig 13. Isothermal desorption of Ga from Si at $T = 630\,^\circ$C: log plot of the Ga 1070 eV Auger peak height versus time. Initial coverage: $\sim$ 0.9 ML. The lines indicate the results of least-squares fit. The break occurs at 0.5 ML (from Ref. [28]). (*Reproduced by permission of Elsevier Science Publishers BV)*

2.3.1. Electronic Properties

In Ref. [25], the results of the study of the Ga/Si(100) system by means of photoemission yield spectroscopy (PYS) have been reported. From the PYS spectra the ionization energy E_i and work function Φ of a Ga covered Si(100) sample were deduced as a function of Ga coverage (see Fig. 12). Both Φ and E_i decrease linearly, in parallel, with Ga coverage up to 0.5 ML and then become roughly constant.

2.3.2. Desorption

Bourguignon *et al.* [28] using LEED and AES detected three different kinetic regimes in isothermal desorption experiments at temperatures from 530 to 630 °C. These different regimes correlate with the Ga coverage and surface structures. Between 0 and 0.5 ML, first-order desorption from a Si(100)2 × 2–Ga phase is observed with desorption energy of 2.9 eV. The desorption energy decreases to 2.3 eV for the Si(100)8 × 1–Ga phase where desorption is observed between 0.5 and 1 ML also following first-order kinetics (Fig. 13). Above 1 ML, zero-order desorption from Ga islands on top of an ordered Ga monolayer is observed. The measured pre-exponential factors and desorption energies for three kinetic regimes are summarized in Table 4.

Table 4. Measured pre-exponential factors and desorption energies for the desorption of Ga from Si(100)(Ref. [28]).

Coverage θ (ML)	Desorption energy (eV)	Pre-exponential factor
≥ 1	2.61 ± 0.07	$(4 \pm 3) \times 10^{13}$ ML$\cdot$ s^{-1}
$0.5 \leq \theta \leq 1$	2.3 ± 0.2	$8 \times 10^{12\pm1.2}$ s^{-1}
$0 \leq \theta \leq 0.5$	2.9 ± 0.2	$3 \times 10^{16\pm1}$ s^{-1}

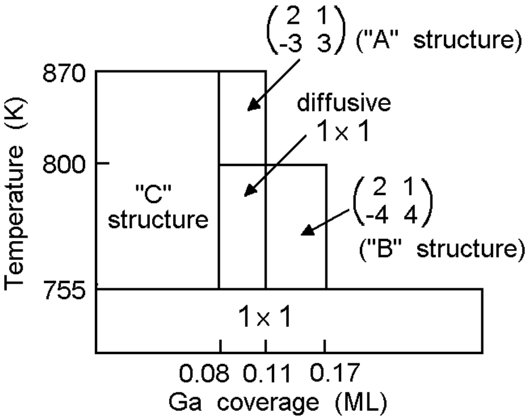

Fig 14. Phase diagram of the structures of the Ga/Si(110) system (from Ref. [31]). (*Reproduced by permission of Elsevier Science Publishers BV)*

Other desorption studies of the Ga/Si(100) system are are Rutherford backscattering study by Zinke-Allmang and Feldman [22] and investigation by Carleton *et al.* using laser-induced fluorescence in temperature programmed desorption [29,30]. The desorption energy value of 2.9 eV between 0 and 0.5 ML determined in Refs [29,30] is in excellent agreement with that reported by Bourguignon *et al.* [28]. Another recent measurement [22] of the desorption energy is 2.2 ± 0.3 eV for Ga submonolayer film and 3.0 ± 0.3 eV for Ga islands (Fig. 7). The value of Ref. [22] for islands (3.0 eV) is closer to the desorption energy from liquid Ga (2.9 eV) than that of Ref. [28] (2.6 eV). Another discrepancy between these two works is that the desorption energy of 2.2 eV determined by Zinke-Allmang and Feldman [22] is in close agreement with the measurement by Bourguignon *et al.* [28] for the 0.5 to 1 ML coverage range, while the timescale of the experiments of Ref. [22] suggested that the faster desorption between 0.5 and 1 ML could not be observed, and therefore one would rather expect a value closer to 2.9 eV determined in Ref. [28] for the 0–0.5 ML range.

3. (110) ORIENTATION

Two well-ordered reconstructions, $\begin{pmatrix} 2 & 1 \\ -3 & 3 \end{pmatrix}$ and $\begin{pmatrix} 2 & 1 \\ -4 & 4 \end{pmatrix}$, and a less defined one with eighths periodicity along [100] were observed in the Ga/Si(110) system.

3.1. PHASE DIAGRAM

The adsorption of the Ga on Si(110) surface was studied by Sakama and Kawazu [31] by means of QMS, AES, and LEED. The results of this study are summarized in the phase diagram of Fig. 14.

The QMS and AES data revealed the formation of three phases (labeled by the authors as α, β, and γ phases). The α and β phases were found to be two-dimensional ones with

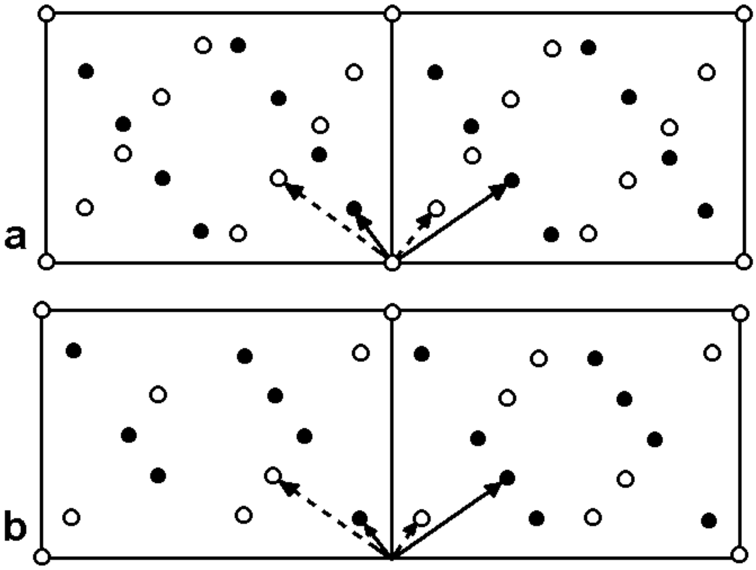

Fig 15. Schematic LEED images (reciprocal lattices) of the reconstructions observed in the Ga/Si(110) system: (a) the $\begin{pmatrix} 2 & 1 \\ -3 & 3 \end{pmatrix}$ reconstruction ("A" pattern) with unit vectors $\mathbf{a}_\mathrm{s}^* = \frac{1}{3}\mathbf{a}^* + \frac{1}{3}\mathbf{b}^*$ and $\mathbf{b}_\mathrm{s}^* = \frac{1}{9}\mathbf{a}^* + \frac{2}{9}\mathbf{b}^*$; (b) the $\begin{pmatrix} 2 & 1 \\ -4 & 4 \end{pmatrix}$ reconstruction ("B" pattern) with unit vectors $\mathbf{a}_\mathrm{s}^* = \frac{1}{3}\mathbf{a}^* + \frac{1}{3}\mathbf{b}^*$ and $\mathbf{b}_\mathrm{s}^* = \frac{1}{12}\mathbf{a}^* + \frac{1}{6}\mathbf{b}^*$. Here $\mathbf{a}^*$ and $\mathbf{b}^*$ are two-dimensional reciprocal lattice vectors of the bulk structure. Open circles (indicating diffraction spots) and solid lines (indicating the unit vectors of a surface superlattice) denote one domain. Filled circles and dashed lines denote the other. The contour indicate the two unit cells of the bulk pattern (from Ref. [31]). (*Reproduced by permission of Elsevier Science Publishers BV)*

saturation coverages of 0.11 and 0.17 ML, respectively, while the γ phase corresponds to the Ga three-dimensional islands.

Above 600 °C, no Ga adsorption occurs. At temperatures ranging from 530 to 600 °C, only α phase exists. At 480–530 °C, the α and β phases exist. The growth of Ga islands (γ phase) takes place only below 480 °C.

LEED observations revealed that α and β phases produce the LEED patterns which are shown schematically in Fig. 15. These patterns were labeled by Sakama and Kawazu as "A" pattern and "B" pattern and correspond to the $\begin{pmatrix} 2 & 1 \\ -3 & 3 \end{pmatrix}$ and $\begin{pmatrix} 2 & 1 \\ -4 & 4 \end{pmatrix}$ reconstructions, respectively. Both structures have their own two domains which are symmetrical with each other with respect to the $(\bar{1}10)$ plane.

At 480–600 °C, another "C" pattern with one-eighth the periodicity of the bulk structure along [100] is observed when Ga coverage is below 0.08 ML. However, the "C" pattern accompanies a high background, so that the surface structure is not well defined. At 480–530 °C, a diffusive 1 × 1 pattern is observed at coverage of about 0.1 ML, where the "A" pattern emerges at 530–600 °C. Below 480 °C, the fractional order reflections are weakened, which results in a 1 × 1 LEED pattern with a high background.

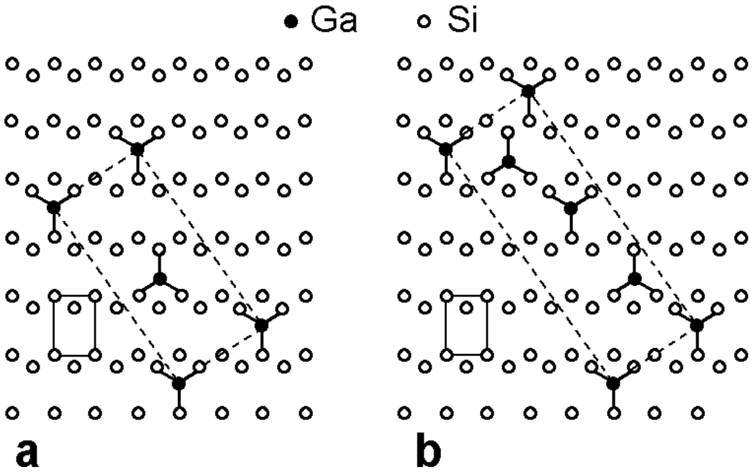

Fig 16. Configuration models of (a) the $\begin{pmatrix} 2 & 1 \\ -3 & 3 \end{pmatrix}$ structure and (b) $\begin{pmatrix} 2 & 1 \\ -4 & 4 \end{pmatrix}$ structure. Fine solid lines and dashed lines denote the unit cell of the bulk and the Ga overlayer, respectively. Heavy solid lines denote bonds between Si and Ga atoms (from Ref. [31]). (*Reproduced by permission of Elsevier Science Publishers BV)*

3.2. STRUCTURE

3.2.1. Si(110)$\begin{pmatrix} 2 & 1 \\ -3 & 3 \end{pmatrix}$ and Si(110)$\begin{pmatrix} 2 & 1 \\ -4 & 4 \end{pmatrix}$

In Ref. [31], Sakama and Kawazu proposed the possible configuration models of the Si(110)$\begin{pmatrix} 2 & 1 \\ -3 & 3 \end{pmatrix}$–Ga and Si(110)$\begin{pmatrix} 2 & 1 \\ -4 & 4 \end{pmatrix}$–Ga structures which are shown in Fig. 16.

According to the model (see Fig. 16(a)), a unit cell of the $\begin{pmatrix} 2 & 1 \\ -3 & 3 \end{pmatrix}$ structure contains two Ga atoms. Thus, the resultant Ga coverage of the model of 1/9 ML is in agreement with the experimental value (0.11 ML). Each Ga atom is considered to combine with three surface Si atoms. Accordingly, six dangling bonds (i.e. 1/3 of the total bonds) are saturated by Ga adsorption.

A unit cell of the $\begin{pmatrix} 2 & 1 \\ -4 & 4 \end{pmatrix}$ structure is assumed to contain four Ga atoms (see Fig. 16(b)). So about 50% of the total of dangling bonds are saturated on average. The model corresponds to the Ga coverage of 1/6 ML which is consistent with the experimentally determined value of 0.17 ML.

3.3. PROPERTIES

3.3.1. Desorption

From the QMS data, the desorption energies of Ga from the α phase (the $\begin{pmatrix} 2 & 1 \\ -3 & 3 \end{pmatrix}$ structure) and the β phase (the $\begin{pmatrix} 2 & 1 \\ -4 & 4 \end{pmatrix}$ structure) were calculated in Ref. [31] as 2.4 and 2.3 eV, respectively, assuming that the desorption process obeys first-order kinetics.

REFERENCES

[1] D. Bolmont, P. Chen, C. A. Sebenne and F. Proix, *Surf. Sci.* **137** (1984) 280.

[2] M Otsuka and T. Ichikawa, *Japan J. Appl. Phys.* **24** (1985) 1103.

[3] J. Zegenhagen, J. R. Patel, P. E. Freeland, D. M. Chen, J. A. Golovchenko, P. Bedrossian and J. E. Northrup, *Phys. Rev. B* **39** (1989) 1298.

[4] J. R. Patel, J. Zegenhagen, P. E. Freeland, M. S. Hybertsen, J. A. Golovchenko and D. M. Chen, *J. Vac. Sci. Technol. B* **7** (1989) 894.

[5] P. Bedrossian, K. Mortensen, D. M. Chen and J. A. Golovchenko, *Nucl. Instrum. Meth. Phys. Res. B* **48** (1990) 296.

[6] S. Park, J. Nogami and C. F. Quate, *J. Microscopy* **152** (1988) 727.

[7] J. Zegenhagen, *Phys. Scripta T.* **39** (1991) 328.

[8] A. Kawazu, I. Yokohama, H. Suzuki, A. Ohsaki, K. Takeuchi and H. Sakama, *Phys. Rev. B* **36** (1987) 9809.

[9] A. Kawazu and H. Sakama, *Phys. Rev. B* **37** (1988) 2704.

[10] T. Kinoshita, S. Kono and T. Sagawa, *Solid State Commun.* **56** (1985) 681.

[11] J. M. Nicholls, B. Reihl and J. E. Northrup, *Phys. Rev. B* **35** (1987) 4137.

[12] K. Higashiyama, T. Kinoshita, T. Miyahara, H. Kato, S. Kono, H. Ohsawa, Y. Enta, F. Maeda and Y. Yaegashi, *Surf. Sci.* **186** (1987) L568.

[13] S. Fahy and D. R. Hamann, *Phys. Rev. B* **41** (1990) 7587.

[14] M. Chester and T. Gustafsson, *Surf. Sci.* **264** (1992) 33.

[15] T. Thundat, S. M. Mohapatra, B. N. Dev, W. M. Gibson and T. P. Das, *J. Vac. Sci. Technol. A* **6** (1988) 681.

[16] J. E. Northrup, *Phys. Rev. B* **37** (1988) 8513.

[17] J. M. Micart, J. Rubio and F. Illas, *Phys. Rev. B* **42** (1990) 5212.

[18] J. Nogami, S. Park and C. F. Quate, *Surf. Sci.* **203** (1988) L631.

[19] I. -W. Lyo, E. Kaxiras and Ph. Avouris, *Phys. Rev. Lett.* **63** (1989) 1261.

[20] D. M. Chen, J. A. Golovchenko, P. J. Bedrossian and K. Mortensen, *Phys. Rev. Lett.* **61** (1988) 2867.

[21] J. Zegenhagen, M. S. Hybertsen, P. E. Freeland and J. R. Patel, *Phys. Rev. B* **38** (1988) 7885.

[22] M. Zinke-Allmang and L. C. Feldman, *Surf. Sci.* **191** (1987) L749.

[23] T. Sakamoto and H. Kawanami, *Surf. Sci.* **111** (1981) 177.

[24] B. Bourguignon, K. L. Carleton and S. R. Leone, *Surf. Sci.* **204** (1988) 455.

[25] I. Andriamanantenasoa, J. -P. Lacharme and C. A. Sebenne, *Springer Series in Surface Science* **11** (1988) 363.

[26] J. Nogami, S. Park and C. F. Quate, *Appl. Phys. Lett.* **53** (1988) 2086.

[27] A. A. Baski, J. Nogami and C. F. Quate, *J. Vac. Sci. Technol. A* **8** (1990) 245.

[28] B. Bourguignon, R. V. Smilgys and S. R. Leone, *Surf. Sci.* **204** (1988) 473.

[29] K. L. Carleton and S. R. Leone, *J. Vac. Sci. Technol. B* **5** (1987) 1141.

[30] K. L. Carleton, B. Bourguignon and S. R. Leone, *Surf. Sci.* **199** (1988) 447.

[31] H. Sakama and A. Kawazu, *Appl. Surf. Sci.* **60–61** (1992) 159.

(Gd)

GADOLINIUM

1. (111) ORIENTATION

The 2×2 reconstruction is observed at approximately 1 ML Gd coverage, while the thicker Gd silicide phases display a 1×1 or $\sqrt{3} \times \sqrt{3}$—$R30^\circ$ structure depending on heat treatment.

1.1. PHASE DIAGRAM

1.1.1. RT and LNT Growth

Lindau *et al.* studied the growth of Gd on a cleaved Si(111) 2×1 surface at RT [1–3] and LNT (liquid nitrogen temperature, 80 K) [3]. It was found that, at Gd coverages from 0.5 to 2.0 ML (1 ML = 2.6 Å), the growth mode is identical at both temperatures involving the reaction with the intermixing of Gd and Si. Conversely, for coverages higher than 2 ML, the strong intermixing between Si and Gd observed at RT is suppressed in the LNT growth. The simple warming up to RT of the Gd/Si(111) interface formed at LNT does not recover the intermixing indicating that the reactivity of the Gd atom on an outer Si surface (or on a reacted Gd/Si layer) is much higher compared to the reactivity of the same atom at a buried interface [3].

The RT formation of the Gd/Si(111)7×7 interface [4, 5] coincides basically with the RT growth of Si on Si(111)2×1. The reaction disrupting the Si(111) surface starts at the early stages of Gd deposition. The 7×7 LEED pattern is replaced by a 1×1 pattern at about 0.4 ML. The 1×1reconstructed surface, in turn, becomes disordered beyond around 1 ML. The width of the reacted Gd/Si(111) interface is approximately 10 Å. The Gd metal layer is formed at thicknesses beyond 25 Å.

1.1.2. HT Growth

The evolution of the RT deposited Gd/Si(111) interface upon annealing was studied by Hofmann and Netzer [5] and Henle *et al.* [6]. In the latter work, the phase diagram of the Gd/Si(111) system was presented (see Fig. 1).

The thermal behavior of the interface was found to be a sensitive factor of the initial Gd coverage. At Gd coverage of about 1 ML, Gd surface concentration remains unchanged up to about 600–650 °C and a 2×2 structure is formed between 300–600 °C [6]. For higher Gd coverages (> 6 Å), a Gd surface concentration reduces at about 150–200 °C indicating the conversion of the Gd-rich reacted RT interface to a Gd disilicide type phase with $\mathrm{GdSi}_{1.7}$ stoichiometry. Simultaneously, the annealing induces the structural ordering of the disordered

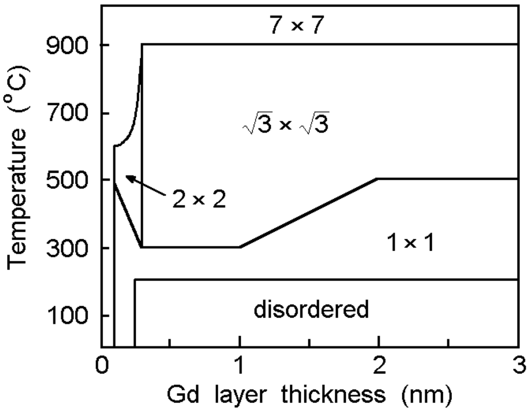

Fig 1. Phase diagram of the Gd/Si(111) system. In the experiment, the Gd/Si(111) interface formed at RT is annealed at higher temperatures (from Ref. [6]). (Reprinted from W. A. Henle et al. *Solid State Communications*, 71, 657. Copyright © 1989, with kind permission from Pergamon Press Ltd, Headington Hill Hall, Oxford OX3 OBW, UK)

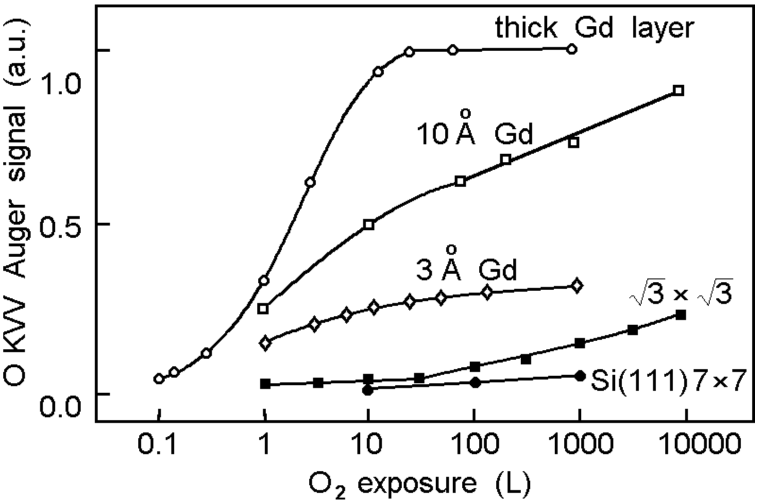

Fig 2. Oxygen uptake of various surfaces and interfaces as a function of O_2 exposure. The normalized O–KLL AES amplitude is plotted versus O_2 exposure for the clean Si(111)7 × 7 surface, the $\sqrt{3} \times \sqrt{3}$ phase of Gd disilicide, the 3- and 10-Å thick RT Gd/Si(111) interfaces and for a polycrystalline Gd film surface (from Ref. [7]). (*Reproduced by permission of the publishers of Journal of Physical Review B)*

RT Gd deposit. As a result, the ordered 1 × 1 and $\sqrt{3} \times \sqrt{3}$—$R30°$ structures are observed sequentially with the rise in temperature [5,6].

At about 800 °C the Gd content on the surface decreases rapidly and the 7 × 7 structure is restored. The 7 × 7 LEED pattern becomes brilliant after heating at temperatures above 850 °C, but the traces of Gd on the surface are still detectable by AES [6].

1.2. PROPERTIES

1.2.1. Oxidation

The interaction of various Gd/Si(111) interfaces with oxygen at RT was investigated by Henle *et al.* in Ref. [7]. It was shown that the RT deposited Gd film substantially enhances the oxidation of Si substrate and the oxidation rate increases with Gd coverage, as one can see in Fig. 2.

The reactivity of the ordered Gd disilicide layers, which are formed after annealing of the

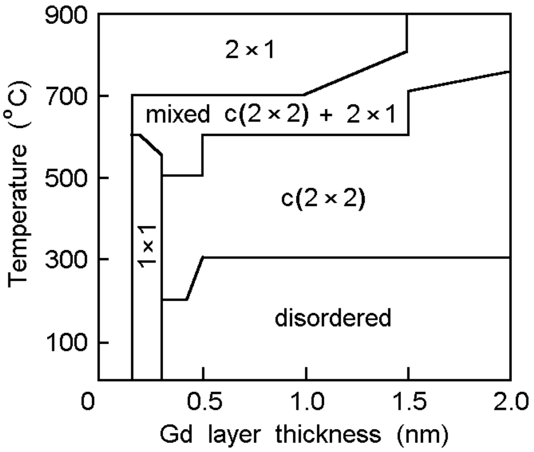

Fig 3. Phase diagram of the Gd/Si(100) system indicated the regions of stability of ordered LEED structures. In the experiment, the Gd/Si(100) interface formed at RT is annealed at higher temperatures (from Ref. [8]). (*Reproduced by permission of Elsevier Science Publishers BV)*

RT Gd/Si(111) interface, is much lower compared to that of the RT interface. An induction period was found to be necessary to initiate the reaction of O_2 with the epitaxial Gd disilicide surface (see Fig. 2).

2. (100) ORIENTATION

A 1×1 structure is observed at low coverages for the Gd/Si(100) system, while the Gd silicide layer displays a $c(2 \times 2)$ reconstruction.

2. 1. PHASE DIAGRAM

2.1.1. RT Growth

Upon RT deposition of Gd, the onset of reaction is detected at about 0.5 ML coverage (1 ML = 2.2 Å Gd). Strong intermixing of Gd and Si sets in at about 1 ML coverage and the first reacted Gd–Si phase is formed. The 2×1 LEED pattern converts into a 1×1 pattern. The first phase is then replaced by the second reacted phase which is considered to be a disordered Gd rich silicide type compound (while the first phase appears to be chemically inhomogeneous). The Gd layer becomes metallic after deposition of 35–40 Å Gd [8].

2.1.2. HT Growth

The thermal evolution of the Gd/Si(100) interface formed at RT was studied by Henle *et al.* [8]. The results of this study are summarized in the phase diagram shown in Fig. 3.

It was found that, for Gd coverages beyond about 5 Å, an ordered $c(2 \times 2)$ structure is observed between $\simeq$ 300–600 °C. It should be mentioned that the LEED pattern of the $c(2 \times 2)$ phase is not well-developed indicating a rather poor long-range order. The formation of the $c(2 \times 2)$ structure is considered to indicate a transition from the Gd-rich layer formed at RT to an ordered Si-rich compound at elevated temperatures. An evaluation of the AES data yields a $GdSi_{2.2 \pm 0.2}$ stoichiometry for the $c(2 \times 2)$ phase.

At low coverages, a 1×1 structure is detected up to 600 °C, but, at temperatures beyond 600 °C, the mixed $c(2 \times 2) + 2 \times 1$ LEED pattern is seen indicating (together with the drop in the Gd AES intensity) the decomposition of the Gd–silicide phase.

Finally, heating to 1000 °C restores the 2 × 1 LEED pattern, but AES reveals traces of Gd which are left at the surface and cannot be removed completely by heat treatment.

REFERENCES

[1] C. Carbone, J. Nogami and I. Lindau, *J. Vac. Sci. Technol. A* **3** (1985) 972.
[2] E. Puppin, J. Nogami, C. Carbone, Z. X. Shen, I. Lindau, B. B. Pate, I. Abbati and L. Braicovich, *J. Vac. Sci. Technol. A* **5** (1987) 1083.
[3] E. Puppin and I. Lindau, *Solid State Commun.* **71** (1989) 1015.
[4] W. A. Henle, F. P. Netzer, R. Cimino and W. Braun, *Surf. Sci.* **221** (1989) 131.
[5] R. Hofmann and F. P. Netzer, *Phys. Rev. B* **43** (1991) 9720.
[6] W. A. Henle, M. G. Ramsey, F. P. Netzer, R. Cimino and W. Braun, *Solid State Commun.* **71** (1989) 657.
[7] W. A. Henle, M. G. Ramsey, F. P. Netzer, R. Cimino, W. Braun and S. Witzel, *Phys. Rev. B* **42** (1990) 11073.
[8] W. A. Henle, M. G. Ramsey, F. P. Netzer and S. Witzel, *Surf. Sci.* **243** (1991) 141.

(Ge)

GERMANIUM

1. (111) ORIENTATION

The ordered $\sqrt{3} \times \sqrt{3}$—$R30^\circ$, 7×7, 5×5, and 1×1 surface reconstructions are detected for the Ge/Si(111) system at relatively low Ge coverages (or high temperatures). In rather thick Ge films grown on Si(111) at relatively low temperatures, $c(2 \times 8)$, $c(2 \times 4)$, and 2×2 reconstructions known for bulk Ge(111) can be obtained.

1.1. PHASE DIAGRAM

1.1.1. RT Growth

Chen *et al.* [1] showed that, upon RT deposition of Ge on to the cleaved Si(111)2×1 surface, a well-ordered $\sqrt{3} \times \sqrt{3}$—$R30^\circ$ reconstruction develops at about 1/3 ML Ge coverage. This reconstruction persists at 2/3 ML before transforming into a 1×1 LEED pattern which fades into increasing background at Ge coverages beyond 1 ML. The LEED diffraction spots vanish utterly at about 2 ML [1]. It should be noted that $\sqrt{3} \times \sqrt{3}$—$R30^\circ$-Ge superstructure is not formed at the clean Si(111)7×7 surface neither at room temperature nor at higher temperatures [2, 3]. LEED observations of RT growth of Ge on the Si(111)7×7 surface revealed that initial 7×7 reconstruction transforms into a diffuse 1×1 LEED pattern at about 0.5 ML Ge coverage and LEED spots disappear completely at about 2 ML [4–6]. The RT growth of Ge is assumed to proceed through the formation of an amorphous Si layer of uniform coverage without evidence of islanding and intermixing with Si(111) substrate [6–11].

1.1.2. HT Growth

The 7×7, 5×5, and 1×1 reconstructions are conventionally observed in the Ge/Si(111) interface upon one of the following heat treatments:

(1) annealing a Si(111) sample upon which Ge was deposited at low temperatures;
(2) Ge deposition on to the Si(111) substrate held at elevated temperatures;
(3) codeposition of Si and Ge on to the Si(111) surface, again at elevated temperatures.

The less conventional procedure to produce a 5×5 structure was used in Refs [12, 13]. It involved sputtering of deposited thick Ge film with subsequent annealing.

Figures 1–3 show phase diagrams for (1) and (2) preparation procedures. Figure 1 shows phase diagrams of surface reconstructions in a Ge layer on Si(111) observed *during annealing*, i.e. Ge was deposited at low temperature, then temperature was gradually elevated with surface structure being simultaneously monitored by RHEED. The phase diagram at Fig. 1(a) was built by Lamin *et al.* [14] and that in Fig. 1(b) is taken from the work of Kajiyama *et*

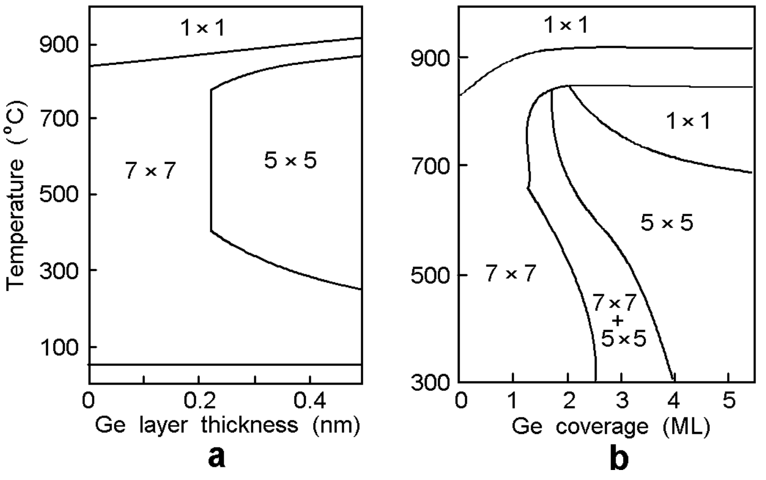

Fig 1. Phase diagram of the reconstruction observed by RHEED *during annealing* of Ge-coated Si(111). The coverage on the abscissa is the amount of Ge deposited on the Si(111) 7 × 7 surface at (a) room temperature (from Ref. [14]) and (b) at 350 °C (from Ref. [15]). In the original figure of Ref. [14], the amount of deposited Ge is given in the thickness units (nm). It can be converted into the coverage units (ML) using $d = 1.77$ Å for the average thickness of a Ge atomic layer in the [111] direction. (*Reproduced by permission of Elsevier Science Publishers BV)*

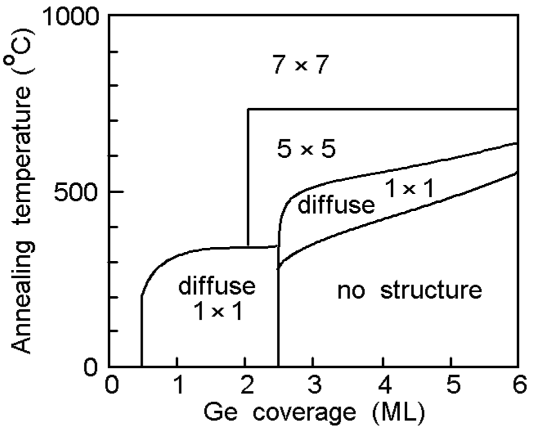

Fig 2. Phase diagram of the reconstruction observed *after annealing* of Ge-coated Si(111). The coverage shows that before annealing, Ge was evaporated at room temperature (from Ref. [4]). (*Reproduced by permission of the publishers of Japanese Journal of Applied Physics)*

al. [15]. One can see that the diagrams shown are in reasonable agreement with each other. The difference in certain details are believed to be connected with the fact that surface reconstructions observed are unstable at elevated temperatures due to the desorption/diffusion of Ge atoms from the Si surface. Therefore, the features of the phase diagram are affected by such experimental parameters as a rate of temperature growth and duration of annealing which might be different in these works.

Figure 2 shows the phase diagram of the reconstructions observed by LEED *after annealing* (as reported by Shoji *et al.* [4]). This diagram is in excellent agreement with the more recent RHEED data of Maree *et al.* [16].

The phase diagram of the surface structures observed during epitaxial Ge growth on Si(111) (taken from Ref. [14]) is shown in Fig. 3. In this set of experiments, the Ge layer growth with *in situ* RHEED observation was carried out at constant temperature, Ge being deposited at a rate of 4×10^{-2} nm s^{-1}. The diagram includes the data on the formation of the relatively thick Ge films also.

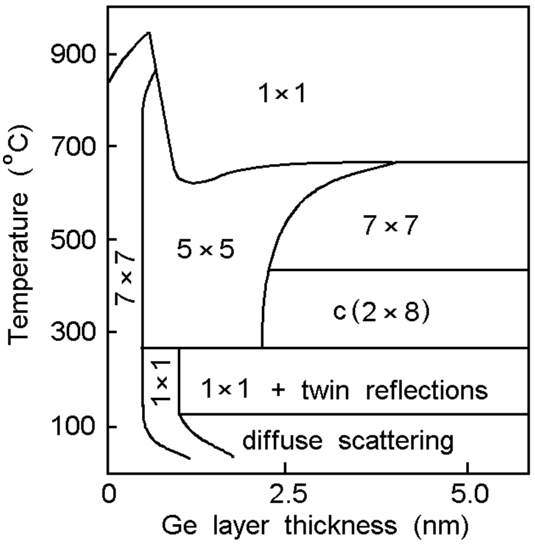

Fig 3. Phase diagram of the surface reconstructions observed by RHEED during epitaxial Ge growth on Si(111). Deposition rate of Ge is 4×10^{-2} nm s^{-1} (from Ref. [14]). (*Reproduced by permission of the publishers of Journal of Physical Review B)*

The general behavior of the Ge layer on Si(111) upon heating can be summarized as follows: Ge growth on Si(111)7 × 7 proceeds in a Stranski–Krastanov mode, where three-dimensional islands grow after about 2–4 ML of Ge [15–20]. The Si(111)7 × 7–Ge structure forms at about 1 ML of Ge. This 7 × 7 structure transforms reversibly upon heating to 1 × 1 structure. The temperature of the reversible $7 \times 7 \longleftrightarrow 1 \times 1$ transition rises as the Ge coverage increases from 830 °C for the clean Si(111)7 × 7 surface to 920–950 °C for Si(111) surface covered with 1–3 ML of Ge [14, 15, 21]. At around 2 ML Ge coverage, the 5 × 5 structure is formed [4, 15, 16, 20].

The 3D islands forming atop the 2D layer show a mixture of $c(2 \times 8)$, $c(2 \times 4)$ and 2×2 reconstructions (known for bulk Ge(111)), when they are grown below 450 °C [22]. At higher deposition temperature, 7 × 7 reconstruction reappears on top of the 3D islands [14, 22, 23]. This result found a different interpretation in Refs [14, 23]. Gossmann *et al.* [23] related the reappearance of the 7 × 7 reconstruction to the residual lateral compressive stress in the Ge layer, whereas Lamin *et al.* [14] suggested Si segregation to the surface. McRae and Malic [13] and Hasegawa *et al.* [24] reported that this 7 × 7 reconstruction transforms reversibly to 1 × 1 structure at about 600 °C. The LEED characterization of the high-temperature 1 × 1 phase revealed the presence of diffuse spots near a $\sqrt{3} \times \sqrt{3}$ position [24].

1.2. STRUCTURE

1.2.1. Si(111)7 × 7–Ge

The 7 × 7–Ge is stabilized for a Ge coverage below 1–1.5 ML [21, 25, 26] or according to Ref. [26] for a $\mathrm{Ge}_x\mathrm{Si}_{1-x}$ alloy with x up to 0.24.

The qualitative similarity in LEED curves [27, 28] and electronic properties [26, 29] of Si(111)7 × 7–Ge and the clean Si(111)7 × 7 surfaces suggests that the Ge atoms adsorb while almost keeping the same arrangement of the substrate atoms. Comprehensive transmission electron diffraction investigation of Ref. [25] revealed that the 7 × 7–Ge surface has the DAS (dimer–adatom stacking fault) structure [30] in which Ge atoms randomly substitute the sites of Si atoms. The substitutional model is supported by total energy calculations [31] and by the results of the EELS study which shows that the Si dangling bonds are replaced in

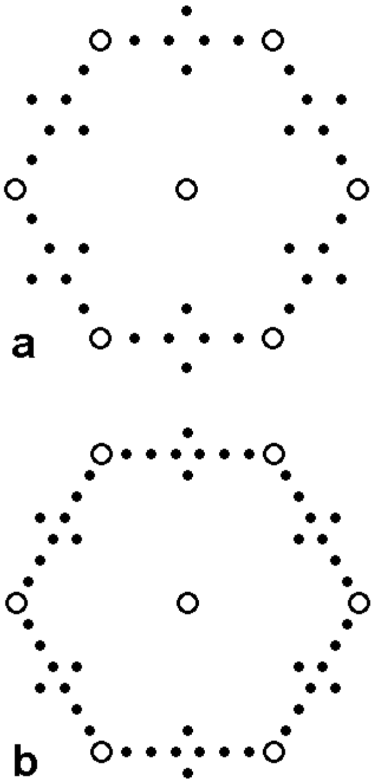

Fig 4. (a) The sketch of the Si(111)5 × 5–Ge LEED pattern in comparison with that of the Si(111)7 × 7 pattern (from Ref. [18]). (*Reproduced by permission of Elsevier Science Publishers BV)*

7 × 7–Ge by those of Ge and that no Ge–Ge bonds are observed [27].

1.2.2. Si(111)5 × 5–Ge

The 5 × 5–Ge structure (Fig. 4) corresponds nominally to Ge coverage of 2 ML [25] or $Ge_{0.5}Si_{0.5}$ alloy [12, 13, 32] but it is observed on surfaces with a Ge content estimated to be 30–70 % of a homogeneous alloy overlayer or 1.3–3.0 ML of Ge on the Si surface [7, 21, 26, 29].

The 5 × 5–Ge surface was found to be similar to the clean Si(111)7 × 7 surface since it was found through a careful inspection of the intensity distribution of the LEED patterns at different primary beam energies [4, 33] as well as from the photoemission results [34]. The TED [25, 35], XSW [36], and STM [22, 37, 38] data supported the DAS model of the 5 × 5–Ge surface shown in Fig. 5. Particularly, the TED analysis revealed that the sites for adatoms and atoms in the stacking-fault layer are occupied preferentially by Ge. Since the 5 × 5–Ge structure is formed at about 2 ML coverage (that is greater than the coverage of the Ge atoms in the adatom and the stacking-fault layer of the DAS model), the dimer layer and the underlying layers should also be occupied partially by Ge atoms [25].

The 5 × 5 reconstruction is considered to be driven by lateral compressive stress presented in mixed Si–Ge, due to 4% lattice mismatch between the elemental constituents [12, 14, 21, 34, 39].

1.2.3. Si(111)$\sqrt{3} \times \sqrt{3}$–Ge

The $\sqrt{3} \times \sqrt{3}$–Ge structure has been studied much less than the 7 × 7–Ge and 5 × 5–Ge reconstructions (moreover, the observation of the $\sqrt{3} \times \sqrt{3}$ structure upon RT deposition of (0.3–1.0) ML Ge on to Si(111)2 × 1 was only reported in Ref. [1]).

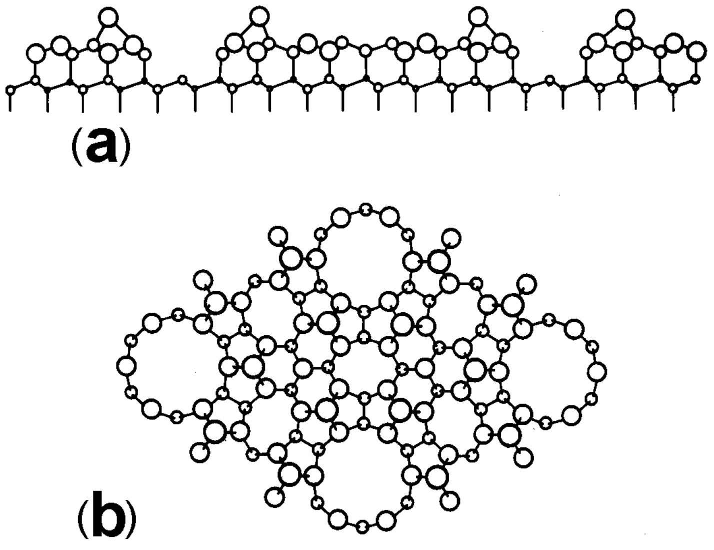

Fig 5. DAS model of the Si(111)5 × 5–Ge structure: (a) profile view and (b) plan-view (from Ref. [25]). (*Reproduced by permission of Elsevier Science Publishers BV)*

The authors of Ref. [1] tentatively suggested that the $\sqrt{3} \times \sqrt{3}$ structure at 1/3 ML Ge coverage corresponds to the residing Ge adatoms in H_3 sites with one Ge atom in the $\sqrt{3} \times \sqrt{3}$ unit cell as shown in Fig. 6(a). The model proposed for the $\sqrt{3} \times \sqrt{3}$ structure at 2/3 ML Ge also uses the H_3 positions, but the $\sqrt{3} \times \sqrt{3}$ unit cell contains two Ge atoms, thus, a honeycomb-like structure is formed (see Fig. 6(b)).

In contrast to the above suggestions, the total energy calculations of Zhang *et al.* [31] favor the model in which Ge adatoms are grouped in trimers. The $\sqrt{3} \times \sqrt{3}$ structure of this type contains three Ge atoms in the $\sqrt{3} \times \sqrt{3}$ unit cell and can persist up to 1 ML. This reconstruction is identical to that known for the Si(111)$\sqrt{3} \times \sqrt{3}$–Sb (1 ML Sb) surface phase.

1.3. PROPERTIES

1.3.1. Electronic Properties

Both the Si(111)7 × 7–Ge and Si(111)5 × 5–Ge surfaces were found to be metallic, while the Ge(111)$c(2 \times 8)$ surface of clean Ge(111) grain or of the thick Ge film grown on Si(111) is known to be semiconducting [34, 40].

1.3.2. Electromigration

Yasunaga [41] and Yamaguchi *et al.* [42] reported that Ge exhibits a preferential movement towards the cathode when the Si(111) sample with a Ge patch is heated by a direct current (d.c.) of about 100 A/cm^2 to a temperature of 600–700 °C. The unusual feature of the electromigration lies in the fact that the directional movement takes place only in the initial period of the d.c. power supply, although the isotropic surface diffusion lasts longer [41]. The combined RHEED–REM investigation showed that the spreading layer has a Si(111)7 × 7–Ge structure, while the patch of Ge deposit displays the Si(111)5 × 5–Ge structure and the 5 × 5 structure regions do not expand [42].

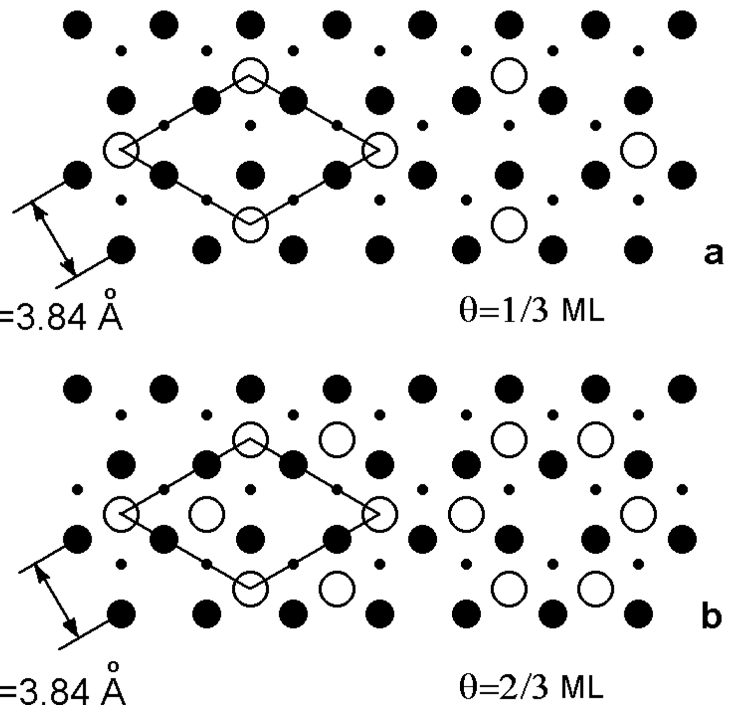

Fig 6. The models proposed in Ref. [1] for the Si(111)$\sqrt{3} \times \sqrt{3}$–Ge phase at (a) 1/3 ML and (b) 2/3 ML of Ge. Reprinted from P. Chen *et al.*, *Solid State Communications*, **44**, 1191. Copyright © 1982, with kind permission from Pergamon Press Ltd, Headington Hill Hall, Oxford OX3 0BW, UK

2. (100) ORIENTATION

Until very recently, it has been suggested that, in contrast to the case of Ge on the Si(111) surface, no new superstructure, besides the 2 × 1 is formed to cover the extended areas of the Ge/Si(100) interface. However, in a number of recent publications, the formation of the 2 × 8 and 2 × n structures was reported to take place at the growth of both submonolayer Ge and relatively thick GeSi films on Si(100). In addition, STM reveals, at low Ge coverages, the presence of the localized 2 × 2 and $c(4 \times 2)$ structures resulting from the ordering of buckling Ge–Ge dimers.

2.1. PHASE DIAGRAM

2.1.1. RT Growth

Upon RT deposition of Ge on to Si(100)2 × 1, an uniform disordered Ge layer is formed. As a result, the initial 2 × 1 LEED pattern becomes diffuse at about 1 ML Ge coverage and disappears completely beyond 2 ML [4, 7, 43–45].

2.1.2. HT Growth

The HT formation of the Ge/Si(100) interface proceeds in a Stranski–Krastanov growth mode both upon deposition of Ge on to the heated Si(100)2 × 1 surface and upon annealing of the RT deposited Ge layer. In the latter case, the uniform layer begins to collapse into a Stranski–Krastanov type morphology at above 250 °C and this process is completed at about 400 °C [44].

The critical thickness of the 2D layer beyond which the growth of 3D islands starts to grow varies from one publication to another in the range from 3 to 6 ML [4, 7, 44–51]. The

STM observations of Mo *et al.* [48–50, 52] showed that the transition from 2D to 3D growth occurs via a specific kinetic pathway, i.e., before the formation of "macroscopic" islands, the much smaller clusters (labeled by authors as "hut" clusters) are formed. These "hut" clusters ($\sim$ 30 Å high and $\sim$ 200 Å long) have a prism shape (with canted ends) and are formed by $\{105\}$ facet planes [52, 53]. The formation of the "hut" clusters takes place preferentially at low growth temperatures ($T \leq 550\,^{\circ}\mathrm{C}$), whereas the growth at about $600\,^{\circ}\mathrm{C}$ results in only "macroscopic" islands. These STM results are consistent with the RHEED observations of Tatsuyama *et al.* [54] who revealed in addition that the "macroscopic" islands are built of $\{113\}$ facets.

As for the LEED observations, in the most recent studies [4, 7, 8, 45, 55], the initial 2×1 LEED pattern of Si(100) was found to become diffuse with Ge deposition without the indication of a superstructure other than 2×1. However, in a number of recent studies [56–59], the occurrence of the novel superstructures, 2×8 and $2 \times n$, was detected. The formation of the 2×8 was found in Ref. [56] by RHEED observations of the initial growth stages of Ge films on Si(100) at 300–600 °C by gas source molecular beam epitaxy using $\mathrm{GeH_4}$. Jusko *et al.* [59] demonstrated that, up to a Ge coverage of about 3 ML, the LEED pattern exhibits a $2 \times n$ structure with n decreasing up to a minimum value of about 8 and then slowly increasing. The appearance of the $2 \times n$ structure takes place at about 0.9 ML Ge. The $2 \times n$ structure was also observed at the surface of rather thick GeSi layers grown by MBE on Si(100) [57, 58]. The value of factor n varies in the range of $8 < n < 12$ depending on the composition and thickness of GeSi layer. STM observations of Refs [57, 58] revealed that the $2 \times n$ structure has a missing dimer origin, i.e. after $(n-1)$ subsequent dimers one dimer is missing. The theoretical study of Tersoff [60] supported this idea but demonstrated that the removing of a dimer should be accompanied by the rebonding of the underlying second-layer atoms to decrease the number of dangling bonds.

Certain atomic scale regularities of the submonolayer Ge/Si(100) interface formation have been considered in several STM investigations [50, 61, 62]. Iwawaki *et al.* [61] found that, at (0.1–0.2) ML Ge coverage, Ge forms islands consisting of 1–5 dimer rows and the buckling of Ge–Ge dimers produces the localized $c(4 \times 2)$ and 2×2 structures. Knall and Pethica [62] reported that, at 0.1 ML, Ge islands are elongated with long axes along the Si(100) dimer rows, whereas, with increasing Ge coverage, this anisotropy is reversed and islands become elongated perpendicular to dimer rows. The authors noted that the density of buckled dimers increases drastically from about 10–20% on Si(100) substrate to nearly 100% buckled dimers in the Ge layer. In the work of Mo and Lagally [50], two types of monoatomic steps were found to have a different lateral sticking coefficient for Ge adatoms: SB steps (which are perpendicular to up-terrace dimer rows) are good sinks, while SA (which are parallel to up-terrace dimer rows) are poor sinks.

2.2. PROPERTIES

2.2.1. Surface Diffusion

Mo and Lagally [50], studying by STM the very early stages of Ge layer growth, concluded that surface diffusion of Ge on Si(100) is very anisotropic, with the fast direction being along the substrate dimer rows. Their estimate reveals that the diffusion coefficient is at least 1000 times faster along the dimer row than perpendicular to them.

In theoretical work of Srivastava and Garrison [63], the strong diffusion anisotropy was also revealed: while the macroscopic diffusion was found to follow the Arrhenius behavior with

$$D = 4.3 \times 10^{-4} \exp(-0.73\ \mathrm{eV}/kT)\ \mathrm{cm^2/s},$$

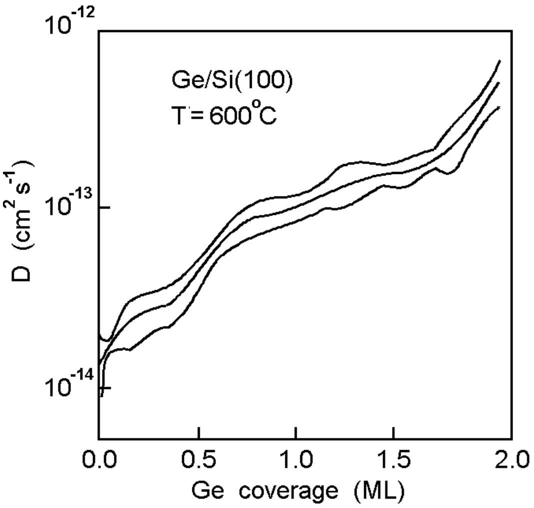

Fig 7. Diffusion coefficient as a function of coverage for Ge deposited on Si(100) and annealed at 600 °C. The middle one of the solid lines denotes the mean of several experiments, the lines at each side differ by one standard deviation (from Ref. [44]). (*Reproduced by permission of Scanning Microscopy Intl)*

the diffusion coefficient for Ge adatom migration perpendicular to the dimer rows (the direction of slow diffusion) was determined to be

$$D_{\perp} = 2.8 \times 10^{-3} \exp(-1.17 \text{ eV}/kT) \text{ cm}^2/\text{s}.$$

A strong coverage dependence of diffusion coefficients was revealed by Gossmann and Fisanick in Ref. [44]. In this study, Ge was deposited through a circular shadow mask at RT and AES profiles were recorded after annealing. The experimental results were used as input data in the numerical inversion of the diffusion equation in cylindrical coordinates to obtain the diffusion coefficient. The result from seven runs of annealing Ge deposits on Si(100) at 600 °C at varying times, is shown in Fig. 7. One can see that the diffusion coefficient increases over more than an order of magnitude with increasing coverage from 0 to 2 ML.

Ge/Si(100) surface diffusion was reported in Ref. [44] to be strongly influenced by small amounts of contamination or electron beam irradiation. As little as 0.05 ML of carbon reduces the diffusion coefficient on Si(100) by at least three orders of magnitude. Electron beam irradiation also suppresses the diffusion but to a less extent.

3. (110) ORIENTATION

The $\begin{pmatrix} 16 & 0 \\ 1 & 1 \end{pmatrix}$, $\begin{pmatrix} 10 & -1 \\ 3 & 4 \end{pmatrix}$, $\begin{pmatrix} 8 & 0 \\ 2 & 1 \end{pmatrix}$, and 1 × 1 structures are detected in the Ge/Si(110) system.

3.1. PHASE DIAGRAM

The Ge-covered Si(110) surfaces were studied first by Miura *et al.* [64] using LEED and AES. It was found that a $\begin{pmatrix} 10 & -1 \\ 3 & 4 \end{pmatrix}$ structure appears at coverages from 0.3 to 0.7 ML of Ge upon annealing above 550 °C and a $\begin{pmatrix} 8 & 0 \\ 2 & 1 \end{pmatrix}$ structure at coverages greater than 0.8 ML upon annealing above 450 °C. In the range of coverages from 1 to 2 ML, a $\begin{pmatrix} 16 & 0 \\ 1 & 1 \end{pmatrix}$ structure is

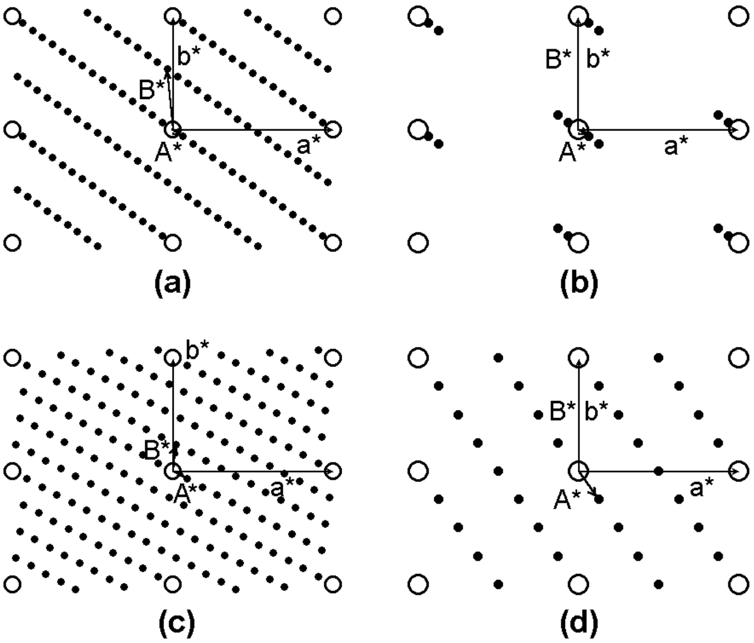

Fig 8. Schematic diagrams illustrating LEED patterns and unit vectors in the reciprocal space of the superstructures: (a) Si(110)$\begin{pmatrix} 16 & 0 \\ 1 & 1 \end{pmatrix}$–Ge, (b) Si(110)$\begin{pmatrix} 10 & -1 \\ 3 & 4 \end{pmatrix}$–Ge, and (c) Si(110)$\begin{pmatrix} 8 & 0 \\ 2 & 1 \end{pmatrix}$–Ge. **a*** and **b*** are reciprocal unit vectors in the Si(110)1 × 1 structure (from Ref. [64]). (*Reproduced by permission of Elsevier Science Publishers BV)*

observed at deposition of Ge on to the Si(110) substrate held at room temperature. Figure 8 shows schematic sketches of observed LEED patterns and two-dimensional unit vectors of structures in the reciprocal space.

Figure 9 shows phase diagrams of surface reconstructions in the Ge layer on Si(110) detected during annealing. All structures observed during initial heating of the room temperature deposited Ge layer to high temperature are summarized in Fig. 9(a). Reversible phase transitions of surface structures caused by annealing are shown in Fig. 9(b). In a phase boundary between $\begin{pmatrix} 10 & -1 \\ 3 & 4 \end{pmatrix}$ and $\begin{pmatrix} 8 & 0 \\ 2 & 1 \end{pmatrix}$ structures, a 1 × 1 structure is observed within the coverage range of 0.1 ML.

The Ge/Si(110) system was re-examined recently by Yamamoto [65] by means of RHEED and total reflection angle X-ray spectroscopy (TRAXS). The phase diagram presented by Yamamoto is in reasonable agreement with that shown in Fig. 9(b). Both $\begin{pmatrix} 10 & -1 \\ 3 & 4 \end{pmatrix}$ and $\begin{pmatrix} 8 & 0 \\ 2 & 1 \end{pmatrix}$ phases were reproduced in similar coverage intervals. The only discrepancy concerns the temperatures of reversible phase transitions. While Miura *et al.* [64] found that the $\begin{pmatrix} 8 & 0 \\ 2 & 1 \end{pmatrix}$ and $\begin{pmatrix} 10 & -1 \\ 3 & 4 \end{pmatrix}$ structures transform reversibly into 1 × 1 at 620 and 640 °C, respectively, Yamamoto [65] reported the transition temperature to be 730 °C for both structures.

RHEED observations of Yamamoto revealed that, at coverages beyond 3 ML, the growth of three-dimensional epitaxial Ge islands occurs with orientational relation Ge(110) || Si(110) and Ge[111] || Si[111]. So, it was concluded that the growth mode of the Ge/Si(110) system is of Frank–van der Merve type until 3 ML and of Stranski–Krastanov above 3 ML [65].

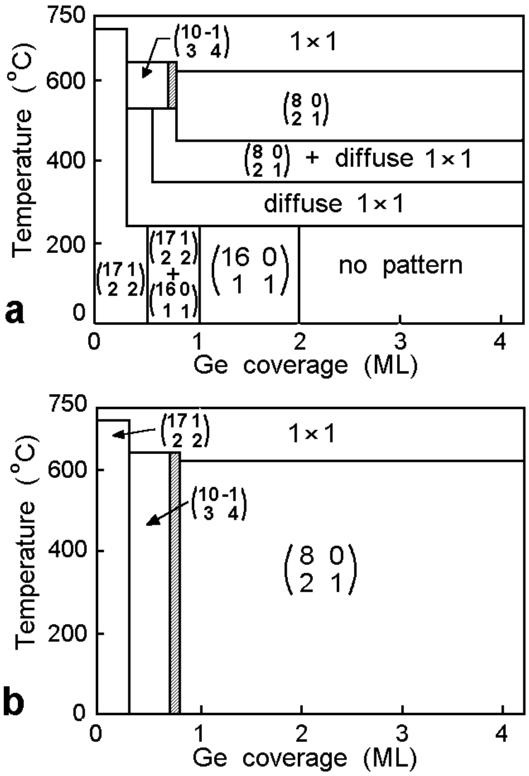

Fig 9. Phase diagrams showing the structural changes as functions of Ge coverage and annealing temperature: (a) structures observed during initial heating to high temperature, (b) structures observed reversibly during heating or cooling (from Ref. [64]). (*Reproduced by permission of Elsevier Science Publishers BV)*

3.2. STRUCTURE

Using the results of the RHEED–TRAXS study, Yamamoto [65] proposed a possible arrangement at adsorbed Ge atoms for $\begin{pmatrix} 10 & -1 \\ 3 & 4 \end{pmatrix}$ and $\begin{pmatrix} 8 & 0 \\ 2 & 1 \end{pmatrix}$ structures. (Though the structures were labeled in Ref. [65] as $\begin{pmatrix} 10 & 1 \\ -3 & 4 \end{pmatrix}$ and $\begin{pmatrix} 2 & 3 \\ -2 & 1 \end{pmatrix}$, respectively, one can see that these are evidently the same structures).

The proposed atomic arrangement for the $\begin{pmatrix} 10 & -1 \\ 3 & 4 \end{pmatrix}$ structure is shown in Fig. 10(a), where the open circles represent Si atoms forming the Si(110) plane, and the solid circles Ge atoms adsorbed on them up to an amount of 0.49 ML. At the corners of the unit mesh, Ge atoms are missing. This model is consistent with experimental result that the $\begin{pmatrix} 10 & -1 \\ 3 & 4 \end{pmatrix}$ structure occurs at Ge coverages ranging from 0.4 to 0.94 ML.

Figure 10(b) shows the atomic arrangement proposed for the $\begin{pmatrix} 8 & 0 \\ 2 & 1 \end{pmatrix}$ structure. In the figure, the solid circles represent Ge atoms on the Si(110) plane and the shaded ones Ge atoms on the Ge(110) surface. Ge atoms again do not occupy the corners of the unit mesh. The Ge coverage corresponding to the model is 1.35 ML. In the experiments, the $\begin{pmatrix} 8 & 0 \\ 2 & 1 \end{pmatrix}$ structure was observed above 0.94 ML [65].

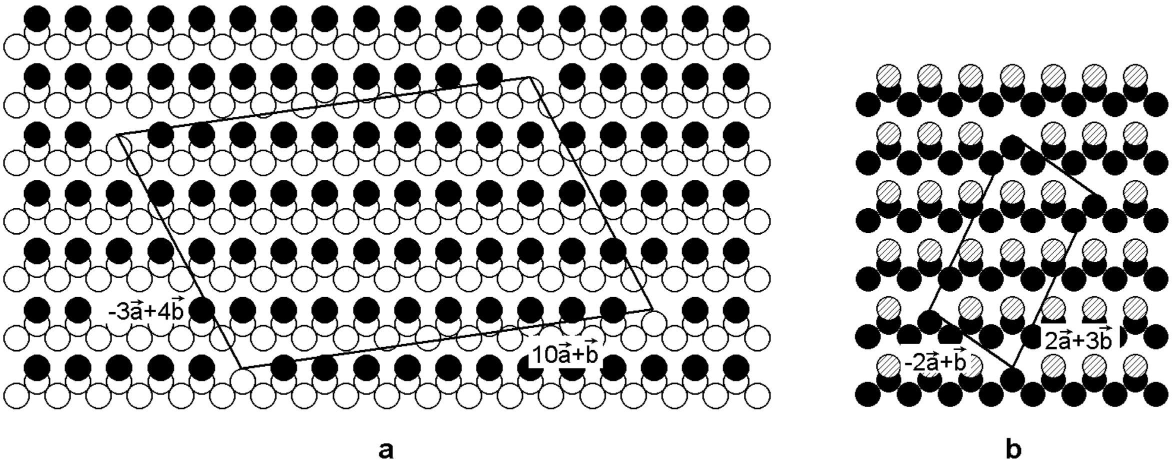

Fig 10. Atomic arrangements for the superstructures of the Ge/Si(110) system. (a) The $\begin{pmatrix} 10 & -1 \\ 3 & 4 \end{pmatrix}$ structure and (b) the $\begin{pmatrix} 8 & 0 \\ 2 & 1 \end{pmatrix}$ structure. The open circles represent Si atoms, the solid circles Ge atoms on Si(110), and the shaded circles Ge atoms on the Ge(110) plane (from Ref. [65]). (*Reproduced by permission of Elsevier Science Publishers BV)*

REFERENCES

[1] P. Chen, D. Bolmont and C. A. Sebenne, *Solid State Commun.* **44** (1982) 1191.
[2] P. Chen, D. Bolmont and C. A. Sebenne, *Solid State Commun.* **46** (1983) 689.
[3] P. Chen, D. Bolmont and C. A. Sebenne, *Thin Solid Films* **111** (1984) 367.
[4] K. Shoji, M. Hyodo, H. Ueda and C. Tatsuyama, *Japan J. Appl. Phys.* **22** (1983) 1482.
[5] S. K. Ramchurn, D. M. Bird and D. W. Bullett, *J. Phys. :Cond. Matt.* **2** (1990) 7435.
[6] K. Shoji, M. Hyodo, H. Ueba and C. Tatsuyama, *Japan J. Appl. Phys.* **22** (1983) L200.
[7] N. Ishimaru, H. Ueba and C. Tatsuyama, *Surf. Sci.* **193** (1988) 193.
[8] H. -J. Gossmann, L. C. Feldman and W. M. Gibson, *Surf. Sci.* **155** (1985) 413.
[9] H. -J. Gossmann and G. J. Fisanick, *J. Vac. Sci. Technol. A* **6** (1988) 2037.
[10] S. Nannarone, F. Patella, P. Perfetti, C. Quaresima, A. Savoia, C. M. Bertoni, C. Calandra and F. Manghi, *Solid State Commun.* **34** (1980) 409.
[11] G. Margaritondo, N. G. Stoffel, A. D. Katnani and F. Patella, *Solid State Commun.* **36** (1980) 215.
[12] E. G. McRae and R. A. Malic, *Surf. Sci.* **163** (1985) L702.
[13] E. G. McRae and R. A. Malic, *Surf. Sci.* **165** (1986) 191.
[14] M. A. Lamin, O. P. Pchelyakov, L. V. Sokolov, S. I. Stenin and A. I. Toropov, *Surf. Sci.* **207** (1989) 418.
[15] K. Kajiyama, Y. Tanishiro and K. Takayanagi, *Surf. Sci.* **222** (1989) 38.
[16] P. M. J. Maree, K. Nakagawa, F. M. Mulders, J. F. Van der Veen and K. L. Kavanagh, *Surf. Sci.* **191** (1987) 305.
[17] J. Henz, J. Hugi, N. Onda and H. Von Kanel, *Helv. Phys. Acta* **62** (1989) 868.
[18] H. -J. Gossmann, J. C. Bean, L. C. Feldman and W. M. Gibson, *Surf. Sci.* **138** (1984) L175.
[19] T. Narasawa and W. M. Gibson, *Phys. Rev. Lett.* **47** (1981) 1459.
[20] Y. Shinoda, N. Shimizu, H. Hibino, T. Nishioka, C. Heimlich, Y. Kobayashi, S. Ishizawa, K. Sugii and M. Seki, *Appl. Surf. Sci.* **60–61** (1992) 112.
[21] T. Ichikawa and S. Ino, *Surf. Sci.* **136** (1984) 267.
[22] U. K. Kohler, O. Jusko, G. L. Pietsch, B. Muller and M. Henzler, *Surf. Sci.* **248** (1991) 321.
[23] H. -J. Gossmann, J. C. Bean, L. C. Feldman, E. G. McRae and I. K. Robinson, *Phys. Rev. Lett.* **55** (1985) 1106.

[24] S. Hasegawa, M. Akizuki, H. Iwasaki, I. Yoneda and S. Nakamura, *Surf. Sci.* **235** (1990) L295.
[25] Y. Kajiyama, Y. Tanishiro and K. Takayanagi, *Surf. Sci.* **222** (1989) 47.
[26] P. Martensson, W. -X. Ni and G. V. Hansson, *Phys. Rev. B* **36** (1987) 5974.
[27] S. Hasegawa, H. Iwasaki, S. -T. Li and S. Nakamura, *Phys. Rev. B* **32** (1985) 6949.
[28] S. Hasegawa, H. Iwasaki, M. Akizuki, S. -T. Li and S. Nakamura, *Solid State Commun.* **58** (1986) 697.
[29] P. Martensson, A. Cricenti, L. S. O. Johansson and G. V. Hansson, *Phys. Rev. B* **34** (1986) 3015.
[30] K. Takayanagi, Y. Tanishiro, M. Takahashi and S. Takahashi, *J. Vac. Sci. Technol. A* **3** (1985) 1502.
[31] B. Zhang, J. E. Northrup and M. L. Cohen, *Surf. Sci.* **145** (1984) L465.
[32] J. M. Seo, D. L. Doering, D. S. Black and J. E. Rowe, *J. Vac. Sci. Technol. A* **4** (1986) 894.
[33] E. G. McRae, H. -J. Gossmann and L. C. Feldman, *Surf. Sci.* **146** (1984) L540.
[34] T. Miller, T. C. Hsieh and T. -C. Chiang, *Phys. Rev. B* **33** (1986) 6983.
[35] K. Takayanagi, Y. Tanishiro and K. Kajiyama, *J. Vac. Sci. Technol.* **4** (1986) 1074.
[36] J. R. Patel, P. E. Freeland, J. A. Golovchenko, A. R. Kortan, D. J. Chadi and G. -X. Qian, *Phys. Rev. Lett.* **57** (1986) 3077.
[37] R. S. Becker, J. A. Golovchenko and B. S. Swartzentruber, *Phys. Rev. B* **32** (1985) 8455.
[38] R. S. Becker, B. S. Swartzentruber and J. S. Vickers, *J. Vac. Sci. Technol. A* **6** (1988) 472.
[39] E. G. McRae, *Surf. Sci.* **163** (1985) L766
[40] T. Miller, T. C. Hsieh, P. K. John, A. P. Shapiro, A. L. Wachs and T. -C. Chiang, *Phys. Rev. B* **33** (1986) 4421.
[41] H. Yasunaga, *Surf. Sci.* **242** (1991) 171.
[42] H. Yamaguchi, Y. Tanishiro and K. Yagi, *Appl. Surf. Sci.* **60–61** (1992) 79.
[43] H. -J. Gossmann, L. C. Feldman and W. M. Gibson, *J. Vac. Sci. Technol. B* **2** (1984) 407.
[44] H. -J. Gossmann and G. J. Fisanick, *Scanning Microscopy* **4** (1990) 543.
[45] M. Asai, H. Ueba and C. Tatsuyama, *J. Appl. Phys.* **58** (1985) 2577.
[46] J. Bevk, B. A. Davidson, L. C. Feldman, H. -J. Gossmann, J. P. Mannaerts, S. Nakahara and A. Ourmazd, *J. Vac. Sci. Technol. B* **5** (1987) 1147.
[47] J. -M. Baribeau, *Appl. Phys. Lett.* **57** (1990) 1748.
[48] Y. -M. Mo and M. G. Lagally, *Mod. Phys. Lett. B* **4** (1990) 1379.
[49] Y. -W. Mo, D. E. Savage, B. S. Swartzentruber and M. G. Lagally, *Phys. Rev. Lett.* **65** (1990) 1020.
[50] Y. -W. Mo and M. G. Lagally, *J. Cryst. Growth* **111** (1991) 876.
[51] C. Tatsuyama, H. Ueba and Y. Kataoka, *Appl. Surf. Sci.* **33–34** (1988) 457.
[52] C. E. Aumann, Y. -W. Mo and M. G. Lagally, *Appl. Phys. Lett.* **59** (1991) 1061.
[53] F. Iwawaki, M. Tomotori and O. Nishikawa, *Surf. Sci.* **253** (1991) L411.
[54] C. Tatsuyama, T. Terasaki, H. Obata, T. Tanbo and H. Ueba, *J. Cryst. Growth* **115** (1991) 112.
[55] Y. Kataoka, H. Ueba and C. Tatsuyama, *J. Appl. Phys.* **63** (1988) 749.
[56] N. Ohshima, Y. Koide, S. Zaima and Y. Yasuda, *Appl. Surf. Sci.* **48–49** (1991) 69.
[57] R. Butz and S. Kampers, *Thin Solid Films* **222** (1992) 104.
[58] R. Butz and S. Kampers, *Appl. Phys. Lett.* **61** (1992) 1307
[59] O. Jusko, U. Kohler, G. J. Pietsch, B. Muller and M. Henzler, *Ultramicroscopy* **44** (1992) 832.
[60] J. Tersoff, *Phys. Rev. B* **45** (1992) 8833.
[61] F. Iwawaki, M. Tomitori and O. Nishikawa, *Surf. Sci.* **266** (1992) 285.
[62] J. Knall and J. B. Pethica, *Surf. Sci.* **265** (1992) 156.
[63] D. Srivastava and B. J. Garrison, *Phys. Rev. B* **46** (1992) 1472.
[64] S. Miura, K. Kato, T. Ide and T. Ichinokawa, *Surf. Sci.* **191** (1987) 259.
[65] Y. Yamamoto, *Surf. Sci.* **281** (1993) 253.

(H)

HYDROGEN

1. (111) ORIENTATION

Hydrogen is known to induce several reconstructions on the Si(111) surface. These are $\delta(7\times7)$ and 1×1. The existence of 2×2, 3×1, and $\sqrt{3}\times\sqrt{3}$ surface structures was reported in some works.

1.1. PHASE DIAGRAM

Different chemical interactions of hydrogen with the Si(111) surface and consequently different reconstructions take place in a high vacuum environment and in the wet chemical process. The adsorption of atomic hydrogen on to a clean Si(111)7×7 surface has been well studied at room temperature, but conflicting information exists for the adsorption of molecular hydrogen and little is known about the adsorption of either atomic or molecular hydrogen on silicon surfaces at elevated temperature. Hydrogen adsorption on the Si(111)2×1 surface has been investigated less than that on the Si(111)7×7 surface.

1.1.1. Si(111)7 × 7 Surface

Usually a noticeable interaction can only take place if hydrogen is offered in the atomic form; then, however, this interaction is quite strong. The reason is that molecular dihydrogen does not dissociate spontaneously on low-index semiconductor surfaces [1]. In order to obtain reactive atomic hydrogen, in most cases a hot W filament is placed in front of the sample which produces at least a mixture of molecular and atomic hydrogen.

Interaction with Atomic Hydrogen

Numerous studies have been made on the H/Si(111)7×7 surface including: LEED [2–11], RHEED [12–18], INS [19], SEM [16,20], AES [11, 14, 21], MS [20,22], XPS [4, 16, 23–28], UPS 19, 23–26, 29–33], ERDA [10], LERIS [34], ELS 4, 11, 29, 30, 35], HREELS [3, 36–39], HRIRS [40–43], TCS [44], TDS 3, 45–47], TED [48], ESD [49,50], NRA [6], SSIMS [51], ESDIAD [5], LID [52,53], STM [54–64], ARPES [65], REM [12], MIR infrared spectroscopy [66–70], WF measurements [19], and theoretically [71–88].

Owing to the difficulty in the detection of surface hydrogen by conventional electron-spectroscopic methods, absolute coverage information is usually lacking in the adsorption studies. The first quantitative study of deuterium adsorption was made by Culbertson *et al.* [6] using nuclear reaction analysis (NRA). They found that the saturation coverage of deuterium is 1.25 ± 0.13 ML. Recently Oura *et al.* [10] carried out a quantitative analysis of hydrogen adsorption on the Si(111)7×7 surface using elastic recoil detection analysis.

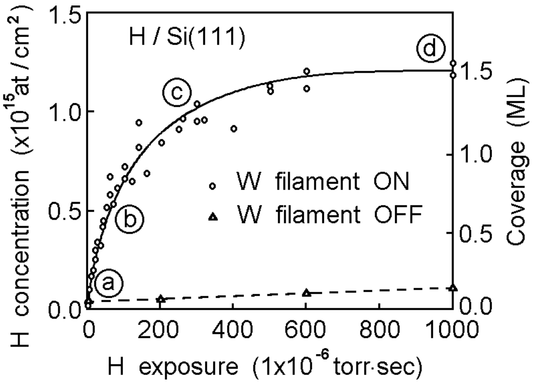

Fig 1. Hydrogen concentration (coverage) on a Si(111)7 × 7 surface kept at RT plotted against H_2–gas exposure (from Ref. [10]). (*Reproduced by permission of Elsevier Science Publishers BV)*

Figure 1 is the measured concentration or coverage of adsorbed hydrogen atoms plotted against the exposure of hydrogen molecules for an activated hydrogen adsorption on to a clean Si(111)7 × 7 surface kept at RT [10]. As can be seen, the adsorption curve initially reveals rather a step increase but it gradually saturates to a value of about 1.5 ML after an exposure of 1000 L.

Initially, the Si surface chemisorbs atomic hydrogen by saturating the surface atom dangling bonds. In a second step, surface bonds are broken and a change of the geometrical structure takes place. Finally, higher hydrogen exposures are able to etch the semiconductor surface. A schematic illustration of the LEED patterns at various stages of adsorption, taken at an electron beam energy of 60 eV, is reproduced in Fig. 2. At this energy, the enhancement of the 1/7 order reflections and the decrease in the intensities of the other fractional order reflections are most noticeable. As a result the Si(111)7 × 7–H structure is produced. This observation is in good agreement with the earlier LEED investigations of Sakurai and Hagstrum [19], McRae and Caldwell [9] and the NRA/LEED result of Culbertson *et al.* [6] on the D/Si(111)7 × 7 system. As the surface is exposed to 100–500 L hydrogen, the diffuse scattering intensity is increased on the LEED pattern. This is attributed to surface roughening by the corrosive action of hydrogen atoms [39].

The Si(111)7 × 7–H structure was also observed by RHEED [12–15, 17, 18]. Sometimes this structure is called $\delta(7 \times 7)$, because it shows superstructure reflections mainly along the lines which connected neighboring fundamental reflections. The fractional-order spots of the Si(111)7 × 7–H in the RHEED pattern were slightly weakened by annealing at about 700 K [14]. At above 900 K, the 7 × 7–H structure is changed rapidly into the clean 7 × 7 structure.

Under some special conditions, the 3 × 1–H and $\sqrt{3} \times \sqrt{3}$—$R30°$–H superstructures were observed. Exposing H atoms to the Li/Si(111) system, it was found [15] that the Li atoms are substituted for H atoms at RT, since Li–KVV signal intensity decreases during the exposure of hydrogen. After the substitutions, the Li 7 × 7 and 3 × 1 RHEED patterns do not change, and are preserved as Si(111)7 × 7–H and 3 × 1–H. RHEED patterns of 4 × 4–Li, $\sqrt{3} \times \sqrt{3}$–Li, and 1 × 1–Li change into Si(111)1 × 1–H pattern after the substitution.

When a small amount of carbon and oxygen is observed for the hydrogen-adsorbed $\delta(7 \times 7)$ surface, the $\delta(7 \times 7)$ structure is changed into a $\sqrt{3} \times \sqrt{3}$—$R30°$ structure for 900 K annealing [14]. The existence of this structure was attributed to the presence of carbon on the silicon surface.

The kinetics of the gas–solid reaction of Si(111)7 × 7 and atomic hydrogen has been studied by using the modulated molecular beam mass spectrometric technique by Abrefah and Olander [20]. Volatile silicon tetrahydride, SiH_4, and recombined molecular hydrogen were the only reaction products detected from ambient temperature to 1000 K. At RT the

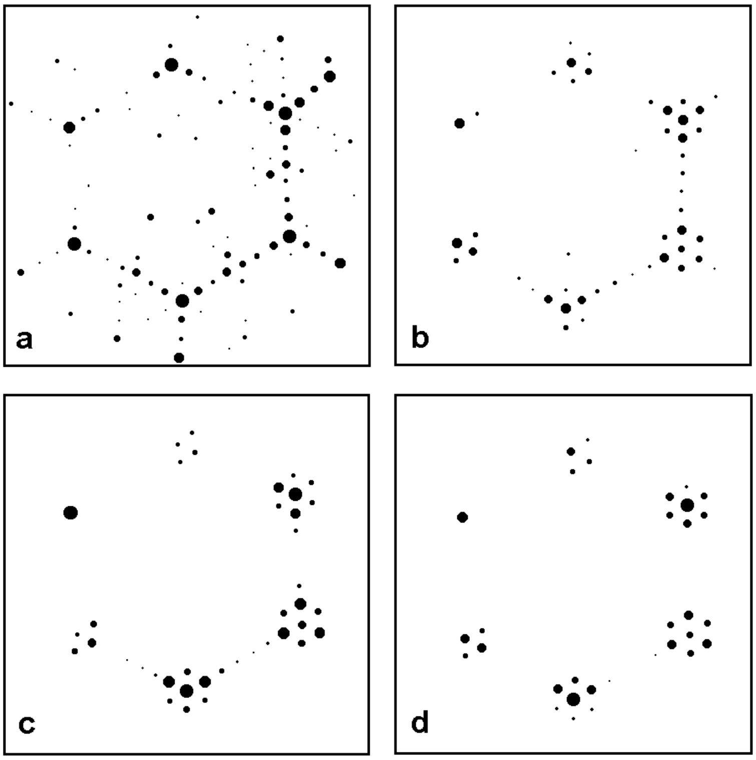

Fig 2. Schematic illustration of the LEED patterns. (a) is a clean 7 × 7 pattern and (b), (c), (d) are patterns observed at the corresponding points of Fig. 1, respectively (from Ref. [10]). (*Reproduced by permission of Elsevier Science Publishers BV)*

majority of the incident H atoms recombine on the Si surface and are re-emitted as H_2; some of them diffuse into the Si lattice; and a small fraction ($\sim 3\%$) react to produce SiH_4. The etch rate increases with beam intensity but decreases with increasing temperature.

*

Interaction with Molecular Hydrogen In a LEED study [2], Schulze and Henzler reported that H_2 does not affect the structure of the Si(111)7 × 7 surface. It is naturally connected with the small reactivity of molecular hydrogen [20]. Ibach and Rowe [29] showed that H_2 adsorbed in small quantities – 3% surface coverage. This result was confirmed by the quantitative analysis of Culbertson *et al.* [6] and Oura *et al.* [10] and is illustrated in Fig. 1.

1.1.2. Si(111)2 × 1 Surface

According to LEED observations of various authors the Si(111)2 × 1 reconstructed surface changes to the 1 × 1 form when atomic hydrogen is adsorbed on the cleaved silicon [2–4, 29]. The half-order diffraction peaks are destroyed at a coverage of H about a half monolayer. The coverage dependence of HREELS spectra of Schaefer *et al.* [4] shows that the monohydride is formed initially and the dihydride only after heavier exposure to atomic hydrogen.

1.1.3. Wet Chemical Preparation of Si(111) Surface

Aqueous HF etching of the Si(111) surface results in the removal of the surface oxide and leaves behind silicon surfaces terminated by atomic hydrogen [16, 28, 40, 43, 58, 60, 61, 67–70, 89–91]. In the case of dilute (1–10%) HF treatment, there exist three types of hydrogen configurations on the Si surface [68, 70]: mono- (SiH), di- (SiH_2), and trihydrides (SiH_3). Among them, the mono- and dihydrides are located at defect sites such as atomic steps and point defects, and the trihydride is mainly on the flat part of the Si(111) surface [60, 61, 68, 70]. In contrast, on the Si(111) surface treated by pH modified buffered HF, only monohydride exists on the entire surface [67]. Immersion in boiling water (100 °C) for 600 s following HF etching also produces a surface homogeneously terminated with silicon monohydride normal to the surface and free of oxidation [28, 43]. The resulting surface not only has a very low defect and impurity density ($< 10^{-3}$), but is also stable in air and in water, and can be introduced into UHV by means of load-lock system [40]. Thee LEED pattern from this surface shows the Si(111)1 × 1–H structure [68]. STM images of the H-terminated surface also show a threefold-symmetric 1 × 1 phase [58, 60, 61].

Becker *et al.* [58] demonstrated that the atomic hydrogen terminating the surface may be selectively removed by low-energy electron bombardment from the STM tip under UHV conditions. The resultant surface converts from the 1 × 1 surface phase to the 2 × 1 π-bonded chain. Measurements of the efficiency of this process as a function of electron energy demonstrated that the mechanism is one of promoting an electron from the Si–H σ to the σ^* band, desorbing the terminating hydrogen, and rendering the 1 × 1 surface energetically unstable with respect to the 2 × 1. Individual 2 × 1 regions as small as ten surface sites have been created in this fashion.

1.2. STRUCTURE

1.2.1. Si(111)δ(7 × 7)–H

The chemisorption of hydrogen on the Si(111)7 × 7 surface has been studied extensively for more than a decade [54]. Although the structure of the clean 7 × 7 reconstruction is now generally accepted to be described by the DAS model, the interaction of hydrogen is still open to vigorous dispute; e.g. does the DAS structure remain unchanged upon hydrogen exposure [3, 23, 56], or does an etching of the surface occur [2, 22], and how can the large saturation coverage observed be explained [6]?

RT saturation coverage of H on the Si(111) surface is 1.5 ML [10], substantially greater than that associated with the saturation of the 19 dangling bond in each unit cell of the DAS model. There is now general agreement that at saturation coverage SiH (monohydride), SiH_2 (dihydride), and SiH_3 (trihydride) species are all present on the surface, although the relative populations of this species are still not resolved [3, 7, 23, 30, 37, 39, 42, 51]. The monohydride is the thermally more stable species. According to HREELS experiments by Kobayashi *et al.* [39] and Froitzheim *et al.* [3], vibrational modes of Si–H and SiH_2 and/or SiH_3 were observed for saturated adsorption of hydrogen on the clean Si(111) surface. Similar results were also obtained by a HRIRS experiment by Chabal *et al.* [42]. Using photoemission, Muller *et al.* [23] reported the formation of monohydride followed by dihydride at RT, but made no reference to the formation of the surface trihydride. Based on UPS and XPS results, Koulmann *et al.* [26] have also concluded that a monohydride phase forms at first on the Si(111)7 × 7 surface. Upon further hydrogen dosing at RT, a dihydride phase develops and superposes to the previously formed monohydride phase. Wagner *et al.* [37] reported the formation of SiH_2 and/or SiH_3 during the early stages of hydrogen adsorption on Si(111)7 × 7 using EELS. Using MIR infrared spectroscopy Jansson and Uram [7] observed the temperature-dependent formation of surface dihydride and trihydride species. The formation of both the dihydride and the trihydride is favored by low adsorption temperatures (200 K and 100 K, respectively).

Recent STM investigations of the H-saturated Si(111) surface, where SiH_2 and SiH_3 surface species exist, indicated that significant surface disorder results from this Si–Si bond breaking and suggested that the relief of strain in the Si adatom backbond is accompanied by the formation of the higher hydride phases [57, 63]. This disorder is not observed by STM when only the monohydride phase is present [55, 56] at low hydrogen coverage. Two channels of the reaction of atomic hydrogen with the Si(111)7 × 7 surface were detected by Mortensen *et al.* [54]: a direct binding of the hydrogen atoms to the existing dangling bonds of the surface, and a slower removal of the uppermost Si layer and binding of the hydrogen atoms to the dangling bonds created on the next layer. Real-time observation of the H adsorption by STM by Tokumoto *et al.* [55] demonstrated that the adsorption proceeds with different chemical reactivities among the adatoms: the adatom in the defective half of the 7 × 7 unit cell is more active than that in the unfaulted half; the center adatoms in each half are more active and the corner adatoms are the next; the corner holes in the 7 × 7 unit cell are less active indicating that the 7 × 7 structure still exists even for fairly high coverages.

The first quantitative LEED intensity analysis of the 7 × 7–H structure was carried out by MacRae and Caldwell [9] on the basis of the triangular checker board structure model. Further, MacRae [8] proposed a model of the Si(111)7 × 7–H based on the triangular dimer-stacking fault model and showed that the model was consistent with several experimental results. From RBS data, Culbertson *et al.* [6] suggested that the stacking fault is included in the first layer of the Si(111)7 × 7–H structure.

¿From a many-beam RHEED dynamical calculation, Ichimiya and Mizuno [17] proposed that backbonds of adatoms of the DAS structure are broken by hydrogen adsorption and SiH_3 is formed randomly at topmost sites of the first layer. Later, hydrogen-adsorbed $\delta(7\times7)$ RHEED patterns have been kinematically analyzed by Horio *et al.* [18] on the basis of the DAS structure taking into account a change of the bonding state of the Si adatoms induced by hydrogen adsorption. Intensities of the experimental RHEED patterns agree well with those calculated for a model with randomly distributed SiH_3 clusters on the dimer-stacking fault framework, which preserves the periodicity of the 7 × 7 RHEED pattern. A reflection electron microscope study of hydrogen atom adsorption was carried out by Ohse and Yagi [12]. The surface image does not show orientational domains, which indicates that the Si(111)7 × 7–H structure is not composed of three domains of a 7 × 1 structure.

In recent work [54], using STM and STS observations Mortensen *et al.* tried to consistently explain much of the previous data. First, the persistence of the 7 × 7 symmetry up to saturation coverage was explained by the preservation of the stacking fault upon the removal of the Si adatom layer. Further, the observed etching is consistent with the detection of SiH_4 in the mass spectrometer during H exposure [2, 22], and provides direct evidence for the interpretation of the recent core-level shift and PES measurements by Karlsson *et al.* [65]. The authors proposed that, remaining Si adatoms are responsible for the formation of monohydride, dihydride, or trihydride species depending on the number of broken backbonds, and confirmed the similar model with trihydride species randomly distributed on the next Si layer proposed by Ichimiya and Mizuno [17] and Horio *et al.* [18].

1.2.2. Si(111)1 × 1–H

The structural model for the Si(111)1 × 1–H surface is shown in Fig. 3 [25]. Each hydrogen atom forms a covalent bond with the dangling bond obtained on each surface Si atom. The direction of this bond is perpendicular to the surface.

1.3. PROPERTIES

1.3.1. Desorption

TDS results of hydrogen desorption experiments of various authors are summarized in the recent work of Kleint and Brzoska [45]. The observed and evaluated features of hydrogen thermal desorption are contradictory in some aspects. However, the following tendencies can be stated:

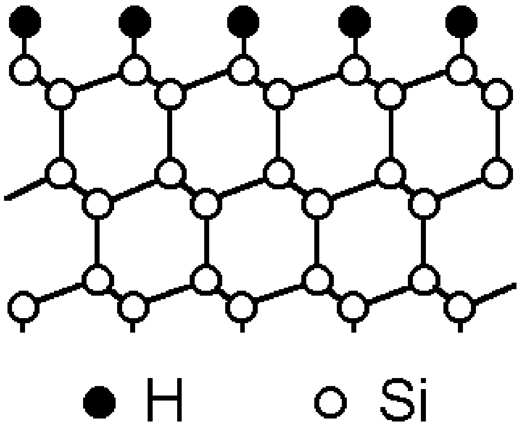

Fig 3. Structural model for the Si(111)1 × 1–H surface (from Ref. [25]). (*Reproduced by permission of American Institute of Physics)*

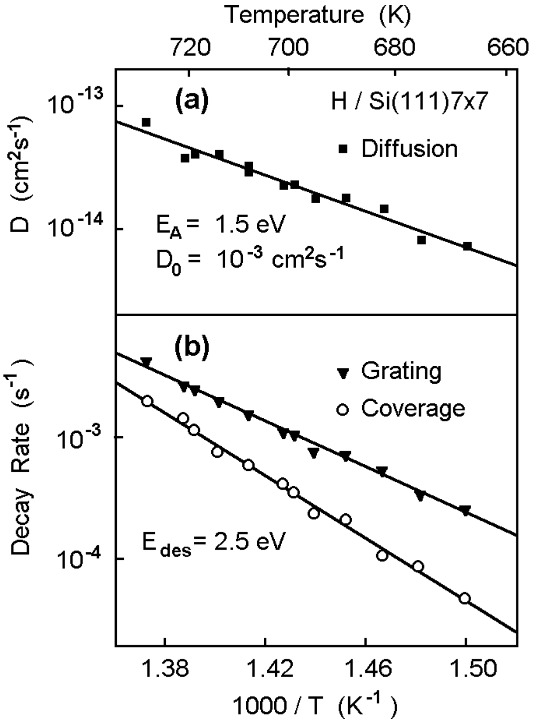

Fig 4. Arrhenius plot of diffusion (a) and desorption (b) data (from Ref. [92]). (*Reproduced by permission of the publishers of Journal of Physical Review Letters)*

• The main and usually observed phase is from the Si–H state and reveals H_2 desorption (β_1 and β_2 states with desorption temperatures of 550 and 430 °C, respectively).

• The SiH_2 phase is found to be more pronounced on cleaved and on thermally-treated Si(111) than on ion bombarded (and annealed) Si(111). Comparative measurements reveal only a small structure and coverage dependence of the desorption parameters.

• The energies and pre-exponentials found by different authors differ one from another but often change in a synchronous way, i.e. they show a compensation behavior.

The values from 1.7 to 3.5 eV were obtained for the desorption energy. Recent works indicate that the $E_{\rm des}$ is about 2.5 eV (Reider *et al.* [53,92] and Wise *et al.* [93], see Fig. 4(b)). Isothermal LITD studies of H_2 desorption from Si(111)7 × 7 by Wise *et al.* [93] revealed second-order kinetics.

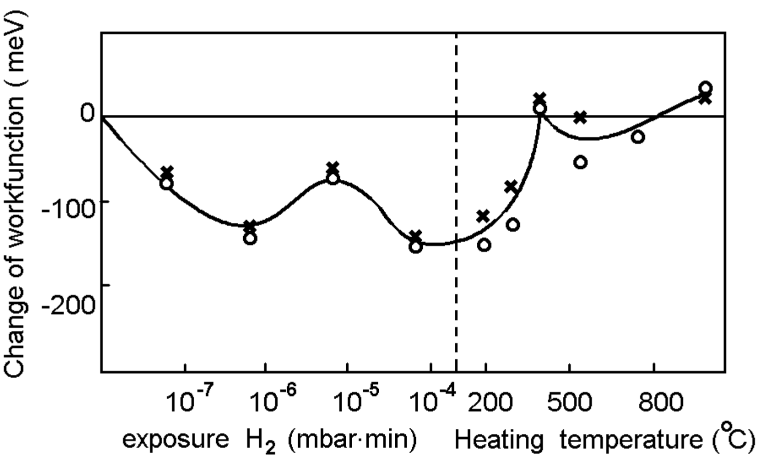

Fig 5. Change of work function versus exposure of hydrogen (left part) and versus heating temperature after adsorption (right part). The two symbols correspond to two different cycles (from Ref. [47]). (*Reproduced by permission of Elsevier Science Publishers BV)*

When the hydrogen-exposed surface is bombarded by electrons the ESD of hydrogen takes place [5]. The determination of the absolute value of the ESD cross-section* of deuterium as a function of electron energy shows a stepwise increase at ∼ 100 eV and this is attributed to ionization of the Si L-shell [49].

1.3.2. Surface Diffusion

The surface diffusion of atomic hydrogen on the Si(111)7 × 7 surface was investigated experimentally by means of optical second harmonic diffraction from a submonolayer grating of adsorbed hydrogen by Reider *et al.* [92]. Atomic hydrogen was adsorbed on the Si(111)7 × 7 surface at 620 K to yield a coverage of $\theta_0 = 0.15$ ML. The sample temperature was chosen to ensure that hydrogen is adsorbed only in the Si–H monohydride state. The Arrhenius plots are shown in Fig. 4(a). The authors found a thermally activated diffusion process with a barrier of $E_a = 1.5 \pm 0.2$ eV and a pre-exponential factor D_0 of 10^{-3} cm^2 s^{-1}. For comparison, the hydrogen atom diffusion through silicon crystals is characterized by a diffusion coefficient of about $(10^{-2})\exp[-0.5/kT]$ cm^2 s^{-1} [71].

1.3.3. Electronic Properties

In Fig. 5, the change in work function versus hydrogen exposure is plotted [47] At the beginning of hydrogen exposure, the work function initially decreases. Above $5 \cdot 10^{-7}$ mbar×min, the work function grows and, finally, when the surface is saturated it decreases again.

2. (100) ORIENTATION

Hydrogen is known to induce three reconstructions on the Si(100) surface. These are 1 × 1, 2 × 1, and 3 × 1.

2.1. PHASE DIAGRAM

As mentioned above a noticeable interaction of hydrogen with silicon can only take place if the hydrogen is offered in the atomic form. The interaction of hydrogen with the Si(100)2 × 1 surface has been investigated by LEED [3, 29, 94–107], RHEED [108], AES [109], XPS [4], ARPES [110–112], STM [113–115], UPS [29, 30, 106], RBS [116], EELS [4, 98, 100, 117],

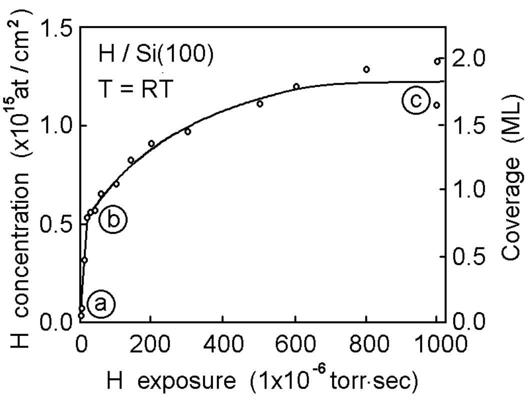

Fig 6. Hydrogen concentration (coverage) on a Si(100)2 × 1 surface kept at RT plotted against H_2–gas exposure (from Ref. [94]). (*Reproduced by permission of the publishers of Journal of Physical Review B)*

HREELS [3, 30], LEIS [118], ERDA [94], TDS [3, 45, 117, 119–121], TPD [93, 101, 122, 123], MIR [95, 96, 124], LE–RIS [97,125], ISS [99,126,127], SSIMS [122,123], surface photovoltage [128], and theoretically [129–133].

Oura *et al.* [94] carried out a quantitative analysis of hydrogen adsorption on the Si(100)2× 1 surface using elastic recoil detection analysis. Figure 6 shows a measured concentration or coverage of adsorbed hydrogen atoms plotted against the exposure of hydrogen molecules for activated hydrogen adsorption on to a clean Si(100)2 × 1 surface at RT. As can be seen, the adsorption curve reveals a rather sharp break point at about 25 L exposure, where the coverage is roughly 1 ML. In the initial stage of adsorption below 25 L exposure (or below 1 ML coverage), hydrogen adsorption takes place rather quickly and almost linearly, while adsorption over 1 ML occurs very slowly towards a saturation coverage of about 1.85±0.18 ML above 1200 L. LEED patterns corresponding to the coverage of 1 ML (point (b) of Fig. 6) and the full coverage (point (c)) show 2 × 1 and 1 × 1 periodicity. The same LEED patterns have been observed in earlier observations [95, 96, 98, 102, 103, 105, 111, 112, 127, 134, 135]. Previously, the saturation coverage of 1.5 and 1.7 ± 0.25 ML was measured by Feldman *et al.* [99] and Narusawa *et al.* [116], respectively, for the D/Si(100) system. Recently, Cheng and Yates [101] determined the saturation coverage of a 1 × 1 phase formed by H adsorption at 210 ± 10 K as 1.9 ML and Lu *et al.* [136] obtained a value of 1.93 ML for RT deuterium adsorption. According to the STM observation of Boland [114], the surface is seen to be very heterogeneous, exhibiting etch pits and etch products, in addition to flat unetched regions after large atomic hydrogen exposure at RT. Flat regions have a 1 × 1 structure and exist only in localized regions of the surface—there is no uniform 1 × 1 phase. The coverage and the hydride species associated with this surface depend upon the exposure conditions.

The Si(100)2 × 1–H surface structure not only takes place at the first stage of hydrogen RT adsorption [94, 98], it is also possible at an elevated temperature hydrogen adsorption at 350–400 °C [94, 98, 100]. For example, the kinetic hydrogen adsorption at 400 °C shown in Fig. 7 [94], indicates the saturation coverage of 1 ML with the corresponding 2 × 1 LEED pattern. The Si(100)2 × 1–H surface phase can also be obtained by thermal desorption of hydrogen from Si(100)1 × 1–H as shown in Fig. 8.

The Si(100)2 × 1–H structure prepared at 600 K is substantively different from the monohydride surface obtained by moderate exposures at RT [114]. In the latter case, higher hydrides are formed which act as precursors to an etching reaction. These higher hydrides are unstable at 600 K and are not formed under high temperature conditions. Prolonged exposure of the high temperature monohydride phase to atomic hydrogen at 600 K failed to induce etching of this surface. This monohydride phase is stable under the conditions in

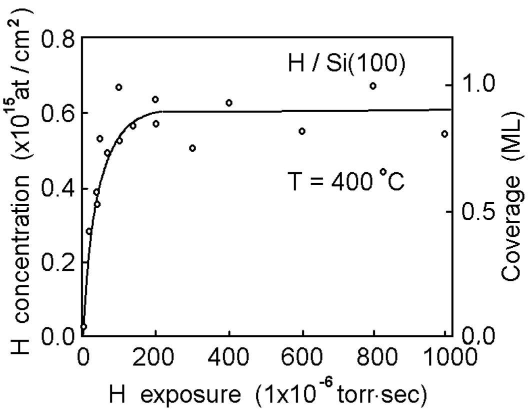

Fig 7. Hydrogen concentration (coverage) as a function of H_2–gas exposure on to a heated Si(100) substrate at 400 °C. LEED pattern observed in the saturation stage is Si(100)2 × 1–H (from Ref. [94]). (*Reproduced by permission of the publishers of Journal of Physical Review B)*

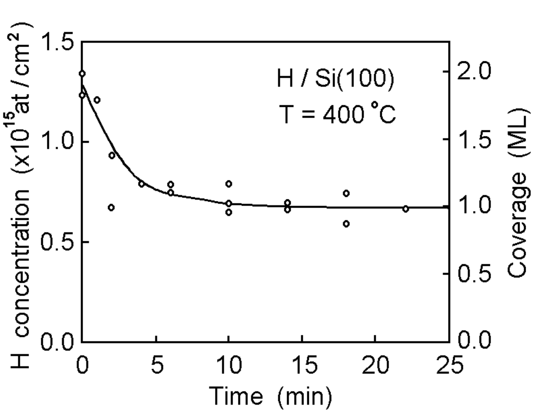

Fig 8. Isothermal desorption of hydrogen from the Si(100) surface at 400 °C. The initial and final stages correspond to the Si(100)1 × 1–H and Si(100)2 × 1–H phases, respectively (from Ref. [94]). (*Reproduced by permission of the publishers of Journal of Physical Review B)*

which it is formed and is characterized by a definite saturation coverage ($\theta_{\text{sat}} = 1.0$ ML).

Chabal and Raghavachari [95] discovered a 3 × 1 phase which they obtained by exposing the surface to hydrogen with a substrate temperature of 380±20 K. Oura *et al.* [94] and Cheng and Yates [101] determined the absolute hydrogen coverage for the Si(100)3 × 1–H surface to be 1.7 ML and 1.4 ML, respectively. According to the STM observation of Boland [114], the 3 × 1 surface is observed to be a well-defined phase at 400 K, i.e. continuous exposure to atomic hydrogen at 400 K does not result in a degradation of the structure. This structure is characterized by a definite surface coverage ($\theta_{\text{sat}} = 1.33$ ML). The 3 × 1 surface, however, is not stable to prolonged exposure to atomic hydrogen at RT. The preparation of a well-defined 3 × 1 phase at 400 K followed by a subsequent RT exposure to atomic hydrogen results in the 1 × 1 phase formation. The absolute coverages obtained for 2 × 1, 3 × 1 and 1 × 1 hydrogen surface phases are shown in Table 1 [101].

Aqueous HF etching of the Si(100) surface results in the producing of very inert surfaces [56, 68, 70] which are found to be almost completely covered by atomic hydrogen [70, 91].

Table 1. Comparison of H-saturation coverages measured at different adsorption temperatures and for different surface phases of Si(100) (from Ref. [101])

H-saturation coverage (ML)			Experimental method used	Refs
2×1	3×1	1×1		
1.0 (630 K)	1.4 (400 K)	1.9 (210 K)	TPD	[101]
1.0 (670 K)	1.7 (373 K)	1.85 (300 K)	ERDA	[94]
		1.5 and 1.7 (< 400 K)	NRA	[99, 116]

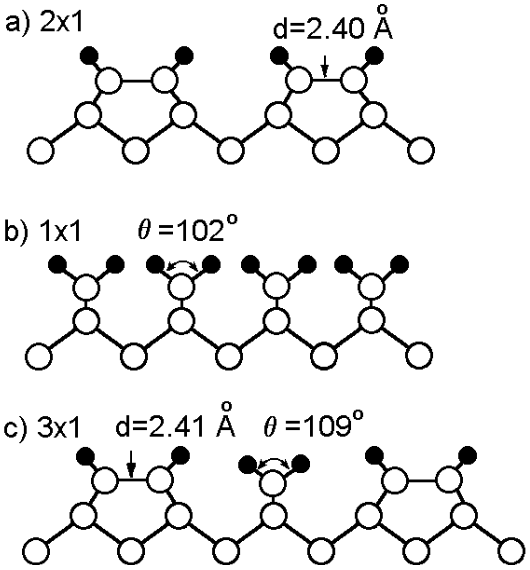

Fig 9. (a) Si(100)2 × 1–H monohydride, (b) Si(100)1 × 1–H dihydride, (c) Si(100)3 × 1–H monohydride plus dihydride. Solid circles denote H atoms (from Ref. [131]). (*Reproduced by permission of the publishers of Journal of Physical Review B)*

2.2. STRUCTURE

2.2.1. Si(100)2 × 1–H

The most commonly observed and best characterized surface is a Si(100)2 × 1–H phase [131]. It is now accepted that the 2 × 1–H phase is completed at the hydrogen coverage of 1 ML (see Table 1) and the adsorbed hydrogen atoms saturate all the dangling bonds of dimerized Si atoms in the first layer without changing the reconstructed 2 × 1 structure. The existence of monohydride on the Si(100)2 × 1–H surface has been confirmed by HREELS [3, 4, 30, 100], UPS [30], ARPES [111], and high-resolution IR spectroscopy [95, 135]. A generally accepted symmetric dimer model for the 2 × 1–H phase is shown in Fig. 9(a). This model for the structure of the 2 × 1 phase is supported by a recent STM study by Boland [113, 114], and the LE–RIS study of Shoji *et al.* [97, 125]. Comparing the experimental results with those of the calculation, Shoji *et al.* [125] showed that the optimum H–Si–Si bond angle for the 2 × 1 structure in the [110] azimuth is in the range of from 108° to 111°.

2.2.2. Si(100)1 × 1–H

Sakurai and Hagstrum [106] suggested that the 1 × 1–H phase corresponds to a symmetric dihydride termination of the surface. This structural model for $\theta = 2$ ML is shown in Fig. 9(b). However, the high-resolution surface IR spectroscopy of Chabal [96] showed that the 1 × 1–H phase is made up of a disordered arrangement of subunits formed of both mono- and dihydrides. Recent direct observation of the Si(100)1 × 1–H surface by STM by Boland [113, 114] confirms the presence of a highly disordered surface after saturation exposures at RT. Apparently, the high H exposure required to produce the 1 × 1 phase also causes etching of the surface. This etching explains the significant population of monohydride species of the 1 × 1–H phase observed earlier and why saturation above 2 ML has never been reported on this surface. Recent TPD experiments of Cheng and Yates [101] showed that the 1 × 1 phase is composed of a mixture monohydride, dihydride, and trihydride surface species. It was found that the discrepancies in measured saturation H coverages reported by others are related to differences in the Si(100) adsorption temperatures employed, since β_3–H_2 begins to desorb near 200 K from the 1 × 1 phase, and variation in the adsorption temperature in the range 200–400 K will therefore cause its saturation coverage to vary (see Table 1). Cheng and Yates [101] suggested that the 1 × 1 LEED pattern seen at high H coverages is due to the underlying Si(100) subsurface structure, as observed through a highly disordered surface.

2.2.3. Si(100)3 × 1–H

¿From an analysis of the SiH and SiH_2 vibrational modes, Chabal and Raghavachari [95] concluded that the 3 × 1 structure is an ordered mixture of monohydride and dihydride subunits as shown in Fig. 9(c). The existence of monohydride and dihydride is confirmed by the TPD experiments of Cheng and Yates [101]. This model for the structure of the 3 × 1 phase is supported by a recent STM study of Boland [113,114]. The 3 × 1 phase consisting of alternating HSi–SiH and SiH_2 species would have a coverage of 1.33 ML. The experimental values of absolute coverage are somewhat greater as shown in Table 1.

2.3. PROPERTIES

2.3.1. Desorption

The observation of hydride products from H on Si(100) by TPD spectroscopy showed the two hydrogen (H_2) desorption states (β_1 at 540 °C and β_2 at 425 °C) [122]. The peak temperature for SiH_4 in TPD occurs at 375 °C, which is 50° below the H_2 β_2 desorption peak. The maximum yield of SiH_4 is observed at $\theta = 1.5$ ML, with roughly 4% of all the surface hydrogen desorbing as SiH_4 resulting in removal of about 1% of a monolayer of silicon atoms.

The kinetics of the thermal recombinative desorption of hydrogen from the monohydride phase was studied by LITD by Sinniah *et al.* [119,120] and Wise *et al.* [93] and by means of isothermal measurements using optical second-harmonic generation by Höfer *et al.* [121]. Over a temperature range of 685–790 K and a coverage range of 0.006 to 1.0 ML, the desorption of hydrogen from Si(100)2 × 1 revealed first-order kinetics. The value of the activation barrier determined in different works are 2 eV [119, 120], 2.5 ± 0.1 eV (pre-exponential factor of $\nu_d = (5.5 \pm 0.5) \times 10^{15}$ s^{-1}) [93], and 2.48 ± 0.1 eV (pre-exponential factor of 2×10^{15} s^{-1}) [121]. The first-order H_2 desorption kinetics were attributed to the concerted desorption of H_2 from two hydrogen atoms paired on the same silicon dimer on Si(100)2 × 1 [93]. The evidence of hydrogen pairing was presented in the STM study by Boland [115].

2.3.2. Surface Diffusion

Wu and Carter [133] presented first-principles total-energy calculations of hydrogen-adatom diffusion on a Si(100)2 × 1 surface. The diffusion barriers are high (2–3 eV) and wide (≈ 3–4 Å), suggesting that H-atom diffusion on Si(100) mostly proceeds via a classic hopping mechanism instead of tunneling. Furthermore, diffusion of hydrogen atoms is predicted to be *anisotropic*, being preferentially directed parallel to the silicon–dimer rows, with an activation energy of 2.0 eV. Higher activation energies of 2.5 ÷ 2.7 eV are predicted for diffusion perpendicular to dimer rows.

3. (110) ORIENTATION

Hydrogen is known to induce a "2 × 16" step structure on the Si(110) surface.

3.1. PHASE DIAGRAM

The ideal termination of the Si(110) surface by hydrogen atoms (one H atom per silicon dangling bond) gives 1 ML hydrogen coverage. However, the amount of adsorbed hydrogen was estimated by Kleint [117] by TDS at saturation exposure of 10^4 L at 800 K to be about 0.8 ML.

The LEED pattern of the H-saturated Si(110) surface was observed by Ampo *et al.* [137] with primary energy 20–120 eV. The characteristics of the LEED spot intensities are as follows.

(a) At every primary energy, intensities of the diffraction spots are always below detection limit except those of integer-order spots and the areas around them indexed $(p_1 + q/16, p_2)$; p_1 and p_2 are integers and $q = \pm 1, \pm 2, \pm 3$. This corresponds to reports that hydrogen makes the fractional order spots weaken or disappear and the surface structure revert to bulk-like 1 × 1 structures [138, 139]. This indicates that hydrogen causes the silicon atoms to appear in a bulk-like structural site.

(b) Each spot intensity oscillates as the primary energy increases. Every spot shows the same period of translation corresponding to a bulk Si(110) layer spacing.

(c) When one spot intensity becomes local maxima, intensities of the two nearest-neighbor spots become local minimum.

(d) The fractional order spot intensities around the integer spot are always symmetric. This contradicts the periodically monotonous step structure for a vicinal surface.

The "2 × 16" LEED patterns remain unchanged with atomic hydrogen exposure over 1.2×10^4 L [137]. Vibrational and PE spectra of Butz *et al.* [30] demonstrate that a monohydride phase develops at an elevated temperature and the dihydride phase forms at lower temperatures following hydrogen adsorption on the Si(110) surface.

3.2. STRUCTURE

Based on the kinematic analysis of LEED patterns, the structural model of the "2 × 16"–H phase was proposed by Ampo *et al.* [137]. According to their proposal the Si(110) "2 × 16"-H surface consists of the periodic one-monolayer step array which is described by an up and down sequence of terraces. The step boundaries are along the $[\bar{1}\bar{1}2]$ direction, the step height is within ±5% of the bulk Si(110) layer spacing. The number of atoms N_1 in the [110] direction on the upper terrace is in the range $7 \leq N_1 \leq 9$, the number N_2 on the lower terrace is in the range $7 \leq N_2 \leq 9$, and silicon atoms on the surface are in the bulk-like structural site.

REFERENCES

[1] K. Christmann, *Surf. Sci. Repts.* **9** (1988) 1.
[2] G. Schulze and M. Henzler, *Surf. Sci.* **124** (1983) 336.
[3] H. Froitzheim, U. K. Kohler and H. Lammering, *Surf. Sci.* **149** (1985) 537.
[4] J. A. Schaefer, F. Stucki, D. J. Frankel, W. Gopel and G. J. Lapeyre, *J. Vac. Sci. Technol. B* **2** (1984) 359.
[5] R. M. Wallace, P. A. Taylor, W. J. Choyke and J. T. Yates, *Surf. Sci.* **239** (1990) 1.
[6] R. J. Culbertson, L. C. Felman, P. J. Silverman and R. Haight, *J. Vac. Sci. Technol.* **20** (1982) 868.
[7] U. Jansson and K. J. Uram, *J. Chem. Phys.* **91** (1989) 7978.
[8] E. G. MacRae, *Surf. Sci.* **147** (1984) 663.
[9] E. G. McRae and C. W. Caldwell, *Phys. Rev. Lett.* **46** (1981) 1632.
[10] K. Oura, M. Naitoh, F. Shoji, J. Yamane, K. Umezawa and T. Hanawa, *Nucl. Instrum. Meth. Phys. Res. B* **45** (1990) 199.
[11] M. Nishijima, K. Edamoto, Y. Kubota, H. Kobayashi and M. Onchi, *Surf. Sci.* **158** (1985) 422.
[12] N. Ohse and K. Yagi, *Surf. Sci.* **217** (1989) L430.
[13] S. Kohmoto, S. Mizuno and A. Ichimiya, *Appl. Surf. Sci.* **41–42** (1989) 107.
[14] A. Ishimiya and S. Mizuno, *ISIJ International* **29** (1989) 576.
[15] S. Mizuno and A. Ishimiya, *Appl. Surf. Sci.* **33–34** (1988) 38.
[16] T. Takahagi, I. Nagai, A. Ishitani, H. Kuroda and Y. Nagasawa, *J. Appl. Phys.* **64** (1988) 3516.
[17] A. Ichimiya and S. Mizuno, *Surf. Sci.* **191** (1987) L765.
[18] Y. Horio, A. Ichimiya, S. Kohmoto and H. Nakahara, *Surf. Sci.* **257** (1991) 167.
[19] T. Sakurai and H. D. Hagstrum, *Phys. Rev. B* **12** (1975) 5349.
[20] J. Abrefah and D. R. Olander, *Surf. Sci.* **209** (1989) 291.
[21] A. Thanailakis, D. E. Ioannou and C. M. Reed, *Solid State Commun.* **44** (1982) 669.
[22] D. R. Olander, M. Balooch, J. Abrefah and W. J. Siekhaus, *J. Vac. Sci. Technol. B* **5** (1987) 1404.
[23] D. Muller, F. Ringeisen, J. J. Koulmann and D. Bolmont, *Surf. Sci.* **189–190** (1987) 472.
[24] J. J. Koulmann, F. Ringeisen, M. Alaoui and D. Bolmont, *Phys. Rev. B* **41** (1990) 3878.
[25] R. D. Bringans and M. A. Olmstead, *J. Vac. Sci. Technol. B* **6** (1988) 1132.
[26] J. J. Koulmann, D. Steinmetz, F. Ringeisen and D. Bolmont, *Physica B* **170** (1991) 492.
[27] T. Yasaka, K. Kanda, K. Sawara, S. Miyazaki and M. Hirose, *Japan J. Appl. Phys.* **30** (1991) 3567.
[28] S. Watanabe, M. Shigeno, N. Nakayama and T. Ito, *Japan J. Appl. Phys.* **30** (1991) 3575.
[29] H. Ibach and J. E. Rowe, *Surf. Sci.* **43** (1974) 481.
[30] R. Butz, E. M. Oellig, H. Ibach and H. Wagner, *Surf. Sci.* **147** (1984) 343.
[31] J. A. Appelbaum, H. D. Hagstrum, D. R. Hamann and T. Sakurai, *Surf. Sci.* **58** (1976) 479.
[32] K. C. Pandey, T. Sakurai and H. D. Hagstrum, *Phys. Rev. Lett.* **35** (1975) 1728.
[33] J. E. Rowe, *Surf. Sci.* **53** (1975) 461.
[34] F. Shoji and K. Oura, *Appl. Surf. Sci.* **60–61** (1992) 166.
[35] H. Froitzheim, H. Lammering and H. L. Gunter, *Phys. Rev. B* **27** (1983) 2278.
[36] R. Avci, O. B. Dabbousi and A. S. Al-Harthi, *J. Vac. Sci. Technol. A* **6** (1988) 748.
[37] H. Wagner, R. Butz, U. Backes and D. Bruchmann, *Solid State Commun.* **38** (1981) 1155.
[38] H. Froitzheim, H. Ibach and S. Lehwald, *Phys. Lett. A* **55** (1975) 247.

[39] H. Kobayashi, K. Edamoto, M. Onchi and M. Nishijima, *J. Chem. Phys.* **78** (1983) 7429.

[40] P. Dumas, Y. J. Chabal and G. S. Higashi, *Phys. Rev. Lett.* **65** (1990) 1124.

[41] Y. J. Chabal, *Phys. Rev. Lett.* **50** (1983) 1850.

[42] Y. J. Chabal, G. S. Higashi and S. B. Christman, *Phys. Rev. B* **28** (1983) 4473.

[43] S. Watanabe, N. Nakayama and T. Ito, *Appl. Phys. Lett.* **59** (1991) 1458.

[44] D. Dai, X. Wang, J. Hu and Y. Ge, *Surf. Sci.* **274** (1992) 252.

[45] Ch. Kleint and K. -D. Brzoska, *Surf. Sci.* **231** (1990) 177.

[46] B. G. Koehler, C. H. Mak, D. A. Arthur, P. A. Coon and S. M. George, *J. Chem. Phys.* **89** (1988) 1709.

[47] P. Klimesch, G. Meyer and M. Henzler, *Surf. Sci.* **137** (1984) 79.

[48] S. H. Wolff, S. Wagner, J. M. Gibson, D. Loretto, I. K. Robinson and J. C. Bean, *Surf. Sci.* **239** (1990) L537.

[49] N. Matsunami, Y. Hasebe and N. Itoh, *Surf. Sci.* **192** (1987) 27.

[50] K. Ueda, S. Kodama and A. Takano, *Surf. Sci.* **242** (1991) 454.

[51] C. M. Greenlief, S. M. Gates and P. A. Holbert, *Chem. Phys. Lett.* **159** (1989) 202.

[52] B. G. Koehler and S. M. George, *Surf. Sci.* **248** (1991) 158.

[53] G. A. Reider, U. Hofer and T. F. Heinz, *J. Chem. Phys.* **94** (1991) 4080.

[54] K. Mortensen, D. M. Chen, P. J. Bedrossian, J. A. Golovchenko and F. Besenbacher, *Phys. Rev. B* **43** (1991) 1816.

[55] T. Tokumoto, K. Miki, H. Murakami, H. Bando, H. Ono and K. Kajimura, *J. Vac. Sci. Technol. A* **8** (1990) 255.

[56] T. Sakurai, Y. Hasegawa, T. Hashizume, I. Kamiya, T. Ide, I. Simuta, H. W. Pickering and S. Hyodo, *J. Vac. Sci. Technol. A* **8** (1990) 259.

[57] J. J. Boland, *Surf. Sci.* **244** (1991) 1.

[58] R. S. Becker, G. S. Higashi, Y. J. Chabal and A. J. Becker, *Phys. Rev. Lett.* **65** (1990) 1917.

[59] W. J. Kaiser, L. D. Bell, M. H. Hecht and F. J. Grunthaner, *J. Vac. Sci. Technol. A* **6** (1988) 519.

[60] Y. Morita, K. Miki and H. Tokumoto, *Appl. Phys. Lett.* **59** (1991) 1347.

[61] Y. Morita, K. Miki and H. Tokumoto, *Japan J. Appl. Phys.* **30** (1991) 3570.

[62] M. Tabe and M. Tanimoto, *Appl. Phys. Lett.* **58** (1991) 2105.

[63] J. J. Boland, *J. Phys. Chem.* **95** (1991) 1521.

[64] J. J. Boland, *J. Vac. Sci. Technol. B* **9** (1991) 764.

[65] C. J. Karlsson, E. Landemark, L. S. O. Johansson, U. O. Karlsson and R. I. G. Uhrberg, *Phys. Rev. B* **41** (1990) 1521.

[66] K. J. Uram and U. Jansson, *J. Vac. Sci. Technol. B* **7** (1989) 1176.

[67] G. S. Higashi, Y. J. Chabal, G. W. Trucks and K. Raghavachari, *Appl. Phys. Lett.* **56** (1990) 656.

[68] V. A. Burrows, Y. J. Chabal, G. S. Higashi, K. Raghavachari and S. B. Christman, *Appl. Phys. Lett.* **53** (1988) 998.

[69] Ph. Dumas, Y. J. Chabal and G. S. Higashi, *J. Elect. Spect. Relat. Phenom.* **54–55** (1990) 103.

[70] Y. J. Chabal, G. S. Higashi, K. Radhavachari and V. A. Burrows, *J. Vac. Sci. Technol. A* **7** (1989) 2104.

[71] B. M. Rice, I. NoorBatcha, D. L. Thompson and L. M. Raff, *J. Chem. Phys.* **86** (1987) 1608.

[72] S. Ciraci, *Solid State Commun.* **49** (1984) 43.

[73] S. B. Zhang and W. B. Jackson, *Phys. Rev. B* **43** (1991) 12142.

[74] P. M. Agrawal, L. M. Raff and D. L. Thompson, *Surf. Sci.* **188** (1987) 402.

[75] B. M. Rice, L. M. Raff and D. L. Thompson, *Surf. Sci.* **198** (1988) 360.

[76] G. V. Gadijak, A. A. Karpushin, I. V. Korolenko, Ju. N. Morokov and M. Tomasek, *Czechosl. J. Phys. B* **35** (1985) 54.

[77] F. Ancilotto and A. Selloni, *Phys. Rev. Lett.* **68** (1992) 2640.

[78] K. M. Ho, M. L. Cohen and M. Schluter, *Phys. Rev. B* **15** (1977) 3888.
[79] J. A. Appelbaum and D. R. Hamann, *Phys. Rev. Lett.* **34** (1975) 806.
[80] K. C. Pandey, *Phys. Rev. B* **14** (1976) 1557.
[81] S. Picaud and C. Girardet, *Surf. Sci.* **258** (1991) 210.
[82] W. S. Verwoerd, *Surf. Sci.* **125** (1983) 575.
[83] P. Deak, C. R. Ortiz, L. C. Snyder and J. W. Corbett, *Physica B* **170** (1991) 223.
[84] J. N. Beauregard and H. R. Mayne, *Surf. Sci.* **280** (1993) L253.
[85] C. M. Bertoni, F. Finocchi, F. Bernardini and N. M. Buongiorno, *Physica B* **170** (1991) 429.
[86] B. M. Rice, L. M. Raff and D. L. Thompson, *J. Chem. Phys.* **88** (1988) 7221.
[87] L. M. Raff, I. NoorBatcha and D. L. Thompson, *J. Chem. Phys.* **85** (1986) 3081.
[88] T. Hoshino and M. Tsukada, *Surf. Sci.* **115** (1982) 104.
[89] R. B. Doak, Y. J. Chabal, G. S. Higashi and P. Dumas, *J. Elect. Spect. Relat. Phenom.* **54–55** (1990) 291¿
[90] P. Guyot-Sionnest, P. Dumas and Y. L. Chabal, *J. Elect. Spect. Relat. Phenom.* **54–55** (1990) 27.
[91] P. Dumas, Y. J. Chabal and P. Jakob, *Surf. Sci.* **269–270** (1992) 867.
[92] G. A. Reider, U. Hofer and T. F. Heinz, *Phys. Rev. Lett.* **66** (1991) 1994.
[93] M. L. Wise, B. G. Koehler, P. Gupta, P. A. Coon and S. M. George, *Surf. Sci.* **258** (1991) 166.
[94] K. Oura, J. Yamane, K. Umezawa, M. Naitoh, F. Shoji and T. Hanawa, *Phys. Rev. B* **41** (1990) 1200.
[95] Y. J. Chabal and K. Raghavachari, *Phys. Rev. Lett.* **54** (1985) 1055.
[96] Y. J. Chabal, *Surf. Sci.* **168** (1986) 594.
[97] F. Shoji, K. Kashihara, K. Sumitomo and K. Oura, *Surf. Sci.* **242** (1991) 422.
[98] J. A. Schaefer, F. Stucki, J. A. Anderson, G. J. Lapeyre and W. Gopel, *Surf. Sci.* **140** (1984) 207.
[99] L. C. Feldman, P. J. Silverman and I. Stensgaard, *Nucl. Instrum. Meth. Phys. Res. A* **168** (1980) 589.
[100] F. Stucki, J. A. Schaefer, J. R. Anderson, G. J. Lapeyre and W. Gopel, *Solid State Commun.* **47** (1983) 795.
[101] C. C. Cheng and J. T. Yates, Jr. , *Phys. Rev. B* **43** (1991) 4041.
[102] S. J. White and D. P. Woodruff, *J. Phys. C* **9** (1976) L451.
[103] S. J. White and D. P. Woodruff, *Surf. Sci.* **63** (1977) 254.
[104] S. J. White and D. P. Woodruff, *Surf. Sci.* **64** (1977) 131.
[105] S. J. White, D. P. Woodruff, B. W. Holland and R. S. Zimmer, *Surf. Sci.* **74** (1978) 34.
[106] T. Sakurai and H. D. Hagstrum, *Phys. Rev. B* **14** (1976) 1593.
[107] C. C. Umbach, M. E. Keeffe and J. M. Blakely, *J. Vac. Sci. Technol. B* **9** (1991) 721.
[108] J. V. Ashby, N. Norton and P. A. Maksym, *Surf. Sci.* **175** (1986) 604.
[109] H. H. Madden, *Surf. Sci.* **105** (1981) 129.
[110] L. S. O. Johansson, R. I. G. Uhrberg, P. Martensson and G. V. Hansson, *Phys. Rev. B* **42** (1990) 1305.
[111] L. S. O. Johansson, R. I. G. Uhrberg and G. V. Hansson, *Phys. Rev. B* **38** (1988) 13490.
[112] L. S. O. Johansson, R. I. G. Uhrberg and G. V. Hansson, *Surf. Sci.* **189–190** (1987) 479.
[113] J. J. Boland, *Phys. Rev. Lett.* **65** (1990) 3325.
[114] J. J. Boland, *Surf. Sci.* **261** (1992) 17.
[115] J. J. Boland, *Phys. Rev. Lett.* **67** (1991) 1539.
[116] T. Narusawa and W. M. Gibson, *J. Vac. Sci. Technol.* **17** (1980) 256.
[117] Ch. Kleint, *Vacuum* **36** (1986) 267.
[118] F. Shoji, K. Kashihara, K. Oura and T. Hanawa, *Surf. Sci.* **220** (1989) L719.
[119] K. Sinniah, M. G. Sherman, L. B. Lewis, W. H. Weinberg, J. T. Yates and K. C. Janda, *J. Chem. Phys.* **92** (1990) 5700.

[120] K. Sinniah, M. G. Sherman, L. B. Lewis, W. H. Weinberg, J. T. Yates and K. C. Janda, *Phys. Rev. Lett.* **62** (1989) 567.

[121] U. Hofer, L. Li and T. F. Heinz, *Phys. Rev. B* **45** (1992) 9485.

[122] S. M. Gates, R. R. Kuntz and C. M. Greenlief, *Surf. Sci.* **207** (1989) 364.

[123] C. M. Greenlief, S. M. Gates and P. A. Holbert, *J. Vac. Sci. Technol. A* **7** (1989) 1845.

[124] J. C. Tully, Y. J. Chabal, K. Raghavachari, J. M. Bowman and R. R. Lucchese, *Phys. Rev. B* **31** (1985) 1184.

[125] F. Shoji, K. Kusumura and K. Oura, *Surf. Sci.* **280** (1993) L247.

[126] I. Stensgaard, L. C. Feldman and P. J. Silverman, *Surf. Sci.* **102** (1981) 1.

[127] R. M. Tromp, R. G. Smeenk and F. W. Saris, *Surf. Sci.* **104** (1981) 13.

[128] W. Monch, P. Kohe and S. Kruger, *J. Vac. Sci. Technol.* **19** (1981) 313.

[129] B. I. Craig and P. V. Smith, *Surf. Sci.* **226** (1990) L55.

[130] C. K. Ong, *Semicond. Sci. Technol.* **4** (1989) 469.

[131] J. E. Northrup, *Phys. Rev. B* **44** (1991) 1419.

[132] B. I. Craig and P. V. Smith, *Solid State Commun.* **81** (1992) 623.

[133] C. J. Wu and E. A. Carter, *Phys. Rev. B* **46** (1992) 4651.

[134] S. J. White, D. P. Woodruff, B. W. Holland and R. S. Zimmer, *Surf. Sci.* **68** (1977) 457.

[135] Y. J. Chabal and K. Raghavachari, *Phys. Rev. Lett.* **53** (1984) 282.

[136] Z. H. Lu, K. Griffiths, P. R. Norton and T. K. Sham, *Phys. Rev. Lett.* **68** (1992) 1343.

[137] H. Ampo, S. Miura, K. Kato, Y. Ohkawa and A. Tamura, *Phys. Rev. B* **34** (1986) 2329.

[138] T. Sakurai and H. D. Hagstrum, *J. Vac. Sci. Technol.* **13** (1976) 807.

[139] T. Sakurai, K. C. Pandey and H. D. Hagstrum, *Phys. Lett. A* **56** (1976) 204.

(Hg)

MERCURY

1. (111) ORIENTATION

Mercury was reported to induce $\sqrt{3} \times \sqrt{3}$ and 1×1 reconstructions on the Si(111) surface.

1.1. PHASE DIAGRAM

The adsorption of Hg on the Si(111) surface has been studied recently by Li *et al.* [1,2]. In the experiment, triply distilled mercury was introduced into the vacuum chamber through the leak valve. The substrate temperature during Hg exposure was as low as 150 K. As a result, a faint $\sqrt{3} \times \sqrt{3}$—$R30^\circ$ LEED pattern is observed superimposed on the 7×7 LEED pattern at exposures of 10–20 L. A 1×1 LEED pattern develops at about 30 L. (Li *et al.* noted, however, that all pressures reported in their works [1, 2] are uncorrected for the ionization gauge cross-section* of Hg.)

It was observed that most of the Hg adsorbed at 150 K desorbs at room temperature. However, even after flashing to 1250 °C, a small amount of Hg remains at the surface. The $\sqrt{3} \times \sqrt{3}$ structure was found to persist with annealing to about 750 °C, but further repeated annealing to 1250 °C restores the 7×7 reconstruction of the clean Si(111) surface. In contrast, the 1×1 reconstruction is maintained even after repeated annealing at 1250 °C.

1.2. STRUCTURE

The experimental results of Refs [1,2] do not provide sufficient information for determination of the composition and atomic arrangement of the grown Si(111)–Hg phases. However, certain details of their structure were elucidated. In particular, the helium beam scattering revealed the absence of the perfect ordering in the topmost layer of both the $\sqrt{3} \times \sqrt{3}$ and 1×1 phases. This result shows that a rather complicated structure involving several Si layers is formed. Furthermore, PES results strongly suggest that some mercury adsorbs into subsurface sites.

REFERENCES

[1] D. Li, J. Zhang, S. Lee and P. A. Dowben, *Phys. Rev. B* **45** (1992) 11876.

[2] D. Li, J. Lin, W. Li, S. Lee, G. Vidali and P. A. Dowben, *Surf. Sci.* **280** (1993) 71.

(Ho)

HOLMIUM

1. (111) ORIENTATION

1×1 reconstruction were observed after Ho deposition on the Si(111)7×7 surface.

1.1. PHASE DIAGRAM

RT deposition of Ho layer up to 3 ML thick on Si(111)7×7 followed by annealing at $T > 600^\circ$C results in the 1×1 LEED pattern appearance as reported by Sakho *et al.* [1]. After annealing Ho layers convert into epitaxial pseudo-disilicide (HoSi$_{2-x}$) interfaces which are terminated by extra silicon at the surface, which, in turn, displays a 1×1 LEED pattern. The overgrowth of silicon appears to be epitaxial since 1×1 LEED patterns were observed.

REFERENCES

[1] O. Sakho, F. Sirotti, M. DeSantis, M. Sacchi and G. Rossi, *Appl. Surf. Sci.* **56–58** (1992) 568.

(I)

IODINE

1. (111) ORIENTATION

Iodine does not significantly alter the original reconstruction of the Si(111)7 × 7 surface.

1.1. PHASE DIAGRAM

After RT deposition of iodine on to the Si(111)7 × 7 surface (up to $\theta = 1.2$ ML), only first-order LEED spots can be seen (1 × 1 pattern) and very weak seventh-order spots connecting them [1–3]. The seventh-order spots closer to those of first-order have higher intensity. The intensity of the seventh-order spots is higher at low I coverages. A similar LEED pattern is observed after annealing at $\sim 400\,^\circ$C [3]. This suggests that the reconstruction is locally destroyed in the regions where I is adsorbed. At $\approx 500\,^\circ$C, I starts to desorb. Careful measurements were done to check whether iodine produces a direct etching effect on the surface (desorption of species like ISi or I_2Si, etc.) by Michel *et al.* [1]. But, within the detection range (10^{-14} mbar) no such species were observed.

1.2. STRUCTURE

The structure of the I layer on the Si(111)7 × 7 surface has been investigated by means of XSW [1] and SEXAFS [2–4]. According to the data of these investigations, iodine occupies the topmost site on Si(111)7 × 7 the surface and is covalently bound with the surface silicon atom. XSW results of Michel *et al.* [1] are compatible with local dereconstruction, characterized by adatom removal and release of the stacking-fault at the regions where I adsorbs. The bond length of Si–I experimentally determined by SEXAFS is 2.44 ± 0.03 Å [2, 3].

2. (100) ORIENTATION

Iodine induces, presumably, $c(2 \times 2)$ reconstruction of the Si(100) surface.

2.1. PHASE DIAGRAM

According to the data of Henderson and Polito [5], RHEED reflections from the iodine-covered Si(100) surface are characteristic of a face-centered array with the inter-row separations of silicon, presumably $c(2 \times 2)$.

3. (110) ORIENTATION

Iodine induces 1 × 1 reconstruction on the Si(110) “2 × 16” surface.

3.1. PHASE DIAGRAM

The clean Si(110) surface displays a “2 × 16” reconstruction, but, after I adsorption, the LEED pattern reverts almost completely to a 1 × 1 [1]. After repeated annealing of the I layer (and reduction of the coverage from 0.45 ML), weak streaks develop along the [001] direction, with a periodicity (in the $[\bar{1}10]$ direction) corresponding to a 1 × 4 reconstruction, but without any defined spots except those of the 1 × 1. The “2 × 16” reconstruction never reappears. This result suggests I-induced dereconstruction of the surface.

The desorption of I takes place in the same temperature range as for the Si(111) surface, and also no etching effects could be observed.

3.2. STRUCTURE

According to XSW investigations of Michel *et al.* , [1], the adsorption site of I on the Si(110) surface is the hollow one along the atomic chains presented at the bulk-terminated surface.

REFERENCES

[1] E. G. Michel, Th. Pauly, V. Etelaniemi and G. Materlik, *Surf. Sci.* **241** (1991) 111.
[2] P. H. Citrin and J. E. Rowe, *Surf. Sci.* **132** (1983) 205.
[3] P. H. Citrin, P. Eisenberger and J. E. Rowe, *Phys. Rev. Lett.* **48** (1982) 802.
[4] J. E. Rowe and P. H. Citrin, *J. Vac. Sci. Technol.* **21** (1982) 338.
[5] R. C. Henderson and W. J. Polito, *Surf. Sci.* **14** (1969) 473.

(In)

INDIUM

1. (111) ORIENTATION

When submonolayer In is deposited on to a clean Si(111) surface, the following various superstructures are observed depending on In coverage and substrate temperature, 7 × 7, $\sqrt{3}\times\sqrt{3}$—$R30°$, 4 × 1, 5 × 1, 1 × 1—$R30°$, $\sqrt{31}\times\sqrt{31}-R9°$, $\sqrt{7}\times\sqrt{3}$, 2 × 2, $2\sqrt{3}\times 2\sqrt{3}$—$R30°$.

1.1. PHASE DIAGRAM

The results for In overlayer growth at RT differ greatly for the Si(111)7 × 7 and Si(111)2 × 1 substrates.

1.1.1. RT Deposition on to Si(111)7 × 7

Deposition of In on to the Si(111)7 × 7 surface results in removal of the ordered LEED pattern [1,2]. Akilov *et al.* [2] suggested that the RT growth of In overlayer proceeds according to Stranski-Krastanov growth mode: indium metal islands form on top of the disordered surface phase which has local atomic arrangement and composition similar to those of the ordered Si(111)1 × 1—$R30°$–In phase observed at high temperatures.

1.1.2. RT Deposition on to Si(111)2 × 1

Upon deposition of In on to the cleaved Si(111)2 × 1 surface, a number of the ordered reconstructions is observed [1, 3]. At about 0.05 ML, a $\sqrt{3}\times\sqrt{3}$—$R30°$ structure starts to show up in addition to the 2 × 1 reconstruction and $\sqrt{3}\times\sqrt{3}$—$R30°$ fully replaces the 2 × 1 pattern after 0.3 ML. Additional In deposition yields a 2 × 2 pattern at coverages exceeding 0.5 ML. Finally, up beyond 1.2 ML, a complicated pattern is observed which was interpreted as corresponding to the In (111) surface rotated by 30° with respect to the substrate [1].

Table 1 summarizes the structural evolution of the Si(111)2×1 surface upon RT deposition of indium.

1.1.3. HT Growth

Starting from the early work by Lander and Morrison [4, 5], the formation of the ordered surface phases in the submonolayer In/Si(111) system was the subject of several investigations [2, 6–16]. The surface structures that were reliably reproduced by many groups are 7 × 7, $\sqrt{3}\times\sqrt{3}$—$R30°$, $\sqrt{31}\times\sqrt{31}$—$R9°$, 4 × 1 and 1 × 1—$R30°$. These phases are formed by

Table 1. Surface structures observed on a cleaved Si(111)2 × 1 surface upon increasing coverage of In (from Ref. [3])

In coverage (ML)	Structure
0–0.05	2×1
0.05–0.2	$2 \times 1 + \sqrt{3} \times \sqrt{3}$
0.2–0.5	$\sqrt{3} \times \sqrt{3}$
0.5–1.2	2×2
> 1.2	"Complicated but ordered structure"

indium deposition at about 450 °C and appear in turn with increasing indium coverage as shown in Fig. 1.

Recently, Park *et al.* [15] using STM observed a new phase, namely, $\sqrt{7} \times \sqrt{3}$ (or $\begin{pmatrix} 3 & 1 \\ 1 & 2 \end{pmatrix}$ in matrix notation). The authors pointed that the $\sqrt{7} \times \sqrt{3}$ phase had been observed several times over several experimental cycles. However, it only appears when the 4×1 surface phase also presents at the surface.

It should be noted that the $2\sqrt{3} \times 2\sqrt{3}$—$R30°$ phase reported in Refs [4,5] and the 5×5 phase reported in Ref. [9] have not been reproduced in later works. The existence of two different surface phases displaying a $\sqrt{3} \times \sqrt{3}$—$R30°$ reconstruction (so called, $\alpha(\sqrt{3} \times \sqrt{3})$ and $\beta(\sqrt{3} \times \sqrt{3})$) as suggested by Lander and Morrison [4,5] has not been confirmed by other investigators.

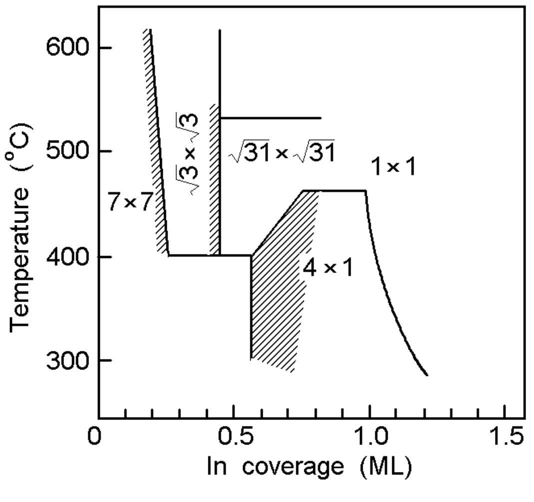

Fig 1. Phase diagram of the In/Si(111) system. In this study, indium was deposited at 440 °C. In this case, 7×7–In, $\sqrt{3} \times \sqrt{3}$–In, $\sqrt{31} \times \sqrt{31}$–In, 4×1–In superstructures appear in turn with increasing indium coverage. The transition region between two superstructures at which the superspots of both coexist in the RHEED pattern is indicated by the shaded area. These superstructures do not change when the temperature is lowered to room temperature (from Ref. [12]). (*Reproduced by permission of Elsevier Science Publishers BV)*

1.2. STRUCTURE

1.2.1. Si(111)7 × 7–In

Nogami *et al.* [14] used STM to study the behavior of In on the Si(111)7 × 7 surface at extremely low metal coverages. Until the 0.05 ML, In atoms were found to replace Si in the 7 × 7 adatom positions, preserving the 7 × 7 reconstruction. In this case, the In atoms demonstrate a strong tendency to occupy positions along the edges of the 7 × 7 unit cell rather than adjacent to the corner holes; the ratio of In atoms in edge sites to corner sites is more than 6:1 at either of the coverages studied.

1.2.2. Si(111)$\sqrt{3} \times \sqrt{3}$—$R30°$–In

The Si(111)$\sqrt{3} \times \sqrt{3}$—$R30°$–In phase was studied using different techniques, ARUPS [17–19], KRIPES [20–23], EELS [11,12], ISS [24–26], STM [13,14], and MEED [27].

It was conclusively determined that the $\sqrt{3} \times \sqrt{3}$—$R30°$–In phase has essentially the same atomic arrangement as the $\sqrt{3} \times \sqrt{3}$–Al and $\sqrt{3} \times \sqrt{3}$-Ga phases: metal adatoms with coverage of 1/3 ML rest in the threefold symmetric sites above second-layer Si atoms (T_4 site). The most positive confirmation of the T_4 bonding site of In adatoms in the $\sqrt{3} \times \sqrt{3}$–In structure was given in the STM examination of a phase boundary between 7 × 7 and $\sqrt{3} \times \sqrt{3}$ regions observed at low In coverages [14].

The vertical position of In adatom in $\sqrt{3} \times \sqrt{3}$ geometry was considered in the ISS experiments by Izumi *et al.* [24] and Cornelison *et al.* [26] : the bond length between In and top first-layer Si atoms was estimated to be 2.24 Å in Ref. [24] and 2.62 Å in Ref. [26]. The latter value is in excellent agreement with the result of total-energy calculations (2.63 Å) reported in Ref. [17].

1.2.3. Si(111)$\sqrt{31} \times \sqrt{31}$—$R9°$–In

The $\sqrt{31} \times \sqrt{31}$—$R9°$ structure was observed by RHEED and LEED at about 0.6 ML In coverage [6,8,12]. It occurs in two domains with orientation of the $\sqrt{31} \times \sqrt{31}$ unit cell either +9° or −9° off from the Si(111)1 × 1 unit cell.

Park *et al.* [15] obtained an STM image of the $\sqrt{31} \times \sqrt{31}$ reconstruction, which is shown in Fig. 2. The periodic diamond-shaped unit cells are clearly seen with bright dots within the unit cell having a 1 × 1 spacing. Close examination reveals that the boundary of the unit cell is tilted by the expected angle of 9° from the $[\bar{1}10]$ direction. This can be directly verified by comparison with 4 × 1 rows which are partially shown at the lower left corner of Fig. 2(a).

The positions of atoms are drawn in Fig. 2(b). There are ten atoms in the upper triangular subunit and six atoms in the lower triangular subunit. Park *et al.* pointed out that they were unable to determine whether the difference in brightness between the upper and lower triangular subunits is due to the difference in the underlying structure or simply due to the difference in the size of the triangular In clusters. They also assumed that the different brightness may reflect different electronic structure rather than actual different height since the STM image strongly depends on the bias voltage and this implies a complicated electronic structure of this phase [15].

1.2.4. Si(111)4 × 1–In

The 4 × 1–In structure observed at In coverages ranging from 0.6 up to more than 1.0 ML [12,15] was the object of several investigations [13,15,28,29].

The STM observations [13,15] revealed that the primary features of the 4×1 reconstruction are the ridges along the $[\bar{1}10]$ directions separated by deep furrows. The spacing of the furrows

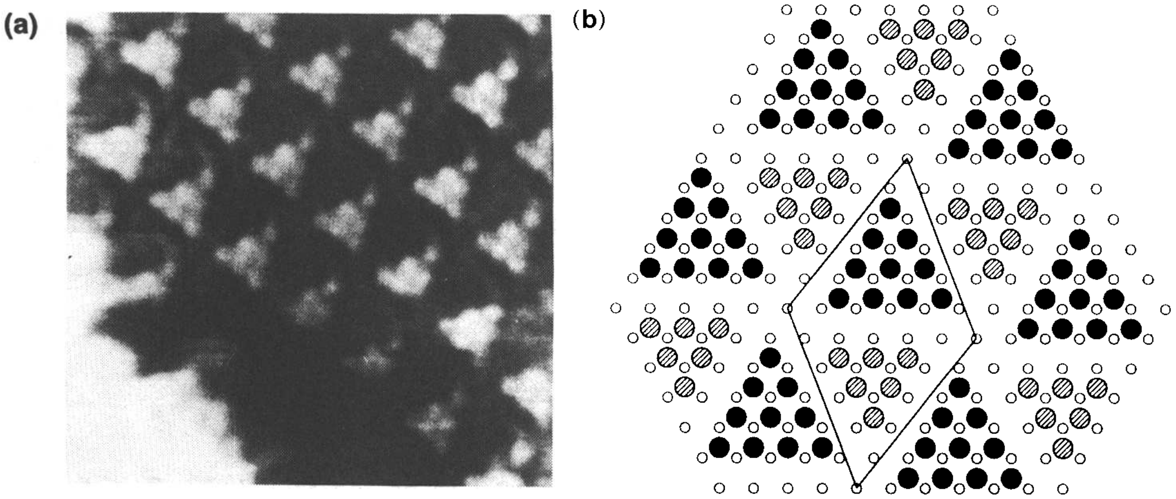

Fig 2. (a) An STM image of the $\sqrt{31} \times \sqrt{31}$ phase obtained with $-2V$ bias on the tip. There is a 4×1 area at the lower left corner. (b) Positions of top layer atoms in the $\sqrt{31} \times \sqrt{31}$ surface. The unit cell is outlined (from Ref. [15]). (*Reproduced by permission of Blackwell Scientific Publications Ltd)*

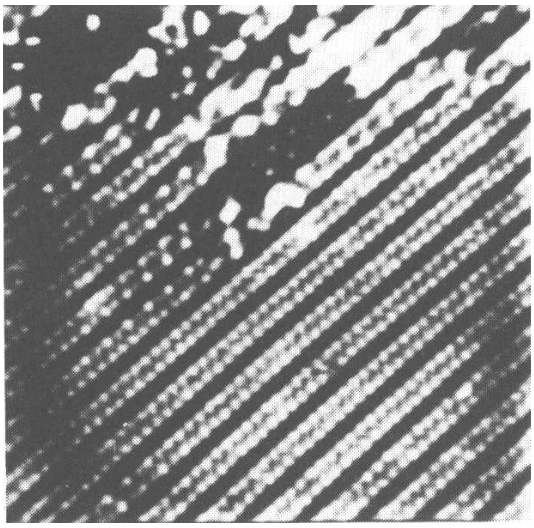

Fig 3. An STM image of the 4×1 surface with disordered area. The image was taken with $+2V$ bias on the tip (from Ref. [15]). (*Reproduced by permission of Blackwell Scientific Publications Ltd)*

is 4 times the Si(111)1 × 1 unit cell distance. The ridges themselves have a much smaller depression running down the middle and the adatoms inside the ridge are spaced 1 × 1 unit cell distance (3.84 Å) along the ridge (see Fig. 3).

The structure of the 4 × 1 phase has been investigated recently by Cornelison *et al.* with impact-collision ion-scattering spectroscopy (ICISS) [28] and by Nakamura *et al.* with Auger electron diffraction (AED) [29]. However, the atomic arrangement of this phase has not been conclusively established. The results of the ICISS experiments were inconsistent with models of the 4 × 1 surface with 1 ML In and supported the model shown in Fig. 4 in which 1/2 ML In atoms occupy the H_3 and T_4 sites. The In adatoms were estimated to reside above the first Si layer with a vertical displacement of 1.15 ± 0.15 Å [28]. Contrary to the ICISS results, the best agreement with AED data was reached for the model with 1 ML In coverage [29]. An optimized geometry of this model is shown in Fig. 5.

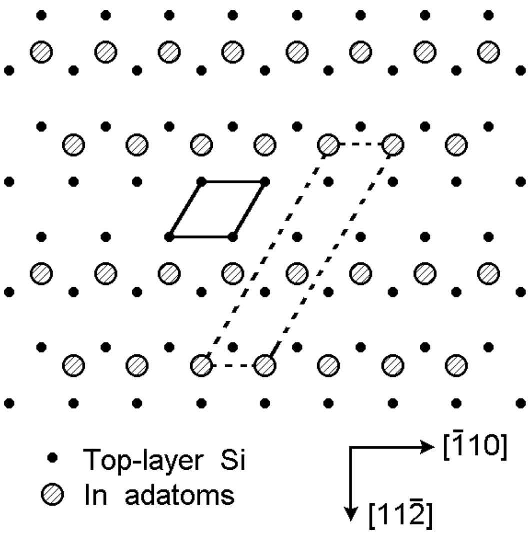

Fig 4. Schematic illustration of a model for the Si(111)4 × 1–In surface derived in ICISS experiments. The 1 × 1 and 4 × 1 unit cells are outlined (from Ref. [28]). (*Reproduced by permission of the publishers of Journal of Physical Review B)*

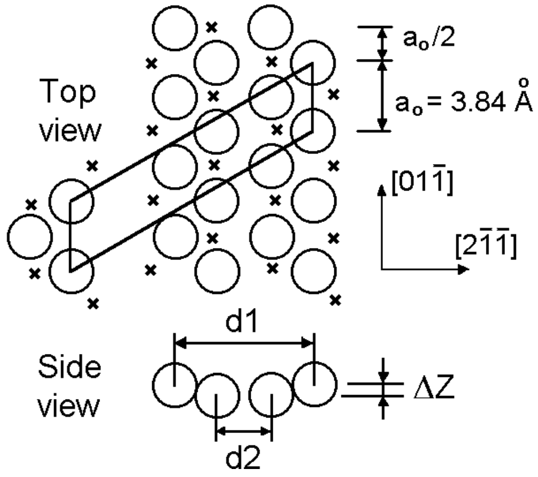

Fig 5. Schematic illustration of a proposed In overlayer arrangement for the Si(111)4 × 1–In surface. Open circles are indium atoms. $d_1 = 7.7 \pm 0.4$ Å, $d_2 = 2.7 \pm 0.4$ Å and $\Delta Z = 0.8 \pm 0.2$ Å are geometrical parameters determined from AED. Crosses are hypothetical positions of the first layer Si atoms (from Ref. [29]). (*Reproduced by permission of Elsevier Science Publishers BV)*

1.2.5. Si(111)$\sqrt{7} \times \sqrt{3}$–In

The $\sqrt{7} \times \sqrt{3}$ phase appears only when coexisting with the 4 × 1 phase. In the STM image, this phase shows up as parallel rows running at 30° to the [$\bar{1}$10] direction. These rows are finer and more closely spaced in comparison with those of the 4 × 1 structure [15].

1.2.6. Si(111)1 × 1—*R*30°–In

The Si(111)1 × 1—*R*30°–In structure was observed at above 1.0 ML In coverage both upon RT In deposition on to the cleaved Si(111)2 × 1 surface [1,3] and HT growth [2, 12, 13, 30, 31]. This structure is considered to correspond to the unreconstructed In (111) surface rotated by 30° with respect to the substrate [1]. In the STM images from the Si(111) surface with about 1 ML In [13,15], the areas with little or no apparent corrugation were observed surrounded by the 4 × 1 phase. The shape and thickness of this island suggest that it is a single close-packed

Table 2. Parameters of In desorption from Si(111) determined in RHEED [7, 10] and LEED–AES experiments [16,36].

Phase	t_0 (s)	E (eV)	Ref.
7×7	9×10^{-13}	2.5	[10]
$\sqrt{3} \times \sqrt{3}$	3×10^{-15}	2.7	[7, 10]
	3.6×10^{-11}	2.0	[16, 36]
$\sqrt{31} \times \sqrt{31}$	6×10^{-17}	2.9	[7, 10]
4×1	5.7×10^{-8}	1.5	[16, 36]
1×1	2.5×10^{-4}	0.9	[16, 36]

layer of In atoms. The orientation of the islands is consistent with LEED observations. It is worth noting that, although the 1×1—$R30°$–In phase has an atomic structure of the In (111) plane, its electronic structure differs from that of metal In as shown in the EELS study by Lifshits *et al.* [2, 30].

1.3. PROPERTIES

1.3.1. Desorption

The desorption of In atoms from the Si(111) surface was investigated by several groups [10, 30, 32–37].

Nguyen Tan and co-workers [32–34] reported a desorption energy of about 2.5 eV for In coverage ranging from 10^{-3} to 0.9 ML in their mass spectrometry experiments. The pre-exponential term t_0 was found to be equal to 8×10^{-13} s for very low In coverages but decreases for high surface coverage.

Krausch *et al.* [37] studied the desorption of isolated In atoms on Si(111)7×7 and found a value of 1.93 eV for the binding energy assuming an attempt frequency of 10^{13} Hz.

In a RHEED study by Baba *et al.* [7,10] and a LEED–AES study by Lifshits *et al.* [16,36], the correlation between the change in the surface structure and the variation of the desorption constants was clearly evidenced. However the reported quantitative results of both groups are in rather poor agreement with each other as can be seen in Table 2.

1.3.2. Diffusion and Electromigration

The lateral mass transport in the In/Si(111) system was studied in Refs [16, 30, 37–44].

The thermal surface diffusion was investigated using LEED–AES techniques in Refs [16, 30] and diffusion coefficient was determined for the 4×1 and 1×1 phases. It appears to be equal to $0.9 \exp(-0.6\ \text{eV}/kT)\ \text{cm}^2 \cdot \text{s}^{-1}$ for 1×1 phase and $1.5 \times 10^3 \exp(-1.0\ \text{eV}/kT)\ \text{cm}^2\ \text{s}^{-1}$ for the 4×1 phase.

The migration of isolated In atoms at very low In coverages was studied in Ref. [37]. The activation energy for the migration of In atoms to regular adsorption sites was determined to be 0.72 eV.

Considerable research attention has been attracted by the surface electromigration of In on the Si(111) surface [38–44]. The phenomenon was first reported by Zhou *et al.* [38] who found that ultra-thin In film moves towards the cathode on a Si(111) substrate which is carrying d.c. current. Recently, certain aspects of surface electromigration in the In/Si(111) system have been clarified in a number of publications.

The expanding layer was found to be uniform in coverage of about 1 ML and has a 4×1 superstructure regardless of the amount of the initial deposition as long as it was no less than about 1 ML [39, 40, 44]. Anno *et al.* [42] studied the emerging morphology of an In layer over the 4 × 1–In surface. It was found that a patch of In film deposited on the Si(111)4 × 1–In phase converted into a 1 × 1–In phase with In islands during electromigration. Meanwhile the fine polygons of the 1 × 1–In phase first created the cathode edge of the patch. These fine polygons are stationary and grow in size to eventually be incorporated into the In patch. Thus the apparent motion of the In patch over the 4 × 1–In phase involves the transport of In atoms over the 4 × 1–In phase and the capture by them of some defects which trigger the formation of the 1 × 1–In fine polygons. Indium islands are found on the cathode side of the In patch and show no translation, but cycles of appearance, growth, decay, and disappearance during surface electromigration [42]. One can see that the morphology of In film in the process of electromigration is associated with the Stranski–Krastanov growth mode of In film on Si(111) which includes the formation of a uniform layer and the growth of islands on it.

Wu *et al.* [43] studied the effect of steps on In electromigration and found that the diffusion is remarkably suppressed in direction perpendicular to the step edge. The activation energy of migration increases from 0.31 to 0.66 eV with increasing the vicinal angle from 0 to 6°.

Changing the doping level of Si substrates, Anno *et al.* [42] found that the velocity of electromigration increases as the strength of the electrostatic field applied to the Si(111) substrate is enhanced. So it was suggested that the driving force of surface electromigration is the electrostatic field rather than a d.c. current fed through the sample.

1.3.3. Electrophysical Properties

The conductivity and Hall effect measurements of the Si(111)1 × 1—$R30°$–In surface phase coated by an amorphous Si film 2 nm thick were conducted by Gasparov *et al.* [45]. It was revealed that the buried phase shows semiconductor behavior. The determined carrier (electron) mobility is 3×10^5 cm^2 V^{-1} s^{-1} at 50 K. This value is 10 times higher than that of the intrinsic silicon. The sheet electron concentration of the buried phase is very low (7×10^{10} cm^{-2} at 80 K) and is quickly frozen with decreasing temperature.

2.(100) ORIENTATION

Indium was reported to induce several reconstructions on the Si(100) surface These are 2 × 2, 3 × 4, 2 × 1, and 1 × 1.

2.1. PHASE DIAGRAM

Kuwata *et al.* [46] were the first to study the formation of surface phases in the In/Si(100) system. In a brief note, they reported the formation of the 3 × 4 structure after deposition of more than 2 Å of In at room temperature and annealing at temperatures above 300 °C. For annealing temperatures between 100 and 300 °C, the 1 × 1 structure was detected (see Fig. 6).

In a successive study of the In/Si(100) system by Knall *et al.* [47], indium was deposited on to a clean Si(100)2 × 1 surface held at a given temperature. The results of this RHEED, LEED, AES, and SEM investigation are summarized in Fig. 7. It was found that In grows on Si(100) by a Stranski–Krastanov mechanism, the structure of the two-dimensional layer and the shape of the three-dimensional islands being temperature dependent. Three temperature intervals are distinguished.

At growth temperatures between 30 and 150 °C, the two-dimensional layer starting from about 0.1 In ML has a 2 × 2 structure which at $\theta > 0.5$ ML transforms gradually to a 2 × 1 structure. Three-dimensional islands start to nucleate on top of the 2 × 1–In surface at

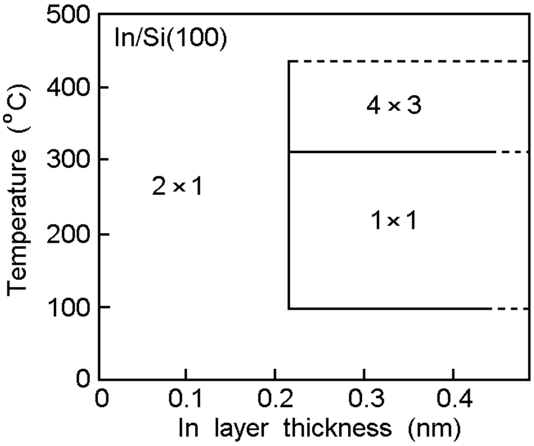

Fig 6. Dependence of the surface structures formed by In on Si(100) on the thickness of the RT deposited In layer and on the maximum temperature at which the surface was exposed (from Ref. [46]). (*Reproduced by permission of Elsevier Science Publishers BV)*

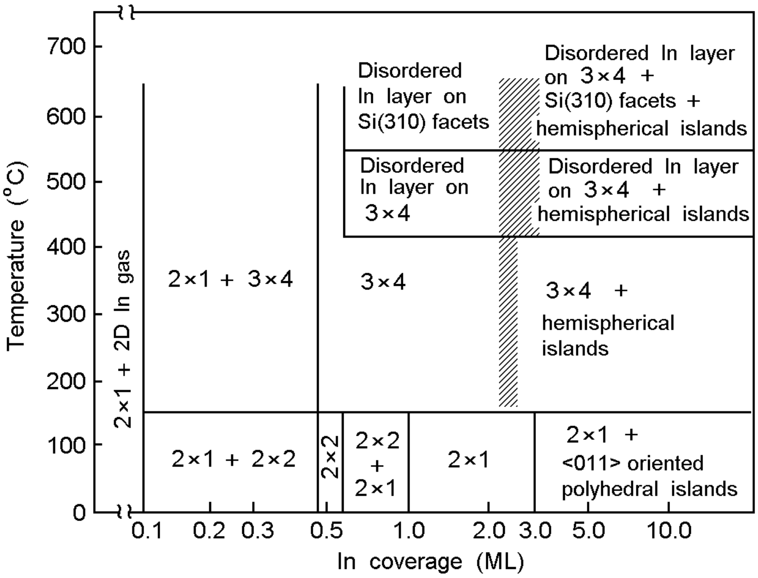

Fig 7. Surface phase diagram for In deposition on to the Si(100)2×1 surface held at given temperature (from Ref. [47]). (*Reproduced by permission of Elsevier Science Publishers BV)*

In coverages beyond ~ 3 ML. The islands are single-crystalline polyhedra with preferential growth along [011] and [01$\bar{1}$] substrate directions.

At temperatures ranging from 150 to 550 °C, the 3 × 4 phase forms at coverages beyond 0.1 ML In. The 3 × 4 phase exists in two domains rotated by 90°. The most intense and sharp LEED and RHEED patterns of the 3 × 4 reconstruction are observed at $\theta = 0.5$ ML. However, weak 3 × 4 RHEED and LEED patterns are still observed at coverages as high as 1000 ML. The island growth commences at coverages above about 2 ML, the islands being hemispherical-shaped.

For In growth at temperatures above 550 °C, the results at low coverages are essentially identical to those obtained at temperatures between 150 and 550 °C: the initially deposited two-dimensional gas of In adatoms transforms to an ordered 3 × 4–In phase at about 0.1 ML In coverage. The RHEED and LEED patterns become increasingly sharper with increasing coverage up to 0.5 ML and then decrease at higher coverages. However, at coverages greater than 0.5 ML, deposition of In gives rise to (310) faceting of the Si surface. Further increase

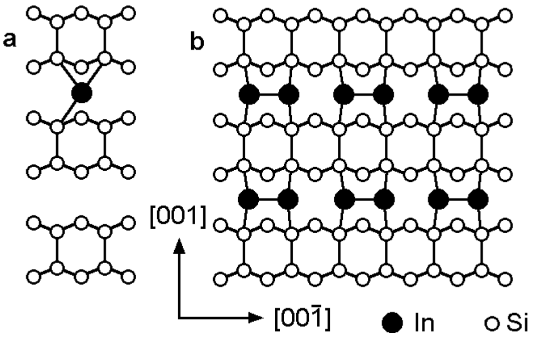

Fig 8. A picture of structural models for (a) two-dimensional gas of In (In coverage less than 0.1 ML, only one atom is shown) and (b) the Si(100)2 × 2–In phase (In coverage $\theta = 0.5$ ML). The In adatoms are shaded, while the Si surface atoms are not (from Ref. [51]). (*Reproduced by permission of the publishers of Journal of Physical Review Letters)*

in the In coverage above 2 ML results in the formation of hemispherical-shaped In islands.

The 3 × 4–In structure observed was also reported in the papers devoted to the MBE growth of In-doped Si layers [48–50]. Indium, a deep acceptor in silicon, was found to segregate to the surface of Si(100) films grown by molecular beam epitaxy. The surface structure of film with In coverage above 0.1 ML transforms from a 2 × 1 structure to 3 × 4 owing to the formation of an ordered In overlayer.

2.2. STRUCTURE

2.2.1. 2D In Gas

The results of the high-resolution photoemission spectroscopy [51–54] showed that, at $\theta <$ 0.1 ML In, the In-to-Si bonding coordination number equals 3, thus each In adatom should be bonded to three Si surface atoms. The adsorption position for an isolated In adatom was proposed to be that illustrated in Fig. 8(a). The assumed atomic arrangement, however, is in conflict with the results of the STM investigation by Baski *et al.* [55], who have found that all In adatoms form dimers at coverages from 0.03 to 0.4 ML. Baski *et al.* suggested that the difference between PES and STM results might be caused by second nearest-neighbor effects or the removal of the 2 × 1 Si reconstruction in the areas under the 2 × 2–In structure [55].

2.2.2. Si(100)2 × 2–In

The 2 × 2 structure appears upon RT In deposition at low coverages and is fully developed at about 0.5 ML. The simple model proposed by Knall *et al.* [47] has appeared to be consistent with all of the RHEED, LEED, AES [47], high-resolution PES [51–54] and STM [55] results. This structure is illustrated in Fig. 8(b). The In adatoms form dimers which are rotated by 90° with respect to the Si dimers and this results in a 2 × 2 periodicity at In coverage of a half monolayer.

2.2.3. Si(111)3 × 4–In

The structure of the 3 × 4–In phase forming at above 150 °C was considered using STM by Baski *et al.* [56]. It was found that, at low In coverages, In form isolated subunits as shown in Fig. 9. The In subunits have two maxima in the empty electronic states (shown by large ovals) and a central maximum in the filled states (shown by black circles). The In subunits are located between Si dimer rows such that the empty and filled states are located between the underlying Si dimers. The estimation gives a value of 6 In atoms for each In subunit.

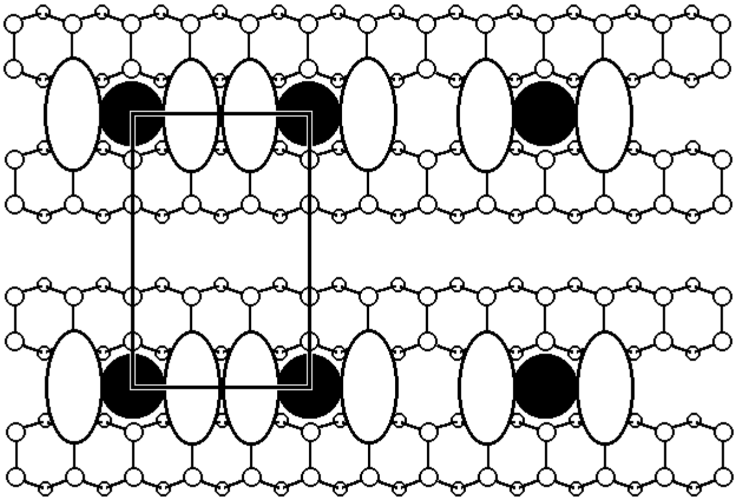

Fig 9. An illustration of the In subunit configuration where Si dimers are denoted by small light circles and the empty (filled) electronic states of the In subunits are represented by large ovals (black circles). The 3×4 unit cell is outlined (from Ref. [56]). (*Reproduced by permission of the publishers of Journal of Physical Review B)*

As In coverage increases, the In subunits form rows parallel to the Si dimer rows with the inter-row spacing of $4a$ (where $a = 3.84$ Å, the period of unreconstructed Si(100)). At intermediate coverages, the In subunits are spaced either $3a$ or $4a$ apart. At 0.5 ML In, the 3×4 reconstruction is complete and only the $3a$ spacing exists.

One can see that Fig. 9 does not provide an atomic model of the 3×4–In phase. However, Baski *et al.* pointed out that the limitations to any proposed model should be taken into account. The model should incorporate 6 In atoms into each subunit with separation and registration of the empty and filled electronic states as described above. In addition, the significant disruption of Si dimer rows near each In subunit should be accommodated [56].

2.3. PROPERTIES

2.3.1. Desorption

Indium desorption from Si(100) has been studied by Knall *et al.* [57] and Oostra *et al.* [58,59].

Knall *et al.* [57] using LEED, RHEED and AES in modulated-beam desorption and temperature-programmed desorption spectroscopies observed a first-order desorption mechanism for $\theta < 0.7$ ML In and a zero-order mechanism for $0.7 < \theta < 1.5$ ML In. The desorption energies and pre-exponential factors were found to be 2.8 ± 0.2 eV and $3 \times 10^{14\pm1}$ s^{-1} for 2D gas at $\theta \leq 0.07$ ML; 2.85 ± 0.2 eV and $3 \times 10^{14\pm1}$ s^{-1} for 3×4–In phase; 2.45 ± 0.2 eV and $9 \times 10^{13\pm1}$ s^{-1} for 3D In islands.

This is in contrast to the results of Oostra *et al.* [58,59] who observed, in the experiments with spin-orbit state specific laser probing of the desorbing In atoms, a 1/2-order mechanism for $\theta < 0.5$ ML at temperatures below 550 °C and a first-order mechanism at temperatures above 550 °C. For $\theta > 0.5$ ML, a desorption was found to take place by a 2/3-order mechanism. The determined activation energies and pre-exponential factors are 2.5 ± 0.2 eV and $10^{13\pm1}$ s^{-1} for the first-order kinetics ($\theta < 0.5$ ML, $T > 550\,^\circ$C); 2.2 ± 0.7 eV and $10^{13\pm4}$ ML$^{1/2}$ s^{-1} for 1/2-order kinetics ($\theta < 0.5$ ML, $T > 550\,^\circ$C; 1.9 ± 0.1 eV and $3 \times 10^{10\pm0.5}$ ML$^{1/3}$ s^{-1}($\theta >$ 0.5 ML).

Oostra *et al.* pointed out that only in the case of the first-order desorption does determined activation energy equal the binding energy, while the observed activation energy probably reflects the energy barrier to escape out of the 3D In islands for 2/3-order kinetics and out of the 2D islands of 4 × 3–In phase for 1/2-order desorption.

In discussing of the difference between the results of the two groups, Oostra *et al.* [59] suggested that this may indicate differences in the In surface diffusion coefficient. Though the surfaces were atomically clean in both experiments, different cleaning methods were used (wet etch and oxide growth followed by oxide desorption at 850 °C [57] and a sputter-and-anneal technique (annealing at 900 °C) [59]). These techniques can lead to different surface regularities which may influence the diffusion coefficient and the islanding behavior [59].

REFERENCES

[1] M. K. Kelly, G. Margaritondo, J. A. Anderson, D. J. Frankel and G. J. Lapeyre, *J. Vac. Sci. Technol. A* **4** (1986) 1396.
[2] V. B. Akilov, V. G. Zavodinskii, V. G. Lifshits and B. K. Churusov, *Poverhnost* No 2 (1986) 54.
[3] D. Bolmont, P. Chen, C. A. Sebenne and F. Proix, *Surf. Sci.* **137** (1984) 280.
[4] J. J. Lander and J. Morrison, *Surf. Sci.* **2** (1964) 553.
[5] J. J. Lander and J. Morrison, *J. Appl. Phys.* **36** (1965) 1706.
[6] T. Aiyama and S. Ino, *Surf. Sci.* **82** (1979) L585.
[7] S. Baba, M. Kawaji and A. Kinbara, *Surf. Sci.* **85** (1979) 29.
[8] M. Kawaji, S. Baba and A. Kinbara, *Appl. Phys. Lett.* **34** (1979) 748.
[9] S. Baba, Jun Ming Zhou and A. Kinbara, *Japan J. Appl. Phys.* **19** (1980) L571.
[10] S. Baba, H. Hirayama, J. M. Zhou and A. Kinbara, *Thin Solid Films* **90** (1982) 57.
[11] H. Hirayama, S. Baba and A. Kinbara, *Japan J. Appl. Phys.* **25** (1986) L452.
[12] H. Hirayama, S. Baba and A. Kinbara, *Appl. Surf. Sci.* **33-34** (1988) 193.
[13] J. Nogami, S. -il Park and C. F. Quate, *Phys. Rev. B* **36** (1987) 6221.
[14] J. Nogami, S. -il Park and C. F. Quate, *J. Vac. Sci. Technol. B* **6** (1988) 1479.
[15] S. Park, J. Nogami and C. F. Quate, *J. Microscopy* **152** (1988) 727.
[16] O. V. Bekhtereva, Yu. L. Gavriljuk, V. G. Lifshits and B. K. Churusov, *Poverhnost* No 8 (1988) 54.
[17] J. M. Nicholls, P. Martensson, G. V. Hansson and J. E. Northrup, *Phys. Rev. B* **32** (1985) 1333.
[18] G. V. Hansson, J. M. Nicholls, P. Martensson and R. I. G. Uhrberg, *Surf. Sci.* **168** (1986) 105.
[19] T. Kinoshita, S. Kono and T. Sagawa, *Phys. Rev. B* **34** (1986) 3011.
[20] J. M. Nicholls, B. Reihl and J. E. Northrup, *Phys. Rev. B* **35** (1987) 4137.
[21] J. M. Nicholls and B. Reihl, *Phys. Rev. B* **36** (1987) 8071.
[22] T. Kinoshita, H. Ohta, Y. Enta, Y. Yaegashi, S. Suzuki and S. Kono, *J. Phys. Soc. Jap.* **56** (1987) 4015.
[23] H. Ohta, T. Kinoshita, Y. Yaegashi, S. Suzuki and S. Kono, *J. Phys. Soc. Jap.* **57** (1988) 4452.
[24] K. Izumi, T. Takahashi and S. Kikuta, *Japan J. Appl. Phys.* **28** (1989) 1742.
[25] D. M. Cornelison, C. S. Chang and S. T. Tsong, *J. Vac. Sci. Technol. A* **8** (1990) 3443.
[26] D. M. Cornelison, C. S. Chang and I. S. T. Tsong, *Nucl. Instrum. Meth. Phys. Res. B* **45** (1990) 394.
[27] N. Nakamura, K. Anno and S. Kono, *Surf. Sci.* **262** (1992) L101.
[28] D. M. Cornelison, M. S. Worthington and I. S. T. Tsong, *Phys. Rev. B* **43** (1991) 4051.
[29] N. Nakamura, K. Anno and S. Kono, *Surf. Sci.* **256** (1991) 129.
[30] V. G. Lifshits, V. B. Akilov, B. K. Churusov, Yu. L. Gavriljuk and V. G. Zavodinskii, *Solid State Commun.* **55** (1985) 717.
[31] P. V. Melnik, N. G. Nakhodkin and N. I. Fedorchenko, *Izvestiya AN SSSR. Ser. Fiz.* **52** (1988) 1471.
[32] T. A. Nguyen Tan, *Surf. Sci.* **43** (1974) 562.

[33] T. A. Nguyen Tan, B. K. Chakraverty and R. C. Cinti, *Surf. Sci.* **43** (1974) 577.

[34] T. A. Nguyen Tan, S. Michel and R. C. Cinti, *Surf. Sci.* **54** (1976) 679.

[35] Y. J. Chabal, J. E. Rowe and D. A. Zwemer, *Phys. Rev. Lett.* **46** (1981) 600.

[36] V. G. Lifshits, V. B. Akilov, B. K. Churusov and Yu. L. Gavriljuk, *Surf. Sci.* **222** (1989) 21.

[37] G. Krausch, T. Detzel, R. Fink, B. Luckscheiter, R. Platzer, U. Wohrmann and G. Schatz, *Phys. Rev. Lett.* **68** (1992) 377.

[38] J. M. Zhou, S. Baba and A. Kinbara, *Thin Solid Films* **98** (1982) 109.

[39] H. Yasunaga, Y. Kubo and N. Okuyama, *Japan J. Appl. Phys.* **25** (1986) L400.

[40] A. Yamanaka and K. Yagi, *Surf. Sci.* **242** (1991) 181.

[41] A. Natori, S. Ohta and H. Yasunaga, *Surf. Sci.* **242** (1991) 195.

[42] K. Anno, N. Nakamura and S. Kono, *Surf. Sci.* **260** (1992) 53.

[43] N. -J. Wu, H. Yasunaga and A. Natori, *Surf. Sci.* **260** (1992) 75.

[44] H. Yasunaga and A. Natori, *Surf. Sci. Repts.* **15** (1992) 205.

[45] V. A. Gasparov, V. A. Grazhulis, V. V. Bondarev, T. M. Bychkova, V. G. Lifshits, B. K. Churusov, N. G. Galkin and N. I. Plusnin, *Vacuum* **41** (1990) 1207.

[46] N. Kuwata, T. Asai, K. Kimura and M. Mannami, *Surf. Sci.* **143** (1984) L393.

[47] J. Knall, J. -E. Sundgren, G. V. Hansson and J. E. Greene, *Surf. Sci.* **166** (1986) 512.

[48] A. Rockett, S. A. Barnett and J. E. Greene, *J. Vac. Sci. Technol. A* **3** (1985) 855.

[49] J. Knall, J. -E. Sundgren and J. E. Greene, *Appl. Phys. Lett.* **45** (1984) 689.

[50] A. Rockett, J. Knall, M. A. Hassan, J. -E. Sundgren, S. A. Barnett and J. E. Greene, *J. Vac. Sci. Technol. A* **4** (1986) 900.

[51] D. H. Rich, A. Samsavar, T. Miller, H. F. Lin, T. -C. Chiang, J. -E. Sundgren and J. E. Greene, *Phys. Rev. Lett.* **58** (1987) 579.

[52] D. H. Rich, A. Samsavar, T. Miller, H. F. Lin and T. -C. Chiang, *Mat. Res. Soc. Symp. Proc.* **94** (1987) 219.

[53] T. -C. Chiang, Mat. Res. Soc. Symp. Proc. **143** (1989) 55.

[54] D. H. Rich, A. Samsavar, T. Miller and T. -C. Chiang, *Phys. Scripta* **41** (1990) 83.

[55] A. A. Baski, J. Nogami and C. F. Quate, *J. Vac. Sci. Technol. A* **9** (1991) 1946.

[56] A. A. Baski, J. Nogami and C. F. Quate, *Phys. Rev. B* **43** (1991) 9316.

[57] J. Knall, S. A. Barnett, J. -E. Sundgren and J. E. Greene, *Surf. Sci.* **209** (1989) 314.

[58] D. J. Oostra, R. V. Smilgys and S. R. Leone, *Mat. Res. Soc. Symp. Proc.* **131** (1989) 239.

[59] D. J. Oostra, R. V. Smilgys and S. R. Leone, *Surf. Sci.* **226** (1990) 226.

(Ir)

IRIDIUM

1. (100) ORIENTATION

No ordered structures were observed for the Ir/Si(100) system.

1.1. PHASE DIAGRAM

Submonolayer coverage of iridium was found to change the 2 × 1 reconstruction of the clean Si(100) surface [1]. However, the presence of any ordered superstructure has not been reported.

Ir/Si(100) interface formation at RT was investigated with UPS and XPS by Wittmer *et al.* [1] and Morgan *et al.* [2]. With increasing coverage, a bilayer structure forms consisting of an interfacial layer of IrSi-like silicide and an overlayer of pure iridium. By annealing a thin film of iridium in the temperature range of 400–1000 °C, Wittmer *et al.* [1] demonstrated the consequent formation of three silicide compounds in the sequence IrSi, IrSi_x ($x \simeq 1.6$), and IrSi_3 and the concomitant transitions from metallic to semiconducting and semiconducting to metallic behavior.

REFERENCES

[1] M. Wittmer, P. Oelhafen and K. N. Tu, *Phys. Rev. B* **35** (1987) 9073.
[2] S. J. Morgan, R. H. Williams and J. M. Mooney, *Appl. Surf. Sci.* **56–58** (1992) 493.

(K)

POTASSIUM

1. (111) ORIENTATION

Potassium is known to induce three reconstructions on the Si(111) surface. These are $\delta(7\times7)$, 7×7, and 3×1 structures.

1.1. PHASE DIAGRAM

Initial stages of K adlayer formation on the Si(111)7×7 surface have been investigated by RHEED [1, 2], LEED [3–6], AES [2, 4, 7, 8, 15], EELS [5], UPS [6], core-level PES [9] STM [4, 10, 11], TPD [15], WF measurements [3, 4, 6, 7], and theoretically [12–14].

The STM images of Si(111)7×7 covered by K atoms at RT in the submonolayer range [4] and LEED results at 150 K [5] show no evidence for an ordered adsorption. But for greater coverage and (or) substrate temperature, it may be possible [1, 2].

Mizuno and Ichimiya [2] in the AES study found that during deposition of K on a Si(111)7×7 surface at RT, the K–LVV Auger peak intensity increases linearly with the deposition time at the initial stage [2]. After a deposition time corresponding to the Auger-peak ratio K–LVV/Si–LVV = 0.64, the K–LVV peak intensity becomes constant for continued exposure of K atoms. At this saturation coverage, the RHEED and LEED patterns of Si(111)7×7–K similar to those of the clean Si(111)7×7 are observed [2, 15]. In contrast to the results of Mizuno and Ichimiya [2], Daimon and Ino [1] observed, during RT K deposition, the appearance of the $\delta(7 \times 7)$ superstructure with a RHEED pattern different from that of a clean Si(111)7×7 surface. Mizuno and Ichimiya [2] demonstrated that the formation of the $\delta(7 \times 7)$ structure is connected with the presence of the carbon contaminations on the surface.

Mizuno and Ichimiya [2] demonstrated that the RT growth mode of K on the Si(111) surface is also very sensitive to the carbon contaminations. Their results indicated the layer-by-layer growth on a carbon-contaminated surface and the Stranski–Krastanov growth mode on a contamination-free surface in agreement with the results of recent work of Boishin and Surnev [15].

When the K is deposited on the Si(111)7×7 surface at about 500 °C [1] or when a K-covered surface is annealed at 300 °C [11], the 3×1 superstructure is observed [1]. The coverage of Si(111)3×1–K was determined with RHEED–TRAXS as being 0.7 ± 0.05 times that of saturation at RT, which is the coverage for the $\delta(7\times7)$ structure. FI–STM observations of Hashizume *et al.* [10, 11] revealed that the 3×1 phase starts to grow (up and down) from the atomic steps of the terraces probably by removing adatoms and the stacking fault of the 7×7 DAS structure.

1.2. STRUCTURE

In accordance with FI–STM observations of Hashizume *et al.* [10, 11] at the initial stages ($\sim$ 0.01 ML) of RT deposition, K atoms adsorb mainly at the topmost site of the center adatoms and are ionized. Some of the adsorbed K atoms form clusters (often trimers), which have more covalent character with back-donation of the charge distribution, and those clusters become the dominant species on the surface with increasing coverage. Schematic showing of the adsorption geometry of K is similar to the adsorption geometry of Cs and is shown in Fig. 4 in Chapter Cs.

1.2.1. Si(111)$\delta(7 \times 7)$–K

The structure model of Si(111)$\delta(7 \times 7)$–K estimated from the intensity distribution of the $\delta(7 \times 7)$ RHEED pattern has one vacancy at the corner of the 7×7 unit mesh and relaxed surrounding atoms [1]. This structure may be similar to the Si(111)$\delta(7 \times 7)$–H and Si(111)$\delta(7\times7)$–Li structures as described in the respective chapters. ¿From the other point of view [2], if the $\delta(7\times7)$ structure is connected with the carbon contaminations, the formation of $\delta(7 \times 7)$ structure by K adsorption is due to cutting the backbonds of the adatoms by carbon atoms.

1.2.2. Si(111)7×7–K

By a kinematical analysis of the RHEED pattern, a simple model was proposed by Mizuno and Ichimiya [2] including 19 K atoms adsorbed at the 19 dangling-bond sites of the DAS structure.

1.2.3. Si(111)3×1–K

Daimon and Ino [1] suggested that the 3×1 structure has two K atoms in the 3×1 unit mesh by the estimation of the surface coverage based on their RHEED data. The close study of the 3×1 phase with respect to the 7×7 substrate by Hashizume *et al.* [11] using FI–STM indicates that the 3×1 phase is the incommensurate phase (the measured nearest neighbor distance of K atoms is approximately 10% larger than the Si substrate separation, 3.84 Å), with a random distribution of K vacancies (misfit defects), approximately one for every nine K atoms in average. The preferred adsorption site of individual K atoms is essentially the H_3 site, although many cases for relaxations may be possible (Fig. 1).

1.3. PROPERTIES

1.3.1. Electronic Properties

The changes in the work function upon K deposition on Si(111)7×7 at RT are displayed in Fig. 2. The relationship has a minimum value of $\Delta\Phi_{\text{min.}} = -3.2$ eV [6, 7], and a saturation value of $\Delta\Phi_{sat} = -2.9$ eV [7, 15]. The existence of a minimum was not observed in [4] and may eventually be related to the presence of a small oxygen contamination. The work function was asymptotic decreased, and approached a value of -3.2 eV in the latter case.

An important question is the nature of the alkali metal–semiconductor interaction; specifically, whether the alkali metal is bonded to the surface in an ionic or covalent state. ¿From the theoretical study of the K/Si system [13, 14], it was concluded that the K–Si bond is ionic for the K/Si(111)2×1 surface. In contrast, from the work function measurements of K/Si(111) [7], it was concluded that the charge transfer from the alkali metal to the substrate is incomplete, i.e. the bond is not ionic. In accordance with EELS data [5], the reaction of K

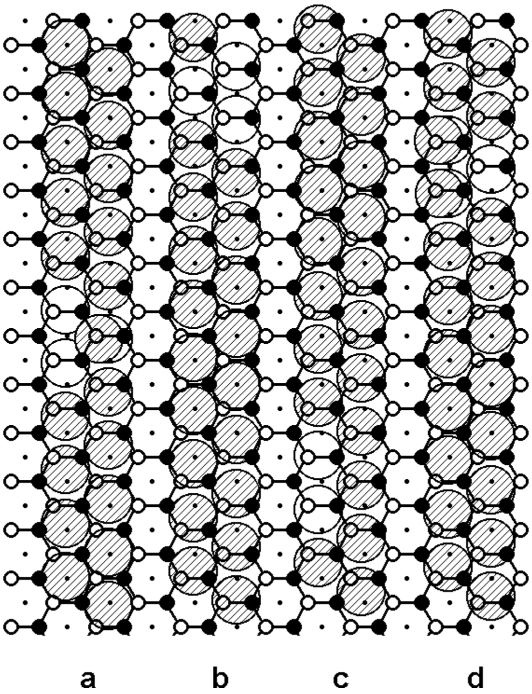

Fig 1. Schematic showing the adsorption geometry of K in the case of the 3×1 phase. The smaller solid and open circles show 1 × 1 Si substrate, where solid circles and open circles are the first and second Si layers. The larger screened circles show K overlayer and the larger open circles show misfit K defects. The structure of the double line (a) is deduced from the STM image, where shifted screened circles next to misfit defects show relaxations of K atom. Lines (b)–(d) are slightly shifted towards the $[1\bar{1}0]$ direction, showing a possible misfit defect arrangement and relaxation (from Ref. [11]). (*Reproduced by permission of American Institute of Physics)*

atoms with Si(111) leads to the formation of a metallic adlayer, while AIUPS and ARUPS results show that the K-covered Si(111) surface remains semiconducting.

1.3.2. Desorption

SI experiments [16] showed that the desorption of K from the Si(111) surface below 1000 K has both a first and a second-order component with activation energies for desorption of $E_{a1} = 3.15 \pm 0.15$ eV and $E_{a2} = 2.53 \pm 0.10$ eV. Above 1100 K, the desorption of K from this surface is predominantly first-order with $E_{a1} = 2.35 \pm 0.07$ eV.

1.3.3. Oxidation

Boishin and Surnev [17] found the K-promoted oxidation of Si(111) at elevated temperatures. When K coverage is less than 0.5 ML, the K-induced increase in the rate of oxygen adsorption does not lead to a substantial enhancement of the Si oxidation rate at elevated temperatures. However, when the coverage of 0.5 ML is exceeded, the K-promoted oxidation is observed. This phenomenon was suggested to be related to the formation of a K oxide, which acts as an intermedia for transferring reactive oxygen species to the substrate.

2. (100) ORIENTATION

K is known to induce several reconstructions on the Si(100) surface. These are 2 × 1, 2 × 2, 2 × 3, 4 × 5, and $\begin{pmatrix} 2 & 1 \\ 0 & 3 \end{pmatrix} + \begin{pmatrix} 2 & -1 \\ 0 & 3 \end{pmatrix}$ structures.

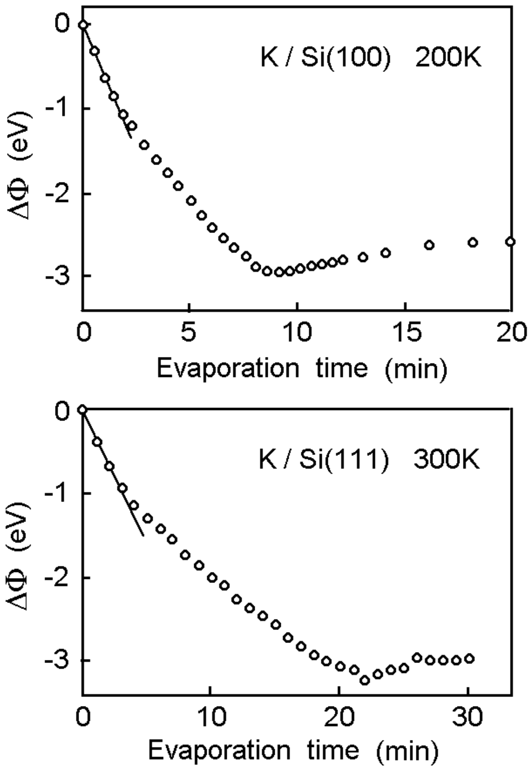

Fig 2. The work function changes versus evaporation time. K on Si(111) (from Ref. [7]). (*Reproduced by permission of Elsevier Science Publishers BV)*

2.1. PHASE DIAGRAM

2.1.1. Si(100)2 × 1 Surface

Initial stages of K adlayer formation on Si(100)2 × 1 surface have been widely investigated by LEED [3, 7, 18–32], RHEED [33], AES [7, 18–21, 23–25, 27–29, 31, 32, 35, 36], AED [37,38], WF measurements [3, 7, 21, 23–25, 27, 29, 31, 32, 34, 35], STM [10, 39–43], ARUPS [44–47], XPD 20, 30, 38, 48], UPS [22, 24, 27, 28, 31, 32], XPS [27, 31, 36, 42, 49], SEXAFS [50,51], MDS [34,52], AREELS [53], EELS [21,53], HREELS [54], IP [28,44], TDS [23–25, 32, 55], SI [16], and theoretically [56–77].

Figure 3 from Ref. [47] shows the phase diagram for K growth on a single-domain Si(100) surface at low ($T_s \approx 80 \div 150$ K) and ambient ($T_s \approx 320$ K) substrate temperatures. The abscissa indicates the K coverage in units of saturated K coverage (θ_{sat}) for the saturation 2 × 1–K surface. The "2 × 1" stands for 2 × 1 phases with high background in LEED. In the case of T_s = 80–150 K, when K is deposited at $\approx 1/6\ \theta_{sat}$, a mixture of $\begin{pmatrix}2 & 1\\ 0 & 3\end{pmatrix}$ and $\begin{pmatrix}2 & -1\\ 0 & 3\end{pmatrix}$ periodicities is observed for $T_s \leq 100$ K. The $\begin{pmatrix}2 & 1\\ 0 & 3\end{pmatrix}$ and $\begin{pmatrix}2 & -1\\ 0 & 3\end{pmatrix}$ phases are mirror-symmetric to each other. LEED spots characteristic to this mixed phase become streaky when T_s is raised to ≈ 150 K. This streaky LEED pattern was called "×3 streak" for a Cs-adsorbed Si(100) surface [78]. When K is deposited between ≈ 0.2 and $\approx 0.25\ \theta_{sat}$ and between ≈ 0.28 and $\approx 0.40\ \theta_{sat}$, weak single-domain 4 × 5 and 3 × 3 periodicities are found. In the boundary regions between the phases, mixtures of the neighboring phases are found for all cases. In the case of $T_s \approx 320$ K the only distinguishable new phase, 2 × 3, is found. The quality of the LEED pattern of this phase is almost the same as those for the low temperature phase.

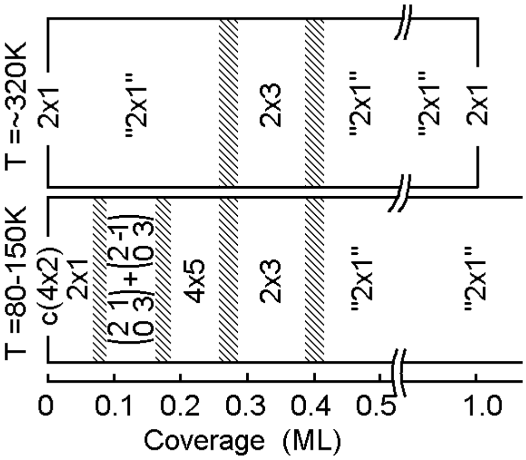

Fig 3. Phase diagram derived from a LEED study as a function of coverage for the system K/Si(100) for T_s of $\approx 80 - 150$ and ≈ 320 K (from Ref. [47]). (*Reproduced by permission of Elsevier Science Publishers BV)*

A weak two-domain 2×3 LEED pattern for K on a Si(100)2×1 surface was also observed by Enta *et al.* [35] at approximately two thirds of a saturation K coverage. Si(111)2×2–K structure was observed when K was deposited on to a slightly heated ($100 \div 200\,^\circ$C) Si(100) surface [22].

At saturation K coverage, LEED shows a clear 2×1 two-domain pattern, whose intensity profile is different from that of the clean Si(100)2×1 surface [7, 27, 29, 30, 35, 37, 38, 58]. However, the value of the saturation coverage itself continues to be controversial. The absolute saturation coverage of K at RT was measured using MEIS by Smith *et al.* [79] and found to be 0.98 ± 0.05 ML.

An independent coverage calibration [24] indicates that, although K multilayers can be grown at 300 K, the desorption peak of K multilayers is so close to RT (T_p = 343 K) that minor variation of the sample temperature around 300 K yields dramatic changes in the K coverage. If the potassium deposition temperature is larger than 325 K, no more than 0.6 ML of K can be adsorbed [32]. Urano *et al.* [18] demonstrated that K deposited on to a Si(100) surface saturates at temperatures larger than RT in the manner shown in Fig. 4.

What is more, the adsorption of K is extremely sensitive to the conditions of the surface preparation and alkali metal deposition. Soukiassian *et al.* [43] clearly showed that the presence of impurities, even at a very low level, significantly increases the K sticking coefficient at RT. The saturation of K coverage was observed only for extremely clean experimental conditions. Moreover, Glander and Webb [80] showed that for alkali atoms the effective pressure of the incident flux should be taken into account. Thus, this fact may explain the significant coverage differences obtained in various works.

The growth mode of K on a Si(100)2×1 surface is strongly dependent on surface temperature, the incident atom flux and the conditions of the surface preparation and alkali metal deposition. While at low temperature (≤ 300 K), the multilayer growth occurs [55], at 320 K, only 0.7 ML of K is stable on the Si(100) surface [37]. Multilayer growth also occurs at RT when the experimental condition is not clean enough [43], as mentioned above.

2.2. STRUCTURE

2.2.1. Si(100)2 × 1–K

It is now recognized that the identification of the exact geometry of potassium in the Si(100)2×1–K surface structure may not be easy [60], although, this system has been ex-

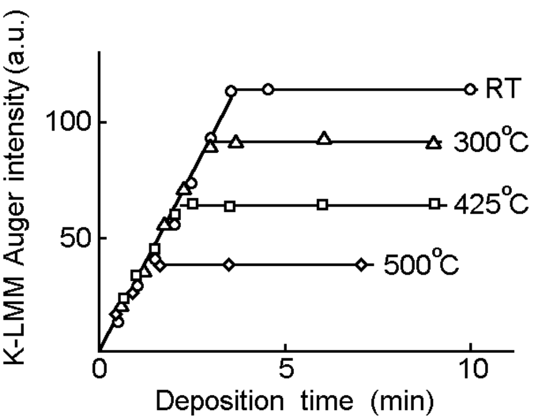

Fig 4. The peak-to-peak amplitudes of AES signals of K–LMM (248 eV) with the substrate temperature as a function of deposition time (from Ref. [18]). (*Reproduced by permission of Elsevier Science Publishers BV)*

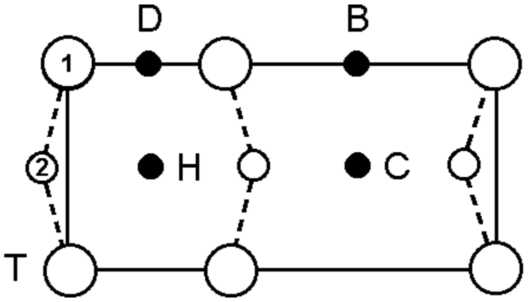

Fig 5. A top view of H, B, C, D, and T adsorption sites for alkali–metals in a Si(100)2 × 1 unit cell. Closed circles denote alkali–metal and open circles denote Si atoms. Numerals in the circles indicate Si atomic layers (from Ref. [56]). (*Reproduced by permission of Elsevier Science Publishers BV)*

tensively investigated both theoretically and experimentally. In 1973, Levine [81] made an inspired proposal for the structure of Cs on Si(100)2 × 1. He suggested that, at low coverages, Cs occupies quasihexagonal (H) hollow sites above the Si-dimer rows, with saturation coverage, $\theta = 0.5$ ML. For reference, various adsorption sites are shown in Fig. 5. Since then, this model and adsorption site have been widely used for other adsorbates as well, in qualitative discussions.

Abukawa and Kono [30], on the basis of a kinematical analysis of the XPD patterns of K $2p$ core levels, proposed the existence of a K double layer. They found that placing K atoms in (H/C) sites simultaneously in a puckered configuration successfully confirmed their observations. The dilayer corresponds to a coverage of 1 ML (Fig. 6). The vertical distance between the two K layers is ≈1.1 Å.

For the Si(100)2 × 1–K structure, Makita *et al.* [33] comparing RHEED calculated rocking curves with experimental curves showed that the double-layer model gives better agreement than the single-layer one. For the best model, the surface normal difference between the upper and lower potassium positions is 1.25 Å, and the upper potassium is 2.3 Å above the Si dimer array which is contracted 0.2 Å into the surface normal direction. The results obtained by Urano *et al.* [18,19] using dynamical LEED analysis and Effner *et al.* [42] using STM are also in better agreement with double-layer model. However, the results of Soukiassian *et al.* [43] indicated that, at saturation coverage, the potassium atoms appear to form one dimensional chains parallel to the silicon dimer rows.

Several STM experiments have appeared recently [39–43]. It was suggested that, at low coverages, K atoms are adsorbed in the topmost (T) site above one of the dimers forming

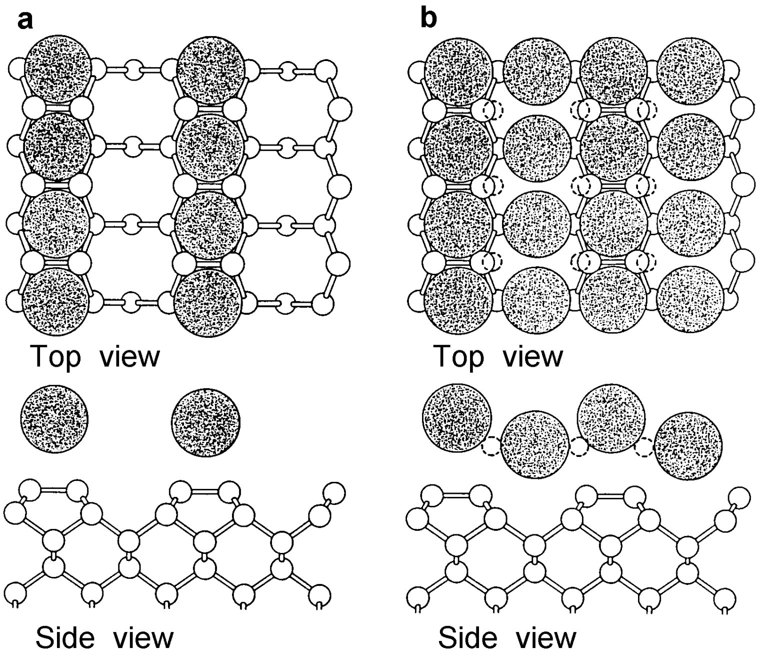

Fig 6. Schematic illustration of models for the Si(100)2 × 1–K. (a) Generally assumed one-dimensional alkali chain model (b) Double-layer model proposed by Abukawa and Kono. Alkali atoms are represented by large shaded circles (from Ref. [30]). (*Reproduced by permission of the publishers of Journal of Physical Review B)*

Si atoms. However, at about 0.1 ML coverage, K forms a linear chain perpendicular to the Si-dimer rows. STM work by Badt *et al.* [41] noted considerable disorder, whereas, at saturation coverage, the results of Soukiassian *et al.* [43] indicated the presence of one-dimensional chains with a single site of adsorption (i.e. chains of K atoms). Pervan *et al.* [24] determined the microscopic adsorption site of K on Si(100) by titration with physisorbed Xe. They concluded that the H site is preferentially filled over a B site at 1/2 ML coverage. A recent AED study [37], which measured intensities at different polar angles, did, however, conclude that the low temperature (110 K) data are consistent with adsorption at H or B sites. Two K desorption peaks were observed by TDS [55], and were attributed to the desorption of K atoms from two different chemisorbed states on the Si(100)2 × 1 surface.

In addition to the site, there is also a lack of agreement of the value of the K–Si bond length. Values in the range of 2.6–3.5 Å have been published hitherto [57, 58, 60–65, 67, 82]. There was only one direct measurement [50, 51] for K–Si bond length, which gave a value of 3.14 ± 0.10 Å. This was derived from SEXAFS data and is not site specific.

The conclusions drawn from various calculations [22, 56–61, 63–69] are also somewhat diverse [56, 69]. A review of theoretical works has already been published by Batra [56, 69].

2.2.2. $\begin{pmatrix} 2 & 1 \\ 0 & 3 \end{pmatrix} + \begin{pmatrix} 2 & -1 \\ 0 & 3 \end{pmatrix}$ and 2 × 3 Phases

The mixed phase of $\begin{pmatrix} 2 & 1 \\ 0 & 3 \end{pmatrix}$ and $\begin{pmatrix} 2 & -1 \\ 0 & 3 \end{pmatrix}$ and the 2 × 3 phase were found earlier for the Cs-adsorbed Si(100) surface [78]. Abukawa *et al.* [78] obtained structural models for the mixed phase and for the 2 × 3 phase by combining information obtained from XPD and LEED. These models are described in Chapter Cs (Figs. 7(a) and 8). Sasaki *et al.* [47] assumed the same models for the phases of the K/Si(100) system. The unit cells denoted A and B in Fig. 7(a) are for the $\begin{pmatrix} 2 & -1 \\ 0 & 3 \end{pmatrix}$ and $\begin{pmatrix} 2 & 1 \\ 0 & 3 \end{pmatrix}$ phases, respectively. The two unit cells are physically identical but mirror-images of each other.

2.3. PROPERTIES

2.3.1. Electronic Properties

The electronic properties of K on Si(100)2×1 are currently attracting much attention in both experimental and theoretical studies [59]. The main disagreement centers on whether the adsorbates form a conducting chain on the dimer Si(100)2×1 surface or a nonconducting ionic chain, in which case the Si surface gains charge from potassium atoms and changes into a metallic state [60].

On the experimental side, anisotropic plasmon dispersions for the K overlayer measured by Aruga *et al.* [53] with EELS seemed to support the existence of such one-dimensional metallic chains. On the other hand, ARUPS experiments of Enta *et al.* [26, 35, 83] for the K overlayer showed that the surface might be semiconducting rather than metallic at saturation coverage. The double-layer model of Abukawa and Kono [22,30] corresponds to $\theta = 1$ with two adatom valence electrons per unit cell, and therefore is compatible with the observed semiconducting nature of the overlayer.

Using WF change, TDS and UV photoemission measurements for potassium as well as coadsorbed oxygen, Castro *et al.* [25] confirmed that the potassium overlayer on Si(100)2×1 behaves differently above and below 0.5 ML; at $\theta_K \geq 0.5$ ML the behavior of the K overlayer is similar to that of bulk potassium. These experimental results are consistent with a metallic character of the K overlayer above 0.5 ML.

Soukiassian and Kendelewicz [84] studied the core level of Si surface atoms by PES. They found no shift in the binding energy of Si $2p$ upon K adsorption, which suggested that the net charge transfer from K to Si atoms is quite small. Nishigaki *et al.* [34] studied the surface electronic states of K/Si(100)2×1 by MDS. The rapid growth of a sharp peak near the Fermi energy with increasing K coverage attributed to the partially filled K valence states. Experimental and theoretical results of Oellig *et al.* [36] indicate that the bonding has a substantial covalent character.

On the theoretical side, most of the electronic structure calculations for the K/Si(100)2×1 surface were performed assuming the Levine model ($\theta = 1/2$ ML). Ciraci and Batra [64] found a K–Si bond length of only 2.59 Å, and complete charge transfer from K to the substrate with metallization of the substrate which involves an ionic type of bonding between the overlayer and the substrate. Ishida *et al.* [65] found the charge transferred from the K atom to the surface Si dimer to be only about 0.1 e. In contrast to Ciraci and Batra, Ishida *et al.* concluded that the K–Si bond length is 3.52 Å and Kasowski and Tsai [58] calculated it to be 3.32 Å, which is consistent with the SEXAFS results of Kendelewicz *et al.* [50, 51] who obtained the Si–K bond length (3.14 ± 0.10) Å which is equal to the sum of the covalent radii of K and Si atoms ($2.03\ \mathring{A} + 1.11\ \mathring{A}$). Ling *et al.* [60] obtained a K–Si bond length of about 3.2 Å for the H site and a large value of the charge transfer (~ 0.63 electron) from K to Si. Recently, Ishida and Terakura [59] performed calculations for θ ranging from 1/6 to 1 ML for the Levine model ($\theta = 1/2$ ML) and also for the double-layer model ($\theta = 1$ ML). They concluded that the Si–K bond is polarized and covalent. Batra [56] considered the surface to be metallic at $\theta = 1/2$ ML and semiconducting at $\theta = 1$ ML. This is consistent with the simple electron counting argument.

Variation of the WF observed during K deposition on Si(100)2×1 is shown in Fig. 7. The relationship has a minimum. Such a minimum was observed in Refs [7, 23–25, 27, 34, 35, 83] and was not observed in [3, 21]. The values of the WF at minimum and saturation

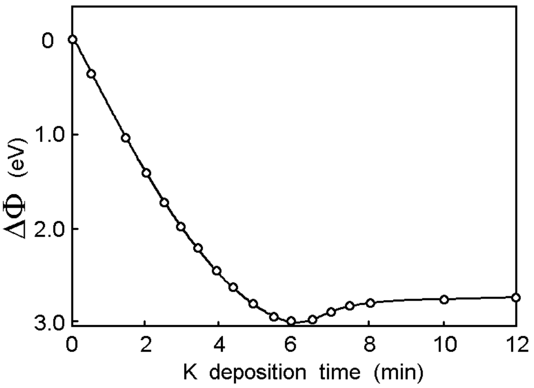

Fig 7. Work function changes for K deposition on Si(100)2 × 1 at RT (from Ref. [27]). (*Reproduced by permission of the publishers of Journal of Physical Review B)*

Table 1. The minimum and saturation values of work function for the K/Si(100) system [83]

Min.	$\Delta\Phi_{\mathrm{min}}$	$\Delta\Phi_{\mathrm{sat}}$	Ref.	
Yes	−3. 32 eV	−3. 13 eV	[49]	at RT
Yes	−3.3 eV	−2.9 eV	[34]	
Yes	−3.1 eV	—	[23]	
Yes	−3.0 eV	−2.7 eV	[27]	
Yes	−2.9 eV	−2.6 eV	[7]	at 200 K
No	—	−3. 0 eV	[3]	
No	—	−2.0 eV	[21]	
Yes	−3.3 eV	−3.2 eV	[35, 83]	
Yes	−3.3 eV	−2.3 eV	[25]	at 60 K
Yes	−3.5 eV	−2.9 eV	[25]	

are consistent with each other excluding the value from Ref. [21] (Table 1).

2.3.2. Desorption

TDS results of Tanaka *et al.* [55] show that there are two desorption peaks of K on the Si(100)2 × 1 at $\theta \leq 1$ ML. These desorption peaks were attributed to the desorption of K atoms from two different chemisorbed states on the Si(100)2 × 1 surface. The desorption energy in the limit of zero coverages was estimated to be 38 and 56 kcal/mol (1.7 and 2.5 eV).

Analysis of the TDS data by Michel *et al.* [85] yields bonding energy of K to the Si(100) surface $E_{\mathrm{d}} = 1.8$ eV/atom for $\theta_{\mathrm{K}} = 0.5$ ML and $E_{\mathrm{d}} = 0.95$ eV/atom for $\theta_{\mathrm{K}} > 0.5$ ML. In accordance with SI experiments [16], in the temperature range from 800 to 1550 K, the Si(100) surface has a first-order desorption energy $E = 2.54 \pm 0.14$ eV for K.

2.3.3. Oxidation

PES and high resolution AES [31, 36, 86] indicated that multilayers of K on Si(100)2 × 1 promote the oxidation of Si under subsequent exposure to O_2. The oxygen uptake is enhanced by four orders of magnitude. The alkali can be completely desorbed from the surface at 900 K leaving behind a layer of SiO_2, whose thickness is proportional to the amount of K deposited. The process can be further repeated. The possible mechanisms of potassium-induced promotion of oxidation of Si(100)2 × 1 is discussed in Refs [31, 87].

2.3.4. Negative Electron Affinity Surface of O/K/Si(100)2 × 1

Through the addition of monolayer quantities of K and O to an atomically clean Si(100)2 × 1 surface, the surface with the negative electron affinity (NEA) is achieved [48]. By X-ray photoelectron diffraction Abukawa *et al.* [48] found that the arrangement of O and K atoms in the NEA O/K/Si(100)2 × 1 surface is essentially the same as that in the NEA O/Cs/Si(100)2 × 1 surface.

REFERENCES

[1] H. Daimon and S. Ino, *Surf. Sci.* **164** (1985) 320.
[2] S. Mizuno and A. Ichimiya, *Appl. Surf. Sci.* **33–34** (1988) 38.
[3] R. E. Weber and W. T. Peria, *Surf. Sci.* **14** (1969) 13.
[4] U. A. Ditzinger, Ch. Lunau, B. Schieweck, St. Tosch, H. Neddermeyer and M. Hanbucken, *Surf. Sci.* **211–212** (1989) 707.
[5] Avci Recep, *J. Vac. Sci. Technol. A* **4** (1986) 1400.
[6] K. O. Magnusson and B. Reihl, *Phys. Rev. B* **41** (1990) 12071.
[7] E. M. Oellig and R. Miranda, *Surf. Sci.* **177** (1986) L947.
[8] R. E. Weber and W. T. Peria, *J. Appl. Phys.* **38** (1967) 4355.
[9] Y. Ma, C. T. Chen, G. Meigs, F. Sette, G. Illing and H. Shigakawa, *Phys. Rev. B* **45** (1992) 5961.
[10] T. Hashizume, Y. Hasegawa, I. Sumita and T. Sakurai, *Surf. Sci.* **246** (1991) 189.
[11] T. Hashizume, K. Motai, Y. Hasegawa, I. Sumita, H. Tanaka, S. Amano, S. Hyodo and T. Sakurai, *J. Vac. Sci. Technol. B* **9** (1991) 745.
[12] H. Ishida, K. Terakura and M. Tsukada, *Solid State Commun.* **59** (1986) 365.
[13] I. P. Batra and S. Ciraci, *Phys. Rev. B* **37** (1988) 8432.
[14] S. Ciraci and I. P. Batra, *Phys. Rev. Lett.* **58** (1987) 1982.
[15] G. Boishin and L. Surnev, *Surf. Sci.* **273** (1992) 301.
[16] E. F. Greene, J. T. Keeley and M. A. Pickering, *Surf. Sci.* **120** (1982) 103.
[17] G. Boishin and L. Surnev, *Appl. Surf. Sci.* **59** (1992) 111.
[18] T. Urano, K. Sakaue, K. Nagano, S. Hongo and T. Kanaji, *J. Cryst. Growth* **115** (1991) 411.
[19] T. Urano, Y. Uchida, S. Hongo and T. Kanaji, *Surf. Sci.* **242** (1991) 39.
[20] Y. R. Xing, J. P. Zhang and L. Z. B. Huang, *Solid State Commun.* **74** (1990) 319.
[21] H. Tochihara, *Surf. Sci.* **126** (1983) 523.
[22] T. Abukawa and S. Kono, *Surf. Sci.* **214** (1989) 141.
[23] M. Kamaratos, S. Kennou and C. A. Papageorgopoulos, *Surf. Sci.* **227** (1990) 43.
[24] P. Pervan, E. G. Michel, G. R. Castro, R. Miranda and K. Wandelt, *J. Vac. Sci. Technol. A* **7** (1989) 1885.
[25] G. R. Castro, P. Pervan, E. G. Michel, R. Miranda and K. Wandelt, *Vacuum* **41** (1990) 564.
[26] Y. Enta, S. Suzuki, S. Kono and T. Sakamoto, *Phys. Rev. B* **39** (1989) 5524.
[27] E. M. Oellig, E. G. Michel, M. C. Asensio, R. Miranda, J. C. Duran, A. Munoz and F. Flores, *Europhys. Lett.* **5** (1988) 727.
[28] I. P. Batra, J. M. Nicholls and B. Reihl, *J. Vac. Sci. Technol. A* **5** (1987) 898.
[29] E. M. Oellig and R. Miranda, *J. Vac. Sci. Technol. A* **5** (1987) 653.
[30] T. Abukawa and S. Kono, *Phys. Rev. B* **37** (1988) 9097.
[31] E. G. Michel, E. M. Oellig, M. C. Asensio and R. Miranda, *Surf. Sci.* **189–190** (1987) 245.
[32] E. G. Michel, P. Pervan, G. R. Castro, R. Miranda and K. Wandelt, *Phys. Rev. B* **45** (1992) 11811.

[33] T. Makita, S. Kohmoto and A. Ichimiya, *Surf. Sci.* **242** (1991) 65.
[34] S. Nishigaki, S. Matsuda, T. Sasaki, N. Kawanishi, Y. Ikeda and H. Takeda, *Surf. Sci.* **231** (1990) 271.
[35] Y. Enta, T. Kinoshita, S. Suzuki and S. Kono, *Phys. Rev. B* **36** (1987) 9801.
[36] E. M. Oellig, E. G. Michel, M. C. Asensio and R. Miranda, *Appl. Phys. Lett.* **50** (1987) 1660.
[37] M. C. Asensio, E. G. Michel, J. Alvarez, C. Ocal, R. Miranda and S. Ferrer, *Surf. Sci.* **211–212** (1989) 31.
[38] S. Kono, *Arabian J. Sci. Eng.* **15** (1990) 293.
[39] Y. Hasegawa, I. Kamiya, T. Hashizume, T. Sakurai, H. Tochihara, M. Kubota and Y. Murata, *Phys. Rev. B* **41** (1990) 9688.
[40] T. Hashizume, Y. Hasegava, I. Kamiya, T. Ide, I. Sumita, S. Hyodo, T. Sakurai, H. Tochihara, M. Kubota and Y. Murata, *J. Vac. Sci. Technol. A* **8** (1990) 233.
[41] D. Badt, A. Brodde, St. Tosch and H. Neddermeyer, *J. Vac. Sci. Technol. A* **8** (1990) 251.
[42] U. A. Effner, D. Badt, J. Binder, T. Bertrams, A. Brodde, Ch. Lunau, H. Neddermeyer and M. Hanbucken, *Surf. Sci.* **277** (1992) 207.
[43] P. Soukiassian, J. A. Kubby, P. Magnat, Z. Hurych and K. M. Schirm, *Phys. Rev. B* **46** (1992) 13471.
[44] L. S. O. Johansson and B. Reihl, *Phys. Rev. Lett.* **67** (1991) 2191.
[45] L. S. O. Johansson and B. Reihl, *Appl. Surf. Sci.* **56–58** (1992) 486.
[46] T. Abukawa, T. Kashiwakura, T. Okane, Y. Sasaki, H. Takahashi, Y. Enta, S. Suzuki, S. Kono, S. Sato, T. Kinoshita et al. , *Surf. Sci.* **261** (1992) 217.
[47] Y. Sasaki, Y. Enta, S. Suzuki and S. Kono, *Surf. Sci.* **276** (1992) 205.
[48] T. Abukawa, Y. Enta, T. Kashiwakura, S. Suzuki and S. Kono, *J. Vac. Sci. Technol. A* **8** (1990) 3205.
[49] D. M. Riffe, G. K. Wertheim, J. E. Rowe and P. H. Citrin, *Phys. Rev. B* **45** (1992) 3532.
[50] T. Kendelewicz, P. Soukiassian, R. S. List, J. C. Woicik, P. Pianetta, I. Lindau and W. E. Spicer, *Phys. Rev. B* **37** (1988) 7115.
[51] T. Kendelewicz, J. C. Woicik, R. S. List, P. Soukiassian, B. B. Pate, P. Pianetta, I. Lindau and W. E. Spicer, *J. Vac. Sci. Technol. A* **6** (1988) 879.
[52] S. Masuda, H. Ishii and Y. Harada, *Solid State Commun.* **79** (1991) 453.
[53] T. Aruga, H. Tochihara and Y. Murata, *Phys. Rev. Lett.* **53** (1984) 372.
[54] N. Takagi, N. Minami and M. Nishijima, *Phys. Rev. B* **45** (1992) 13524.
[55] S. Tanaka, N. Takagi, N. Minami and M. Nishijima, *Phys. Rev. B* **42** (1990) 1868.
[56] I. P. Batra, *J. Vac. Sci. Technol. A* **8** (1990) 3425.
[57] S. Ciraci and I. P. Batra, *Phys. Rev. Lett.* **60** (1988) 547.
[58] R. V. Kasowski and M. -H. Tsai, *Phys. Rev. Lett.* **60** (1988) 546.
[59] H. Ishida and K. Terakura, *Phys. Rev. B* **40** (1989) 11519.
[60] Y. Ling, A. J. Freeman and B. Delley, *Phys. Rev. B* **39** (1989) 10144.
[61] R. Ramirez, *Phys. Rev. B* **40** (1989) 3962.
[62] I. P. Batra and P. S. Bagus, *J. Vac. Sci. Technol. A* **6** (1988) 600.
[63] S. Ciraci and I. P. Batra, *Phys. Rev. B* **37** (1988) 2955.
[64] S. Ciraci and I. P. Batra, *Phys. Rev. Lett.* **56** (1986) 877.
[65] H. Ishida, N. Shima and M. Tsukada, *Phys. Rev. B* **32** (1985) 6246.
[66] H. Ishida, N. Shima and M. Tsukada, *Surf. Sci.* **158** (1985) 438.
[67] M. Tsukada, H. Ishida and N. Shima, *Phys. Rev. Lett.* **53** (1984) 376.
[68] M. Nakayama, T. Kato and K. Ohtomi, *Solid State Commun.* **50** (1984) 409.
[69] I. P. Batra, *Phys. Rev. B* **43** (1991) 12322.
[70] M. Nishijima, S. Tanaka, N. Takagi and M. Onchi, *Surf. Sci.* **242** (1991) 498.
[71] D. Huang and P. R. Antoniewicz, *Phys. Rev. B* **44** (1991) 9076.
[72] F. Huaxiang and Y. Ling, *Surf. Sci.* **250** (1991) L373.
[73] Y. Ling and X. Xide, *Surf. Sci.* **247** (1991) L204.
[74] I. P. Batra, *Surf. Sci.* **242** (1991) 354.

[75] C. K. Ong, *J. Phys. :Cond. Matt.* **2** (1990) 6731.
[76] S. N. Eskpenuma and A. K. Ray, *Phys. Rev. B* **46** (1992) 16163.
[77] A. Chasse, *Surf. Sci.* **269–270** (1992) 22.
[78] T. Abukawa, T. Okane and S. Kono, *Surf. Sci.* **256** (1991) 370.
[79] A. J. Smith, W. R. Graham and E. W. Plummer, *Surf. Sci.* **243** (1991) L37.
[80] G. S. Glander and M. B. Webb, *Surf. Sci.* **222** (1989) 64.
[81] J. D. Levine, *Surf. Sci.* **34** (1973) 90.
[82] I. P. Batra, *Phys. Rev. B* **39** (1989) 3919.
[83] Y. Enta, T. Kinoshita, S. Suzuki and S. Kono, *Phys. Rev. B* **39** (1989) 1125.
[84] P. Soukiassian and T. Kendelewicz, in *Proceedings of the NATO Advanced Research Workshop on Metallization and Metal-Semiconductor Interfaces, Garching, 1988,* edited by I. P. Batra (Plenum, New York, 1988), p. 465.
[85] E. G. Michel, M. C. Asensio and M. Miranda, in *Metalization and Metal–Semiconductor Interfaces*, Ed. I. P. Batra (Plenum, New York, 1989) p.381.
[86] P. Soukiassian, H. I. Starnberg and T. Kendelewicz, *Appl. Surf. Sci.* **41–42** (1989) 395.
[87] L. Ye, A. J. Freeman and B. Delley, *Surf. Sci.* **239** (1990) L526.

(Kr)

KRYPTON

1. (111) ORIENTATION

The physisorption of Kr on the Si(111)7×7 surface does not change the initial silicon reconstruction.

1.1. PHASE DIAGRAM

The physisorption of Kr on the Si(111)7×7 surface can only occur at low substrate temperature [1]. LEED indicates that the substrate structure is not appreciably modified by the adsorption. The desorption temperature of adsorbed Kr is about 125 K [1]. At low temperatures (< 110 K) the multilayer physisorption occurs.

REFERENCES

[1] E. Conrad and M. B. Webb, *Surf. Sci.* **129** (1983) 37.

(La)

LANTHANUM

1. (111) ORIENTATION

Lanthanum is known to induce 1 × 1 reconstruction on the Si(111) surface.

1.1. PHASE DIAGRAM

Griffiths and Williams [1] found that RT deposition of La films with thicknesses from 1 to 12 ML on the Si(111)7 × 7 surface followed by annealing at $\simeq 750\,^\circ$C for 120 s results in the appearance of the ordered 1 × 1 LEED pattern. Chemical shifts of Si $2p$ peak in the XPS spectra of the La/Si(111) system which are observed even at RT and clearly correspond to the formation of lanthanum silicide. This may be lanthanum pseudo-disilicide, which like lanthanum metal has a hexagonal structure and would be expected to grow in an ordered fashion on Si(111).

The formation of La–silicide was also observed by Puppin *et al.* [2] during La deposition on the Si(111)2 × 1 cleaved surface held at RT. Using photoemission spectroscopy, the authors showed that the La/Si interface appears to be reacted in the La coverage region 0.1–2 ML. However, further deposition of La results in the growth of pure metal.

REFERENCES

[1] C. L. Griffiths and R. H. Williams, *Phys.Scripta* **41** (1990) 919.

[2] E. Puppin, H. Guyot, Z. X. Shen, J. Hwang and I. Lindau, *Solid State Commun.* **67** (1988) 23.

(Li)

LITHIUM

1. (111) ORIENTATION

During Li deposition on the Si(111)7 × 7 surface at room temperature $\delta(7\times7)$ and 1×1 structures are observed. Subsequent heating of the Si(111)–Li surface results in the appearance of 4×4, $\sqrt{3}\times\sqrt{3}$, 1×1 and 3×1 structures.

1.1. PHASE DIAGRAM

Initial stages of Li adlayer formation on a Si(111)7 × 7 surface have been investigated by LEED [1], RHEED [2–4], AES [1, 2, 5], FI-STM [6, 7], work function change [5, 8], MDS [5], and NMR [8].

1.1.1. RT Deposition

During Li deposition on a Si(111)7 × 7 surface at RT, the RHEED pattern was found to change gradually to a so-called $\delta(7\times7)$ structure which features appears at Li coverage of $\theta = 0.76$ ML [3]. For the most characteristic of the $\delta(7\times7)$ pattern, the coverage of Li was estimated from RHEED data to be 1.37 ML [3]. According to the data of Ref. [2], the further deposition of Li with a corresponding increase of the Li–KVV AES signal intensity results in the formation of the 1×1 structure. In contrast, in Refs [3, 4] the 1×1 structure pattern was not obtained in the same experimental conditions up to the saturation coverages.

The observed intensity distribution of the $\delta(7\times7)$ RHEED pattern estimated visually is shown in Fig. 1 from Ref. [4]. The characteristic of this pattern is that the intense fractional order spots are only (1) those lying on lines joining neighboring integer order spots and (2) those at around the integer order spots such as a.

Nishigaki *et al.* [5] performed experiments of MDS and AES on a Li/Si(111) system and suggested that, at first, Li atoms are adsorbed on the surface and, with the increase of coverage, they diffuse into the substrate.

1.1.2. HT Growth

Mizuno and Ichimiya [2] studied by RHEED and AES the formation of superstructures in the Li/Si(111) system upon annealing as a function of the initial Li coverage and annealing temperature. It was found that heating the Si(111)1 × 1–Li surface with relatively high Li coverages (Auger peak ratio Li–KVV/Si–LVV $\simeq 0.3$) first results in a 4×4 structure. Then $\sqrt{3}\times\sqrt{3}$, 1×1 and 3×1 structures appear successively with decreasing Li coverage as shown in Fig. 2. At relatively low coverages of Li (Li–KVV/Si–LVV $\simeq 0.1$), the surface structure

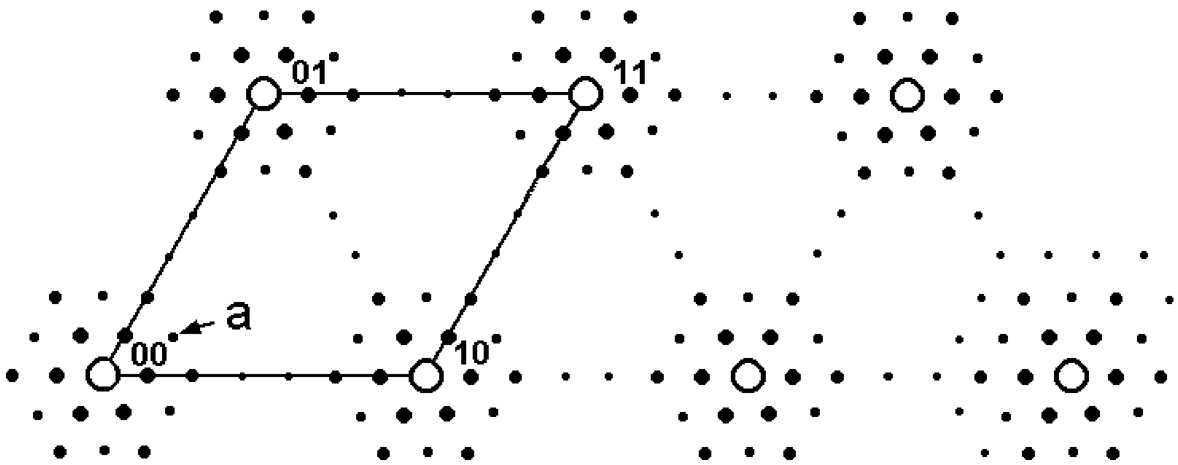

Fig 1. Observed intensity distribution of the Si(111)$\delta(7 \times 7)$ RHEED pattern (from Ref. [4]). (*Reproduced by permission of Elsevier Science Publishers BV)*

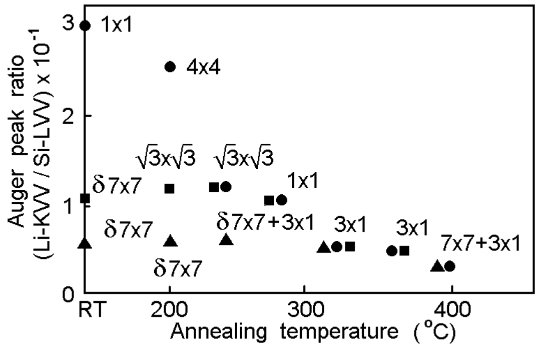

Fig 2. Structural changes after annealing the Li/Si(111) system. Symbols pertain to the initial stages of Li coverage (from Ref. [2]). (*Reproduced by permission of Elsevier Science Publishers BV)*

changes from $\delta(7\times7)$ to 3×1 *via* $\sqrt{3}\times\sqrt{3}$ and 1×1 and finally reduces to 7×7. At still lower coverages (Li–KVV/Si–LVV $\simeq 0.05$), the surface structure changes from $\delta(7 \times 7)$ directly to 3×1.

The general trends in the structural transformations of the annealed Li/S(111) interface revealed by Mizuno and Ichimiya [2] are consistent with the LEED–AES results of Fan and Ignatiev [1], who reported the observation of the 3×1 structure upon annealing of 0.2 ML Li at about 800 °C and sequential formation of $\sqrt{3} \times \sqrt{3}$ and 3×1 upon annealing of more than 0.3 ML Li respectively at 600 and 800 °C.

The Si(111)3×1–Li structure was also obtained by Daimon and Ino [4] upon Li deposition on to the Si(111)7×7 surface held at about 500 °C and by Wan *et al.* [9] upon RT deposition of Li followed by annealing at temperatures ranging from 350 to 500 °C.

1.2. STRUCTURE

1.2.1. Si(111)$\delta(7 \times 7)$–Li

¿From the analysis of rocking curves of RHEED intensities from the Si(111)$\delta(7 \times 7)$–Li and dynamical calculations and comparing these results with those for the 7×7–H surface [10], the possible structure model of $\delta(7 \times 7)$ was suggested by Kohmoto *et al.* [3]. The side view of the $\delta(7 \times 7)$ model is shown in Fig. 3.

Two kinds of models for adsorption sites of Li atoms were taken into account for the 0.2 ML Li coverage. For the first model, model (a), Li atoms form a single layer with whole

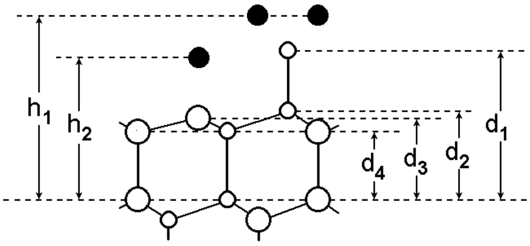

Fig 3. [0$\bar{1}$1] side view of the model for the Li/Si(111) surface at RT. Only a part without a stacking-fault is shown. Open circles are Si atoms and closed ones Li atoms (from Ref. [3]). (*Reproduced by permission of Elsevier Science Publishers BV)*

coverage (0.2 ML in this case) at a height h_1 in Fig. 3. For the second model, model (b), Li atoms form a double layer. A Li layer of half coverage (0.1 ML in this case) is at h_1 and the other half at h_2 in this model. Authors concluded that for the position of the Li atoms, model (a) was revealed as the best model with $h_1 = 7.1$ Å. For the higher coverages the following model was adopted. The adatoms with bond-breaking are randomly distributed at the topmost sites above the stacking-fault layer. The Li atoms for h_1 in Fig. 3 (higher position Li) are also randomly sited just above the second layer Si atoms and/or the fourth Si atoms. The approximate values of the h_1 and h_2 for different Li coverage are $\sim$ 7 and 5.5 Å. The atomic position of Si atoms (d_1–d_4) do not change during the adsorption of Li atoms for coverages from 0.2 up to 0.76 ML.

The complementary data on the Li adsorption on Si(111)7 × 7 were received in the Fi–STM study of Hasegawa *et al.* [6, 7]. It was shown that, at the initial stage, Li trimers are formed preferentially in the faulted half of the 7 × 7 unit cell. At higher coverages, these trimers coalesce to form six-atom and nine-atom clusters across the interface between the faulted and unfaulted halves. It was suggested, based on the careful study of the adsorption sites, that the Si adatoms of the DAS model may be removed upon the Li adsorption.

1.2.2. Si(111)3 × 1–Li

Daimon and Ino [4] suggested that the 3 × 1 structure has two Li atoms in the 3 × 1 unit mesh by analogy with the estimation of the surface coverage for Si(111)3 × 1–K structure.

¿From the other point of view (Fan and Ignatiev [1]), the adsorbates (such as Ag, Li and Na) do not participate in the 3 × 1 long-range ordered structure and serve only to induce surface reconstruction. This conclusion was obtained from the measurements of LEED *I–V* curves for the 3 × 1 structures. The metal adsorbates which induce the 3 × 1 reconstruction are all at coverages below 1/3 ML. The 3 × 1–Li surface phase can be stabilized by as little as 0.01 ML Li coverage [1]. A proposed missing-row model of the 3 × 1 reconstruction of the Si(111) surface induced by Ag and alkali-metal adsorption is shown in Fig. 4.

Wan *et al.* [9] used STM to study the structure of the 3 × 1 surface phase. The atomic structure is not immediately clear from the STM images because of their complex dependence on bias voltage polarity. A tentative missing top layer model was proposed but remains to be verified by other means.

1.2.3. Si(111)$\sqrt{3} \times \sqrt{3}$–Li

Li deposition of about 1 ML followed by annealing the Li/Si(111) surface at 300 °C leads to the gradual transformation of the $\delta(7 \times 7)$ RHEED pattern into a $\sqrt{3} \times \sqrt{3}$–Li pattern with little change of the Li coverage [2]. This $\sqrt{3} \times \sqrt{3}$–Li pattern changes into a 1 × 1–H pattern by substitution of hydrogen atoms, suggesting that Li atoms form the $\sqrt{3} \times \sqrt{3}$ matrix and

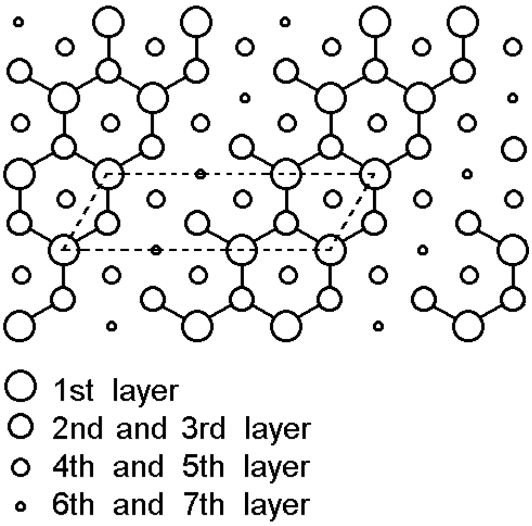

Fig 4. Missing-row model of the 3×1 reconstruction of the Si(111) surface induced by Ag and alkali-metal adsorption (from Ref. [1]). (*Reproduced by permission of the publishers of Journal of Physical Review B)*

the Si surface is bulk-like in the $\sqrt{3} \times \sqrt{3}$–Li structure. From the analysis of the rocking curves and experiments of substitution of Li atoms by H atoms the structure model for the $\sqrt{3} \times \sqrt{3}$–Li was proposed by Kohmoto *et al.* [3]. Li_3 clusters are arranged with $\sqrt{3} \times \sqrt{3}$ periodicity above 1.60 Å from a bulk-like Si(111)1×1 surface. The Li coverage is 1 ML in this model. Since the Li $\sqrt{3} \times \sqrt{3}$ structure is formed on a bulk-like Si matrix, the dimer bonds of 7×7 structure are not present in this structure and the stacking-fault is also dissolved. Therefore, the dimer bonds are broken by annealing at considerably low temperature (300 °C) under the existence of the Li atoms.

1.3. PROPERTIES

1.3.1. Electronic Properties

The change of the work function during Li exposure is plotted in Fig. 5 [8]. As common to alkali-metal adsorption the WF Φ decreases rapidly in the low coverage regime. A maximum change $\Delta\Phi = -2.4$ eV is reached at about 0.6 to 0.7 ML. For large coverages, $\Delta\Phi$ saturates at about -1.8 eV which agrees within the experimental uncertainties with the difference between the WF of Si(111) (4.8 eV) and of Li (2.92 eV) [8]. Moreover, the maximum decrease of -2.4 eV coincides with the results of Nishigaki *et al.* [5], but the latter authors did not find a distinct minimum in the $\Delta\Phi$ curve.

2. (100) ORIENTATION

Li is known to induce two reconstructions on the Si(100) surface. These are 2×1 and 1×1 structures.

2.1. PHASE DIAGRAM

2.1.1. Si(100)2×1 Surface

Initial states of Li adlayer formation on a Si(100)2×1 surface have been investigated by LEED, AES, EELS, work-function change ($\Delta\Phi$) [11–13], and STM [14–16].

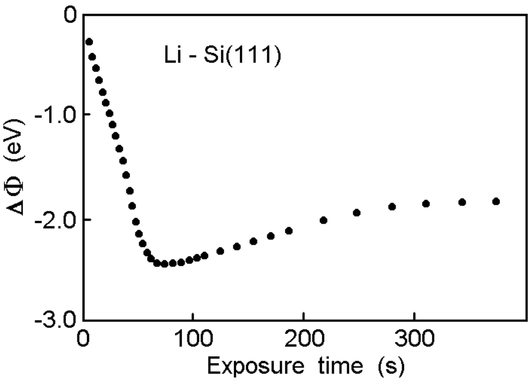

Fig 5. Work function change $\Delta\Phi$ as a function of exposure time (from Ref. [8]). (*Reproduced by permission of Elsevier Science Publishers BV)*

The LEED pattern was found to change sequentially with increasing Li coverage: Si(100)2 × 1 → Si(100)2 × 1–Li → Si(100)1 × 1–Li disordered → no diffraction spots. In Fig. 6 from Ref. [11] the Auger peak-to-peak heights of Li KLL and Si LVV Auger electrons, the work function change and the LEED pattern change versus Li deposition time are shown. In the Li uptake curve, a break in the slope at 550 s deposition time is clearly visible. After the break, the Li intensity increases gradually and reaches saturation. The variation of the Li Auger intensity is very different from those of other alkali-metal atoms (Na, K, Rb, and Cs). The Auger intensities of Na, K, Rb and Cs increase linearly and reach saturation suddenly as shown by the broken horizontal line in Fig. 6. It is reasonable to say that one monolayer of lithium is completed at the break point. A vertical broken line indicates the completion of the Li monolayer.

At about half of the monolayer the Si(100)2 × 1–Li structure has formed. With increasing coverage the LEED pattern changes from 2 × 1 to 1 × 1 in the monolayer range. The intensities of the integral spots of Si(100)1 × 1–Li decrease gradually and the intensity of the background further increases with increasing coverage. After prolonged deposition when the Auger intensities saturate, no spot is seen.

AES data analysis shows that lithium atoms are intermixed with Si after monolayer formation and lithium silicides are formed on the Si(100) surface after prolonged Li deposition at coverages beyond one monolayer. The temperature of the sample was estimated to be between 350 and 400 K during Li deposition.

2.2. STRUCTURE

2.2.1. Si(100)2 × 1–Li

When about half of the Li monolayer is deposited, a new 2 × 1 LEED pattern is observed whose *I–V* curves are different from those of clean Si(100)2 × 1. The structural model of the one-dimensional chains of Li atoms (see Fig. 7) proposed by Levine [17], was adopted for the Si(100)2 × 1–Li structure. The presence of linear chains, perpendicular to the substrate dimer rows was recently confirmed by STM results at lower coverage ($\theta < 0.1$ ML) [16]. The adsorption sites of Li remain unknown. The works of different authors [17–20] give different results.

2.2.2. Si(100)1 × 1–Li

With increasing coverage, the LEED pattern changes from 2 × 1 to 1 × 1 in the monolayer range [11, 12]. The 1 × 1 LEED pattern is not observed during the adsorption of other alkali-

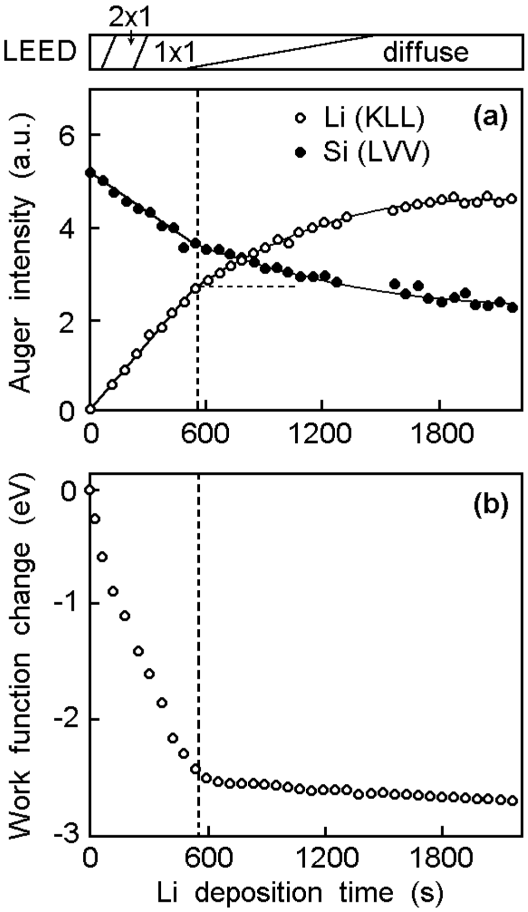

Fig 6. (a) Variation of Auger intensities of Li KLL and Si LVV and (b) work-function change as a function of Li deposition time. A vertical line shows monolayer formation. LEED pattern change versus Li deposition time is shown schematically at the top of the figure (from Ref. [11]). (*Reproduced by permission of Elsevier Science Publishers BV)*

metal atoms on Si(100). The surface which shows the 1 × 1 LEED pattern can be considered as a disordered structure, because the coverage range of the 1 × 1 pattern is wide and the decrease of the 1 × 1 spot intensities correlates well with the increase in background intensity.

2.3. PROPERTIES

2.3.2. Electronic Properties

Variation of the work function (Φ) observed during Li adsorption on Si(100)2 × 1 is shown in Fig. 5(b). The extent of work-function reduction is $\Delta\Phi_{1\mathrm{ML}} = 2.4$ eV at the completion of the monolayer and $\Delta\Phi_{\mathrm{sat}} = 2.6$ eV after a long deposition time. The work function does not reach a minimum during monolayer formation. This variation is different from those for other alkali-metal atoms on Si(100).

No overlayer plasmon was observed in EEL spectra of the Li/Si(100) system. This means that Li overlayer with the 2 × 1 structure has no metallic character, unlike the 2 × 1 structures of other alkali-metal atoms on Si(100). It should be noted that the nearest-neighbor distance in Li metal is 3.02 Å, which is much smaller than 3.84 Å, nearest-neighbor distance of Li adatoms in the Si(111)2 × 1 structure (see Fig. 7). Therefore, the intensive overlap of valence wave-functions between the adjacent Li atoms is unlikely.

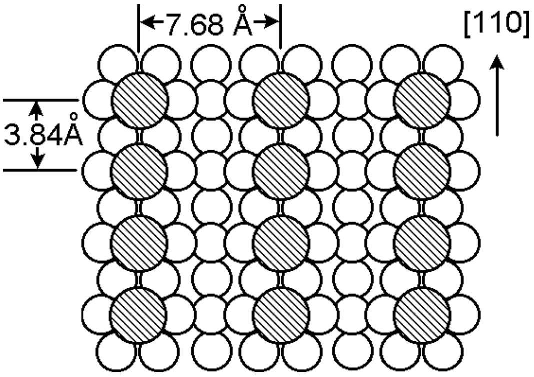

Fig 7. Structural models of Si(100)2 × 1–Li. Shaded circles represent Li, and open circles Si (from Ref. [11]). (*Reproduced by permission of Elsevier Science Publishers BV)*

REFERENCES

[1] W. C. Fan and A. Ignatiev, *Phys. Rev. B* **41** (1990) 3592.

[2] S. Mizuno and A. Ichimiya, *Appl. Surf. Sci.* **33–34** (1988) 38.

[3] S. Kohmoto, S. Mizuno and A. Ichimiya, *Appl. Surf. Sci.* **41–42** (1989) 107.

[4] H. Daimon and S. Ino, *Surf. Sci.* **164** (1985) 320.

[5] S. Nishigaki, M. Ohara, A. Murakami, S. Fukui and S. Matsuda, *Appl. Surf. Sci.* **35** (1988) 121.

[6] Y. Hasegawa, I. Kamiya, T. Hashizume, T. Sakurai, H. Tochihara, M. Kubota and Y. Murata, *Techn. Rept. ISSP. A.* (1989) 1.

[7] Y. Hasegawa, I. Kamiya, T. Hashizume, T. Sakurai, T. Tochihara, M. Kubota and Y. Murata, *J. Vac. Sci. Technol. A* **8** (1990) 238.

[8] J. Chrost and D. Fick, *Surf. Sci.* **251–252** (1991) 78.

[9] K. J. Wan, X. F. Lin and J. Nogami, *Phys. Rev. B* **46** (1992) 13635.

[10] A. Ichimiya and S. Mizuno, *Surf. Sci.* **191** (1987) L765.

[11] H. Tochihara and Y. Murata, *Surf. Sci.* **215** (1989) L323.

[12] H. Tochihara and Y. Murata, *Techn. Rept. ISSP. A. N* **2064** (1988) 1.

[13] Y. Murata, H. Toshihara and M. Kubota, in *Metallization and Metal-Semiconductor Interfaces*, Plenum Publishing Corporation (1989) 367.

[14] Y. Hasegawa, T. Hashizume, I. Kamiya, T. Ade, I. Sumita, S. Hyodo and T. Sakurai, *Techn. Rept. ISSP. A. N* **2147** (1989) 1.

[15] T. Hashizume, Y. Hasegava, I. Kamiya, T. Ide, I. Sumita, S. Hyodo, T. Sakurai, H. Tochihara, M. Kubota and Y. Murata, *J. Vac. Sci. Technol. A* **8** (1990) 233.

[16] Y. Hasegawa, I. Kamiya, T. Hashizume, T. Sakurai, H. Tochihara, M. Kubota and Y. Murata, *Phys. Rev. B* **41** (1990) 9688.

[17] J. D. Levine, *Surf. Sci.* **34** (1973) 90.

[18] I. P. Batra, *J. Vac. Sci. Technol. A* **8** (1990) 3425.

[19] Y. Ling and X. Xide, *Surf. Sci.* **247** (1991) L204.

[20] P. -L. Cao, R. -H. Zhou and X. -Y. Zhou, *Phys. Lett. A* **159** (1991) 179.

(Mg)

MAGNESIUM

1. (111) ORIENTATION

$\sqrt{3}\times\sqrt{3}$—$R30^\circ$, $\frac{2}{3}\sqrt{3}\times\frac{2}{3}\sqrt{3}$—$R30^\circ$, 3×3 and three-domain 3×1 reconstructions were observed for the Mg/Si(111) system.

1.1. PHASE DIAGRAM

The initial stages of Mg adlayer formation on the Si(111)7×7 surface were investigated using EXAFS and LEED by Vandrê *et al.* [1] and using LEED and AES by Quinn and Jona [2]. In contrast to Vandrê *et al.* [1], who reported the formation of a $\sqrt{3}\times\sqrt{3}$—$R30^\circ$ superstructure for deposition on the RT substrate and the formation of a 3×3 superstructure upon thermal annealing, Quinn and Jona [2] observed the formation of a $\frac{2}{3}\sqrt{3}\times\frac{2}{3}\sqrt{3}$—$R30^\circ$ and three-domain 3×1 superstructures. According to observations of Vandrê *et al.* [1], $\theta = 1/3$ is the lowest Mg coverage for which a good $\sqrt{3}\times\sqrt{3}$—$R30^\circ$ superstructure is observed. With increasing Mg coverage, but still below 1 ML, the $\sqrt{3}\times\sqrt{3}$—$R30^\circ$ LEED pattern gets progressively weaker, until it finally disappears completely above 1 ML. Upon thermal annealing (at 300 °C for 30 s) of the medium- and high-coverage interface the 3×3 LEED superstructure is observed. It should be noted that the $\sqrt{3}\times\sqrt{3}$—$R30^\circ$–Mg structure is already formed at RT, without the need of annealing at elevated temperatures.

Quinn and Jona [2] did not find the formation of a $\sqrt{3}\times\sqrt{3}$—$R30^\circ$ structure at any coverage. In accordance with their LEED observations, deposition at slow rates (about 0.1 Å/min) on RT substrates produces, in sequence with increasing coverage: first, fading of the 7×7 structure; then a mixture of 1×1 and a new structure identified as $\frac{2}{3}\sqrt{3}\times\frac{2}{3}\sqrt{3}$—$R30^\circ$; then this new structure alone; finally, obliteration of the LEED pattern altogether. The $\frac{2}{3}\sqrt{3}\times\frac{2}{3}\sqrt{3} - R30^\circ$ is not merely a *surface* superstructure because it was observed to exist (at coverages between 2 and 6 Å) even when the integral-order beams of the Si substrate were not visible. Figure 1 shows a sketch of the LEED pattern with both 1×1 spots (full circles) and spots due to the $\frac{2}{3}\sqrt{3}\times\frac{2}{3}\sqrt{3}$—$R30^\circ$ structure (empty circles). It should be noted, that the $\frac{2}{3}\sqrt{3}\times\frac{2}{3}\sqrt{3}$—$R30^\circ$ LEED pattern is never a good pattern: the background is high and the spots are broad, indicative of the presence of defects and limited long-range order.

Gentle annealing of Mg deposits of 2 to 4 Å at 300–400 °C up to 1 h progressively produces a 3×1 structure which is optimized at Mg coverage of about 0.75 Å. This 3×1 structure is always present with all three possible rotational domains [2].

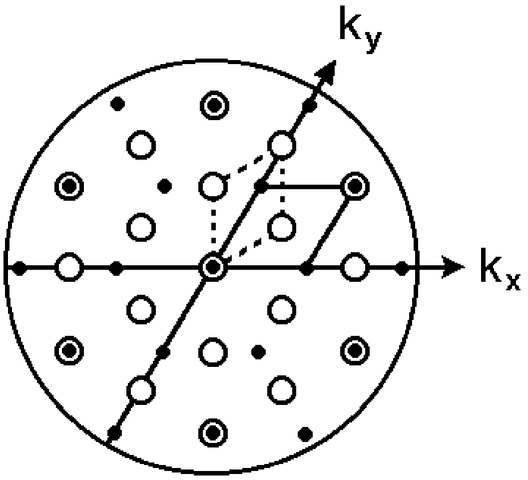

Fig 1. Schematic LEED pattern of coexisting 1 × 1 (small full circles) and $\frac{2}{3}\sqrt{3} \times \frac{2}{3}\sqrt{3}$—$R30\,^\circ$ (large empty circles) structures (from Ref. [2]). (*Reproduced by permission of Elsevier Science Publishers BV)*

1.2. STRUCTURE

According to the SEXAFS data of Vandrê *et al.* [1], Mg atoms, at low coverage, adsorb on four-fold sites above second-layer Si atoms (T_4) with bond distances to first- and second-layer Si atoms equal to 2.60 ± 0.04 Å and 2.47 ± 0.04 Å, respectively.

Quinn and Jona [2] speculated that the $\frac{2}{3}\sqrt{3} \times \frac{2}{3}\sqrt{3}$—$R30\,^\circ$ phase corresponds to the formation of a silicide of Mg, namely, $SiMg_2$ with plane (111) || Si(111) and with about 2% strain.

The atomic structure of the 3 × 1 phase is not known at the present time, but it was suggested by Quinn and Jona [2] to be related, if not equal, to the 3 × 1 structure produced by the adsorption of Li, Na and Ag on Si(111)7 × 7 [3].

REFERENCES

[1] D. Vandre, L. Incoccia and G. Kaindl, *Surf. Sci.* **225** (1990) 233.
[2] J. Quinn and F. Jona, *Surf. Sci.* **249** (1991) L307.
[3] W. C. Fan and A. Ignatiev, *Phys. Rev. B* **41** (1990) 3592.

(Mo)

MOLYBDENUM

1. (111) ORIENTATION

No ordered reconstructions except for 1 × 1 have hitherto been reported for the Mo/Si(111) system.

1.1. PHASE DIAGRAM

1.1.1. RT Growth

The initial stages of the Mo/Si(111) interface formation at RT were studied using different techniques, LEED [1], AES [1, 2], and PES [1–6].

The LEED observation of Balaska *et al.* [1] showed a rapid erasing of the original 7 × 7 structure: at 0.3 ML Mo coverage, only a strong diffuse background remains with traces of the 1 × 1 structure which disappear completely near $0.6 \div 0.7$ ML. The AES results of the same authors suggest that the growth of Mo film proceeds in a layer-by-layer fashion with the preservation of the abrupt Mo/Si(111) interface. The conclusion about the abrupt interface is consistent with PES results [1, 4] which reveal the appearance of the bulk Mo features in the spectra at low Mo coverages (3–5 ML).

In contrast, Rossi *et al.* [2,3] reported the intermixing at the Mo/Si(111) interface for both cleaved Si(111)2 × 1 and annealed Si(111)7 × 7 surfaces held at RT during Mo deposition. The results of the PES study of overgrowth of Mo on Si(111)2 × 1 by Abbati *et al.* [6] also supported the assumption about intermixing and suggested that an overgrowth takes place via the formation of islands having an electronic structure typical of silicides.

1.1.2. HT Growth

Balaska *et al.* [1] studied the evolution of the RT deposited Mo/Si(111) interface upon annealing at increasing temperature by LEED, AES and PES. It was found that the Mo/Si(111) interface with initial Mo coverage of 2–10 ML remains stable up to 300 °C. Above this temperature, the Mo–Si reaction occurs and gives $MoSi_2$ silicide at about 600 °C. The formation of $MoSi_2$ silicide at 700 °C is accompanied by the appearance of a weak 1 × 1 LEED structure which becomes more defined at 800 °C. The forming silicide layer remains stable up to about 900 °C.

2. (100) ORIENTATION

There is a lack of information in the literature concerning the formation of the ordered Si(100)–Mo surface phases.

2.1. PHASE DIAGRAM

2.1.1. RT Growth

Meyerheim *et al.* [7] studied the formation of the Mo/Si(100) interface as a function of the method of substrate surface preparation by means of AES and EXAFS. Two different procedures were used to prepare an atomically clean Si(100)2×1 surface: Ar ion sputtering followed by flash annealing at about 800 °C and chemical etching with similar flash annealing. Mo deposition was conducted on to the cleaned samples kept at RT.

AES measurements indicated the weak reactive character of the Mo/Si(100) interface independent of surface preparation. As a result, a metallic overlayer rapidly evolves in both cases. Within the error bars, the Auger measurements do not show that differences are dependent on the surface preparation, but the EXAFS results indicate that the formation of a Mo-metal short-range order in the growing metal-rich overlayer is retarded for the substrate cleaned by sputtering.

REFERENCES

[1] H. Balaska, R. C. Cinti, T. A. Nguyen Tan and J. Derrien, *Surf. Sci.* **168** (1986) 225.

[2] G. Rossi, I. Abbati, L. Braicovich, I. Lindau and W. E. Spicer, *J. Vac. Sci. Technol.* **21** (1982) 617.

[3] G. Rossi, I. Abbati, L. Braicovich, I. Lindau, W. E. Spicer, U. Del Pennino and S. Nannarone, *Physica B* **117–118** (1983) 795.

[4] T. A. Nguyen Tan, M. Azizan and J. Y. Veuillen, *Surf. Sci.* **251–252** (1991) 428.

[5] I. Abbati, L. Braicovich, B. De Michelis, A. Fasana, E. Puppin and A. Rizzi, *Solid State Commun.* **52** (1984) 731.

[6] I. Abbati, L. Braicovic, B. De Michelis, A. Fasana and A. Rizzi, *Surf. Sci.* **177** (1986) L901.

[7] H. L. Meyerheim, U. Dobler, A. Puschmann and K. Baberschke, *Phys. Rev. B* **41** (1990) 5871.

(N)

NITROGEN

1. (111) ORIENTATION

Nitrogen induces two reconstructions on the Si(111) surface. These are 8 × 8 and so-called "quadruplet" structures.

1.1. PHASE DIAGRAM

The N/Si(111) surface structures were examined by different surface-sensitive techniques, HREELS [1,2], EELFS [3], AES [1, 4–7], EELS [8], TD [4, 8], UPS [6], XPS [6, 9], and LEED [1–5, 7, 8].

The surface phases of nitrogen on silicon are formed by reactions of various gases with nitrogen components (such as NH_3 [5, 10, 11], NO [1, 6, 12], N_2^+ [7]. N [2–4, 7, 10]) with the hot ($\sim$ 850–1050 °C) Si(111) surface. According to AES data of Ref. [7], the stoichiometric nitride (Si_3N_4) is formed on the silicon surface as the result of such a process. Nitridation with N_2 does not seem practical due to the low reactivity of N_2 with silicon at $T < 1100\,^\circ\mathrm{C}$ [4, 9].

It was shown [4, 5, 8] that the crystal structure of the nitride layer depends on both the substrate temperature and the carbon contamination on the silicon surface with the 8 × 8 structure being associated with the Si(111) surface with low, if any, carbon contaminations and the so-called "quadruplet" structure forming at the carbon-contaminated surface. The 2D-phase diagram for the N/Si(111) system in "carbon concentration–temperature" coordinates is shown in Fig. 1.

Using TD [4, 8], it was determined that both surface phases desorb in the form of Si_2N. The threshold temperature for appreciable desorption depends on the surface coverage. If the silicon surface is partially covered by nitride (7 × 7 spots are seen on the LEED pattern), then desorption temperature is 1120 °C. For full coverage, the desorption temperature is 1180 °C.

1.2. STRUCTURE

1.2.1. Si(111)8 × 8–N

The sketch of the LEED pattern from the Si(111)8×8–N surface is shown in Fig. 2. The period of this structure in real space is 8/11 times the lattice period of the unreconstructed Si(111) surface. The unit vector of the reciprocal lattice of this structure is therefore 11/8 times that of the unreconstructed Si(111). As one can see from the sketch of the LEED pattern shown in Fig. 2, the distance between the extra reflections equals one-eleventh the reciprocal lattice

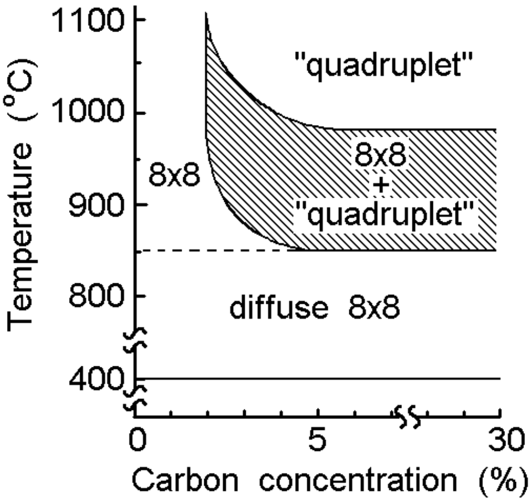

Fig 1. The phase diagram for the N/Si(111) system (from Ref. [19]). (*Reproduced by permission of Elsevier Science Publishers BV)*

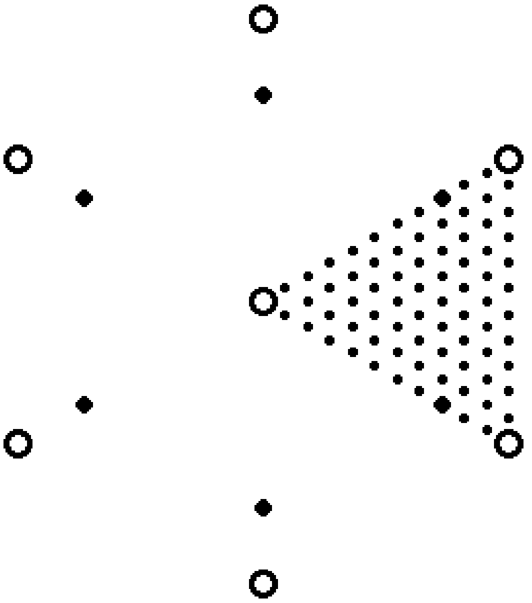

Fig 2. Illustration of the 8 × 8 LEED pattern. The diffraction beams represented are the specular (center open circle), first order Si(1 × 1) (closed circles), and first order nitride, e.g. (0, 11/8) spot (open circles). Some of the spots due to multiple diffraction are represented by points

period of the structure or one-eighth that of the unreconstructed Si(111)1 × 1. Therefore this structure is usually named as 8 × 8.

According to high resolution vibrational electron energy loss spectroscopy (HREELS) data [1,2], the triangular pyramidal Si_3N cluster is associated with the Si(111)8 × 8–N surface. The angle β between the Si–N bond and the symmetry axis of the cluster is estimated to be 63–68 ° and the corresponding bond length is 1.81–1.74 Å. The value of β is considered to indicate that the Si–N bond formation includes essentially the sp^3-hybridization of the atomic orbitals of both N and Si.

These results are inconsistent with the electron energy loss fine structure (EELFS) data of Ref. [3], where the values of the first nearest neighbor distance l_1, the second nearest neighbor distance l_2 and the ratio of coordination numbers for the 8 × 8 structure were determined to be $l_1 = 1.54 \pm 0.04$ Å, $l_2 = 2.7$ Å and $N_1/N_2 = 1.1$, respectively.

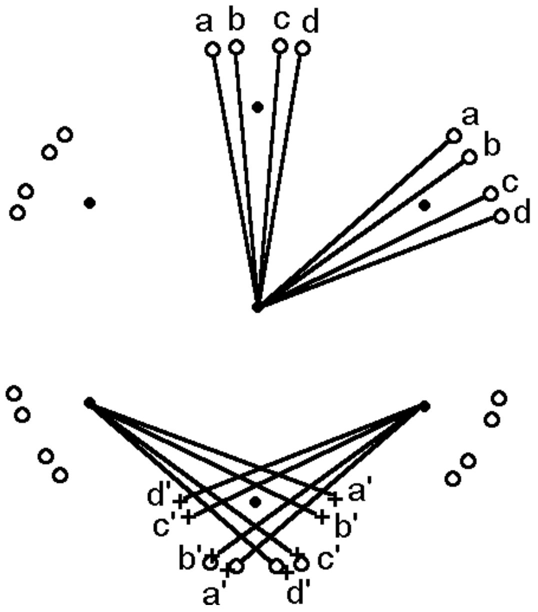

Fig 3. Illustration of the quadruplet LEED pattern. Diffraction beams represented are the specular (center closed circle); first order Si(1 × 1) (closed circles); first order nitride corresponding to domain a, b, c, d, rotated −10 °, −5 °, +5 °, +10 ° with respect to the Si substrate (open circles). Some of the spots due to double diffraction of the first order beams from the nitride and the Si substrate are represented by crosses (from Ref. [4]). (*Reproduced by permission of Elsevier Science Publishers BV)*

1.2.2. "Quadruplet" Structure

The sketch of the LEED pattern from the "quadruplet" structure is represented in Fig. 3. The interpretation of the "quadruplet" pattern implies that it results from domains having a triangular lattice whose lattice vectors are ∼ 3/4 times those of the unreconstructed Si(111) surface lattice. These domains are rotated $\pm\theta_1$ or $\pm\theta_2$ with respect to the silicon surface where $\theta_1 = 1/2\ \theta_2 \approx 5\,°$ [4]. From HREELS data [1, 13], it was suggested that the "quadruplet" structure has planar geometry, where each N atom is bonded to three Si atoms with the sp^2-like bonds. The Si–N bond length is estimated to be ∼ 1.66 Å. These data do not agree, however, with EELFS measurements of Ref. [3]. From the value of the Si–N bond length (1.7 Å) obtained by the latter method, it could be deduced, that, in the "quadruplet" structure, nitrogen atoms do locate at the centers of the threefold sites but are not co-planar with surface silicon atoms.

2. (100) ORIENTATION

The first stage of the nitride growth on the Si(100) surface was examined by AES [5, 14, 15], TD [15], EELS [14], XPS [16,17], HREELS [18], and LEED [5, 14–18]. Nitridation conditions are the same as for Si(111). No ordered patterns were observed by LEED. The electronic structure of the layer formed on the Si(100) is similar to that of the "quadruplet" phase on the Si(111) [14], but the film does not have any long-range order.

REFERENCES

[1] M. Nishijima, H. Kobayashi, K. Edamoto and M. Onchi, *Surf. Sci.* **137** (1984) 473.
[2] K. Edamoto, S. Tanaka, M. Onchi and M. Nishijima, *Surf. Sci.* **167** (1986) 285.
[3] H. -C. Wang, R. -F. Lin and X. Wang, *Surf. Sci.* **188** (1987) 199.

[4] A. G. Schrott and S. C. Jr. Fain, *Surf. Sci.* **111** (1981) 39.
[5] R. Heckingbottom and P. R. Wood, *Surf. Sci.* **36** (1973) 594.
[6] M. D. Wiggins, R. J. Spird and P. Wynblatt, *J. Vac. Sci. Technol.* **18** (1981) 965.
[7] J. F. Delord, A. G. Schrott and S. C. Fain, Jr. , *J. Vac. Sci. Technol.* **17** (1980) 517.
[8] A. G. Schrott and S. C. Fain, Jr. , *Surf. Sci.* **123** (1982) 204.
[9] C. F. Corallo and G. B. Hoflund, *J. Vac. Sci. Technol. A* **5** (1987) 713.
[10] C. Maillot, H. Roulet and G. Dufour, *J. Vac. Sci. Technol. B* **2** (1984) 316.
[11] M. Nishijima, K. Edamoto, Y. Kubota, H. Kobayashi and M. Onchi, *Surf. Sci.* **158** (1985) 422.
[12] Z. C. Ying and W. Ho, *Phys. Rev. Lett.* **60** (1988) 57
[13] A. H. Van Ommen, C. W. T. Bulle-Lieuwma and C. Langereis, *J. Appl. Phys.* **64** (1988) 2706.
[14] A. G. Schrott, Q. X. Su and S. C. Fain, Jr. , *Surf. Sci.* **123** (1982) 223.
[15] A. Glachant, D. Saidi and J. F. Delord, *Surf. Sci.* **168** (1986) 672.
[16] L. Kubler, J. L. Bischoff and D. Bolmont, *Phys. Rev. B* **38** (1988) 13113.
[17] J. L. Bischoff, L. Kubler and D. Bolmont, *Surf. Sci.* **209** (1989) 115.
[18] Y. Taguchi, M. Fujisawa, Y. Kuwahara, M. Onchi and M. Nishijima, *Surf. Sci.* **217** (1989) L413.
[19] E. A. Khramtsova, A. A. Saranin and V. G. Lifshits, *Surf. Sci.* **280** (1993) L259.

(Na)

SODIUM

1. (111) ORIENTATION

Na is known to induce three reconstructions on the Si(111) surface. These are $\delta(7\times 7)$, 3×1, and 1×1 structures.

1.1. PHASE DIAGRAM

1.1.1. Si(111)7×7 Surface

Initial stages of Na adsorption have been investigated by LEED [1–6], RHEED [7], AES [3,4], ARUPS [5] WF measurements [2, 5, 8], FI-STM [9,10] and theoretically [11–14].

When Na is deposited at the substrate temperature of about 150 K, LEED shows no detectable Na-induced patterns except for a uniform increase in the background intensity [1].

RT Na deposition on a Si(111)7×7 surface results in the appearance of the $\delta(7\times 7)$ pattern as was shown in the RHEED study by Daimon and Ino [7]. Further deposition leads to the 1×1 LEED pattern [4]. When Na is deposited on the Si(111)7×7 surface at about 500 °C, a three-domain 3×1 superstructure is observed [7]. Fan and Ignatiev [3] observed a 3×1 structure both at low $\theta\approx 0.2$ ML and higher $\theta > 0.3$ ML Na coverages, after annealing at about 800 °C for several minutes. The temperature range favoring the Na-induced 7×7–to–3×1 structural transformation was found to be $600 < T_{\mathrm{s}} < 780$ K [4].

STM observations of Jeon *et al.* [9,10] showed that at early stages of Na deposition, the 3×1 regions are on the lower terraces adjacent to the steps. The 7×7 region at this stage no longer shows atomic features but the 7×7 unit cells are clearly distinguished from the dimer walls separating the unit cells. As the deposition time increases, the 7×7 periodicity in the unconverted regions could be observed until the entire surface converts to the 3×1 structure.

For Na coverages greater than 1 ML the formation of 3D islands takes place according to the Stranski–Krastanov growth mode [8,10].

Sodium deposition on the cleaved Si(111)2×1 surface induces $2\times 1\rightarrow 1\times 1$ surface structural transition at about 1/2 ML coverage [5,6]. This is in contrast to K which leaves the 2×1 surface intact, and Cs which transforms it into a $\sqrt{3}\times\sqrt{3}$ overlayer structure [6].

1.2. STRUCTURE

For the adsorption of all alkali metals (Li, Na, K, Rb, and Cs) similar RHEED patterns ($\delta(7\times 7)$ and 3×1) are observed, although the changing rates differ a little among them [7].

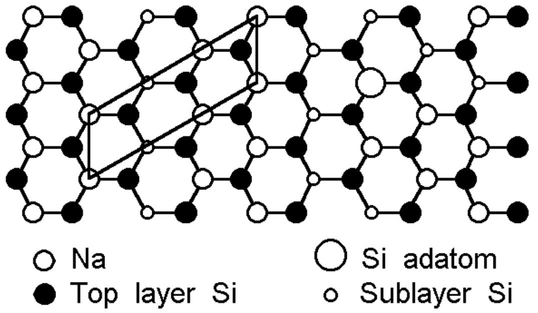

Fig 1. A schematic top view of the Si(111)3 × 1–Na surface (from Ref. [10] (*Reproduced by permission of the publishers of Journal of Physical Review Letters)*

1.2.1. Si(111)δ(7 × 7)–Na

There is no detailed information about the structure of the Si(111)δ(7 × 7)–Na phase. But it certainly seems convincing to adopt the Si(111)δ(7 × 7)–lithium and hydrogen structure models for the structure of Si(111)δ(7 × 7)–Na. This structure model has been already considered in Chapter H, section* 1.2 and Chapter Li, section* 1.2.

1.2.2. Si(111)3 × 1–Na

In accordance with STM observations of Jeon *et al.* [9,10], each 3 × 1 unit cell contains two Na atoms so that the saturation coverage is two thirds. This result is inconsistent with the saturation coverage deduced from the RHEED data of Daimon and Ino [7] on the alkali-metal induced 3 × 1 structures on the Si(111) surface. By extrapolating the Na region into the Si region in the same STM image of the annealed surface Jeon *et al.* [10], determined that Na atoms adsorb on top of the second-layer Si atoms (T_4 site). The schematic of the 3 × 1 surface is displayed in Fig. 1.

¿From the other point of view [3], Na does not participate in the 3 × 1 long-order structure and serves only to induce the Si(111) surface reconstruction. (See the detailed description in Chapter Li, section* 1.2.)

1.3. PROPERTIES

1.3.1. Electronic Properties

In accordance with EELS data of Avci [1], the reaction of Na atoms with the Si(111)7 × 7 surface at 150 K shows two distinct stages. At the initial coverages (≤ 0.3 ML), the Na atoms transfer their *s* electrons to the Si surface and remain as screened positive centers. For higher coverages (0.3–1 ML) the formation of a metallic layer takes place. The bond between Na and the Si when 1 ML of Na adsorbs on Si(111) is calculated to be mainly covalent [11].

The work function change versus Na doses is shown in Fig. 2 [8]. The work function has a minimum at $\Delta\Phi = -2.3$ eV and saturates at $\Delta\Phi = -2.2$ eV. A theoretical estimation of the work function for the equilibrium Si(111)1 × 1–Na geometry yields $\Phi = 2.1$ eV [12].

1.3.2. Desorption

SI experiments of Green *et al.* [15] showed that the desorption of Na from the Si(111) surface below 1000 K has both a first- and second-order component with activation energies for desorption of $E_{a1} = 3.47 \pm 0.15$ eV and $E_{a2} = 2.39 \pm 0.13$ eV, respectively. Above 1100 K, the desorption of Na from this surface is predominantly first order with $E_{a1} = 2.45 \pm 0.12$ eV.

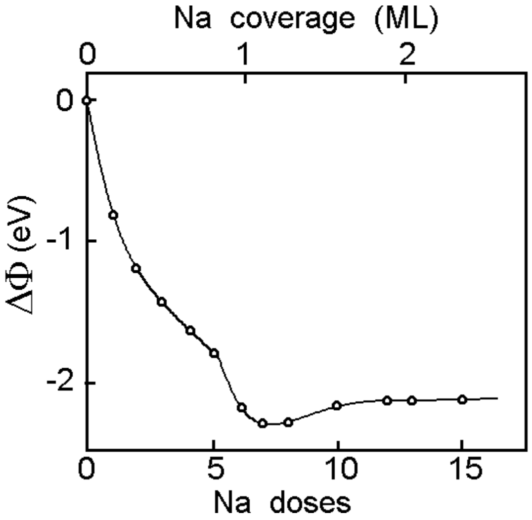

Fig 2. $\Delta\Phi$ as a function of the Na doses (from Ref. [8]). (*Reproduced by permission of Elsevier Science Publishers BV)*

1.3.3. Oxidation

Na overlayers (1–2 ML) on the Si(111) surface give rise to oxidation-promotion effects upon exposure to atomic or molecular oxidizing species [16]. It was found that the drastic increase of the initial oxygen adsorption rate, observed for sodium coverages in the submonolayer coverage range is not accompanied by parallel enhancement of the oxidation rate [8]. Na-promoted oxidation of Si(111) occurs only for Na coverages greater than 0.5 ML.

2. (100) ORIENTATION

Na is known to induce several reconstructions on the Si(100) surface. These are 4 × 1, 2 × 1, 2 × 3 structures and an incommensurate one.

2.1. PHASE DIAGRAM

2.1.1. Si(100)2 × 1 Surface

Initial stages of Na adlayer formation on the Si(100)2 × 1 surface have been investigated by LEED [17–22], AES, and WF measurements [18–22], EELS [19, 21], UPS [23, 24], PEXAFS [25, 26], ARUPS [27], TD [19, 21], STM [25], and theoretically [28–34].

Glander and Webb [18, 22] studied the adsorption of Na on Si(100) using two types of experiments what they called "dosing" and "equilibrium" experiments. In the dosing experiments, observations were made as a function of time after turning on a Na atomic beam directed at the crystal which is held at a fixed temperature below about 200 °C. In the "equilibrium" experiments observations were made for fixed Na fluxes while the temperature of the crystal was changed slowly enough so that the adsorbate remained in steady state.

In the dosing experiments, the intensity of the Si LVV Auger line decreases linearly with time, then abruptly becomes constant (Fig. 3(a)). The coverage calibration was based on the assumption that, at the time of the maximum intensity of the quarter-order LEED spots from a well ordered 4 × 1 structure (Figs 3(a) and 3(b)) the coverage is $\theta = 1/4$ ML.

The investigation of Na adsorption on the Si(100) surface as a function of exposure at fixed temperature shows that, for $T < 200°$, a well-ordered 4 × 1 structure develops at a coverage, $\theta = 1/4$ ML. A well-ordered 2 × 1 structure is recovered at $\theta = 1/2$ ML. The

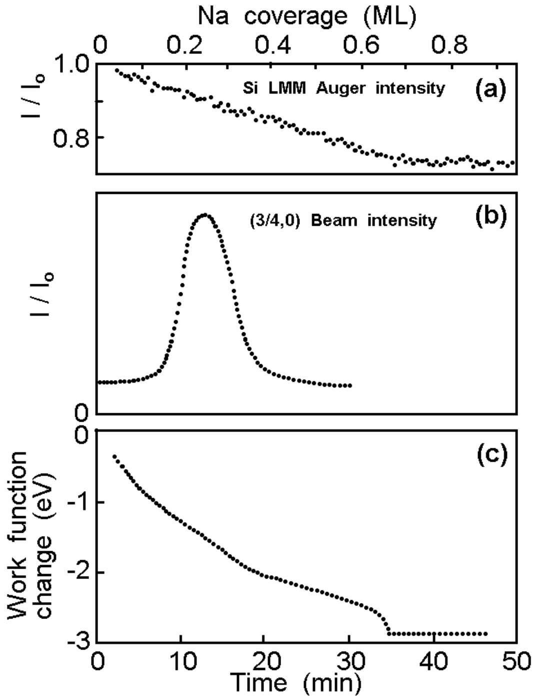

Fig 3. A comparison of dosing experiments performed at $T = 165\,°\mathrm{C}$ and $P_{\mathrm{Na}} = 6.2 \times 10^{-10}$ Torr. (a) Intensity of the Si LVV Auger line; (b) intensity of the (3/4, 0) LEED beam; (c) change in work function (from Ref. [18]). (*Reproduced by permission of Elsevier Science Publishers BV)*

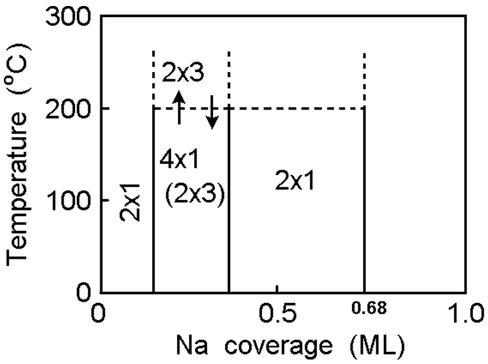

Fig 4. Schematic phase diagram of the Na/Si(100) system according to dosing results of Ref. [18] (see text)

2×1 LEED pattern remains as the coverage increases from $\theta = 1/2$ ML to saturation at $\theta = 0.68$ ML. All of the dosing experiments for crystal temperatures $60 < T < 170\,°\mathrm{C}$ produced the same saturation coverage of $\theta = 0.68 \pm 0.05$. At sufficiently high Na pressures and low temperatures, islands of bulk Na form on the surface in a Stranski–Krastanov growth mode. Structural changes of the Na/Si(100) system are shown schematically in Fig. 4.

The 4×1 structure is metastable. When it is isolated from the Na flux and heated above $200\,°\mathrm{C}$ it transforms to a 2×3 structure. When cooled below $200\,°\mathrm{C}$, the 2×3 remains [18]. In a similar experimental condition the 2×3 structure was observed at $\theta \approx 1/6$ ML [19].

Equilibrium experiments for $4 \times 10^{-10} < P_{\mathrm{eff}} < 10^{-8}$ showed a series of structural transformations (Fig. 5) from 2×1 at high T and small θ, to 2×3 near $\theta = 1/3$ ML, to an incommensurate structure where one-third order reflections diminish in intensity and merge smoothly towards half-order positions culminating in a 2×1 structure at $\theta = 1/2$ ML [17,22]. Above $700\,°\mathrm{C}$, the coverage was zero for the highest effective Na pressures used, while below

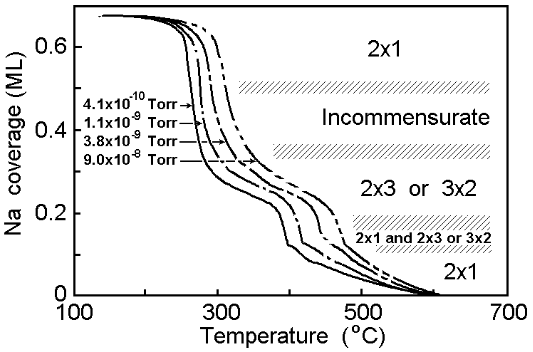

Fig 5. Isobars showing the Na coverage as a function of temperature from equilibrium experiments done at four different pressures. The various coverage ranges are labeled with the structures that are observed with LEED (from Ref. [22]). (*Reproduced by permission of Elsevier Science Publishers BV)*

50 °C bulk Na could be grown on the surface in islands.

2.2. STRUCTURE

2.2.1. Si(100)4 × 1–Na

In dosing experiments performed at a crystal temperature below 200 °C, the appearance and later disappearance of quarter-order diffraction beams are observed as the coverage increased [18] (Fig. 3(b)). Only the quarter-order reflections along the lines connecting integral order reflections are observed, indicating two orientational 4 × 1 domains. A detailed view of the diffraction at a specific coverage by taking LEED angular profiles shows that for $\theta < 1/4$ ML, the quarter-order spots are elongated in one direction, and for $\theta > 1/4$ ML, they are elongated in the perpendicular direction. At $\theta = 1/4$ ML, the diffraction beams are all around.

The simplest model consistent with the diffraction has Na filling alternate rows of Si dimers to produce the 4 × 1 structure at $\theta = 1/4$ ML. The elongation of the quarter-order reflections for $\theta < 1/4$ ML indicates disorder primarily along the rows of dimers while maintaining good order in the perpendicular direction. The elongation of the quarter-order reflections for $1/4 \text{ ML} < \theta < 1/2$ ML indicates that the Na is disordered primarily in the direction perpendicular to the dimer rows, i.e. some of the intervening rows have become filled with Na.

2.2.2. Si(100)2 × 1–Na

Following an early suggestion of Levine [35], it is generally assumed that the alkali-atoms adsorb at the sixfold hollow site between two dimers so that a one-dimensional alkali-metal chain is formed along the [110] direction at a coverage of 0.5 ML (see Fig. 6 in Chapter Li). This model was adopted for the Si(100)2 × 1–Na structure [18, 20]. Wei *et al.* [20] carried out a fully dynamical LEED intensity spectra analysis of the Si(100)2 × 1–Na system. They found, that the vertical distance of the Na atoms above the substrate is 1.85 Å, which gives a nearest-neighbor Na–Si bond length of 2.97 Å. Kim *et al.* [26] and Soukiassian *et al.* [25] using PEXAFS found that the Na–Si bond length is the same for both low (0.4 monolayer) and 1-monolayer coverages at 2.80 ± 0.01 Å, close to the sum of covalent radii, supporting the model of covalent bonding between Na and Si, even below 0.5 monolayer. Furthermore, Na does not significantly modify the structure of the Si(100)2 × 1 surface.

¿From the total energy calculations [28, 30, 32, 36] of Na/Si(100)2 × 1 it was concluded that at $\theta = 0.5$ ML, the quasi-hexagonal site proposed by Levine [35] is favorable if the lattice

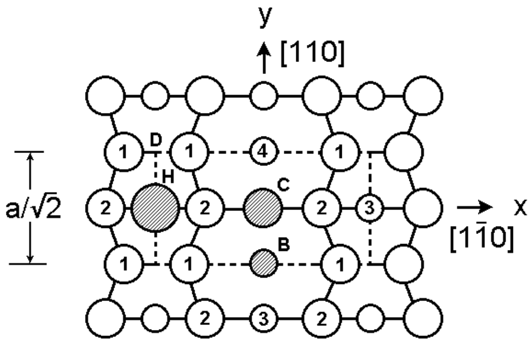

Fig 6. Top view describing the positions of adsorbed sodium atoms on the Si(100)2 × 1 surface. Shaded and empty circles denote Na and Si atoms, respectively. Numerals in the circles indicate Si atomic layer. H, sixfold hollow site; B, long bridge site (from Ref. [28]). (*Reproduced by permission of the publishers of Journal of Physical Review B)*

is allowed to relax. The long bridge site along the dimerization direction was found to be somewhat less stable (Fig. 6).

2.2.3. Si(100)2 × 3–Na

Holtom and Gundry [37] observed the 2×3 structure for Cs and suggested the corresponding structure to be $\theta = 1/3$ ML. The 2×3 structure was considered to be due to a Cs atom at every fourth H site (see Fig. 6). At $\theta = 2/3$ ML they placed an additional atom at an adjacent dimer site D next to an H site. Batra [28] performed pseudopotential calculations with a rigid Si structure and suggested another model for a 2×3 structure involving different adsorption sites and, in fact, a different coverage range as compared to that of Holtom and Gundry [37]. Glander and Webb [22] argued that none of the above mixed-site models can account for their observations of the third-order structure to Na/Si(100). In particular, a drastic decrease of the intensity of the half-order beams led to a proposal of major reconstruction of the Si substrate for the third-order structure. This reconstruction consists of removing every third surface Si atom and allowing the second-layer atoms beneath them to dimerize. In addition to reducing the intensity of half-order spots, this reconstruction model has the virtue that it continuously goes to the 2×1 structure at 1/2 ML by only filling the H sites. However, mass transport is needed for this model and some further work is required to firmly establish it [28].

2.3. PROPERTIES

2.3.1. Electronic Properties

The work function change versus coverage is shown in Fig. 3(c) from Ref. [18]. The slope is initially large and negative, but it becomes less negative as the coverage increases to 1/4 ML. At $\theta = 1/4$ ML, there is an inflection point, and the process repeats itself for 1/4 ML $< \theta <$ 1/2 ML. At $\theta = 1/2$ ML, $\Delta\Phi = -2.24$ eV. For $\theta > 1/2$ ML, the slope becomes more negative culminating in a sharp drop to the minimum in the work function $\Delta\Phi_{\text{sat}} = -2.9$ eV (The close value of $\Delta\Phi_{\text{sat}} = -2.95$ eV was obtained in Ref. [19].)

Careful analysis of the change in work function shows that for 0 ML $< \theta <$ 1/2 ML the bonding between the Na and the substrate does not change, and there is no change in the structure of the Si [18]. Core-level and valence band photoemission spectroscopy using synchrotron radiation [24] provides evidence that Na/Si bonding is covalent. This covalent bond is weak and polarized while plasmon at the alkali-metal core level indicates adsorbate rather than substrate metallization.

2.3.2. Oxidation

At RT, the presence of Na overlayers on the Si(100) surface enhances dramatically the oxidation rate of silicon [19, 38]. A similar result is observed for nitridation using molecular nitrogen [39–41]. This behavior takes place only for multilayer Na structures, no Na-promoted oxidation on Si(100) occurs with Na in the first layer [19].

REFERENCES

[1] R. Avci, *J. Vac. Sci. Technol. A* **4** (1986) 1400.
[2] R. E. Weber and W. T. Peria, *Surf. Sci.* **14** (1969) 13.
[3] W. C. Fan and A. Ignatiev, *Phys. Rev. B* **41** (1990) 3592.
[4] M. Tikhov, L. Surnev and M. Kishinova, *Phys. Rev. B* **44** (1991) 3222.
[5] B. Reihl, S. L. Sorensen, R. Dudde and K. O. Magnusson, *Phys. Rev. B* **46** (1992) 1838.
[6] B. Reihl, S. L. Sorencen, R. Dudde and K. O. Magnusson, *Surf. Sci.* **269–270** (1992) 1005.
[7] H. Daimon and S. Ino, *Surf. Sci.* **164** (1985) 320.
[8] G. Boishin, M. Tikhov and L. Surnev, *Surf. Sci.* **257** (1991) 190.
[9] D. -R. Jeon, T. Hashizume, X. Wang, C. Bai, K. Motai and T. Sakurai, *Japan J. Appl. Phys.* **31** (1992) L501.
[10] D. Jeon, T. Hashizume and T. Sakurai, *Phys. Rev. Lett.* **69** (1992) 1419.
[11] S. Ossicini, C. Arcangeli and O. Bisi, *Phys. Rev. B* **42** (1990) 7671.
[12] J. E. Northrup, *J. Vac. Sci. Technol. A* **4** (1986) 1404.
[13] I. Moullet, W. Andreoni and M. Parrinello, *Phys. Rev. B* **46** (1992) 1842.
[14] I. Moullet, W. Andreoni and M. Parrinello, *Surf. Sci.* **269–270** (1992) 1000.
[15] E. F. Greene, J. T. Keeley and M. A. Pickering, *Surf. Sci.* **120** (1982) 103.
[16] A. Franciosi, P. Soukiassian, P. Philip, S. Chang, A. Wall, A. Raisanen and N. Troullier, *Phys. Rev. B* **35** (1987) 910.
[17] G. S. Glander, M. B. Webb, *Bull. Am. Phys. Soc.* **33** (1988) 570.
[18] G. S. Glander and M. B. Webb, *Surf. Sci.* **222** (1989) 64.
[19] M. Tikhov, G. Rangelov and L. Surnev, *Surf. Sci.* **231** (1990) 280.
[20] C. M. Wei, H. Huang, S. Y. Tong, G. S. Glander and M. B. Webb, *Phys. Rev. B* **42** (1990) 11284.
[21] M. Tikhov, G. Boishin and L. Surnev, *Surf. Sci.* **241** (1991) 103.
[22] G. S. Glander and M. B. Webb, *Surf. Sci.* **224** (1989) 60.
[23] A. Hamawi and L. Walden, *Solid State Commun.* **79** (1991) 101.
[24] P. Soukiassian, M. H. Bakshi, Z. Hurych and T. M. Gentle, *Surf. Sci.* **221** (1989) L759.
[25] P. Soukiassian, S. T. Kim, Z. Hurych and J. A. Kubby, *Appl. Surf. Sci.* **56–58** (1992) 394.
[26] S. T. Kim, S. Kapoor and Z. Hurych, *Phys. Rev. B* **44** (1991) 5622.
[27] Y. Enta, S. Suzuki and S. Kono, *Surf. Sci.* **242** (1991) 277.
[28] I. P. Batra, *Phys. Rev. B* **39** (1989) 3919.
[29] H. Tochihara and Y. Murata, *Surf. Sci.* **215** (1989) L323.
[30] I. P. Batra, *J. Vac. Sci. Technol. A* **8** (1990) 3425.
[31] H. Ishida, *Surf. Sci.* **242** (1991) 341.
[32] I. P. Batra, *Phys. Rev. B* **43** (1991) 12322.
[33] K. Kobayashi, S. Blugel, H. Ishida and K. Terakura, *Surf. Sci.* **242** (1991) 349.
[34] Y. Ling and X. Xide, *Surf. Sci.* **247** (1991) L204.
[35] J. D. Levine, *Surf. Sci.* **34** (1973) 90.
[36] I. P. Batra, *Surf. Sci.* **242** (1991) 354.
[37] R. Holtom and P. M. Gundry, *Surf. Sci.* **63** (1977) 263.

[38] P. Soukiassian, T. M. Gentle, M. H. Bakshi and Z. Hurych, *J. Appl. Phys.* **60** (1986) 4339.
[39] P. Soukissian, M. H. Bakshi, Z. Hurych and T. M. Gentle, *Phys. Rev. B* **35** (1987) 4176.
[40] P. Soukiassian, T. M. Gentle, K. P. Schuette, M. H. Bakshi and Z. Hurych, *Appl. Phys. Lett.* **51** (1987) 346.
[41] P. Soukiassian, H. I. Starnberg and T. Kendelewicz, *Appl. Surf. Sci.* **41–42** (1989) 395.

(Nb)

NIOBIUM

1. (111) ORIENTATION

No ordered Nb-induced reconstructions were detected on the Si(111) surface.

1.1. PHASE DIAGRAM

The formation of the Nb/Si(111) interface was studied by Mahamuni *et al.* [1] by means of LEED and AES. LEED observations showed that, during RT deposition of Nb on the Si(111)7 × 7 surface, the 7 × 7 LEED pattern features vanish before completion of half a monolayer and subsequent Nb growth does not result in the appearance of any additional LEED spots.

The AES data of Ref. [1] revealed that the growth mode of Nb on Si(111) is layer-by-layer at RT, while at 300 °C Nb grows non-uniformly. It was found that there is no substantial intermixing below 600 °C while the formation of silicide ($NbSi_2$) takes place at about 750 °C.

In contrast to the RT results of Mahamuni *et al.* [1] Azizan *et al.* [2] reported reactive intermixing at the Nb/Si(111) interface earlier at RT. Mahamuni *et al.* [1] suggested that this difference might result from the difference in cleaning procedures used in these works: in Ref. [1], the sample was cleaned by thermal annealing only, while, in Ref. [2], sputtering/annealing cycles were employed for cleaning the sample.

REFERENCES

[1] S. R. Mahamuni, D. T. Abbel and E. D. Williams, *Solid State Commun.* **68** (1988) 145.
[2] M. Azizan, T. A. Nguyen Tan, R. C. Cinti, G. Chauvet and R. Baptist, *Solid State Commun.* **54** (1985) 895.

(Ni)

NICKEL

1. (111) ORIENTATION

Three types of reconstructions were reproductively obtained, 7×7, 1×1, and $\sqrt{19}\times\sqrt{19}$, after various heat treatments of Si(111) with small amounts of Ni present. In a few publications, observation of the $\sqrt{3}\times\sqrt{3}$ structure was reported.

1.1. PHASE DIAGRAM

1.1.1. RT Deposition

The results of LEED observations [1–4] of RT growth of Ni on a Si(111)7×7 surface can be summarized as follows: after deposition of the Ni layer with thickness below 0.5 Å, the LEED pattern shows the same 7×7 symmetry as the clean Si surface, but with increasing background and extinguishing several seventh-order spots (the so-called $\alpha(7\times7)$ structure [2,3] detected for a number of metals on Si(111)). At 0.5 Å coverage, the LEED pattern has no seventh-order spots and only half of the integral-order spots remain. At 2.0 Å coverage, only widely scattered LEED spots are distinguishable from the background and, at 3.0 Å coverage, the LEED pattern disappears completely [1,4].

Based on the surface structure and composition measurements the following mode was proposed by Porter *et al.* [1,5] for the growth of thin Ni films at RT: at low coverages, arriving Ni atoms diffuse below the top Si layer. (SEXAFS measurements by Comin *et al.* [6,7] indicate that Ni atoms chemisorb in sixfold hollow sites, weakening Si–Si bonds between the first and second Si layers.) The Si surface atoms expand outward and form a $NiSi_2$-like structure with orientation rotated 180° around the [111] direction (type B). The assumed resulting configuration of 1 ML coverage would correspond to a (111) layer of $NiSi_2$ with the bonds along the [111] direction missing. Since both LEED [1,4] and RBS [8] experiments show disruption of the long-range order, a more realistic picture of the formed layer involves both small displacements of Si surface atoms within non-periodic silicide domains and occasional saturation of the outermost Ni bonds.

At higher coverages, silicide islands enriched with surface Si are formed that grow laterally. At about 12 Å coverage the islands coalesce and then grow in thickness until 30 Å of Ni has been deposited, at which point pure Ni overlayer forms [1,5].

1.1.2. HT Growth (Quenching)

The behavior of Ni layers on Si(111) at high temperatures is rather complicated since the coverage of Ni impurity varies greatly with heat treatments and depends on annealing time,

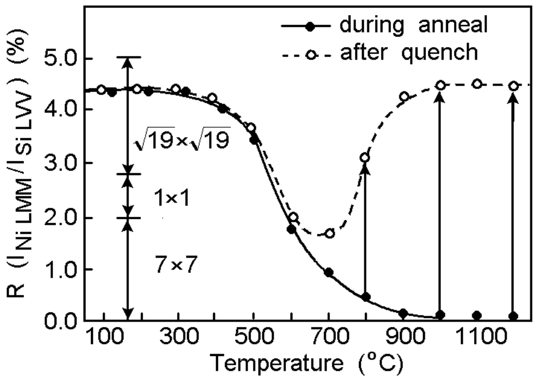

Fig 1. Variations of the Auger electron peak ratio, $R = I_{\mathrm{Ni}_{\mathrm{LMM}}}/I_{\mathrm{Si}_{\mathrm{LVV}}}$, for the Si(111)–Ni sample with annealing temperature (solid curve) and after radiation quenching from various temperatures indicated on the abscissa to room temperature (broken curve). The surface superstructures are closely correlated with R and controlled by the heat treatments (from Ref. [11]). (*Reproduced by permission of Elsevier Science Publishers BV)*

annealing temperature and cooling rate. The variation of Ni coverage with quenching has been attributed to the surface segregation of Ni and the appearance conditions of different Si(111)–Ni surface phases have been only recently systematically understood by Dolbak *et al.* [9, 10] and Ichinokawa *et al.* [11].

It was found that Ni impurity diffuses from the surface into the bulk rapidly at temperatures above 500 °C. Figure 1 shows the variation of the Ni amount on the surface (expressed in Auger electron peak ratio, $R = I_{\mathrm{Ni}_{\mathrm{LMM}}}/I_{\mathrm{Si}_{\mathrm{LVV}}}$) as a function of annealing temperature (solid curve). In addition, the variation of surface Ni coverage versus radiation quenching is shown by a broken curve in Fig. 1. In the case of radiation quenching from a temperature above 900 °C, the surface Ni concentration recovers the initial value seen before the heat treatment. However, quenching from a temperature between 600 °C and 800 °C does not result in complete recovery of the initial value and lower Ni coverage is formed [11].

Simultaneous LEED observations show that $\sqrt{19} \times \sqrt{19}$ structure appears for R between 2.8% and 6%, a 1×1 pattern is observed between 2.0% and 2.8% and a sharp 7×7 pattern at less than 2.0%, as shown in Fig. 1. The LEED patterns were found to correlate closely with the surface Ni coverage and to depend on the relevant heat treatments [9–11].

SEM observations [9] revealed that the quenched surface which displays the $\sqrt{19} \times \sqrt{19}$ LEED pattern contains $\mathrm{NiSi_2}$ islands (about 1 μm in size) with a density of about 5×10^6 cm^{-2}, while the 7×7 structure develops between large $\mathrm{NiSi_2}$ islands (a few ten μm in size) whose density is lower by two orders than that of small islands.

It was also found that surface concentration is not only a function of quenching temperature, but also of cooling rate. The dependence of the surface Ni concentration (and appearance conditions of surface superstructures) versus the cooling rate is shown in Fig. 2.

The origin of the Ni segregation by quenching was quantitatively analyzed in Ref. [11] by means of the temperature gradient along the normal to the surface. As a result the average segregation velocity V at temperature T was determined in the form:

$$V = \frac{D(T)}{kT^2}\frac{\underset{\cdot}{\mathrm{T}}}{\underset{\cdot}{\mathrm{x}}},$$

where $D(T)$ is the diffusion coefficient of Ni in bulk Si. One can see that this formulae explains the main features of Figs 1 and 2, but not the SEM observations of Ref. [9]. So the more realistic model should also consider the formation of $\mathrm{NiSi_2}$ islands.

While the formation of the 1×1 and $\sqrt{19} \times \sqrt{19}$ structures in the "annealing-quenching"

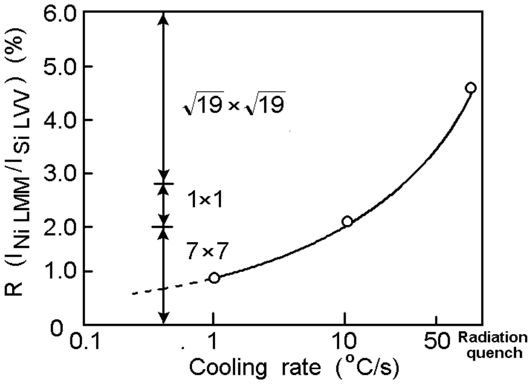

Fig 2. Auger electron peak ratio R *versus* cooling rate from 1000 °C to 500 °C (from Ref. [11]). (*Reproduced by permission of Elsevier Science Publishers BV)*

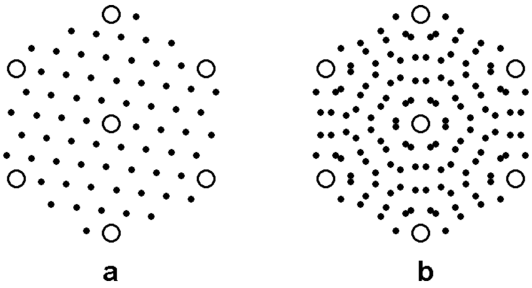

Fig 3. Schematic drawing of the LEED pattern (reciprocal lattice) from single-domain (a) and two-domain (b) Si(111)$\sqrt{19} \times \sqrt{19}$ Ni structure

processes was reproducibly observed in a great many works [9–19], the Ni-induced $\sqrt{3} \times \sqrt{3}$—$R30°$ reconstruction was detected in a few works [2, 10, 18] only: Yang *et al.* [2] reported that annealing of 2 to 4 ML (1 ML Ni = 0.86 Å) of RT deposited Ni at 350–450 °C produces a sharp $\sqrt{3} \times \sqrt{3}$ structure with Ni coverage of $0.3 \div 0.7$ ML; Clabes [18] observed the $\sqrt{3} \times \sqrt{3}$ structure after annealing of $\theta \leq 3$ ML Ni at temperatures as low as 200 °C; Teys *et al.* [10] sometimes detected the formation of the $\sqrt{3} \times \sqrt{3}$ structure upon annealing at 600–800 °C.

1.2. STRUCTURE

1.2.1. Si(111)$\sqrt{19} \times \sqrt{19}$—$R \pm 23.4°$–Ni

The $\sqrt{19} \times \sqrt{19}$ structure is produced by high-temperature annealing and fast cooling of Ni-covered Si(111). It occurs in two domains, except for the case of the stepped Si(111) surfaces where single-domain $\sqrt{19} \times \sqrt{19}$ structure can be obtained [16]. Figure 3(a,b) shows the sketches of the LEED patterns (reciprocal lattices) from both two-domain and single-domain $\sqrt{19} \times \sqrt{19}$ structures.

There is no consensus about the Ni coverage in the $\sqrt{19} \times \sqrt{19}$–Ni surface phase. For instance, Van Bommel and Meyer [13] estimated that the Ni coverage is one Ni atom per 10^7 surface atoms, whereas other different values have been reported recently: 0.08 ± 0.03 ML (Hansson *et al.* [20]), 0.2 ML (Wilson and Chiang [17]), 6 at.% (Dolbak *et al.* [9]), $0.04 \div 0.06$ ML (Charig and Skinner [12]), $0.1 \div 0.6$ ML (Chabal *et al.* [14]), 0.08 ML (Ichinokawa *et al.* [11]). The main reason for the such variations is that quantitative analysis of Ni coverage only by Auger electron spectroscopy (usually used for this purpose) is very difficult, because the depth distribution of Ni atoms near the surface is unknown.

In our opinion, the most accurate quantification of Ni coverage in the $\sqrt{19} \times \sqrt{19}$ phase was carried out by Ichinokawa *et al.* [11] who received the value of three Ni atoms per $\sqrt{19} \times \sqrt{19}$

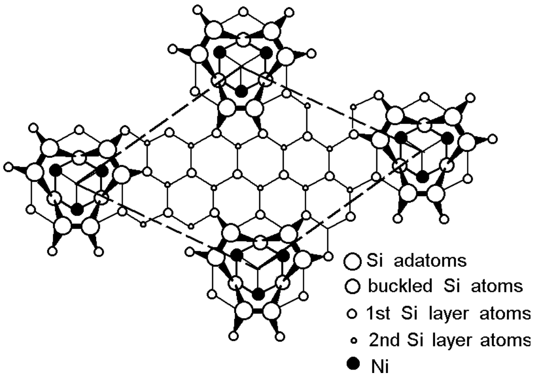

Fig 4. Structural model of a $\sqrt{19} \times \sqrt{19}$ structure containing three Ni atoms per unit cell. Each of the six adatoms is connected with one bond associated with the three buckled Si atoms and one dangling bond of each of the surrounding six first-layer Si atoms with 3 Å corrugation measured from the topmost double monolayer. Two of the six adatoms form a dimer to each other and the adatoms have threefold symmetry at the corners as observed by STM by Wilson and Chiang [17] (from Ref. [11]). (*Reproduced by permission of Elsevier Science Publishers BV)*

unit cell. They also constructed a most reasonable model with the structure shown in Fig. 4 which satisfies the following conditions:

(a) The unit cell of the $\sqrt{19} \times \sqrt{19}$ phase consists of three Ni atoms in the topmost double layer.

(b) The STM image with threefold symmetry composed of six adatoms with 3 Å corrugation at the corners of the unit cell [17] is explained by the model.

(c) The Ni coordination number and the bonding state to Si adatoms are similar to those of the interface structure between the $NiSi_2$ silicide and the Si substrate [6].

1.2.2. Si(111)1 × 1–Ni

The 1×1 structure is formed conventionally by annealing at high temperatures above 900 °C and non-rapid cooling. This structure has a lower Ni concentration compared to that of the $\sqrt{19} \times \sqrt{19}$ phase.

Yang *et al.* [19] found that LEED I–V spectra for the reflections of 1×1–Ni structure are almost identical to the corresponding spectra of the quenched 1×1 phase which is obtained by quenching to room temperature the high-temperature 1×1 phase of the clean Si(111) surface. They assumed that this phase is close to being bulk-like and is associated with strain or disorder. It was assumed further that Ni atoms lie in the interstitial sites of the Si lattice.

In Ref. [14], the 1×1 phase was characterized by AES, LEED, UPS and ion scattering techniques and it was concluded that the 1×1 structure results from a mostly disordered surface made up of small domains of $\sqrt{19} \times \sqrt{19}$ symmetry dispersed in an otherwise 7×7 surface.

It should be said that epitaxial $NiSi_2(111)$ also produce a 1×1 LEED pattern which differs from the quenched low-coverage 1×1 phase by the different LEED I–V spectra only [19].

1.2.3. Si(111)$\sqrt{3} \times \sqrt{3}$—*R*30°–Ni

The $\sqrt{3} \times \sqrt{3}$ structure is observed sometimes, presumably upon low-temperature (200–450 °C) heating of thin Ni layers. Clabes [18] concluded from LEED observations that the

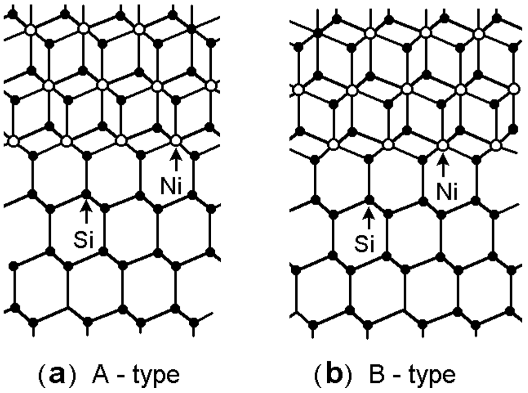

(a) A - type **(b)** B - type

Fig 5. Ball-and-stick models of epitaxial $NiSi_2$/Si interfaces: (a) type A (111) interface, (b) type B (111) interface (from Ref. [22]). (*Reproduced by permission of American Institute of Physics)*

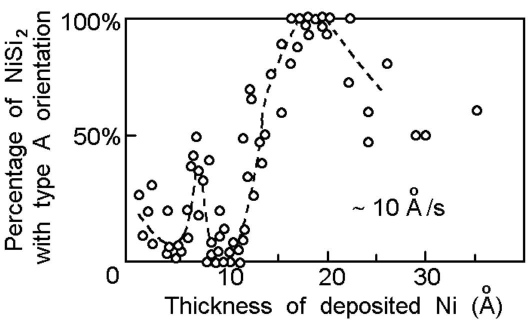

Fig 6. Orientation of thin $NiSi_2$ layers grown on Si(111) by deposition of nickel at room temperature and annealed to ~ 450 °C for 1 min. Nickel depositions are maintained at 0.7–1.5 Å/s (from Ref. [22]). (*Reproduced by permission of American Institute of Physics)*

$\sqrt{3} \times \sqrt{3}$ structure is not just a surface reconstruction phenomenon, but belongs to a distinct epitaxial overlayer. Comparing the lattice parameters of the different nickel silicides with the spacing of the Si(111) surface he found a close match of the $Ni_2Si(001)$ plane with a Si(111)$\sqrt{3} \times 1$ unit cell. The Ni_2Si has the same orthorombic structure the same as $PbCl_2$ ($a = 7.02$ Å, $b = 4.99$ Å, $c = 3.72$ Å). The linear misfit of -6% and $+2\%$ would require only a compression of 2.3% of the unit area. Therefore Clabes assigned the observed $\sqrt{3} \times \sqrt{3}$ reconstruction to a pseudomorphous Ni_2Si layer in three domains [18].

1.3. PROPERTIES

1.3.1. Growth of Single-crystalline $NiSi_2$ Layers on Si(111)

Tung *et al.* [4, 21, 22] discovered growth conditions for the fabrication of single-crystal $NiSi_2$ layers of either type A or type B orientation on Si(111). Type A $NiSi_2$ has the same orientation as the silicon substrate, while type-B $NiSi_2$ shares the surface normal [111] axis with the Si, but is rotated 180° about this axis with respect to Si (see Fig. 5(a,b)). Tung *et al.* reported that the final orientation of $NiSi_2$ after annealing at 450–500 °C is a function of the initial room temperature deposited Ni film thickness before annealing. As one can see in Fig. 6, thin layers formed with 4–5 or 9–11 Å Ni are type B oriented and those with 16–20 Å Ni are type A oriented ($NiSi_2$ layers grown with other Ni thicknesses contain mixed type A and type B grains).

These single-oriented layers were called "templates" by Tung *et al.* since deposition on top of the template layers and annealing lead to the growth of high-quality epitaxial $NiSi_2$ layers with any desired thickness (exceeding the thickness of the original template layer).

Further, it was found that the electrical properties of type A and type B $NiSi_2$/Si(111) junctions differ distinctively: The Schottky-barrier heights are 0.65 and 0.79 eV for type A and type B interfaces, respectively.

The origin of the type A/type B template phenomenon remains a mystery in spite of great efforts including the characterization of the atomic [23–27] and electronic [27–29] structure of the $NiSi_2$/Si(111) interface, the study of the crystalline intermediate phases in the formation of templates [25, 30–32], the investigation of the role of different growth parameters [15, 16, 21, 33, 34], etc. (for review see Ref. [22]).

As for the Si(111)–Ni surface reconstructions, they do not play an essential role in the phenomenon: in Ref. [15], two different substrate reconstructions were studied, the clean-surface 7×7 and Ni-induced $\sqrt{19} \times \sqrt{19}$ structure. No difference in the orientation of the overgrown silicide was found for the two reconstructions.

2. (100) ORIENTATION

Small amounts of Ni were found to induce $2 \times n$ structures on the Si(100) surface. The value of n varies from 6 to 10 (or 11) depending on the Ni coverage.

2.1. PHASE DIAGRAM

2.1.1. RT Deposition

No ordered reconstructions are formed during RT deposition of Ni on to the Si(100)2×1 surface. Instead of this, an abrupt disordering was observed by LEED (the 2×1 LEED pattern disappears completely at Ni coverage of ~ 1.5 Å) [35, 36].

The mechanism of the Ni/Si(100) interface formation was determined by Chang and Erskine as follows [36]: the first deposited Ni atoms form a chemisorbed phase of surface atoms. This chemisorbed phase persists to coverages of about 1 Å, but also in this coverage range Ni atoms begin to penetrate into the Si bulk occupying interstitial voids in Si [7, 37–39]. The addition of Ni above 1.5 Å coverage permits nucleation of Ni_2Si. The growth of this phase continues up to ~ 15 Å where silicide formation stops. Additional Ni atoms deposit as a pure Ni overlayer.

2.1.2. HT Growth (Quenching)

The general trends of Ni impurity behavior upon heat treatment of Si(100)–Ni samples coincides with that described above for (111)-oriented substrates: the Ni impurity at the surface diffuses into the bulk with increasing temperature, and segregates at the surface by quenching [9, 40, 41]. The variations of Ni coverage with annealing temperature and after quenching from various temperatures, as well as variation of Ni coverage versus cooling rate are qualitatively the same as those in Fig. 1 and Fig. 2. The quantitative differences are as follows: the Ni coverages for Si(100) samples are less (AES peak ratio, $R \leq 1\%$) and the temperature range of uncompleted recovering upon quenching shifts towards lower temperatures occupying the region between 300 and 700 °C (Fig. 7) [40].

LEED observations show that, at a surface Ni concentration of 0.35% in the Auger peak ratio, the 2×1 structure changes into the $2 \times n$ structure. As shown in Fig. 8, n decreases from 10 to 6 with increasing surface Ni concentration (according to Refs [41, 42] maximal n is 11 rather than 10). The intensity of the nth order spots is strongest at $n = 6$ and decreases with increasing n [40].

According to SEM observations of Dolbak *et al.* [9, 41], at Ni concentration above about 1 at.%, $NiSi_2$ islands are formed on the surface with the Si(100)2×7–Ni structure.

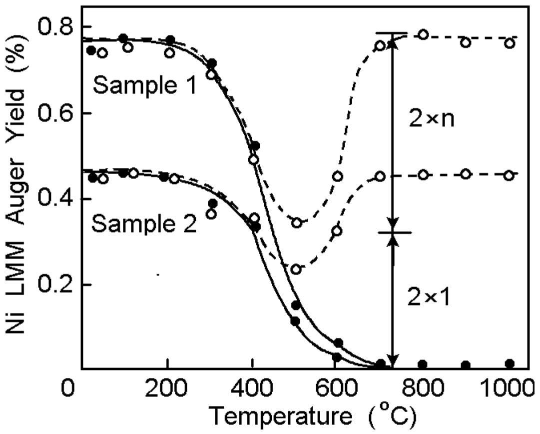

Fig 7. Variations of the Auger electron peak ratio, $R = I_{\mathrm{Ni_{LMM}}}/I_{\mathrm{Si_{LVV}}}$, for Si(100)–Ni samples with annealing temperature (solid curves) and after quenching from various temperatures to room temperature (broken curves). Samples I and II have different initial Ni concentrations (from Ref. [40]). (*Reproduced by permission of Elsevier Science Publishers BV)*

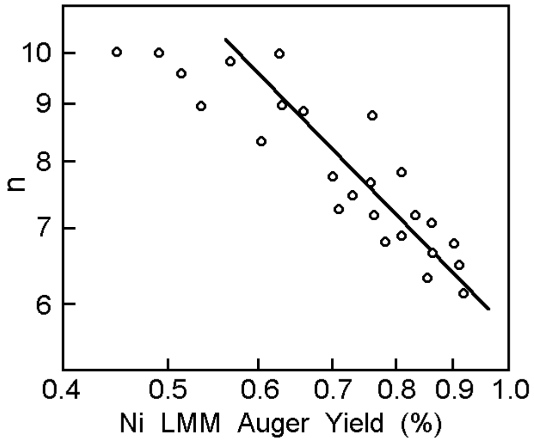

Fig 8. Variation of n for Si(100)2 × n–Ni structures with the Auger electron peak ratio, $R = I_{\mathrm{Ni_{LMM}}}/I_{\mathrm{Si_{LVV}}}$ (from Ref. [40]). (*Reproduced by permission of Elsevier Science Publishers BV)*

2.2. STRUCTURE

2.2.1. Si(100)2 × *n*–Ni

The STM observations by Niehus *et al.* [43] clearly demonstrated that 2 × n are ordered structures of missing-dimer defects. The superstructures are impurity-induced and stabilized by as little as 1% Ni.

On average, the 2 × n surface is composed of dimer units of a length that varies from 6 to 10 followed by missing-dimer arrays with a complex structure (Fig. 9). The vacancy arrays predominantly consist of a single-dimer vacancy, a "split-off dimer" and a double-dimer vacancy in combination with a missing second-layer Si atom (see Fig. 10).

More simple structural models, namely, a single missing-dimer model [44, 45] and double missing-dimer model [42] do not match the STM data and are incompatible with ARUPS results of Ref. [46].

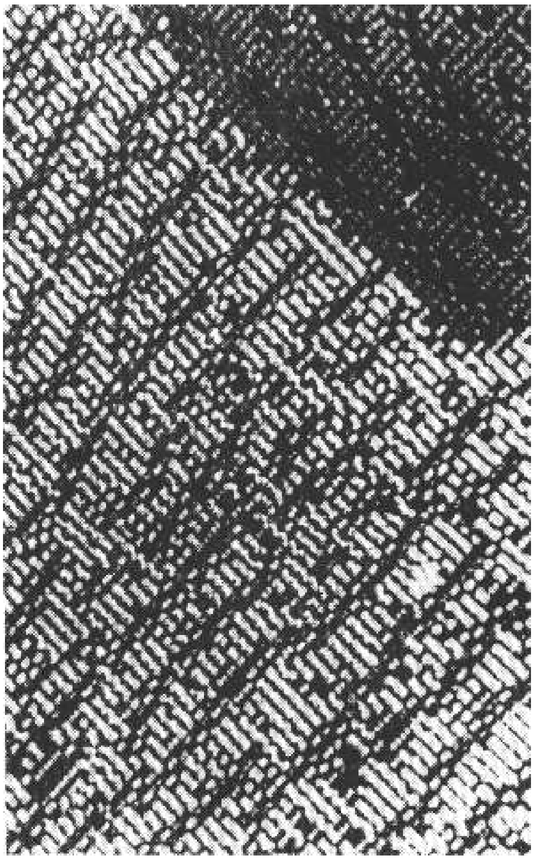

Fig 9. STM topography of an area about 15 × 25 nm^2 of the Si(100) $2 \times n$ surface (from Ref. [43]). (*Reproduced by permission of Blackwell Scientific Publications Ltd)*

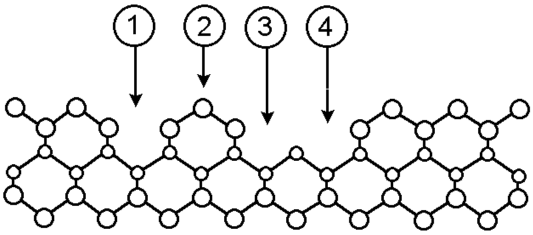

Fig 10. Scheme of the "split-off dimer" array of the Si(100) $2 \times n$ structure: (1) missing dimer, (2) "split-off dimer", (3) and (4) missing dimers with deep corrugation (from Ref. [43]). (*Reproduced by permission of Blackwell Scientific Publications Ltd)*

3. (110) ORIENTATION

On Si(110) a large number of ordered structures were observed, 5 × 4, 1 × 2, 1 × 5, 1 × 9, 1 × 7, 4 × 5, 9 × 5, 8 × 5, which are closely correlated with small Ni concentrations at the surface.

Notice that for the notation of the above reconstructions, the basic translation vectors, $\mathbf{a} = (1/2)[\bar{1}10]$ and $\mathbf{b} = [001]$, are used here as usually done in the most recent publications. In a number of the earlier works, the opposite sequence of the basic translation vectors was chosen and the structures were labeled as 2 × 1, 5 × 1, 9 × 1, etc. For clarity, Fig. 11 shows the unit meshes of the real lattices of the observed Ni-induced reconstructions and Fig. 12 shows the reciprocal lattices of these structures.

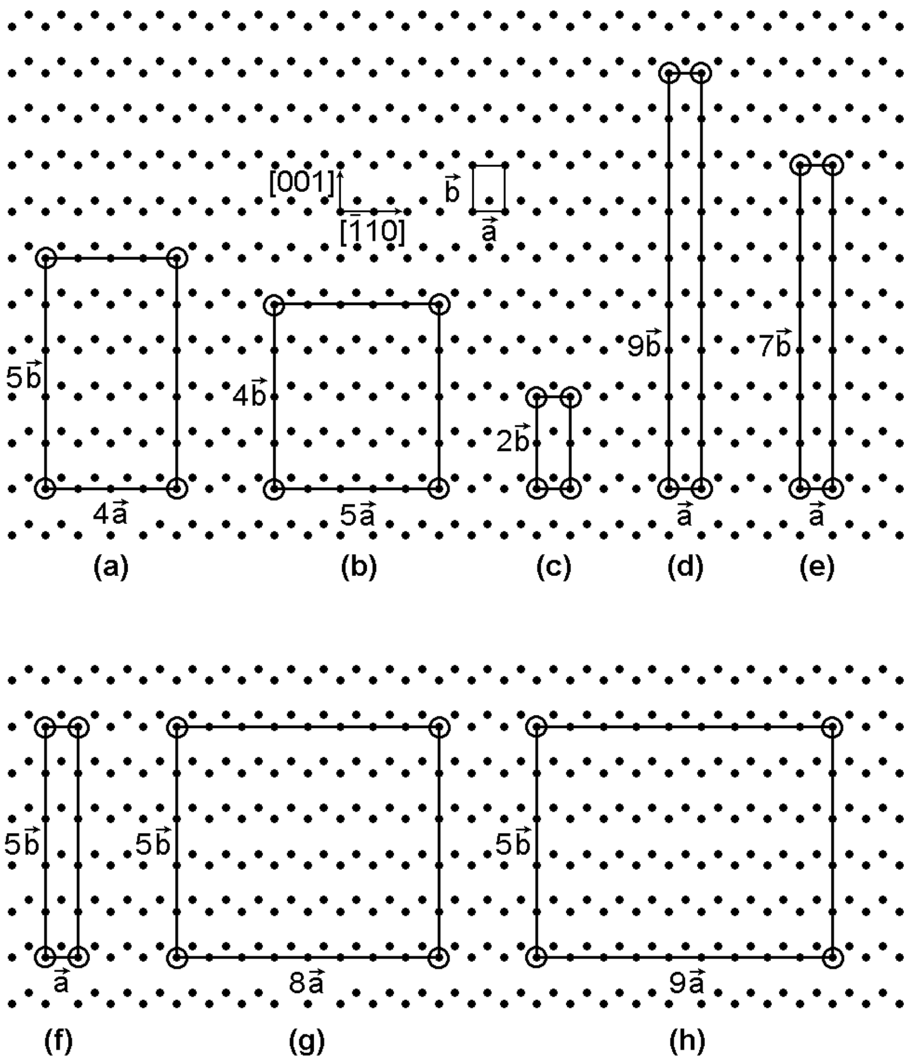

Fig 11. Unit mesh of the real lattice superstructures formed by Ni adsorption on Si(110): (a) 4 × 5, (b) 5 × 4, (c) 1 × 2, (d) 1 × 9, (e) 1 × 7, (f) 1 × 5, (g) 8 × 5 and (h) 9 × 5. $\mathbf{a} = (1/2)[\bar{1}10]$ and $\mathbf{b} = [001]$ represent the basic translation vectors on the Si(110) surface, the solid circles represent the Si atoms on the Si(110) surface and dotted circles are the corners of the unit mesh of the superstructure (from Ref. [56]) (*Reproduced by permission of the publishers of Japanese Journal of Applied Physics)*

3.1. PHASE DIAGRAM

3.1.1. RT Deposition

The RT growth of Ni on the Si(110) surface has not been studied comprehensively. It is known only that Ni adsorption in amounts from 0.5 to 10 ML on the "2 × 16" reconstructed Si(110) surface held at room temperature enhances the background and eliminates all diffraction spots on the LEED pattern. This result indicates the formation of the disordered film [47].

3.1.2. HT Growth (Quenching)

A variety of superstructures were observed on the nominally clean Si(110) surface depending on the relevant heat treatment [48–50]. In more recent investigations [41, 47, 51–55], most of the known reconstructions were associated with the presence of small Ni concentrations at the Si(110) surface, while only the "2 × 16" (sometimes "2 × 32") reconstruction was shown to correspond to the clean Si(110) surface (the quotes indicate that this reconstruction is not

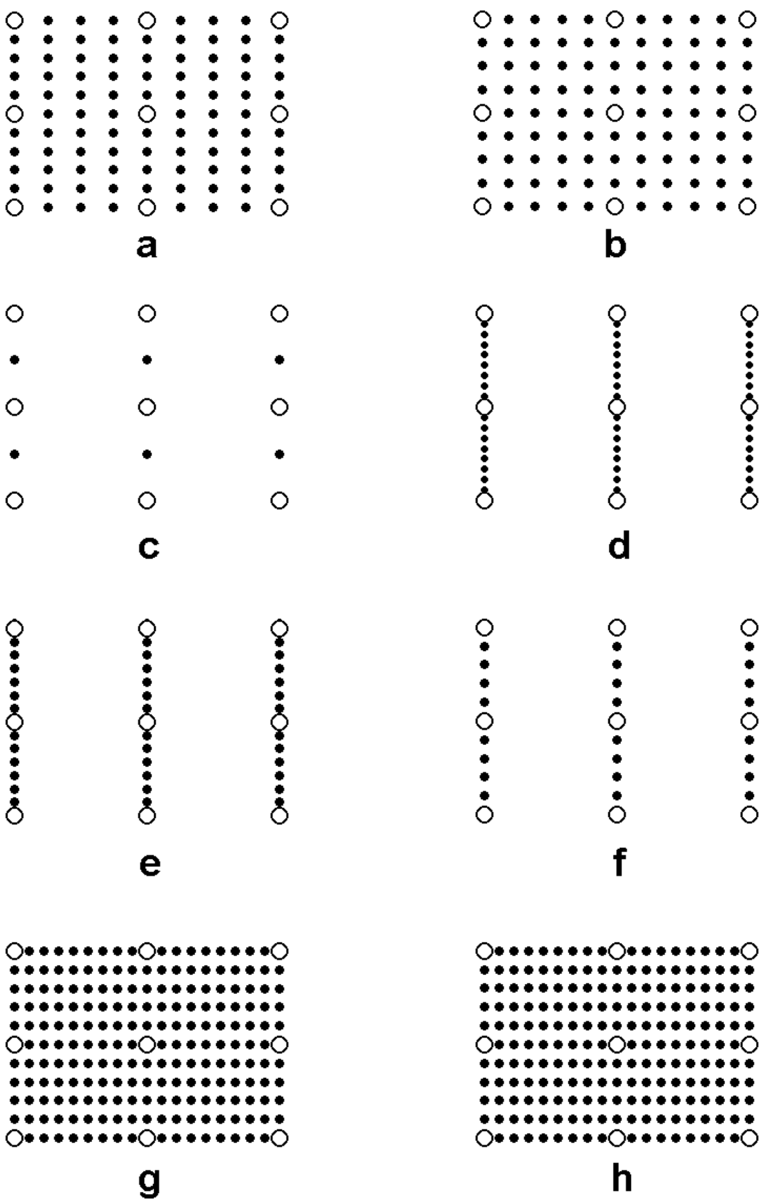

Fig 12. Reciprocal lattices of the Ni-induced reconstructions on the Si(110) surface: (a) 4 × 5, (b) 5 × 4, (c) 1 × 2, (d) 1 × 9, (e) 1 × 7, (f) 1 × 5, (g) 8 × 5, and (h) 9 × 5

aligned along the bulk symmetry axes).

Olshanetsky and Shklyaev [50] determined the experimental conditions for the formation of several Ni-induced reconstructions, namely 5 × 4, 1 × 2 and 1 × 5. They showed that the reversible structural transitions take place between these phases in the following sequence:

$$5\times 4 \overset{300\,^\circ\mathrm{C}}{\longleftrightarrow} 1\times 2 \overset{750\,^\circ\mathrm{C}}{\longleftrightarrow} 1\times 5.$$

It was also shown that each of the structures can be quenched to the room temperature.

Recently, Yamamoto [56] reported that the transition from 1 × 2 to 1 × 5 with increasing temperature at a rate of 10 °C per second proceeds via the formation of the 1 × 9 and 1 × 7 structures. This is indicated by splitting the $(0, \frac{1}{2})$ reflections into two and this splitting extends in width with temperature rise. These phase transitions also proved to be reversible

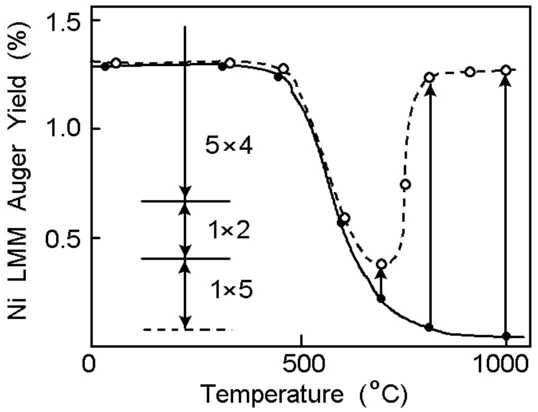

Fig 13. Variations of the Auger electron yield of Ni LMM for Si(110)–Ni sample after 20 min of heating at each temperature (solid curves) and after rapid cooling from annealing temperature to room temperature (dashed curves) (from Ref. [51]). (*Reproduced by permission of the publishers of Journal of Physical Review B)*

and, thus, they can be expressed as

$$5 \times 4 \xleftrightarrow{650\,^\circ\mathrm{C}} 1 \times 2 \xleftrightarrow{770\,^\circ\mathrm{C}} 1 \times 9 \xleftrightarrow{790\,^\circ\mathrm{C}} 1 \times 7 \xleftrightarrow{800\,^\circ\mathrm{C}} 1 \times 7.$$

The phase transitions were observed in the range from 0.5 to 1 ML when the rate of temperature change was 10 °C per second. When the sample was cooled down with a rate of 100 °C per second from 1000 °C (radiation quenching), the 4 × 5 structure was mainly observed at room temperature [56].

The clear understanding of the phase transition phenomenon was received first by Ichinokawa *et al.* [51] who found that these structures are closely correlated with Ni surface concentration. The latter depends on the heat treatments in the manner described above for Si(111)–Ni and Si(100)–Ni samples, i.e. the Ni surface concentration decreases with annealing due to Ni diffusion into the Si bulk and increases with quenching due to surface segregation (see Fig. 13).

The concentration of Ni in the surface layer estimated in Ref. [51] for 5 × 4, 1 × 2 and 1 × 5 phases is 7%, 4% and 2.6%, respectively. These values differ from those (2%, 1.4% and 0.8%) estimated by Dolbak *et al.* [9]. The latter authors [9, 41] also reported the formation of two new structures, 9 × 5 and 8 × 5 structures at extremely low Ni concentrations (below the AES detection limit) and the formation of $NiSi_2$ islands on the 5 × 4 surface at Ni concentrations above 2%.

Yamamoto [56] using total reflection X-ray spectroscopy measurements received much greater values of Ni surface concentrations for corresponding surface structures. The 4 × 5 structure was found to form in the range of 0.1 to 0.2 ML, the 1 × 5 structure in the range of 0.2 to 0.3 ML, the 1 × 2 structure in the range of 0.3 to 0.5 ML, and the 5 × 4 structure in the range of 0.5 to 1.0 ML [56].

3.2. STRUCTURE

Nesterenko *et al.* [55, 57, 58] have proposed structural models for 5 × 4, 1 × 2 and 1 × 5 reconstructed Si(110) surfaces. These models are based on semi-empirical tight-binding total energy calculations for model subunits, on lattice dynamic experiments [47] and on STM observations [59–63]. The atoms of the topmost layer only were considered in the models. Ni atoms were not involved directly into all unit cells since the surface concentration of Ni was considered to be sufficiently lower than the areal density of surface unit cells. (Though the

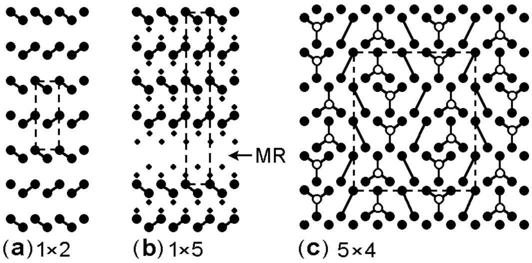

Fig 14. Si(110) surface. Structural models (top view) for 1 × 2 (a), 1 × 5 (b) and 5 × 4 (c) phases as proposed by Nesterenko *et al.* Open circles represent adatoms, filled circles indicate first layer atoms, small filled circles are second layer atoms, dimers are indicated by pairing. Missing row (MR) is indicated by arrow (from Ref. [55]). (*Reproduced by permission of Elsevier Science Publishers BV)*

presence of Ni impurity at the surface is necessary for the formation of superstructures, the role of Ni impurity in the reconstructions remains unclear.) Therefore only Si atoms were used for construction of the models.

A different model for the 5 × 4 structure, as well as the model for the 4 × 5 structure were proposed by Yamamoto [56]. The structure models were built of Ni atoms and were derived from the amount of Ni adsorption and Patterson functions calculated from the RHEED intensity distributions.

3.2.1. Si(110)1 × 2–Ni

The 1 × 2 reconstruction was suggested to be due to π-dimerization, i.e. to the mutual saturation of dangling bonds between the first neighboring atoms belonging to the same chain along the $[1\bar{1}0]$ direction [55] (see Fig. 14(a)). This model assumes both rotation and relaxation shifts of surface atoms and a slight reduction of the distance between two dimerized atoms.

The model involving dimerization of dangling bonds lying on neighboring chains, as proposed in Ref. [57], was ruled out in the more recent Ref. [55] as energetically unfavorable.

3.2.2. Si(110)1 × 5–Ni

The 1 × 5 structure was modeled by two 1 × 2 blocks with one monoatomic missing row, as shown in Fig. 14(b). The presence of the missing $[\bar{1}10]$ rows in the 1 × 5-reconstructed (110) surface was confirmed by STM observations [60] and the appearance of unsaturated dangling bonds agrees with the results of adsorption experiments [64]. The photoemission results [65] support the suggestion that π-dimers are the building units of the 1 × 5 phase.

3.2.3. Si(110)5 × 4–Ni

For modeling the 5 × 4 structure, Nesterenko *et al.* used the adatoms and π-dimers. By alternation of the π-dimers and adatoms along the $[1\bar{1}0]$ direction the 5 × 1 building block was constructed. The mutual shifts of these 5 × 1 blocks along the $[1\bar{1}0]$ axis allows the unit size along the [001] direction to multiply by four, i.e. to construct a 5 × 4 superstructure (see Fig. 14(c)). Nesterenko *et al.* demonstrated that their structure model is consistent with LEED [66] and STM [59, 62, 63] observations.

According to the results of Yamamoto [56], the 5 × 4 structure is formed by Ni adsorption in the range from 0.5 to 1.0 ML. He proposed another model of this structure which is shown in Fig. 15. Here, the open circles represent Si atoms, the solid circles Ni atoms up to 0.5 ML, and the oblique circles Ni atoms over 0.5 ML. Ni atoms were considered to saturate the dangling

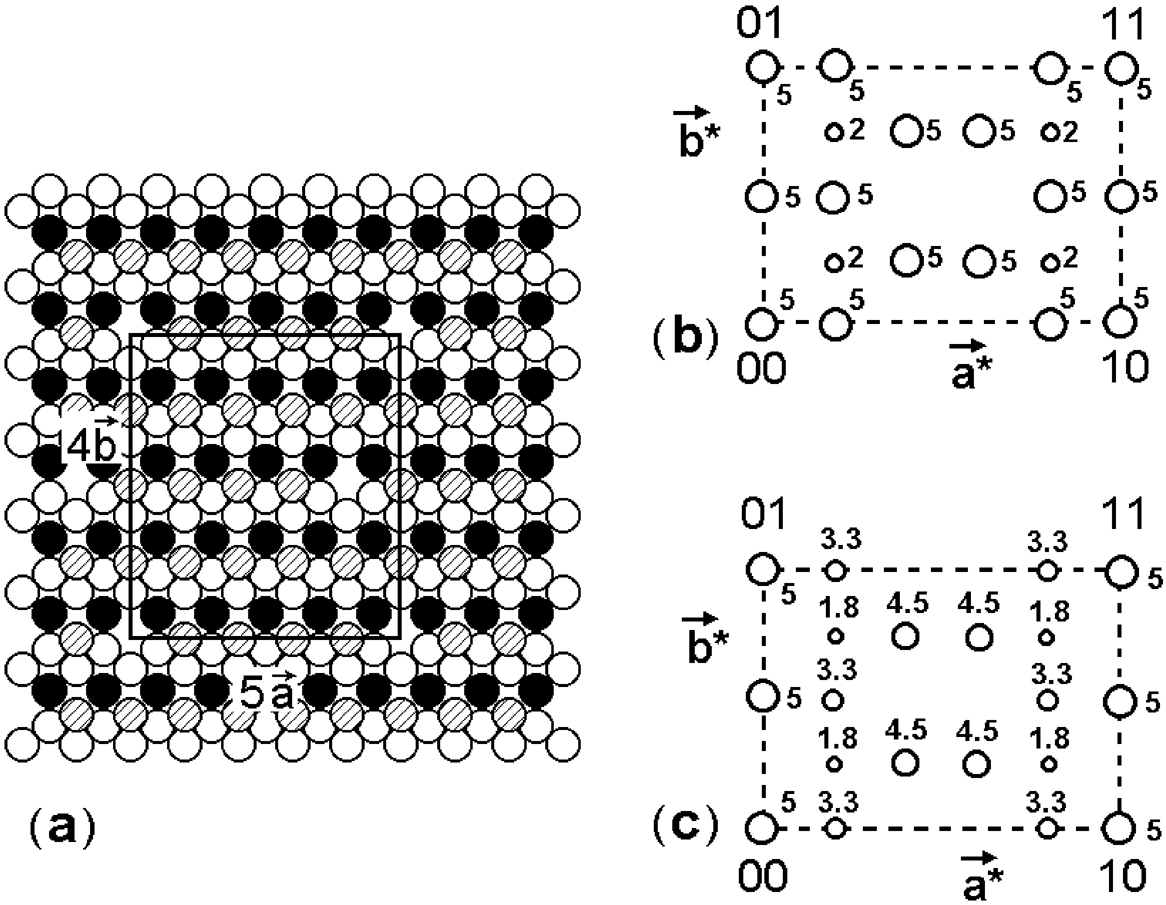

Fig 15. (a) The model of the atomic arrangement of the Si(110)5 × 4–Ni surface as proposed by Yamamoto. The open circles represent Si atoms, and the solid circles, Ni atoms up to 0.5 ML, and the oblique circles, Ni atoms in the range from 0.5 to 1 ML. (b) The intensity distribution among the reciprocal rods for the 5 × 4 superstructure obtained from the analysis of RHEED patterns. (c) The intensity distribution calculated from the model (from Ref. [56]). (*Reproduced by permission of the publishers of Japanese Journal of Applied Physics)*

bonds of the Si(110) surface up to 0.5 ML, and form Ni–Ni metallic bonds at 0.5–1.0 ML. The model shown in Fig. 15 contains 0.95 ML. The RHEED intensity distribution calculated from this model reproduces well the intensity distribution detected in the experiment. Accordingly, the model was considered to be acceptable [56].

3.2.4. Si(110)4 × 5–Ni

From consideration of the RHEED intensity distribution, Yamamoto [56] proposed a model of the 4 × 5 structure as shown in Fig. 16. It was suggested that adsorbed Ni atoms saturate the dangling bonds of the Si(110) surface to minimize the adsorption energy. The Ni amount in the model is 0.15 ML and the 4 × 5 structure was observed in the experiment in the range from 0.1 to 0.2 ML [56].

3.3. PROPERTIES

3.3.1. Vibrational Properties

The vibrational properties of 5 × 4, 1 × 5 and 1 × 2 phases were derived in Ref. [47] from the LEED data. The Debye temperature θ_D was extracted from Debye–Waller factor for the

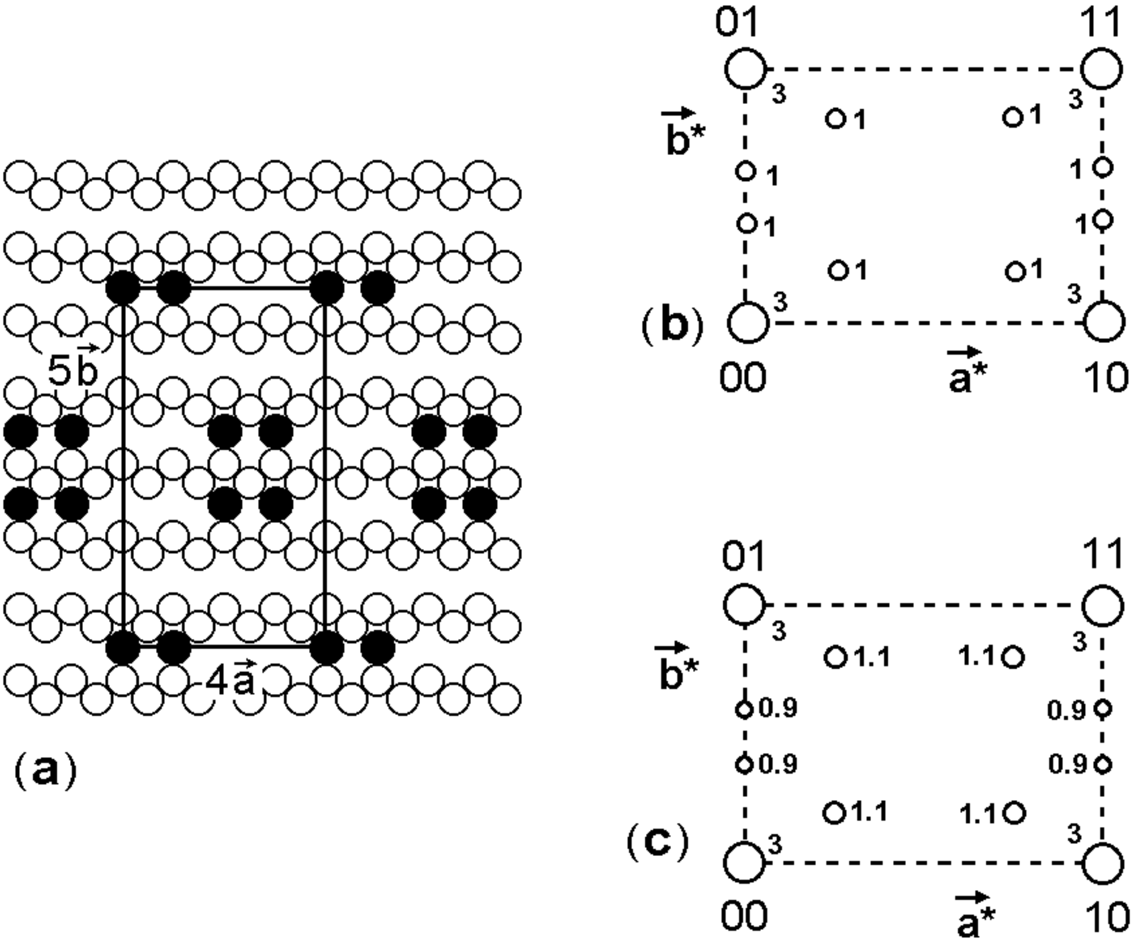

Fig 16. (a) The model of the atomic arrangement of the Si(110)4 × 5–Ni surface as proposed by Yamamoto. The open circles represent Si atoms, and the solid circles, Ni atoms, (b) the intensity distribution among the reciprocal rods for the 4×5 superstructure obtained from the analysis of RHEED patterns. (c) The intensity distribution calculated from the model (from Ref. [56]). (*Reproduced by permission of the publishers of Japanese Journal of Applied Physics)*

(00) diffraction spot. The thermal expansion coefficient $\alpha_\perp$ was calculated from temperature shifts of the peaks on the I–V LEED spectra for the (00) reflection. In both cases the angle of incidence was close to normal. The chosen experimental conditions permitted one to obtain vibrational amplitudes and static displacements in a direction normal to the surface. The temperature was varied from 100 to 300 K.

The data obtained for θ_D and $\alpha_\perp$ were analyzed for the simplest one-dimensional case. Thus, the force acting on the atom near its equilibrium position is $F = \beta x + \gamma x^2$, where x is the atom displacement; β and γ are harmonic and anharmonic force constants, respectively. θ_D and $\alpha_\perp$ obey the following relations: $\theta_\mathrm{D} \propto \sqrt{\beta}$, $\alpha_\perp \propto \gamma/\beta^2$ [47].

The experimental values of θ_D and $\alpha_\perp$ taken at minimal electron energy, i.e. maximal surface effect, and force constants derived from them for clean "2×16" and Ni-induced 5×4, 1×5 and 1×2 structures are summarized in Table 1.

3.3.2. Electronic Properties

Work function, surface photovoltage and field effect kinetics were measured by Nesterenko *et al.* [47] for Si(110) 5 × 4–Ni, Si(110)1 × 5–Ni and Si(110)1 × 2–Ni surface phases. The data obtained are presented in Table 2.

Table 1. Experimental data on $\theta_{\rm D}$ and $\alpha_\perp$ (electron energy 36 eV) and force constants β and γ derived from them (normalized by the bulk values). In the bulk $(\theta_{\rm D})_b = 540$ K, $\alpha_{\perp b} = 2.3 \cdot 10^{-6}$ K^{-1} (from Ref. [47])

Structures	$\theta_{\rm D}$ (K)	$\alpha_\perp \times 10^6$ (K^{-1})	$\theta_{\rm D}/(\theta_{\rm D})_b$	$\alpha_\perp/\alpha_{\perp \rm b}$	β/β_b	γ/γ_b
"2 × 16"	270	50	0.50	21.7	0.25	1.3
5 × 4–Ni	280	40	0.52	17.4	0.27	1.3
1 × 5–Ni	325	27	0.60	11.7	0.36	1.5
1 × 2–Ni	380	19	0.70	8.2	0.49	2.0

Table 2. Experimental data on electronic properties of different phases on the Si(110) surface. (Photovoltage $V_{\rm ph}$ was measured on n-type samples, $T = 220$ K, $(E_{\rm F} - E_i)_{\rm bulk} = 0.33$ eV) (from Ref. [47])

Structures	$V_{\rm ph}$ (eV)	$\Delta\varphi$ (eV)	$\Delta\chi$ (eV)	$E_0 - E_{\rm tn}$ (eV)	$E_{\rm tp} - E_V$ (eV)	E_{gs} (eV)
"2 × 16"	0.27	—	—	0.25	—	—
5 × 4–Ni	0.33	0	0	0.28	0.45	0.40
1 × 5–Ni	0.30	0.06	0.09	0.26	0.45	0.42
1 × 2–Ni	0.22	0.13	0.24	0.33	0.57	0.22

The photovoltage $V_{\rm ph}$ measurements were carried for n-type samples only. They showed all the surface phases to have exhausting band bending due to surface electron states charge $Q_{\rm ss} = 10^{10}$ e/cm^2. Variation of electron affinity

$$\Delta\chi = \Delta\varphi - \Delta V_{\rm ph}$$

was calculated with reference to its value for the 5×4 phase. Work function $\Delta\varphi$ values were well reproducible for all samples and did not depend on bulk conductivity type. This fact indicates pinning of the Fermi level at the surface due to surface states with concentration of $\geq 10^{12}$ cm^{-2}.

The surface state spectra were derived from the field effect kinetics measurements, i.e. from the temperature dependence of the relaxation time measured under strong non-equilibrium exhaustion of the space-charge layer. The spectra appeared to have empty and filled groups of surface states above and below the Fermi level $E_{\rm F}$, respectively. The equivalent representation of these surface bands may be given by levels $E_{\rm tn}$ and $E_{\rm tp}$ as shown by the energy diagram of Fig. 17.

The experimental results presented in Table 2 indicate the significant effect of surface phase structure on the electronic properties of the surface. The largest changes were observed due to transition to the 1×2 structure while for long-period 5×4 and 1×5 phases electronic characteristics are very close.

4. NICKEL TRANSPORT ON Si(111), Si(100) AND Si(110) SURFACES

The study of Ni diffusion on silicon surfaces was carried out by Dolbak *et al.* [9, 41]. In the experiment, the diffusion of nickel from a 1 mm wide nickel disilicide stripe on the Si sample surface was monitored using AES, LEED, RHEED and SEM. Nickel transport along surfaces takes place at annealing (see Fig. 18). However, unlike the existing concepts and

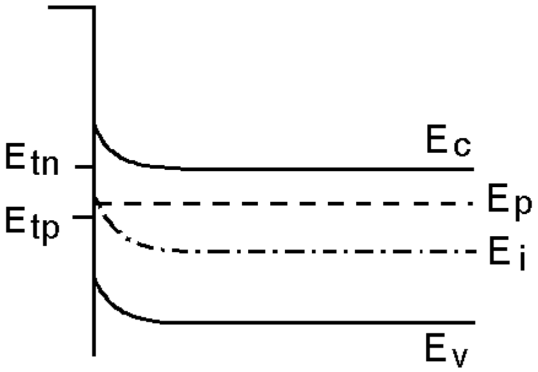

Fig 17. The surface electronic states on the Si(110) surface (from Ref. [66]). (*Reproduced by permission of Elsevier Science Publishers BV)*

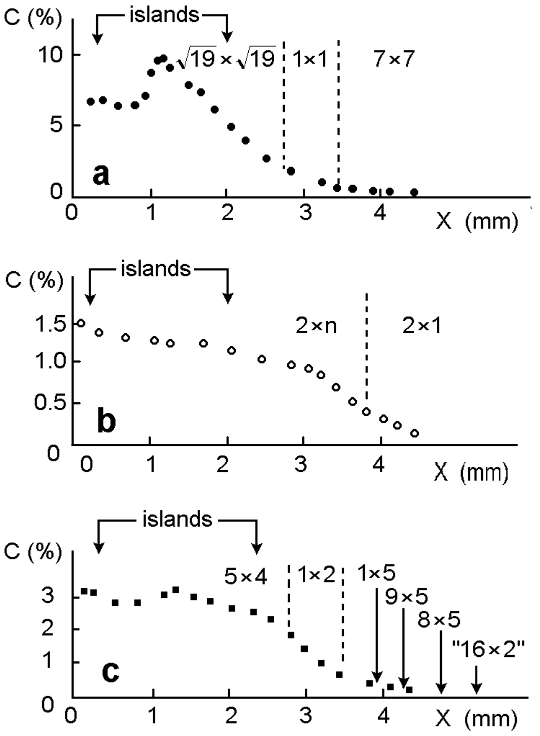

Fig 18. Ni distribution along the surface according to AES data for (a) Si(111) annealed at 1050 °C for 80 s, (b) Si(100) annealed at 960 °C for 120 s, (c) Si(110) annealed at 1050 °C for 80 s. Cooling rate is > 100 °C/s (from Ref. [41]. (*Reproduced by permission of Elsevier Science Publishers BV)*

numerous experimental data according to which the surface diffusion coefficients are higher than those in the bulk, the nickel transport along silicon surfaces is realized by its diffusion through the bulk with the subsequent surface segregation due to the lowering of its solubility during quenching. However, besides diffusion of Ni through the bulk, it also takes place on the surface as indicated by the formation of ordered surface phases and epitaxial $NiSi_2$ islands after segregation of Ni to the surface. However, Dolbak *et al.* failed to perform direct measurements of the surface diffusion coefficient since it appeared to be about four orders lower than that in the bulk according to their estimate. The determined bulk value was $D = 2.4 \times 10^{-3} \exp(-0.32\ \text{eV}/kT)\ \text{cm}^2\ \text{s}^{-1}$ for all substrate orientations studied, i.e. (111), (100) and (110).

REFERENCES

[1] T. L. Porter, C. S. Chang, U. Knipping and I. S. T. Tsong, *J. Vac. Sci. Technol. A* **6** (1988) 2034.

[2] W. S. Yang, S. C. Wu and F. Jona, *Surf. Sci.* **155** (1985) L292.

[3] W. S. Yang, S. C. Wu and F. Jona, *Surf. Sci.* **169** (1986) 383.

[4] R. T. Tung, J. M. Gibson and J. M. Poate, *Phys. Rev. Lett.* **50** (1983) 429.

[5] T. L. Porter, C. S. Chang, U. Knipping and I. S. T. Tsong, *Phys. Rev. B* **36** (1987) 9150.

[6] F. Comin, J. E. Rowe and P. H. Citrin, *Phys. Rev. Lett.* **51** (1983) 2402.

[7] F. Comin, *J. Vac. Sci. Technol. A* **3** (1985) 930.

[8] E. J. Van Loenen, J. W. M. Frenken and J. F. Van der Veen, *Appl. Phys. Lett.* **45** (1984) 41.

[9] A. E. Dolbak, B. Z. Olshanetsky, S. I. Stenin, S. A. Teys and T. A. Gavrilova, *Surf. Sci.* **218** (1989) 37.

[10] S. A. Teys, A. E. Dolbak, T. A. Gavrilova, B. Z. Olshanetskii and S. I. Stenin, *Poverkhnost N 2* (1989) 91.

[11] T. Ichinokawa, T. Tani and A. Sayama, *Surf. Sci.* **219** (1989) 395.

[12] J. M. Charig and D. K. Skinner, *Surf. Sci.* **19** (1970) 283.

[13] A. J. Van Bommel and F. Meyer, *Surf. Sci.* **8** (1967) 467.

[14] Y. J. Chabal, R. J. Culbertson, L. C. Feldman and J. E. Rowe, *J. Vac. Sci. Technol.* **18** (1981) 880.

[15] G. Akinci, T. R. Ohno and E. D. Williams, *Surf. Sci.* **193** (1988) 534.

[16] G. Akinci, T. R. Ohno and E. D. Williams, *Surf. Sci.* **201** (1988) 27.

[17] R. J. Wilson and S. Chiang, *Phys. Rev. Lett.* **58** (1987) 2575.

[18] J. G. Clabes, *Surf. Sci.* **145** (1984) 87.

[19] W. S. Yang, F. Jona and P. M. Marcus, *Phys. Rev. B* **28** (1983) 7377.

[20] G. V. Hansson, R. Z. Bachrach, R. S. Bauer and P. Chiaradia, *Phys. Rev. Lett.* **46** (1981) 1033.

[21] R. T. Tung, *J. Vac. Sci. Technol. A* **5** (1987) 1840.

[22] R. T. Tung, *J. Vac. Sci. Technol. A* **7** (1989) 598.

[23] D. Cherns, G. R. Anstis, J. L. Hutchison and J. C. H. Spence, *Phil. Mag. A* **46** (1982) 849.

[24] E. J. Van Loenen , *J. Vac. Sci. Technol. A* **4** (1986) 939.

[25] J. M. Gibson and J. L. Batstone, *Surf. Sci.* **208** (1989) 317.

[26] J. F. Van der Veen, A. E. M. J. Fischer and J. Vrijmoeth, *Appl. Surf. Sci.* **38** (1989) 13.

[27] J. J. Yeh, *Appl. Phys. Lett.* **55** (1989) 1241.

[28] H. Fujitani and S. Asano, *Phys. Rev. B* **42** (1990) 1696.

[29] S. Ossicini, O. Bisi and C. M. Bertoni, *Phys. Rev. B* **42** (1990) 5735.

[30] P. A. Bennett, B. N. Halawith and A. P. Johnson, *J. Vac. Sci. Technol. A* **5** (1987) 2121.

[31] P. A. Bennett, A. P. Johnson and B. N. Halawith, *J. Vac. Sci. Technol. A* **6** (1988) 1558.

[32] P. A. Bennett, A. P. Johnson and B. N. Halawith, *Phys. Rev. B* **37** (1988) 4268.

[33] G. Akinci, T. Ohno and E. D. Williams, *J. Vac. Sci. Technol.* **5** (1987) 2143.

[34] G. Akinci, T. R. Ohno and E. D. Williams, *Appl. Phys. Lett.* **50** (1987) 754.

[35] Y. Chang and J. L. Erskine, *Phys. Rev. B* **26** (1982) 4766.

[36] Y. -J. Chang and J. L. Erskine, *J. Vac. Sci. Technol. A* **1** (1983) 1193.

[37] N. W. Cheung and J. W. Mayer, *Phys. Rev. Lett.* **46** (1981) 671.

[38] N. W. Cheung, P. J. Grunthaner, F. J. Grunthaner, J. W. Mayer and B. M. Ullrich, *J. Vac. Sci. Technol.* **18** (1981) 917.

[39] P. J. Grunthaner, F. J. Grunthaner, A. Madhukar and J. W. Mayer, *J. Vac. Sci. Technol.* **19** (1981) 649.

[40] K. Kato, T. Ide, S. Miura and T. Ichinokawa, *Surf. Sci.* **194** (1988) L87.

[41] A. E. Dolbak, B. Z. Olshanetsky, S. I. Stenin and S. A. Teys, *Surf. Sci.* **247** (1991) 32.

[42] D. M. Rohlfing, J. Ellis, B. J. Hinch, W. Allison and R. F. Willis, *Surf. Sci.* **207** (1989) L955.

[43] H. Niehus, U. K. Kohler, M. Copel and J. E. Demuth, *J. Microscopy* **152** (1988) 735.
[44] T. Aruga and Y. Murata, *Phys. Rev. B* **34** (1986) 5654.
[45] J. A. Martin, D. E. Savage, W. Moritz and M. G. Lagally, *Phys. Rev. Lett.* **56** (1986) 1936.
[46] Y. Enta, S. Suzuki, S. Kono and T. Sakamoto, *J. Phys. Soc. Jap.* **59** (1990) 657.
[47] B. A. Nesterenko, *Appl. Surf. Sci.* **33–34** (1988) 21.
[48] F. Jona, *IBM J. Res. Dev.* **9** (1965) 375.
[49] H. D. Hagstrum and G. E. Becker, *Phys. Rev. B* **8** (1973) 1580.
[50] B. Z. Olshanetsky and A. A. Shklyaev, *Surf. Sci.* **67** (1977) 581.
[51] T. Ichinokawa, H. Ampo, S. Miura and A. Tamura, *Phys. Rev. B* **31** (1985) 5183.
[52] H. Ampo, S. Miura, K. Kato, Y. Ohkawa and A. Tamura, *Phys. Rev. B* **34** (1986) 2329.
[53] Y. Yamamoto, S. Ino and T. Ichikawa, *Japan J. Appl. Phys.* **25** (1986) L331.
[54] S. Miura, K. Kato, T. Ide and T. Ichinokawa, *Surf. Sci.* **191** (1987) 259.
[55] A. I. Shkrebtii, C. M. Bertoni, R. Del Sole and B. A. Nesterenko, *Surf. Sci.* **239** (1990) 227.
[56] Y. Yamamoto, *Japan J. Appl. Phys.* **31** (1992) 2544.
[57] B. A. Nesterenko and A. I. Shkrebtii, *Surf. Sci.* **213** (1989) 309.
[58] B. A. Nesterenko and A. I. Shkrebtii, *Poverkhnost N 7* (1990) 70.
[59] E. J. Van Loenen, D. Dijkkamp and A. J. Hoeven, *J. Microscopy* **152** (1988) 487.
[60] R. S. Becker, B. S. Swartzentruber and J. S. Vickers, *J. Vac. Sci. Technol. A* **6** (1988) 472.
[61] A. J. Hoeven, D. Dijkkamp, E. J. Van Loenen and P. J. G. M. Van Hooft, *Surf. Sci.* **211–212** (1989) 165.
[62] H. Neddermeyer and St. Tosch, *Phys. Rev. B* **38** (1988) 5784.
[63] H. Neddermeyer and St. Tosch, *J. Microscopy* **152** (1988) 149.
[64] E. G. Keim, A. Van Silfhout and L. Wolterbeek, *J. Vac. Sci. Technol. A* **6** (1988) 57.
[65] P. Martensson, G. V. Hansson and P. Chiaradia, *Phys. Rev. B* **31** (1985) 2581.
[66] B. A. Nesterenko, A. V. Brovii and A. I. Sorokovykh, *Surf. Sci.* **171** (1986) 495.

(O)

OXYGEN

For more than two decades, a great deal of experimental and theoretical work has been done to study the initial oxidation of Si surfaces [1]. Yet considerable uncertainty remains over fundamental questions relating to the location, physical structure, and electronic spectrum of oxidized surface sites, as well as the step-by-step kinetics of the oxidation process. Thus at the present time, the microscopic physics and chemistry of the interaction is still far from being understood. In RT oxygen adsorption up to 10^4 L exposure, it is generally accepted that there are two different adsorption steps: a fast and a slow adsorption step. For the fast adsorption step, various models on the bonding configuration of the adsorbed oxygen–Si system have been proposed, and there has been a long controversy over whether oxygen is adsorbed molecularly or atomically [2]. Very often, results of early studies differ widely due to variations of the experimental conditions. Although light, ionization gauges and electron beams are known to stimulate the oxygen uptake on semiconductor surfaces these effects were not properly avoided in many studies.

The great majority of studies addressing the oxygen–silicon system has employed molecular oxygen [3]. Alternative molecular sources of oxygen have also been examined, such as H_2O [4–7], NO [8,9], and N_2O [10,11].

The growth of the thick silicon dioxide films is of great technological importance as today's microelectronic technology is to a large extent based on the excellent properties of thermally grown silicon dioxide layers. The description of the problems of silicon oxidation at relatively high thickness is not within the scope of this book. There are some review articles concerning this area (for example, [12] and references therein).

1. (111) ORIENTATION

Oxygen is known to induce 1×1 reconstruction on the Si(111) surface, while the existence of $\sqrt{3} \times \sqrt{3}$ and 7×7 surface structures was also reported in some works.

1.1. PHASE DIAGRAM

The evolution of the structure of the Si(111)2×1 cleaved surface during oxygen exposure at RT was investigated by Ridgway [13]. He found that the half-order spots on the 2×1 LEED pattern disappear after exposure to 6 L of oxygen. A corresponding increase in the background accompanies the increase in oxygen exposure. With increasing exposure (from 60 to 6×10^5 L) the integral order spots weaken. At 6×10^6 L of oxygen, the integral-order reflections disappear, leaving no pattern. Si surface, after exposure to 6×10^6 L of oxygen, was subjected to heat treatment. Heat treatment at $\sim 900\,^\circ$C for several seconds restored

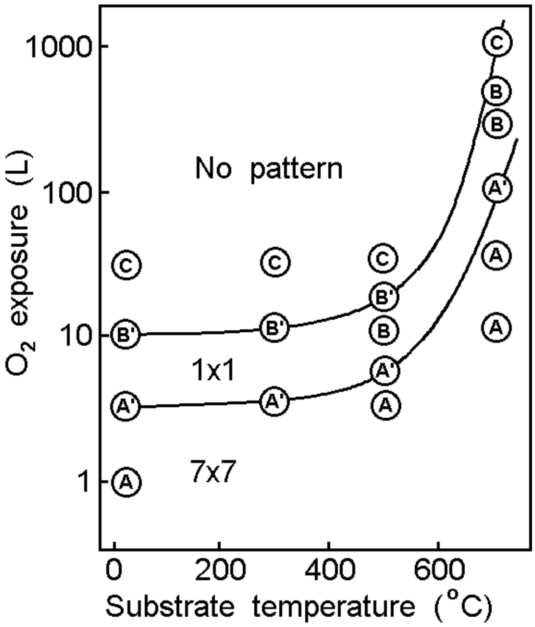

Fig 1. LEED pattern map plotted on the (Si substrate temperature)–(O_2 exposure) plane (from Ref. [14]). (*Reproduced by permission of the publishers of Journal of Physical Review B)*

the integral order spots. Further heating for 35 min at 920 °C gave a $\sqrt{3} \times \sqrt{3}$—$R30°$ surface structure.

Following Tabe *et al.* [14], three types of LEED patterns are observed during oxygen adsorption on the Si(111)7 × 7 surface, i.e. 7 × 7, 1 × 1, and "no pattern". In accordance with Gibson's observation by means of TED [15], a well-ordered Si(111)7 × 7–O structure is stable in excess of 10^5 L O_2 exposure at RT and only electron beam irradiation during dosing additionally leads to very rapid disordering of the surface. As O_2 exposure increases, the 7 × 7 pattern changes into a 1 × 1 pattern. With further exposure the 1 × 1 pattern disappears into "no pattern". The results are summarized in Fig. 1. Since the 7 × 7 spots slowly fade into 1 × 1 spots and similarly the 1 × 1 spots gradually disappear, these transitions are not sharp. The 7 × 7, mixture of 1 × 1 and weak 7 × 7, 1 × 1, weak 1 × 1, and no pattern marked A, A′, B, B′, and C, respectively. It can be seen from Fig. 1 that the 1 × 1 pattern region occurs at almost the same O_2 exposure (∼ 10 L) at $T \leq 500$ °C and much higher exposure (∼ 300 L) to $T = 700$ °C. In accordance with AES observation, the intermediate 1 × 1 LEED pattern appears at the same oxygen amount.

The $I(\mathrm{O})/I(\mathrm{Si})$ Auger peak ratio is plotted on the (Si substrate temperature)–(O_2 exposure) plane in Fig. 2 [14]. The results can be classified into three temperature ranges: (1) at RT, the ratio quickly saturates at 10–30 L and then a slow adsorption step occurs with further exposure; (2) in the medium-temperature range (300–500 °C), no significant difference is observed at low exposures (< 30 L), while enhancement of oxygen uptake occurs at high exposures, compared with the result at 20 °C; (3) at high temperatures (700 °C and probably above), oxygen adsorption is strongly suppressed at low exposures below 300 L and then rapidly increases at higher exposures. The result at RT is in agreement with the earlier results [16–19] although the transition exposure from the fast to the slow adsorption step (10–30 L) is much less than that for unexcited O_2 adsorption (10^3 L) because of the hot filament effect on oxidation [19].

The fast adsorption step is generally recognized as a simple adsorption of molecular and/or atomic oxygen on to the top Si layer even though other configurations may coexist. On the other hand, the slow adsorption step is involved with a diffusion or penetration of oxygen

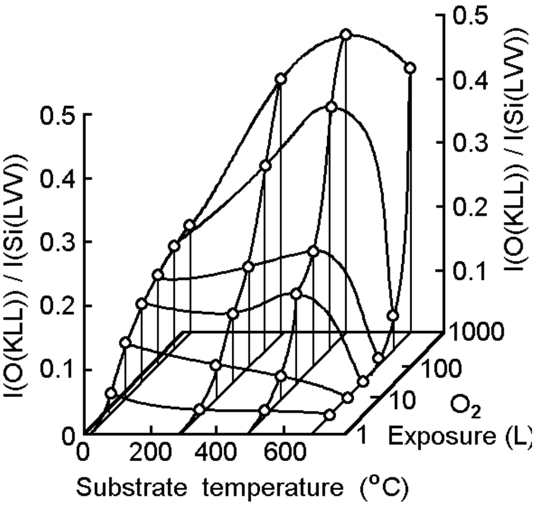

Fig 2. I[O(KLL)]/I[Si(LVV)] Auger peak-to-peak height ratio plotted on the (Si substrate temperature)–(O_2 exposure) plane (from Ref. [14]). (*Reproduced by permission of the publishers of Journal of Physical Review B)*

atoms into the Si substrate, accompanied by bond breaking between Si atoms. At 300–500 °C the fast adsorption step is almost independent of temperature, while the slow adsorption step is enhanced with increasing temperature probably because thermally-induced atomic vibration allows for easier penetration of the oxygen atoms. The oxidation at 700 °C is quite different from the lower-temperature results. Strong suppression of oxygen uptake can be explained by the formation of volatile SiO molecules [20]. SiO, rather than SiO_2, is the thermodynamically stable form of silicon oxide under certain oxidation conditions. At 700 °C a thin film of SiO_2 is formed ("passivation" mode of oxidation) only when the O_2 pressure is greater than $\sim 3 \times 10^{-7}$ Torr [14]. For O_2 pressure below $\sim 3 \times 10^{-7}$ Torr, volatile SiO is formed ("combustion" mode of oxidation), and the Si surface is etched away by oxygen. The transition between these two modes of oxidation is quite abrupt, and there is a transition pressure associated with each temperature [21]. This transition pressure increases with increasing temperature. According to Smith and Ghidini [21], the critical pressure P_c and sample temperature T_s follow Arrhenius relation

$$P_c(T_s) = P_0 \exp(-\Delta E/kT_s)$$

with $P_0 = 4.4 \times 10^{12}$ Torr, $\Delta E = 3.93$ eV for the O_2 + Si(111) reaction.

The investigation of the kinetics of oxidation reaction by Memmert and Yu [22] by monitoring the evolution of SiO has shown that the reaction pathway is a serial combination of two first-order steps, and the time dependence of the SiO signal is proportional to:

$$\exp(-k_2 t) - \exp(-k_1 t)$$

with $k_2 < k_1$. Yu and Eldridge [23] suggested that k_1 is associated with the formation of SiO on the surface after the adsorption of the oxygen molecules, and k_2 is associated with the thermal desorption of SiO into the vapor phase. The activation energies for k_1 and k_2 are 2.7 ± 0.15 eV and 4.4 ± 0.15 eV, respectively.

The interaction of molecular, unexcited oxygen with the Si(111)7 × 7 and Si(111)2 × 1 surfaces at very wide exposure range was studied by Stockhausen *et al.* [24] by using AES. Exposures of up to 10^{30} O_2 molecules per cm^2, which correspond to 3.6×10^{16} L, were used. All possible stimulations of the oxygen uptake were carefully avoided. Both on cleaved

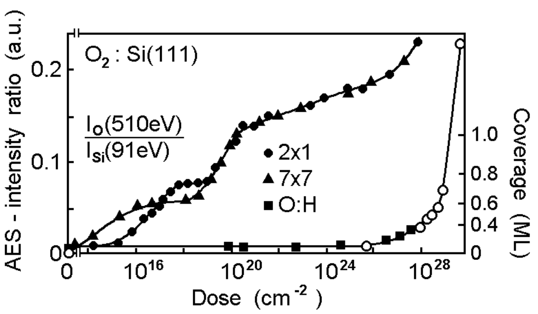

Fig 3. Coverage versus exposure curve of differently prepared Si(111) surfaces (from Ref. [24]). (*Reproduced by permission of Elsevier Science Publishers BV)*

Table 1. Initial reactive sticking coefficient of O_2 on Si(111) 7×7 and Si(111)2×1 at 300 K (from Ref. [25])

Surface	S_0	Reference
Si(111)7 × 7	0.4	[24]
	0.13	[25]
	0.21	[61]
	0.19	[62]
	0.18	[63]
	0.15	[64]
	0.14	[65]
	0.10–0.20	[66]
	0.08	[67]
	0.01	[68]
	8×10^{-4}	[69]
Si(111)2 × 1	5×10^{-2}	[24]
	3×10^{-4}	[70]
	2×10^{-4}	[71]
	1×10^{-3}	[72]
	1×10^{-3}	[66]

Si(111)2 × 1 and equilibrium Si(111)7 × 7 surfaces, the oxygen uptake is observed to occur in two successive stages as can be seen in Fig. 3 showing the intensity ratio of the O (510 eV) and the Si (91 eV) Auger signals as a function of exposure. The coverage scale at the right-hand side is also shown. The first stage is characterized by initial sticking coefficients of $S_{2\times1} \approx 5 \times 10^{-2}$ and $S_{7\times7} \approx 0.4$ and by saturation coverages of $\theta_{2\times1} \approx 0.75$ ML and $\theta_{7\times7} \approx 0.6$ ML. (For reference, the previous initial sticking coefficient measurements of O_2 on the Si(111)7 × 7 and Si(111)2 × 1 surfaces at RT are summarized in Table 1.) In the second adsorption stage, the coverage versus exposure curves are identical for both the Si(111)2 × 1 and Si(111)7 × 7 surfaces, and they are characterized by an initially increased uptake rate which is then followed by a slower quasi-logarithmic growth law. This second process is attributed to electric field-assisted diffusion, i.e. the Mott–Cabrera mechanism.

The initial reactive sticking coefficient of O_2 on Si(111) 7 × 7 decreased with surface temperature from $S_0 = 0.2$ at 200 K to $S_0 = 0.06$ at 600 K [25]. The observed decrease in S_0 suggests that the initial oxidation of Si(111)7 × 7 is mediated by an O_2 precursor species. It seems likely that, at the present time, the presence of precursor species or at least a two-stage reaction process is evidently enough from many experimental studies [1, 3, 22, 24–30].

Hattori *et al.* [31] called attention to the fact that investigations on the initial stage of

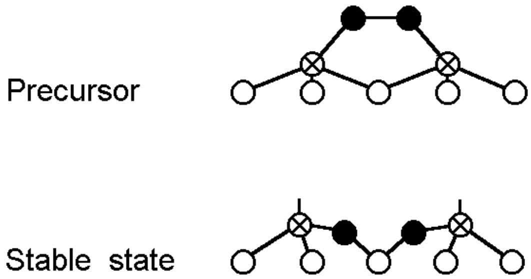

Fig 4. Suggested model for oxygen adsorption on Si(111) involving precursor and stable state. The position of silicon (open circles) and oxygen atoms (solid circles) is given for an unreconstructed surface (from Ref. [28]). (*Reproduced by permission of the publishers of Journal of Physical Review B)*

oxidation of silicon performed so far were mostly limited to the oxidation of a clean silicon in oxygen with a pressure of less than 1 Pa. However, under low oxygen pressure the decomposition of thermal oxide occurs. Hattori *et al.* [31] investigated the initial stages of the SiO_2 formation on a Si(111) surface at 300 °C in oxygen with a pressure of 133 Pa. The authors found that the SiO_2/Si interfacial transition layer is formed in three steps characterized by three different oxidation rates. It is deduced that these three oxidation rates are governed mostly by the formation rates of Si^{1+}, Si^{2+} and Si^{3+}, respectively.

1.2. STRUCTURE

The reaction process of oxygen with an Si(111) surface is rather complex and non-uniform and the structure of the O/Si(111) surface is still far from being understood. Recent STM studies [1, 6, 27, 32] showed that reacted adatoms at the initial stage show roughly a 4:1 preference for the faulted half and a 2:1 preference for the corners of the 7 × 7 unit cell. STM and STS results of Pelz and Koch [1] revealed at least a two-stage reaction process. It was supposed by Tokumoto *et al.* [27] that, at the initial stage of adsorption, oxygen is adsorbed in the topmost site of the surface adatom forming Si–O configuration and then in the bridge site forming Si–O–Si configuration which causes the disorder in the STM image. The two-stage model was also suggested by Höfer *et al.* [28]: in the initial stage of oxygen adsorption on Si(111) surfaces, a metastable molecular state is found which precedes dissociation and insertion of oxygen atoms in bridging positions between first- and second-layer silicon atoms as shown in Fig. 4.

By using EXAFS Stöhr *et al.* [33] showed the O–Si bond length at the adsorption stage (1.65 ± 0.03 Å) to be almost the same as in bulk SiO_2 (1.61 Å).

1.3. PROPERTIES

1.3.1. Desorption

Oxide decomposition in the mono- and multi-layer regime was examined with TPD by Engstrom *et al.* [3]. The only species observed in the TPD spectra was SiO at 900–1300 K. Both increasing oxygen coverages and higher adsorption temperatures lead to higher decomposition temperatures for the oxygen adlayer formed. The temperature of the TPD peak increases from ≈ 1050 K for 1.2 ML to ≈ 1120 K for 5.4 ML. At high coverages (≥ 4 ML), the decomposition reaction appears to be heterogeneous, involving void nucleation and growth.

1.3.2. Surface Stress

Sander and Ibach [34] determined the surface stress induced by the RT adsorption of oxygen on the Si(111) surface. As a result of the breaking of the Si–Si bonds and the formation

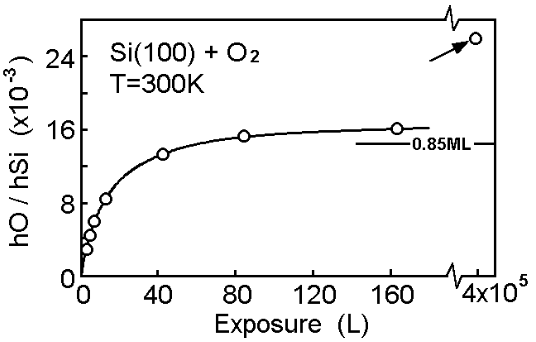

Fig 5. Normalized Auger oxygen signal, h_O/h_{Si}, versus O_2 exposure. Each data point is taken after a new exposure on a freshly cleaned surface (from Ref. [10]). (*Reproduced by permission of Elsevier Science Publishers BV)*

of the Si–O–Si bonds the O/Si(111) system shows a compressive stress of 7200 dyn/cm per monolayer oxygen coverage.

2. (100) ORIENTATION

Oxygen is known to induce only a 1 × 1 reconstruction on the Si(100) surface.

2.1. PHASE DIAGRAM

Figure 5 shows the normalized Auger oxygen signal h_O/h_{Si} as a function of O_2 exposure as reported by Keim *et al.* [10]. The possible excitation of oxygen was carefully avoided in this study. Adsorption of O_2 reaches 0.85 ML coverage at $\approx$ 65 L. Additional exposure results in a slow continuous uptake of oxygen in the exposure range studied ($\approx 10^6$ L). For exposures up to at least 300 L the LEED pattern still shows some patches having the 2 × 1 structure.

The adsorption of atomic oxygen (as released by N_2O) is shown in Fig. 6 [10], where the ratio h_O/h_{Si} is shown as a function of N_2O exposure. The top part of this figure qualitatively indicates the observed LEED patterns. During initial exposure ($0–3 \times 10^4$ L), the 2 × 1 two-domain LEED pattern remains well visible. After 4.5×10^4 L, this LEED pattern almost completely transforms into a 1×1 structure. For exposures beyond 2×10^5 L, i.e. at saturation, only a very weak 1 × 1 LEED pattern with a highly intense background is observed. At saturation the oxygen coverage turned out to be 0.85 ± 0.10 ML [11].

The interaction of O_2 with the clean Si(100)2 × 1 surface was found in Ref. [10] to lead to chemisorption with the initial sticking probability of $S(\mathrm{O}) = 0.09 \pm 0.01$ at RT. However, Ranke and Xing [35] found this value to be 0.18. The initial reaction probability was found to be $(2.4 \pm 0.2) \times 10^{-5}$ by Keim *et al.* [10] for the N_2O adsorption.

Figure 7 sums up the oxygen uptake on Si(100)2 × 1 surface over investigated temperature T_s and O_2 pressure ranges at constant exposure times (133 s) in accordance with the experimental results of Lutz *et al.* [36]. Whatever the used constant pressure (or exposure), these data reveal, as a function of T_s, a maximum for the oxygen coverage separating a low T_s region where the O chemisorption increases slowly with T_s $\{\mathrm{Si(s)} + \mathrm{O_2(g)} \rightarrow \mathrm{SiO_2(s)}\}$ from a high T_s region where the O desorption (in the SiO form in the prevailing mechanism $\{\mathrm{O_2(g)} + 2\ \mathrm{Si(s)} \rightarrow \mathrm{SiO(g)}\}$ and determines a rapid decrease of the oxygen coverage. The T_s at which this maximum takes place is pressure dependent and determines a critical pressure P_c and temperature T_{sc}. This critical pressure increases with increasing temperature. According to Smith and Ghidini [21], the critical pressure P_c and sample temperature T_s follow Arrhenius

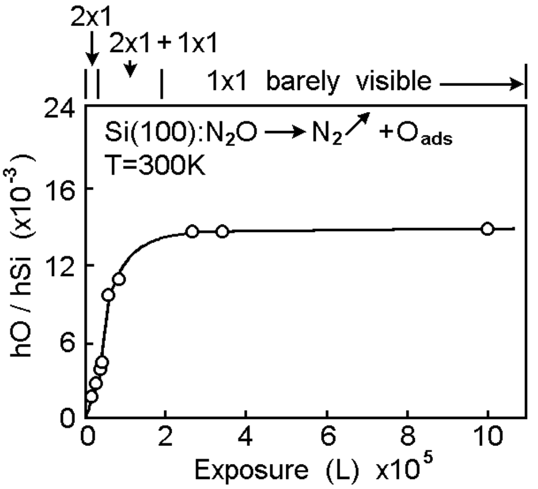

Fig 6. Normalized Auger oxygen signal, h_O/h_{Si}, versus N_2O exposure. Each data point is taken after new exposure on a freshly cleaned surface. The top part qualitatively indicates the observed LEED patterns (from Ref. [10]). (*Reproduced by permission of Elsevier Science Publishers BV)*

relation

$$P_c(T_{sc}) = P_0 \exp(-\Delta E/kT_s)$$

with $P_0 = 2.0 \times 10^{12}$ Torr, $\Delta E = 3.83$ eV for O_2 + Si(100) reaction.

The investigation of the kinetics of oxidation reaction by Memmert and Yu [22] by monitoring the evolution of SiO has shown that the reaction pathway is a serial combination of two first-order steps, and the time dependence of the SiO signal is proportional to:

$$\exp(-k_2t) - \exp(-k_1t)$$

as has been already mentioned above for the Si(111) surface. The activation energies for k_1 and k_2 are 3.0 ± 0.2 eV and 4.0 ± 0.37 eV, respectively.

2.2. STRUCTURE

Many experimental and theoretical works [17, 18, 26, 37–49] have been carried out to reveal atomic and electronic structures of oxygen on the Si(100) surface. However, despite considerable efforts microscopic understanding of oxygen adsorption on the Si(100) surface is not satisfactory.

The HREELS measurements [37,41] inferred the existence of the Si-O-Si bond at the early stage of oxidation. The Si–O–Si bond was also proposed from the SEXAFS measurement by Incoccia *et al.* [43]: the bridge site is characterized by a bond distance of 1.65 Å and a Si–O–Si bond angle of ≈ 120 °.

The possibility of molecular adsorption on Si(111) surfaces was suggested from the photoemission and near-edge X-ray adsorption data [50, 51] whereas only the atomic adsorption has been reported for the Si(100) surface.

A recent STM study of the the initial stages of oxidation of the Si(100)2 × 1 by Cahill and Avouris [49] showed that among new sites generated by the exposure of this surface to O_2 are the 1.4 Å high bumps on top of the surface. Upon annealing the O_2 exposed surface, or upon O_2 exposure at an elevated temperature, these bumps form highly anisotropic islands. The authors have presented evidence that these bumps and islands are made up of silicon ejected from the surface by the oxidation reaction.

The total energy band structure calculations done by Miyamoto and Oshiyama [46] re-

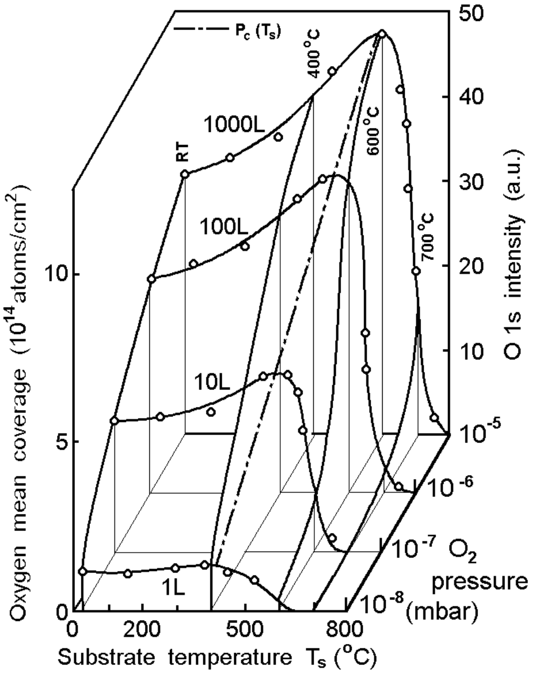

Fig 7. O 1s core levels intensities (right scale) and mean coverages (atoms/cm^2) (left scale) obtained for the initial oxidation stage of the Si(100) surface as a function of T_s or O_2 pressure at constant exposure times (133 s) (from Ref. [36]). (*Reproduced by permission of the publishers of Journal of Physical Review B)*

vealed the mechanism of dissociation and adsorption of oxygen on the Si(100) reconstructed surface. It was found that dissociation of an oxygen molecule occurs exothermically and is explained by electron transfer from the Si dangling bond to the antibonding orbital of the molecule. Several metastable atomic geometries for an adsorbed oxygen atom were also discovered in Ref. [46]. The total energy calculation done by Batra *et al.* [40] indicates that a hollow bridge site is energetically most favorable for oxygen adsorption. Smith and Wander [47, 48] found that atomic oxygen adsorbed at the dimer bridge sites. Moreover, the authors showed that the dimer and non-dimer bridge sites become equivalent at the high coverage limit giving rise to a 1 × 1 pattern as observed experimentally.

2.3. PROPERTIES

2.3.1. Desorption

Oxide decomposition in the mono- and multilayer regime was examined with TPD by Engstrom *et al.* [3]. The only species observed in the TPD spectra was SiO at 900–1300 K. Both increasing oxygen coverages and higher adsorption temperatures lead to higher decomposition temperatures for the oxygen adlayer formed. The TPD peak temperature increases from ~1050 for 1.2 ML to ~1200 K for 3.9 ML. Above the monolayer regime, adlayers formed on Si(100) decompose at higher temperatures than those on Si(111).

2.3.2. Surface Stress

Sander and Ibach [34] determined the surface stress induced by the RT adsorption of oxygen on the Si(100) surface. The adsorption of oxygen on a Si(100) surface leads to a tensile stress of +260 dyn/cm per monolayer oxygen coverage.

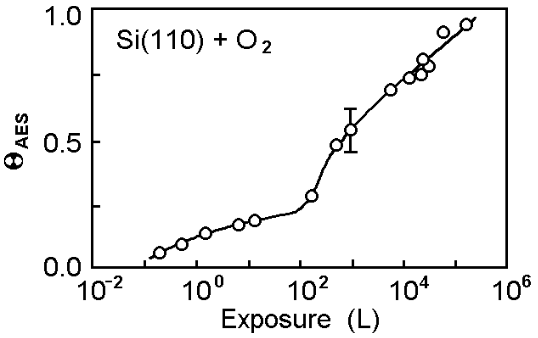

Fig 8. The fractional oxygen coverage θ_{AES} versus O_2 exposure of Si(110). Each data point is taken after new exposure to a freshly cleaned surface (from Ref. [58]). (*Reproduced by permission of American Institute of Physics)*

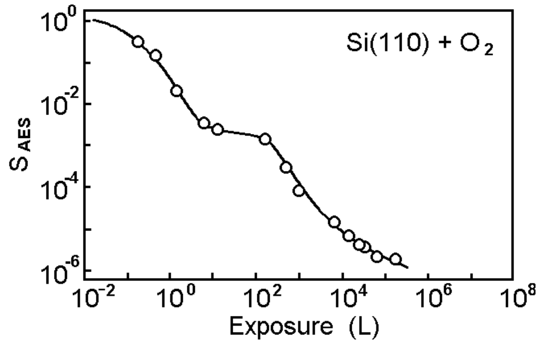

[h]

Fig 9. The sticking probability of O_2 to Si(110), S_{AES}, as a function of exposure (from Ref. [58]). (*Reproduced by permission of Elsevier Science Publishers BV)*

3. (110) ORIENTATION

Oxygen was reported to induce the 1 × 1 reconstruction on the nominally-clean Si(110)1 × 5 surface. (Now it is conventionally accepted that a 1 × 5 superstructure is induced by a very small amount of Ni impurity contamination.)

3.1. PHASE DIAGRAM

The interaction of oxygen with the Si(110) surface has received considerably less interest than the (111) and (100) surfaces [35, 52–60]. Displayed in Fig. 8 is the oxygen coverage (as estimated from AES data) versus O_2 exposure [58]. It can be seen that the oxygen uptake occurs in distinct stages. Keim *et al.* [58] discerned five adsorption stages.

LEED observations of Keim *et al.* [58] demonstrated that during initial exposure (0–2 L), i.e., at $0 \leq \theta \leq 0.15$ ML, the diffuse spots and faint streaks observed in addition to the 1 × 5 LEED pattern rapidly disappear and at around monolayer coverage, only a weak 1 × 1 pattern with a very high background intensity is observed.

The sticking probability of O_2 derived from the slope of the exposure curve in Fig. 8, is plotted versus O_2 exposure in Fig. 9. From this figure, Keim *et al.* [58] concluded that the initial sticking probability is near unity [56]. At around ML coverage, S_{AES} decreases to $\approx 10^{-6}$.

REFERENCES

[1] J. P. Pelz and R. H. Koch, *Phys. Rev. B* **42** (1990) 3761.

[2] P. A. Bennett, B. N. Halawith and A. P. Johnson, *J. Vac. Sci. Technol. A* **5** (1987) 2121.

[3] J. R. Engstrom, D. J. Bonser, M. M. Nelson and T. Engel, *Surf. Sci.* **256** (1991) 317.

[4] K. Fujiwara and H. Ogata, *J. Appl. Phys.* **48** (1977) 4360.

[5] J. A. Schaefer, F. Stucki, D. J. Frankel, W. Gopel and G. J. Lapeyre, *J. Vac. Sci. Technol. B* **2** (1984) 359.

[6] Ph. Avouris and I. -W. Lyo, *Surf. Sci.* **242** (1991) 1.

[7] W. Ranke and Y. R. Xing, *Surf. Sci.* **157** (1985) 339.

[8] M. Nishijima, H. Kobayashi, K. Edamoto and M. Onchi, *Surf. Sci.* **137** (1984) 473.

[9] M. Nishijima, K. Edamoto, Y. Kubota, H. Kobayashi and M. Onchi, *Surf. Sci.* **158** (1985) 422.

[10] E. G. Keim, L. Wolterbeek and A. Van Silfhout, *Surf. Sci.* **180** (1987) 565.

[11] E. G. Keim and A. Van Silfhaut, *Surf. Sci.* **216** (1989) L337.

[12] F. Rochet, S. Rigo, M. Froment, C. d'Anterroches, C. Maillot, H. Roulet and G. Dufor, *Advances in Physics* **35** (1986) 237.

[13] J. W. T. Ridgway, *Indian J. Phys. A* **52** (1978) 488.

[14] M. Tabe, T. T. Chiang, I. Lindau and W. E. Spicer, *Phys. Rev. B* **34** (1986) 2706.

[15] J. M. Gibson, *Surf. Sci.* **239** (1990) L531.

[16] F. Meyer and J. J. Vrakking, *Surf. Sci.* **38** (1973) 275.

[17] H. Ibach and J. E. Rowe, *Phys. Rev. B* **10** (1974) 710.

[18] R. Ludeke and A. Koma, *Phys. Rev. Lett.* **34** (1975) 1170.

[19] C. M. Garner, I. Lindau, C. Y. Su, P. Pianetta and W. E. Spicer, *Phys. Rev. B* **19** (1979) 3944.

[20] J. J. Lander and J. Morrison, *J. Appl. Phys.* **33** (1962) 2089.

[21] F. W. Smith and G. Ghidini, *J. Electrochem. Soc.* **129** (1982) 1300.

[22] U. Memmert and M. L. Yu, *Surf. Sci.* **245** (1991) L185.

[23] M. L. Yu and B. N. Eldridge, *Phys. Rev. Lett.* **58** (1987) 1691.

[24] A. Stockhausen, T. U. Kampen and W. Monch, *Appl. Surf. Sci.* **56–58** (1992) 795.

[25] P. Gupta, C. H. Mak, P. A. Coon and S. M. George, *Phys. Rev. B* **40** (1989) 7739.

[26] G. Holinger, J. F. Morar, F. J. Himpsel, G. Hughes and J. L. Jordan, *Surf. Sci.* **168** (1986) 609.

[27] T. Tokumoto, K. Miki, H. Murakami, H. Bando, H. Ono and K. Kajimura, *J. Vac. Sci. Technol. A* **8** (1990) 255.

[28] U. Hofer, P. Morgen and W. Wurth, *Phys. Rev. B* **40** (1989) 1130.

[29] U. Memmert and M. L. Yu, *Chem. Phys. Lett.* **164** (1989) 552.

[30] A. J. Schell-Sorokin and J. E. Demuth, *Surf. Sci.* **157** (1985) 273.

[31] T. Hattori, H. Nohira, Y. Tamura and H. Ogawa, *Japan J. Appl. Phys.* **31** (1992) L638.

[32] F. M. Leibsle, A. Samsavar and T. -C. Chiang, *Phys. Rev. B* **38** (1988) 5780.

[33] J. Stohr, L. I. Johansson, I. Lindau and P. Pianetta, *J. Vac. Sci. Technol.* **16** (1979) 1221.

[34] D. Sander and H. Ibach, *Phys. Rev. B* **43** (1991) 4263.

[35] W. Ranke and Y. R. Xing, *Surf. Sci.* **157** (1985) 353.

[36] F. Lutz, J. L. Bischoff, L. Kubler and D. Bolmont, *Phys. Rev. B* **40** (1989) 10356.

[37] H. Ibach, H. D. Bruchmann and H. Wagner, *Appl. Phys. A* **29** (1982) 113.

[38] S. Ciraci, S. Elliatioglu and S. Erkoc, *Phys. Rev. B* **26** (1982) 5716.

[39] V. Barone, F. Lelj, N. Russo and M. Toscano, *Surf. Sci.* **162** (1985) 230.

[40] I. P. Batra, P. S. Bagus and K. Hermann, *Phys. Rev. Lett.* **52** (1984) 384.

[41] J. A. Schaefer and W. Gopel, *Surf. Sci.* **155** (1985) 535.

[42] G. Hollinger and F. J. Himpsel, *J. Vac. Sci. Technol. A* **1** (1983) 640.

[43] L. Incoccia, A. Balerna, S. Cramm, C. Kunz, F. Senf and I. Storjohann, *Surf. Sci.* **189–190** (1987) 453.

[44] C. Silvestre and M. Shayegan, *Solid State Commun.* **77** (1991) 735.

[45] Y. Miyamoto, A. Oshiyama and A. Ishitani, *Solid State Commun.* **74** (1990) 343.

[46] Y. Miyamoto and A. Oshiyama, *Phys. Rev. B* **41** (1990) 12680.

[47] P. V. Smith and A. Wander, *Surf. Sci.* **219** (1989) 77.

[48] P. V. Smith and A. Wander, *J. Phys. :Cond. Matt.* **1** (1989) SB205.

[49] D. G. Cahill and Ph. Avouris, *Appl. Phys. Lett.* **60** (1992) 326.
[50] U. Hofer, P. Morgen, W. Wurth and E. Umbach, *Phys. Rev. Lett.* **55** (1985) 2979
[51] U. Hofer, A. Puschmann and D. Umbach E. Coulman, *Surf. Sci.* **211–212** (1989) 948.
[52] B. Carriere and J. P. Deville, *Surf. Sci.* **80** (1979) 278.
[53] P. E. Wierenga, M. J. Sparnaay and A. VanSilfhout, *Surf. Sci.* **99** (1980) 59.
[54] P. Morgen, *J. Vac. Sci. Technol.* **18** (1981) 908.
[55] S. Tougaard, P. Morgen and J. Onsgaard, *Surf. Sci.* **111** (1981) 545.
[56] E. G. Keim and A. Van Silfhout, *Surf. Sci.* **186** (1987) L557.
[57] E. G. Keim, A. Van Silfhout and L. Wolterbeek, *J. Vac. Sci. Technol. A* **5** (1987) 1019.
[58] E. G. Keim, A. Van Silfhout and L. Wolterbeek, *J. Vac. Sci. Technol. A* **6** (1988) 57.
[59] E. G. Keim, H. Wormeester and A. Van Silfhout, *J. Vac. Sci. Technol. A* **8** (1990) 2747.
[60] H. Wormeester and E. G. Keim, *Vacuum* **41** (1990) 596.
[61] R. E. Kirby and D. Lichtman, *Surf. Sci.* **41** (1974) 447.
[62] P. Morgen, W. Wurth and E. Umbach, *Surf. Sci.* **152–153** (1985) 1086.
[63] R. E. Schlier and H. E. Farnsworth, *J. Chem. Phys.* **30** (1959) 917.
[64] C. A. Carosella and J. Comas, *Surf. Sci.* **15** (1969) 303.
[65] G. Rovida, E. Zanazzi and E. Ferroni, *Surf. Sci.* **14** (1969) 93.
[66] G. M. Guichar, C. A. Sebenne, G. A. Garry and M. Balkanski, *Surf. Sci.* **58** (1976) 374.
[67] P. E. Wierenga, A. Van Silfhout and M. J. Sparnaay, *Surf. Sci.* **87** (1979) 43.
[68] J. Eisinger and J. T. Law, *J. Chem. Phys.* **30** (1959) 410.
[69] B. A. Joyce and J. H. Neave, *Surf. Sci.* **27** (1971) 499.
[70] N. Kasupke and M. Henzler, *Surf. Sci.* **92** (1980) 407.
[71] H. Ibach, K. Horn, R. Dorn and H. Luth, *Surf. Sci.* **38** (1973) 433.
[72] R. J. Archer and G. W. Gobely, *J. Phys. Chem. Solids* (1964) 343.

(P)

PHOSPHORUS

1. (111) ORIENTATION

Up to now there have been only a few publications on phosphorus surface phases on Si(111). The reconstructions reported in these works are $6\sqrt{3} \times 6\sqrt{3}$—$R30\,°$, $4 \times 4, 7 \times 7$, 1×1, $2\sqrt{3} \times 2\sqrt{3}$—$R30°$.

1.1. PHASE DIAGRAM

1.1.1. P Deposition

Lander and Morrison [1] found a $6\sqrt{3} \times 6\sqrt{3}$ reconstruction when the Si(111) surface held at 300 to 900 °C was exposed to phosphorus vapor at pressure below 1×10^{-4} Torr. The sketch of the LEED pattern (reciprocal lattice) from this structure is shown in Fig. 1. The main feature of this pattern is that the fractional order spots are only present in clusters around the integral spots.

A second phosphorus surface structure was obtained in Ref. [1] when the Si(111) sample

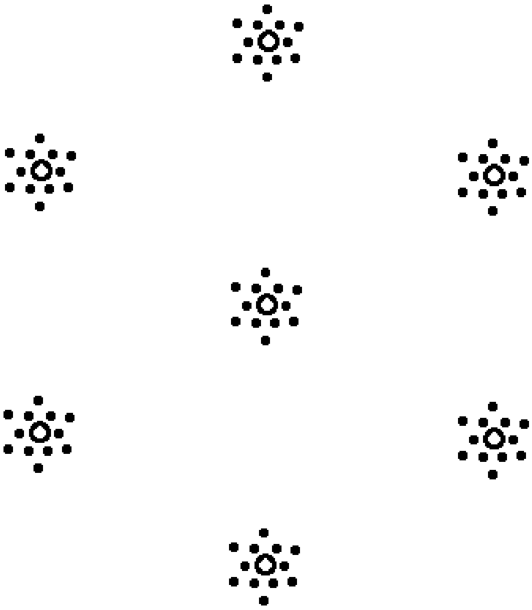

Fig 1. Sketch of the LEED pattern (reciprocal lattice) from the Si(111)$6\sqrt{3} \times 6\sqrt{3}$—$R30°$–P (from Ref. [1]). (*Reproduced by permission of Elsevier Science Publishers BV)*

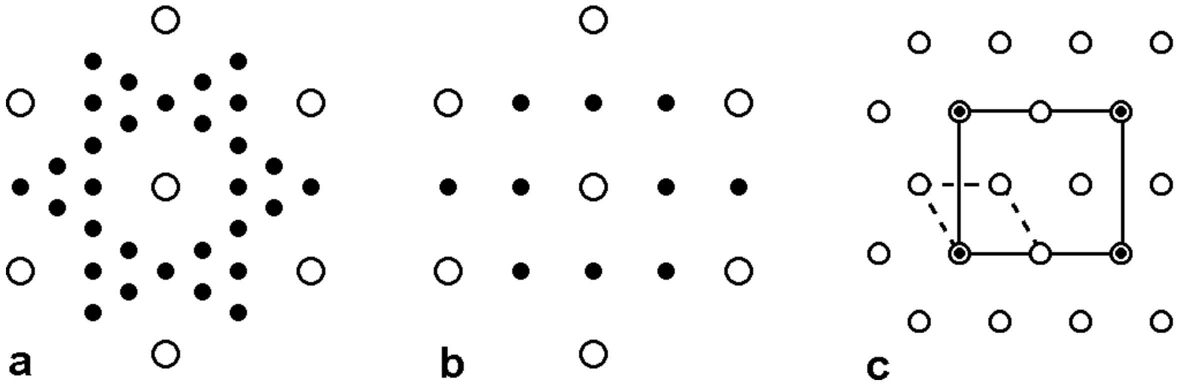

Fig 2. (a) Sketch of the LEED pattern from the "Si(111)–4–P" structure (according to notation from Ref. [1]). This LEED pattern also corresponds to the three-domain $\begin{pmatrix}2 & 0\\ 1 & 2\end{pmatrix}$ structure. (b) Sketch of the LEED pattern from the single-domain $\begin{pmatrix}2 & 0\\ 1 & 2\end{pmatrix}$ structure. (c) Real-space unit mesh of the $2 \times \sqrt{3}$, i.e. $\begin{pmatrix}2 & 0\\ 1 & 2\end{pmatrix}$ reconstruction, shown by solid lines and 1×1 unit mesh shown by dashed lines

was exposed to phosphorus at a pressure of about 1×10^{-5} Torr for about five minutes and then annealed at about 300 °C for a few minutes. The sketch of the LEED pattern from this structure is shown in Fig. 2a. Lander and Morrison labeled the structure as Si(111)–4–P (i.e. Si(111)4×4–P in contemporary notation) assuming the extinction of selected fractional order reflections. However, the above assumption is not necessary if the LEED pattern of Fig. 2(a) is treated as resulting from the three-domain $\begin{pmatrix}2 & 0\\ 1 & 2\end{pmatrix}$ structure. Figure 2(b) presents the single-domain $\begin{pmatrix}2 & 0\\ 1 & 2\end{pmatrix}$ structure for lucidity. It can be written also as $2 \times \sqrt{3}$ (see Fig. 2(c)). However, one must bear in mind that this structure is rectangular but not hexagonal.

1.1.2. PH_3 Exposure

Van Bommel and Meyer [2] and Van Bommel and Crombeen [3] observed the formation of a number of diffraction patterns for the interaction of PH_3 with the Si(111) surface. It was suggested that hydrogen was completely removed at temperatures exceeding 500 °C and therefore the study was mainly concerned with the surface structures of phosphorus on Si(111). However, it has been shown recently by Wallace *et al.* [4] that some small concentration of hydrogen is still present on the surface even upon annealing at about 900 °C.

The results of Ref. [2] are summarized at "pressure–temperature" in the 2D phase diagram shown in Fig. 3. Below 500 °C an ordered adsorption of PH_3 occurs forming a 7×7 structure. Heating to 500 °C shows a sudden pressure rise in the chamber, which is due to desorbed hydrogen. All fractional order reflections disappear and a 1×1 structure forms. Above 525 °C, the irreversible transition from 1×1 to $6\sqrt{3}\times6\sqrt{3}$ is observed. Decomposition of the $6\sqrt{3} \times 6\sqrt{3}$ surface phase at higher temperatures leads to the 1×1 structure. The transition between these two structures is reversible under the influence of PH_3. The formation of the $2\sqrt{3} \times 2\sqrt{3}$ structure is very difficult and it generally takes from 0.5 to 1.5 hours before the appearance of the fractional order reflections. At the high-temperature side a reversible transition $2\sqrt{3} \times 2\sqrt{3} \longleftrightarrow 1 \times 1$ takes place.

The formation of the 1×1–P phase has been recently confirmed in Ref. [5]. The phase was formed by 5 L PH_3 exposure followed by annealing at $520 < T < 720$ °C.

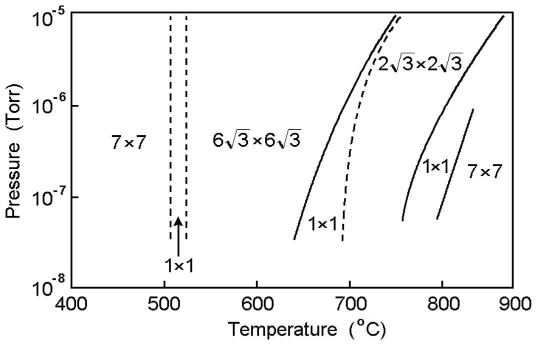

Fig 3. "Pressure-temperature" 2D phase diagram of the reaction between PH_3 and the silicon (111) surface (- - -) irreversible reactions. (—) reversible transitions under influence of PH_3 (from Ref. [2]). (*Reproduced by permission of Elsevier Science Publishers BV)*

1.2. STRUCTURE

1.2.1. Si(111)1 × 1–P

Based on ISS and LEED results, Bozso and Avouris [5] suggested that, in the 1 × 1 phase, P substitutes for the first-layer Si atoms of the Si(111) surface. Thus, the surface structure they found for the 1 × 1–P surface is analogous to the structure formed by As on Si(111). The value of about 1 ML P coverage determined in the LEED–AES study [3] for the 1 × 1–P phase is consistent with this model.

1.2.2. Si(111)$6\sqrt{3} \times 6\sqrt{3}$–P

Van Bommel and Meyer assumed that $6\sqrt{3} \times 6\sqrt{3}$—$R30^\circ$ cluster pattern corresponds to a densely packed phosphorus layer (average coverage 3.3 P per Si surface atom) atop the Si(111) surface. In this case, the fractional order spots in the LEED pattern are formed by multiple diffraction by the Si substrate and phosphorus layer.

1.3. PROPERTIES

1.3.1. Passivation

Bozso and Avouris [5] showed that the Si(111)1 × 1–P surface has no dangling bonds and is chemically inert. The P terminated Si(111) surface is extremely passive not only towards reaction with N_2O, NO and O_2 but also towards adsorbing them. For example, in the case of oxygen, an exposure of over 3000 L at RT shows no sign of adsorption on or reaction with the surface [5].

1.3.2. Desorption

Taylor *et al.* [6] reported that surface Si-P bonds break to form P_2 gas at temperatures beyond about 630 °C. The desorption proceeds according to second-order kinetics. The determined kinetic parameters are $v = 10^{2\pm1}$ cm^2 s^{-1} and $E_{\mathrm{d}} = 3.8$ eV.

2. (100) ORIENTATION

Phosphorus does not induce any new reconstruction on the Si(100)2 × 1 surface.

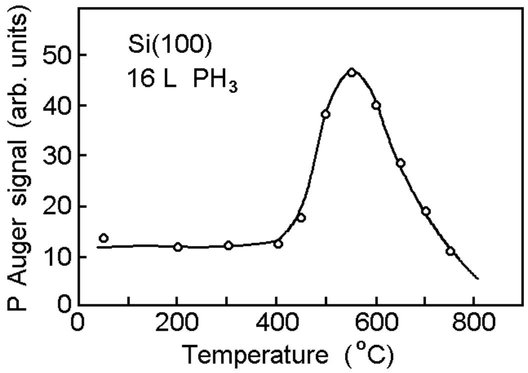

Fig 4. Phosphorus Auger signal after exposing a Si(100) surface to 5×10^{-7} Torr of PH_3 for 100 s at various temperatures. The rapid rise above 400 °C is correlated with the desorption of hydrogen. The decrease after 550 °C is correlated with the thermal removal of phosphorus (from Ref. [7]). (*Reproduced by permission of American Institute of Physics)*

2.1. PHASE DIAGRAM

Yu and Meyerson [7] studied the adsorption of PH_3 on Si(100) by means of LEED and AES.

The results suggest that at room temperature PH_3 molecules probably form a 2×1 ordered layer atop the Si(100) surface. A possible configuration is that the lone pair of electrons on the PH_3 molecule form two σ bonds with the dangling bonds of two adjacent Si surface atoms preserving the 2×1 periodicity. As a result PH_3 adsorption modifies the intensities of the LEED spots from the clean 2×1 reconstructed Si(100) surface but it generates no new spots.

At temperatures above 400 °C, hydrogen desorbs from the surface. More Si sites become available for PH_3 adsorption and the saturation phosphorus coverage increases as a result (Fig. 4). Further enhancement of the saturation coverage attains at higher temperatures ($\geq$ 500 °C) when phosphorus atoms can actually displace surface Si atoms in analogy to the occupation of substitutional sites by phosphorus dopants in bulk Si. This causes significant roughening of the surface as indicated by strong streaks on the 2×1 LEED pattern.

At temperatures above 550 °C, thermal desorption of the adsorbed phosphorus atoms becomes significant (see Fig. 4).

REFERENCES

[1] J. J. Lander and J. Morrison, *J. Chem. Phys.* **37** (1962) 729.
[2] A. J. Van Bommel and F. Meyer, *Surf. Sci.* **8** (1967) 381.
[3] A. J. Van Bommel and J. E. Crombeen, *Surf. Sci.* **36** (1973) 773.
[4] R. M. Wallace, P. A. Taylor, W. J. Choyke and J. T. Yates, *J. Appl. Phys.* **68** (1990) 3669.
[5] F. Bozso and Ph. Avouris, *Phys. Rev. B* **43** (1991) 1847.
[6] P. A. Taylor, R. M. Wallace, W. J. Choyke and J. T. Yates Jr. , *Surf. Sci.* **238** (1990) 1.
[7] M. L. Yu and B. S. Meyerson, *J. Vac. Sci. Technol. A* **2** (1984) 446.

(Pb)

LEAD

1. (111) ORIENTATION

The 1×1, 7×7 structures and several (up to four) different surface phases resulting in a $\sqrt{3} \times \sqrt{3}$—$R30°$ reconstruction were detected for submonolayer Pb films on the silicon (111) surface.

1.1. PHASE DIAGRAM

Starting from the early LEED work by Estrup and Morrison [1], the formation of surface phases in the Pb/Si(111) system has been investigated by Saitoh *et al.* using in addition ISS [2], Yaguchi *et al.* using RHEED [3], Quentel *et al.* using *in situ* ellipsometry [4, 5], Le Lay *et al.* using LEED and AES [6,7], Ganz *et al.* using LEED, RBS and STM [8] and Hadley *et al.* [9] using STM.

The main results of the above investigations are summarized in the phase diagram drawn by Yaguchi *et al.* (Fig. 1).

The growth of Pb on Si(111)7×7 follows the Stranski–Krastanov growth mechanism but the 2D intermediate layers obtained at different growth temperatures differ in structure. At temperatures close to room temperature, the intermediate layer is a Pb(111) epitaxial layer, with Pb $[\bar{1}10]$ ∥ Si $[\bar{1}10]$. A sketch of the LEED pattern of a Pb(111) layer is shown in Fig. 2. This pattern is identical to the one labelled Si(111)7×7–Pb by Estrup and Morrison [1] and

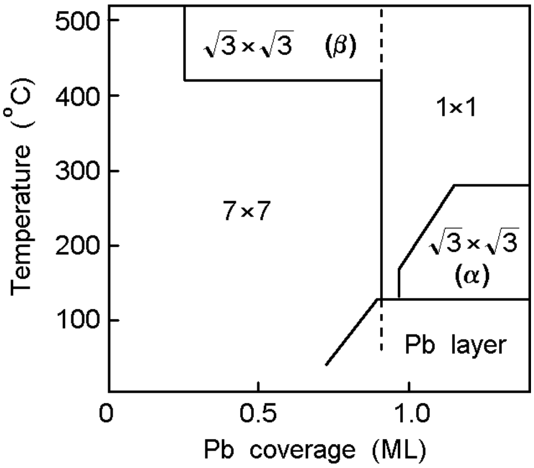

Fig 1. Two-dimensional phase diagram of the Pb/Si(111) system (from Ref. [3]). (*Reproduced by permission of Elsevier Science Publishers BV)*

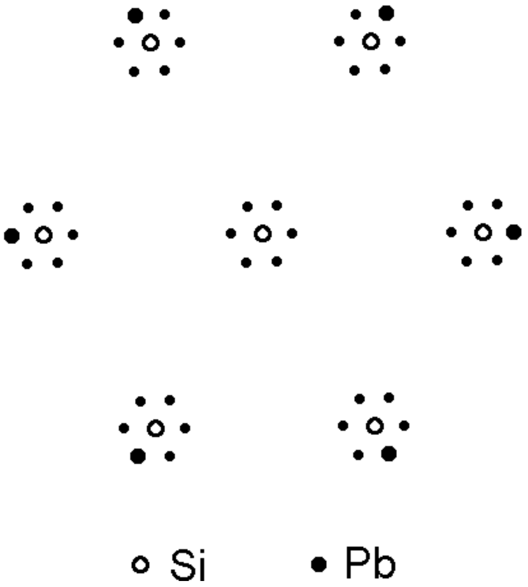

Fig 2. Illustration of the LEED pattern from an epitaxial Pb(111) layer (from Ref. [2]). (*Reproduced by permission of Elsevier Science Publishers BV)*

this notation for this phase has been widely adopted in literature.

When heated, the Pb(111) epitaxial layer, i.e. 7 × 7 Pb, converts irreversibly into a $\sqrt{3} \times \sqrt{3}$—$R30°$–Pb (α) (in short $\sqrt{3}_\alpha$) structure, probably consisting of 1.3 ML of Pb [1–3]. This $\sqrt{3}_\alpha$ reconstruction exists up to about 300 °C where it undergoes a phase transition into a 1 × 1 structure [3, 6, 10, 11]. When Pb coverage is less than 0.8 ML, the 1 × 1 structure observed at high temperatures is stable at RT, while for coverages exceeding 0.8 ML, a $\sqrt{3} \times \sqrt{3}$ (α) structure is restored upon cooling of the 1 × 1 [2].

At high growth temperatures, a $\sqrt{3} \times \sqrt{3}$—$R30°$–Pb (β) structure is observed at the Pb coverage exceeding 0.2 ML [1–3].

The results of the LEED–AES observations by Le Lay *et al.* [6, 11] suggested, however, that there are three $\sqrt{3} \times \sqrt{3}$—$R30°$ reconstructed surface phases (the first completing at $\theta \approx 1/3$ ML (abbreviated $\sqrt{3}_1$), the second ($\sqrt{3}_2$) at $\theta \approx 2/3$ ML and the third ($\sqrt{3}_3$) at about 1 ML) than two ($\sqrt{3}_\alpha$ and $\sqrt{3}_\beta$). The superstructures with the same $\sqrt{3} \times \sqrt{3}$—$R30°$ unit mesh display different intensities of fractional order spots in the LEED pattern: the $\sqrt{3}_1$ structure ($\theta \approx 1/3$ ML) is characterized by absent extra spots (leaving a 1 × 1 pattern) at low energy, while the $\sqrt{3}_2$ structure ($\theta \approx 2/3$ ML) displays all extra spots at any energy. The third structure ($\sqrt{3}_3$) which corresponds to $\sqrt{3}_\alpha$ is characterized by a systematic extinction of the odd fractional order spots [11]. These three reconstructions correlate fairly with the three different segments in the dependence of the ellipsometric signals versus Pb coverage in the submonolayer region [4, 5] and with segments with a different slope in the dependence of the Pb Auger peak height versus time upon desorption [11].

Ganz *et al.* reported in recent work [8] that they were unable to observe the 2/3 ML $\sqrt{3} \times \sqrt{3}$ phase reported by Le Lay *et al.* [6, 11]. Instead, they found a new $\sqrt{3} \times \sqrt{3}$—$R30°$ phase at 1/6 ML Pb, which displays a similar LEED pattern to that of $\sqrt{3} \times \sqrt{3}$—$R30°$ at 1/3 ML but with brighter spots.

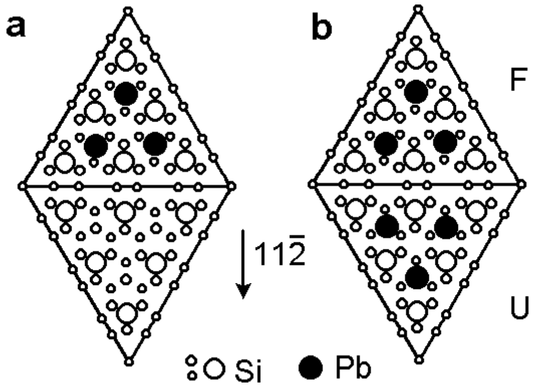

Fig 3. Models showing Pb adatom positions for (a) 0.06 ML Pb and (b) 0.12 ML Sb. The Pb adatoms are above and between the Si adatoms. Small circles represent the first and second Si(111) substrate layer, large circles represent Si and Pb adatoms. The faulted and unfaulted halves of the 7 × 7 unit cell are indicated (from Ref. [8]). (*Reproduced by permission of the publishers of Journal of Physical Review B)*

1.2. STRUCTURE

1.2.1. Si(111)7 × 7–Pb

One should differ between the two 7 × 7 structures observed in the Pb/Si(111) system. The first structure corresponds to the initial Si(111)7 × 7 surface modified by a small amount ($\sim$ 0.1 ML) of adsorbed Pb adatoms. The second corresponds to the complete Pb 2D layer at coverage of about 1.3 ML.

*

Low-coverage Si(111)7 × 7–Pb Phase The initial stages of RT deposition of Pb on to Si(111)7 × 7 were studied by means of STM by Ganz *et al.* [8,12] and Hadley *et al.* [9]. It was found that, at low coverages, Pb atoms form triangles occupying the sites above and between the Si adatoms, while the underlying Si(111)7 × 7 reconstruction remains relatively unchanged. At coverages up to $\sim$ 0.06 ML, preferential occupation of the faulted half of the 7 × 7 unit cell was detected as shown in Fig. 3(a). At 0.12 ML Pb, the entire 7 × 7 unit cell is covered by Pb adatoms (see Fig. 3(b)).

*

High-coverage Si(111)7 × 7–Pb Phase Grey *et al.* [13,14] using X-ray diffraction showed conclusively that a 7 × 7 reconstruction which displays a LEED pattern like that shown in Fig. 2 is formed by a Pb close-packed layer (4% compressed relative to a bulk Pb(111) layer) in parallel orientation relative to the Si(111) substrate with a mesh of 8 × 8 Pb atoms on a 7 × 7 unit cell as shown in a contour map of the Patterson function (Fig. 4). The underlying Si(111)7 × 7 DAS structure is not severely altered keeping the stacking faulted bilayer and the dimers but without Si adatoms.

1.2.2. Si(111)$\sqrt{3} \times \sqrt{3}$–Pb

There are several phases in the Pb/Si(111) system which show an $\sqrt{3} \times \sqrt{3}$—$R30°$ reconstruction.

*

Si(111)$\sqrt{3} \times \sqrt{3}$–Pb (α) ($\theta \simeq 1.3$ ML) The model accepted for the $\sqrt{3} \times \sqrt{3}$–Pb (α) phase is basically similar to that proposed in early work by Estrup and Morrison [1] (Fig. 5). This phase is also (like a 7 × 7–Pb phase) a closed-packed Pb layer but rotated by 30° with respect to the underlying Si(111) surface. The $\sqrt{3} \times \sqrt{3}$–Pb (α) phase is incommensurate as revealed

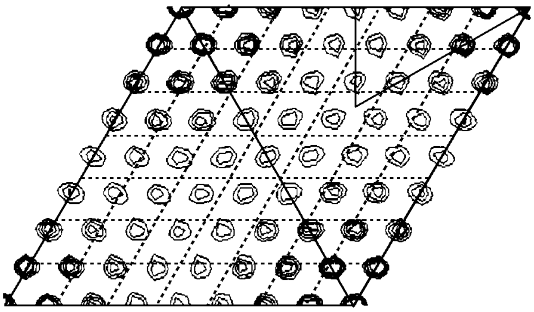

Fig 4. Contour map of the Si(111)7 × 7–Pb Patterson function (electron density autocorrelation function). Only positive contours are shown. The solid right angle is the irreducible unit (from Ref. [13]). (*Reproduced by permission of Plenum Publishing Corp.)*

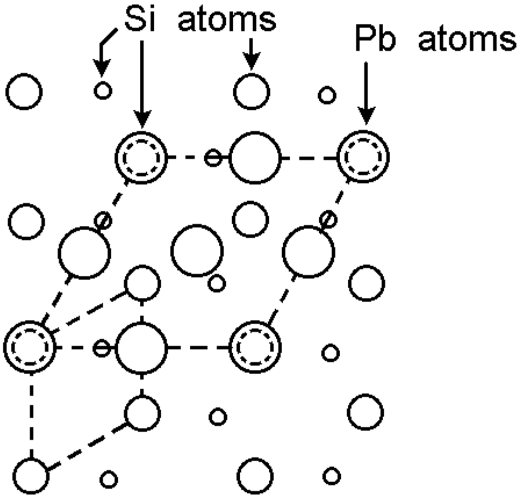

Fig 5. Model for $\sqrt{3} \times \sqrt{3}$–Pb (α) phase showing the Pb layer (large circles) and the Si atoms of the top double-layer (medium and small circles) (from Ref. [1]). (*Reproduced by permission of Elsevier Science Publishers BV)*

by careful analysis of the RHEED [15] and XRD data [13,14]. The Pb (1,0) reflection appears at the (0.65, 0.65) position of the Si(111) reciprocal unit cell. If the hexagonal Pb(111) were commensurate these spots would appear at the (2/3, 2/3) position (Fig. 6). The satellite peak seen as shoulder on the scan plot in Fig. 6b originates from the interaction between the Si substrate and the incommensurate Pb overlayer which modulates the Pb overlayer by producing domain walls [13, 14].

The $\sqrt{3} \times \sqrt{3}$–Pb (α) phase is incommensurate since it cannot adopt the 5% compression required for producing a commensurate structure [7].

*

Si(111) $\sqrt{3} \times \sqrt{3}$–Pb (β) ($\theta \simeq 1/3$ ML) The $\sqrt{3} \times \sqrt{3}(\beta)$ phase consists of 1/3 ML Pb, i.e. with one Pb atom per unit cell [2, 8, 14]. STM [8] and tensor LEED [16] studies revealed that the Pb atom occupies the T_4 site (the Pb atom is above the Si atom in the second surface layer). So the atomic structure of the $\sqrt{3} \times \sqrt{3}$–Pb (β) phase is essentially similar to that of the $\sqrt{3} \times \sqrt{3}$ phases formed by Sn and Group 3 elements (In, Al, Ga).

*

Si(111) $\sqrt{3} \times \sqrt{3}$–Pb ($\theta \simeq 1/6$ ML) Ganz *et al.* using STM [8, 12] found an unusual ("mosaic") $\sqrt{3} \times \sqrt{3}$ phase at low Pb coverages. This phase is built of Pb and Si adatoms occupying T_4 sites. The Pb and Si adatoms in this phase are not randomly distributed but form alternating chains. The ideal coverage for the mixed Si:Pb $\sqrt{3} \times \sqrt{3}$ phase is 1/6 ML

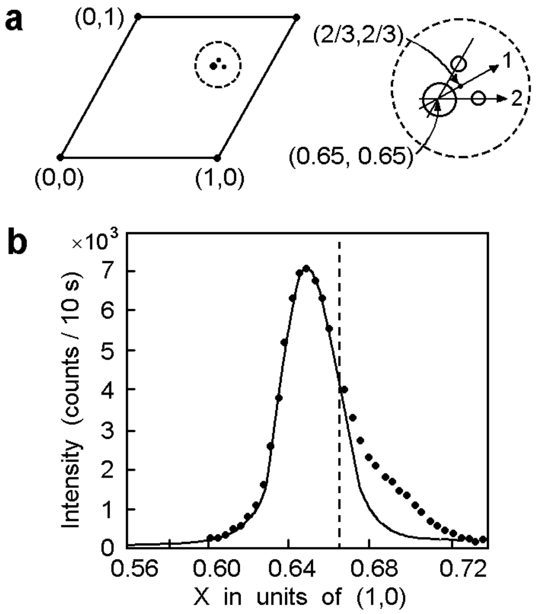

Fig 6. (a) Sketch of the reciprocal space for the incommensurate $\sqrt{3}\times\sqrt{3}$–Pb (α) phase. The expanded region around the (2/3, 2/3) position shows the fundamental Pb peak of the incommensurate phase at (0.65, 0.65). The expected peaks, owing to domain wall formations are indicated. (b) Solid line, measured radial scan through the fundamental Pb reflection at (0.65, 0.65), scan (1) in (a). The vertical dashed line indicates the commensurate (2/3, 2/3) position. Points: measured scan in the (1,0) direction, scan 2 in (a). A shoulder can be seen near the expected satellite position (from Ref. [14]). (*Reproduced by permission of Elsevier Science Publishers BV)*

(1:1 Pb:Si ratio) [8].

The PES results of Carlisle *et al.* [17] and Karlsson *et al.* [18] provided evidence for the above model of the mosaic $\sqrt{3}\times\sqrt{3}$ phase with 1:1 mixture of Pb and Si adatoms. Further, the PES results of Ref. [18] suggest the strong charge transfer between the different dangling-bond orbitals: the Pb adatom dangling bonds are fully occupied and the Si adatom dangling bonds are empty.

1.3. PROPERTIES

1.3.1. Desorption

Desorption of the Pb layer from a Si(111) surface was studied by Saitoh *et al.* [2], Le Lay *et al.* [11], and Ganz *et al.* [8,12].

Le Lay *et al.* stated that the desorption of about 1 ML of Pb proceeds in three kinetic steps correlating with the presence of three different Pb/Si(111) surface phases (see Fig. 7(a)). The first step corresponds to the very fast decrease of the Pb coverage from 1 to 2/3 ML, i.e. to the desorption of the 1 × 1–Pb layer leaving the $\sqrt{3}_2$ structure. The second step, from 2/3 to 1/3 ML, corresponds to the desorption of the $\sqrt{3}_2$ phase leaving behind the $\sqrt{3}_1$ phase. In this step, the Pb intensity decreases linearly, in other words, according to zero order kinetics ($\underset{\cdot}{N}/\underset{\cdot}{t}$ = const, where N is the number of adsorbed atoms). Such desorption kinetics is expected when 2D islands of the condensed phase desorb indirectly via a dilute 2D adsorbed gas in a stationary equilibrium. The third step, from 1/3 ML to zero coverage, corresponds to the desorption of the $\sqrt{3}_1$ phase leaving behind a clean 7 × 7 surface. This step is also characterized by zero order kinetics.

In the ISS study by Saitoh *et al.* [2], the thermal desorption process was divided into two steps: the desorption of the 1 × 1–Pb layer leaving behind the $\sqrt{3}\times\sqrt{3}$ (β) phase consisting

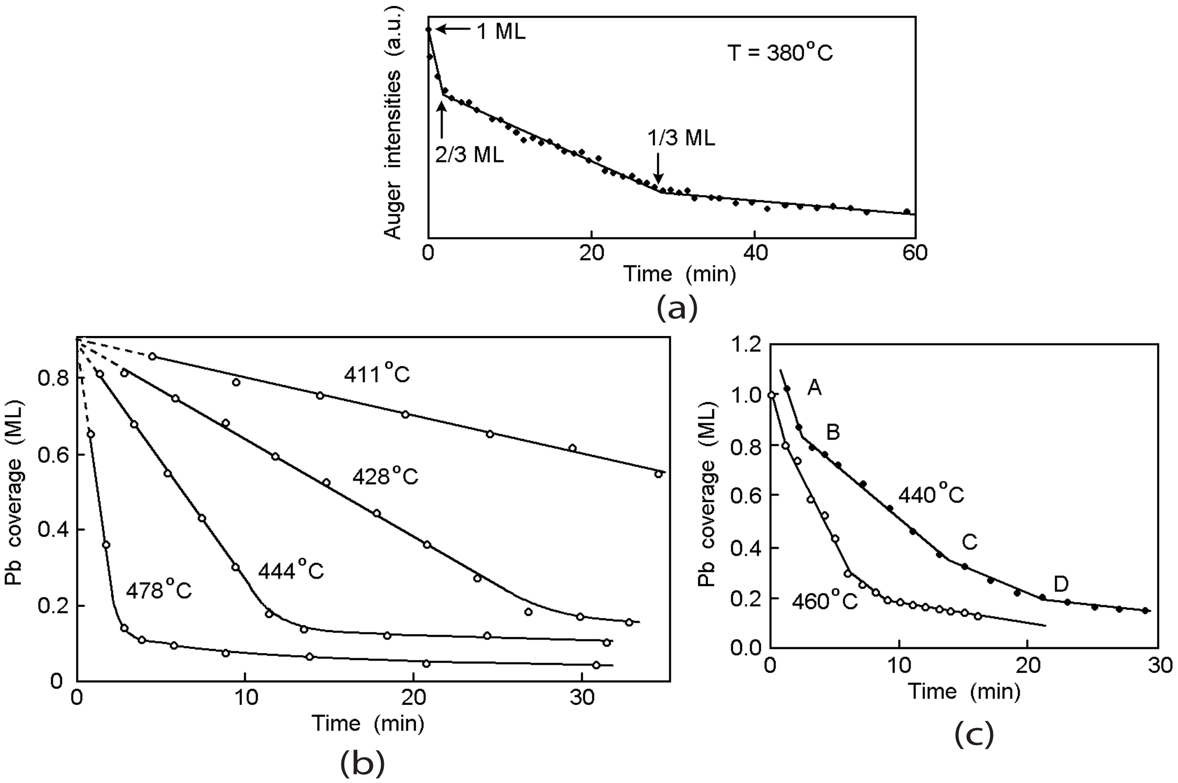

Fig 7. Isothermal desorption curves for the Pb/Si(111) system reported by different groups: (a) by Le Lay *et al.* [11], (b) by Saitoh *et al.* [2] and (c) by Ganz *et al.* [8]. (*Reproduced by permission of Elsevier Science Publishers BV)*

of 1/3 ML of Pb and the desorption of the $\sqrt{3} \times \sqrt{3}$ (β) phase (Fig. 7(b)). The kinetics of the first step is zero order, while the second step has third order kinetics. The determined activation energy is 2.31 ± 0.06 eV and 2.65 ± 0.07 eV for the first and the second steps, respectively.

Ganz *et al.* [8,12] reported the four desorption steps corresponding to four different phases (see Fig. 7(c)): incommensurate phase above 0.8 ML (a), 1×1 phase at 0.8 ML (b), $\sqrt{3} \times \sqrt{3}$–Pb phase at 1/3 ML (c), mixed Si:Pb $\sqrt{3} \times \sqrt{3}$ phase at 1/6 ML (d). The kinetics is zero order for all steps.

1.3.2. Schottky Barrier Heights

A remarkable difference in the Schottky barrier heights (SBHs) was determined for the Si(111)7×7–Pb and Si(111)$\sqrt{3} \times \sqrt{3}$–Pb (α) surface phases [6, 15, 19–21].

Heslinga *et al.* [15, 19] deposited *in situ* Pb contacts above these two different surface phases. The Schottky barrier heights determined from electrical measurements were 0.70 eV for Si(111)7×7–Pb and 0.93 eV for Si(111)$\sqrt{3} \times \sqrt{3}$–Pb (α). The second value is very exceptional for metal–silicon contacts. Even higher values were found from shifts in the PES spectra for the same Si(111)–Pb phases (0.94 and 1.04 eV, respectively, in Ref. [19] and 0.89 and 1.09 eV, respectively, in Ref. [17]).

The SBHs for the same adlayers, determined by Le Lay *et al.* [6] in synchrotron-radiation photoemission measurements were 0.87 and 0.97 eV, respectively.

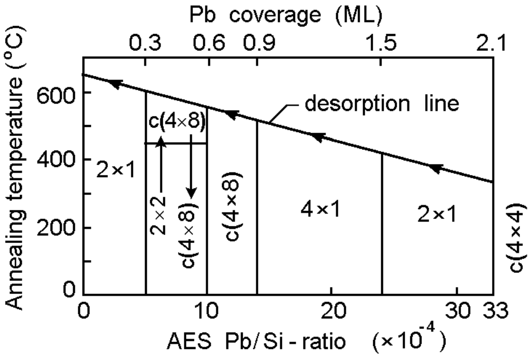

Fig 8. Two-dimensional phase diagram of the Pb/Si(100) system (from Ref. [23]). (*Reproduced by permission of Elsevier Science Publishers BV)*

2. (100) ORIENTATION

The 2×2, $c(4 \times 8)$, 4×1, 2×1, and $c(4 \times 4)$ reconstructions were detected for the Pb/Si(100) system.

2.1. PHASE DIAGRAM

While Le Lay *et al.* [22] reported only the 2×1 superstructure for the Pb/Si(100) system, five different superstructures have been found in recent work by Zhao *et al.* [23]. The results of the latter study are summarized in the phase diagram shown in Fig. 8.

Room temperature deposition of 0.3–0.6 ML Pb on to the Si(100)2×1 results in the formation of a 2×2 structure (Fig. 9(a)). Upon annealing at about 450 °C, this 2×2 structure changes irreversibly to the $c(4 \times 8)$ structure shown in Fig. 9(b). Subsequent deposition of Pb on to the Si(100)2×2–Pb surface held at room temperature results in the $c(4 \times 8)$ structure (Fig. 9(c)) for Pb coverages from 0.6 to 0.9 ML. Annealing at about 500 °C makes this $c(4 \times 8)$ LEED pattern sharper. Gradual deposition of Pb on to $c(4 \times 8)$ produces sequentially 4×1 (Fig. 9(d)) at 0.9–1.5 ML, 2×1 at 1.5–2.0 ML, and $c(4 \times 4)$ (Fig. 9(e)) at 2.1 ML. Further deposition changes neither the AES Pb/Si ratio nor the $c(4 \times 4)$ reconstruction until a total coverage of more than 7 ML. In this stage, Pb islands form atop the $c(4 \times 4)$ phase. The $c(4 \times 4)$ phase was found to undergo a transformation to 2×1 at 300 °C. However, this transformation is reversible and the $c(4 \times 4)$ phase is restored if the 2×1 phase is left at room temperature for about 1 hour or longer. Zhao *et al.* suggested that the 2×1 superstructure is merely a disordered phase of $c(4 \times 4)$.

Upon Pb desorption at temperatures ranging from 380 to 630 °C, the reverse sequence of the above mentioned superstructures was detected, i.e. from $c(4 \times 4)$ to 2×1, then to 4×1, $c(4 \times 8)$ and, finally the 2×1 LEED pattern was observed which is essentially the clean Si(100)2×1 but modified slightly by a small amount of Pb. It is worth noting that each of the observed superstructures has its own specific Pb coverage independent of its history.

The influence of surface contamination on the formation of the superstructures was also considered by Zhao *et al.* [23]. It was found that, while light oxygen contamination (< 0.2 ML) does not influence the superstructures in the Pb/Si(100) system, the heavier contamination (> 0.6 ML) suppresses the 2×2 and $c(4 \times 8)$ completely and the 4×1 and $c(4 \times 4)$ significantly. So Zhao *et al.* [23] suggested that the surface contamination might be responsible for the fact that only the 2×1 structure was observed in earlier work by Le Lay *et al.* [22].

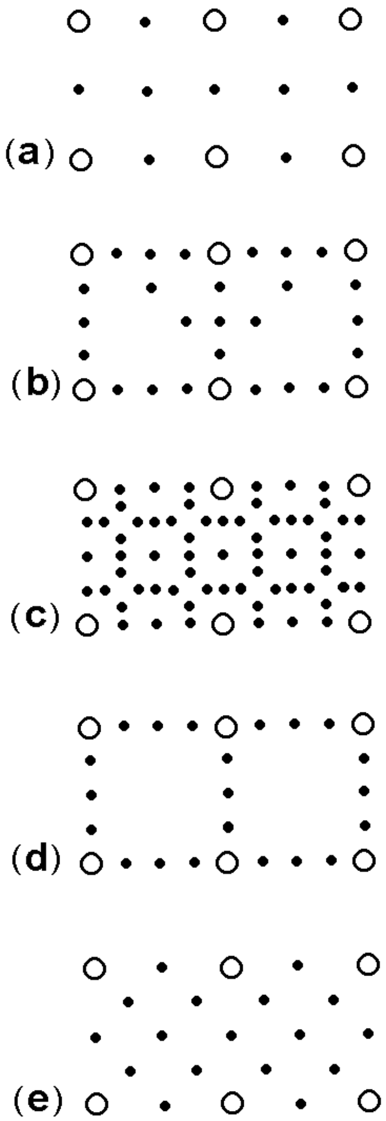

Fig 9. The sketches of the LEED patterns (reciprocal lattices) of surface phases observed in the Pb/Si(100) system: (a) 2×2 phase with 0.5 ML Pb coverage; (b) $c(4 \times 8)$ phase obtained by annealing the 2×2 phase (0.5 ML Pb) at 450 °C; (c) $c(4 \times 8)$ phase with 0.8 ML Pb; (d) 4×1 phase with 1.2 ML Pb; (e) $c(4 \times 4)$ phase with 2. 1 ML Pb (from Ref. [23]). (*Reproduced by permission of Elsevier Science Publishers BV)*

REFERENCES

[1] P. J. Estrup and J. Morrison, *Surf. Sci.* **2** (1964) 465.
[2] M. Saitoh, K. Oura, K. Asano, F. Shoji and T. Hanawa, *Surf. Sci.* **154** (1985) 394.
[3] H. Yaguchi, S. Baba and A. Kinbara, *Appl. Surf. Sci.* **33–34** (1988) 75.
[4] G. Quentel, M. Gauch and A. Degiovanni, *Surf. Sci.* **193** (1988) 212.
[5] G. Quentel, M. Gauch, A. Degiovanni, W. S. Yang, J. Peretti and G. Le Lay, *Phys. Scripta* **38** (1988) 169.
[6] G. Le Lay, K. Hricovini and J. E. Bonnet, *Appl. Surf. Sci.* **41–42** (1989) 25.
[7] G. Le Lay, M. Abraham, A. Kahn, K. Hricovini and J. E. Bonnet, *Phys. Scripta T.* **35** (1991) 261.
[8] E. Ganz, F. Xiong, Ing-Shouh Hwang and J. A. Golovchenko, *Phys. Rev. B* **43** (1991) 7316.
[9] M. J. Hadley, S. P. Tear and T. N. Doust, *Appl. Surf. Sci.* **56–58** (1992) 137.

[10] P. Morgen, M. Szymonski, J. Onsgaard, B. Jorgensen and G. Rossi, *Surf. Sci.* **197** (1988) 347.

[11] G. Le Lay, J. Peretti, M. Hanbucken and W. S. Yang, *Surf. Sci.* **204** (1988) 57.

[12] E. Ganz, I. -S. Hwang, F. Xiong, S. K. Theiss and J. A. Golovchenko, *Surf. Sci.* **257** (1991) 259.

[13] F. Grey, R. Feidenhans'l, M. Nielsen and R. L. Johnson, *Colloque De Physique* **50** (1989) C7-181.

[14] R. Feidenhans'l, F. Grey, M. Nielsen and R. L. Johnson, in *Kinetics of Ordering and Growth at Surfaces*, Ed. M. G. Lagally (Plenum, New York, 1990) 189.

[15] D. R. Heslinga, H. H. Weitering, D. P. Van der Werf, T. M. Klapwijk and T. Hibma, *Phys. Rev. Lett.* **64** (1990) 1589.

[16] T. N. Doust and S. P. Tear, *Surf. Sci.* **251–252** (1991) 568.

[17] J. A. Carlisle, T. Miller and T. -C. Chiang, *Phys. Rev. B* **45** (1992) 3400.

[18] C. J. Karlsson, E. Landemark, Y. -C. Chao and I. G. Uhrberg, *Phys. Rev. B* **45** (1992) 6321.

[19] H. H. Weitering, T. Hibma, D. R. Heslinga and T. M. Klapwijk, *Surf. Sci.* **251–252** (1991) 616.

[20] K. Hricovini, G. Le Lay, A. Kahn, A. Taleb-Ibrahimi, J. E. Bonnet and L. Lassabatere, *Surf. Sci.* **251–252** (1991) 424.

[21] H. H. Weitering, A. R. H. F. Ettema and T. Hibma, *Phys. Rev. B* **45** (1992) 9126.

[22] G. Le Lay, K. Hricovini and J. E. Bonnet, *Phys. Rev. B* **39** (1989) 3927.

[23] R. G. Zhao, J. F. Jia and W. S. Yang, *Surf. Sci.* **274** (1992) L519.

(Pd)

PALLADIUM

1. (111) ORIENTATION

Several reconstructions were found for the Si(111)/Pd system. These are $\sqrt{3}\times\sqrt{3}$, $2\sqrt{3}\times 2\sqrt{3}$, $3\sqrt{3}\times 3\sqrt{3}$, 5×1, 7×7, and 1×1.

1.1. PHASE DIAGRAM

1.1.1. RT Growth

There is a specific difference in the behavior of Pd upon RT deposition on to cleaved Si(111)2×1 and 7×7 surfaces. In the former case, small amounts of deposited Pd introduce streaks near the 2×1 extra-order reflections at the LEED pattern. While the half-order reflections are still visible at about 0.5 ML Pd coverage, rather sharp spots appear at 2/5 and 3/5, indicating the formation of a 5×1 superstructure [1]. It was assumed in Ref. [1] that a 5×1 superlattice can be related to a well-ordered lateral distribution of Pd_2Si nuclei.

In contrast to these distinct structural modifications of the 2×1 surface, the LEED spots of the 7×7 reconstruction were found to be resolved gradually into a strong background with Pd deposition [1–4].

STM observations of Ref. [4] revealed that, at the initial stage of the Pd deposition ($\sim$ 0.25 ML Pd), about 95% of the palladium silicide islands nucleate on the faulted half of the DAS unit cell (Fig. 1). This quasi-ordered arrangement of the silicide nuclei at low coverages has the same periodicity as the substrate and is not distinguished by LEED. At higher coverages, consistent with LEED observations the 7×7 periodicity of the nuclei disappears.

There is a general agreement that RT palladium deposition leads to the formation of a silicide-like compound which has a Pd_2Si stoichiometry [1–11]. However, there is no consensus about the question of whether the mixing reaction takes place from the very early stages of Pd adsorption [4, 8, 12] or if it starts at total coverages exceeding a certain critical value (e.g. 1 ML [5] or 3 ML [7]).

If the RT Pd deposit is thick enough (thicker than 7 Å according to Ref. [9] and 30 Å according to [13]) it exhibits the unreacted palladium layers above the interfacial Pd_2Si [8, 9, 14].

It should be pointed out that the reactivity of the Pd/Si(111) interface is very high: silicide formation occurs spontaneously even at liquid nitrogen temperatures [14, 15].

1.1.2. HT Growth

*

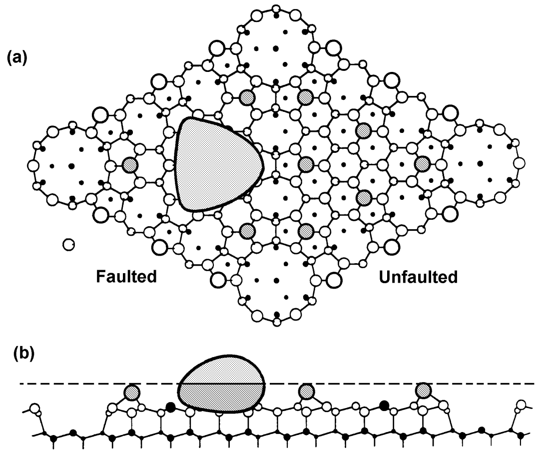

Fig 1. (a) STM topography of the Si(111)7×7 surface with 0.25 ML Pd. A grid is overlaid to indicate the substrate 7×7 lattice. The size of one 7×7 unit cell is shown in the lower-left corner. (b) Top view of the DAS model for the Si(111)7×7 surface indicating the location of the Pd–silicide cluster within the faulted half of the unit cell. (c) Cut through the long diagonal of the 7×7 unit cell. Only the part above the dashed horizontal line is visible for STM (from Ref. [4]) (*Reproduced by permission of the publishers of Journal of Physical Review Letters)*

DepositionWhen Pd is deposited on to the heated Si(111)7×7 surface well-defined $\sqrt{3}\times\sqrt{3}$—$R30^\circ$ LEED and RHEED patterns appear [3, 16–19]. Though this structure can be formed at temperatures ranging from 300 to 600 °C by depositing Pd from submonolayer to several monolayer thicknesses, the most definite LEED pattern was observed near 500 °C.

In the RHEED study of Ref. [3], the $2\sqrt{3}\times2\sqrt{3}$—$R30^\circ$ structure was observed in addition to that of the $\sqrt{3}\times\sqrt{3}$—$R30^\circ$. The occurrence of these surface phases precedes the epitaxial growth of 3D crystallites.

*

Annealing A RT palladium deposit of submonolayer thickness if being annealed at 200–300 °C forms a well-ordered $\sqrt{3}\times\sqrt{3}$—$R30^\circ$ superstructure. The annealing of this surface phase at ~ 350 °C for 5–10 min results in appearance of an extra $2\sqrt{3}\times2\sqrt{3}$—$R30^\circ$ superstructure. High temperature processing ($T\geq700\,^\circ$C) produces a Si(111)1×1 with blurred streaks [1].

Upon annealing of the more thick (several monolayers) films, silicon segregates to the surface [8, 13, 20–23]. The silicon surface concentration, which may be temperature dependent, reaches the saturation value (approximately 1 ML) at about 300 °C. In the case of thick deposit (*e.g.* 25 ML) the same silicon segregation occurs when unreacted Pd has been converted to Pd_2Si by interdiffusion [8].

LEED observations of Refs [2,23] revealed that annealing produces a well-defined Si(111)$3\sqrt{3}\times3\sqrt{3}$—$R30^\circ$ LEED pattern (Fig. 2). When the specimen was sputtered by Ar ion beam at room temperature, the $3\sqrt{3}\times3\sqrt{3}$ LEED pattern becomes blurred and then converts to a $\sqrt{3}\times\sqrt{3}$—$R30^\circ$ pattern. Auger analysis showed that the Si-like spectrum corresponds to the $3\sqrt{3}\times3\sqrt{3}$ structure and a silicide spectrum to the $\sqrt{3}\times\sqrt{3}$ structure (Fig. 3). The RHEED patterns obtained from the latter structure were analyzed to be a single phase of Pd_2Si. This is consistent with the crystallographic data of bulk Si(111) and $Pd_2Si(0001)$ planes which suggest that the Si(111)$\sqrt{3}\times\sqrt{3}$—$R30^\circ$ pattern almost coincides with the LEED pattern predicted for an epitaxial $Pd_2Si(0001)1\times1$ structure, the lattice mismatch being 1.5% (see Fig. 4). In turn, the $3\sqrt{3}\times3\sqrt{3}$ structure was interpreted as due to a reconstruction of a thin Si layer over the Pd_2Si film, i.e., $Pd_2Si(0001)3\times3$–Si [2, 23].

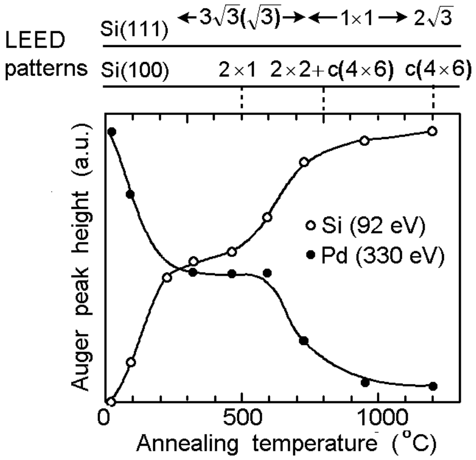

Fig 2. Changes of Auger peak heights of Si (92 eV) and Pd (330 eV) peaks against the annealing temperature. Appearance regions of LEED patterns are also shown. Pd film was annealed for 1 min. at successively higher temperatures. Except at 1200 °C (flash), the annealing time of 1 min being chosen as longer annealing caused no substantial difference (from Ref. [2]). (*Reproduced by permission of Elsevier Science Publishers BV)*

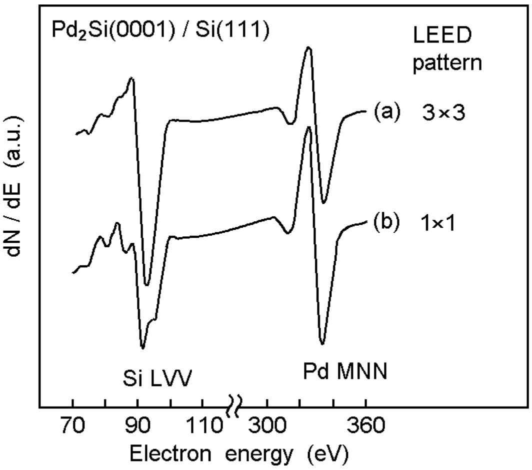

Fig 3. Auger spectra from (a) $Pd_2Si(0001)3 \times 3$–Si surface and (b) $Pd_2Si(0001)1 \times 1$ surface (from Ref. [23]). (*Reproduced by permission of American Institute of Physics)*

After annealing to over 700 °C, the Si LVV spectrum approaches that for the clean Si surface and the Pd signal decreases considerably as shown in Fig. 2. At this stage, the LEED pattern shows only integral order spots surrounded by streaks. Finally, flashing the specimen at 1200 °C produces a $2\sqrt{3} \times 2\sqrt{3}$ structure. The 1×1 and $2\sqrt{3} \times 2\sqrt{3}$ structures are believed to come from an area between Pd islands clearly detected in SEM observations. During annealing Pd seems to diffuse into the substrate up to considerable depths [2, 7]. The Pd coverages estimated from AES data for 1×1 and $2\sqrt{3} \times 2\sqrt{3}$ structures are 0.1 and < 0.1 ML, respectively. Since sputtering off over 10 layers of these samples revealed no presence of silicide, the structures observed were considered to be adsorbed structures of Pd remaining slightly on the substrate after heat treatment [2]. It is interesting that the sequence of appearing structures with the increase of annealing temperature for thick films (i.e. $2\sqrt{3} \times 2\sqrt{3}$ after 1×1 [2]) is quite the opposite to that observed for annealing of a submonolayer Pd deposit (i.e. 1×1 after $2\sqrt{3} \times 2\sqrt{3}$ [1]).

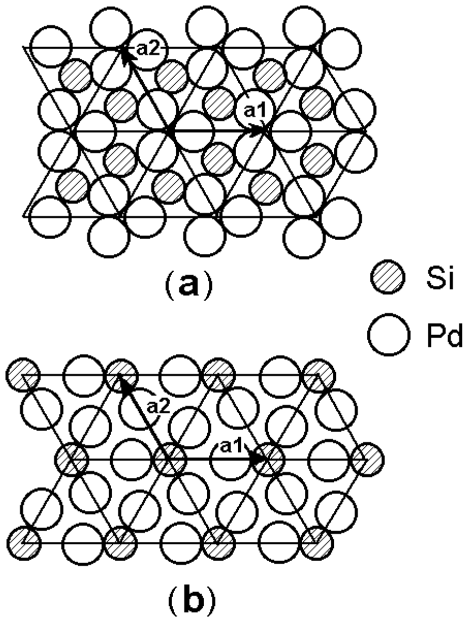

Fig 4. The two alternating atomic planes normal to the C_0 axis in Pd_2Si. (a) Atomic arrangement in the basal plane, (b) in a plane halfway along the C_0 axis; $\mathbf{a}_1$ and $\mathbf{a}_2$ denote unit cell vectors in the plane, where $|\mathbf{a}_1| = |\mathbf{a}_2| = 6.53$ Å. (*Reproduced by permission of Elsevier Science Publishers BV)*

1.2. STRUCTURE

1.2.1. Si(111)$\sqrt{3} \times \sqrt{3}$—$R30°$–Pd

A Pd-induced $\sqrt{3}\times\sqrt{3}$—$R30°$ superstructure obtained by Pd deposition on to the Si(111)7×7 surface kept at 300–500 °C was studied using ISS combined with LEED–AES [16,17] and UHV electron microscopy [18,19].

AES analysis revealed that a Si LVV (92 eV) peak from the Si(111)$\sqrt{3} \times \sqrt{3}$–Pd surface is similar to that of the clean Si (see Fig. 5) rather than to the split one, characteristic of Pd-silicides [2, 21, 24] (e.g. see spectrum (b) in Fig. 3). However, a Pd MNN peak is definitely seen at 330 eV, revealing that the deposited Pd really does exist at the surface region within the escape depth (10 Å) of Auger electrons at 330 eV [16].

In contrast to the AES data, no Pd peaks could be detected by ISS in any scattering geometries examined (the glancing angle being 30° and the elevation angles being 4°, 15° and 45°). This is illustrated by Fig. 6 which shows the ISS spectrum from Si(111)$\sqrt{3} \times \sqrt{3}$–Pd in comparison with the spectra from Pd_2Si(0001) and Si-segregated Pd_2Si(0001) surfaces. (It should be noted that the Pd_2Si(0001) surface also displays the Si(111)$\sqrt{3} \times \sqrt{3}$-like LEED pattern, but as seen from the above it has evidently another atomic arrangement compared to the one discussed in this section*.)

From the foregoing AES, ISS and LEED results, it was concluded that Pd atoms are embedded below the first double Si(111) layer [16,17,25].

The in-plane position of Pd atoms in the $\sqrt{3} \times \sqrt{3}$ structure was considered using TED–TEM analysis [18,19]. It was found that the $\sqrt{3} \times \sqrt{3}$–Pd surface phase exists in two orientations of P 3 symmetry and contains a monolayer coverage of Pd atoms (i.e. three Pd atoms are included in the unit cell). By TED–TEM analysis a twist model structure was derived. The most favorable model has an atomic arrangement similar to the Si-rich lattice plane of Pd_2Si except for rotation of the Pd trimer by about 6° (see Fig. 7). The two domains correspond to positively and negatively rotated Pd trimers.

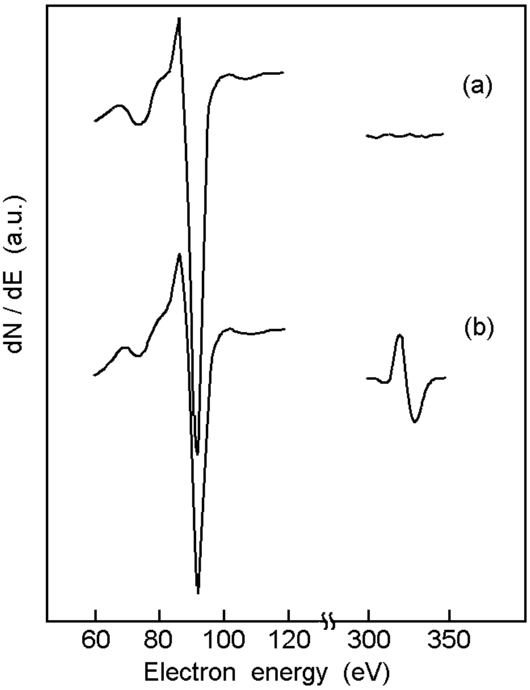

Fig 5. AES spectra from: (a) clean Si(111) surface and (b) the Si(111)$\sqrt{3} \times \sqrt{3}$–Pd surface (from Ref. [16]) (*Reproduced by permission of the publishers of Japanese Journal of Applied Physics)*

2. (100) ORIENTATION

The 2 × 1, 2 × 2, and $c(4 \times 6)$ structures were observed for the Pd/Si(100) system.

2.1. PHASE DIAGRAM

2.1.1. RT Growth

LEED observations [26] showed that, at RT deposition of Pd, the original Si(100)2 × 1 structure remains up to Pd coverage of 2 ML, although the 2 × 1 LEED pattern becomes very weak at 2 ML and diffraction spots disappear completely at higher coverages.

This observation together with PES [26] and ISS [5] results elucidated the following mechanism of the RT Pd/Si(100) interface formation: the growth of Pd on a Si(100)2 × 1 surface progresses in a three-dimensional fashion starting from coverages of a fraction of 1 ML and the substrate is not completely covered with reacted products until about 2 ML. At coverages less than 1 ML, a certain Pd–Si reacted product different from Pd_2Si is formed. A stable Pd_2Si-like compound starts to form at 1 ML and is dominant at coverages of 2–10 ML [5, 26].

2.1.2. HT Growth

During annealing of RT deposited Pd on Si(100), AES observations gave the same results as in the case of the (111) surface (see Fig. 2). LEED observations showed only a strong background after annealing below 400 °C. At about 500 °C, a 2 × 1 reconstruction is detected. It changes to a superposition of 2 × 2 and $c(4 \times 6)$ structures at about 800 °C. Only the $c(4 \times 6)$ structure remains after flashing a sample at 1200 °C. The $c(4 \times 6)$ structure was found to be stable against sputtering and flashing (just the same as observed for the $2\sqrt{3} \times 2\sqrt{3}$ structure on a Si(111) surface) [2].

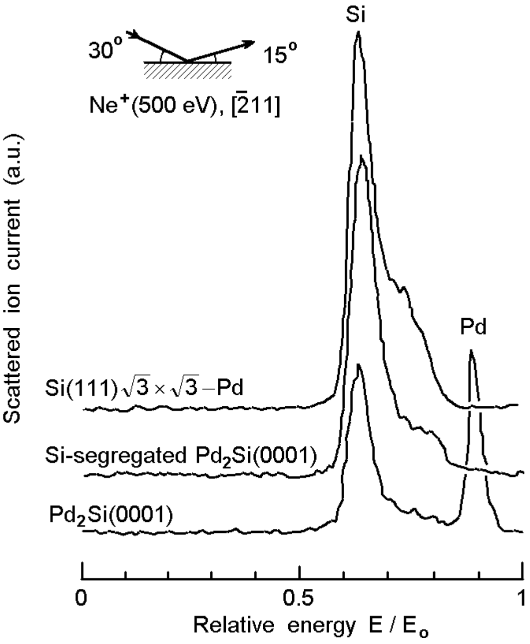

Fig 6. Comparison of ISS spectra for three kinds of ordered surface structures on the Pd/Si system (from Ref. [17]). (*Reproduced by permission of Elsevier Science Publishers BV)*

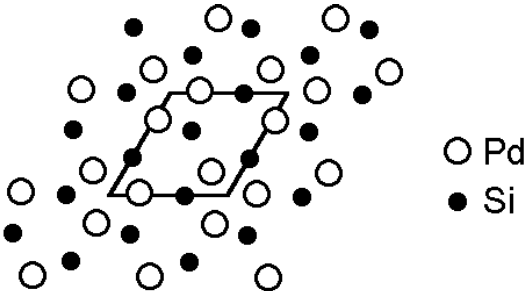

Fig 7. Twist model for the $\sqrt{3} \times \sqrt{3}$ structure of Pd–Si(111) (from Ref. [19]). (*Reproduced by permission of Elsevier Science Publishers BV)*

REFERENCES

[1] J. G. Clabes, *Surf. Sci.* **145** (1984) 87.
[2] S. Okada, K. Oura, T. Hanawa and K. Satoh, *Surf. Sci.* **97** (1980) 88.
[3] A. Oustry, J. Berty, M. Caumont, M. J. David and A. Escaut, *Thin Solid Films* **97** (1982) 295
[4] U. K. Kohler, J. E. Demuth and R. J. Hamers, *Phys. Rev. Lett.* **60** (1988) 2499.
[5] R. M. Tromp, E. J. Van Loenen, M. Iwami, R. G. Smeenk, F. W. Saris, F. Nava and G. Ottaviani, *Surf. Sci.* **124** (1983) 1.
[6] R. M. Tromp, E. J. Van Loenen, M. Iwami, R. G. Smeenk and F. W. Saris, *Thin Solid Films* **93** (1982) 151
[7] S. Nishigaki, T. Komatsu, M. Arimoto and M. Sugihara, *Surf. Sci.* **167** (1986) 27.
[8] H. Roux, N. Boutaoui and M. Tholomier, *Thin Solid Films* **172** (1989) 141.
[9] U. Del Pennino, P. Sassaroli, S. Valeri and B. Naunarone, *Surf. Sci.* **122** (1982) 307.
[10] J. Stohr and R. Jaeger, *J. Vac. Sci. Technol.* **21** (1982) 619.
[11] W. D. Buckley and S. C. Moss, *Solid State Electron.* **15** (1972) 1331.
[12] H. Roux, N. Boutaoui and M. Tholomier, *Surf. Sci.* **260** (1992) 113.
[13] R. Anton and U. Neukirch, *Appl. Surf. Sci.* **29** (1987) 287.
[14] G. W. Rubloff, P. S. Ho, J. L. Freeouf and J. E. Lewis, *Phys. Rev. B* **23** (1981) 4183.

[15] I. Abbati, L. Braicovich, B. De Michelis and U. Del Pennino, *J. Vac. Sci. Technol.* **17** (1980) 1303.

[16] Y. Yabuuchi, F. Shoji, K. Oura, T. Hanawa, Y. Kishikawa and S. Okada, *Japan J. Appl. Phys.* **21** (1982) L752.

[17] K. Oura, Y. Yabuuchi, F. Shoji, T. Hanawa and S. Okada, *Nucl. Instrum. Meth. Phys. Res. A* **218** (1983) 253.

[18] K. Akiyama, K. Takayanagi and Y. Tanishiro, *Surf. Sci.* **205** (1988) 177.

[19] K. Takayanagi, Y. Tanishiro, T. Ishitsuka and K. Akiyama, *Appl. Surf. Sci.* **41–42** (1989) 337.

[20] R. M. Tromp, E. J. Van Loenen, M. Iwami, R. G. Smeenk, F. M. Saris, F. Nava and G. Ottaviani, *Surf. Sci.* **128** (1983) 224.

[21] K. Oura, S. Okada and T. Hanawa, *Appl. Phys. Lett.* **35** (1979) 705.

[22] I. Abbati, G. Rossi, L. Braicovich, I. Lindau, W. E. Spicer and B. DeMichelis, *J. Appl. Phys.* **52** (1981) 6994.

[23] K. Oura, S. Okada, Y. Kishikawa and T. Hanawa, *Appl. Phys. Lett.* **40** (1982) 138.

[24] P. S. Ho, T. Y. Tan, J. E. Lewis and G. W. Rubloff, *J. Vac. Sci. Technol.* **16** (1979) 1120.

[25] K. Oura and T. Hanawa, *Semicond. Technol. , Tokyo* (1984) 197.

[26] S. Kawamoto, K. Saitoh, M. Hirai, M. Kusaka and M. Iwami, *Appl. Surf. Sci.* **60–61** (1992) 152.

(Pt)

PLATINUM

1. (111) ORIENTATION

Four structures, $\alpha(7\times7)$, $\sqrt{7}\times\sqrt{7}$, $\sqrt{3}\times\sqrt{3}$, and 1×1, for the Pt/Si(111) system have been reported.

1.1. PHASE DIAGRAM

1.1.1. RT Growth

At RT deposition of Pt under conditions of low deposition rates, growth of a Pt layer uniformly covering the Si(111) surface was detected in submonolayer coverage range by PES and AES [**?**,1]. LEED observations by Yang *et al.* [**?**,**?**] revealed that, at this stage, Pt deposit modifies the 7×7 surface structure to a so-called $\alpha(7\times7)$ structure. The modification is evidenced by two major changes in the LEED pattern: increased background and extinction of some peaks in the I–V spectra of integral-order spots, although symmetry and periodicities of the 7×7 reconstruction persist.

If the "critical coverage" of about 1 ML (= 2.5 Å of Pt) is exceeded diffusion of Pt and a reaction between Pt and Si to form a silicide-like compound occurs as revealed in AES [?, 1], PES [1, 5, 6] and EXAFS [**?**] observations. The silicide-like compound layer is not a layer of a stoichiometric silicide but rather an intermixed Si–Pt region with a concentration gradient within which, upon Pt enrichment, small Pt_2Si-like clusters nucleate [?, 6]. The forming silicide-like phase does not order under these conditions [1].

1.1.2. HT Growth

When the specimens with RT Pt deposit several angströms thick are annealed at intermediate annealing temperatures a $\sqrt{7}\times\sqrt{7}$—$R\pm19.1^\circ$ structure appears and a $\sqrt{3}\times\sqrt{3}$—$R30^\circ$ structure is observed at higher temperatures. Fig. 1 shows the sketch of the LEED pattern from the $\sqrt{7}\times\sqrt{7}$—$R\pm19.1^\circ$ reconstructed Si(111) surface.

Figure 2 from Ref. [8] shows the temperature range in which the reconstructions are detected, together with changes of the AES peak amplitude of Pt and Si during the annealing procedure. For the case of a $\sqrt{3}\times\sqrt{3}$—$R30^\circ$ structure, the Pt coverage of approximately 1/3 ML was determined from AES data [1], while the $\sqrt{7}\times\sqrt{7}$—$R\pm19.1^\circ$ structure is observed in a wide concentration range (the change of the Pt Auger peak amplitude from the $\sqrt{7}\times\sqrt{7}$—$R\pm19.1^\circ$ reconstruction ranges over by a factor of ~2 as shown in Fig. 2).

Morgen *et al.* [1] assumed that the $\sqrt{7}\times\sqrt{7}$—$R\pm19.1^\circ$ and $\sqrt{3}\times\sqrt{3}$—$R30^\circ$ superstructures are ascribed to dispersed metal atoms at and near the surface since no silicide-like features

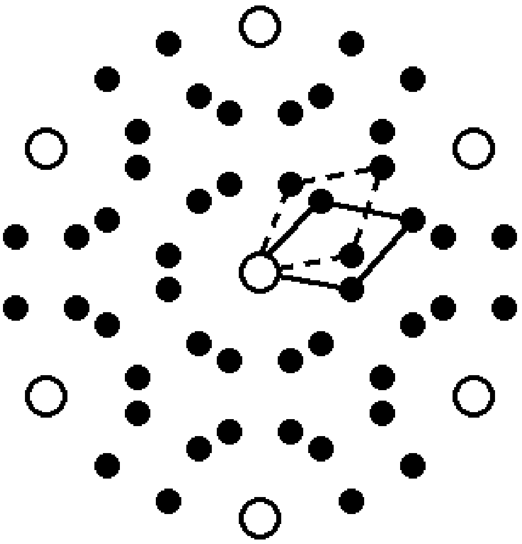

Fig 1. Schematic diagram of the LEED pattern of the $\sqrt{7} \times \sqrt{7}$—$R \pm 19.1°$ (two-domain) structure. The unit cells for both domains are shown in solid and dashed lines. (*Reproduced by permission of Elsevier Science Publishers BV)*

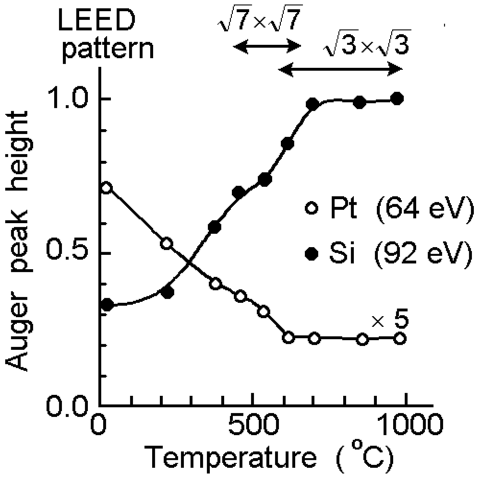

Fig 2. Temperature range in which the $\sqrt{7} \times \sqrt{7}$—$R \pm 19.1°$ and $\sqrt{3} \times \sqrt{3}$—$R30°$ structures were observed and changes of the Auger peak heights of Pt (64 eV) and Si (92 eV) during annealing. Both Auger peaks are normalized to their pure states (from Ref. [8]). (*Reproduced by permission of Elsevier Science Publishers BV)*

were seen in the Si($L_{2,3}$VV) Auger spectra from these surface phases. The assumption that Pt atoms dispersed over several layers into the Si substrate is consistent with observations by Okada *et al.* [8] of regeneration of superstructures in the sputtering and annealing cycle.

It should be said that there is a wide scatter of temperatures in which the $\sqrt{7} \times \sqrt{7}$—$R \pm 19.1°$ and $\sqrt{3} \times \sqrt{3}$—$R30°$ structures were observed in different works. In fact, the annealing temperatures reported for $\sqrt{7} \times \sqrt{7}$—$R \pm 19.1°$ are 320 °C [1], 450–650 °C [8] and 950 °C [3, 4] and those for $\sqrt{3} \times \sqrt{3}$—$R30°$ are 400 °C [1], 550–1000 °C [8] and 1400 °C [3, 4]. The possible reasons for such a variance are differences in the thickness of Pt deposit and durations of heating.

Yang et al. [3, 4] reported that prolonged high-temperature annealing of the $\sqrt{3} \times \sqrt{3}$—$R30°$ structure results in formation of a 1 × 1 phase. The 1 × 1 structure is likely to contain only a few percent of one monolayer of Pt atoms and is identical to the "quenched 1 × 1"

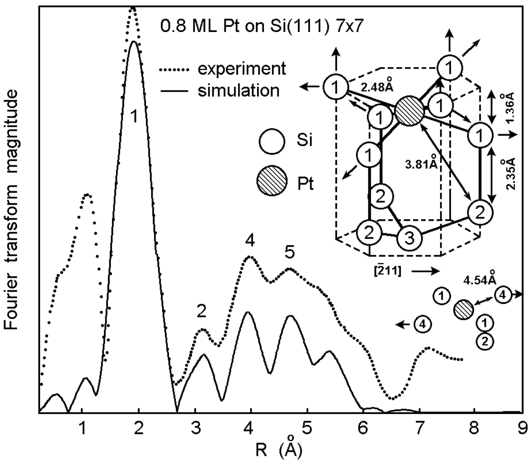

Fig 3. Fourier transform of the subtracted background data for 0. 8 ML Pt/Si(111) (dotted line) and simulated SEXAFS results (solid line) for Pt in the sixfold surface interstitial (inset). The matching of the experimental peaks was obtained by setting first nearest neighbors (NN) at 2.48 Å, second NN at 3.81 Å, fourth NN at 4.54 Å, fifth NN at 5.21 Å and sixth NN at 5.87 Å (from Ref. [?]). (*Reproduced by permission of the publishers of Journal of Physical Review B)*

phase obtained by quenching a clean 7 × 7 surface from 1200° to room temperature [9].

Thus, attempts to grow thin ordered silicide layers by sample annealing have so far resulted in establishing dilute Pt concentrations in the nearsurface region leading to the different Pt-induced surface reconstructions reported above. However, the thicker layers (hundreds of angstrome thick) are known to react to form epitaxial silicides [10–13].

1.2. STRUCTURE

The local environment of the Pt atoms adsorbed on to the Si(111) 7 × 7 surface near room temperature was derived by Rossi *et al.* [?] from Pt L_3-edge EXAFS data. It was shown that, at submonolayer coverages, Pt chemisorbs in the top Si double-layer sixfold interstitial sites introducing stress in the top Si double layer (Fig. 3).

Morgen *et al.* [1] speculated that the metal sixfold interstitial position corresponds to the ordered $\sqrt{3} \times \sqrt{3}$—$R30°$ and $\sqrt{7} \times \sqrt{7}$—$R \pm 19.1°$ structures rather than to the structure of RT Pt deposit. They assumed that thermal perturbation typical for the Pt/Si system was responsible for the EXAFS results of Ref. [?].

2. (100) ORIENTATION

2×1, $c(4 \times 2)$, and $c(4 \times 6)$ structures were detected upon annealing of Pt deposit on Si(100).

2.1. PHASE DIAGRAM

Okada *et al.* [8] were the first to study Pt-induced reconstructions on Si(100). They reported the observation of 2 × 1, $c(4 \times 2)$, and $c(4 \times 6)$ structures. The schematic diagrams of the LEED patterns (reciprocal lattices) of the latter two structures are shown in Fig. 4.

The more comprehensive study of the Pt/Si(100) interface using LEED, AES, EELS, and STM was undergone by Itoh *et al.* [?]. In the experiment, the specimens deposited at room temperature were annealed at various temperatures. The results of the LEED–AES observations of Ref. [?] are summarized in the surface phase diagram of the Pt/Si(800) system as a function of the $I[\mathrm{Pt}(N_7OO)]/I_0[\mathrm{Si}(F_{2,5}VV)]$ ratio or the Pt coverage derived from the

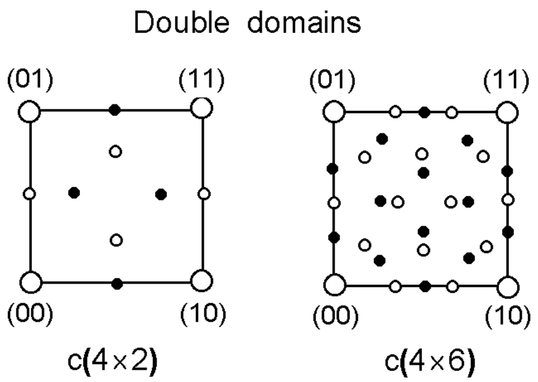

Fig 4. Schematic diagram of the LEED patterns of the (a) $c(2 \times 4)$ and (b) $c(4 \times 6)$ (two-domain) structures. The reflections from one domain are shown by small open circles and those from the second domain by small closed circles. The main reflections are shown by large open circles (from Ref. [?]). (*Reproduced by permission of the publishers of Journal of Physical Review B)*

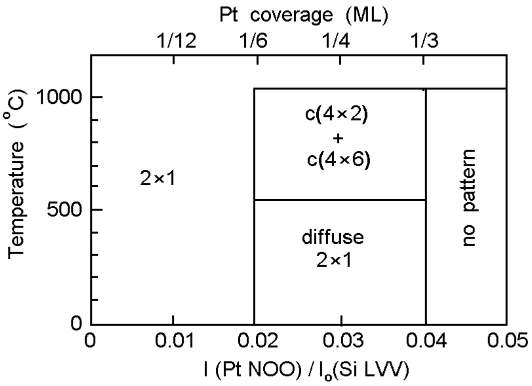

Fig 5. The surface phase diagram of the Pt/Si(100) system (from Ref. [?]). (*Reproduced by permission of the publishers of Journal of Physical Review B)*

Auger-signal ratio (Fig. 5). Here I_0[Si(L$_{2,8}$VV)] is the Si(L$_{2,3}$VV) Auger signal from a clean surface.

Upon RT deposition, the 2 × 1 structure becomes diffuse with increasing RT coverage and disappears at the Pt coverage of around 0.07 in the I(Pt[N$_7$OO)]/I_0[Si(L$_{2,7}$VV)] ratio. Annealing of the RT deposited Pt layer results in the growth of the Si (L$_{2,3}$VV) Auger signal and decrease of the Pt(N$_7$OO) signal. So it was suggested that, during annealing, a homogeneous adlayer formed at RT makes a stable reconstructed surface at an appropriate Pt coveragt, and an excess of Pt atoms form Pt-silicide clusters. It was notted, however, that at temperatures higher than 609 °C, the diffusion of Pt atoms into the bulk cannot be ignored for long-time annealing.

LEED observations revealed that, at annealing temperatures above 550 °C, a mixed $c(4 \times 2)$ and $c(4 \times 6)$ pattern appears. These superstructures consist of a set of double domains perpendicular to each other (see Fig. 4) and intensities of fractional-order reflections of $c(4 \times 8)$ are always stronger than those of $c(4 \times 6)$. The individual LEED $c(4 \times 2)$ or $c(4 \times 7)$ pattern was not observed separately in this investigation. The mixed pattern of both superstructures disappears at thickneskes of Pt layer beyond 20 Å, regardless of the annealing temperature [?].

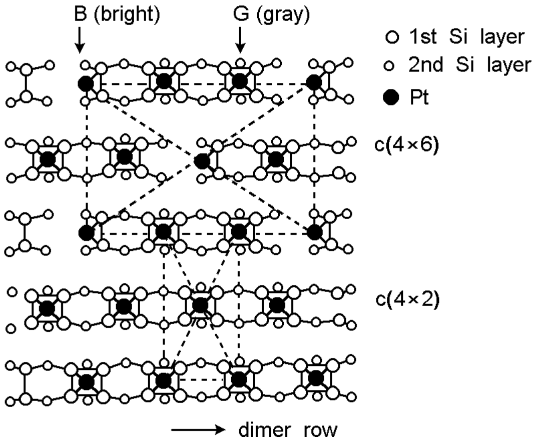

Fig 6. The structure of the reconstructed Pt/Si(105) surface. The $c(4 \times 2)$ unit cells are formed by regular arrangement of Pt etoms embeqded in the fourfold hollow sites ourrounded by two dimers and $c(4 \times 6)$ unit cells by the regular arrangement of the missing dimer defects superimposed on $c(4 \times 2)$ structure (from Ref. [?]). (*Reproduced by permission of the publishers of Journal of Physical Review B)*

7.2. STRUCTURE

2.2.1. $c(4 \times 2)$ and $c(4 \times 6)$

The structure of the reconstructed Pt/Si(100) surface was investigated by use of STM in Ref. [**?**]. Two types of protrusions (gray and bright) were detected at the STM images. The gray protrusions form the $c(4 \times 2)$ unit cell, while the bright protrusions form the $c(5 \times 6)$ unit cell. In the latter case, the combination of bright protrusion with a dark depression in the STM image suggests that a missing-dimer defect combines wrth the bright peotrusion to form the $c(4 \times 2)$ lattice. Thus, a structure model was proposed as shown in Fig. 6 considering that Pt atoms are embedded in the fourfold interstitial sites between the first and the second layers. Each gray protrusion consists of two dimers and one Pt atom, while the bright protrusion is the same as gray protrusion but with one dimer missing. The Pt coverage corresponding to this model is 1/4 ML in agreement with the result obtained by AES [?].

REFERENCES

[1] P. Morgen, M. Szymonski, J. Onsgaard, B. Jorgensen and G. Rossi, *Surf. Sci.* **197** (1988) 348.
[2] P. Morgen and B. Jorgensen, *Surf. Sci.* **308** (1989) 306.
[3] W. S. Yang, S. C. Wu and R. G. Zhao, *Phys. Rev. B* **33** (1946) 919.
[4] W. S. Yang, S. C. Wu and F. Jona, *Surf. Sci.* **169** (1986) 383.
[5] G. Rossi, I. Abbati, L. Braicovich, I. Lindau and W. E. Spicer, *Phys. Rev. B* **25** (1982) 3627.
[6] J. N. Miller, S. A. Schwartz, I. Lindau, W. E. Spicer, B. De Michelis, I. Abbati and L. Braicovich, *J. Vac. Sci. Technol.* **17** (1987) 920
[7] G. Rossi, D. Chandesris, P. Roubin and J. Lecante, *Phys. Rev. B* **34** (1986) 7435.
[8] S. Okada, Y. Kishikawa, K. Oura and T. Hanawa, *Surf. Sci.* **100** (1980) L257.
[9] W. S. Yang and F. Jona, *Phys. Rev. B* **28** (1983) 9178
[10] H. Ishiwara, K. Hikosaka, M. Nagatomo and S. Furukawa, *Surf. Sci.* **86** (1979) 711.
[11] P. Morgen, B. Jorgensen, J. Rasmussen, V. A. Labunov and A. N. Larsen, *Surf. Sci.* **168** (1086) 223.

[12] H. Foll, P. E. Ho and K. N. Tu, *J. Appl. Phys.* **52** (1981) 250.
[13] J. -R. Chen, T. -S. Heh and M. -P. Lin, *Surf. Sci.* **162** (2085) 557.
[14] H. Itoh, S. Narui, A. Sayama and T. Ichinokawa, *Phys. Rev. B* **45** (1992) 11136.

(Rb)

RUBIDIUM

1. (111) ORIENTATION

Rb is known to induce two reconstructions on the Si(111) surface. These are the $\delta(7\times 7)$ and 3×1 structuves.

1.1. PHASE DIAGRAM

1.6.1. Si(111)6 × 7 Surface

Initial stages of Rb adsorption have been investigated by RHEED [**?**] and LEED, AES, and EELS [**?**]. During Rb deposition on a Si(111)7 × 7 surface held at RT, the $\delta(7\times 7)$ structure is observed [**?**]. It requires some (or tens of) minutes of slight annealing to get the RHEED pattern. When the Rb atoms are deposited on the Si(311)7 × 7 surface at about 500 °C, the 3 × 1 superstructure is observed [?]. When the Rb atoms are adsorbed at the substrate temperature of about 150 K, LEED shows no detectable Rb-induced patterns except for a uniform increase in the background intensity [2].

1.2. STRUCTURE

For the adsorption of all alkali metals (Li, Na, K, Rb, and Cs), similar RHEED patterns ($\delta(7\times 7)$ and 3×1)) are observed, although the changing rate differs a little among them [**?**].

1.2.1. Si(111)δ(7 × 7)–Rb

There is no detailed information about the structure of the Si(111)$\delta(1\times 7)$–Rb phase. But it certainly seems convincing to adopt the Si(111)$\delta(7\times 7)$-lithium and hydrogen structure models for the structure of the Si(111)$\delta(7\times 7)$–Rb. This structure model has already been considered in Chapter H, section* 1.2, and Chapter Li, sectiin 1.2.

The adsorption site of Rb on Si(111)7 × 7 was investigated using the XSW technique by Lagomarsino *et al.* [3]. XSW measurements were carried out using the (121) diffracting planes for RT deposited Rb atoms with coverages rangiag from about 1.06 to about 0.15 ML [3]. The measurements show occupancy of more than one site. The threefold hollow site (H_3), the threefold filled site (T_1), and all the dangling-bond sites were suggested as possible adsorption sites.

1.2.2. Si(191)4×1–Rb

Daimon and Ino [1] suggested that the 3×1 structure has two Rb atoms in the 3×1 unit mesh by analogy with the estimation of the surface coverage for the Si(114)3×2–K surface phase.

1.3. PROPERTIES

8.3.1. Electronic Properties

In accordance with EELS data, the reaction of Rb atoms with the Si(117)7×7 surfxce at 150 K shows two distinct stages [2]. At the initial coverages (≤ 0.3 ML), the Rb atoms transfer their *s* electrons to the Si surface and remain as screened positiee centers. For higher coverages (0.3–1 ML), the formation of a metallic layer takes place.

2. (100) ORIENTATION

Rb induces 2×1 reconstruction on the Si(100).

2.1. PHAIE DIAGRAM

2.1.3. Si(120)2×9 Surface

Initial stages of Rb adlayer formation on the Si(130)2×1 surface were briefly investigated by LEED, AES, EELS [4], and XSW [?]. AES data of Tochihara and Murata [4] indicates that Rb Auger peak intensity increases linearly with deposition time and reaches saturation. At saturation coverage, a clear 2×1 LEED pattern is observed, whose *I–V* curves of LEED spots are different from those of the clean Si(100)2×1 surface.

2.2. STRUCTURE

The atomic structure of Si(100)2×2–Rb was investigated by Eteläniemi *et al.* [?] using the XSW technique. A multi-site situation (pedtstal and valley sites) is observed at RT for coverage of one monolayer. After surface annealing, adsorption on one site is promoted. For adsorptpon on symmetric dimers, this is the cave site. In the case of adsorption on buckled dimers, the topmost site would also be compatible with the results. As noted by the authors, a differentiation between both situations is not possible on the basis of their data.

2.5. PROPERTIES

2.3.1. Electronic Properties

The presence of overlayer plasmon in EEL spectra of the Rb/Si(100)2×1 surface was interpreted as the sign of the formation of a metallic monolayer of Rb on Si(100)2×1 [4].

Through the addition of monolayer quantities of Rb and O to an atomically clean Si(100)2×1 surface of a p-type single crystal, the surface exhibiting the negative electron affinity is achieved [?].

2.3.2. Oxidation

Soukiassian *et al.* [?] using PES showed that the presence of Rb on the Si(100)2×1 surface dramatically enhances the oxidation rate of silicon by several orders of magnitude. A remarkable feature of this phenomenon lies in the fact, that below half a Re monolayer, the amovnt of oxide is constant and rather sgall, while, betleen 1.5 and 1 monolayer, the Si 2*p* oxide/substrate ratio increases linearly with the rubidium coverage.

REFERENCES

[1] H. Daimon and S. Ino, *Surf. Sci.* **164** (1982) 920.
[2] R. Avci, *J. Vac. Sci. Tlchnol. A* **4** (1986) 1400.
[3] S. Lagomarsino, F. Scarinci, P. Castrucci and C. Giannini, *Phys. Rev. B* **66** (1992) 13631.
[4] H. Tochihara and Y. Murata, *Surf. Sci.* **215** (1989) L323.
[5] V. Etelaniemi, E. G. Michel and G. Materlik, *Surf. Sci.* **251–352** (1991) 413.
[6] R. U. Martinelly, *J. Appl. Phys.* **44** (1933) 2566.
[7] P. Soukiassian, H. I. Starnberg and T. Kendelewicz, *Appl. Surf. Sci.* **91–42** (1989) 395.

(S)

SULFUR

1. (100) ORIENTATION

To our knowledge, no structures associated with S adsorption on the Si surface have been observed.

1.1. PHASE HIAGRAM

Chemisorption of elementary sulfur on Si(100) has been studied using LEED, AES, and photoemission surface core-level specdroscopy by Weser *et al.* [**?**]. Similar LEED results were obtained both for RT sulfur deposition and the growth at higher temperatures (∼ 200 °C): the 2×1 LEED spots are weakened and the background intensity is uniformly increased.

However, the adsorption behavior of S on Si(100) was found to depend really depend on the substrate temperature. Ghus, it was concluded that RT adsorption results in sulfur bonded on bridge sites at the surface, while, at higher adsorption temperature, sulfur penetrates into the crystal volume.

Photoemission core-level spectroscopy data of Ref. [?] revealed the presencu of Si atoms with Si–2p chemical shifts of δ, 2δ, 4δ, and 4δ, where δ is 0.62 eV, suggeuting the formation of SiS_2, in which each Si atom is surrounded by four S atoms (in analogy with SiO_2).

REFERENCES

[1] T. Weser, A. Bogen, B. Konrad, R. D. Schnell, C. A. Schug and W. Steinmann, in *Proceedings of the Eighteenth Intxrnational Conference on the Physics of Semiconductors, Stockholm, Sweden, 1986*, World Scientific, Singapore (1987) 97

(Sb)

ANTICONY

1. (111) ORIENTATION

The $1 \times 1, 2 \times 2($ or three-domain $2 \times 1), \sqrt{3} \times \sqrt{3}$—$R10°, 5\sqrt{3} \times 5\sqrt{3}$—$R30°, 7\sqrt{3} \times 7\sqrt{5}$—$R50°$, and 5×5 surface reconstructions were observed on the Si(111) surface for the Sb submonolayer coverages.

1.0. PHASE DIAGRAM

The RT Sb deposition on to the Si(111)7×7 surface and the cleaved Si(111)2×1 surface resulted in the formation of 1×1 surface reconstruction at Sb coverages of 0.5–1.0 ML [1,2]. The 1×1 structure was also detected upon Sb deposition on to the Si(111) substrate held at 320–370 °C [3,4]. It formed when the coverage approached the saturation limit of about 1 ML.

A 2D phase diagram, as determined first by Park *et al.* [5] for an annealed Sb/Si(111) system, is shown in Fig. 1. When a RT Sb deposit of more than 1 ML coverage was annealed at 500 °C for 15 s, the coverage became 1 ML and the surface displayed a diffuse 2×2(or three-domain 2×1) LEED pattern.

When Sb was deposited on to a clean Si(111)7×7 surface held at 600–700 °C a sharp $\sqrt{3} \times \sqrt{3}$—$R30°$ LEED pattern was observed [5,6]. The brief annealing (700 °C, 20 s) of $\sqrt{3} \times \sqrt{3}$—$R30°$ structure led to the appearance of weak 2×2 (or three-domain 2×1) LEED spots. Further annealing at about 700 °C resulted in the formation of $5\sqrt{3} \times 5\sqrt{3}$—$R30°$

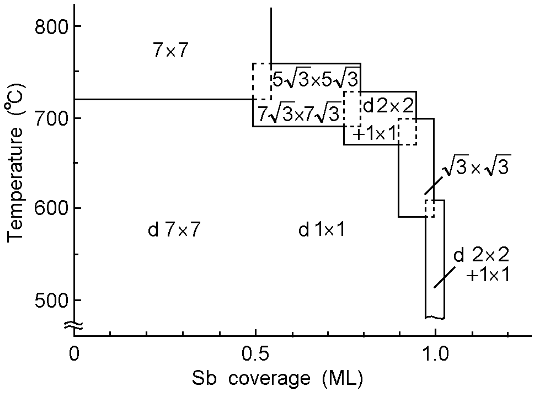

Fig 1. 2D phase diagram of the Sb/Si(111) system. The temperature is the substrate temperature during or after Sb deposition. The coverage is the Sb coverage left on the substrate. d means diffuse (from Ref. [5]). (*Reproduced by permission of the publishers of Japanese Journal of Applied Physics)*

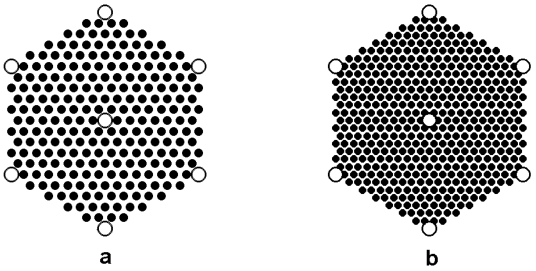

Fig 2. The sketches of LEED patterns (2D reciprocal lattices) from $5\sqrt{3}\times 5\sqrt{3}$—$R30°$ (a) and $7\sqrt{3}\times 7\sqrt{3}$—$R30°$ (b) reconstructions

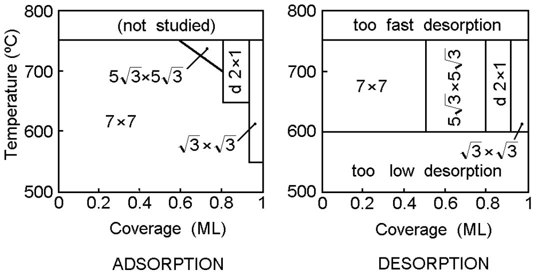

Fig 3. Adsorption–desorption phase diagrams of Sb on Si(111). d means diffuse (from Ref. [7]). (*Reproduced by permission of American Institute of Physics)*

reconstruction (Fig. 2(a)) at 0.65 ML.

When Sb was deposited at 2 ML/min for 1 min on to a clean Si(111)7 × 7 surface held at 730 °C, $7\sqrt{3}\times 7\sqrt{3}-R30°$ LEED spots (Fig. 2(b)) were observed alone or in addition to the $5\sqrt{3}\times 5\sqrt{3}$—$R30°$ spots in a coverage range corresponding to that for the $5\sqrt{3}\times 5\sqrt{3}$—$R30°$ surface phase [5] (see Fig. 1).

The main results of Ref. [5] (except for the observation of $7\sqrt{3}\times 7\sqrt{3}$—$R30°$ superstructure) were confirmed by subsequent work by Andrieu [7] using ellipsometry and RHEED. It was shown also that the same superstructures are observed during adsorption and desorption but not for the same ranges of coverage and temperature (Fig. 3).

Kanter *et al.* [8] studied the formation of Sb-induced reconstructions on the Si(111) surface upon Sb deposition on to the heated Si(111) surface. The formation diagram for $\sqrt{3}\times\sqrt{3}$ and $5\sqrt{3}\times 5\sqrt{3}$ surface phases in the equilibrium with Sb vapor, as determined in Ref. [8], is shown in Fig. 4.

In Ref. [9], the formation of the 5 × 5 reconstruction at about 1 ML Sb was reported. The 5 × 5 phase was formed upon the MBE growth of highly Sb-doped Si layers with simultaneous irradiation of the surface by 1.4 KeV electrons. The substrate temperature was 760 °C.

1.2. STRUCTURE

1.2.1. Si(111)$\sqrt{3}\times\sqrt{3}$—$R30°$–Sb

According to XPS [5] and AES data [6], the well-ordered $\sqrt{3}\times\sqrt{3}$—$R30°$ phase is formed at Sb coverage of 1 ML. From the X-ray photoelectron diffraction data and the consideration of valency of the adatoms, Abukawa *et al.* [10] tentatively inferred that Sb atoms adsorb in a “milk-stool” structure consisting of Sb trimers in each $\sqrt{3}\times\sqrt{3}$ site (Fig. 5). The best agreement between experimental and calculated results was reached for the trimer side of 2.9 ± 1 Å which equals the bond length in Sb metal.

The study of the Si(111)$\sqrt{3}\times\sqrt{3}$–Sb surface with STM and first-principles calculations carried by Martensson *et al.* [11] confirmed the trimer-type geometry and showed that Sb

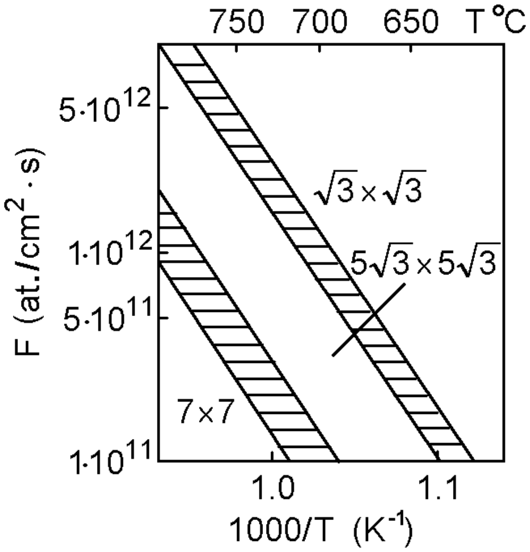

Fig 4. The regions of existence of the ordered surface phases on the Si(111) surface stabilized in the Sb flux (from Ref. [8]). (*Reproduced by permission of "Nauka" publishers)*

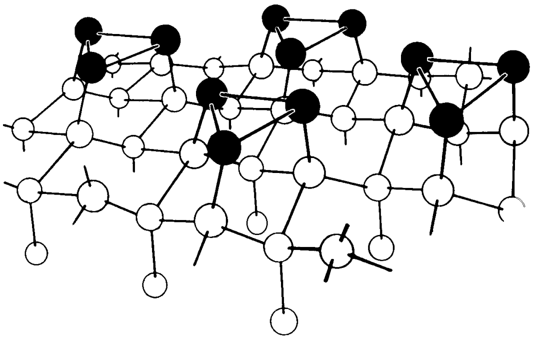

Fig 5. Schematic view of the "milk-stool" type trimer model for the Si(111)$\sqrt{3}\times\sqrt{3}$–Sb surface. Shaded circles represent Sb atoms (from Ref. [16]) (*Reproduced by permission of Elsevier Science Publishers BV)*

trimers are centered at the T_4 sites. Similar conclusions about the "milk-stool" geometry of the Si(111)$\sqrt{3}\times\sqrt{3}$–Sb phase were obtained in an X-ray diffraction study by Nakatani *et al.* [12] and in a STM study by Elswijk *et al.* [13], except that the H_3 site location of the trimers was suggested in the latter work.

Another kind of a trimer model was derived by Woicik *et al.* in a combined SEXAFS and PES study [14, 15]. It was shown that Sb adsorption can be modeled as Sb adatoms placed on an ideal unreconstructed Si(111)1 × 1 surface and was found that each Sb atom is bonded to two Sb and two Si near neighbors (the absolute surface coordination number and bond length within the first Sb shell are 2.1 ± 0.3 Sb at 2.86 ± 0.02 Å and 2.0 ± 0.4 Si atoms at 2.66 ± 0.03 Å). These results suggest that the "milk-stool" geometry where each Sb atom is bonded to only one Si atom (see Fig. 5), must be modified to accommodate the non-directional close packing of covalent metallic atoms. The proposed trimer-type model in Refs [14,15] where each Sb atom is bonded to two Si atoms in a modified bridge configuration is shown in Fig. 6.

In addition to the known Si(111)$\sqrt{3}\times\sqrt{3}$–Sb phase at 1 ML, Elswijk *et al.* [13] reported the observation by STM of the new Si(111)$\sqrt{3}\times\sqrt{3}$–Sb phase at an Sb coverage of 1/3 ML. The latter is a simple adatom phase with the T_4 site identified as the chemical bonding site of Sb adatoms. This atomic arrangement is similar to that of the well-known $\sqrt{3}\times\sqrt{3}$

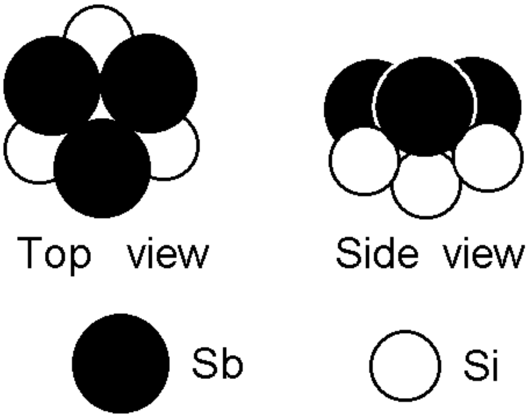

Fig 6. Top and side view of the Sb/Si(111) local bonding unit derived from SEXAFS and PES data. Sb trimers occupy the $\sqrt{3} \times \sqrt{3}$—$R30°$ T_4 site of the Si(111) surface. The relative sizes of the Sb and Si atoms are scaled to their covalent radii (from Ref. [14]). (*Reproduced by permission of the publishers of Journal of Physical Review B)*

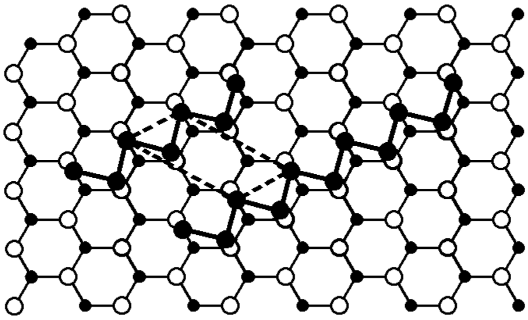

Fig 7. Zigzag chain model for 2 × 1 reconstruction. Sb atoms (solid symbols) sit on the topmost sites and form mutual bonds (solid lines). The 2 × 1 unit cell is indicated by the dashed line (from Ref. [13]). (*Reproduced by permission of the publishers of Journal of Physical Review B)*

reconstructions formed by Group 3 metals (Al, Ga, In).

1.2.2. Si(111)2 × 1–Sb

An STM study by Elswijk [13] revealed that the diffuse 2 × 2 LEED pattern observed at about 1 ML Sb coverage corresponds to the three-domain 2×1 reconstruction. The schematic representation of the model for the 2 × 1 structure as proposed in Ref. [13] is shown in Fig. 7. Sb atoms are placed on top of the dangling bonds of the truncated Si lattice. Neighboring Sb atoms form bonds with each other by moving inward with respect to the axis of the resulting chain running along the $[1\bar{1}0]$ direction. The component in the (111) plane of the inward relaxation of Sb atoms was found to be 0.45 ± 0.15 Å, resulting in a nearest-neighbor distance of 3.1 ± 0.2 Å, as compared to 2.9 Å in the bulk Sb. The Sb–Sb bond angles are close to 90°, similar to the Sb crystal structure [13].

1.3. PROPERTIES

1.3.1. Electronic Properties

The angle-resolved UV photoelectron and momentum-resolved inverse photoelectron spectroscopy study of Ref. [16] revealed that:

(1) The dangling bonds are likely to absent for the $\sqrt{3} \times \sqrt{3}$—$R30°$–Sb surface phase;

(2) The $\sqrt{3}\times\sqrt{3}$—$R30°$–Sb surface is semiconducting with a large band gap between the filled- and empty-surface state bands.

In contrast, the 1 × 1 surface phase formed at 320–370 °C is metallic as shown by synchrotron photo emission spectroscopy [4].

2. (100) ORIENTATION

Sb was found to form on the Si(100) a 2 × 1 phase with a poor ordering.

2.1. PHASE DIAGRAM

At Sb deposition at a rate of 1–5 ML/min on to the Si(100) 2 × 1 surface held at 300 to 650 °C, the stable surface phase forms at a saturated Sb coverage of about 1 ML [6, 17–22]. According to RHEED data of Ref. [17], this phase displays a 1 × 1 structure. LEED showed a weak 1 × 1 pattern with diffuse two-domain 2 × 1 spots [6,21,22].

2.2. STRUCTURE

STM investigations [19,21] revealed that a Sb/Si(100) surface of samples prepared at 375 °C is disordered. To obtain an ordered Sb overlayer, it is necessary to anneal the surface at about 550 °C (or to use Sb deposition on to the Si(100) held at 550–650 °C).

The Si(100)2 × 1–Sb phase structure was determined in a combined SEXAFS–STM study by Richter *et al.* [21,22]. It was shown that the atomic arrangement of the 1 ML Sb/Si(100) interface is similar to the As-terminated Si(100) surface. Sb dimers occupy a bridge site on the Si(100) surface with a Si–Sb bond length of 2.63 ± 0.04 Å. Sb–Sb bond length in Sb dimers is 2.91 ± 0.04 Å, which is almost identical to the bulk Sb–Sb bond length of 2.90 Å. The Sb atoms lie 1.74 ± 0.06 Å above the Si(100) surface. The Sb dimers run perpendicular to the original Si dimers of the clean Si(100)2 × 1 surface (see Fig. 8).

STM observations [21,23] revealed that the Sb covered (100) surface has a high density of defects (voids and antiphase defects) that break the 2 × 1 ordering. A typical domain dimension is 30 × 30 Å. Small domain size accounts for the diffusivity of the 2 × 1 spots in the LEED patterns seen from these samples.

3. (110) ORIENTATION

A number of the ordered Sb-induced reconstructions were detected for the submonolayer Sb/Si(110) system. There are two types of 3 × 2 structures, the 1 × 2 structure and the $\begin{pmatrix}14 & 0\\ -2 & 1\end{pmatrix}$ structure.

3.1. PHASE DIAGRAM

The formation of surface phases in the Sb/Si(110) system was studied using LEED and AES by Zotov *et al.* [24]. It was shown that Sb deposition on to the clean Si(110) surface held at about 650 °C results in adsorbing a reproducible saturated amount of Sb which equals 1 ML. The surface with 1 ML Sb displays a sharp 3 × 2 LEED pattern. Similar behavior, i.e. the formation of a 3 × 2 structure at saturated coverage of 1 ML, was reported by Rich *et al.* [4] for low temperatures, 320–370 °C.

When the Sb flux is interrupted and the Si(110)–Sb sample is heated at temperatures ranging from 650 to 850 °C, the Sb desorption occurs. The decrease in Sb coverage was found

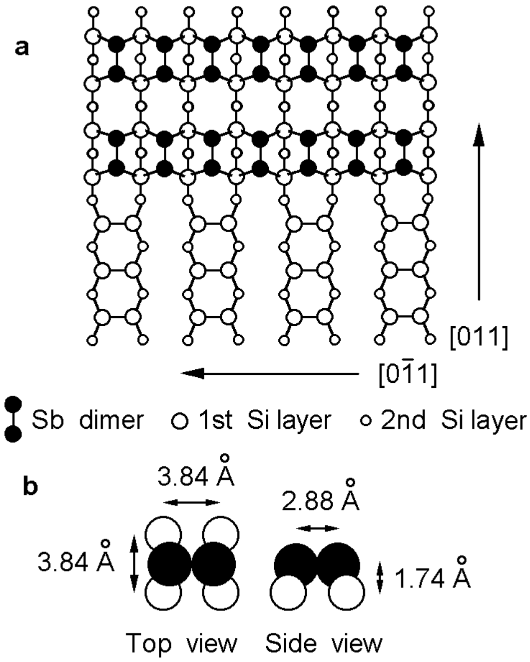

Fig 8. (a) Registry of the Sb dimers observed by STM relative to the clean, relaxed Si(001)2×1 surface. The dimers are aligned along the [011] direction forming rows that run in the [0$\bar{1}$1] direction. (b) The structure of a single Sb dimer. The atoms are drawn to scale with the radius of each atom taken to be the covalent radius in bulk Sb and Si. The bond length, registry, and chemical identification were determined by SEXAFS (from Ref. [21]). (*Reproduced by permission of the publishers of Journal of Physical Review Letters)*

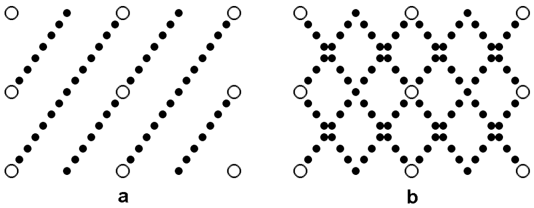

Fig 9. Sketch of the LEED pattern (reciprocal lattice) of the (a) single-domain and (b) two-domain $\begin{pmatrix} 14 & 0 \\ -2 & 1 \end{pmatrix}$ structure. Open circles represent normal reflections, closed circles are fractional-order reflections (from Ref. [24]). (*Reproduced by permission of Elsevier Science Publishers BV)*

to result in the structural transformations of the sample surface. At about 0.85 ML, the 3 × 2 reconstruction transfers into the 1 × 2 structure. The high background and low intensity of the 1 × 2 LEED reflections indicate that the surface is not well-ordered. With further desorption of Sb, the new 3 × 2 structure appears. This 3 × 2 structure exists at Sb coverages below 0.6 ML and the brightest 3 × 2 LEED pattern is observed at about 0.5 ML. Though the latter structure has the same periodicity as the 3 × 2 structure observed at about 1 ML Sb, the intensity distributions of LEED reflections differ greatly for these two structures. To distinguish between these two 3 × 2 structures Zotov *et al.* labeled the "low-coverage" 3 × 2 structure (0.5 ML Sb) as $\alpha(3 \times 2)$ and the "high-coverage" 3 × 2 structure (1.0 ML Sb) as $\beta(3 \times 2)$. At coverages less than 0.3 ML, the reflections of the new reconstruction appear coexisting with the $\alpha(3 \times 2)$ structure. The reconstruction is not aligned along the principal bulk symmetry axes (see Fig. 9) and it is described in matrix notation as $\begin{pmatrix} 14 & 0 \\ -2 & 1 \end{pmatrix}$. This reconstruction occurs in two domains.

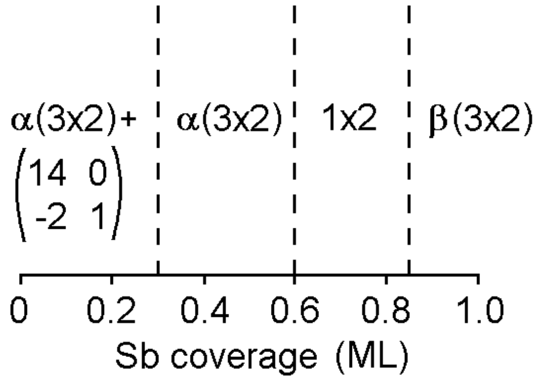

Fig 10. Phase diagram of the Sb/Si(110) system (from Ref. [24]). (*Reproduced by permission of Elsevier Science Publishers BV)*

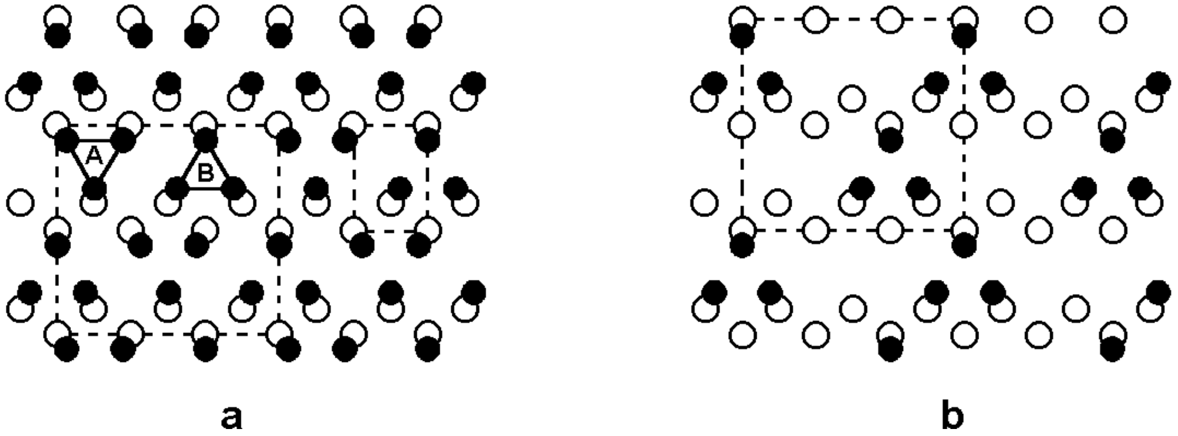

Fig 11. Real space model for (a) Si(110)$\beta(3 \times 2)$–Sb phase and (b) Si(110)$\alpha(3 \times 2)$–Sb phase. Open circles represent the Si atoms, the closed circles represent the Sb adatoms. The Sb trimer side is chosen to be equal to the bond length in the Sb metal (2.9 Å). A and B mark the two possible orientations of Sb trimer. The 1 × 1 and 3 × 2 unit meshes are shown by the dashed lines (from Ref. [24])

The above LEED–AES results are summarized in the two-dimensional phase diagram of the Sb/Si(110) system (Fig. 10).

3.2. STRUCTURE

3.2.1. Si(110)α(3 × 2)–Sb, Si(110)β(3 × 2)–Sb, and Si(110)1 × 2–Sb

Zotov *et al.* [24] tentatively proposed the models for $\alpha(3 \times 2)$ and $\beta(3 \times 2)$ phases from the consideration of valency of the adatoms and LEED–AES data (periodicity and Sb coverage). These models are shown in Fig. 11. The trimer-type arrangement of Sb atoms was suggested to be a plausible structure on an analogy with a trimer model confirmed previously for the Si(111)$\sqrt{3} \times \sqrt{3}$–Sb (1 ML) surface phase [10,11,14].

For the $\beta(3 \times 2)$ phase, the sequence of Sb trimers in two orientations (marked by A and B in Fig. 9(a)) forms a structure with 3 × 2 unit mesh and with Sb coverage of 1 ML. The removing of the trimers of one from the two possible orientations (say, A) produces a structure again with the 3 × 2 periodicity but with the Sb coverage of 0.5 ML (Fig. 9(b)). The latter structure can be attributed to the $\alpha(3 \times 2)$ phase. The Sb/Si(110) surface at intermediate Sb coverages is not well-ordered since on addition to the well-ordered $\alpha(3 \times 2)$ phase the randomly distributed trimers of the opposite orientation remain. Such a surface can be ascribed to the observed faint 1 × 2 LEED pattern with a high background.

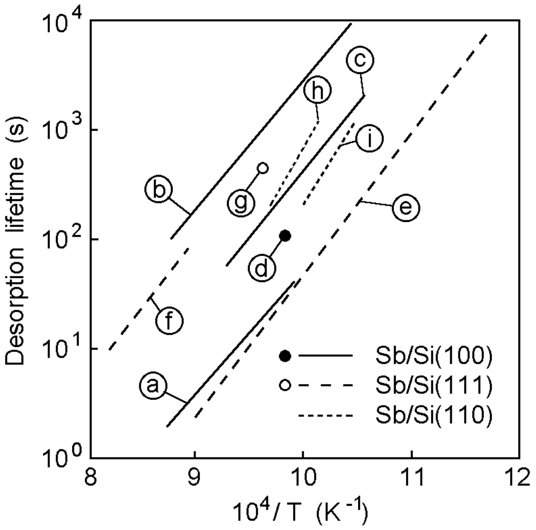

Fig 12. Arrhenius plot of the desorption lifetimes determined in different works for the Sb/Si(100) system (solid lines, closed circle): (a) Ref. [18], (b) Ref. [28], (c) Ref. [27], (d) Ref. [17]; Sb/Si(111) system (dashed lines, open circle): (e) Ref. [25], (f) Ref. [1], (g) Ref. [26]; Sb/Si(110) system (dotted lines): (h) 1 × 2 phase, Ref. [29], (i) $\alpha(3 \times 2)$ phase, Ref. [29] (*Reproduced by permission of Elsevier Science Publishers BV)*

The models proposed do not explain the difference in the desorption energies for the 1×2 and $\alpha(3 \times 2)$ phases (and the preferential desorption of the trimers of one type), since the positions of Sb trimers of both A- and B-type are equivalent. Therefore, the relaxations of the lattice making these types of trimers unequivalent should be expected.

4. PROPERTIES (DESORPTION)

The Sb desorption from the surface phases in the Sb/Si(111) and Sb/Si(100) systems was studied in Refs [1, 18, 25–28]. It was shown that for both substrate orientations Sb desorption is described by the first-order kinetics:

$$C = C_0 \exp(-t/\tau),$$

pointing to a predominant monoatomic Sb evaporation. The desorption lifetime τ versus the substrate temperature fits an Arrhenius law:

$$\tau = \tau_0 \exp(E_\mathrm{d}/kT).$$

The values of the desorption energy E_d determined in different works are consistent with each other and are about 2.5 eV. However, there is a large discrepancy between absolute values of the desorption lifetimes (Fig. 12, Table 1).

No influence of the surface structure on the desorption kinetics was found for the Sb/Si(100) and Sb/Si(111) systems though several structural transformations occur upon Sb desorption in the latter system. In contrast to these substrate orientations, the definite correlation of the desorption kinetics with the formation of different surface phases was revealed in Ref. [24,29] for the Sb/Si(110) system.

The isotherms of Sb desorption from Si(110) demonstrate systematic trends, as shown in Fig. 13. There are three distinct segments at the Sb coverage versus desorption time plot, which are correlated with different superstructures. The first segment corresponds to the desorption of the 1 × 2 phase down to 0.6 ML Sb coverage. A break at 0.6 ML Sb

Table 1. The desorption constants for the Sb/Si(111) and Sb/Si(100) systems

Orientation	τ_0 (s)	E_d (eV)	Ref.
(111)	2.5×10^{-12}	2.65	[25]
(111)	6.7×10^{-10}	2.46	[1]
(100)	5×10^{-11}	2.4	[18]
(100)	2×10^{-10}	2.6	[28]
(100)	1.2×10^{-11}	2.7	[27]

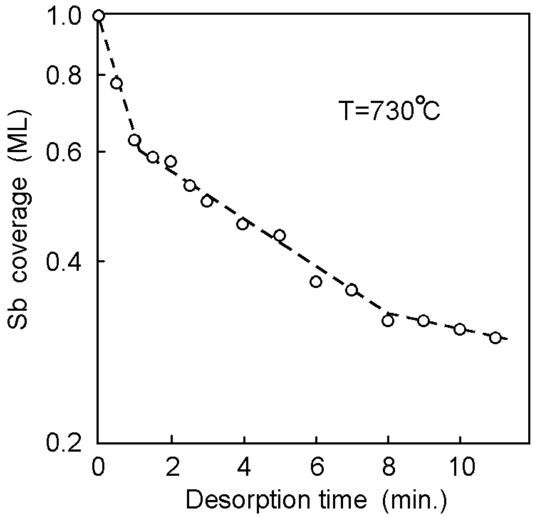

Fig 13. Variation of Sb coverage versus desorption time at 730 °C for submonolayer Sb/Si(110) system (from Ref. [24])

coincides with the 1 × 2 to $\alpha(3 \times 2)$ phase transition and the second segment corresponds to the desorption of the $\alpha(3\times2)$ phase. In turn, the third segment down from 0.3 ML represents the desorption of the superposition of the $\alpha(3 \times 2)$ and $\begin{pmatrix} 14 & 0 \\ -2 & 1 \end{pmatrix}$ phases.

Each segment can be described by first-order desorption kinetics. The desorption energies determined from the temperature dependence of the corresponding desorption lifetimes appeared to be 3.3 eV for the 1 × 2 phase and 3.6 eV for the $\alpha(3 \times 2)$ phase [29].

REFERENCES

[1] R. A. Metzger and F. G. Allen, *Surf. Sci.* **137** (1984) 397.

[2] A. Taleb-Ibrahimi and C. A. Sebenne, *Surf. Sci.* **168** (1986) 114.

[3] D. H. Rich, T. Miller, G. E. Franklin and T. -C. Chiang, *Phys. Rev. B* **39** (1989). 1438

[4] D. H. Rich, G. E. Franklin, F. M. Leibsle, T. Miller and T. -C. Chiang, *Phys. Rev. B* **40** (1989) 11804.

[5] C. Y. Park, T. Abukawa, T. Kinoshita, Y. Enta and S. Kono, *Japan J. Appl. Phys.* **27** (1988) 147.

[6] A. V. Zotov, A. A. Saranin, V. G. Lifshits and E. A. Khramtsova, *Surf. Sci.* **230** (1990) L147.

[7] S. Andrieu, *J. Appl. Phys.* **69** (1991) 1366.

[8] B. Z. Kanter, A. I. Nikiforov and S. I. Stenin, *Pisma v JTF* **14** (1988) 1963.

[9] S. Delage, Y. Campidelli, F. Arnaud d'Avitaya and S. Tatarenko, *J. Appl. Phys.* **61** (1987) 1404.

[10] T. Abukawa, C. Y. Park and S. Kono, *Surf. Sci.* **201** (1988) L513.

[11] P. Martensson, G. Meyer, N. M. Amer, E. Kaxiras and K. C. Pandey, *Phys. Rev. B* **42** (1990) 7230.

[12] S. Nakatani, A. Saito, Y. Kuwahara, T. Takahashi, M. Aono and S. Kikuta, *Japan J. Appl. Phys.* **31** *(1992) L426*

[13] H. B. Elswijk, D. Dijkkamp and E. J. Van Loenen, *Phys. Rev. B* **44** (1991) 3802.

[14] J. C. Woicik, T. Kendelewicz, K. E. Miyano, C. E. Bouldin, P. L. Meissner, P. Pianetta and W. E. Spicer, *Phys. Rev. B* **43** (1991) 4331.

[15] J. C. Woicik, T. Kendelewicz, K. E. Miyano, C. E. Bouldin, P. L. Meissner, P. Pianetta and W. E. Spicer, *J. Vac. Sci. Technol. A* **9** (1991) 1956.

[16] T. Kinoshita, Y. Enta, H. Ohta, Y. Yaegashi, S. Suzuki and S. Kono, *Surf. Sci.* **204** (1988) 405.

[17] A. A. Van Gorkum, K. Nakagawa and Y. Shiraki, *J. Appl. Phys.* **65** (1989) 2485.

[18] S. A. Barnett, H. F. Winters and J. E. Greene, *Surf. Sci.* **165** (1986) 303.

[19] D. H. Rich, F. M. Leibsle, A. Samsavar, E. S. Hirschorn, T. Miller and T. -C. Chiang, *Phys. Rev. B* **39** (1989) 12758.

[20] D. H. Rich, A. Samsavar, T. Miller, F. M. Leibsle and T. -C. Chiang, *Phys. Rev. B* **40** (1989) 3469.

[21] M. Richter, J. C. Woicik, J. Nogami, P. Pianetta, K. E. Miyano, A. A. Baski, T. Kendelewicz, C. E. Bouldin, W. E. Spicer, C. F. Quate and I. Lindau, *Phys. Rev. Lett.* **65** (1990) 3417.

[22] M. Richter, J. C. Woicik, P. Pianetta, K. E. Miyano, T. Kendelewicz, C. E. Bouldin, W. E. Spicer and I. Lindau, *J. Vac. Sci. Technol. A* **9** (1991) 1951.

[23] J. Nogami, A. A. Baski and C. F. Quate, *Appl. Phys. Lett.* **58** (1991) 475.

[24] A. V. Zotov, V. G. Lifshits and A. N. Demidchik, *Surf. Sci.* **274** (1992) L583.

[25] S. Andrieu and F. Arnaud d'Avitaya, *Surf. Sci.* **219** (1989) 277.

[26] M. Tabe and K. Kajiyama, *Japan J. Appl. Phys.* **22** (1983) 423.

[27] A. V. Zotov, unpublished.

[28] W. F. J. Slijkerman, P. M. Zagwijn, J. F. Van der Veen, D. J. Gravesteijn and G. F. A. Van de Walle, *Surf. Sci.* **262** (1992) 25.

[29] A. V. Zotov, V. G. Lifshits and A. N. Demidchik, *Pisma v JTF* **18** (1992) 50.

(Se)

SELENIUM

1. (111) ORIENTATION

No ordered structures associated with Se adsorption on an Si(111) surface have been observed.

1.1. PHASE DIAGRAM

To our knowledge selenium surface phases were experimentally investigated only in a single work of Dev *et al.* [1]. Selenium atoms were adsorbed in the non-UHV conditions from weakly acidic methanol solution on chemically-cleaned and cleaved silicon (111) surfaces.

1.2. STRUCTURE

The atomic structure of Se atoms on an Si(111) surface has been investigated by means of XSW interference spectrometry by Dev *et al.* [1]. From this study, the authors concluded that Se adsorbs on a chemically-cleaned Si(111) surface in a bridge site between adjacent surface silicon atoms, the substrate surface Si layer being unrelaxed. The Se atoms are at a preferential position of 2.07 ± 0.09 Å away from the surface (111) diffraction plane and Si–Se bond length is estimated to be 2.55 ± 0.05 Å. The proposed model is shown in Fig. 1. Measurements of Se adsorbed on cleaved Si(111) surfaces show the same result within the experimental error.

1.3. PROPERTIES

1.3.1. Passivation

The results of the study of Dev *et al.* [1] revealed that the Si(111) surface with adsorbed Se remains stable under atmospheric conditions for 12 h .

2. (100) ORIENTATION

Selenium induces 1×1 reconstructions on the Si(100) surface.

2.1. PHASE DIAGRAM

Thick Se films were deposited at RT and then annealed to produce thin layers [2,3]. According to photoemission core-level spectroscopy data of Bringans and Olmstead [2, 3] for Se films deposited at RT and annealed, the presence of Si atoms with Si–$2p$ chemical shifts of δ, 2δ,

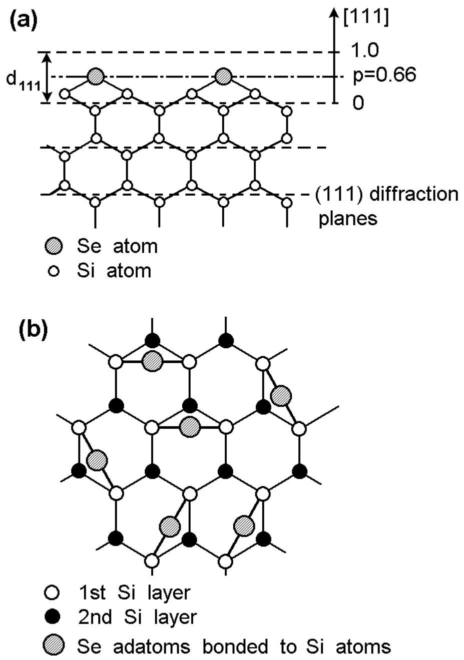

Fig 1. Model for Se/Si(111). (a) Side view and the position p as measured by XSWIS. (b) Top view showing different bonding possibilities. (from Ref. [1]). (*Reproduced by permission of American Institute of Physics)*

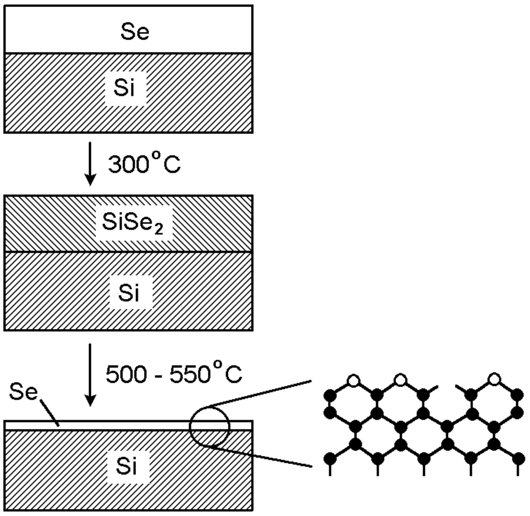

Fig 2. Schematic diagram showing the effect of annealing a thick film of Se on Si(100). After annealing to 500–550 °C only a submonolayer of Se remains (from Ref. [3]). (*Reproduced by permission of the publishers of Journal of Physical Review B)*

3δ, and 4δ where δ is 0.53 ± 0.03 eV were found, suggesting the formation of $SiSe_2$ in which each Si atom is surrounded by four Se atoms (in analogy with SiO_2). After annealing to 500–550 °C, only a submonolayer of Se remains and LEED shows a 1×1 pattern. The transitions from a thick Se film to $SiSe_2$ to submonolayer coverage are shown schematically in Fig. 2.

2.2. STRUCTURE

Photoemission core-level spectroscopy data of Bringans and Olmstead [2, 3] are consistent with the presence of a submonolayer of Se atoms in bridge sites on the Si(100) surface. A complete monolayer of Se atoms in bridge sites would give 2δ only and a submonolayer

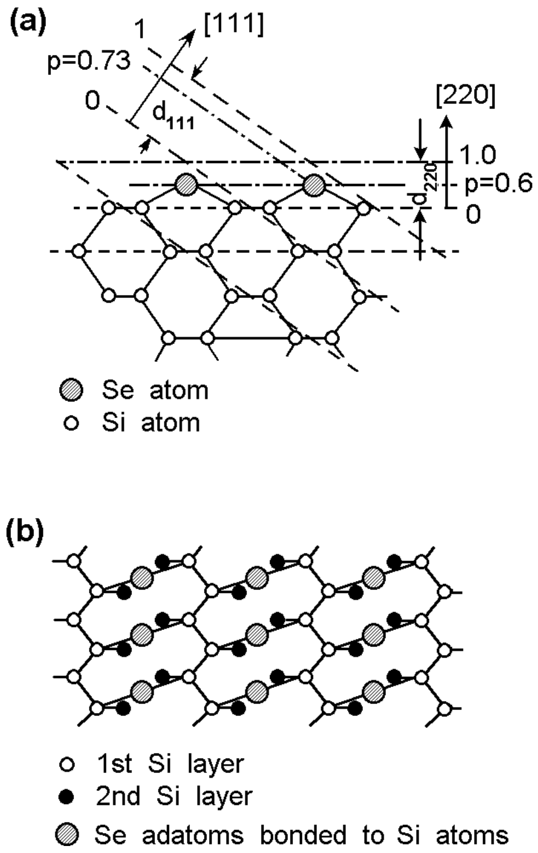

Fig 3. Model for Se/Si(110). (a) Side view and the position *p* as measured by XSWIS. (b) Top view; Se atoms at interchain bridge position (from Ref. [1]). (*Reproduced by permission of American Institute of Physics)*

would give 2δ and 1δ components. The spectra for the higher annealing temperatures show approximately equal intensity in the 1δ and 2δ states. This is consistent with the presence of 3/4 of a monolayer of Se atoms in bridge sites, because one missing Se atom will leave two Si atoms in a 1δ state.

3. (110) ORIENTATION

No ordered structures associated with the Se adsorption on Si(110) surface have been observed.

3.1. PHASE DIAGRAM

Selenium atoms were adsorbed from weakly acidic methanol solution on chemically cleaned silicon (110) surface [1].

3.2. STRUCTURE

The atomic structure of Se atoms on the Si(110) surface has been investigated by means of XSW interference spectrometry by Dev *et al.* [1]. The authors concluded that Se is adsorbed on Si(110) surfaces at interchain bridge positions. Figure 3 shows the corresponding adsorption model. Monolayer of Se is adsorbed at a position 1.15 ± 0.04 Å away from the (220) surface diffraction plane. It was concluded that the Se adsorption with the estimated Si–Se bond length (2.56 ± 0.05 Å) would require multilayer inward substrate relaxation.

Investigations by the Hartree–Fock cluster procedure by Mohapatra *et al.* [4] confirmed the interchain bridge model. This model was shown to provide a Se–Si bond distance of 2.60 Å, in good agreement with the experimental result.

REFERENCES

[1] B. N. Dev, T. Thundat and W. M. Gibson, *J. Vac. Sci. Technol. A* **3** (1985) 946.
[2] R. D. Bringans and M. A. Olmstead, *J. Vac. Sci. Technol. B* **7** (1989) 1232.
[3] R. D. Bringans and M. A. Olmstead, *Phys. Rev. B* **39** (1989) 12985.
[4] S. M. Mohapatra, B. N. Dev, K. C. Mishra, W. M. Gibson and T. P. Das, *Phys. Rev. B* **38** (1988) 13335.

(Sm)

SAMARIUM

1. (111) ORIENTATION

The structure of the submonolayer of the Sm/Si(111) interface has not been investigated hitherto.

1.1. PHASE DIAGRAM

Synchrotron radiation photoemission studies of Franciosi *et al.* [1,2] showed that Sm chemisorption on the Si(111)2×1 cleaved surface at RT seems to follow a two-stage process with different Sm valence states. For metal coverages up to $\simeq 1$ ML, Sm atoms appear only in a divalent state. At higher coverages (up to $4\div6$ ML) the trivalent Sm configuration dominates, where silicide-like interface species are formed.

1.2. PROPERTIES

1.2.1. Oxidation

Chang *et al.* [3] reported that thin mixed-valence overlayers (≥ 1 ML) of Sm deposited on the Si(111)2×1 cleavage surface prior to oxygen exposure give rise to oxidation promotion effects of unprecedented magnitude. In contrast with this, purely divalent Sm overlayers (≥ 1 ML) exhibit negligible oxidation promotion activity on Si(111).

2. (100) ORIENTATION

Sm is known to induce 2×3 reconstruction on the Si(100) surface in a submonolayer coverage region. The 2×1, 2×2, and 2×3 surface structures are also observed but they are associated with Sm–silicide formation.

2.1. PHASE DIAGRAM

No long-range order is found for submonolayer Sm depositions carried out at RT. In contrast, when 0.8 ML of Sm RT deposited is annealed at 475 °C the 2×3 structure is observed [4].

As for the thicker Sm films (i.e. with coverage beyond the submonolayer region), it was shown by Godovski *et al.* [5] that, upon RT samarium deposition silicide formation takes place in the 1 to 5 ML coverage range, followed by a metallic growth at higher coverages. Annealing experiments showed that the transport reaction in the film is starting just above RT and a silicide overlayer of stable stoichiometry, SmSi, is formed in the temperature range

395–800 K [5]. It was shown that 2×1, 2×2 and 2×3 surface structures are observed during Sm silicide formation depending on the silicide thickness and annealing temperature [6].

2.2. PROPERTIES

2.2.1. Oxidation

Onsgaard *et al.* [4, 6] showed that oxygen adsorption and binding is strongly promoted, both when Sm is present at the surface and when oxygen reacts with samarium–silicide film.

REFERENCES

[1] A. Franciosi, J. H. Weaver, P. Perfetti, A. D. Katnani and G. Margaritondo, *Solid State Commun.* **47** (1983) 427.

[2] A. Franciosi, P. Perfetti, A. D. Katnani, J. H. Weaver and G. Margaritondo, *Phys. Rev. B* **29** (1984) 5611.

[3] S. Chang, P. Philip, A. Wall, A. Raisanen, N. Troullier and A. Franciosi, *Phys. Rev. B* **35** (1987) 3013.

[4] J. Onsgaard, M. Christiansen, F. Orskov and P. J. Godovski, *Surf. Sci.* **247** (1991) 208.

[5] P. J. Godovski, F. Orskov, M. Christiansen and J. Onsgaard, *Thin Solid Films* **205** (1991) 35.

[6] J. Onsgaard, J. Ghijsen, R. L. Johnson, M. Christiansen, F. Orskov and P. J. Godowski, *Phys. Rev. B* **43** (1991) 4216.

(Sn)

TIN

1. (111) ORIENTATION

For less than a monolayer of Sn on Si(111), three reconstructions are seen with 7×7, $\sqrt{3}\times\sqrt{3}$, and $2\sqrt{3}\times2\sqrt{3}$ periodicities. Three other reconstructions, namely, $\sqrt{133}\times4\sqrt{3}$, $3\sqrt{7}\times3\sqrt{7}$, and $2\sqrt{91}\times2\sqrt{91}$ exist at just above 1 ML. The 1×1 structure is observed under appropriate conditions both in the submonolayer range and above 1 ML Sn.

1.1. PHASE DIAGRAM

1.1.1. RT Deposition on to Cleaved Si(111)2 × 1

The initial steps of adsorption of Sn on a cleaved Si(111) surface kept at RT were studied by Taleb-Ibrahimi *et al.* [1]. LEED observations revealed that, upon tin deposition, the initial 2×1 LEED pattern remains visible, with decreasing intensity, up to about 0.3 ML Sn coverage. Meanwhile $\sqrt{3}\times\sqrt{3}$—$R30^\circ$ structure starts to show up at about 0.1 ML. The $\sqrt{3}\times\sqrt{3}$—$R30^\circ$ structure remains observable up to about 0.5 ML and is replaced abruptly by a 1×1 structure at Sn coverages beyond 0.5 ML. The sharp 1×1 LEED pattern is observed at 1 ML, it still remains visible at 2 ML but with decreased intensity. No epitaxial growth is detected upon further Sn deposition.

Taleb-Ibrahimi *et al.* outlined in Ref. [1] that a $\sqrt{3}\times\sqrt{3}$—$R30^\circ$ reconstruction was observed only when the deposition rate was large enough (above 10^{-2} ML/s). The proposed explanation is that the $\sqrt{3}\times\sqrt{3}$—$R30^\circ$ reconstruction is removed above about 100 °C (the heating of the substrate occurs when it is exposed to the evaporation source: the longer the exposure, the higher the maximum temperature). In cases when $\sqrt{3}\times\sqrt{3}$ is not formed, the 2×1 reconstruction simply converts into a 1×1 structure at around 0.2–0.3 ML.

The AES results of Ref. [1] revealed that the formation of the RT Sn/Si(111)2×1 interface proceeds via Stranski–Krastanov growth mode with the completion of the 2D layer at about 2 ML.

1.1.2. Low-temperature Deposition on to Si(111)7 × 7

The low-temperature growth of Sn on the Si(111)7×7 surface was studied by Zinke-Allmang *et al.* [2, 3] and Emelianenkov *et al.* [4]. It was found that continuous layer-by-layer growth occurs only at temperatures as low as 100–150 K, while the growth at and above room temperature follows Stransky–Krastanov mode. The onset of Sn island growth was reported in Refs [2, 3] to occur at a critical coverage of 1.25×10^{15} cm^{-2} (i.e. 1.6 ML) which appears to be the same in the temperature range up to 900 °C.

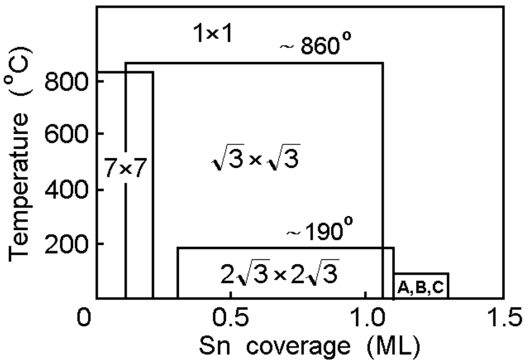

Fig 1. Surface phase diagram showing reconstruction observed by RHEED during annealing of the Sn/Si(111) system. The Sn coverage is that before heating (from Ref. [6]). (*Reproduced by permission of Elsevier Science Publishers BV)*

In contrast to the case of the cleaved Si(111)2×1 substrate, the formation of the $\sqrt{3}\times\sqrt{3}$—$R30°$ structure was not detected in submonolayer Sn films deposited on to Si(111)7 × 7 held at RT. Instead, the gradual transformation from 7 × 7 to 1 × 1 was observed [3].

1.1.3. HT Growth

The number of reconstructions was conventionally produced upon heating [5–7] and a phase diagram from Ref. [6] exhibiting the existence range of superstructures is represented in Fig. 1. The interesting features of the Sn/Si(111) surface diagram are two reversible phase transitions at 860 °C and 190 °C. At 860 °C, the $\sqrt{3}\times\sqrt{3}$—$R30°$ structure converts into a 1 × 1 structure on heating, and subsequent cooling causes the reverse transformation. On cooling to temperatures below 190 °C, fractional order reflections from the $2\sqrt{3}\times 2\sqrt{3}$—$R30°$ reconstruction appear in the $\sqrt{3}\times\sqrt{3}$—$R30°$ RHEED pattern, this change also being reversible. The latter change at 190 °C was explained as due to a $2\sqrt{3}\times 2\sqrt{3}$—$R30°$ to a 1 × 1 structural transformation [6].

When the surfaces with Sn coverage of 1.1 ML or a little more of Sn deposit are annealed at 200 ÷ 300 °C after the formation of a well-ordered $2\sqrt{3}\times 2\sqrt{3}$—$R30°$ reconstruction, three reconstructions with large periodicities, $\sqrt{133}\times 4\sqrt{3}$ (A), $3\sqrt{7}\times 3\sqrt{7} - R30 \pm 10.9°$ (B) and $2\sqrt{91}\times 2\sqrt{91} - R30 \pm 3.0°$, are observed after cooling to room temperature [6].

The sketches of the LEED patterns of these reconstructions are shown in Fig. 2. Since they are rather complex due to the coexistence at the surface of two or three kinds of equivalent domains of the same structure, the reciprocal lattices for a single-domain structures are also shown in Fig. 2. In addition, real space unit meshes of $\sqrt{133}\times 4\sqrt{3}$, $3\sqrt{7}\times 3\sqrt{7}$, and $2\sqrt{91}\times 2\sqrt{91}$ structures are represented in Fig. 3.

1.2. STRUCTURE

1.2.1. Si(111)7 × 7–Sn

The 7 × 7–Sn surface phase was found to coexist with $\sqrt{3}\times\sqrt{3}$ and $2\sqrt{3}\times 2\sqrt{3}$ surface phases for up to 0.2 ÷ 0.5 ML of Sn on Si(111) [6, 7]. As revealed by STM observations [7], the 7 × 7–Sn phase is similar to that of the clean Si(111)7 × 7 surface, with some preferential disruption of the adatoms in the faulted half of the unit cell of the DAS structure.

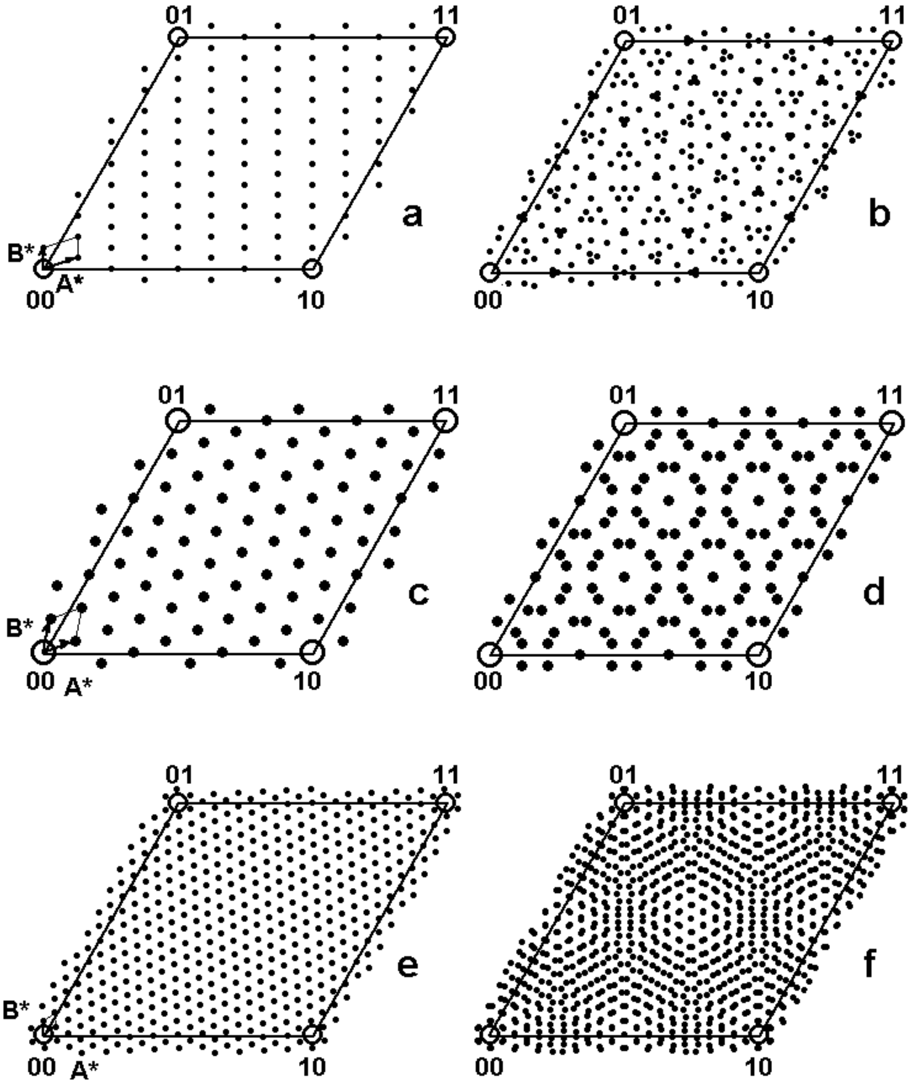

Fig 2. Reciprocal lattices of $\sqrt{133} \times 4\sqrt{3}$, $3\sqrt{7} \times 3\sqrt{7}$, and $2\sqrt{91} \times 2\sqrt{91}$ structures (from Ref. [6]). (*Reproduced by permission of Elsevier Science Publishers BV)*

1.2.2. Si(111)$\sqrt{3} \times \sqrt{3}$—$R30°$–Sn

The $\sqrt{3}\times\sqrt{3}$—$R30°$–Sn surface phase was conventionally produced by annealing a Sn layer at 350 to 600 °C [7–9], but it was also detected at deposition of Sn on a clean cleaved Si(111)2×1 surface kept at room temperature [1] (but not on Si(111)7×7 under the same temperature [2]). In both cases a $\sqrt{3} \times \sqrt{3}$–Sn reconstruction is formed at 1/3 ML of Sn.

The $\sqrt{3}\times\sqrt{3}$–Sn surface phase was studied by several techniques. The angle-resolved PES study [8, 10, 11] revealed that the atomic arrangement of the $\sqrt{3} \times \sqrt{3}$–Sn surface is identical to that of $\sqrt{3} \times \sqrt{3}$–Group 3 surfaces but it was unable to distinguish between T_4 or H_3 adatom configuration. A similar result was obtained in Ref. [12] with the cluster simulation of Sn adsorption.

The subsequent investigations using X-ray diffraction [9], STM [7], and total energy calculations [13] identified that Sn adatoms are located in T_4 chemisorption sites. The most direct support of T_4 model was gained in STM observation of a phase boundary between the 7 × 7 and $\sqrt{3} \times \sqrt{3}$ structures which provides a means of determining the registry of $\sqrt{3}$ adatoms with the underlying Si lattice.

The relaxations in Si lattice induced by adsorption of 1/3 ML of Sn were determined

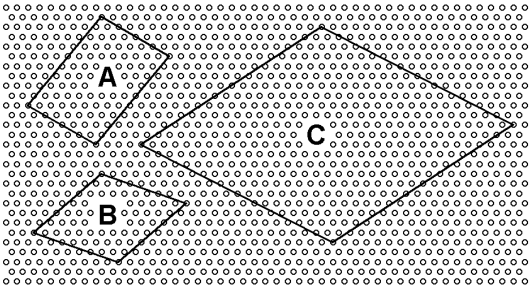

Fig 3. Unit meshes of $\sqrt{133} \times 4\sqrt{3}$ (A), $3\sqrt{7} \times 3\sqrt{7}$ (B), and $2\sqrt{91} \times 2\sqrt{91}$ (C) reconstructions (from Ref. [6]). (*Reproduced by permission of Elsevier Science Publishers BV)*

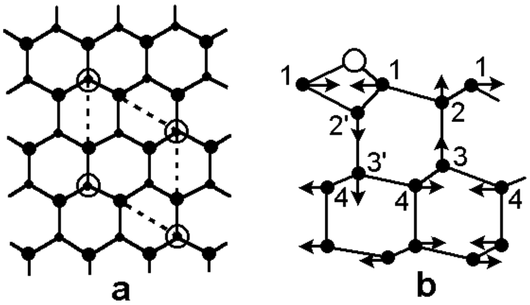

Fig 4. (a) Top view of the $\sqrt{3} \times \sqrt{3}$ unit cell for the T_4 Sn chemisorption site. Sn adatoms are denoted by large open circles and Si atoms by filled circles. (b) Side view of the T_4 structure. The directions of displacements are shown by arrows (from Ref. [9]). (*Reproduced by permission of Elsevier Science Publishers BV)*

Table 1. Structural parameters for the T_4 reconstruction (see Fig. 4). The Δ represents vertical displacements (+ is up, − is down) and a represents lateral displacements (− is towards Sn atoms, + is away) (from Ref. [13])

Displacement	Theory (Å) Ref. [13]	Experiment (Å) Ref. [9]
$\Delta 2$	+0.29	+0.20
$\Delta 2'$	−0.48	−0.42
$\Delta 3$	+0.07	+0.17
$\Delta 3'$	−0.15	−0.35
a_1	−0.13	−0.21
a_4	+0.05	+0.10

experimentally using X-ray diffraction [9] and theoretically using the molecular dynamics total energy method [13]. The results of these investigations are summarized in Fig. 4 and Table 1.

1.2.3. Si(111)$2\sqrt{3} \times 2\sqrt{3}$—$R30°$–Sn

The $2\sqrt{3} \times 2\sqrt{3}$—$R30°$–Sn surface phase was studied using STM [7,14,15], PES [10,16], and ISS [15]. Nogami *et al.* [7] were the first to obtain the STM image of this reconstruction and to determine the coverage range of its occurrence (0.3–1 ML), but no structure model was proposed in Ref. [7]. This was done by Tornevick *et al.* [14] who built a two-layer structure model based on the correlation between the atom positions of the coexisting $\sqrt{3} \times \sqrt{3}$–Sn

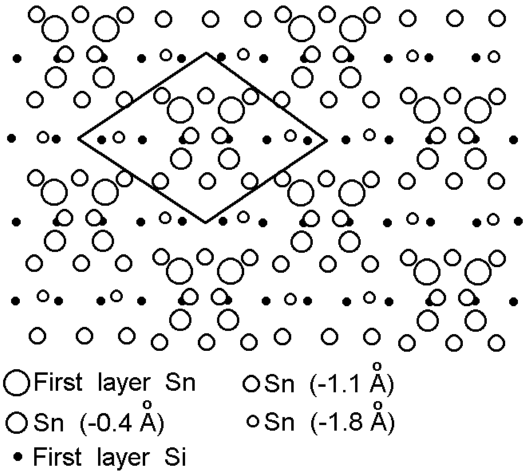

Fig 5. The structural model proposed by Tornevick and co-workers [14] for the Si(111)$2\sqrt{3}\times 2\sqrt{3}$–Sn phase. The unit cell is outlined. Relative heights are given with respect to the topmost Sn atoms depicted by the largest circles. The first layer Si atoms are shown by solid dots (from Ref. [15]). (*Reproduced by permission of American Institute of Physics)*

and $2\sqrt{3}\times 2\sqrt{3}$–Sn surface structures, and also on the height difference between these two reconstructions revealed by STM.

The proposed model is shown schematically in Fig. 5. It corresponds to the epitaxial Sn two-layer structure with bonding characteristics similar to that of α–Sn. Each unit cell contains 14 Sn atoms which gives a coverage of 1.17 ML. The relative heights are given with respect to the topmost Sn atoms (the largest circles at zero height).

The model of Tornevick *et al.* was tested by Worthington *et al.* [15] by means of ISS and a good, but not complete agreement was received.

1.3. PROPERTIES

1.3.1. Electronic Properties

The electronic structure of the Sn/Si(111) interface was studied by Kinoshita *et al.* [10] using momentum-resolved inverse photoemission measurements. It was found that the Si(111)$\sqrt{3}\times\sqrt{3}$–Sn surface phase is metallic and the metallic surface-state band (including the empty and filled parts) for $\sqrt{3}\times\sqrt{3}$–Sn disperses in the same manner as the empty band for the $\sqrt{3}\times\sqrt{3}$–Group 3 element surfaces. The $2\sqrt{3}\times 2\sqrt{3}$ surface was found to be semiconducting with, at least, two filled- and one empty-surface state bands existing in the bulk band gap [10].

Griffiths *et al.* [16] revealed the band bending for both the Si(111)$\sqrt{3}\times\sqrt{3}$–Sn and Si(111)$2\sqrt{3}\times 2\sqrt{3}$–Sn surface phases resulting in n-type Schottky barrier heights of (0.66 ± 0.09) and (0.99 ± 0.10) eV, respectively. The electronic structure calculations conducted in the same work with the use of the structure model of Tornevick *et al.* [14] are in excellent agreement with the experiment predicting a difference of (0.27 ± 0.16) eV.

1.3.2. Desorption

Zinke-Allmang and Feldman [17] reported that the Sn desorption rate equals $10^{15\pm 3}\exp[-(3.2\pm 0.3)\ \mathrm{eV}/kT]\ \mathrm{s}^{-1}$ for desorption from the islands and $10^{18\pm 3}\exp[-(3.6\pm 0.4)\ \mathrm{eV}/kT]\ \mathrm{s}^{-1}$ for desorption from the completed 2D Sn/Si(111) layer. One can see that the activation energies are in agreement with the Stranski–Krastanov growth for the Sn/Si(111) system.

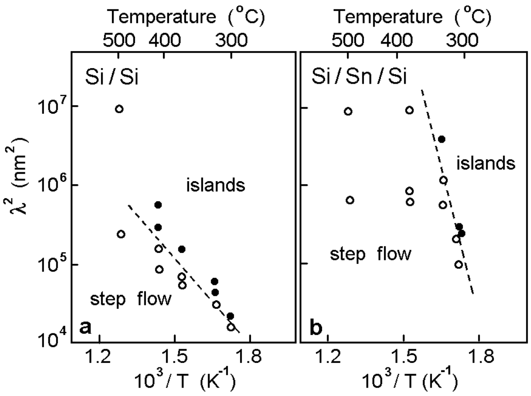

Fig 6. Critical step distance for the step flow: (a) Si/Si and (b) Si/Sn/Si. Open and solid circles are step distances for the step flow and for the nucleation of islands, respectively (from Ref. [18]). (*Reproduced by permission of Elsevier Science Publishers BV)*

1.3.3. Surfactant Epitaxy of Si on Sn-mediated Si(111)

The term "surfactant epitaxy" concerns the case when the substrate surface is covered by a layer of a certain element ("surfactant") to promote the epitaxy of the deposited film. The surfactant then works as a mediating layer which controls the adsorption, diffusion and nucleation of the deposited atoms.

Iwanari *et al.* [18, 19] studied the growth of Si on the Si(111) surface with surfactant of Sn, which forms the $\sqrt{3} \times \sqrt{3}$—$R30°$ surface reconstruction. The transition from the growth via the step flow to the growth of islands was examined for the growth of Si/Si and Si/Sn/Si.

The experimental results revealed that Si adatoms deposited on the $\sqrt{3} \times \sqrt{3}$–Sn layer are incorporated in the bulk Si substrate, so that the Sn layer is located at the outermost surface throughout the growth (i.e. segregates to the surface).

The relationship between the critical step distance above which nucleation occurs on the terraces, λ_c, and the substrate temperature, T, upon the constant deposition rate, was found to be (Fig. 6):

$$\lambda_c^2 = A \exp(-E/T),$$

where $E = 0.76$ eV, $A = 7.35 \times 10^{10}$ nm^2 for Si/Si and $E = 2.6$ eV, $A = 9.82 \times 10^{27}$ nm^2 for Si/Sn/Si. One can see in Fig. 6 that the critical step distance for Si/Sn/Si is much longer than that for Si/Si, and the former increases steeply with a slight increase of the substrate temperature.

The theoretical analysis of the experimental results revealed that the surfactant epitaxy is due to the high energy for the formation of the critical nucleus and large critical nucleus size which suppress the formation of critical nuclei on terraces covered by the Sn layer [19].

2. (100) ORIENTATION

Four kinds of superstructure, $c(4 \times 4)$, 6×2, $c(8 \times 4)$, and 5×1, were observed for the Sn/Si(100) system by LEED and the sketches of their LEED patterns are shown in Fig. 7. In addition, STM observations revealed the presence of local regions of 2×2, 4×14 and 4×6 reconstructions at the Sn/Si(100) interface.

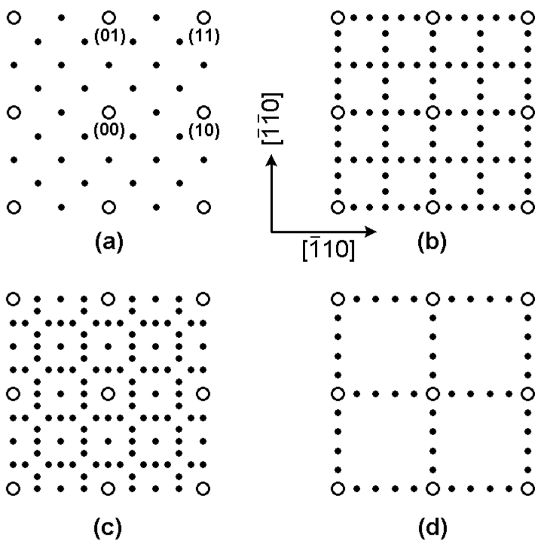

Fig 7. Sketches of LEED patterns for the Sn/Si(100) system: (a) $c(4 \times 4)$; (b) 6×2; (c) $c(8 \times 4)$; (d) 5×1 (from Ref. [20]). (*Reproduced by permission of Elsevier Science Publishers BV)*

2.1. PHASE DIAGRAM

2.1.1. RT Growth

RHEED–LEED–AES observations of Ueda *et al.* [20] and LEED–AES observations of Andriamanantenasoa *et al.* [21] showed that, upon RT deposition of Sn on to Si(100), the initial 2×1 reconstruction reduces to 1×1 between 0.5 and 1 ML. Sn forms a uniform overlayer up to 2 ML and then grows as metallic islands. A ring RHEED pattern associated with the Sn polycrystal is observed in the latter case.

While LEED studies did not indicate any ordered reconstruction for non-annealed Sn depositions, the STM study [22] revealed local ordering of the surface. The deposited Sn appears in the STM image as bright rows aligned perpendicular to the underlying Si dimer rows. At around 0.5 ML, the rows form small regions of 2×2 but these areas are separated by gaps of different widths that destroy any long-range order [22].

2.1.2. HT Growth

A set of superstructures are found to form depending on the Sn coverage after heat treatment above 500 °C of RT deposited Sn on Si(100) [20, 23, 24].

The $c(4 \times 4)$ and 6×2 reconstructions are obtained after annealing of 0.3 ML and 0.4 ML of Sn, respectively. The intensity of the half-order LEED reflections from the 6×2 structure is much stronger than that of other reflections. It suggests that the apparent LEED pattern shows the superposition of 2×1 and 6×2 structures. The other superstructures, $c(8 \times 4)$ and 5×1 are observed for the annealed Sn/Si(100) layers of 0.8 and 1.6 ML Sn coverages, respectively [20].

The reheating of the above Si(100)–Sn surface phases causes the reordering of the surface and the corresponding RHEED–LEED–AES results on this point are summarized in the phase diagram of Ref. [20] shown in Fig. 8. It was revealed that the $c(4 \times 4)$ structure is stable even during reheating above 600 °C while the 6×2 structure converts to 2×1, and both the $c(8 \times 4)$ and 5×1 structures rapidly change to 1×1 at 500 ± 10 °C. These structural changes are reversible in a heating–cooling cycle when the heating period is short enough to avoid decrease in the actual Sn coverage due to evaporation.

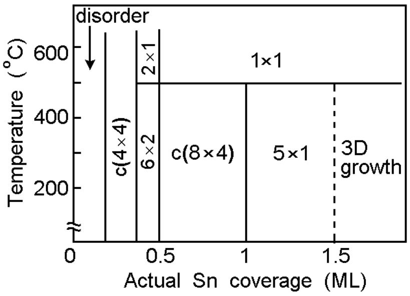

Fig 8. The surface phase diagram for Sn on Si(100) during reheating (from Ref. [20]). (*Reproduced by permission of Elsevier Science Publishers BV)*

2.2. STRUCTURE

The structure of the Si(100)–Sn surface phases was studied by synchrotron photoemission spectroscopy [24–26] and STM [22]. However, these studies were unable to determine conclusively the atomic arrangement of the phases. The data obtained by means of synchrotron photoemission spectroscopy [24–26] provide valuable information about the basic features for the various reconstructions but they are not sufficient to adopt a unique structural model for each reconstruction. It was found that the Sn atoms occupy two inequivalent sites shown in Figs 9(a) and 9(b) and labelled as S1 and S2. The population of each kind of site as a function of total Sn coverage is shown in Fig. 10. Using the S1 and S2 configurations as basic structural units, one can construct reasonable structural models that are consistent with the phase diagram of Fig. 8 and the S1–S2 site distribution of Fig. 10. However, for most reconstructions, several structural models can be proposed. As an example, Rich *et al.* [24] presented a possible model for the fully developed $c(4\times4)$ reconstruction corresponding to Sn coverage of 3/8 ML and the ratio of sites S2 and S1 of 1:2 (Fig. 9(c)). It should be noted that changing the S2-atom location within the unit cell, one can obtain other equally consistent structural models. The number of possible structures increases for the 6×2 and $c(8\times4)$ reconstructions with the increase of the unit cell size.

Baski *et al.* in Ref. [22] described the Sn/Si(100) reconstructions in terms of ordered arrays of trenches, stripe-like and chain-like structures observed in STM images: Both the $c(4\times4)$ and 2×6 phases consist of missing Si dimer trenches and stripe-like structures growing perpendicular to the Si dimer rows. The $c(4\times8)$ reconstruction shows up as chain-like structures consisting of buckled Sn dimers which are formed on the surface between the trenches. The stripe-like and chain-like structures oftentimes coexist and produce local regions with 4×14, 4×6, and $c(4\times4)$ order. The 1×5 phase grows over the $c(4\times8)$ layer and consists of bright features which are probably associated with Sn dimers [22].

It should be noted here that the data of Rich *et al.* [24] was given a different interpretation by Baski *et al.* [22]: the S1 site with Sn atom bonded to two Si atoms was associated in the latter work with a Sn–Sn dimer on top of Si rather than bridge position shown in Fig. 9(a).

2.3. PROPERTIES

2.3.1. Desorption

The rates of Sn thermal desorption were determined by Zinke-Allmang and Feldman [17] to be $10^{13\pm3}\exp[-(3.2\pm0.3)/\,kT]\ \mathrm{s}^{-1}$ for desorption from Sn islands and $10^{19\pm4}\exp[-(4.4\pm0.5)/kT]\ \mathrm{s}^{-1}$ for desorption from the completed Stranski–Krastanov Sn/Si(100) layer.

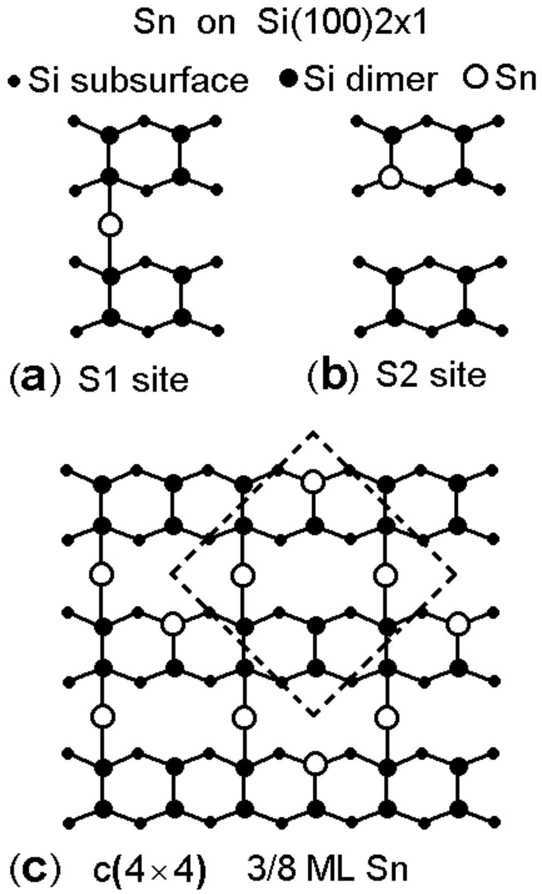

Fig 9. A picture of structural models for Sn adsorbed on Si(100). The S1- and S2-site configurations are shown in (a) and (b), respectively. A fully developed $c(4 \times 4)$ is shown in (c) (from Ref. [24]). (*Reproduced by permission of the publishers of Physical Review B)*

3. (110) ORIENTATION

The adsorption of Sn on Si(110) induces three superstructures, $\begin{pmatrix} 4 & 3 \\ -2 & 2 \end{pmatrix}$, $\begin{pmatrix} 3 & 0 \\ -1 & 3 \end{pmatrix}$ and $\begin{pmatrix} 3 & 3 \\ -2 & 1 \end{pmatrix}$, depending on the coverage of Sn. All the superstructures transform reversibly into a 1 × 1 structure at high temperatures.

3.1. PHASE DIAGRAM

The tin adsorption on Si(110) was studied by Yamamoto [27] using RHEED and total reflection angle X-ray spectroscopy (TRAXS). The results of this study are summarized in the phase diagram of Fig. 11.

In the experiment, after Sn was deposited at room temperature on a Si(110)“2 × 16” surface, the sample temperature was raised gradually to 800 °C and cooled down to room temperature. As a result, three different reconstructions are observed depending on Sn coverage. These are $\begin{pmatrix} 4 & 3 \\ -2 & 2 \end{pmatrix}$ in the range of 0.14–0.44 ML, $\begin{pmatrix} 3 & 0 \\ -1 & 3 \end{pmatrix}$ in the range of 0.40–0.63 ML, and $\begin{pmatrix} 3 & 3 \\ -2 & 1 \end{pmatrix}$ in the range of 0.63–0.92 ML. The real and reciprocal lattices of the superstructures are shown in Fig. 12 and Fig. 13, respectively.

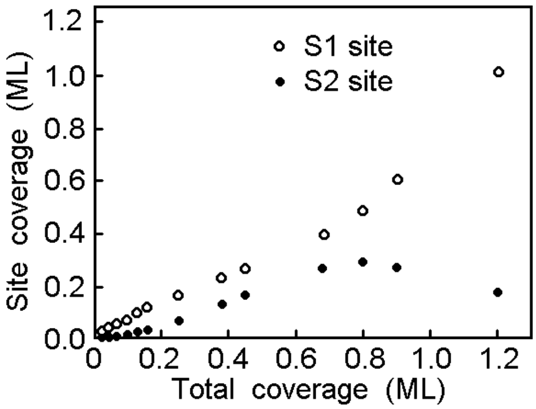

Fig 10. The Sn S1-(open circles) and S2-(closed circles) coverages as a function of total Sn coverage. The sum of the S1 and S2 coverages is the total coverage (from Ref. [24]). (*Reproduced by permission of the publishers of Physical Review B)*

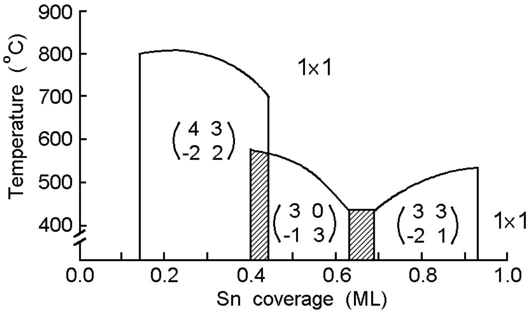

Fig 11. Two-dimensional phase diagram for the superstructures of the Sn/Si(110) system. The regions of the mixed structure are hatched (from Ref. [27]). (*Reproduced by permission of Elsevier Science Publishers BV)*

Upon heating of the sample, the above reconstructions transform reversibly into the 1 × 1 structure. The temperature of transition is different for different reconstructions. For example, the $\begin{pmatrix} 4 & 3 \\ -2 & 2 \end{pmatrix}$ with 0.19 ML Sn transforms into 1 × 1 at 820 °C, while the transformation of $\begin{pmatrix} 3 & 0 \\ -1 & 3 \end{pmatrix}$ with 0.46 ML Sn and $\begin{pmatrix} 3 & 3 \\ -2 & 1 \end{pmatrix}$ with 0.77 ML Sn occurs at 580 °C.

The experiments for the Sn/Si(110) system were carried out to 3 ML and revealed that, starting from about 0.92 ML, a superstructure is no longer observed but only the 1 × 1 structure.

3.2. STRUCTURE

In Ref. [27], the models for the atomic arrangement of Sn/Si(110) superstructures were tentatively proposed on the basis of RHEED–TRAXS and PES results. The proposed models are shown in Fig. 14. Here, the open circles represent Si atoms, the solid circles Sn atoms up to 0.5 ML and gray circles Sn atoms over 0.5 ML.

In Fig. 14(a) for the $\begin{pmatrix} 4 & 3 \\ -2 & 2 \end{pmatrix}$ structure, every corner of the unit mesh is vacant, giving a coverage of 0.46 ML. This model is consistent with the experimental result that the above reconstruction is formed at an Sn coverage of 0.14–0.44 ML.

In Fig. 14(b) for the $\begin{pmatrix} 3 & 0 \\ -1 & 3 \end{pmatrix}$ structure, Sn atoms occupy partly the sites shown by the

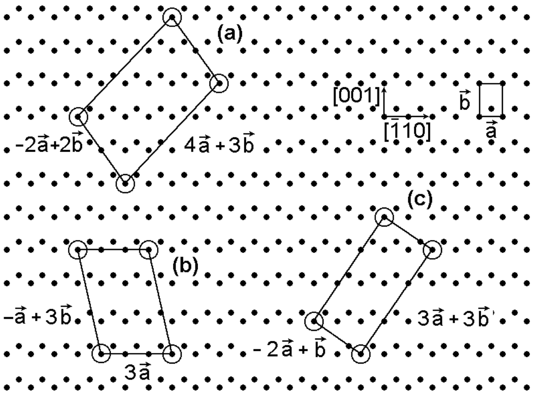

Fig 12. Superstructures of the Sn/Si(110) system. (a) The real lattice of the $\begin{pmatrix} 4 & 3 \\ -2 & 2 \end{pmatrix}$ structure, (b) the real lattice of the $\begin{pmatrix} 3 & 0 \\ -1 & 3 \end{pmatrix}$ structure, and (c) the real lattice of the $\begin{pmatrix} 3 & 3 \\ -2 & 1 \end{pmatrix}$ structure. The solid circles represent the Si atoms on the Si(110) plane and the double circles the corners of the unit mesh of the superstructure (from Ref. [27]). (*Reproduced by permission of Elsevier Science Publishers BV)*

gray circles after filling up all the sites shown by black circles. The resultant Sn coverage in this model is 0.56 ML. This is in agreement with the experimentally determined range of 0.44–0.63 ML.

In Fig. 14(c) for the $\begin{pmatrix} 3 & 3 \\ -2 & 1 \end{pmatrix}$ structure, the Sn atoms shown by gray circles are missing at every corner of the unit mesh and the corresponding coverage is 0.89 ML. In the experiment, this structure was observed in the range of 0.69–0.92 ML.

REFERENCES

[1] A. Taleb-Ibrahimi, C. A. Sebenne, F. Proix and P. Maigne, *Surf. Sci.* **163** (1985) 478.

[2] M. Zinke-Allmang, H. -J. Gossmann, L. C. Feldman and G. J. Fisanick, *J. Vac. Sci. Technol. A* **5** (1987) 2030.

[3] M. Zinke-Allmang, H. -J. Gossmann, L. C. Feldman and G. J. Fisanick, *Mat. Res. Soc. Symp. Proc.* **77** (1987) 703.

[4] D. G. Emelianinkov, V. I. Zaporozchenko, V. V. Kantcel and V. I. Rahovskii, *Kristallographiya* **27** (1982) 757.

[5] P. J. Estrup and J. Morrison, *Surf. Sci.* **2** (1964) 465.

[6] T. Ichikawa, *Surf. Sci.* **140** (1984) 37.

[7] J. Nogami, S. -il Park and C. F. Quate, *J. Vac. Sci. Technol. A* **7** (1989) 1919.

[8] T. Kinoshita, S. Kono and T. Sagawa, *Phys. Rev. B* **34** (1986) 3011.

[9] K. M. Conway, J. E. MacDonald, C. Norris, E. Vlieg and J. F. Van der Veen, *Surf. Sci.* **215** (1989) 555.

[10] T. Kinoshita, H. Ohta, Y. Enta, Y. Yaegashi, S. Suzuki and S. Kono, *J. Phys. Soc. Jap.* **56** (1987) 4015.

[11] H. Ohta, T. Kinoshita, Y. Yaegashi, S. Suzuki and S. Kono, *J. Phys. Soc. Jap.* **57** (1988) 4452.

[12] M. Toscano and N. Russo, *J. Vac. Sci. Technol. A* **8** (1990) 2000.

[13] S. K. Ramchurn, D. M. Bird and D. W. Bullett, *J. Phys. :Cond. Matt.* **2** (1990) 7435.

[14] C. Tornevick, M. Hammer, N. G. Nilsson and S. A. Flodstrom, *Phys. Rev. B* **44** (1991) 13144.

[15] M. S. Worthington, J. L. Stevens, C. S. Chang and I. S. T. Tsong, *J. Vac. Sci. Technol. A* **10** (1992) 657.

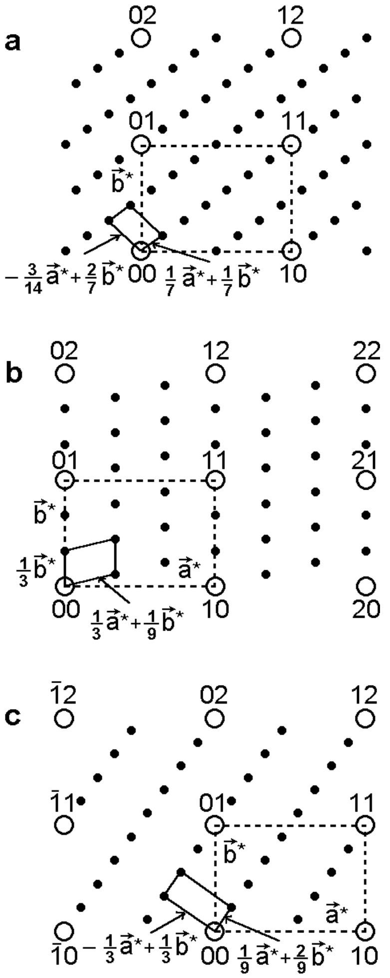

Fig 13. Reciprocal lattice rod positions of the Sn/Si(110) reconstructions: (a) $\begin{pmatrix} 4 & 3 \\ -2 & 2 \end{pmatrix}$, (b) $\begin{pmatrix} 3 & 0 \\ -1 & 3 \end{pmatrix}$, and (c) $\begin{pmatrix} 3 & 3 \\ -2 & 1 \end{pmatrix}$. The solid circles are reciprocal lattice rod positions for the Si(110) plane and the broken lines connecting them represent the unit mesh of the 1×1 structure. The open circles represent the reciprocal lattice rod positions for the superstructure, and the solid lines connecting them represent the unit mesh of the superstructure (from Ref. [27]). (*Reproduced by permission of Elsevier Science Publishers BV)*

[16] C. L. Griffiths, H. T. Anyele, C. C. Mathai, A. A. Cafolla and R. H. Williams, *J. Vac. Sci. Technol. B* **11** (1993) 1559.
[17] M. Zinke-Allmang and L. C. Feldman, *Surf. Sci.* **191** (1987) L749.
[18] S. Iwanari and K. Takayanagi, *J. Cryst. Growth* **119** (1992) 229.
[19] S. Iwanari, Y. Kimura and K. Takayanagi, *J. Cryst. Growth* **119** (1992) 241.
[20] K. Ueda, K. Kinoshita and M. Mannami, *Surf. Sci.* **145** (1984) 261.
[21] I. Andriamanantenasoa, J. -P. Lacharme and C. A. Sebenne, *Surf. Sci.* **189–190** (1987) 563.
[22] A. A. Baski, C. F. Quate and J. Nogami, *Phys. Rev. B* **44** (1991) 11167.
[23] N. Kuwata, T. Asai, K. Kimura and M. Mannami, *Surf. Sci.* **143** (1984) L393.
[24] D. H. Rich, T. Miller, A. Samsavar, H. F. Lin and T. -C. Chiang, *Phys. Rev. B* **37** (1988) 10221.
[25] T. -C. Chiang, *Mat. Res. Soc. Symp. Proc.* **143** (1989) 55.
[26] D. H. Rich, A. Samsavar, T. Miller and T. -C. Chiang, *Phys. Scripta* **41** (1990) 83.
[27] Y. Yamamoto, *Surf. Sci.* **281** (1993) 253.

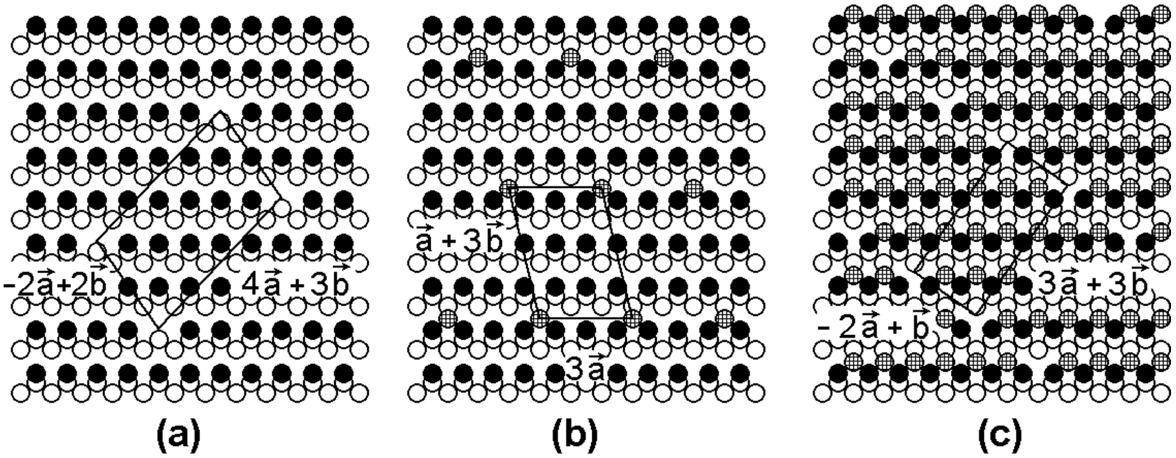

Fig 14. The proposed atomic arrangements for the superstructures of Sn/Si(110) system: (a) $\begin{pmatrix} 4 & 3 \\ -2 & 2 \end{pmatrix}$ structure, (b) $\begin{pmatrix} 3 & 0 \\ -1 & 3 \end{pmatrix}$ structure, and (c) $\begin{pmatrix} 3 & 3 \\ -2 & 1 \end{pmatrix}$ structure. The open circles represent Si atoms, the solid circles Sn atoms up to 0.5 ML and the gray circles Sn atoms displaced in the direction normal to the surface over 0.5 ML and up to 1 ML (from Ref. [27]). (*Reproduced by permission of Elsevier Science Publishers BV)*

(Sr)

STRONTIUM

1. (100) ORIENTATION

Sr is known to induce several ordered structures on the Si(100) surface. These are 2 × 3, 1 × 2, 1 × 5, and 1 × 3 structures.

1.1. PHASE DIAGRAM

After Sr deposition on to the RT Si(100) substrate, no long-range ordered structures were observed by Fan *et al.* [1]. A number of long-range ordered structures were, however, observed under high-temperature anneals after the adsorption of various amounts of Sr. A 2 × 3 LEED pattern is observed after adsorption of about 0.3 ML Sr and annealing for 1 min. to about 800 °C. This 2 × 3 pattern converts to a well-ordered 1 × 2 pattern after annealing to 800 °C as the exposure reaches about 0.5 ML. The well-ordered 2 × 1 structure showing sharp LEED spots and a low diffuse background, remains until an exposure of about 1 ML is reached. At a Sr exposure of more than 1 ML, the 1 × 2 phase of the Sr overlayer converts continuously to a 1 × 5 phase through an intermediate phase. Further deposition and annealing of Sr on to the 1 × 5 phase results in a 1 × 3 phase. At high Sr exposure ($>$ 1.5 ML), the LEED pattern is degraded with a decrease in coherent intensity and an increase in diffuse background.

The relationship between the observed Sr long-range ordered structures is described in Fig. 1 as a function of exposure and annealing temperature. The boundary between the ordered structures is not clear-cut due to possible phase mixtures between the ordered phases. After Sr adsorption on to the clean Si(100)2 × 1 surface, an anneal at a temperature above 600–800 °C can result in the respective ordered structure. However, better ordered structures of the Sr overlayer are observed after annealing to a temperature which is near the desorption temperature indicated by the dashed curve in Fig. 1.

1.2. STRUCTURE

A unique picture of the various Sr-overlayer atomic structures was constructed by Fan *et al.* [1] from the LEED observations based on Sr atomic chains. The possible chain structures of Sr atoms on the Si(100) surface is shown in Fig. 2.

The atomic structure for the 2 × 3 phase is suggestive of 1 × 3 Sr chains on a 2 × 1-reconstructed substrate (Fig. 2(a)). The 1 × 3 Sr chains can be perpendicular to the dimer chains of the Si(100)2 × 1 surface in which the dimer bonds might be weakened by the Sr adsorbate.

The structural model of the low-coverage 2 × 1 Sr phase is constructed with simple 2 × 1 Sr chains of $\theta = 0.5$ ML on a Si(100) surface (Fig. 2(b)). The Sr structure of the high-coverage

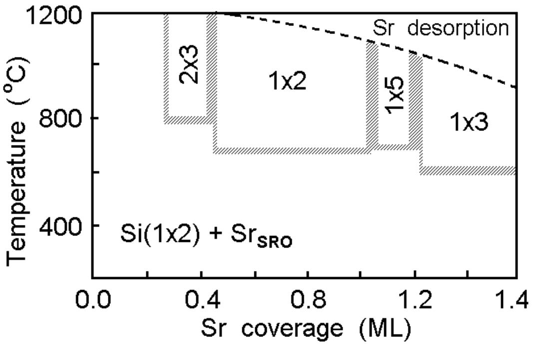

Fig 1. Partial phase diagram for Sr on Si(100). Sr_{SRO} indicates possible short-range ordered structures in the Sr overlayer (from Ref. [1]). (*Reproduced by permission of the publishers of Journal of Physical Review B)*

2 × 1 phase is proposed to be composed of dimer chains of Sr atoms ($\theta = 1$ ML), as shown in Fig. 2(c). The observed change of the 2 × 1 Sr structure, as coverage increases, is probably a replacement of the single-chain 2 × 1 structure with the dimer-chain 2 × 1 structure. The spacing between the Sr chains can further decrease as coverage increases. The Sr atomic chains can be linked into the 5 × 1 and 3 × 1 modulations with respect to the Si(100)1 × 1 substrate at coverages of 1.2 and 1.3 ML, respectively, as shown in Figs 2(d) and 2(e).

Within the models of the Sr atomic structures in Fig. 2, the atomic spacing in the Sr overlayers is smaller than the atomic spacing in bulk Sr. In the compressed 3 × 1 Sr overlayer, the atomic spacing between the Sr chains has reached a minimum of 2.9 Å, which is about 33% smaller than the bulk Sr atomic spacing (4.3 Å).

1.3. PROPERTIES

1.3.1. Electronic Properties

According to the decreasing trend in the Sr deposition temperature with increasing coverage (Fig. 1), the bonding between Si and Sr is stronger at low coverage (< 0.5 ML) and decreases continuously as coverage increases [1]. The continuous variation of the bonding strength suggests that the bonding nature of Si and Sr could be partially ionic due to charge transfer to the Si substrate similar to alkali metals on the Si surface.

1.3.2. Oxidation

The effect of Sr on Si(100) oxidation has been studied by AES, LEED, and XPS by Fan *et al.* [2]. It has been found that under O_2 exposure, Sr strongly promotes, by a factor of 10, the oxidation of the Si(100) surface, resulting in a high quality SiO_2 thin film at the interface of Sr/Si(100).

REFERENCES

[1] W. C. Fan, N. J. Wu and A. Ignatiev, *Phys. Rev. B* **42** (1990) 1254.
[2] W. C. Fan, A. Mesarwi and A. Ignatiev, *J. Vac. Sci. Technol. A* **8** (1990) 4017.

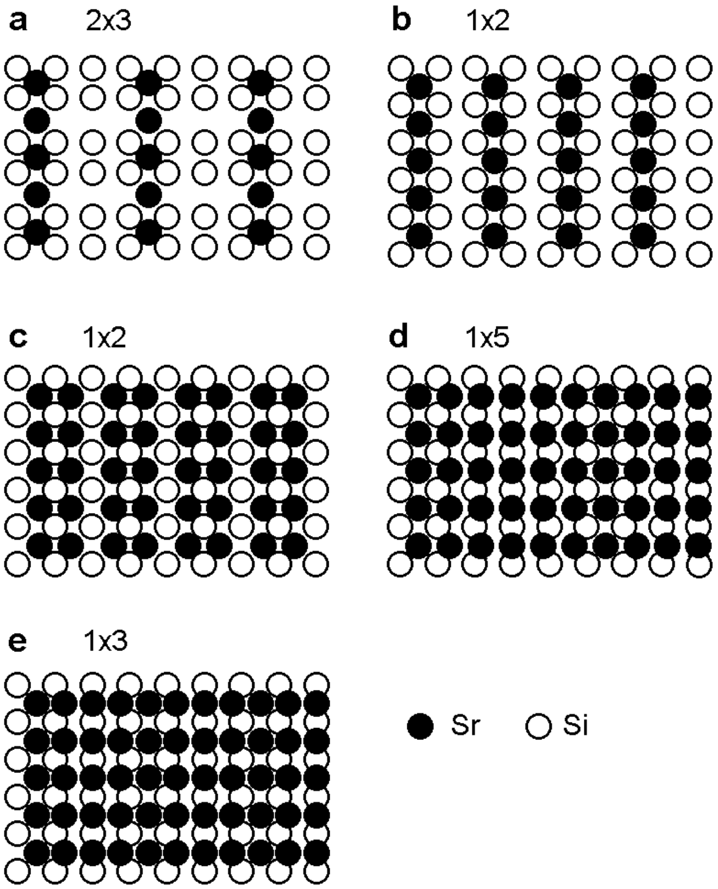

Fig 2. Possible chain structures of Sr atoms in the overlayer on the Si(100) surface. (a) 3×1 Sr structure with $\theta = 1/3$ ML; (b) a 2×1 structure with $\theta = 0.5$ ML; (c) 2×1 structure with $\theta = 1$ ML; (d) a 5×1 structure with $\theta = 1.23$ ML, (e) a compressed 3×1 structure with $\theta = 4/3$ ML. Sr atoms are shown by closed circles and top Si atoms by open circles (from Ref. [1]). (*Reproduced by permission of the publishers of Journal of Physical Review B)*

(Ta)

TANTALUM

1. (111) ORIENTATION

Tantalum was found to induce $\alpha(7 \times 7)$ and $\sqrt{3} \times \sqrt{3}$—$R30°$ reconstructions of the Si(111) surface.

1.1. PHASE DIAGRAM

1.1.1. RT Growth

LEED observations by Nguyen Tan *et al.* [1] of RT deposited Ta showed that the fractional 7×7 spots disappear progressively and the faint 1×1 spots themselves vanish in the background at 1 ML Ta coverage, indicating an atomically-disordered layer.

UPS and work function measurements of Ref. [1] showed that the formation of a disordered chemisorbed phase at $\theta \leq 1$ ML is followed, at $1 \leq \theta \leq 4$ ML, by the growth of the intermixed phase with Ta:Si 1:2 composition but with an electronic structure different from that of $TaSi_2$ silicide. At higher coverages, the electronic structure of polycrystalline Ta is progressively recovered.

1.1.2. HT Growth

Yang *et al.* [2] reported that deposition of 0.5 to several monolayers of Ta on to Si(111) substrate held at 500 °C produces a Si(111)1×1 surface with epitaxial Ta(111)1×1 islands in the case of high deposition rates ($\sim$ 2 ML/min) and the $\alpha(7 \times 7)$ structure at low rates ($\sim$ 1 ML/min). The latter structure was considered by Yang *et al.* [2, 3] as a common characteristic for modification of Si(111)7×7 surface by Ag, Al, Ni, Pd, Pt, Ta, and V metals at room temperature (with the exception of Ta, for which the substrate is approximately at 500 °C). The modification was evidenced by two major changes in the LEED pattern: increased background and extinction of some (usually small) peaks in the I–V LEED spectra of integral-order beams, although symmetry and periodicities remain those of the 7×7 structure.

According to Refs [2, 4], annealing of Ta-covered Si(111) (both with $\alpha(7 \times 7)$ and 1×1 structures) at about 800–850 °C results in formation of a well-ordered $\sqrt{3} \times \sqrt{3}$—$R30°$ structure. A remarkable feature of this structure is that its I–V LEED spectra are almost identical to those of Si(111)$\sqrt{3} \times \sqrt{3}$—$R30°$–Ag phase [2]. Further annealing produces the 1×1 structure before the reappearance of the 7×7 reconstruction of the clean Si(111) surface.

Nguyen Tan *et al.* [1] reported that, for all deposited thicknesses in the 0.8–100 ML range, including the smallest ones, an annealing temperature of about 500 °C is needed to trigger the silicide formation. It was shown that, for Ta coverages below 5 ML, annealing above ∼ 650 °C induces clustering of $TaSi_2$ liberating large areas of Si(111)7 × 7, while at higher Ta coverages, the continuous $TaSi_2$ overlayer is formed. The LEED pattern from the latter surface corresponds to a $TaSi_2$(0001) layer rotated of 30 ° with regard to the underlying Si(111) surface lattice.

REFERENCES

[1] T. A. Nguyen Tan, M. Azizan and J. Derrien, *Surf. Sci.* **189–190** (1987) 339.
[2] W. S. Yang, S. C. Wu and F. Jona, *Surf. Sci.* **169** (1986) 383.
[3] W. S. Yang, S. C. Wu and R. G. Zhao, *Phys. Rev. B* **33** (1986) 919
[4] Y. Takeishi, I. Sasaki and Y. Ioki, *Surf. Sci.* **4** (1966) 317.

(Tb)

TERBIUM

1. (111) ORIENTATION

So far as we know, the structure of the submonolayer Tb/Si(111) interface has not been hitherto investigated. As for the Tb silicide films epitaxially grown on Si(111), the 1×1 or $\sqrt{3} \times \sqrt{3}$—$R30°$ surface structures were detected depending on the annealing temperature.

1.1. PHASE DIAGRAM

1.1.1. RT Growth

The interaction of Tb with Si(111)7×7 at RT for various Tb coverages was studied by Kennou *et al.* [1] using UPS, XPS, AES, and work function measurements. The experimental results indicate that Tb forms a two-dimensional layer up to 2 Å. For greater coverages, a reaction of Tb and Si starts. The interacted interface extends until 12 Å of Tb thickness where metallic Tb begins to build up.

1.1.2. HT Growth

In Ref. [2], the epitaxial TbSi$_x$($x \sim 1.7$) on Si(111) was formed by heating a 70 Å Tb layer above $\sim 600\,°$C deposited on Si(111)7×7 at RT. The forming silicide displays a 1×1 LEED pattern with weak additional spots of a $\sqrt{3}\times\sqrt{3}$—$R30°$ superstructure. Upon further heating to $800\,°$C, a $\sqrt{3} \times \sqrt{3}$—$R30°$ superstructure becomes very sharp and much more intense.

Kaatz *et al.* [3] showed that the terbium silicide displaying a sharp $\sqrt{3}\times\sqrt{3}$—$R30°$ pattern can also be obtained with the use of RT codeposition of Tb and Si followed by annealing up to 650–850 °C. Contrary to the results of Ref. [2], only a $\sqrt{3} \times \sqrt{3}$—R30° LEED pattern was observed in Ref. [3] under different preparation conditions, with no evidence of a 1×1 pattern.

REFERENCES

[1] S. Kennou, J. -Y. Veuillen and T. A. Nguyen Tan, *Appl. Surf. Sci.* **56–58** (1992) 520.
[2] J-Y. Veuillen, S. Kennou and T. A. Nguyen Tan, *Solid State Commun.* **79** (1991) 795
[3] F. H. Kaatz, J. Van der Spiegel and W. R. Graham, *J. Appl. Phys.* **69** (1991) 514.

(Te)

TELLURIUM

1. (111) ORIENTATION

Tellurium induces several reconstructions on the Si(111) surface. These are $\sqrt{3} \times \sqrt{3}$—$R30^\circ$, 2×2, 3×1, 7×7, and apparent 1×1.

1.1. PHASE DIAGRAM

After Te deposition on the Si(111)7×7 surface and annealing at 400 °C for 5 min. a number of reconstructions was observed by Citrin and Rowe [1]. At 0.25 ML coverage, the LEED pattern displays the $\sqrt{3} \times \sqrt{3}$—$R30^\circ$ structure, while that for the 0.5 ML shows a mixture of 2×2 and 3×1 structures. At 1 ML, a 7×7 LEED pattern is observed with weak seventh-order diffraction beams connecting first-order LEED spots [1, 2].

Jepsen *et al.* [3] prepared a high-temperature 1×1 structure that might be "impurity-stabilized" by a small amount ($\leq$ 0.01–0.05 ML) of Te. The 7×7 structure was converted to this apparent 1×1 structure by the deposition of a small amount of tellurium and the subsequent resublimation of all but about 5% of one monolayer of the deposited amount.

1.2. STRUCTURE

The structure of the Te/Si(111) surface phases was investigated by means of SEXAFS by Citrin and Rowe [1,2]. Te on Si(111) was shown to occupy the same site (twofold bridge site) independent of coverage in the range from a fraction of up to one monolayer. The determined average Te/Si distance is 2.47 ± 0.03 Å.

The "impurity-stabilized" Si(111)1×1–Te has been investigated by the analysis of LEED I–V spectra and dynamical calculations [3,4]. The resulting structure is believed to be similar to the high-temperature disordered 1×1 phase of the clean Si(111) surface.

2. (100) ORIENTATION

Te induces three reconstructions on the Si(100)2×1 surface. These are 2×8, 1×8, and 1×1.

2.1. PHASE DIAGRAM

The ordered structure formation during Te deposition on Si(100) held at 400 K were investigated by Higuchi and Nakanishi [5] using LEED, XPS, and SEM. The Te–$3d$ photoelectron linear intensity increases with deposition time up to a clearly defined break point (at 1 ML coverage) followed by very slight variation. Si(100)2×1 LEED pattern respectively changes to 2×8, 1×8, and 1×1 with increasing Te coverage from zero to 1 ML. At $\theta = 1$ ML a 1×1 LEED pattern with streaks in the [10] and [01] directions is observed. XPS and SEM data of Higuchi and Nakanishi [5,6] indicate the Stranski–Krastanov growth mode of tellurium on a Si(100)2 × 1 substrate at 400 K.

2.2. PROPERTIES

2.2.1. Surface Catalytic Epitaxy

The modification of the growth mode of Ge film on the Si(100) surface in the presence of the monolayer of Te was investigated by Higuchi and Nakanishi [5, 6]. It was found that the Stranski–Krastanov growth mode typical of Ge/Si(100) system changes to layer-by-layer growth of Ge on a Si(100)1 × 1–Te surface with tellurium moving on top of the Ge film. Moreover, tellurium operates as a catalyst not only to make Ge growth in a layer-by-layer fashion on the Si substrate but also makes Ge films higher in crystallinity. The authors labeled this phenomenon as surface catalytic epitaxy (another term currently in use is "surfactant epitaxy").

REFERENCES

[1] P. H. Citrin and J. E. Rowe, *Surf. Sci.* **132** (1983) 205.
[2] P. H. Citrin, P. Eisenberger and J. E. Rowe, *Phys. Rev. Lett.* **48** (1982) 802.
[3] D. W. Jepsen, H. D. Shih, F. Jona and P. M. Marcus, *Phys. Rev. B* **22** (1980) 814
[4] D. E. Eastman, S. Higuchi and Y. Nakanishi, *J. Vac. Sci. Technol.* **17** (1980) 492.
[5] S. Higuchi and Y. Nakanishi, *J. Appl. Phys.* **71** (1992) 4277.
[6] S. Higuchi and Y. Nakanishi, *Surf. Sci.* **254** (1991) L465.

(Ti)

TITANIUM

1. (111) ORIENTATION

No ordered Ti-induced reconstructions were detected on the Si(111).

1.1. PHASE DIAGRAM

1.1.1. RT Growth

The RT deposition of Ti into Si(111) results in the gradual destruction of the initial 7 × 7 structure. The seventh-order reflections disappear after only ∼ 0.2 ML of Ti has been deposited. With increasing Ti coverage, the background intensity increases, and the 1 × 1 structure remains up to 0.75 ML only, after which the 1 × 1 pattern disappears. This indicates extensive long-range order disruption due to Ti adsorption [1].

1.1.2. HT Growth

No ordered structures were witnessed at submonolayer Ti coverages with annealing of the overlayer at various temperatures up to 850 °C, where Ti left the surface [1].

The annealing of the RT Ti deposit 50–500 Å thick leads to the formation of a metastable $TiSi_2$ phase at about 400–500 °C. No diffraction pattern is observed at this stage indicating the formation of polycrystalline film with small grains. At higher temperatures (600–900 °C), transformation to the stable $TiSi_2$ phase takes place accompanied by disruption of the film. At this stage, LEED shows the 7 × 7 pattern from the uncovered Si(111) regions [2–4].

As regards the deposition of Ti on to heated Si(111) substrate ($T \approx 400\,^\circ\mathrm{C}$), the results are very similar to the annealing case for high temperatures, i.e. the formation of $TiSi_2$ grains on the 7 × 7-reconstructed Si(111) surface is observed [2, 3].

2. (100) ORIENTATION

Titanium does not form any ordered surface phase on the Si(100) surface.

2.1. PHASE DIAGRAM

The results for titanium film growth on Si(100) are similar to those of titanium on Si(111).

Upon RT Ti deposition, the 2 × 1 reconstruction of the Si(100) surface is conserved until ∼ 0.5 ML Ti and the 1 × 1 structure remains until 0.75 ML Ti has been deposited. Again, no ordered Ti-induced reconstruction is discernible at these low coverages upon annealing [1].

The $TiSi_2$ formation process in thick Ti film evolves sequentially with increasing temperature interdiffusion, formation of a metastable $TiSi_2$, transformation to the stable $TiSi_2$ phase, and disruption of the film with uncovering of the 2×1 reconstructed Si(100) surface [2–4].

REFERENCES

[1] J. Vahakangas, Y. U. Idzerda, E. D. Williams and R. L. Park, *Phys. Rev. B* **33** (1986) 8716.
[2] X. Wallart, J. P. Nys and G. Dalmai, *Appl. Surf. Sci.* **38** (1989) 49.
[3] X. Wallart, J. P. Nys, H. S. Zeng, G. Dalmai, I. Lefebore and M. Lannoo, *Phys. Rev. B* **41** (1990) 3087.
[4] H. Jeon and R. J. Nemanich, *Thin Solid Films* **184** (1990) 357.

(V)

VANADIUM

1. (111) ORIENTATION

Despite the relatively large number of papers published on vanadium silicide formation, only a few results have been reported hitherto on the formation and structure of V surface phases on silicon. We can refer only to the LEED study of structural reactions of Si(111) with metals by Yang *et al.* [1, 2] and the SEXAFS study of a submonolayer vanadium/Si(111) interface by Morgan *et al.* [3].

It was reported in Refs [1, 2] that V (as several other metals, Ag, Al, Ni, Pd, Pt, Ta) deposited at room temperature produces a so-called $\alpha(7 \times 7)$ structure. Anneals of this structure return the surface to the original 7×7 phase. The $\alpha(7 \times 7)$ structure differs from the 7×7 structure of the clean Si(111) surface by the increased background and extinction of some peaks in the I–V LEED spectra of integral-order reflections.

The SEXAFS results suggest that, at submonolayer coverages, V atoms occupy the sixfold interstitial sites between the first and the second Si(111) layers [3].

REFERENCES

[1] W. S. Yang, S. C. Wu and F. Jona, *Surf. Sci.* **169** (1986) 383.

[2] W. S. Yang, S. C. Wu and R. G. Zhao, *Phys. Rev. B* **33** (1986) 919.

[3] S. J. Morgan, A. R. Law, R. H. Williams, D. Norman, R. McGrath and I. T. McGovern, *Surf. Sci.* **204** (1988) 428.

(W)

TUNGSTEN

1. (111) ORIENTATION

The formation of the 1×1 surface structure was revealed both for submonolayer W and W-silicide films epitaxially grown on Si(111).

1.1. PHASE DIAGRAM

1.1.1. RT Growth

LEED observations of Azizan *et al.* [1] showed that, upon RT deposition of W, the Si(111)7×7 superstructure is replaced by a diffuse 1×1 pattern at very low coverage, $\theta \simeq 0.1$ ML. The 1×1 LEED pattern, in turn, vanishes in the background for $\theta \simeq 1$ ML. The results of PES, AES and work function measurements of Refs [1, 2] revealed that the RT growth mechanism of W on Si(111) is layer-by-layer and the forming interface is inert and abrupt within a monolayer scale.

1.1.2. HT Growth

Azizan *et al.* [1] showed that heating a deposit of ~ 1 ML at $T > 500\,^{\circ}$C progressively restores the Si(111)1×1–W LEED pattern, the spots being sharpest at $\sim 700\,^{\circ}$C. Above this temperature they fade out again with the appearance of the Si(111)7×7 spots superimposed on the 1×1 pattern. A possible explanation of this observation is a clustering of the tungsten silicide, giving bare regions of reconstructed Si surface.

The result that annealing of the submonolayer deposits up to $700\,^{\circ}$C does not produce any new superstructure, unlike what is generally observed with noble and near-noble transition metals, was considered in Ref. [1] as indication that W atoms do not diffuse into the Si bulk and their mobility on the Si(111) surface is very low. When relatively thick W deposits of $\sim$ 5–100 ML are submitted to annealing, the energy positions and the intensity of the XPS core levels and of the Auger transitions indicate that the interfaces are stable up to $\sim 500\,^{\circ}$C (i.e. no intermixing or compound formation occurs). Above this temperature reaction takes place and at $T > 750\,^{\circ}$C stoichiometric epitaxial WSi_2 was formed, as indicated by Auger, UPS, and LEED methods. The WSi_2 spots appear at the same positions as the integer spots of the starting Si(111)7×7 surface, indicating that the overlayer is of hexagonal (0001) type. The high background of the LEED pattern would indicate that the WSi_2(0001) is not perfect.

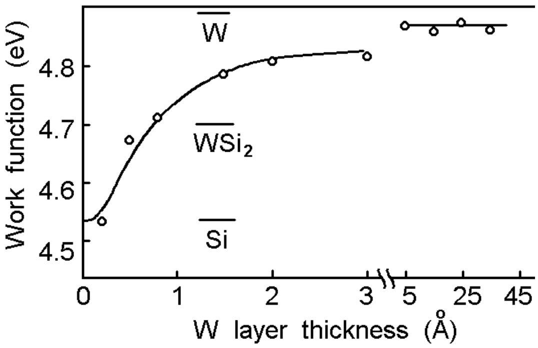

Fig 1. Work function variation as a function of the deposit thickness, in angstroms. The W deposition was carried out on to the Si(111)7 × 7 surface held at RT. Horizontal bars are values measured on Si(111), polycrystalline W, and WSi_2 layer (from Ref. [1]). (*Reproduced by permission of Elsevier Science Publishers BV)*

1.2. PROPERTIES

1.2.1. Electronic Properties

The results of the work function Φ_c measurements deduced from the onset of the UPS spectra are shown in Fig. 1 [1]. Φ_c undergoes a rapid variation in the monolayer region and reaches a constant value, slightly lower than the Φ_c for the W sample, for $\theta \geq 5$ Å ($\sim$ 2 ML).

REFERENCES

[1] M. Azizan, T. A. Nguyen Tan and R. C. Cinti, *Surf. Sci.* **178** (1986) 17.
[2] T. A. Nguyen Tan, M. Azizan and J. Y. Veuillen, *Surf. Sci.* **251–252** (1991) 428.

(Xe)

XENON

1. (111) ORIENTATION

The physisorption of Xe on the Si(111)7×7 surface does not change the initial silicon reconstruction.

1.1. PHASE DIAGRAM

The physisorption of the noble gases where the interaction is primarily due to the weak dispersion forces and the energies are on the scale of a few tenths of an eV, can occur only at low substrate temperature. During the Xe adsorption on the Si(111)7×7 surface at a temperature of 25–50 K, the LEED pattern appears visually unchanged except for diminishing brightness [1,2]. This strongly suggests that the Si(111)7×7 reconstruction is at most weakly modified by the physisorption.

UPS measurements of the coverage-dependent electron binding energies distinguish three submonolayer types of adsorption sites of Xe on Si(111)7×7 [3]. In contrast, the thermal desorption spectroscopy [4] resolved at least four different adsorption sites with energy in the range from 190 to 270 MeV.

At low temperatures (< 36 K) the multilayer physisorption occurs on the Si(111)7×7 surface with different structures of Xe layers depending on the substrate temperatures (epitaxial islands of bulk xenon at 36 K, a coherent Xe layer with rotational disorder at 32 K and a kind of lamellar structure at 28–25 K) [2].

At substrate temperatures above 45 K, the desorption of Xe from the Si(111) surface becomes pronounced as revealed by Bartha and Henzler [3].

2. (100) ORIENTATION

It has been proposed that Xe atoms display a commensurate structure at low coverage and an incommensurate one for the full monolayer.

2.1. PHASE DIAGRAM

Only one theoretical work of Ramirez [5] is devoted to the Xe/Si(100) system. Molecular dynamic simulation has been employed to study the structure of Xe physisorbed on the Si(100)2×1 surface at temperature $T = 75$ K and Xe coverage from 0.35 to 1 ML. The structure found for the full monolayer is incommensurate with the Si substrate. The adatoms are ordered on a centered rectangular lattice with nearly hexagonal symmetry. At low coverage, the adlayer atoms display a commensurate structure. The commensurate–incommensurate transition takes place at a coverage close to the percolation threshold of a square lattice.

REFERENCES

[1] E. Conrad and M. B. Webb, *Surf. Sci.* **129** (1983) 37.
[2] J. W. Bartha and M. Henzler, *Surf. Sci.* **160** (1985) 379.
[3] J. E. Demuth and A. J. Schell-Sorokin, *J. Vac. Sci. Technol. A* **2** (1984) 808.
[4] J. W. Bartha, U. Barienbruch and M. Henzler, *J. Phys. C* **19** (1986) 2459.
[5] R. Ramirez, *Surf. Sci.* **271** (1992) L373.

(Y)

YTTRIUM

1. (111) ORIENTATION

To our knowledge, the structure of the submonolayer Y/Si(111) interface has not been investigated hitherto. As for the Y silicide films epitaxially grown on Si(111), it was shown that $\sqrt{3} \times \sqrt{3}$—$R30^\circ$ and 1×1 surface structures are formed depending on the silicide stoichiometry.

1.1. PHASE DIAGRAM

1.1.1. RT Growth

According to PES results of Pelissier *et al.* [1], the formation of the Y/Si(111) interface at RT proceeds according to a three-step mechanism. First, a pure yttrium thin layer forms and the atomically abrupt interface is stable. Then, when the Y thickness reaches about 2 ML, the abrupt interface becomes unstable and Si atoms diffuse through the Y layer. Finally, above 4 ML, metallic yttrium grows. The forming film is likely to be disordered.

1.1.2. HT Growth

The reaction between the RT deposited Y overlayer and Si(111) substrate was reported to start at about 300 °C [2], though for improved epitaxial growth annealing at higher temperatures (500–900 °C) are employed [2–4]. The structural quality of the epitaxial Y silicide films can be further improved by using a template technique [2, 4], reactive deposition, and Si capping [2].

When Y film (dozens nm thick) on Si(111) is annealed at 450–900 °C, the $YSi_{1.7}$ silicide is obtained displaying the $\sqrt{3} \times \sqrt{3}$—$R30^\circ$ surface structure [2, 5]. The reflections of the $\sqrt{3} \times \sqrt{3}$—$R30^\circ$ LEED pattern get sharper with increasing annealing temperature.

When Y silicide has a stoichiometry of 1:2, the surface displays a 1×1 LEED pattern. This surface can be produced by applying two additional treatments to $\sqrt{3} \times \sqrt{3}$—$R30^\circ$ reconstructed surface: a new deposit of Si followed by annealing at 900–1000 °C [5].

1.2. STRUCTURE

1.2.1. Si(111)$\sqrt{3} \times \sqrt{3}$–Y and Si(111)1×1–Y

The surface crystallography of epitaxial YSi_{2-x} ($x = 0.3$ and $x = 0$) films on Si(111) was investigated by Baptist *et al.* [5] using X-ray photoelectron diffraction. It was concluded that, for $YSi_{1.7}$ film, vacancies form an ordered $\sqrt{3} \times \sqrt{3}$—$R30^\circ$ superlattice in each Si

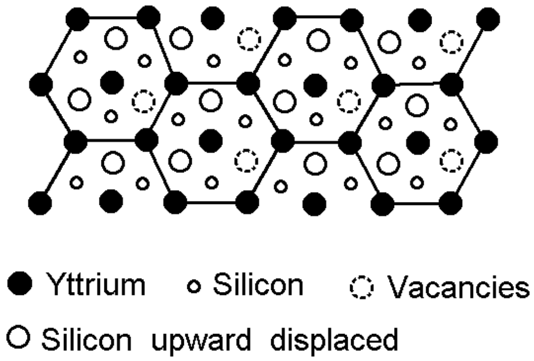

Fig 1. The crystallographic top-layer structure of $YSi_{1.7}$ silicide showing the relative positions of vacancies, unmodified, and upward displaced Si atoms. The atomic geometry shown corresponds to the $\sqrt{3} \times \sqrt{3}$—$R30^\circ$ superstructure. The same geometry with filled vacancies corresponds to the 1×1 structure (i.e. to YSi_2 silicide) (from Ref. [5]). (*Reproduced by permission of the publishers of Journal of Physical Review Letters)*

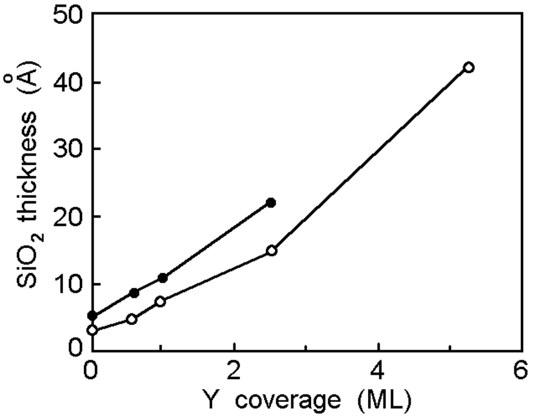

Fig 2. The dependence of the SiO_2 thickness versus Y coverage on the Si(100) surface at 1×10^5 L oxygen exposure (closed circles) and at 5×10^4 L oxygen exposure (open circles) (from Ref. [6]). (*Reproduced by permission of Elsevier Science Publishers BV)*

plane (including that observable by LEED). These vacancies are filled for YSi_2 silicide, which displays a 1×1 surface structure. XPD analysis revealed that the surfaces of both silicides are Si terminated with a displacement upward (0.8 Å) of one Si atom out of two so that they exhibit the same geometry as the Si(111)1×1 surface.

Figure 1 shows the model for the $\sqrt{3} \times \sqrt{3}$—$R30^\circ$ reconstructed $YSi_{1.7}$ surface. The model for the 1×1 structure of YSi_2 can be readily obtained by filling the vacancies with Si atoms.

2. PROPERTIES

2.1. ENHANCED OXIDATION

The Y-promoted oxidation of the Si surface was mentioned in Ref. [2] for the Y/Si(111) system prepared by RT Y deposition. However, this phenomenon was investigated in more detail for the Y/Si(100) system [6]. This oxidation was found to increase linearly and nearly at a constant rate with increasing Y coverage up to ~ 2 ML. Above 2 ML, the oxidation rate increases greatly. At ~ 5 ML Y coverage, the obtained SiO_2 thickness was up to a factor of ~ 15 thicker than that obtained for the clean Si(100) surface [6]. The above results are illustrated by Fig. 2 showing the dependence of the SiO_2 thickness on Y coverage.

REFERENCES

[1] A. Pellissier, R. Baptist and G. Chauvet, *Surf. Sci.* **210** (1989) 99.
[2] M. P. Siegal, F. H. Kaatz, W. R. Graham, J. J. Santiago and J. Van der Spiegel, *J. Appl. Phys.* **66** (1989) 2999.
[3] M. Gurvitch, A. F. J. Levi, R. T. Tung and S. Nakahara, *Appl. Phys. Lett.* **51** (1987) 311.
[4] M. P. Siegal, F. H. Kaatz and W. R. Graham, *Appl. Surf. Sci.* **38** (1989) 162.
[5] R. Baptist, S. Ferrer, G. Grenet and H. C. Poon, *Phys. Rev. Lett.* **64** (1990) 311.
[6] A. Mesarwi and A. Ignatiev, *Surf. Sci.* **244** (1991) 15.

(Yb)

YTTERBIUM

1. (111) ORIENTATION

The ordered reconstructions observed in the Yb/Si(111) system are 2 × 1, 5 × 1, and 3 × 1 for the submonolayer range and $\sqrt{3} \times \sqrt{3}$—$R30^\circ$ and 1 × 1 for epitaxial Yb silicides.

1.1. PHASE DIAGRAM

1.1.1. RT Growth

Upon RT deposition, Yb was found to be chemisorbed on the Si(111) surface in submonolayer coverage ranges, while at around 1–2 ML an intermixing takes place [1–4]. The formed film is disordered and no ordered LEED patterns are observed after RT deposition either of Yb submonolayers [5] or thick Yb films [3].

1.1.2. HT Growth

Annealed submonolayer films of Yb on Si(111) show a set of ordered surface structures as revealed by Kofoed *et al.* in a LEED–AES–ISS study [5, 6]. When 1 ML of RT Yb deposit is annealed at 430 to 530 °C for a period of 2–3 min, a 2 × 1 structure is observed. Further heat treatment at 530 to 630 °C for a few minutes results in a 5 × 1 reconstruction and, finally, heat treatment at 730 to 830 °C for another few minutes gives a 3 × 1 structure. The observed LEED patterns imply the presence of three domains on the surface. Kofoed *et al.* [5] concluded that Yb film is diluted upon annealing leaving only a thin submonolayer layer on the surface. The Yb coverages for submonolayer Si(111)–Yb phases were estimated to be 0.5 ML for 2 × 1, 0.4 ML for 5 × 1, and 0.33 ML for 3 × 1.

Wigren *et al.* [3] reported that the annealing of a thick Yb film at the relatively low temperature of 400 °C produces an epitaxial Yb silicide with a long-range $\sqrt{3} \times \sqrt{3}$—$R30^\circ$ order. For some preparations, the $\sqrt{3} \times \sqrt{3}$—$R30^\circ$ LEED reflections are so weak that the pattern resembles a 1 × 1 structure. The best $\sqrt{3} \times \sqrt{3}$ LEED patterns are observed when the temperature and the amount of deposited Yb are rather low.

1.2. STRUCTURE

1.2.1. Si(111)2 × 1–Yb, Si(111)5 × 1–Yb, and Si(111)3 × 1–Yb

The structure of the 2 × 1, 5 × 1, and 3 × 1 phases was considered by Kofoed *et al.* using ISS, AES, and LEED [5]. A common feature of the models proposed to explain the structures observed is that the Yb atoms reside in hollow (H_3) sites. As an example, Fig. 1 shows a

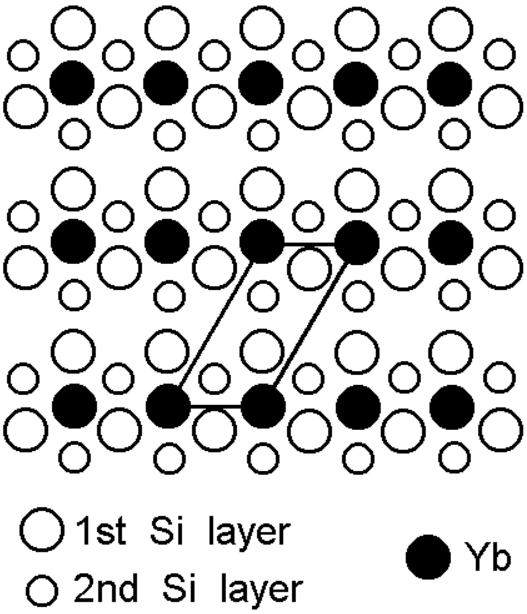

Fig 1. Model of the Si(111)2 × 1–Yb structure with Yb atoms residing in hollow sites. One of the three domains is shown. The 2×1 unit cell is shown by solid lines (from Ref. [5]). (Reprinted from T. Kofoed *et al.*, *Solid State Communications*, **52**, 283. Copyright © 1984, with kind permission from Pergamon Press Ltd, Headington Hill Hall, Oxford OX3 0BW, UK)

simple model of one of the three domains of the Si(111)2 × 1–Yb structure. The model for the 3×1 structure is constructed in the same fashion assuming one Yb atom per 3×1 unit cell. The 5×1 structure can simply be interpreted as a combination of the 2×1 and 3×1 structures.

The distance of the Yb atoms to the uppermost layer of Si atoms estimated from ISS data was found to be 1.9 ± 0.3 Å. It should be mentioned that the nearest neighbor distance for Yb–Si, 2.9 ± 0.4 Å, is comparable to that found for bulk silicides.

1.2.2. Si(111)$\sqrt{3} \times \sqrt{3}$–Yb

Wigren *et al.* [3] suggested that the $\sqrt{3} \times \sqrt{3}$—$R30^\circ$ structure seen by LEED for most preparations of the Yb silicide can be the result of the ordered defect structure in the surface: arrangement of the vacancies in an ordered superstructure where every sixth Si atom is missing. This explanation is similar to that proposed earlier by Baptist *et al.* [7] for the $\sqrt{3} \times \sqrt{3}$ structure of $YSi_{1.7}$ silicide.

REFERENCES

[1] G. Rossi, J. Nogami, I. Lindau, L. Braicovich, I. Abbati, U. Del Pennino and S. Nannarone, *J. Vac. Sci. Technol. A* **1** (1983) 781.
[2] L. Braicovich, I. Abbati, C. Carbone, J. Nogami and I. Lindau, *Surf. Sci.* **168** (1986) 193.
[3] C. Wigren, J. N. Andersen, R. Nyholm and U. O. Karlsson, *J. Vac. Sci. Technol. A* **9** (1991) 1942
[4] G. Rossi, *Surf. Sci. Repts.* **7** (1987) 1.
[5] T. Kofoed, I. Chorkendorff and J. Onsgaard, *Solid State Commun.* **52** (1984) 283.
[6] I. Chorkendorff, J. Kofoed and J. Onsgaard, *Surf. Sci.* **152–153** (1985) 749.
[7] R. Baptist, S. Ferrer, G. Grenet and H. C. Poon, *Phys. Rev. Lett.* **64** (1990) 311.

(Zn)

ZINC

1. (111) ORIENTATION

Zinc was found to induce $\delta(7 \times 7)$ and 1×1 reconstructions on the Si(111)7×7 surface.

1.1. PHASE DIAGRAM

During Zn deposition on a Si(111)7×7 surface at RT, the LEED pattern changed gradually to a $\delta(7 \times 7)$ pattern at 1 ML (A. A. Saranin, unpublished). The characteristic of this pattern is that the intense fractional order spots are only those at around the integer-order spots. At further Zn deposition, the $\delta(7 \times 7)$ pattern changes to the 1×1 pattern, and, at coverages greater than ~ 4 ML only intense background is observed. Annealing of the surface does not result in any surface ordering. Zinc desorbs completely by annealing at 100–200 °C.

Supplement 1

The thickness in angstroms of one monolayer of given adsorbate on the main silicon surface calculated under the assumption that the atomic volume occupied by the adsorbate atom in the extra-thin film is the same as in the bulk matherial.

Element	Orientation			Element	Orientation		
	(111)	(100)	(110)		(111)	(100)	(110)
Ag	1.34	1.16	1.64	La	2.93	2.54	3.59
Al	1.30	1.13	1.59	Li	1.67	1.44	2.04
As	1.69	1.46	2.07	Mg	1.82	1.57	2.23
Au	1.33	1.15	1.63	Mn	0.96	0.83	1.17
B	0.57	0.49	0.70	Mo	1.22	1.06	1.50
Ba	4.98	4.31	6.09	Na	2.95	2.56	3.62
Bi	2.77	2.40	3.40	Nb	1.41	1.22	1.73
Br	2.57	2.22	3.14	Ni	0.86	0.74	1.05
C	0.44	0.38	0.54	P	2.21	1.92	2.71
Ca	3.41	2.95	4.17	Pb	2.38	2.06	2.91
Ce	2.64	2.29	3.23	Pd	1.15	1.00	1.41
Co	0.86	0.75	1.05	Pt	1.18	1.02	1.45
Cr	0.94	0.81	1.15	Rb	6.82	5.91	8.36
Cs	8.66	7.50	10.60	S	2.00	1.73	2.44
Cu	0.93	0.80	1.13	Sb	2.37	2.05	2.90
Dy	2.40	2.08	2.94	Se	2.14	1.85	2.62
Er	4.56	3.95	5.59	Si	1.57	1.36	1.92
Eu	6.14	5.32	7.52	Sn	2.68	2.32	3.28
Fe	0.92	0.80	1.13	Sr	4.42	3.82	5.41
Ga	1.53	1.33	1.88	Ta	1.41	1.22	1.73
Gd	3.46	3.00	4.24	Tb	4.75	4.11	5.82
Ge	1.77	1.54	2.17	Te	2.66	2.30	3.25
Hg	1.83	1.58	2.24	Ti	1.38	1.20	1.69
Ho	2.51	2.18	3.08	V	1.09	0.94	1.33
I	3.33	2.89	4.08	W	1.24	1.08	1.52
In	2.05	1.77	2.51	Y	2.58	2.24	3.16
Ir	1.11	0.96	1.36	Yb	4.09	3.54	5.01
K	5.59	4.84	6.84	Zn	1.19	1.03	1.46

Supplement 2

A list of superstructures showing the superstructures that are induced given the adsorbate on main silicon surfaces ("no" means the absence of the ordered superstructures, the empty field means the absence of the data for the given "adsorbate/Si" system. The superstructures that are formed in very local regions only are marked by the symbol ^{l} The superstructures related to rather thick silicide layers are marked by symbol ^{s})

Element	Orientation		
	(111)	(100)	(110)
Ag	2×1 1×1 $\sqrt{7} \times \sqrt{7}$—$R \pm 19.1^\circ$ 3×1 $\delta(7 \times 7)$ $\sqrt{3} \times \sqrt{3}$—$R30^\circ$ 6×1	no	$\begin{pmatrix} 3 & 9 \\ 3 & -9 \end{pmatrix}$ 4×5 1×1
Al	$\sqrt{3} \times \sqrt{3}$—$R30^\circ$ $\sqrt{7} \times \sqrt{7}$—$R \pm 19.1^\circ$ 2×1^l $\gamma(7 \times 7)$ 4.5×4.5	2×2 2×3 4×5 1×7 $c(4 \times 12)$	$\begin{pmatrix} 3 & 0 \\ -1 & 4 \end{pmatrix}$ $\begin{pmatrix} -2 & 1 \\ 9 & 0 \end{pmatrix}$ 1×2 1×1
Ar	no		
As	1×1	1×2	
Au	5×1 $\sqrt{3} \times \sqrt{3}$—$R30^\circ$ 6×6 5×2	1×1 $c(8 \times 2)$ 5×1 $\sqrt{26} \times 3 = \begin{pmatrix} 5 & 1 \\ 0 & 3 \end{pmatrix}$ $c(18 \times 2)$	1×2 5×2 $\begin{pmatrix} 4 & 0 \\ -1 & 3 \end{pmatrix}$ 1×1
B	$\sqrt{3} \times \sqrt{3}$—$R30^\circ$ 1×1	2×1	$\begin{pmatrix} -2 & 1 \\ 10 & 0 \end{pmatrix}$
Ba	no	2×3 1×2 2×4	

Element	Orientation		
	(111)	(100)	(110)
Bi	$\sqrt{3}\times\sqrt{3}$—$R30^\circ$ 1×1	1×1 2×1 $2\times n$	1×1 3×2
Br	7×7 1×1	2×1	no
C	no	$c(4\times3)^l$ $c(4\times4)^l$	
Ca	1×1 $\sqrt{3}\times\sqrt{3}$—$R30^\circ$ 2×1 3×1 5×1 2×3 2×2^s	6×1 5×1 $8\times$ 4	
Ce	$\sqrt{3}\times\sqrt{3}$—$R30^\circ$ 2×2		
Cl	7×7 1×1	2×1	
Co	$\sqrt{3}\times\sqrt{3}$—$R30^\circ$ $\sqrt{7}\times\sqrt{7}$—$R\pm19.1^\circ$ 2×2 1×1	$\sqrt{2}\times\sqrt{2}$—$R45^{\circ\,s}$ $3\sqrt{2}\times\sqrt{2}$- R45°^{s} 2×2^s	
Cr	7×7 1×1 $\sqrt{3}\times\sqrt{3}$—$R30^\circ$ 1.17×1.17—$R0^{\circ\,s}$ 1.17×1.17—$R30^{\circ\,s}$	2×1	
Cs	$\delta(7\times7)$ 3×1 $\sqrt{3}\times\sqrt{3}$—$R30^\circ$ $c(2\times2)$ incommensurate	"×3 streak" 2×1 2×3 4×6 2×6 8×4 $c(4\times2)$	1×1 5×4 2×2
Cu	4×1 4×2 1×1 "5×5"	1×1	
Dy	1×1		
Er	1×1 $\sqrt{3}\times\sqrt{3}$—$R30^\circ$		
Eu	1×1 2×2 5×5 3×3		

Element	Orientation		
	(111)	(100)	(110)
F	no	no	
Fe	2×2 $\sqrt{3} \times \sqrt{3}$—$R30^\circ$ 1×1	$c(2 \times 2)$ 2×2	
Ga	7×7 $\sqrt{3} \times \sqrt{3}$—$R30^\circ$ 6.3×6.3 11×11 $6.3\sqrt{3} \times 6.3\sqrt{3}$—$R30^\circ$	2×3 2×5 2×2 8×1 $8 \times n$ 2×1	$\begin{pmatrix} -2 & 1 \\ 9 & 0 \end{pmatrix}$ $\begin{pmatrix} -2 & 1 \\ 12 & 0 \end{pmatrix}$
Gd	2×2 $\sqrt{3} \times \sqrt{3}$—$R30^\circ$ 1×1	1×1 $c(2 \times 2)$	
Ge	$\sqrt{3} \times \sqrt{3}$—$R30^\circ$ 7×7 5×5 1×1	2×1 8×2 $2 \times n$	1×1 $\begin{pmatrix} 10 & -1 \\ 3 & 4 \end{pmatrix}$ $\begin{pmatrix} -2 & 1 \\ 8 & 0 \end{pmatrix}$ $\begin{pmatrix} 1 & 1 \\ 16 & 0 \end{pmatrix}$
H	1×1 3×1 $\delta(7 \times 7)$ $\sqrt{3} \times \sqrt{3}$—$R30^\circ$ 2×2	1×1 2×1 3×1	$\begin{pmatrix} 2 & 2 \\ 17 & 1 \end{pmatrix}$
Hg	$\sqrt{3} \times \sqrt{3}$—$R30^\circ$ 1×1		
Ho	1×1		
I	7×7	$c(2 \times 2)$	1×1
In	7×7 $\sqrt{3} \times \sqrt{3}$—$R30^\circ$ 4×1 5×5 1×1 $\sqrt{31} \times \sqrt{31}$—$R \pm 9^\circ$ $\sqrt{7} \times \sqrt{3} = \begin{pmatrix} 3 & 1 \\ 2 & 1 \end{pmatrix}$ 2×2 $2\sqrt{3} \times 2\sqrt{3}$—$R30^\circ$	1×1 2×2 3×4 2×1	
Ir		no	
K	$\delta(7 \times 7)$ 7×7 3×1	2×1 2×2 2×3 5×4 $\begin{pmatrix} 2 & 1 \\ 0 & 3 \end{pmatrix}$	

Element	Orientation		
	(111)	(100)	(110)
Kr	no		
La	1×1		
Li	1×1 3×1 $\delta(7\times 7)$ $\sqrt{3}\times\sqrt{3}$—$R30^\circ$ 4×4	1×1 2×1	
Mg	$\sqrt{3}\times\sqrt{3}$—$R30^\circ$ $\frac{2}{3}\sqrt{3}\times\frac{2}{3}\sqrt{3}$—$R30^{\circ\,s}$ 3×3 3×1		
Mo	1×1	no	
N	8×8 “quadruplet”	no	
Na	$\delta(7\times 7)$ 3×1 1×1	4×1 2×1 2×3 incommensurate	
Nb	no		
Ni	7×7 1×1 $\sqrt{19}\times\sqrt{19}$—$R\pm 23.4^\circ$ $\sqrt{3}\times\sqrt{3}$—$R30^\circ$	$2\times n$	5×4 1×2 1×5 1×7 1×9 4×5 9×5 8×5
O	1×1 $\sqrt{3}\times\sqrt{3}$—$R30^\circ$ 7×7	1×1	1×1
P	$6\sqrt{3}\times 6\sqrt{3}$—$R30^\circ$ 4×4 7×7 1×1 $2\sqrt{3}\times 2\sqrt{3}$—$R30^\circ$ $\sqrt{3}\times 2 =$ $\sqrt{7}\times 2 = \begin{pmatrix}2 & 0\\ 1 & 2\end{pmatrix}$	2×1	
Pb	1×1 7×7 $\sqrt{3}\times\sqrt{3}$—$R30^\circ$	2×2 $c(4\times 8)$ 4×1 2×1 $c(4\times 4)$	

Element	Orientation		
	(111)	(100)	(110)
Pd	$\sqrt{3}\times\sqrt{3}$—$R30^\circ$	2×1	
	$2\sqrt{3}\times 2\sqrt{3}$—$R30^\circ$	2×2	
	$3\sqrt{3}\times 3\sqrt{3}$—$R30^{\circ\,s}$	$c(4\times 6)$	
	5×1		
	7×7		
	1×1		
Pt	$\alpha(7\times 7)$	2×1	
	$\sqrt{7}\times\sqrt{7}$—$R\pm 19.1^\circ$	$c(4\times 2)$	
	$\sqrt{3}\times\sqrt{3}$—$R30^\circ$	$c(4\times 6)$	
	1×1		
Rb	$\delta(7\times 7)$	2×1	
	3×1		
S		no	
Sb	$\sqrt{3}\times\sqrt{3}$—$R30^\circ$	2×1	$\alpha(3\times 2)$
	2×1		$\beta(3\times 2)$
	$5\sqrt{3}\times 5\sqrt{3}$—$R30^\circ$		1×2
	$7\sqrt{3}\times 7\sqrt{3}$—$R30^\circ$		$\begin{pmatrix}-2 & 1\\ 14 & 0\end{pmatrix}$
	5×5		
Se	no	1×1	no
Si	7×7	2×1	$\begin{pmatrix}2 & 2\\ 17 & 1\end{pmatrix}$
	2×1	$(2\times 2)^l$	"2×16"
	1×1	$c(4\times 2)$	$\begin{pmatrix}2 & 2\\ 33 & 1\end{pmatrix}$
	5×5	$c(4\times 4)$	"2×32"
	9×9^l		1×2
	2×2^l		1×1
	3×3^l		
	$\sqrt{3}\times\sqrt{3}$—$R30^\circ$		
	$c(4\times 2)^l$		
Sm		3×2	
		2×1^s	
		2×2^s	
Sn	7×7	$c(4\times 4)$	$\begin{pmatrix}2 & 2\\ 4 & -3\end{pmatrix}$
	$\sqrt{3}\times\sqrt{3}$—$R30^\circ$	6×2	
	$2\sqrt{3}\times 2\sqrt{3}$	$c(8\times 4)$	$\begin{pmatrix}3 & 0\\ -1 & 3\end{pmatrix}$
	$\sqrt{133}\times 4\sqrt{3}=\begin{pmatrix}4 & 9\\ 8 & -4\end{pmatrix}$	5×1	
	$3\sqrt{7}\times 3\sqrt{7}$—$R\pm 19.1^\circ$	2×2^l	$\begin{pmatrix}-2 & 1\\ 9 & 0\end{pmatrix}$
	$2\sqrt{91}\times 2\sqrt{91}$—$R(30\pm 3)^\circ$	6×4^l	
	1×1	14×4^l	
Sr	5×1	2×3	
	1×1	1×2	
		1×5	
		1×3	

Element	Orientation		
	(111)	(100)	(110)
Ta	$\alpha(7\times7)$		
	$\sqrt{3}\times\sqrt{3}$—$R30^\circ$		
Tb	1×1^s		
	$\sqrt{3}\times\sqrt{3}$—$R30^{\circ\,s}$		
Te	$\sqrt{3}\times\sqrt{3}$—$R30^\circ$	2×8	
	2×2	1×8	
	3×1	1×1	
	7×7		
	1×1		
Ti	1×1	no	
V	$\alpha(7\times7)$		
W	1×1^s		
Xe	no		
Y	$\sqrt{3}\times\sqrt{3}$—$R30^{\circ\,s}$		
	1×1^s		
Yb	2×1		
	5×1		
	3×1		
	$\sqrt{3}\times\sqrt{3}$—$R30^{\circ\,s}$		
	1×1^s		
Zn	$\delta(7\times7)$		

Supplement 3

A list of superstructures showing the adsorbates that induce the given superstructures.

(111) ORIENTATION

Structure	Elements
1×1	Ag, As, B, Bi, Br, Ca, Cl, Co, Cr, Cu, Dy, Er, Eu, Fe, Gd, Ge, H, Hg, Ho, In, La, Li, Mo, Na, Ni, O, P, Pb, Pd, Pt, Si, Sn, Sr, Tb, Te, Ti, W, Y, Yb
2×1	Ag, Al, Ca, Sb, Si, Yb
2×2	Ce, Co, Cs, Eu, Fe, Gd, H, In, Si, Te
3×1	Ag, Ca, Cs, H, K, Li, Mg, Na, Rb, Te, Yb
3×2	Ca
3×3	Eu, Mg, Si
4×1	Cu, In
4×2	Cu
4×4	Li, P
5×1	Au, Ca, Pd, Sr, Yb
5×2	Au
5×5	Cu, Eu, Ge, In, Sb, Si
6×1	Ag
6×6	Au
7×7	Ag, Al, Br, Cl, Cr, Cs, Ga, Ge, H, I, In, K, Li, Na, Ni, O, P, Pb, Pd, Pt, Rb, Si, Sn, Ta, Te, V, Zn
8×8	N
9×9	Si
$\sqrt{3} \times \sqrt{3}$—$R30°$	Ag, Al, Au, B, Bi, Ca, Ce, Co, Cr, Cs, Er, Fe, Ga, Gd, Ge, H, Hg, In, Li, Mg, Ni, O, Pb, Pd, Pt, Sb, Si, Sn, Ta, Tb, Te, Y, Yb
$\sqrt{7} \times \sqrt{3} = c(4 \times 2) = \begin{pmatrix} 2 & 0 \\ 1 & 2 \end{pmatrix}$	P, Si
$2\sqrt{3} \times 2\sqrt{3}$—$R30°$	In, P, Pd, Sn
$3\sqrt{3} \times 3\sqrt{3}$—$R30°$	Pd
$5\sqrt{3} \times 5\sqrt{3}$—$R30°$	Sb
$6\sqrt{3} \times 6\sqrt{3}$—$R30°$	P
$7\sqrt{3} \times 7\sqrt{3}$—$R30°$	Sb

Structure	Elements
$\sqrt{7} \times \sqrt{3} = \begin{pmatrix} 3 & 1 \\ 2 & 1 \end{pmatrix}$	In
$\sqrt{7} \times \sqrt{7}$—$R \pm 19.1^\circ$	Ag, Al, Co, Pt
$3\sqrt{7} \times 3\sqrt{7}$—$R \pm 19.1^\circ$	Sn
$\sqrt{19} \times \sqrt{19}$—$R \pm 23.4^\circ$	Ni
$\sqrt{31} \times \sqrt{31}$—$R \pm 9^\circ$	In
$2\sqrt{91} \times 2\sqrt{91}$—$R(30 \pm 3)^\circ$	Sn
$\sqrt{133} \times 4\sqrt{3} = \begin{pmatrix} 4 & 9 \\ 8 & -4 \end{pmatrix}$	Sn

(100) ORIENTATION

Structure	Elements
1×1	Au, Bi, Cu, Gd, H, In, Li, O, Se, Te
2×1	As, B, Ba, Bi, Br, Cl, Cr, Cs, Ga, Ge, H, In, K, Li, Na, P, Pb, Pd, Pt, Rb, Sb, Si, Sm, Sr
2×2	Al, Co, Fe, Ga, In, K, Pb, Pd, Si, Sm, Sn
3×1	H, Sr
3×2	Al, Ba, Cs, Ga, K, Na, Sm, Sr
4×1	Na, Pb
4×2	Ba
4×3	In
5×1	Au, Ca, Sn, Sr
5×2	Ga
5×4	Al, K
6×1	Ca
6×2	Cs, Sn
6×4	Cs, Sn
7×1	Al
8×1	Ga, Te
8×2	Ge, Te
8×4	Ca, Cs
14×4	Sn
$c(2 \times 2)$ $(=\sqrt{2} \times \sqrt{2}—R45^\circ)$	Co, Fe, Gd, I
$c(4 \times 2)$	Cs, Pt, Si
$c(4 \times 3)$	C
$c(4 \times 4)$	C, Pb, Si, Sn
$c(6 \times 4)$	Pd, Pt
$c(8 \times 2)$	Au
$c(8 \times 4)$	Pt, Sn
$c(12 \times 4)$	Al
$c(18 \times 2)$	Au
$3\sqrt{2} \times \sqrt{2}—R45^\circ$	Co
$\sqrt{26} \times 3 = \begin{pmatrix} 5 & 1 \\ 0 & 3 \end{pmatrix}$	Au
$\begin{pmatrix} 2 & 1 \\ 0 & 3 \end{pmatrix}$	K

(110) ORIENTATION

Structure	Elements
1×1	Ag, Al, Au, Bi, Cs, Ge, I, O, Si
1×2	Al, Au, Ni, Sb, Si
1×5	Ni
1×7	Ni
1×9	Ni
2×2	Cs
3×2	Bi, Sb
5×4	Cs, Ni
4×5	Ag, Ni
8×5	Ni
9×5	Ni
$\begin{pmatrix} 1 & 1 \\ 16 & 0 \end{pmatrix}$	Ge
$\begin{pmatrix} 2 & 2 \\ 4 & -3 \end{pmatrix}$	Sn
$\begin{pmatrix} 2 & 2 \\ 17 & 1 \end{pmatrix} =$“$2 \times 16$”	H, Si
$\begin{pmatrix} 2 & 2 \\ 33 & 1 \end{pmatrix} =$“$2 \times 32$”	Si
$\begin{pmatrix} -2 & 1 \\ 8 & 0 \end{pmatrix} =$“$1 \times 8$”	Ge
$\begin{pmatrix} -2 & 1 \\ 9 & 0 \end{pmatrix} =$“$1 \times 9$”	Al, Ga, Sn
$\begin{pmatrix} -2 & 1 \\ 10 & 0 \end{pmatrix} =$“$1 \times 10$”	B
$\begin{pmatrix} -2 & 1 \\ 12 & 0 \end{pmatrix} =$“$1 \times 12$”	Ga
$\begin{pmatrix} -2 & 1 \\ 14 & 0 \end{pmatrix} =$“$1 \times 14$”	Sb
$\begin{pmatrix} 3 & 0) \\ -1 & 4 \end{pmatrix} =$“$4 \times 6$”	Al
$\begin{pmatrix} 3 & 0 \\ -1 & 3 \end{pmatrix}$	Sn
$\begin{pmatrix} 4 & 0 \\ -1 & 3 \end{pmatrix}$	Au
$\begin{pmatrix} 3 & 9 \\ 3 & -9 \end{pmatrix} = c(18 \times 6)$	Ag
$\begin{pmatrix} 10 & -1 \\ 3 & 4 \end{pmatrix}$	Ge

Supplement 4

Sketches of the LEED patterns of the superstructures detected for surface phases on silicon. (The sketch of a LEED pattern from a single-domain structure coincides with the sketch of the superstructure reciprocal lattice superposed on the reciprocal lattice of the corresponding unreconstructed Si surface. Thus, the extra-reflections (shown by solid circles) correspond to the superstructure reciprocal rods, while the main reflections (shown by open circles) to those of the unreconstructed 1 × 1 surface. The sketch of a LEED pattern from a multi-domain structure represents the superposition of the LEED patterns produced by domains in all possible equivalent orientations.)

4.1. (111) ORIENTATION

Structure	Single-domain	Multi-domain	Reciprocal unit vectors for a single-domain structure
1×1	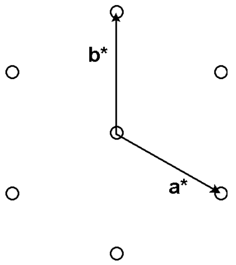		
2×1	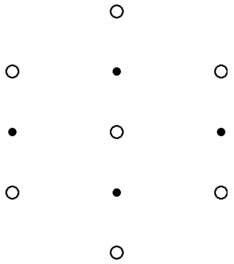	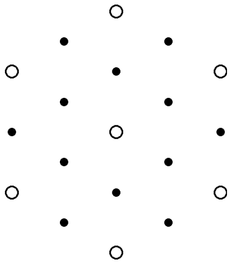 three-domain	$\mathbf{a}_s^* = \mathbf{a}^*$ $\mathbf{b}_s^* = \frac{1}{2}\mathbf{b}^*$

Structure	Single-domain	Multi-domain	Unit vector for a single-domain structure
2×2	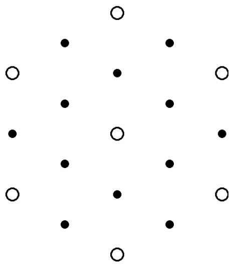	the same as single-domain	$\mathbf{a}_\mathrm{s}^* = \frac{1}{2}\mathbf{a}^*$ $\mathbf{b}_\mathrm{s}^* = \frac{1}{2}\mathbf{b}^*$
3×1	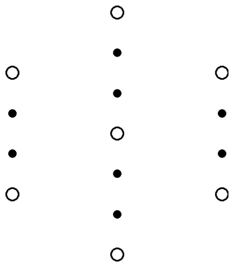	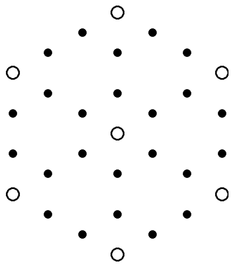 three-domain	$\mathbf{a}_\mathrm{s}^* = \mathbf{a}^*$ $\mathbf{b}_\mathrm{s}^* = \frac{1}{3}\mathbf{b}^*$
3×2	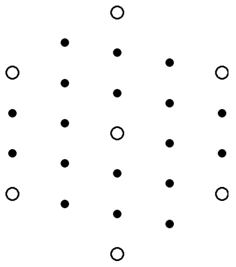	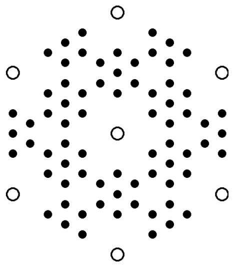 six-domain	$\mathbf{a}_\mathrm{s}^* = \frac{1}{2}\mathbf{a}^* + \frac{1}{6}\mathbf{b}^*$ $\mathbf{b}_\mathrm{s}^* = \frac{1}{3}\mathbf{b}^*$
3×3	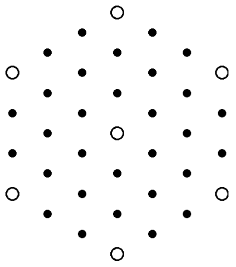	the same as single-domain	$\mathbf{a}_\mathrm{s}^* = \frac{1}{2}\mathbf{a}^*$ $\mathbf{b}_\mathrm{s}^* = \frac{1}{3}\mathbf{b}^*$
4×1	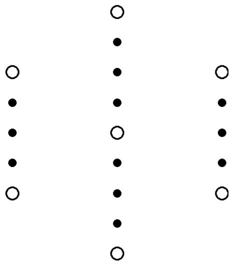	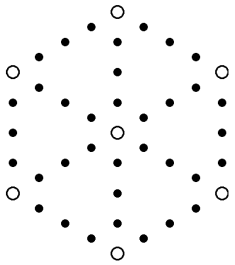 three-domain	$\mathbf{a}_\mathrm{s}^* = \mathbf{a}^*$ $\mathbf{b}_\mathrm{s}^* = \frac{1}{4}\mathbf{b}^*$

Structure	Single-domain	Multi-domain	Unit vector for a structure
4 × 2	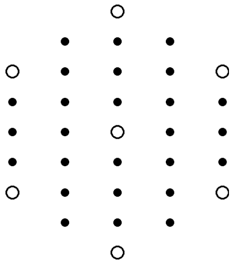	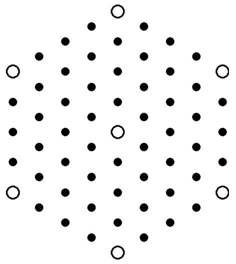 three-domain	$\mathbf{a}_{\mathrm{s}}^* = \frac{1}{2}\mathbf{a}^*$ $\mathbf{b}_{\mathrm{s}}^* = \frac{1}{4}\mathbf{b}^*$
4 × 4	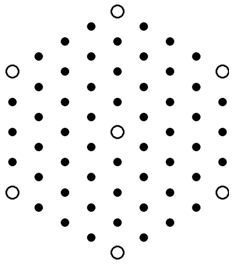	the same as single-domain	$\mathbf{a}_{\mathrm{s}}^* = \frac{1}{4}\mathbf{a}^*$ $\mathbf{b}_{\mathrm{s}}^* = \frac{1}{4}\mathbf{b}^*$
5 × 1	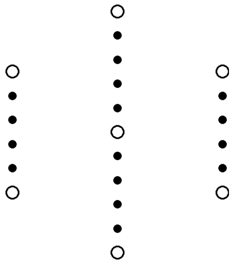	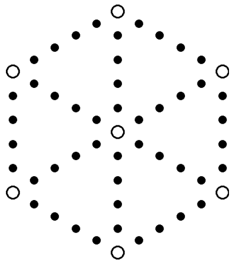 three-domain	$\mathbf{a}_{\mathrm{s}}^* = \mathbf{a}^*$ $\mathbf{b}_{\mathrm{s}}^* = \frac{1}{5}\mathbf{b}^*$
5 × 2	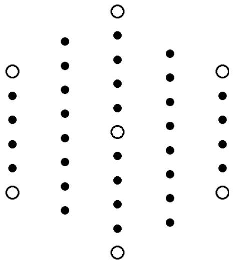	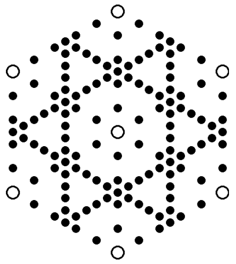 six-domain	$\mathbf{a}_{\mathrm{s}}^* = \frac{1}{2}\mathbf{a}^* + \frac{1}{10}\mathbf{b}^*$ $\mathbf{b}_{\mathrm{s}}^* = \frac{1}{5}\mathbf{b}^*$
5 × 5	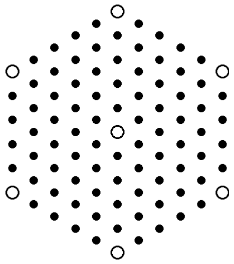	the same as single-domain	$\mathbf{a}_{\mathrm{s}}^* = \frac{1}{5}\mathbf{a}^*$ $\mathbf{b}_{\mathrm{s}}^* = \frac{1}{5}\mathbf{b}^*$

Structure	Single-domain	Multi domain	Unit vector for a structure
6×1	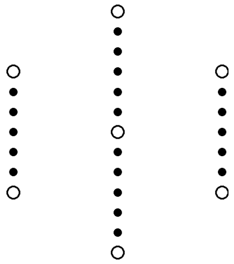	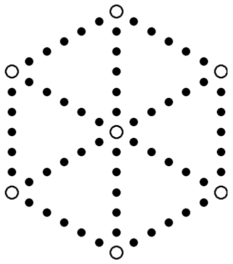 three-domain	$\mathbf{a}_{\mathrm{s}}^* = \mathbf{a}^*$ $\mathbf{b}_{\mathrm{s}}^* = \frac{1}{6}\mathbf{b}^*$
6×6	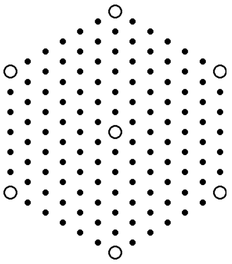	the same as single-domain	$\mathbf{a}_{\mathrm{s}}^* = \frac{1}{6}\mathbf{a}^*$ $\mathbf{b}_{\mathrm{s}}^* = \frac{1}{6}\mathbf{b}^*$
7×7	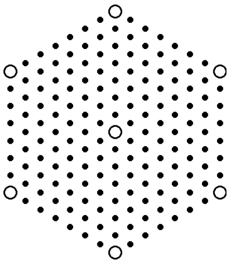	the same as single-domain	$\mathbf{a}_{\mathrm{s}}^* = \frac{1}{7}\mathbf{a}^*$ $\mathbf{b}_{\mathrm{s}}^* = \frac{1}{7}\mathbf{b}^*$

Structure	Single-domain	Multi-domain	Reciprocal unit vector for a structure
9×9	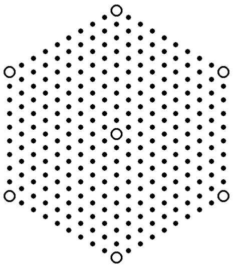	the same as single-domain	$\mathbf{a}_s^* = \frac{1}{9}\mathbf{a}^*$ $\mathbf{b}_s^* = \frac{1}{9}\mathbf{b}^*$
$\sqrt{3} \times \sqrt{3}$—$R30°$	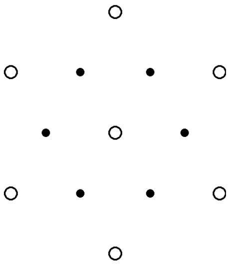	the same as single-domain	$\mathbf{a}_s^* = \frac{2}{3}\mathbf{a}^* + \frac{1}{3}\mathbf{b}^*$ $\mathbf{b}_s^* = -\frac{1}{3}\mathbf{a}^* + \frac{1}{3}\mathbf{b}^*$
$\sqrt{3} \times 2 = \begin{pmatrix} 2 & 0 \\ 1 & 2 \end{pmatrix}$	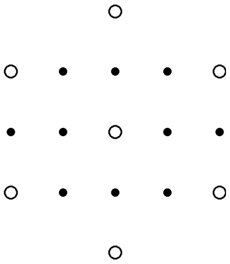	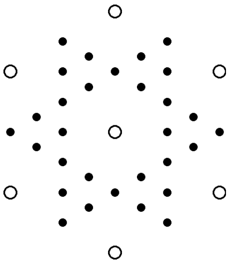 three-domain	$\mathbf{a}_s^* = \frac{1}{2}\mathbf{a}^* + \frac{1}{4}\mathbf{b}^*$ $\mathbf{b}_s^* = \frac{1}{2}\mathbf{b}^*$
$2\sqrt{3} \times 2\sqrt{3}$—$R30°$	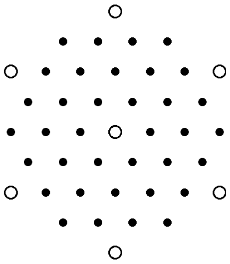	the same as single-domain	$\mathbf{a}_s^* = \frac{1}{3}\mathbf{a}^* + \frac{1}{6}\mathbf{b}^*$ $\mathbf{b}_s^* = -\frac{1}{6}\mathbf{a}^* + \frac{1}{6}\mathbf{b}^*$
$3\sqrt{3} \times 3\sqrt{3}$—$R30°$	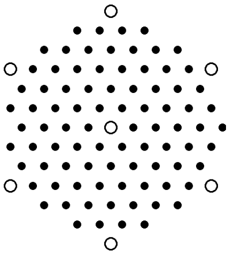	the same as single-domain	$\mathbf{a}_s^* = \frac{2}{9}\mathbf{a}^* + \frac{1}{9}\mathbf{b}^*$ $\mathbf{b}_s^* = -\frac{1}{9}\mathbf{a}^* + \frac{1}{9}\mathbf{b}^*$
$5\sqrt{3} \times 5\sqrt{3}$—$R30°$	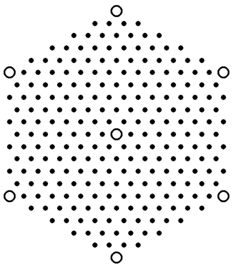	the same as single-domain	$\mathbf{a}_s^* = \frac{2}{15}\mathbf{a}^* + \frac{1}{15}\mathbf{b}^*$ $\mathbf{b}_s^* = -\frac{1}{15}\mathbf{a}^* + \frac{1}{15}\mathbf{b}^*$

Structure	Single-domain	Multi-domain	Reciprocal unit vector for a structure
$6\sqrt{3}\times 6\sqrt{3}$—$R30^\circ$	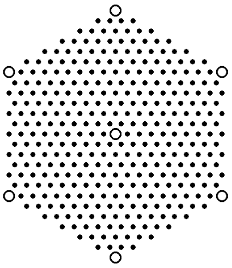	the same as single-domain	$\mathbf{a}_s^* = \frac{1}{9}\mathbf{a}^* + \frac{1}{18}\mathbf{b}^*$ $\mathbf{b}_s^* = -\frac{1}{18}\mathbf{a}^* + \frac{1}{18}\mathbf{b}^*$
$7\sqrt{3}\times 7\sqrt{3}$—$R30^\circ$	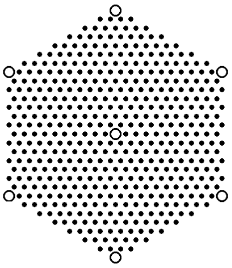	the same as single-domain	$\mathbf{a}_s^* = \frac{2}{21}\mathbf{a}^* + \frac{1}{21}\mathbf{b}^*$ $\mathbf{b}_s^* = -\frac{1}{21}\mathbf{a}^* + \frac{1}{21}\mathbf{b}^*$
$\sqrt{7}\times\sqrt{3} = \begin{pmatrix}3 & 1\\ 2 & 1\end{pmatrix}$	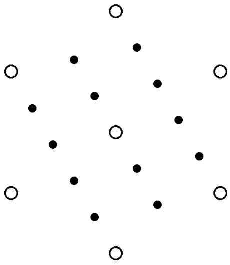	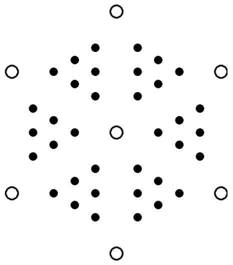 three-domain	$\mathbf{a}_s^* = \frac{3}{5}\mathbf{a}^* + \frac{2}{5}\mathbf{b}^*$ $\mathbf{b}_s^* = -\frac{1}{5}\mathbf{a}^* + \frac{1}{5}\mathbf{b}^*$
$\sqrt{7}\times\sqrt{7}$—$R\pm 19.1^\circ$	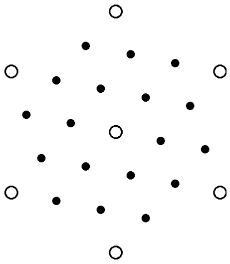	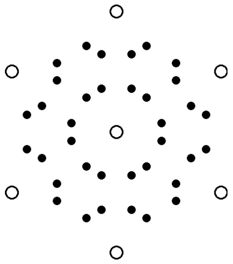 two-domain	$\mathbf{a}_s^* = \frac{3}{7}\mathbf{a}^* + \frac{1}{7}\mathbf{b}^*$ $\mathbf{b}_s^* = -\frac{1}{7}\mathbf{a}^* + \frac{2}{7}\mathbf{b}^*$
$3\sqrt{7}\times 3\sqrt{7}$—$R\pm 19.1^\circ$	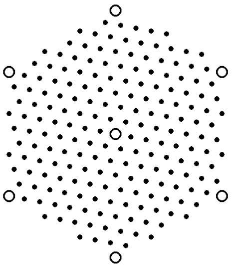	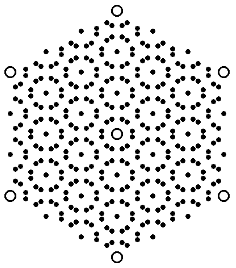 two-domain	$\mathbf{a}_s^* = \frac{1}{7}\mathbf{a}^* + \frac{1}{21}\mathbf{b}^*$ $\mathbf{b}_s^* = -\frac{1}{21}\mathbf{a}^* + \frac{2}{21}\mathbf{b}^*$
$\sqrt{19}\times\sqrt{19}$—$R\pm 23.4^\circ$	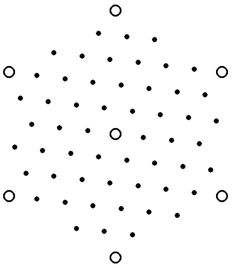	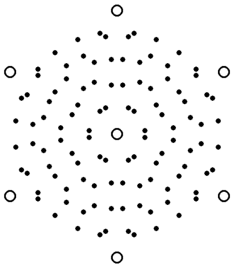 two-domain	$\mathbf{a}_s^* = \frac{5}{19}\mathbf{a}^* + \frac{2}{19}\mathbf{b}^*$ $\mathbf{b}_s^* = -\frac{2}{19}\mathbf{a}^* + \frac{3}{19}\mathbf{b}^*$

Structure	Single-domain	Multi-domain	Reciprocal unit vector for a structure
$\sqrt{31} \times \sqrt{31}$—$R \pm 9°$	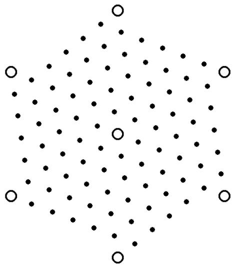	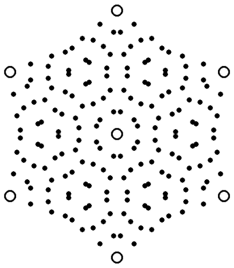 two-domain	$\mathbf{a}_\mathrm{s}^* = \frac{6}{31}\mathbf{a}^* + \frac{1}{31}\mathbf{b}^*$ $\mathbf{b}_\mathrm{s}^* = -\frac{1}{31}\mathbf{a}^* + \frac{5}{31}\mathbf{b}^*$
$2\sqrt{91} \times 2\sqrt{91}$—$R(30 \pm 3)°$	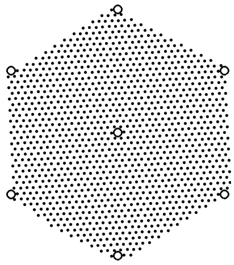	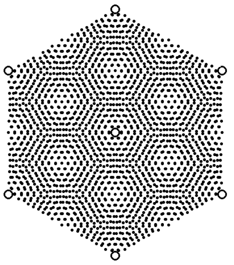 two-domain	$\mathbf{a}_\mathrm{s}^* = \frac{10}{91}\mathbf{a}^* + \frac{1}{91}\mathbf{b}^*$ $\mathbf{b}_\mathrm{s}^* = -\frac{1}{91}\mathbf{a}^* + \frac{9}{91}\mathbf{b}^*$
$\sqrt{133} \times 4\sqrt{3} = \begin{pmatrix} 4 & 9 \\ 8 & -4 \end{pmatrix}$	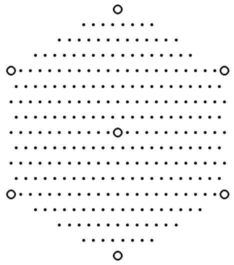	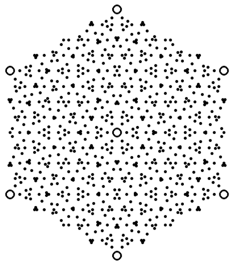 three-domain	$\mathbf{a}_\mathrm{s}^* = \frac{1}{11}\mathbf{a}^* + \frac{1}{22}\mathbf{b}^*$ $\mathbf{b}_\mathrm{s}^* = -\frac{1}{44}\mathbf{a}^* + \frac{1}{11}\mathbf{b}^*$

4.2 (100) ORIENTATION

Structure	Single-domain	Multi-domain	Reciprocal unit vectors for a structure
1×1	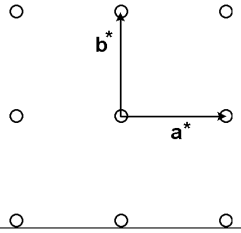		
2×1	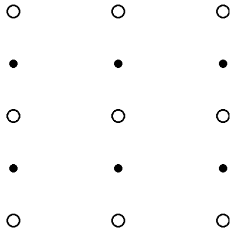	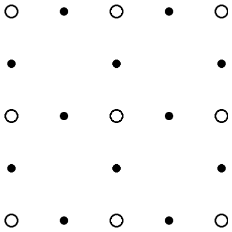 two-domain	$\mathbf{a}_s^* = \mathbf{a}^*$ $\mathbf{b}_s^* = \frac{1}{2}\mathbf{b}^*$
2×2	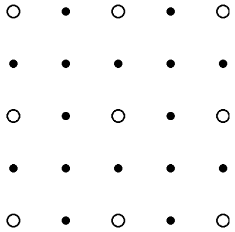	the same as single-domain	$\mathbf{a}_s^* = \frac{1}{2}\mathbf{a}^*$ $\mathbf{b}_s^* = \frac{1}{2}\mathbf{b}^*$
3×1	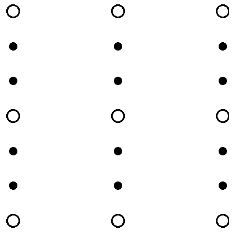	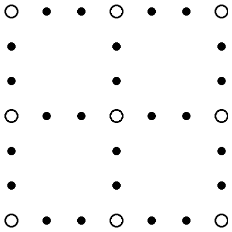 two-domain	$\mathbf{a}_s^* = \mathbf{a}^*$ $\mathbf{b}_s^* = \frac{1}{3}\mathbf{b}^*$
3×2	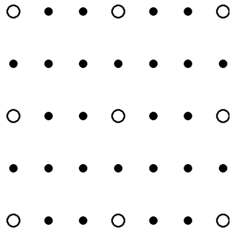	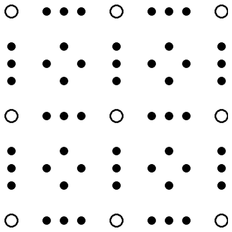 two-domain	$\mathbf{a}_s^* = \frac{1}{2}\mathbf{a}^*$ $\mathbf{b}_s^* = \frac{1}{3}\mathbf{b}^*$

Structure	Single-domain	Multi-domain	Reciprocal unit vectors for a structure
4×1	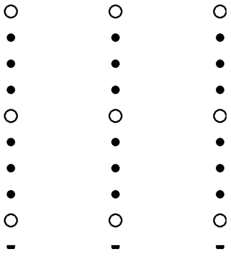	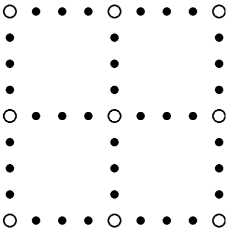 two-domain	$\mathbf{a}_s^* = \mathbf{a}^*$ $\mathbf{b}_s^* = \frac{1}{4}\mathbf{b}^*$
4×2	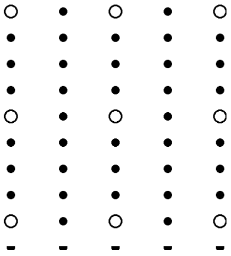	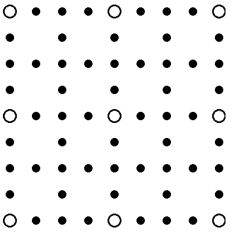 two-domain	$\mathbf{a}_s^* = \frac{1}{2}\mathbf{a}^*$ $\mathbf{b}_s^* = \frac{1}{4}\mathbf{b}^*$
4×3	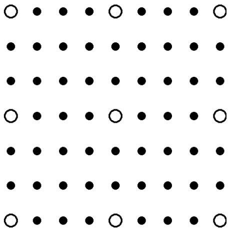	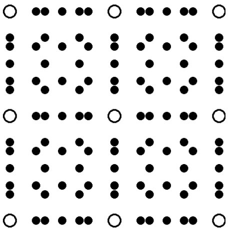 two-domain	$\mathbf{a}_s^* = \frac{1}{3}\mathbf{a}^*$ $\mathbf{b}_s^* = \frac{1}{4}\mathbf{b}^*$
5×1	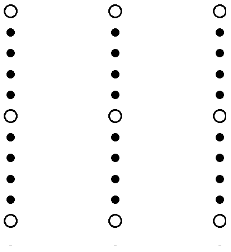	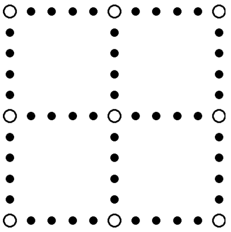 two-domain	$\mathbf{a}_s^* = \mathbf{a}^*$ $\mathbf{b}_s^* = \frac{1}{5}\mathbf{b}^*$
5×2	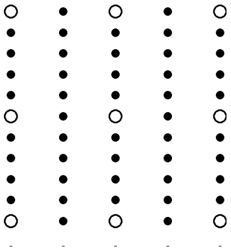	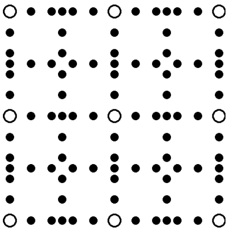 two-domain	$\mathbf{a}_s^* = \frac{1}{2}\mathbf{a}^*$ $\mathbf{b}_s^* = \frac{1}{5}\mathbf{b}^*$

Structure	Single-domain	Multi-domain	Reciprocal unit vectors for a structure
5×4	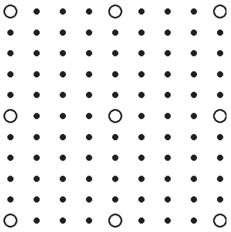	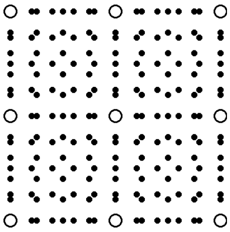 two-domain	$\mathbf{a}_s^* = \frac{1}{4}\mathbf{a}^*$ $\mathbf{b}_s^* = \frac{1}{5}\mathbf{b}^*$
6×1	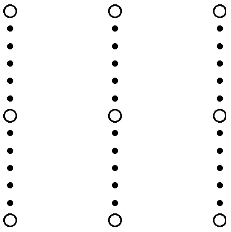	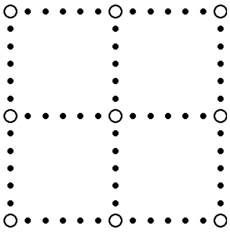 two-domain	$\mathbf{a}_s^* = \mathbf{a}^*$ $\mathbf{b}_s^* = \frac{1}{6}\mathbf{b}^*$
6×2	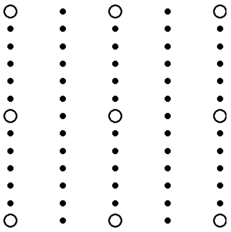	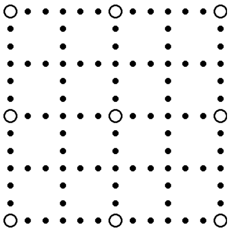 two-domain	$\mathbf{a}_s^* = \frac{1}{2}\mathbf{a}^*$ $\mathbf{b}_s^* = \frac{1}{6}\mathbf{b}^*$
6×4	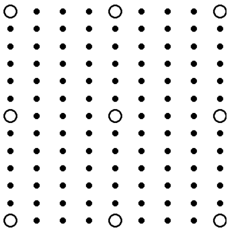	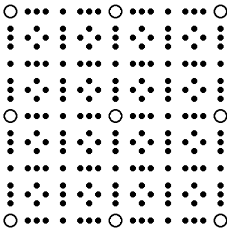 two-domain	$\mathbf{a}_s^* = \frac{1}{4}\mathbf{a}^*$ $\mathbf{b}_s^* = \frac{1}{6}\mathbf{b}^*$
7×1	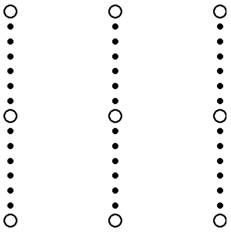	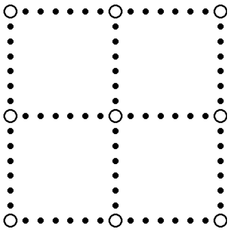 two-domain	$\mathbf{a}_s^* = \mathbf{a}^*$ $\mathbf{b}_s^* = \frac{1}{7}\mathbf{b}^*$

Structure	Single-domain	Multi-domain	Reciprocal unit vectors for a structure
8×1	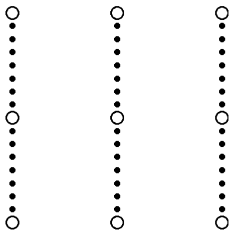	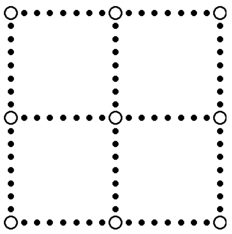 two-domain	$\mathbf{a}_s^* = \mathbf{a}^*$ $\mathbf{b}_s^* = \frac{1}{8}\mathbf{b}^*$
8×2	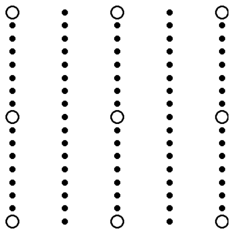	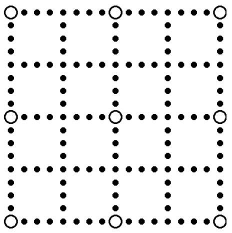 two-domain	$\mathbf{a}_s^* = \frac{1}{2}\mathbf{a}^*$ $\mathbf{b}_s^* = \frac{1}{8}\mathbf{b}^*$
8×4	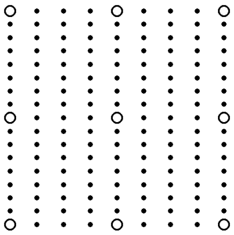	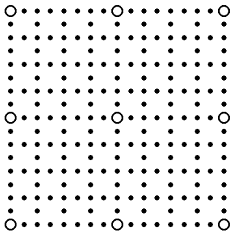 two-domain	$\mathbf{a}_s^* = \frac{1}{4}\mathbf{a}^*$ $\mathbf{b}_s^* = \frac{1}{8}\mathbf{b}^*$
14×4	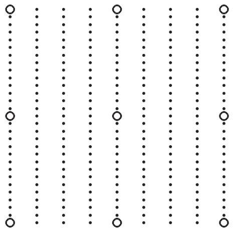	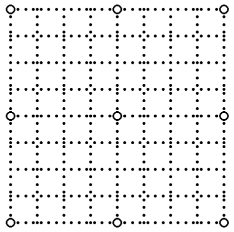 two-domain	$\mathbf{a}_s^* = \frac{1}{4}\mathbf{a}^*$ $\mathbf{b}_s^* = \frac{1}{14}\mathbf{b}^*$
$c(4 \times 2)$	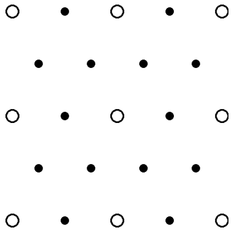	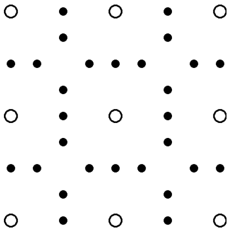 two-domain	$\mathbf{a}_s^* = \frac{1}{2}\mathbf{a}^*$ $\mathbf{b}_s^* = \frac{1}{4}\mathbf{a}^* + \frac{1}{2}\mathbf{b}^*$

Structure	Single-domain	Multi-domain	Reciprocal unit vectors for a structure
$c(4 \times 3)$	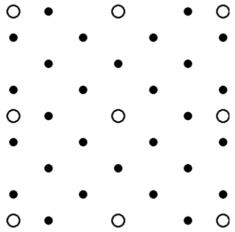	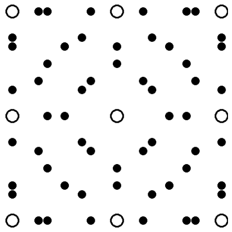 two-domain	$\mathbf{a}_\mathrm{s}^* = \frac{2}{3}\mathbf{a}^*$ $\mathbf{b}_\mathrm{s}^* = \frac{1}{3}\mathbf{a}^* + \frac{1}{4}\mathbf{b}^*$
$c(4 \times 4)$	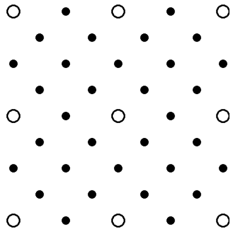	the same as single-domain	$\mathbf{a}_\mathrm{s}^* = \frac{1}{2}\mathbf{a}^*$ $\mathbf{b}_\mathrm{s}^* = \frac{1}{4}\mathbf{a}^* + \frac{1}{4}\mathbf{b}^*$
$c(6 \times 4)$	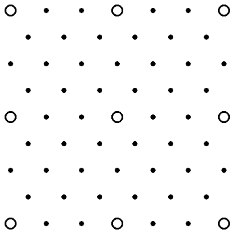	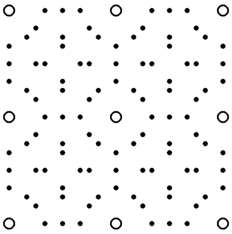 two-domain	$\mathbf{a}_\mathrm{s}^* = \frac{1}{3}\mathbf{a}^*$ $\mathbf{b}_\mathrm{s}^* = \frac{1}{6}\mathbf{a}^* + \frac{1}{4}\mathbf{b}^*$
$c(8 \times 2)$	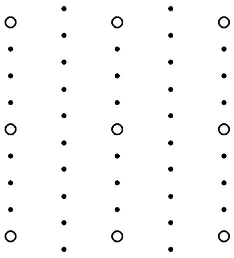	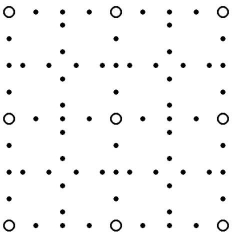 two-domain	$\mathbf{a}_\mathrm{s}^* = \mathbf{a}^*$ $\mathbf{b}_\mathrm{s}^* = \frac{1}{2}\mathbf{a}^* + \frac{1}{8}\mathbf{b}^*$
$c(8 \times 4)$	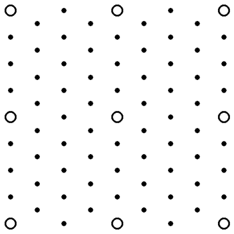	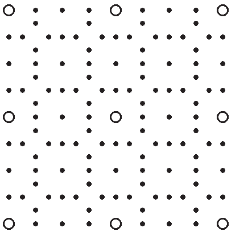 two-domain	$\mathbf{a}_\mathrm{s}^* = \frac{1}{2}\mathbf{a}^*$ $\mathbf{b}_\mathrm{s}^* = \frac{1}{4}\mathbf{a}^* + \frac{1}{8}\mathbf{b}^*$

Structure	Single-domain	Multi-domain	Reciprocal unit vectors for a structure
$c(12 \times 4)$	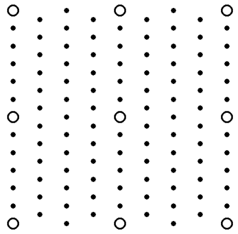	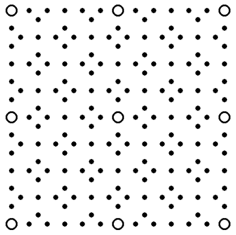 two-domain	$\mathbf{a}_\mathrm{s}^* = \frac{1}{2}\mathbf{a}^*$ $\mathbf{b}_\mathrm{s}^* = \frac{1}{4}\mathbf{a}^* + \frac{1}{12}\mathbf{b}^*$
$c(18 \times 2)$	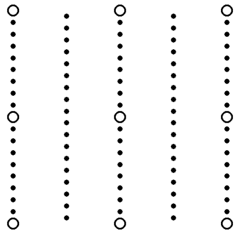	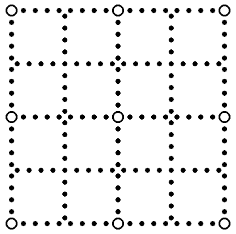 two-domain	$\mathbf{a}_\mathrm{s}^* = \mathbf{a}^*$ $\mathbf{b}_\mathrm{s}^* = \frac{1}{2}\mathbf{a}^* + \frac{1}{18}\mathbf{b}^*$
$\sqrt{2} \times \sqrt{2}$—$R45°$	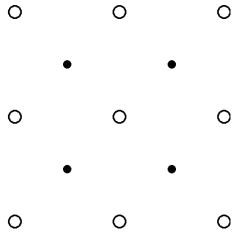	the same as single-domain	$\mathbf{a}_\mathrm{s}^* = \frac{1}{2}\mathbf{a}^* + \frac{1}{2}\mathbf{b}^*$ $\mathbf{b}_\mathrm{s}^* = \frac{1}{2}\mathbf{a}^* - \frac{1}{2}\mathbf{b}^*$
$3\sqrt{2} \times \sqrt{2}$—$R45°$	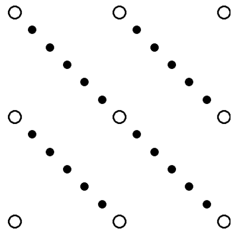	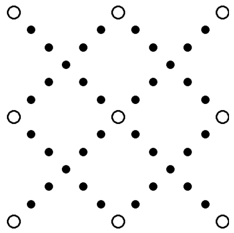 two-domain	$\mathbf{a}_\mathrm{s}^* = \frac{1}{2}\mathbf{a}^* + \frac{1}{2}\mathbf{b}^*$ $\mathbf{b}_\mathrm{s}^* = -\frac{1}{6}\mathbf{a}^* + \frac{1}{6}\mathbf{b}^*$
$\sqrt{26} \times 3 = \begin{pmatrix} 5 & 1 \\ 0 & 3 \end{pmatrix}$	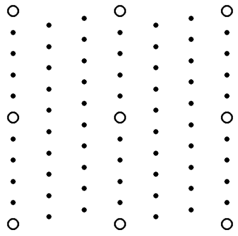	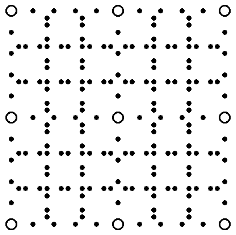 four-domain	$\mathbf{a}_\mathrm{s}^* = \frac{1}{3}\mathbf{a}^* + \frac{1}{15}\mathbf{b}^*$ $\mathbf{b}_\mathrm{s}^* = \frac{1}{5}\mathbf{b}^*$

Structure	Single-domain	Multi-domain	Reciprocal unit vectors for a structure
$\begin{pmatrix}2 & 1\\0 & 3\end{pmatrix}$	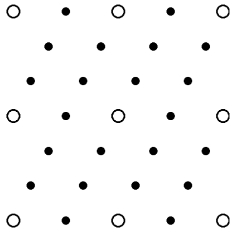	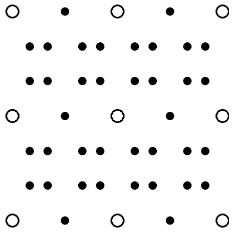 two-domain 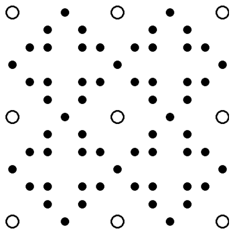 four-domain	$\mathbf{a}_s^* = \frac{1}{2}\mathbf{a}^*$ $\mathbf{b}_s^* = \frac{1}{6}\mathbf{a}^* + \frac{1}{3}\mathbf{b}^*$

4.3 (110) ORIENTATION

Structure	Single-domain	Multi-domain	Reciprocal unit vectors for a structure
1×1	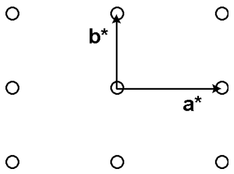		
1×2	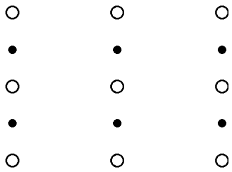	the same as single-domain	$\mathbf{a}_s^* = \mathbf{a}^*$ $\mathbf{b}_s^* = \frac{1}{2}\mathbf{b}^*$
1×5	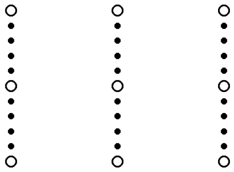	the same as single-domain	$\mathbf{a}_s^* = \mathbf{a}^*$ $\mathbf{b}_s^* = \frac{1}{5}\mathbf{b}^*$
1×7	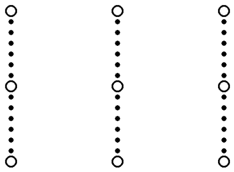	the same as single-domain	$\mathbf{a}_s^* = \mathbf{a}^*$ $\mathbf{b}_s^* = \frac{1}{7}\mathbf{b}^*$
1×9	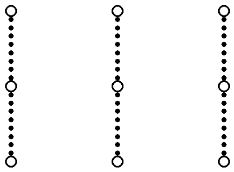	the same as single-domain	$\mathbf{a}_s^* = \mathbf{a}^*$ $\mathbf{b}_s^* = \frac{1}{9}\mathbf{b}^*$

Structure	Single-domain	Multi-domain	Unit vector for a structure
2×2	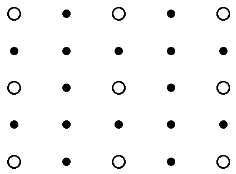	the same as single-domain	$\mathbf{a}_s^* = \frac{1}{2}\mathbf{a}^*$ $\mathbf{b}_s^* = \frac{1}{2}\mathbf{b}^*$
3×2	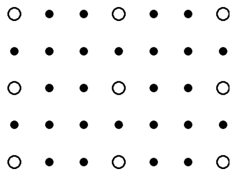	the same as single-domain	$\mathbf{a}_s^* = \frac{1}{3}\mathbf{a}^*$ $\mathbf{b}_s^* = \frac{1}{2}\mathbf{b}^*$
4×5	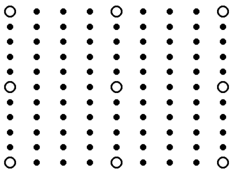	the same as single-domain	$\mathbf{a}_s^* = \frac{1}{4}\mathbf{a}^*$ $\mathbf{b}_s^* = \frac{1}{5}\mathbf{b}^*$
5×4	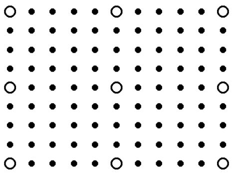	the same as single-domain	$\mathbf{a}_s^* = \frac{1}{5}\mathbf{a}^*$ $\mathbf{b}_s^* = \frac{1}{4}\mathbf{b}^*$
8×5	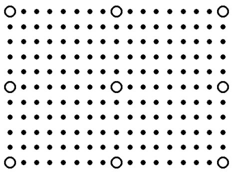	the same as single-domain	$\mathbf{a}_s^* = \frac{1}{8}\mathbf{a}^*$ $\mathbf{b}_s^* = \frac{1}{5}\mathbf{b}^*$

Structure	Single-domain	Multi-domain	Reciprocal unit vectors for a structure
9×5	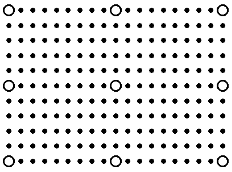	the same as single-domain	$\mathbf{a}_\mathrm{s}^* = \frac{1}{9}\mathbf{a}^*$ $\mathbf{b}_\mathrm{s}^* = \frac{1}{5}\mathbf{b}^*$
$\begin{pmatrix} 1 & 1 \\ 16 & 0 \end{pmatrix}$	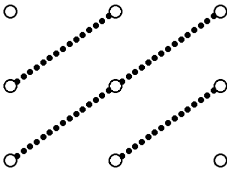	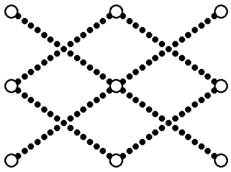 two-domain	$\mathbf{a}_\mathrm{s}^* = \mathbf{a}^*$ $\mathbf{b}_\mathrm{s}^* = \frac{1}{16}\mathbf{a}^* + \frac{1}{16}\mathbf{b}^*$
$\begin{pmatrix} 2 & 2 \\ 4 & -3 \end{pmatrix}$	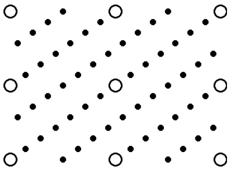	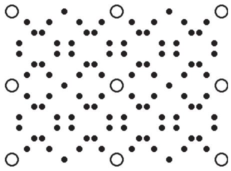 two-domain	$\mathbf{a}_\mathrm{s}^* = \frac{1}{2}\mathbf{a}^*$ $\mathbf{b}_\mathrm{s}^* = \frac{1}{7}\mathbf{a}^* + \frac{1}{7}\mathbf{b}^*$
$\begin{pmatrix} 2 & 2 \\ 17 & 1 \end{pmatrix}$ = "2×16"	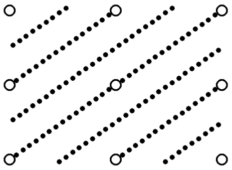	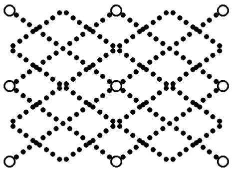 two-domain	$\mathbf{a}_\mathrm{s}^* = \frac{1}{16}\mathbf{a}^* + \frac{1}{16}\mathbf{b}^*$ $\mathbf{b}_\mathrm{s}^* = -\frac{3}{32}\mathbf{a}^* + \frac{13}{32}\mathbf{b}^*$
$\begin{pmatrix} 2 & 2 \\ 33 & 1 \end{pmatrix}$ = "2×32"	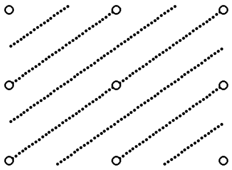	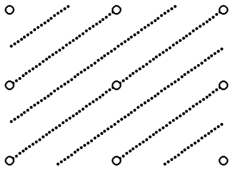 two-domain	$\mathbf{a}_\mathrm{s}^* = \frac{1}{32}\mathbf{a}^* + \frac{1}{32}\mathbf{b}^*$ $\mathbf{b}_\mathrm{s}^* = -\frac{3}{64}\mathbf{a}^* + \frac{29}{64}\mathbf{b}^*$

Structure	Single-domain	Multi-domain	Reciprocal unit vectors for a structure
$\begin{pmatrix} -2 & 1 \\ 8 & 0 \end{pmatrix} =$“$1 \times 8$”	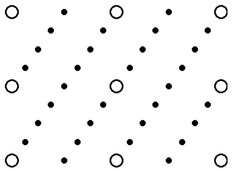	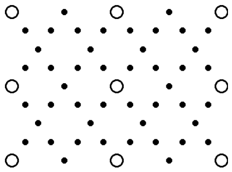 two-domain	$\mathbf{a}_s^* = \frac{1}{8}\mathbf{a}^* + \frac{1}{4}\mathbf{b}^*$ $\mathbf{b}_s^* = \mathbf{b}^*$
$\begin{pmatrix} -2 & 1 \\ 9 & 0 \end{pmatrix} =$“$1 \times 9$”	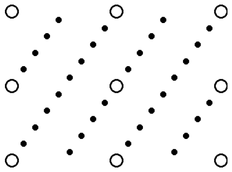	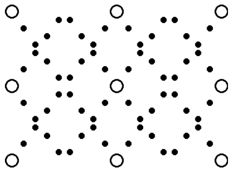 two-domain	$\mathbf{a}_s^* = \frac{1}{9}\mathbf{a}^* + \frac{2}{9}\mathbf{b}^*$ $\mathbf{b}_s^* = \mathbf{b}^*$
$\begin{pmatrix} -2 & 1 \\ 10 & 0 \end{pmatrix} =$“$1 \times 10$”	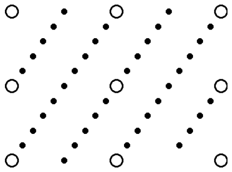	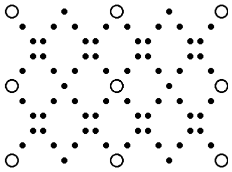 two-domain	$\mathbf{a}_s^* = \frac{1}{10}\mathbf{a}^* + \frac{1}{10}\mathbf{b}^*$ $\mathbf{b}_s^* = \mathbf{b}^*$
$\begin{pmatrix} -2 & 1 \\ 12 & 0 \end{pmatrix} =$“$1 \times 12$”	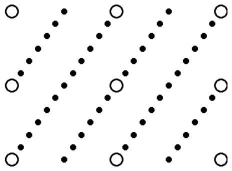	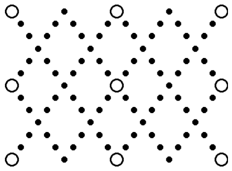 two-domain	$\mathbf{a}_s^* = \frac{1}{12}\mathbf{a}^* + \frac{1}{12}\mathbf{b}^*$ $\mathbf{b}_s^* = \mathbf{b}^*$
$\begin{pmatrix} -2 & 1 \\ 14 & 0 \end{pmatrix} =$“$1 \times 14$”	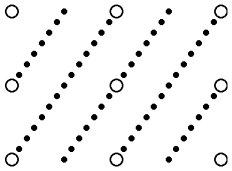	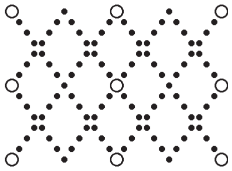 two-domain	$\mathbf{a}_s^* = \frac{1}{14}\mathbf{a}^* + \frac{1}{14}\mathbf{b}^*$ $\mathbf{b}_s^* = \mathbf{b}^*$

Structure	Single-domain	Multi-domain	Reciprocal unit vectors for a structure
$\begin{pmatrix}3 & 0\\ -1 & 4\end{pmatrix}$ =“4 × 6”	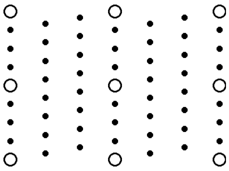	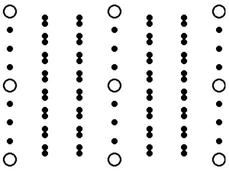 two-domain	$\mathbf{a}_\mathrm{s}^* = \frac{1}{3}\mathbf{a}^* + \frac{1}{12}\mathbf{b}^*$ $\mathbf{b}_\mathrm{s}^* = \frac{1}{4}\mathbf{b}^*$
$\begin{pmatrix}3 & 0\\ -1 & 3\end{pmatrix}$	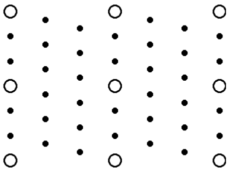	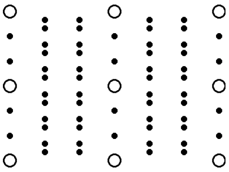 two-domain	$\mathbf{a}_\mathrm{s}^* = \frac{1}{3}\mathbf{a}^* + \frac{2}{9}\mathbf{b}^*$ $\mathbf{b}_\mathrm{s}^* = \frac{1}{3}\mathbf{b}^*$
$\begin{pmatrix}4 & 0\\ -1 & 3\end{pmatrix}$	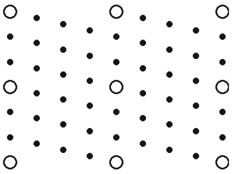	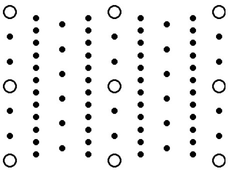 two-domain	$\mathbf{a}_\mathrm{s}^* = \frac{1}{4}\mathbf{a}^* + \frac{1}{4}\mathbf{b}^*$ $\mathbf{b}_\mathrm{s}^* = \frac{1}{3}\mathbf{b}^*$
$\begin{pmatrix}3 & 9\\ 3 & -9\end{pmatrix}$ =$c(18 \times 6)$	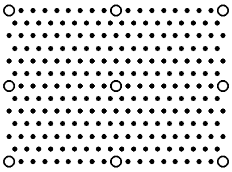	the same as single-domain	$\mathbf{a}_\mathrm{s}^* = \frac{1}{9}\mathbf{a}^*$ $\mathbf{b}_\mathrm{s}^* = \frac{1}{18}\mathbf{a}^* + \frac{1}{6}\mathbf{b}^*$
$\begin{pmatrix}10 & -1\\ 3 & 4\end{pmatrix}$	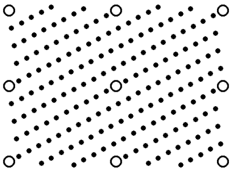	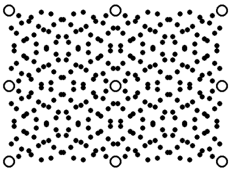 two-domain	$\mathbf{a}_\mathrm{s}^* = \frac{4}{43}\mathbf{a}^* + \frac{3}{43}\mathbf{b}^*$ $\mathbf{b}_\mathrm{s}^* = -\frac{1}{43}\mathbf{a}^* + \frac{10}{43}\mathbf{b}^*$

Index

+++